

Undergraduate Lecture Notes in Physics

Sylvie Braibant
Giorgio Giacomelli
Maurizio Spurio

Particles and Fundamental Interactions

An Introduction to Particle Physics

Second Edition

Undergraduate Lecture Notes in Physics

For further volumes:
<http://www.springer.com/series/8917>

Undergraduate Lecture Notes in Physics (ULNP) publishes authoritative texts covering topics throughout pure and applied physics. Each title in the series is suitable as a basis for undergraduate instruction, typically containing practice problems, worked examples, chapter summaries, and suggestions for further reading.

ULNP titles must provide at least one of the following:

- An exceptionally clear and concise treatment of a standard undergraduate subject.
- A solid undergraduate-level introduction to a graduate, advanced, or non-standard subject.
- A novel perspective or an unusual approach to teaching a subject.

ULNP especially encourages new, original, and idiosyncratic approaches to physics teaching at the undergraduate level.

The purpose of ULNP is to provide intriguing, absorbing books that will continue to be the reader's preferred reference throughout their academic career.

Sylvie Braibant • Giorgio Giacomelli
Maurizio Spurio

Particles and Fundamental Interactions

An Introduction to Particle Physics



Springer

Sylvie Braibant
Department of Physics and INFN
University of Bologna
Viale Berti Pichat 6/2
40126 Bologna
Italy
sylvie.braibant@bo.infn.it

Giorgio Giacomelli
Department of Physics and INFN
University of Bologna
Viale Berti Pichat 6/2
40126 Bologna
Italy
giacomelli@bo.infn.it

Maurizio Spurio
Department of Physics and INFN
University of Bologna
Viale Berti Pichat 6/2
40126 Bologna
Italy
maurizio.spurio@bo.infn.it

ISSN 2192-4791 e-ISSN 2192-4805
ISBN 978-94-007-2463-1 e-ISBN 978-94-007-2464-8
DOI 10.1007/978-94-007-2464-8
Springer Dordrecht Heidelberg London New York

Library of Congress Control Number: 2011940974

© Springer Science+Business Media B.V. 2012

No part of this work may be reproduced, stored in a retrieval system, or transmitted in any form or by any means, electronic, mechanical, photocopying, microfilming, recording or otherwise, without written permission from the Publisher, with the exception of any material supplied specifically for the purpose of being entered and executed on a computer system, for exclusive use by the purchaser of the work.

Printed on acid-free paper

Springer is part of Springer Science+Business Media (www.springer.com)

Preface

This book aims to provide the basis of theoretical and phenomenological knowledge of the structure of matter at the subatomic level. It is organized in such a way that it can be used by undergraduate students specialized either in particle or nuclear physics. It starts presenting the general concepts at the simplest level which does not require previous knowledge of the field, except for the basic quantum mechanics. The students are gradually guided towards the more advanced arguments presented in Chapters from 9 to 13, generally addressed to graduate and PhD students in experimental high-energy physics. A special emphasis is placed on experimental and phenomenological aspects of the field and how measurements and theory interplay in the development of particle physics. A list of other introductory texts, work reviews and some specialized publications is reported in the bibliography. The book is based on the author's experience in the undergraduate and graduate lecture courses at the University of Bologna, Italy.

After an introduction on fundamental concepts, Chaps. 2 and 3 deal with experimental methods developed to “see” particles, from accelerators to analyses of some experiments, highlighting the methodologies and detection techniques. In Chap. 4, the electromagnetic interaction (which is familiar to the student) is used to recall some theoretical arguments and to outline the formalism that shall be used for the weak and strong interactions. A standard description of invariance and conservation principles is given in Chap. 6. The hadron structure and the static quark model, together with its intrinsic limits, are discussed in Chap. 7. Chapter 8 deals with the weak interactions and the neutrino (from Pauli's hypothesis of its existence and its experimental discovery, to the conservation of three neutrino flavors). Chapter 9 describes the e^+e^- collisions, from the discovery of the heavier c, b quarks up to the high precision tests of the electromagnetic and weak interactions at the LEP collider. Chapter 10 discusses the deep inelastic scattering experiments which were used to understand the dynamic quark model of hadrons. It also includes the study of hadron-hadron interactions at high energies, up to the LHC collider. The more advanced mathematical formalism of the Standard Model, including the need for the Higgs boson, is the topic of Chap. 11. The fact that the observed Universe is made of matter, with virtually no antimatter, is a fundamental observation which

challenges the Standard Model. The mechanism (i.e., the CP violation) which seems necessary to produce the particle–antiparticle asymmetry is described in Chap. 12. In addition, the situation after the recent experimental discovery of the neutrino oscillation mechanism is discussed. Chapter 13 presents some aspects of the physics beyond the Standard Model, and the connections between microphysics, astrophysics and cosmology. The most striking demonstration of the interconnection between the microcosm and macrocosm, or between particle physics, astrophysics and cosmology, is given by the periodic table of elements. For this reason, the book ends with Chap. 14, where fundamental aspects of interactions between nucleons and the physics of nuclei are presented.

More than 150 problems are proposed and are available on the Springer website. Full solutions and some extended and highlighted arguments are proposed in a companion *problems and solutions* book.

We thank many colleagues for their cooperation and suggestions, particularly when this book was in the form of notes for students. In particular, we thank Y. Becherini, M. Fabbri, M. Giorgini, P. Giacomelli, and all the colleagues of the former OPAL and MACRO groups (now CMS, OPERA and ANTARES) at the Bologna University. We are grateful to many students for their suggestions and questions that have allowed us to set this work in a way that we hope will be useful for many. Although we have tried to be meticulous, we will be grateful to anyone who wishes to send corrections, improvements or simple observations.

Bologna

Sylvie Braibant, sylvie.braibant@unibo.it
Giorgio Giacomelli, giacomelli@bo.infn.it
Maurizio Spurio, maurizio.spurio@unibo.it

Contents

1	Historical Notes and Fundamental Concepts	1
1.1	Introduction	1
1.2	The Discovery of Particles	3
1.3	The Concept of the Atom and Indivisibility	5
1.4	The Standard Model of Microcosm – Fundamental Fermions and Bosons	9
2	Particle Interactions with Matter and Detectors	11
2.1	Introduction	11
2.2	Passage of Charged Particles Through Matter	12
2.2.1	Energy Loss Through Ionization and Excitation	12
2.2.2	“Classical” Calculation of Energy Loss Through Ionization	13
2.2.3	Bremsstrahlung	20
2.3	Photon Interactions	22
2.3.1	Photoelectric Effect	22
2.3.2	Compton Scattering	23
2.3.3	Pair Production	25
2.4	Electromagnetic Showers	25
2.5	Neutron Interactions	28
2.6	Qualitative Meaning of a Total Cross-Section Measurement	29
2.7	Techniques of Particle Detection	30
2.7.1	General Characteristics	30
2.8	Ionization Detectors	32
2.9	Scintillation Counters	35
2.10	Semiconductor Detectors	38
2.11	Cherenkov Counters	39
2.12	The Bubble Chamber	40
2.13	Electromagnetic and Hadronic Calorimeters	42
3	Particle Accelerators and Particle Detection	45
3.1	Why Do We Need Accelerators?	45

3.1.1	The Center-of-Mass (c.m.) System	47
3.1.2	The Laboratory System.....	47
3.1.3	Fixed Target Accelerator and Collider	48
3.2	Linear and Circular Accelerators.....	49
3.2.1	Linear Accelerators	49
3.2.2	Circular Accelerators	50
3.3	Colliders and Luminosity	52
3.3.1	Example: the CERN Accelerator Complex	53
3.4	Conversion of Energy into Mass	54
3.4.1	Use of Fixed Target Accelerators	55
3.4.2	Baryonic Number Conservation.....	57
3.5	Particle Production in a Secondary Beam	57
3.5.1	Time-of-Flight Spectrometer	57
3.6	Bubble Chambers in Charged Particle Beams	61
3.6.1	Conservation Laws.....	61
3.6.2	The Electron “Spiral”	64
3.6.3	Electron-Positron Pair	65
3.6.4	An Electron-Positron “Tree”	66
3.6.5	Charged Particle Decays.....	67
4	The Paradigm of Interactions: The Electromagnetic Case	73
4.1	The Interaction Between Electric Charges	74
4.1.1	The EM Coupling Constant	76
4.1.2	The Quantum Theory of Electromagnetism	78
4.2	Some Quantum Mechanics Concepts	78
4.2.1	The Schrödinger Equation.....	79
4.2.2	Klein–Gordon Equation	80
4.2.3	Dirac Equation	81
4.3	Transition Probabilities in Perturbation Theory	82
4.4	The Bosonic Propagator	85
4.5	Cross-Sections and Lifetime: Theory and Experiment.....	86
4.5.1	The Cross-Section	86
4.5.2	Particle Decay and Lifetime	88
4.6	Feynman Diagrams	90
4.7	A Few Examples of Electromagnetic Processes.....	93
4.7.1	Rutherford Scattering	93
4.7.2	$e^+e^- \rightarrow \mu^+\mu^-$ Process.....	97
4.7.3	Elastic Scattering $e^+e^- \rightarrow e^+e^-$ (Bhabha Scattering).....	98
4.7.4	$e^+e^- \rightarrow \gamma\gamma$ Annihilation	99
4.7.5	Some QED Checks	99
5	First Discussion of the Other Fundamental Interactions	101
5.1	Introduction	101
5.2	The Gravitational Interaction.....	101
5.3	The Weak Interaction	103
5.4	The Strong Interaction	106

5.5	Particle Classification	109
5.5.1	Classification According to <i>Stability</i>	110
5.5.2	Classification According to the <i>Spin</i>	110
5.5.3	Classification According to the Baryon and Lepton Numbers	111
6	Invariance and Conservation Principles	113
6.1	Introduction	113
6.2	Invariance Principle Reminder	114
6.2.1	Invariance in Classical Mechanics	114
6.2.2	Invariance in Quantum Mechanics	115
6.2.3	Continuous Transformations: Translations and Rotations	117
6.3	Spin-Statistics Connection	118
6.4	Parity	119
6.5	Spin-Parity of the π Meson	122
6.5.1	Spin of the π Meson	122
6.5.2	Parity of the π Meson	123
6.5.3	Particle–Antiparticle Parity	125
6.6	Charge Conjugation	126
6.6.1	Charge Conjugation in Electromagnetic Processes	127
6.6.2	Violation of C in the Weak Interaction	128
6.7	Time Reversal	129
6.8	<i>CP</i> and <i>CPT</i>	131
6.9	Electric Charge and Gauge Invariance	133
7	Hadron Interactions at Low Energies and the Static Quark Model	135
7.1	Hadrons and Quarks	135
7.1.1	The Yukawa Model	136
7.2	Proton-Neutron Symmetry and the Isotopic Spin	137
7.3	The Strong Interaction Cross-Section	139
7.3.1	Mean Free Path	140
7.4	Low Energy Hadron-Hadron Collisions	142
7.4.1	Antibaryons	143
7.4.2	Hadron Resonances	144
7.5	Breit–Wigner Equation for Resonances	148
7.5.1	The $\Delta^{++}(1232)$ Resonance	150
7.5.2	Resonance Formation and Production	151
7.5.3	Angular Distribution of Resonance Decay Products	152
7.6	Production and Decay of Strange Particles	154
7.7	Classification of Hadrons Made of u, d, s Quarks	156
7.8	The $J^P = 3/2^+$ Baryonic Decuplet	158
7.8.1	First Indications for the Color Quantum Number	160
7.9	The $J^P = 1/2^+$ Baryonic Octet	162
7.10	Pseudoscalar Mesons	163

7.11	The Vector Mesons	165
7.12	Strangeness and Isospin Conservation	167
7.13	The Six Quarks.....	168
7.14	Experimental Tests on the Static Quark Model.....	170
7.14.1	Leptonic Decays of Neutral Vector Mesons	170
7.14.2	Lepton Pair Production	171
7.14.3	Hadron-Hadron Cross-Sections at High Energies	172
7.14.4	Baryon Magnetic Moments	173
7.14.5	Relations Between Masses	175
7.15	Searches for Free Quarks and Limits of the Model	177
8	Weak Interactions and Neutrinos.....	179
8.1	Introduction	179
8.2	The Neutrino Hypothesis and the β Decay	180
8.2.1	Nuclear β Decay and the Missing Energy	180
8.2.2	The Pauli Desperate Remedy.....	181
8.2.3	How World War II Accelerated the Neutrino Discovery	183
8.3	Fermi Theory of Beta Decay	184
8.3.1	Neutron Decay	185
8.3.2	The Fermi Coupling Constant from Neutron β Decay	186
8.3.3	The Coupling Constant α_W from Fermi Theory.....	187
8.4	Universality of Weak Interactions (I)	187
8.4.1	Muon Lifetime	187
8.4.2	The Sargent Rule.....	189
8.4.3	The Puppi Triangle	189
8.5	The Discovery of the Neutrino	190
8.5.1	The Poltergeist Project.....	190
8.6	Different Transition Types in β Decay.....	194
8.6.1	The Cross-Section of the β -Inverse Process	197
8.7	Lepton Families	198
8.8	Parity Violation in β Decays	201
8.9	The Two-Component Neutrino Theory	204
8.10	Charged Pion Decay	205
8.11	Strange Particle Decays	208
8.12	Universality of Weak Interactions (II). The Cabibbo Angle	211
8.13	Weak Interaction Neutral Current	213
8.14	Weak Interactions and Quark Eigenstates	215
8.14.1	The WI Hamiltonian and the GIM Mechanism	215
8.14.2	Hints on the Fourth Quark from WI Neutral Currents .	217
8.14.3	The Six Quarks and the Cabibbo– Kobayashi–Maskawa Matrix	218

8.15	Discovery of the W^\pm and Z^0 Vector Bosons	220
8.16	The V-A Theory of CC Weak Interaction.....	222
8.16.1	Bilinear Forms of Dirac Fermions	222
8.16.2	Current–Current Weak Interaction	225
9	Discoveries in Electron-Positron Collisions	229
9.1	Introduction	229
9.2	Electron-Positron Cross-Section and the Determination of the Number of Colors	231
9.2.1	The Process $e^+e^- \rightarrow \gamma \rightarrow \mu^+\mu^-$	232
9.2.2	The Color Quantum Number	232
9.3	The Discovery of Charm and Beauty Quarks.....	234
9.3.1	Mesons with c, \bar{c} Quarks	234
9.3.2	The J/ψ Resonance Properties	235
9.3.3	Mesons with b, \bar{b} Quarks	236
9.4	Spectroscopy of Heavy Mesons and α_S Estimate	237
9.5	The τ Lepton	238
9.6	LEP Experiments and Examples of Events at LEP	239
9.6.1	The LEP Detectors	239
9.6.2	Events in 4π Detectors at LEP	243
9.7	e^+e^- Collisions at $E_{cm} \sim 91$ GeV. The Z^0 Boson	248
9.7.1	The Z^0 Resonance	248
9.7.2	Z^0 Total and Partial Widths	249
9.7.3	Measurable Quantities, Γ_{invis} and the Number of Light Neutrino Families	251
9.7.4	Forward–Backward Asymmetries A_{FB}	253
9.7.5	Multihadronic Production Model	256
9.8	e^+e^- Collisions for $\sqrt{s} > 100$ GeV at LEP2	257
9.8.1	$e^+e^- \rightarrow W^+, W^-, Z^0Z^0$ Cross-Sections	258
9.8.2	The W Boson Mass and Width	261
9.8.3	Measurement of α_S	262
9.8.4	The Higgs Boson Search at LEP	262
10	High Energy Interactions and the Dynamic Quark Model	265
10.1	Introduction	265
10.2	Lepton–Nucleon Interactions at High Energies	265
10.3	Elastic Electron-Proton Scattering	269
10.3.1	Kinematic Variables	269
10.3.2	Proton Form Factors	270
10.4	Inelastic ep Cross-Section	275
10.4.1	Partons in the Nucleons: Their Nature and Spin	278
10.4.2	Electric Charge of the Partons.....	280
10.5	Cross-Section for CC $\nu_\mu N$ Interactions	282
10.5.1	Comparison with Experimental Data	287
10.5.2	The Neutrino-Nucleon Cross-Section.....	288

10.6	“Naive” and “Advanced” Quark Models.....	290
10.6.1	Q^2 -Dependence of the Structure Functions	290
10.6.2	Summary of DIS Results	294
10.7	High Energy Hadron-Hadron Collisions.....	296
10.8	Total and Elastic Cross-Sections at High Energy	298
10.8.1	Elastic Differential Cross-Sections	298
10.8.2	Total Cross-Sections	301
10.9	High Energy Inelastic Hadron Collisions at Low- p_t	302
10.9.1	Outline on High Energy Nucleus-Nucleus Collisions..	303
10.10	The LHC and the Search for the Higgs Boson	305
10.10.1	Higgs Boson Production in pp Collisions	306
10.10.2	Higgs Boson Decays.....	308
10.10.3	Search Strategies at LHC	309
11	The Standard Model of the Microcosm	313
11.1	Introduction	313
11.2	Weak Interaction Divergences and Unitarity Problem	314
11.3	Gauge Theories	316
11.3.1	Choice of the Symmetry Group	317
11.3.2	Gauge Invariance	318
11.4	Gauge Invariance in the Electroweak Interaction	322
11.4.1	Lagrangian Density of the Electroweak Theory	323
11.5	Spontaneous Symmetry Breaking. The Higgs Mechanism	325
11.6	The Weak Neutral Current.....	330
11.7	The Fermion Masses	333
11.8	Parameters of the Electroweak Interaction	334
11.8.1	Electric Charge Screening in QED.....	336
11.8.2	Higher Order Feynman Diagrams, Mathematical Infinities and Renormalization in QED	337
11.9	The Strong Interaction	338
11.9.1	Quantum Chromodynamics (QCD)	338
11.9.2	Color Charge Screening in QCD	341
11.9.3	Color Factors	342
11.9.4	The Strong Coupling Constant α_S	343
11.10	The Standard Model: A Summary	343
12	CP-Violation and Particle Oscillations	347
12.1	The Matter-Antimatter Asymmetry Problem	347
12.2	The $K^0 - \bar{K}^0$ System	348
12.2.1	Time Development of a K^0 Beam. K_1^0 Regeneration. Strangeness Oscillations	350
12.3	CP -Violation in the $K^0 - \bar{K}^0$ System	353
12.3.1	The Formalism and the Parameters of CP -Violation ...	354

12.4	What is the Reason for CP-Violation?	358
12.5	CP -Violation in the $B^0 - \bar{B}^0$ System.....	360
12.5.1	Future Experiments	364
12.6	Neutrino Oscillations	364
12.6.1	The Special Case of Oscillations Between Two Flavors	365
12.6.2	Three Flavor Oscillations.....	367
12.6.3	The Approximation for a Neutrino with Dominant Mass.....	368
12.6.4	Neutrino Oscillations in Matter	370
12.7	Neutrinos from the Sun and Oscillation Studies.....	371
12.8	Atmospheric ν_μ Oscillations and Experiments	376
12.8.1	Long Baseline Experiments	379
12.9	Effects of Neutrino Oscillations	381
13	Microcosm and Macrocosm	385
13.1	The Grand Unification	386
13.1.1	Proton Decay	389
13.1.2	Magnetic Monopoles	390
13.1.3	Cosmology. First Moment of the Universe	391
13.2	Supersymmetry (SUSY)	392
13.2.1	Minimal Standard Supersymmetric Model (MSSM)	393
13.2.2	Supergravity (SUGRA). Superstrings.....	397
13.3	Composite Models	397
13.4	Particles, Astrophysics and Cosmology	400
13.5	Dark Matter	403
13.6	The Big Bang and the Primordial Universe.....	407
14	Fundamental Aspects of Nucleon Interactions	415
14.1	Introduction	415
14.2	General Properties of Nuclei	417
14.2.1	The Chart of Nuclides	419
14.2.2	Nuclear Binding Energy	420
14.2.3	Size of the Nuclei	421
14.2.4	Electromagnetic Properties of the Nuclei.....	424
14.3	Nuclear Models	424
14.3.1	Fermi Gas Model	425
14.3.2	Nuclear Drop Model	426
14.3.3	Shell Model	429
14.4	Properties of Nucleon-Nucleon Interaction.....	431
14.5	Radioactive Decay and Dating	433
14.5.1	Cascade Decays	434
14.6	γ Decay.....	436

14.7	α Decay.....	437
14.7.1	Elementary Theory of α Decay	439
14.7.2	Lifetime Calculation of the $^{238}_{92}U$ Nucleus	440
14.8	β Decay	441
14.8.1	Elementary Theory of Nuclear β -Decay.....	443
14.9	Nuclear Reactions and Nuclear Fission.....	444
14.9.1	Nuclear Fission	445
14.9.2	Fission Nuclear Reactors	447
14.10	Nuclear Fusion in Astrophysical Environments.....	448
14.10.1	Fusion in Stars	449
14.10.2	Formation of Elements Heavier than <i>Fe</i> in Massive Stars	451
14.10.3	Earth and Solar System Dating.....	454
14.11	Nuclear Fusion in Laboratory	455
Appendix A	459
A.1	Periodic Table [P08]	460
A.2	The Natural Units in Subnuclear Physics	461
A.3	Basic Concepts of Relativity and Classical Electromagnetism ...	462
A.3.1	The Formalism of Special Relativity.....	462
A.3.2	The Formalism of Classical Electromagnetism	464
A.3.3	Gauge Invariance of the Electromagnetism.....	466
A.4	Dirac Equation and Formalism.....	467
A.4.1	Derivation of the Dirac Equation.....	467
A.4.2	General Properties of the Dirac Equation.....	469
A.4.3	Properties of the Dirac Equation Solutions	472
A.4.4	Helicity Operator and States	475
A.5	Physical and Astrophysical Constants [P08]	478
References	481
Index	487

Chapter 1

Historical Notes and Fundamental Concepts

1.1 Introduction

Elementary particle physics deals with the search and the study of the ultimate constituents of matter as well as of their interactions. Within common usage, the term *elementary particle* is considered to be a synonym of the *ultimate constituent* of matter. It is with such a conviction that the first scientists in this particular field of physics have attributed the name of elementary particle to objects that are not really as such: as the *atom* (which etymologically means indivisible in Greek) is in fact quite divisible, the largest part of elementary particles (the protons for instance) are also not truly elementary.

With the increase of experimental knowledge, the actual definition of the elementary particle underwent an evolution: in the 1940s, it only applied to a few submicroscopic “objects” that were thought of as new indivisible “atoms;” about thirty years ago, it was instead attributed to a few tens of objects, without worrying that they were indeed elementary. Currently, the term elementary particle denotes some particles such as the electron (e^-), the muon (μ^-) and the tau (τ^-) and the corresponding neutrinos (ν_e, ν_μ, ν_τ), which are globally called *leptons*, and the *quarks*. Free quarks were never observed as they are confined inside *hadrons*. This term includes a stable object (the proton), several particles with relatively long lifetimes (as the neutron and the Λ^0 hyperon) and many resonances having very short lifetimes.

The *quarks* and *leptons*, currently considered to be the ultimate constituents of matter, are *fermions*, that is, half-integer spin particles; they can be thought as *matter particles*. Fermions obey the Fermi-Dirac statistics.

A description of the structure of matter cannot be complete without considering the interactions (forces) that “join” the particles and more generally that regulate the interactions amongst them. The *strong, weak, electromagnetic* and *gravitational* interactions were identified. Each interaction has its own quantum field, namely, the *force particles* that relay the interaction. These are particles with integer spin, called *bosons* as they obey the Bose-Einstein statistics. The *photons* mediate

Table 1.1 Fundamental fermions and bosons in the standard model of the microcosm

Fermions			Bosons		
$\begin{pmatrix} u \\ d \end{pmatrix}$	$\begin{pmatrix} c \\ s \end{pmatrix}$	$\begin{pmatrix} t \\ b \end{pmatrix}$	Quarks	Fundamental Interactions	Mediators
$\begin{pmatrix} \nu_e \\ e^- \end{pmatrix}$	$\begin{pmatrix} \nu_\mu \\ \mu^- \end{pmatrix}$	$\begin{pmatrix} \nu_\tau \\ \tau^- \end{pmatrix}$	Leptons	Strong Electromagnetic Weak	8 gluons γ W^+, W^-, Z^0
First family	Second family	Third family		Gravitational	Graviton
			Higgs Boson		H^0

the electromagnetic interaction, the W^+ , W^- and Z^0 vector bosons the weak interaction, the eight gluons the strong interaction and the hypothetical graviton the gravitational interaction. The bosons must be included in the lists of elementary particles and ultimate constituents.

It should be noted that for every fermion exists an antifermion, that is, an antiparticle having the same mass and spin of the corresponding particle, though with opposite electric charge and magnetic dipole moment.

Currently, the stable particles are: the photon γ , the neutrinos and the antineutrinos, the electron e^- , the positron e^+ , the proton p and the antiproton \bar{p} ; all the others are unstable. The six leptons (electron, muon, tau and their neutrinos) and the corresponding six antileptons, the six quarks (d, u), (b, t) (s, c) and the corresponding six antiquarks are considered to be the *ultimate fermionic constituents* of matter. We will also see that quarks (and antiquarks) appear in three different colors (and anticolors). To these ultimate fermionic constituents, the force carriers of the fundamental interactions, the vector bosons, must be added (see Table 1.1). To further complete the picture, one needs to introduce the *scalar (spin 0) Higgs boson*. The Higgs boson has not yet been observed; it is thought to be the main ingredient in the mechanism that attributes mass to the particles.

Only the electron, the proton and the neutron directly enter the composition of the stable terrestrial matter. The photon is created when transitions occur amongst two states. In the radioactive decays, particles and antiparticles (such as the positron) are produced. Any particle can be created in collisions between two high energy particles thanks to a process of transformation of energy in mass. The fact that there are so many particles and that so few constitute the present stable matter cannot be currently explained. It is also unclear as to why the *ultimate fermionic constituents* appear in three families, each constituted of two leptons and two quarks, and each being a replica of the same type, see Table 1.1. The first family includes ν_e, e^-, u, d ; the second one includes ν_μ, μ^-, c, s ; the third one includes ν_τ, τ^-, t, b . For each fermion of every family, one has the corresponding antifermion (antiparticle).

In order to probe structures with ever smaller dimensions, one must study high energies collisions between particles. It is therefore necessary to have powerful accelerators. The physics laws that describe the collisions between two particles

become simpler at high energies in the sense that the laws acquire a larger degree of mathematical symmetry. Besides, at high energies one has unification of forces: the electromagnetic and weak unification (*electroweak interaction*) has already been verified and models exist for the Great Unification (GUT) of the electroweak interaction with the strong one; some models attempt to describe a super unification. We may be close to a deeper level of comprehension of the “building blocks” of the forces and of the laws of the *microcosm*. In addition, we have became aware that laws governing the structure of the matter are connected to the structure of the Universe and its evolution following the Big Bang.

Regarding the study of the interactions between constituents, the fundamental notions of quantum mechanics and possibly of its mathematical formalism are required. The terminology and some concepts may appear complicated initially, and thus a second reading is recommended for a better understanding. Finally, one should notice that the terminology used for classifying the observed particles was historically introduced in a rather chaotic way.

1.2 The Discovery of Particles

At the beginning of the 1930s (when Hitler was entering into power in Germany and after the great Wall Street stock market crash), only the proton, electron and photon were known. Nevertheless, it was known that an ionizing radiation was constantly bombarding the terrestrial surface. In 1912, Victor Hess (Nobel laureate in 1936) showed by using aerostatic balloons that the level of ionizing radiation increased with increasing altitude. Therefore, the measured radiation could not be of terrestrial origin. This radiation was called *cosmic radiation*. In the following years, it became more evident that the particles present in this radiation could be divided into two categories: those coming from the extraterrestrial space (the *primary cosmic rays*) and the secondary component produced by the interaction of primary cosmic rays with the terrestrial atmosphere, that is, the *secondary cosmic rays*.

The flow of primary cosmic rays (CR) is about $1,000 \text{ cm}^{-2} \text{ s}^{-1}$ and is mainly constituted of protons ($\sim 85\%$), the nuclei of helium ($\sim 10\%$) and heavier nuclei ($\sim 1\%$). Electrons only account for $\sim 2\%$. Starting in the 1930s, the experimental techniques for the detection and measurement of some physics quantities (e.g., electric charge, mass, lifetime) of particles present in the secondary cosmic rays started to become more refined. Particularly, Patrick Blackett (Nobel laureate in 1948) used a cloud chamber inside a magnetic field that bent the trajectory of charged particles. For a long time, particle physics was identified with that of the cosmic rays. This superposition remained well after the end of the Second World War, when particle accelerators started to be developed. With the advent of accelerators, the paths of particle physics and that of the cosmic rays (which later became that of *astroparticle physics*) disentangled, though they have actually reconnected in recent years (as we will see in Chaps. 12 and 13).

Using Blackett’s experimental techniques, in 1932, Anderson (Nobel laureate in 1936) discovered a particle with the same mass of the electron, though with

opposite electric charge. It was the antielectron, that is, the antiparticle predicted by the quantum theory of the electron developed a few years before by Dirac (Nobel laureate in 1933). Immediately afterwards, in 1934, James Chadwick (Nobel laureate in 1935) experimentally identified a particle with a mass similar to that of the proton, though without electric charge: *the neutron*.

In 1937, Anderson together with Neddermeyer again discovered a particle of intermediate mass between that of the proton and that of the electron: they called this new particle the *meson*. For some time, it was thought that this particle was the *mediator* particle of the interactions between protons and neutrons for the formation of nuclei. A theoretical model created by Hideki Yukawa (Nobel laureate in 1949) predicted the existence of a particle with a mass very close to that of the just discovered meson. Nevertheless, actually during World War II in Rome, Conversi, Pancini and Piccioni showed in a famous experiment that the meson of Anderson and Neddermeyer (nowadays called the *muon*) could not be the particle predicted by Yukawa. Even if the theory of Yukawa (as we will see later) does not properly describe the physics of nuclei, the predicted particle (the *pion*) was discovered in 1947 by Lattes, Occhialini and Powell in secondary cosmic rays using nuclear emulsions (i.e., sophisticated photographic films) at high altitudes.

Nonetheless, in 1947, in the interactions of cosmic rays in a cloud chamber with magnetic field, particles with a particularly strange behavior were discovered. They were thus named *strange* particles. As we will see, particles containing a quark of mass higher than that of the quarks that compose protons and neutrons had just been discovered (this was obviously understood only a few years later). Finally, Pauli at the beginning of the 1930s had hypothesized the existence of an elusive particle without mass and electric charge: the *neutrino*. However, one had to wait until 1954 to experimentally observe it (thanks to the advent of nuclear reactors).

With the advance of accelerators, the discovery of many new particles was made possible; most of them are subject to the strong interaction and are named *hadrons*. The fermionic particles that do not strongly interact were named *leptons*. Etymologically, the term lepton means a particle of small mass. However, now that it includes the τ^- , heavier than the proton, the term lepton simply denotes the fermions that do not strongly interact. This is yet another example of the typical contradiction between the etymology of the word and the latest results obtained in this field of research.

The development of particle physics following World War II has been amazing, with continuous surprises, quite a collection of discoveries and a lot of systematic work. For instance, without pretension of completeness: the discovery of the antiproton (1955), the classification of the hadrons in terms of quarks; the discovery of the parity violation in the weak interaction. After the discovery of the two types of neutrinos, electronic (1956) and muonic (1963), followed the discovery of the hadronic resonances and the scheme of classification based on SU(3) (1960s and 1970s). Furthermore, the list of developments continues with the discovery of the hyperon Ω^- with strangeness $S = -3$ (1963), the evidence for quarks and gluons (1960s), the increasing with energy of the total hadronic cross-sections (1971–1974), the discovery of the neutral current weak interaction,

the quark c (1974) and b (1976), the electroweak unification (1970s and 1980s), the W^+ , W^- and Z^0 vector bosons (1983), the quark t (1995), and the neutrino oscillations (1998).

There was a continuous exchange between theories and experiments. Starting from simple models to more elaborated ones, complete theories were finally reached. In the experimental field, a rapid technological progress took place. The first experiences were conducted by only a few physicists with small accelerators, using less than five counters with simple “homemade” electronics. The actual experiments are performed with circular accelerators with radius measuring several kilometers (or linear accelerators several kilometers long), detectors with thousand of counters, chambers of various types, elaborated electronics and high-speed computers. Because of these huge dimensions, the principal experiments involve hundreds and sometimes thousands of physicists. The ramifications of such research are sometimes formidable: from the applications and uses of accelerators in the medical field, to the birth at the CERN of the *World-Wide Web (WWW)*, i.e., the system of interlinked hypertext documents accessed via the Internet.

1.3 The Concept of the Atom and Indivisibility

As previously mentioned, towards the end of the nineteenth century, the word “atom,” i.e., indivisible, was attributed to objects that were actually quite divisible. The same error was repeated for many “elementary particles.” Now, one speaks instead of the “ultimate constituent,” knowing that perhaps they will not be as such. In fact, some physicists already speak about *subconstituents*!

One must wonder why so many errors have been made in attributing the title of indivisibility to objects that did not deserve it. One may also ask if the concept of an indivisible object is a relative concept: a concept that depends on particular environmental conditions, for example, on the temperature.

Let us illustrate this evolutionary concept with an ideal experiment. We consider a gas of particles placed in a container, for example, nitrogen (N_2) gas in a room. To the environment pressure of one atmosphere and to the temperature of 20°C , equal to 293 K , the nitrogen molecules can be considered as indivisible objects, the Democritus atoms. In fact, the gas can be thought of as constituted of many little balls, the molecules, of small dimensions (some 10^{-8} cm) with respect to the volume of the room, so that they can be considered almost point-like. These molecules move in a disordered way, each of them independently from the others. The mean velocity of the molecules $\langle v \rangle$ is related to the temperature according to

$$\frac{3}{2}KT = \frac{1}{2}m\langle v^2 \rangle \quad (1.1)$$

where K is the Boltzmann constant and T is the absolute temperature. The mean velocity of the nitrogen (N_2) molecules at the room temperature is

$$\sqrt{\langle v^2 \rangle} = \sqrt{\frac{3KT}{m}} = \sqrt{\frac{3 \cdot 1.38 \cdot 10^{-23} \cdot 293}{28 \cdot 1.66 \cdot 10^{-27}}} \simeq 510 \text{ m s}^{-1}. \quad (1.2)$$

The mean kinetic energy of the nitrogen molecules is

$$T_K = \frac{1}{2}m\langle v^2 \rangle = \frac{3}{2}KT \simeq 3.8 \cdot 10^{-2} \text{ electron Volt (eV)}. \quad (1.3)$$

Molecules traveling in the vacuum collide with the walls of the container and rebound, producing a pressure on the container walls. The collisions between two molecules are relatively rare and are completely elastic; the long distance forces between molecules are negligible. Under these conditions, the molecules can be considered as fundamental objects, namely, the “Democritus atom.”

Suppose that we raise the temperature of the gas. At the submicroscopic level, the effect is the increases of the molecules mean velocity and thus of their kinetic mean energy. The disordered motion is the same, though everything happens more quickly; in particular, the impact on the walls is more frequent and consequently the pressure on the walls is higher.

We continue to increase the temperature: except for the increasing pressure, nothing new happens for a little while. When the temperature becomes very high (as the kinetic energy of molecules), molecules can be excited after collision. This corresponds to an inelastic collision: part of the kinetic energy is transformed into the excitation energy of a molecule. Shortly after being excited (a fraction of a millionth of a second), the molecule de-excites, emitting infrared or visible electromagnetic radiation. Our gas is now more complex: it is constituted of molecules, excited molecules and electromagnetic radiation.

If we continue to raise the temperature, one reaches a given critical value (order of a thousand of Kelvin degrees) for the nitrogen molecules. At this temperature, the mean kinetic energy of the molecules is about a tenth of eV; but a small fraction of molecules have an energy notably greater than that average. It can therefore happen that in a collision, one or both nitrogen molecules fragment into two nitrogen atoms. We have therefore a situation with nitrogen molecules and atoms, excited molecules and electromagnetic radiation.

For higher temperatures, a simplification occurs: when every single molecule has fragmented into atoms, one can say that the gas is only formed

of nitrogen atoms plus visible electromagnetic radiation. In this situation, we may believe that the “Democritus atom” is the nitrogen atom.

Let us again raise the temperature, and therefore the mean kinetic energy of the nitrogen atoms, see Fig. 1.1. Again, nothing new happens for a little while, then the process which happened for the molecules repeats itself for the atoms. First, the collision energy is large enough to excite the atoms; then, it becomes large enough to ionize them, i.e., to extract an electron from an atom. Our gas is now made of electrons, positive ions of nitrogen (i.e., atoms with a missing electron) and electromagnetic radiation which is more energetic than that present to lower temperatures. A gas of this type, with electrons, positive ions and photons, is present in the external layers of the Sun, particularly in the photosphere.

Proceeding with our ideal experiment, by continuing to increase the temperature, we will reach other phases corresponding to nitrogen atoms without two electrons, then without three, etc., until all the electrons will be stripped from the nitrogen atom. The new type of gas is made of positive nitrogen nuclei, electrons and high-energy photons (X-rays). This complex gas is called a plasma, i.e., a state made of positive and negative electric charges and electromagnetic radiation. This is the fourth state of matter which is abundant in the Universe because it is present in the stars. At this point, we could say that the “Democritus atoms” are the electrons and the nuclei. The plasma cannot be contained because the container walls would be destroyed by collision of the gas particles (if the number density of gas particles is large). It must be “confined” with the mean of magnetic fields using, for example, a Tokamak apparatus, where the nuclear fusion and magnetic confinement is studied (Sect. 14.11).

A further increase of the collision energy induces the fragmentation of the nitrogen nuclei into neutrons and protons. (From an experimental point of view, it is however easier to reach the same observation using high energy collisions between an electron and a nucleus, or even between two nuclei.) While protons are stable, neutrons decay after few minutes in a proton, an electron and an electron antineutrino, $n \rightarrow p e^- \bar{\nu}_e$. Our gas is now made of electrons, protons, electromagnetic radiation (γ -rays) plus $\bar{\nu}_e$. Antineutrinos do not have electric charge and have a tiny probability to interact with other particles; therefore, they quickly leave the region where they have been produced.

The proton, neutron, electron, photon and the antineutrino were for a long time all considered “elementary particles.” It can be hypothesized that in some part of the Universe, there exists a plasma of protons, neutrons and electrons (perhaps at the center of the neutron stars). Protons and neutrons are not really elementary. One believes that by further raising the temperature, another transition should be observed, passing to a new type of gas that should have as elementary objects the leptons, the quarks, the

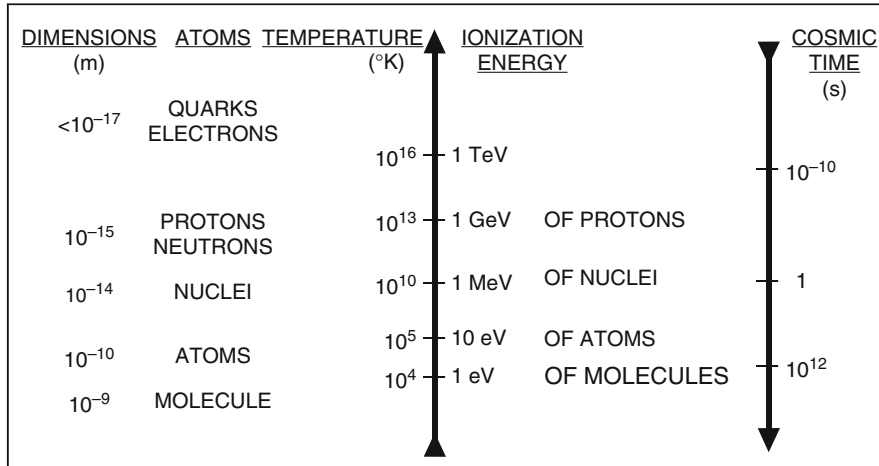


Fig. 1.1 Scale of dimensions in meters for various types of “atoms” and scale of “ionization” energies, i.e., the necessary energies to extract a constituent from the considered “atom.” The temperatures corresponding to the considered energies and the cosmic time when the Universe had that temperature starting from the Big Bang are also shown

photons and the gluons, see Fig. 1.1. This new state of the matter should be reachable for temperatures larger than $10^{15} K$ (i.e., for collision energies higher than 100 GeV), under the condition of large density. The state with quarks and gluons is called quark-gluon plasma. (Could it be the fifth state of the matter?) The discovery of this possible fifth state of matter is one of the objectives of the new LHC (Large Hadron Collider) accelerator at CERN.

We have perhaps reached the end of our ideal experiment in the sense that in the collisions between two particles, it is not possible to reach higher collision energies, that is, higher temperatures. At this level of knowledge, “Democritus atoms” have been identified; it is necessary to specify that some of them, the leptons and the quarks, can be really thought of as “atoms,” while the photons and gluons can respectively be thought of as the transmitters of the electromagnetic and strong interactions (all can be considered as point-like). Here, a more elaborated discussion shall pursue concerning the fundamental interactions (gravitational, weak, electromagnetic and strong), their unification and the possible symmetries amongst the “matter particles” (the leptons and the quarks) and the “force particle” (the photon, the gluons and the intermediate bosons W^+ , W^- and Z^0).

Proceeding with our ideal experiment at even more elevated temperatures, can a gas of new, smaller, and more “elementary” particles be hypothesized? Some believe that is the case.

It is reasonable to think that a gas of particles constituted the primitive Universe immediately following the Big Bang. Indeed, one can imagine that the primitive Universe was a warm gas of tiny, but very massive particles. The gas has cooled down with increasing time, leading successively to a gas composed of less heavy particles, then to a “gas” of quarks, gluons and leptons, to a “gas” of protons and electrons, to a gas of atomic nuclei and electrons and finally to a gas of atoms and molecules. Therefore, the study of high temperature gas allows us to study situations typical of the early Universe: the higher the temperature, the closer we are to the initial conditions of the Big Bang. The higher temperatures reached in laboratory in collisions between two leptons or quarks are obtained at energies in the center of mass of hundreds of GeV, i.e., around 10^{15} K, corresponding to the temperature that existed slightly less than a billionth of a second (see Eq. 1.5) after the Big Bang.

Figure 1.1 illustrates “atoms” found in our ideal experience proceeding towards smaller dimensions. A scale of temperature is also illustrated, together with the corresponding energy, determined through the relationship

$$\text{Kinetic energy (eV)} = 3KT/2 \simeq 1.3 \cdot 10^{-4} T(\text{K}), \quad (1.4)$$

i.e., $1 \text{ eV} = 7,740 \text{ K}$.

Finally, a temporal scale is also shown starting from the Big Bang using the relationship [W08]

$$t(s) \simeq 2.25 \cdot 10^{20} / T^2(\text{K}^2). \quad (1.5)$$

1.4 The Standard Model of Microcosm – Fundamental Fermions and Bosons

According to the so-called *Standard Model of the Microcosm* (SM), the ultimate constituents (fundamental) of matter are quarks and leptons, i.e., point-like fermions with spin 1/2. We can consider them as the smaller known objects. The quarks and the leptons can be classified into three “families” as shown in Table 1.1 and in Table 1.2. The quarks u , c , t have electric charge equal to +2/3 times that of the proton, while the quarks d , s , b have electric charge equal to -1/3. The neutrinos ν_e , ν_μ and ν_τ have a null electric charge. The first family includes the quarks u , d and the leptons ν_e , e^- . The ordinary matter is constituted of quarks u , d and of electrons e^- . The second and third families seem to be “replicas” of the first one. The quarks and the leptons of the second and third families can be produced in collisions between high energy particles.

The particles that mediate the four fundamental forces are the photon for the electromagnetic interaction, the intermediate vector bosons W^+ , W^- and Z^0 for the weak interaction, and the eight gluons for the strong interaction. These particles, unlike those listed before, are bosons, that is, they have integer spin equal to one.

Table 1.2 (a) Leptons and quarks (spin 1/2 fermions) first family. (b) Leptons and quarks second and third families

First family				
	Symbol	Q	L_e	B
Leptons	ν_e	0	1	—
	e^-	-1	1	—
Quarks	u	+2/3	—	+1/3
	d	-1/3	—	+1/3

Q is the electric charge in unit of the proton charge, L_e is the electronic lepton number, B the baryonic number.

2^d	3^{rd}
ν_μ	ν_τ
μ^-	τ^-
c	t
s	b

The Standard Model does not consider the gravitational interaction that may be neglected in the microcosm at the attainable energies.

The four fundamental forces seem to be each very different from the other. In collisions between high energy particles, it was possible to verify that the electromagnetic and weak interaction are tightly entangled and that one therefore can speak of electroweak interaction. The attainable energies with accelerators (actual and future) do not allow one to directly verify the theories that foresee a further unification of the electroweak force with the strong one (Theories of Grand Unification (GUT)). One can only hope to observe indirect effects through experiments without accelerators.

The Higgs boson, H^0 is also listed in Table 1.1. The Higgs boson has not yet been experimentally observed; its existence is postulated to resolve inconsistencies in theoretical physics and attempts are being made to find the particle by experiment, using the Large Hadron Collider (LHC) at CERN and the Tevatron at Fermilab.

All particles with electric charge are subject to the *electromagnetic interaction*. Lepton and quarks are also subject to the weak interaction. In particular, the *neutrinos*, being uncharged, are only subject to the weak interaction. The particles composed of *quarks* (the *hadrons*) are subject to the strong interaction. Hadrons are known in two topologies: those constituted by three quarks (the *baryons*, as the proton and neutron) and those constituted by a quark-antiquark pair (the *mesons*). As for leptons, antiquarks also exist and particles composed of three antiquarks are called antibaryons. As will be discussed later, the number of *baryons* and *leptons* is conserved. This means that, as described by the relationship $E = mc^2$, the energy can be converted in mass in the form of particles; nevertheless, the total number of baryons and leptons must be conserved. If an electron is produced, it must be created in association with a positron (its antiparticle, with electric charge and leptonic number of opposite sign) as expected from the Dirac theory.

Chapter 2

Particle Interactions with Matter and Detectors

2.1 Introduction

What does it mean to *see* a particle? From the epistemological point of view, to observe an object means to detect the light reflected by its surface. The light is nothing else than a component of the electromagnetic radiation that can be detected by the human eye. The dimensions of the particles are such that the electromagnetic wave is undisturbed: the visible light wavelength ranges from 400 to 700 nm (corresponding to the color range from violet to red) and is quite larger than the dimension of an atom (~ 0.1 nm). The only possibility is therefore to detect the emitted radiation when the particles interact with matter. A particle detector is a *translator* that connects, through adequate amplifications, one of our sensory organs (or a computer) with the effect produced by the interaction of the particle to be detected with matter. Particle physics is based on experiments in which particle interactions are studied thanks to the use of more or less sophisticated detectors.

In this chapter, the main processes occurring in the interaction of radiation with matter and the experimental techniques to detect them are briefly described. The term *radiation* refers to both charged (electrons, protons, etc.) and neutral particles (photons, neutrons, etc.) with energies greater than the keV. The study of these processes of radiation-matter interaction is of fundamental importance since they are at the base of the methods of particle detection; they determine the sensitivity and the efficiency of any experimental apparatus, and are therefore necessary in order to understand the operation of detectors and experiments.

The radiation “sees” the matter as an aggregate of constituents (electrons, atomic nuclei, nucleons, quarks, etc.) separated by distances larger than their dimensions. The radiation-matter interaction depends on the probability of interaction between an incident particle and a target particle, i.e., on the type of fundamental interaction involved (e.g., strong, electromagnetic, weak) and on the incident particle energy. Sometimes, the target may be a whole atom; more often, it is an atomic electron. For instance, for a beam of low energy neutrons (up to a few MeV), the most probable collision arises between a neutron and an atomic nucleus. However, at

higher energies, it may arise between a neutron and a nucleon of an atomic nucleus; at even higher energies, the interaction can occur between a quark of the neutron and a quark of a nucleon.

Particle detectors are based on the fact that when particles cross a given medium, they *excite* and *ionize* it. The gas counters (e.g., the Geiger counter) detect the electrons produced through ionization of the medium atoms; these electrons are then accelerated in a strong electric field, producing a small measurable electric signal. The scintillation counters are instead based on the detection of the light emitted through de-excitation of the medium atoms. For this reason, the principles of particle – matter interactions through excitation and/or ionization are described in the first part of this chapter. The detection techniques are in continuous evolution and in the second part we shall synthetically illustrate the basic principles of operation of the main particle detectors, making references to specialized texts for more detailed studies (e.g., [L87]).

2.2 Passage of Charged Particles Through Matter

2.2.1 Energy Loss Through Ionization and Excitation

A fast charged particle that moves in a given medium loses energy almost constantly and is slightly deflected from its initial direction. These two effects are the result of two types of collisions:

1. Inelastic collisions with the atomic electrons of the medium, particularly with those more external; these collisions produce **ionization** and/or **excitation** of the atoms of the medium; an excited atom de-excites, emitting one or more photons. These collisions are the main source of energy loss of the incident charged particle.
2. Elastic collisions with the nuclei. These collisions are less frequent; in practice, they do not cause a loss of energy, but a variation in the direction of the incident particle.

The collisions described in 1 and 2 statistically occur a large number of times per path length unit of the incident particle. For particles heavier than the electron (or positron), the cumulative effect of the collisions may be considered as a continuous effect along the whole trajectory of the particle. The energy loss in every collision (of the order of a few tens of eV) is a tiny fraction of the total kinetic energy of the incident particle. However, since the number of collisions in a dense medium is very large, it results in a measurable energy loss which for fast particles is of the order of $2 \text{ MeV g}^{-1} \text{ cm}^2$ of crossed material (that is, $\sim 2 \text{ MeV}$ for every cm of crossed material with the water density). Moreover, such an average energy loss has small fluctuations and varies slowly with the incident particle energy.

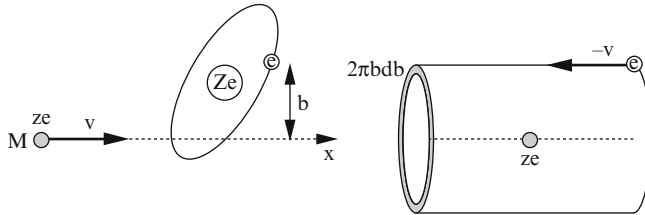


Fig. 2.1 Scheme of a Coulomb interaction between a particle and the electrons of a medium in a cylindrical layer at a distance b from the trajectory of the particle

The lightest relativistic particles, particularly the electrons, besides the normal energy loss through ionization and excitation, have another important source of energy loss: the *bremsstrahlung* process, that is, the emission of a high-energy photon. For this reason, they are discussed in a dedicated section.

2.2.2 “Classical” Calculation of Energy Loss Through Ionization

Let us consider a heavy particle with electric charge ze , mass M , and speed v that travels through some medium with atomic number Z and density ρ . We must consider the collisions with the atomic electrons. Figure 2.1 sketches the collision of the projectile particle with a target electron located at a distance b (the so-called impact parameter). If the incident particle has a mass $M \gg m_e$ where m_e is the electron mass, it is practically not deflected and may be considered in motion on a rectilinear trajectory. The speed of the atomic electron is much smaller than the speed of the particle. Therefore, the electron can be regarded as stationary during the collision. This hypothesis is easily demonstrable from the atomic theory: the speed of the atomic electrons is of the order of $(c\alpha_{EM}/n)$, where $\alpha_{EM} = 1/137$ is the fine structure constant and n is the principal quantum number. In the collision, the impulse delivered to the target electron is

$$I = \int F dt = e \int E_\perp dt = e \int E_\perp \frac{dt}{dx} dx = e \int E_\perp \frac{dx}{v}. \quad (2.1)$$

We have only taken into account the component of the electromagnetic field, E_\perp , perpendicular to the trajectory of the fast particle thanks to the symmetry of the problem. Using the Gauss theorem on a cylinder of radius b and infinite length, one can write (in the Gauss-cgs system)

$$\int E_\perp 2\pi b dx = 4\pi ze \Rightarrow \int E_\perp dx = \frac{2ze}{b} \quad (2.2)$$

and therefore (if $v = \text{constant}$),

$$I = \frac{2ze^2}{vb}. \quad (2.3)$$

The energy δE received by the electron located at a distance b is

$$\delta E(b) = \frac{I^2}{2m_e} = \frac{2z^2e^4}{m_e v^2 b^2}. \quad (2.4)$$

When the projectile particle travels a short distance dx in a medium with electron density N_e , the energy imparted to the electrons in a layer of the medium at a distance from b to $b + db$ from the trajectory is

$$-dE(b) = \delta E(b) N_e dv = \frac{4\pi z^2 e^4}{m_e v^2} N_e \frac{db}{b} dx. \quad (2.5)$$

The elementary volume is $dv = 2\pi b db dx$. The total energy loss per path length unit is obtained, integrating (2.5) from a value b_{min} to b_{max} . The choice of b_{min} to b_{max} has to be made in order to prevent the value of the integral to become infinite, which is obviously unphysical: b_{min} has to be slightly larger than zero because (2.5) diverges for $b_{min} \rightarrow 0$; b_{max} should not be infinite because in this case, the collision would last indefinitely, contrarily to the hypothesis that the electron stays stationary. The integration gives

$$-\frac{dE}{dx} = \frac{4\pi z^2 e^4}{m_e v^2} N_e \ln \frac{b_{max}}{b_{min}}. \quad (2.6)$$

The negative sign indicates that the incident particle loses energy. The problem is now only connected to the determination of b_{min} and b_{max} .

To determine b_{min} , we consider the maximum energy that the electron can receive in a collision. Classically, in a central collision, the electron can gain the energy $\frac{1}{2}m_e(2v)^2$. Keeping special relativity in mind, such a quantity becomes $2\gamma^2 m_e v^2$, where $\gamma = (1 - \beta^2)^{-1/2}$, $\beta = v/c$, $p = m_e v \gamma$. Placing this value in (2.4), one has

$$\frac{2z^2 e^4}{m_e v^2 b_{min}^2} = 2\gamma^2 m_e v^2 \Rightarrow b_{min} = \frac{ze^2}{\gamma m_e v^2}. \quad (2.7)$$

For b_{max} , let us recall that the electrons are bound in atoms with orbital frequencies ν . If the whole process of collision happens in a time comparable or greater than the revolution period $\tau = 1/\nu$, the collision is adiabatic and the electron does not receive any energy (it receives it in the first phase and loses it in the second one). It is therefore necessary to hypothesize that the collision occurs in a brief time compared to the period τ . The typical time of interaction is classically $t = b/v$ and relativistically $t/\gamma = b/(\gamma v)$. From this last relation, one has

$$\frac{b}{\gamma v} \leq \tau = \frac{1}{\nu} \Rightarrow b_{max} = \frac{\gamma \nu}{\nu}. \quad (2.8)$$

In an atom, there are different bound states, each with a different frequency v ; we have thus used an average frequency \bar{v} in (2.8). The maximum value for b is consequently $b_{max} = \gamma v/\bar{v}$. Placing this value and that of (2.7) in (2.6), one has

$$-\frac{dE}{dx} = \frac{4\pi z^2 e^4}{m_e v^2} N_e \ln \frac{\gamma^2 m_e v^3}{ze^2 \bar{v}}. \quad (2.9)$$

This is the *classical Bohr's formula*. It gives a reasonable description of the energy loss for helium nuclei (α particles) and heavier nuclei. However, it does not properly describe the energy loss of lighter particles, for example, the protons, despite the fact that it contains the essential characteristics of the energy loss due to collisions with atomic electrons.

A better approximation including relativistic effects is given by the *Bethe-Bloch formula*. Equation (2.9) is modified to take into account the mean ionization potential of the medium and the maximum energy transferred to the electron. Moreover, one has to consider two additional terms: the δ correction known as *the density effect* and the *C shell correction*. After these changes, (2.9) becomes

$$-\frac{dE}{dx} = 2\pi N_a m_e r_e^2 c^2 \rho \frac{Z}{A} \frac{z^2}{\beta^2} \left[\ln \left(\frac{2m_e \gamma^2 v^2 W_{max}}{I^2} \right) - 2\beta^2 - \delta - 2\frac{C}{Z} \right] \quad (2.10)$$

where

$$r_e = e^2/m_e c^2 = 2.818 \cdot 10^{-13} \text{ cm classical electron radius}$$

$$N_e = N_A \cdot Z \cdot \rho / A$$

$$2\pi N_a r_e^2 m_e c^2 = 0.1535 \text{ MeV g}^{-1} \text{ cm}^2$$

$$m_e = \text{electron mass} = 0.55110 \text{ MeV}/c^2 = 9.110 \cdot 10^{-31} \text{ kg}$$

$$N_A = \text{Avogadro's number} = 6.022 \cdot 10^{23} \text{ mol}^{-1}$$

$$I = \text{mean ionization (excitation) potential of the target}$$

$$Z, A = \text{atomic number and atomic weight of the absorber medium}$$

$$\rho = \text{material density}$$

$$ze = \text{charge of the incident particle}$$

$$\beta = v/c \text{ of incident particle}$$

$$\gamma = 1/\sqrt{1-\beta^2}$$

$$\delta = \text{density effect correction (important at high energy)}$$

$$C = \text{shell correction(already important at low energy)}$$

$$W_{max} = \text{maximum kinetic energy imparted to an } e^- \text{ in a single collision}$$

$$\simeq 2m_e c^2 (\beta \gamma)^2, \text{ for } M \gg m_e$$

Note that:

- The *mean ionization (excitation) potential* I has a value of ~ 10 eV, and it is actually difficult to calculate. It is estimated on the basis of dE/dx experimental measurements. In a medium with $Z < 13$, one has a semi-empirical formula $I/Z \simeq 12 + 7/Z$ (eV).

- The *relativistic rise* of dE/dx in the logarithmic term is due to the relativistic increase in the laboratory system of the transverse component of the electric field, E_{\perp} , by a factor γ . Since E_{\parallel} remains unchanged, the field flattens and extends so that *distant collisions* increase as $\ln(\beta\gamma)$. In dense materials, the relativistic slope is reduced because of the effects of density.
- The *density effect*. The relativistic effect implies that at high β , target electrons with large values of b are involved in the interaction; however, these electrons are screened by electrons closer to the projectile particle trajectory. This effect is larger in materials of high density (solids and liquids) than in gases. In solids and for high values of $\beta\gamma$, the density effect reduces the dE/dx relativistic rise by about a factor of two.
- The *shell correction* takes into account the effects that occur when the speed of the incident particle is comparable or smaller than the atomic electron orbital speed. In this case, the approximation of a stationary electron with respect to the incident particle is not as good. However, the correction that is derived from it is relatively small.

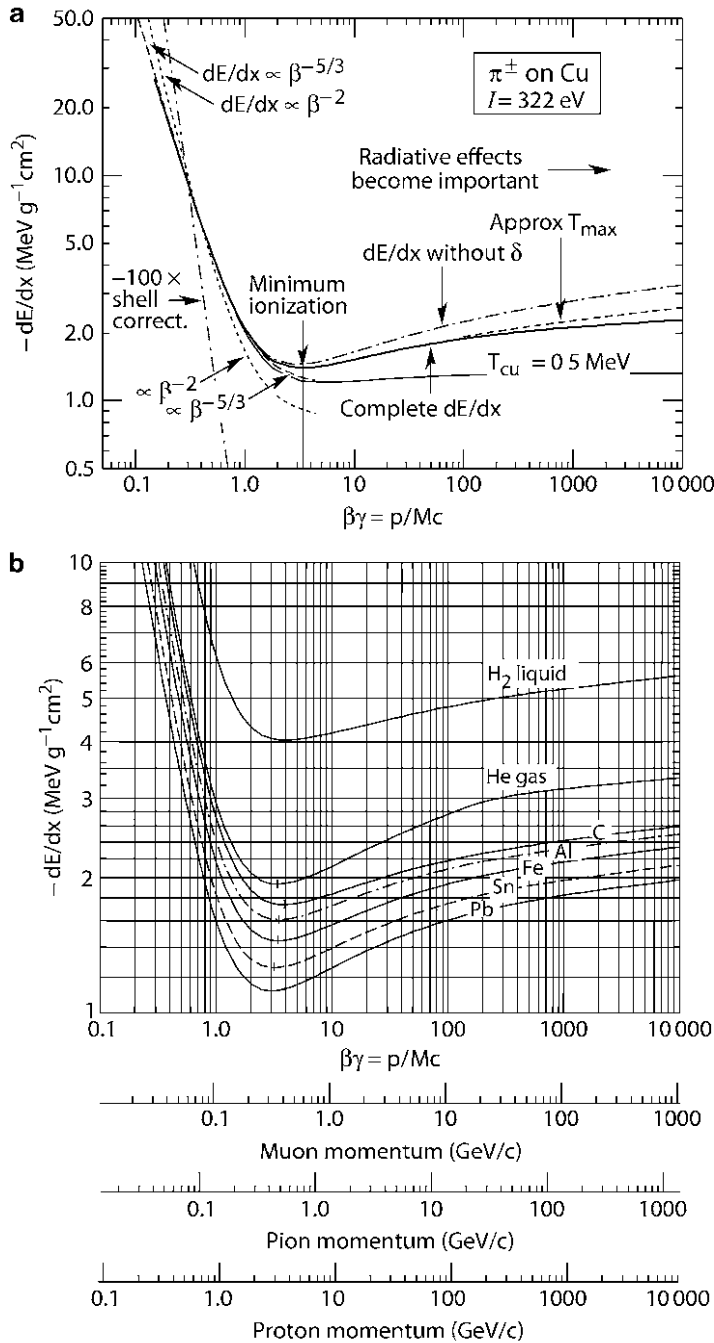
Figure 2.2a illustrates the behavior of the energy loss as a function of $\beta\gamma$ of the incident particle; some definitions are given (for instance, the *energy loss at the minimum ionization* and the *relativistic rise*). Note that from (2.10), the energy loss only depends on $\beta\gamma$, or better, since relativistically $p = Mv\gamma = M\beta\gamma c$, from $\beta\gamma = p/Mc$. From Eq. 2.10, it is then possible to formulate the so-called “scaling laws” which allow one to calculate the energy loss of a particle with mass m_1 , energy E_1 and electric charge z_1 starting from m_2 , E_2 , z_2 :

$$-\frac{dE_2}{dx}(E_2) \simeq -\frac{z_2^2}{z_1^2} \frac{dE_1}{dx} \left(E_2 \frac{m_1}{m_2} \right). \quad (2.11)$$

Figure 2.2b shows the difference in energy loss in liquid hydrogen ($Z/A = 1$), gaseous materials (He , $Z/A = 0.5$) and in solid materials with $Z/A \simeq 0.5$. It can be observed that the specific energy loss at the minimum ionization is $(dE/dx)_{min} \simeq 1.5 \text{ MeV g}^{-1} \text{ cm}^2$, while it can be considered approximately constant at high energies, $(dE/dx) \simeq 2 \text{ MeV g}^{-1} \text{ cm}^2$.

The formula (2.10) can be integrated in order to determine the *range*, that is, the total path length of a particle that loses energy only through ionization. The result is shown in Fig. 2.3.

Fig. 2.2 (a) Energy loss through ionization for π^{\pm} mesons in copper. The general behavior is shown together with some definitions and corrections due to the density effect (responsible for the smaller relativistic rise) and two different approximations at low energies. (b) Mean energy loss in liquid hydrogen (bubble chamber), gaseous helium, carbon, aluminum, iron, tin, and lead. The horizontal scale is in $\beta\gamma$ units, which is independent of the incident particle type. The underlying scales indicate the momentum for μ , π and p , respectively. The energy loss curves show a minimum for $\beta\gamma = 3$, that is, $pc \simeq 3Mc^2$ [P08]



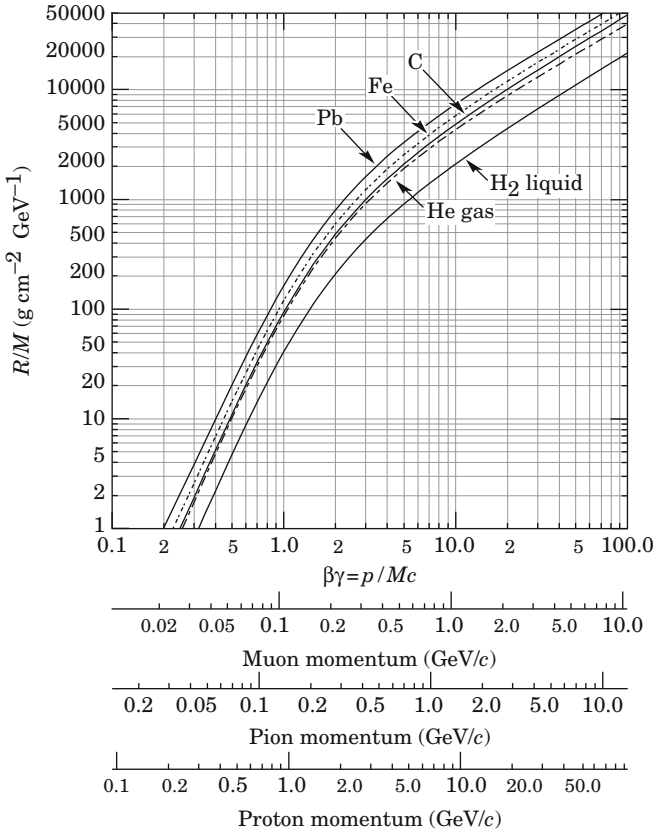


Fig. 2.3 “Range” of charged particles, normalized to the mass M of the particle (relationship valid for $> 0.4 \text{ GeV}$) in liquid hydrogen (bubble chamber), helium gas, carbon, iron and lead [P08] as a function of the $\beta\gamma$ of the particle. For example, for a proton of 200 MeV energy, $\beta\gamma \simeq 0.2$ (see Fig. 2.2b) and we read $R/M \times M \simeq 1 \text{ g cm}^{-2}$, equivalent to 1 cm of water. For 1 GeV protons, the range is $R \simeq 100 \text{ g cm}^{-2}$

Hadron therapy with nuclei. The concept of the range of a particle has a very important application in the medical field. Hadron therapy is the most recent relative of conventional radiotherapy, which uses X-rays. Hadron therapy instead uses beams of protons, carbon ions or neutrons. For instance, protons accelerated to 200 MeV or carbon ions accelerated to $4,700 \text{ MeV}$ may be used to irradiate deep tumors by following the tumor contour with millimetric precision, allowing one to preserve the surrounding healthy tissue.

The accelerated hadrons are able to destroy sick tissues mostly at the end of their range in the body of the patient, where the tumor is situated. This is evident from Fig. 2.2, where it can be seen that the energy loss for slowing

down particles (that is, at the end of range) is very high. A beam of charged hadrons therefore releases the greatest part of its destructive energy on the target tumor. The dose received at the tumor can therefore be very high while the healthy tissue is saved. Hadron therapy was initially specially relevant for tumors located in the cranial base or along the vertebral column and for ocular cancers. Recently, hadron therapy has successfully treated pediatric tumors, tumors residing in the central nervous system, prostate, liver, and of the gastroenterological apparatus.

Many countries are investing in this anticancer tool. The clinics which use proton accelerators largely dominate, and the number of new clinics has rapidly increased in the last few years. In 2008, there was nearly the same number of clinics in Europe (11), North America (8) and Japan (8), and more than 16 clinics will enter into operation within the next 5 years [2L07]. The total number of patients treated with protons was about 10,000 in 1993 and 50,000 in 2006, that is, the progression appears to be exponential. Many excellent clinics exist or are in construction in Europe. A dedicated heavy ion therapy clinic is being constructed in Heidelberg (Germany). The construction of ETOILE, the French National Hadron Therapy Centre, was approved by the French Ministries of Health and Research in 2006. This carbon therapy clinic will be built within the framework of a Public – Private Partnership near Lyon. The TERA Foundation [2w1] aims at the development of the techniques based on the use of hadrons and, more generally, of the applications of physics and computer science for medicine and biology. In particular, in Italy, since 2001, the South National Laboratories of INFN are operating a beam of 62 MeV protons used to treat ocular melanoma and other non-deep tumors. In 2003, the TERA Foundation completed the specifications and the technical design of the CNAO, the Italian National Centre for Oncologic Hadron Therapy aiming at the treatment of deep tumors with protons and carbon ions, which will be built in Pavia.

An appreciable fraction of the energy lost through ionization can be delivered more “violently” to some electrons which consequently acquire a relatively high energy and therefore have a relatively longer path length: they are the so-called *knock-on electrons* and they have enough energy to ionize (they are the so-called δ rays along the path of a charged particle). The number of δ rays increases with the energy of the primary particle. Fluctuations in the energy loss through ionization are mainly due to the small number of energetic knock-on electrons. Some detectors, for example, the Nuclear Track detectors, are sensitive to the *Restricted Energy Loss (REL)*, that is, the energy deposited in a cylinder, having for an axis the direction of the particle of about 100 Å diameter, corresponding to δ rays with less than 200 eV energy.

2.2.3 Bremsstrahlung

The *bremsstrahlung* is the emission of a photon from an electron deflected by a nucleus; it is a process due to the electromagnetic interaction that produces a large energy loss. The bremsstrahlung dominates the energy loss with respect to the energy losses through ionization and excitation for high $\beta\gamma$. Given the small mass, this already happens for a few tens of MeV in the case of electrons in lead and hundreds of MeV for lighter materials; for muons, it only becomes important for energies larger than 0.5 TeV.

In Sect. 4.6, the Feynman diagrams will be illustrated; we shall obtain a qualitative and intuitive dependence of the probability (or better, of a quantity that we shall call the cross-section) of the bremsstrahlung process, resulting in $\sigma \approx Z^2\alpha_{EM}^3$, where Z is the atomic number of the medium nuclei. The process can be seen as a slowing down of the incident electron caused by the nuclear Coulomb field: the amplitude of the emitted radiation is inversely proportional to the electron mass. The cross-section is proportional to $1/m_e^2$. Therefore, one has $\sigma \approx Z^2\alpha_{EM}^3/m_e^2c^4$. For a higher mass particle, σ is smaller since the squared mass appears in the denominator. It can be derived that the energy loss per path length unit is

$$-\left(\left\langle \frac{dE}{dx} \right\rangle\right)_{rad} \simeq \frac{4N_a Z^2\alpha_{EM}^3 (\hbar c)^2}{m_e^2 c^4} E \ln \frac{183}{Z^{1/3}}, \quad (2.12)$$

where $N_a = \text{number of atoms cm}^{-3} = \rho N_A / A$ and N_A is the Avogadro's number. The logarithmic term has its origin in the “screening” of the nucleus from the atomic electrons and therefore the cross-section is limited. The mathematical demonstration and more precise formulas are given in [J99].

Figure 2.4a shows how for electrons *the energy loss through radiation* linearly increases with the electron energy. Besides, note that for $E \geq 20$ MeV, the energy loss through radiation is higher than that through ionization. The *critical energy* is defined as the value for which the energy loss through radiation is equal to that of the energy loss through ionization (the definition given by Rossi [L87] is slightly different). An approximate formula for the electron critical energy in materials with a different Z is that of Bethe–Heitler, that is,

$$E_c \simeq 1600 m_e c^2 / Z. \quad (2.13)$$

Critical energy values for some material elements are given in Table 2.1.

For energies much higher than the critical energy, energy loss through radiation is practically the only one to be considered. In this situation, the integration of (2.12) gives

$$E = E_0 e^{-x/L_{rad}} \quad (2.14)$$

where E_0 is the initial energy, E is the energy after a thickness x of material. The *radiation length*, L_{rad} , is the length after which the energy E_0 of the incident

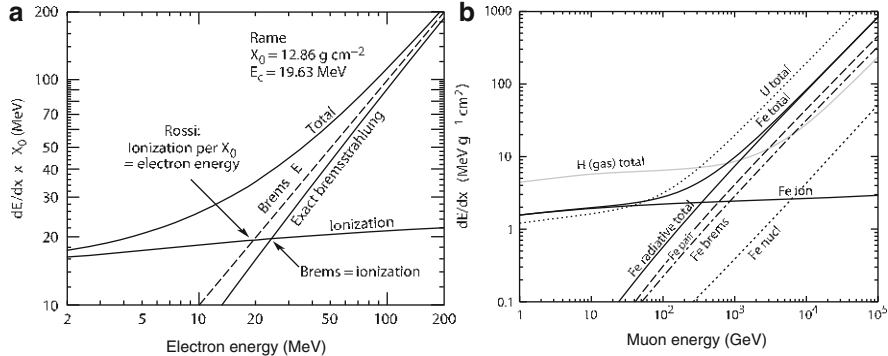


Fig. 2.4 (a) Electron energy loss in copper as a function of the electron energy. The excitation and ionization contribution (*ionization*) remains roughly constant with increasing energy. Instead, the term due to the energy loss through radiation (*bremsstrahlung*) increases. The intersecting point of the two curves defines the *critical energy*. In this figure, it corresponds to about 20 MeV. (b) Muon energy loss in hydrogen, iron and uranium as a function of the muon energy. Energy loss through excitation and ionization is indicated only for the iron (*Fe ion*). The value of the critical energy is found at a few hundred GeV. The different behavior of the muons in comparison to the electrons is due to the mass difference: $m_\mu \simeq 200 m_e$ [P08]

Table 2.1 Radiation length, path length (radiation length divided by the medium density) and critical energy in various material absorbers

Medium	L_{rad} (g cm ⁻²)	$\frac{L_{rad}}{\rho}$ (cm)	E_C (MeV)
Air	36.20	30050	83
H ₂ O	36.08	36.1	93
Pb	6.37	0.56	9.5
Cu	12.86	1.43	25
Al	24.01	8.9	51
Fe	13.84	1.76	27.4

electron is reduced to E_0/e , where e is Nepero's constant. An approximate formula for the radiation length L_{rad} (often indicated as X_0) is

$$X_0 = L_{rad} \simeq \frac{716.4 [\text{g cm}^{-2}] A}{Z(Z + 1) \ln(287/\sqrt{Z})}. \quad (2.15)$$

It must be emphasized that the energy loss through radiation may suffer strong fluctuations from the mean value given in (2.12). The number of photons and their energy fluctuate as well. The probability to emit a photon of high energy is much smaller than that to emit one of low energy.

The bremsstrahlung may also happen on target electrons. The considerations made on the electron energy loss through radiation are also valid for other higher mass charged particles with an equivalent value of $\beta\gamma$.

2.3 Photon Interactions

The behavior of photons in matter is very different from that of charged particles. Indeed, the photons are not subject to the numerous inelastic collisions with atomic electrons. The main photon interactions are the photoelectric effect, Compton scattering (including Thomson and Rayleigh collisions) and pair production. In general, photons are more penetrating (in matter) than charged particles; a beam of photons is not degraded in energy, but is attenuated in intensity according to the formula

$$I(x) = I(0) e^{-\mu x} \quad (2.16)$$

where μ is the *photon attenuation coefficient*

$$\mu = N_a \sigma = \sigma N_A \rho / A \quad (2.17)$$

where N_A = Avogadro's number, ρ = medium specific mass, A = molecular or atomic weight, N_a = atomic density, and σ = the total cross-section. The mean free path $\lambda = 1/\mu$ of photons as a function of their energy and for various materials is given in Fig. 2.5.

2.3.1 Photoelectric Effect

In the photoelectric effect, a photon is absorbed by an atomic electron with the consequent emission of an electron, $\gamma e^- \rightarrow e^-$. To conserve momentum, the photoelectric effect can only happen with bound electrons; the rest of the atom

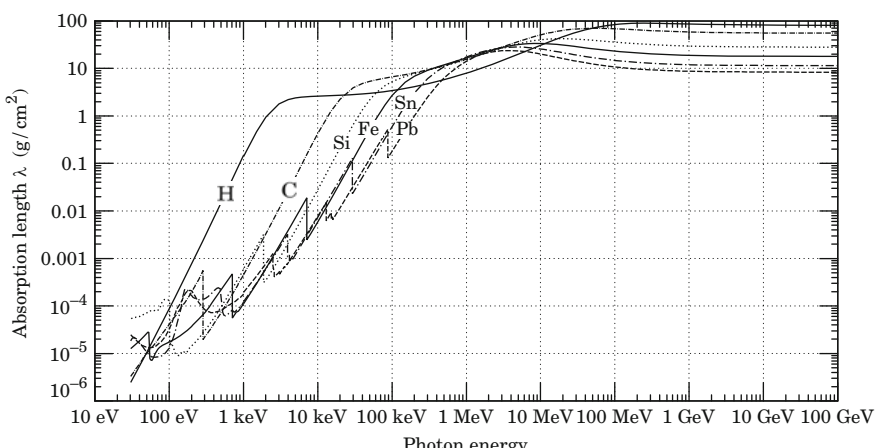


Fig. 2.5 Photon mean free path (in g cm^{-2}) as a function of photon energy for various elemental absorbers [P08]. The mean free path λ is the inverse of the attenuation coefficient μ (2.17)

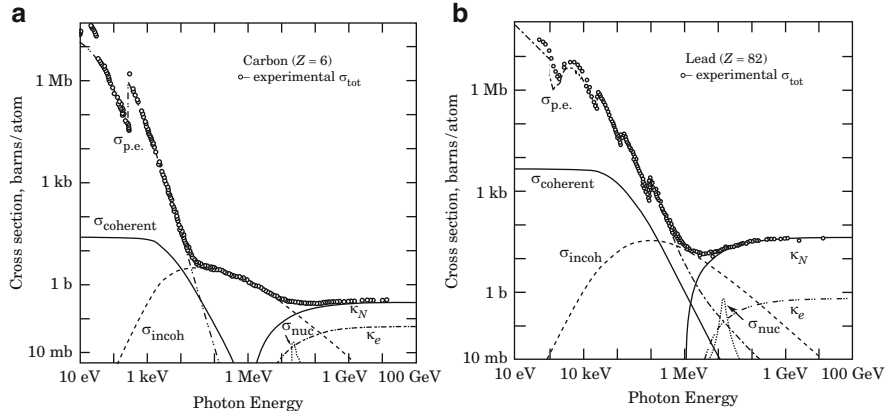


Fig. 2.6 Total cross-section (circles at the top) for photons (a) in carbon and (b) in lead as a function of the photon energy. In the figure are also shown the partial cross-sections for the following processes: $\sigma_{\text{p.e.}}$ for the photoelectric effect on atomic electrons; σ_{coherent} for elastic collisions on atoms (Rayleigh scattering); σ_{incoh} for Compton scattering on electrons; κ_N for pair production in a nuclear field; κ_e for pair production in the field of an electron; σ_{nuc} for photon absorption in nuclei [P08]

recoils. The energy of the emitted electron is given by $E_e = h\nu - h\nu_0$, where $h\nu_0$ is the electron binding energy. Figure 2.6 shows the cross-section for the photoelectric effect as a function of photon energy for C and Pb elements. The cross-section strongly decreases with increasing energy and becomes very small for energies larger than 100 keV. One should also note the series of peaks corresponding to the ionization energy of the K-shell electrons¹ and to the higher order shell electrons, that is, L, M, etc.

The calculation of the photoelectric cross-section is complicated; for energies greater than the K-edge and smaller than m_ec^2 , the following approximate formula is valid, that is,

$$\sigma_{\text{pe}} \simeq 4\alpha_{EM}^2 \sqrt{2}Z^5 \sigma_0 (m_ec^2/h\nu)^{7/2} \quad (2.18)$$

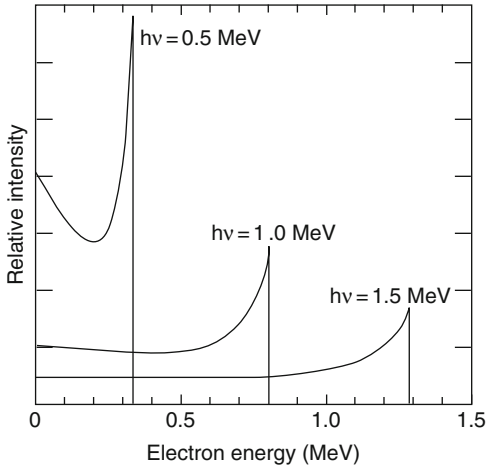
per atom, with $\sigma_0 = 8\pi r_e^2/3 = 6.65 \cdot 10^{-25} \text{ cm}^2 = \text{Thomson cross-section}$, where r_e is the electron classical radius and $\alpha_{EM} = 1/137$. The Thomson cross-section is the cross-section for the elastic process $\gamma e^- \rightarrow \gamma e^-$ for energies approaching zero. One should note the dependence from Z^5 of the traversed medium.

2.3.2 Compton Scattering

The Compton scattering consists of an elastic collision of a photon with an electron, $\gamma e^- \rightarrow \gamma e^-$. The electrons in ordinary matter are bound electrons; if the incident

¹The peak due to photons with energy slightly higher than the binding energy of the K-shell atomic electrons is called the K-edge.

Fig. 2.7 Energy distribution of the recoiling Compton electrons for various energies $h\nu$ of the incident photon



photon has an energy much higher than that of the bound electrons, these can be considered as free. The kinematics of Compton scattering gives the following expression for the photon energy after the collision, $h\nu'$, that is,

$$h\nu' = \frac{h\nu}{1 + \Gamma(1 - \cos \theta)} \quad (2.19)$$

where $\Gamma = h\nu/m_e c^2$. Quantum electrodynamics allow one to compute the Compton scattering cross-section (*Klein–Nishina formula*)

$$\frac{d\sigma}{d\Omega} = \frac{r_e^2}{2} \frac{1}{[1 + \Gamma(1 - \cos \theta)]^2} \left(1 + \cos^2 \theta + \frac{\Gamma^2(1 - \cos \theta)^2}{1 + \Gamma(1 - \cos \theta)} \right) \quad (2.20)$$

where r_e is the electron classical radius.

The integration of the Klein–Nishina formula gives the total cross-section of Compton scattering as shown in Fig. 2.6 (σ_{incoh}). It should be noted that such a process is dominant in the few tens of keV region for C and a few MeV for Pb.

To evaluate the energy response of some detectors, for example, scintillation counters, it is important to know the energy distribution of the recoiling electrons in Compton scattering. This distribution is shown in Fig. 2.7 for different energies of the incident photons. One should note that the maximum in intensity corresponds to the maximum energy allowed by the kinematics

$$T_{max} = h\nu \frac{2\Gamma}{1 + 2\Gamma} \quad (2.21)$$

(it is referred to as the *Compton edge*). In the classical low energy limit, the Klein–Nishina formula reduces to the Thomson formula, $\sigma_0 = 8\pi r_e^2/3$.

The *Rayleigh scattering* (denoted $\sigma_{coherent}$ in Fig. 2.6) is the elastic diffusion of a photon on an atom taken as a whole. It is referred to as a coherent scattering. Given the high atomic mass, no energy is transferred to the medium.

2.3.3 Pair Production

In the *pair production* process, a photon converts into an e^+e^- pair: $\gamma + Z \rightarrow Z + e^+ + e^-$, where Z is an atomic nucleus or an electron. This reaction has a threshold energy of $2m_e c^2 = 1.022$ MeV. The lowest order Feynman diagram is similar to the bremsstrahlung one, as will be explained in Chap. 4.

The differential cross-section has a complicated mathematical form. The more common practical formula is that of Bethe–Heitler; the integrated cross-section is shown in Fig. 2.6, and is indicated as κ_N and κ_e . Note that the pair production process in the Coulomb field of atomic nuclei (κ_N) dominates for energies of the incident photon larger than a few MeV. For higher energies, $h\nu \gg 137 m_e c^2 Z^{-1/3}$, one can use the formula obtained considering a complete *screening* of the atomic electrons, that is,

$$\sigma_{\kappa_N} \simeq aZ^2 \alpha_{EM} r_e^2 \left\{ \frac{7}{9} [\ln(183 Z^{1/3}) - f(Z)] - \frac{1}{54} \right\}. \quad (2.22)$$

The pair production on the electron (κ_e curves of Fig. 2.6) is given by an equation similar to that with $Z = -1$. To take it into account, it is sufficient to substitute Z^2 with $Z(Z + 1)$. From this latest formula, the following mean free path can be obtained, that is,

$$\frac{1}{\lambda_{pair}} = N_a \sigma_{\kappa_e} \simeq \frac{7}{9} Z(Z + 1) N_a r_e^2 \alpha_{EM} [\ln(183 Z^{-1/3}) - f(Z)]. \quad (2.23)$$

Note that the expression for λ_{pair} is quite similar to that for the radiation length. Indeed, one has

$$\lambda_{pair} \simeq \frac{9}{7} L_{rad}. \quad (2.24)$$

2.4 Electromagnetic Showers

In matter, a high energy photon converts into an electron-positron pair; each e^- (e^+) is able to radiate energetic photons through bremsstrahlung. These radiated photons can convert into pairs that, for example, radiate. In conclusion, one has an *electromagnetic shower* (*electromagnetic cascade*) with a large number of photons, electrons and positrons. The process continues up to when the energies of the

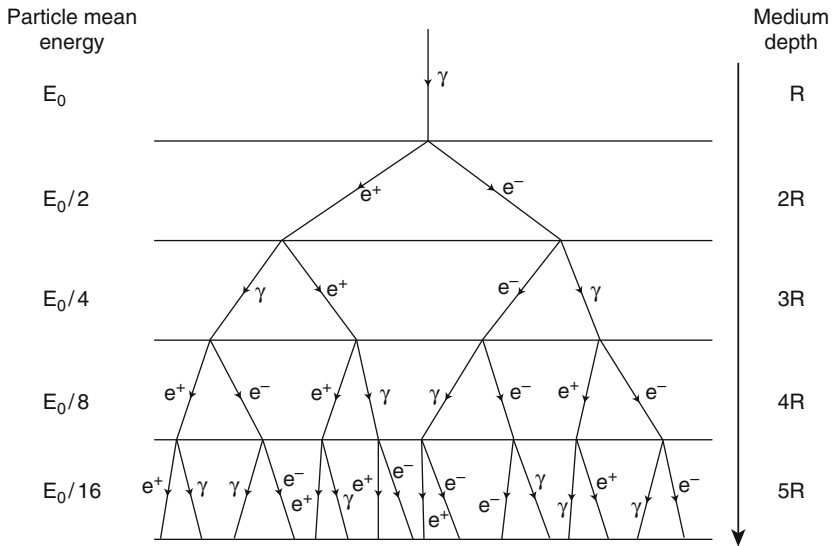


Fig. 2.8 Simplified scheme of an electromagnetic cascade development initiated from a γ

electrons and positrons go below the critical energy, that is, when they lose energy only through ionization and excitation.

The cascade development is a statistical process. It can be visualized in a simple way with the following intuitive method. The primary photon of energy E_0 converts into an e^+e^- pair after a radiation length L_{rad} and the electron or positron mean energy is $E_0/2$ (see Fig. 2.8). In the next radiation length, the electron and positron both emit one bremsstrahlung photon having approximately half the energy of the charged particle that emitted it. At this point, after two L_{rad} , one has two photons and an e^+e^- pair. In the following radiation length (at three L_{rad}), each of the two photons is converted into an e^+e^- pair, while the previous e^+e^- pair has radiated two photons. Now, the number of particles is therefore $8 = 2^3$, of which six are e^+, e^- and two are γ s; the mean energy of any of these particles is $E_0/8$. Continuing with the cascade, after t radiation lengths, the number of γ, e^-, e^+ particles is $N \simeq 2^t$, each of them with a mean energy $E_N \simeq E_0/2^t$. The same result would be obtained for a cascade initiated from an e^- instead of a γ . Note that we have measured the medium thickness in radiation lengths, $t = x/L_{rad}$.

One can now ask what is the maximum penetration of the cascade. Measuring the energy in unit of critical energy, E/E_c , one has

$$E_{t_{max}} \simeq \frac{E_0}{2^{t_{max}}} = E_c, \quad \text{from which: } t_{max} \simeq \frac{\ln(E_0/E_c)}{\ln 2}. \quad (2.25)$$

For energies lower than E_c , the dominant mechanism of energy loss of the electrons is not bremsstrahlung, but the “continuous” processes of excitation-ionization which

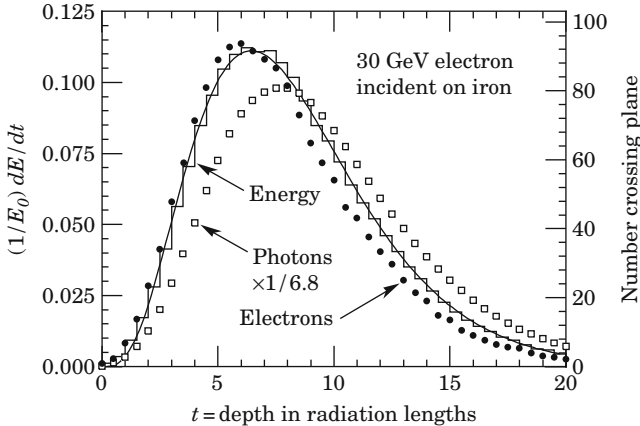


Fig. 2.9 Simulation of an electromagnetic cascade started by a 30 GeV incident electron on iron. The left scale shows the percentage of the deposited energy per radiation length. The black dots are the total number of electrons with energy greater than 1.5 MeV; the squares are the number of photons with $E_\gamma > 1.5$ MeV (right scale) [P08]

do not allow the multiplication of the number of particles. The maximum number of particles present in the cascade at a given instant is therefore

$$N_{max} \simeq E_0/E_c. \quad (2.26)$$

This simple model only gives a qualitative idea: the number of particles in a cascade increases exponentially up to the maximum. When the maximum number has been reached, the number of particles subsequently decreases gradually. The detailed analysis of the form of an electromagnetic cascade requires the use of Monte Carlo methods. Figure 2.9 shows the result of the simulation of an electromagnetic cascade. Note that the electromagnetic cascade is fully contained in about 20–25 radiation lengths.

Monte Carlo Simulations. Monte Carlo techniques are methods of statistical simulations based on the use of sequences of pseudo-random numbers for the resolution of problems, in particular for estimating the parameters of an unknown distribution. Monte Carlo methods are particularly useful when the complexity of the problem makes it impossible or very difficult to reach an analytical solution or a solution with traditional numerical methods. In the case of particle detector simulations, sequences of pseudo-random numbers are used to produce and follow the parameters of some particles, statistically varying event by event (the vertex from which a particle is originated, the

energy/momentum of the particle, the point of impact in the detector, the statistical fluctuations in the energy loss, etc.,) in order to reproduce a situation as close as possible to reality.

2.5 Neutron Interactions

The neutron, as the photon, has no electric charge; but it has a magnetic dipole moment, through which it can interact electromagnetically. Neutron interaction with matter is dominated by the strong interaction; in practice, the cross-section varies with the energy (speed) of the neutrons. Different energy regions may be considered:

High energy neutrons for kinetic energies $T_n > 100 \text{ MeV}$. In this region, neutrons behave as protons, with a total cross-section between 40 and 60 mb (see Sect. 7.3). The study of the neutrons in this energy range is part of the typical studies of particle physics. The study at smaller energies is included in the nuclear physics field and may have important technical and engineering implications.

Fast neutrons with $200 \text{ keV} < T_n < 40 \text{ MeV}$.

Epithermal neutrons with $0.1 \text{ keV} < T_n < 100 \text{ keV}$.

Thermal or slow neutrons when they have kinetic energies comparable to the energies typical of the thermal motion in materials, that is, $T_n \sim KT \sim (1/40) \text{ eV}$.

Cold and ultra-cold neutrons for kinetic energies of the order of milli-eV (meV) and micro-eV (μeV).

For energies smaller than 100 MeV, the neutrons are subject to different processes:

1. Elastic collision with a nucleus, $n + A \rightarrow n + A$. The elastic scattering is the most important process for MeV energies.
2. Inelastic collision with a nucleus excitation, $nA \rightarrow nA^*$, etc. The excited nucleus de-excites with the emission of γ rays. Also, these processes are important for MeV energies.
3. Radiative neutron capture from a nucleus: $n + (Z, A) \rightarrow \gamma + (Z, A + 1)$; the cross-section for this process is inversely proportional to the speed and therefore becomes large at low energies.
4. Nuclear capture reactions of the type (n, p) , (n, d) , (n, α) , etc. This cross-section has a dependence of the type $1/v$ and therefore the processes become important for thermal neutrons.
5. Nuclear fission, that is, the neutron capture with breakup of the nucleus (heavy) in two fragments and emission of a few neutrons (thermal and fast). Fission is more probable for slow neutrons.

In nuclear physics and for engineering purposes, it is usually necessary to slow down the fast neutrons. The most important process for obtaining neutron deceleration is through elastic collisions with nuclei with which other processes do not occur. The material which is widely used is ^{12}C for which about 110 elastic collisions are needed to actually slow down a neutron of 1 MeV to thermal energies of $(1/40)\text{eV}$. In hydrogen, about 17 collisions are needed.

2.6 Qualitative Meaning of a Total Cross-Section Measurement

If the collisions between two particles were analogous to those between two billiard balls, elastic collisions and the interaction probability would not depend on the speed of the incident particle, but would remain constant for any speed. However, if the balls collide at very high speeds, the billiard balls can break, particularly in the case of central collisions. Collisions in which the billiard balls break are referred to as inelastic collisions. With an increase in speed, the rate of inelastic collisions increases, while the elastic collision rate decreases, though the total probability of a collision remains the same.

The situation at the level of atomic and nuclear collisions and of particles is more complicated and less intuitive. Indeed, we have elastic collisions, inelastic collisions in which the complex system breaks, inelastic processes in which the internal system is modified, as, for example, in the case of an atom in which an electron is brought in a more external orbit, and finally, high energy collisions in which the energy is transformed into mass and new particles are created. The probability of every type of collision can be measured through a quantity called the *cross-section*, which is of enormous importance in high energy physics. The total cross-section is the sum of elastic and inelastic cross-sections, which may also have different contributions. In conclusion, several reasons exist as to why one expects that the total cross-section may strongly vary with the energy of the incident particles.

If the projectiles would have dimensions much smaller than those of the targets, if there were no wave-like effects and if the forces would have a short range of action, the cross-section would represent the transverse area (section) of every target. If the projectiles have comparable dimensions to those of the targets, then one would measure a quantity that depends on the dimensions of both the projectile and the target. This is the case of the greatest part of the collisions between particles.

The fact that particles are also waves implies that at the edges of every object involved in the collision, an elastic diffractive effect occurs. Moreover, in the submicroscopic world, it is not always possible to clearly separate the effects due to the type of interaction from those due to the effective dimensions of the objects. The cross-sections of neutrinos, photons and mesons on protons are very different because the interactions are respectively caused by the weak, electromagnetic and strong interaction and because the mesons are, in reality, complex objects. One may hope to gather the essence of the interactions eliminating spurious effects, considering in detail the total cross-sections in the limit of the highest energies (that

is, where the associated wavelength is very small) and in the case of the collisions between the “most elementary” constituents that we presently know. The unit used to measure the cross-section is the cm^2 ; in practice, the atomic cross-sections are measured in barn (b), $1 \text{ barn} = 10^{-24} \text{ cm}^2$. The cross-section of collisions between hadrons are of the order of a few tens of mb, $1 \text{ mb} = 10^{-3} \text{ b} = 10^{-27} \text{ cm}^2$. We shall return to the meaning of the cross-section later.

2.7 Techniques of Particle Detection

The subatomic particles are too small to be observed through optical methods, though they can be indirectly “observed” through the mechanisms of transfer of energy in matter. In the previous paragraphs, we have seen that the fast charged particles ionize and excite, along their trajectories, the atoms of the traversed medium. This is the principle of operation of all types of detectors. The information is transformed into electric signals that are then analyzed with electronic methods. The ionization detectors directly exploit the produced ionization, gathering the ionization electrons and positive ions (usually in a gas), and transforming them into electronic signals. In the first half of the 1900s, the *ionization chamber*, *proportional counter* and the *Geiger-Müller counter* were developed. These detectors have undergone only a few changes and are still used in the laboratory. The *multiwire proportional chamber* (MWPC), the *drift chamber*, the *time projection chamber* (TPC) and others were invented at the beginning of the 1960s. These detectors are all based on the principle of the proportional counter, though they are larger and more sophisticated.

In the scintillation counters, the light emitted in the de-excitation of the atoms and in the molecules excited by the passage of a fast charged particle is used. Various types of scintillation counters are used in experiments.

In some types of detectors, for example, bubble chambers, along the path of the particle, the ionization induces a variation of state of the medium; in others, as in nuclear emulsions, the ionization of the medium activates a chemical process which is then completed with film development.

In order to be detected, the neutral particles, as the photon, must interact and produce charged particles (these last particles are those that are actually “observed”). In the following, the simpler types of detectors are schematically described, distinguishing the electronic detectors from other types. Detailed descriptions and information can be found in specialized sites and books [2w2].

2.7.1 General Characteristics

A detector sensitive to all types of radiation for all energies does not exist. Every detector is sensitive to some type of radiation in a given energetic range. A detector

Table 2.2 Typical values of some of the parameters of particle detectors

Detector	Time resolution (s)	Dead time (s)	Spatial resolution (cm)	Typical volume (cm ³)
Ionization chamber, prop. counter.	10^{-9}	10^{-8}	— ^a	$1\text{--}10^5$
Limited streamer tubes	$10^{-8}\text{--}10^{-7}$	$10^{-4}/\text{m}^{\text{c}}$	1	$10^2\text{--}10^6$
Multiwire proportional chamber	10^{-9}	10^{-8}	10^{-1}	$10^3\text{--}10^6$
Drift chamber	$10^{-9}\text{--}10^{-8}$	$10^{-7}\text{--}10^{-5}$	10^{-2}	$10^4\text{--}10^6$
Time projection chamber	$10^{-9}\text{--}10^{-8}$	$10^{-5}\text{--}10^{-4}$	10^{-2}	$10^6\text{--}10^7$
Geiger-Müller tube	10^{-6}	10^{-3}	— ^a	$1\text{--}10^4$
Semiconductor counter ^b	10^{-8}	10^{-6}	$10^{-3}\text{--}10$	10
Spark chamber	$0.2 \cdot 10^{-9}$	10^{-8}	— ^a	$1\text{--}10^5$
Cherenkov counter	10^{-9}	10^{-8}	— ^a	$1\text{--}10^5$
Nuclear emulsion	—	—	$5 \cdot 10^{-5}$	$10\text{--}10^4$
Nuclear track detector	—	—	$3 \cdot 10^{-4}$	$10\text{--}10^6$
Cloud chamber	10^{-2}	100	0.05	10^5
Bubble chamber	10^{-3}	1	$10^{-3}\text{--}0.1$	$10^4\text{--}10^7$
Scintillation chamber	10^{-7}	10^{-3}	0.05	$10^4\text{--}10^6$
Streamer chamber	10^{-8}	10^{-3}	0.1	10^6
TRD	10^{-8}	10^{-6}	1	$10^5\text{--}10^6$
Cryogenic counter	10^{-5}	10^{-4}	10	10^2

^aDepends on apparatus dimensions and segmentation

^bThe spatial resolution is given for a single counter for a microstrip detector

^cDead time per meter of a single crossed streamer tube

possesses specific operational characteristics which are illustrated in the following in a schematic way (see Table 2.2).

Detector efficiency ϵ : Detector efficiency ϵ is the probability that a detector records a radiation that traverses it; it is given by the ratio between the number of recorded events N_{rec} and the N particles that traverse the detector, $\epsilon = N_{\text{rec}}/N$ (with $0 \leq \epsilon \leq 1$). It is usually studied through simulation methods (Monte Carlo methods) based on the knowledge of the detecting process of the geometry and the mass of the detector or of the intrinsic background, for example. It can be experimentally measured using a beam of known particles.

Response time of the detector: It is connected to the intrinsic time that the detector takes to form an electronic signal after the arrival of the radiation (excluding the delays introduced, for example, by the cables). To obtain a good response, the pulse rise time should be as brief as possible. The response time is usually a Gaussian distribution for which the half-width at half-maximum can be considered as the **time resolution** σ_t . Time resolutions are below 1 ns for scintillation counters and Cherenkov detectors, 1 ms for bubble chambers; for some detectors, a response time is not defined (nuclear emulsions and nuclear track detectors) (see Table 2.2). The duration of the signal is important because during this time, a second event may not be recorded. The **dead time** is the time between the passage of a particle and

the moment at which the detector is ready to record the passage of the next particle (during the dead time, the apparatus is not sensitive). The length of the signal, the electronics used, and the recovery time of the detector (see the example of the Geiger counter) influence the dead time. They vary from 10^{-8} to 100 s.

Spatial resolution: It is the precision with which the passage of a charged particle is located in space. It varies from about $1 \mu\text{m}$ for nuclear emulsions to $5\text{--}10 \mu\text{m}$ for silicon microstrip detectors, to many centimeters for a Cherenkov counter.

Energy resolution: Energy resolution is connected to the possibility of a detector to distinguish two close energies. If the signals are separate in time, the energy resolution is the half-width of the energy distribution, measured, for example, in a “test beam” with particles of known energy. If the two signals are too close in time, a more refined analysis must be performed. Besides, for scintillators, it is necessary to take into account the asymmetrical distribution with a long tail towards high energies, the so-called *Landau tail*.

2.8 Ionization Detectors

We shall not describe all of the ionizing particle detectors based on the discharges in gas in detail. One should remember that to create an electron-positive ion pair in a gaseous medium, it is necessary to provide a mean energy of about 30 eV, a value which depends on the gas and not on the properties of the ionizing particles. One should also remember that the ionization potential varies from about 10 eV in the more complex molecules to about 24 eV in the noble gases (see Table 2.3).

One simpler detector that uses a gas is the **ionization chamber (or counter)** (see Fig. 2.10a); it is usually made of a vessel within which two electrode plates are inserted, filled with a noble gas at a pressure close to the atmospheric one. In absence of ionizing particles that cross the chamber, there is no appreciable continuous electric current. If a fast charged particle crosses the chamber, the ions produced by the particle passage are all collected in two electrodes; this process creates a small electric current (current pulse) for a short time of the order of a

Table 2.3 Excitation potential, ionization potential and mean energy to produce an electron-ion pair in various gases. In general, the lower the values, the more sensitive the detector

	Excitation potential (eV)	Ionization potential (eV)	Mean energy (eV)
H ₂	10.8	15.4	37
He	19.8	24.6	41
N ₂	8.1	15.5	35
Ne	16.6	21.6	36
Ar	11.6	15.8	26
Xe	8.4	12.1	22
CO ₂	10.0	13.7	33
C ₄ H ₁₀		10.8	23

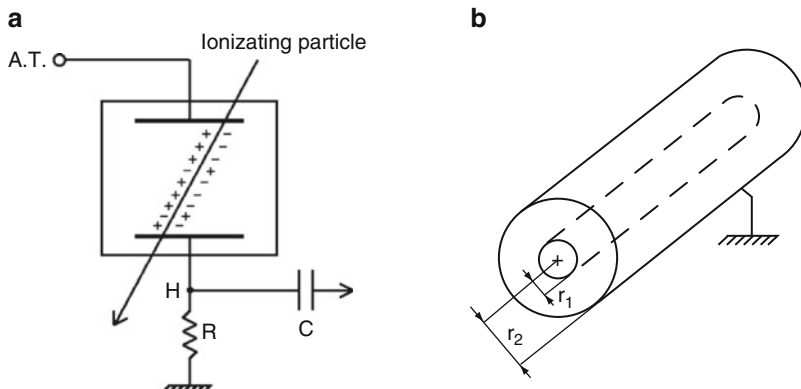


Fig. 2.10 (a) Ionization chamber: geometry and operating scheme. The path of a fast charged particle producing positive ions and electrons is indicated. The voltage drop in point H passes through the capacitor C and proceeds towards the counting electronic system. (b) Coaxial cylindrical electrodes. The electric field has a dependence of the type $E(r) = V/[r \ln(r_2/r_1)] \approx 1/r$. The ion multiplication happens in the region of the intense electric field close to the internal conductor

few nanoseconds. In the scheme of Fig. 2.10a, the electric current pulse becomes a voltage pulse in point H because the electric current decreases the voltage in H. This pulse can pass through the capacitor C and is sent to an amplifier and to a counting electronic system.

For the **proportional counters** (Fig. 2.10b), the operating voltage is such that the electrons, produced by the ionization of the gas at the passage of the particle, are multiplied in a proportional way to the initial ionization, resulting in a measurable avalanche of electric charges.

From a historical point of view, the **Geiger counter** is the most famous gas detector. The Geiger counter has a cylindrical electrode structure with a wire anode and the cathode that serves as an external wall. The generator's resistance R is usually quite large ($10\text{--}100\text{ M}\Omega$). The Geiger counter works in the quasi-independent Townsend discharge regime. The discharge regards the whole tube because in the point where the initial ionization avalanche (streamer) happens, many photons are emitted. These photons ionize the molecules of the particular gas used and the ionized zone propagates along the whole wire up to involving the whole counter. The operating voltages are about 1–3 kV.

With a Geiger counter, high current pulses for a duration of a few microseconds are obtained. After a discharge, it takes quite some time before the tube is ready to detect the next particle: the dead time is of the order of milliseconds.

The electronic detectors presented (and others not mentioned here, e.g., the limited streamer tubes and the resistive plate chambers) cannot provide precise information on the trajectory of a particle unless a thin segmentation is realized. Until 1968, precise information on the particle trajectory was obtained using photographic methods applied to bubble chambers, spark chambers, etc. In 1968,

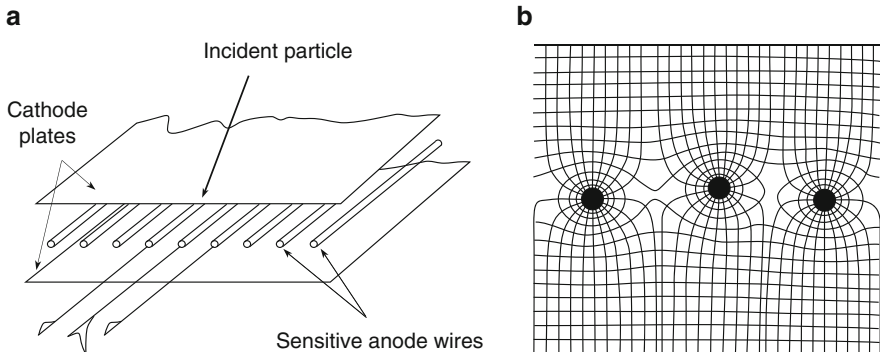


Fig. 2.11 (a) Configuration of a multiwire proportional chamber. Every wire performs as a single proportional counter. The signals from the wires closest to the trajectory are positive while those from more distant wires are negative. (b) Configuration of the electric field lines for a MWPC [2C70]

Charpak (Nobel laureate in 1992) invented the multiwire proportional chamber. This was the beginning of a technology which allowed electronic detectors to measure positions with resolutions of $50\text{--}100\,\mu\text{m}$, energy loss dE/dx sampled many times along the trajectory, elevated time resolutions, etc., thus leading the way to many new applications.

The basic configuration of a *multiwire proportional chamber* (MWPC) is shown in Fig. 2.11a: it consists of a plane of parallel wires (anodes) typically with $2\,\text{mm}$ spacing placed in the medium between two cathode plates typically $1.5\,\text{cm}$ apart. The electric field lines are illustrated in Fig. 2.11b. The passage of an ionizing particle produces positive ions and electrons in the gas inside the chamber. These last ones drift toward the nearest wire: part of the path happens where the electric field is constant: they have a motion with a constant speed because of the energy loss in the collisions (viscous motion). In the zone close to the wire, where the potential has a $1/r$ dependence, a multiplication of electrons occurs. In the closest wire (or in the closest wires in the case of particles with nonperpendicular incidence in the chamber), a (proportional) positive pulse is produced. However, in the adjacent wires, negative pulses are generated. Every wire corresponds to a single proportional counter with separate acquisition electronics (an amplifier, an ADC converter, a logic signal for TDC, etc.).

This chamber can provide a spatial coordinate, for example, x , with a precision of a fraction of the wire spacing d , typically $\sigma_x \simeq d/\sqrt{12} \simeq 1\,\text{mm}$. One can operate a second chamber with wires rotated by 90° in order to obtain information on the y coordinate with the same precision. A third chamber with wires at 45° is sometimes used to eliminate any ambiguity in the reconstruction. The response time is only a few ns, while the chamber efficiency is of the order of 98–99%.

Instead of using a second chamber for the y coordinate, the method of the *charge division* can be used: the collected charge at the extremity of a resistive wire (e.g., at

the left side) is proportional to the distance between the point in which the particle is passed and the extremity of the wire. If Q_L, Q_R are the electric charges collected respectively at the left and right parts of the wire, one has $y = \ell Q_L / (Q_L + Q_R)$, where ℓ is the wire length. The precisions are not so good (up to $\sim 1\%$ of the wire length) and it is difficult to maintain a good stability in time. An evolution of the multiwire proportional chamber is the **drift chamber**: the information on the y coordinate is obtained through the measurement of the secondary electron *drift time*, $t = d/v$ with respect to a “trigger” signal.

2.9 Scintillation Counters

Figure 2.12 shows the scheme of a scintillation counter consisting of: (1) a *scintillator* material whose atoms and molecules are excited by the passage of a charged particle; in the de-excitation, a certain quantity of light is emitted, i.e., a certain number of photons. The scintillator is coupled (2) directly or through a *light guide* to (3) a *photomultiplier*; a photomultiplier is made of a *photocathode* where the light photons are converted into electrons through the photoelectric effect, and by a *multiplier* of electrons (constituted by a series of *dynodes*) which produces an electric signal which may then be amplified by an electronic *amplifier*. The photomultiplier is connected to (4) a *base* containing an adequate circuit providing the appropriate voltages for the photomultiplier dynodes. (5) A cage made of ferromagnetic material (*mu-metal*, an alloy of 80% nickel and 20% iron) minimizes the effects of the magnetic fields, including the Earth one.

A scintillator (see Table 2.4) must have a good efficiency to convert the deposited energy in light. Besides, the light must be emitted quickly.² Finally, the scintillator must be transparent to the radiations that it emits and the light must be emitted in a spectral band compatible with the photomultiplier response.

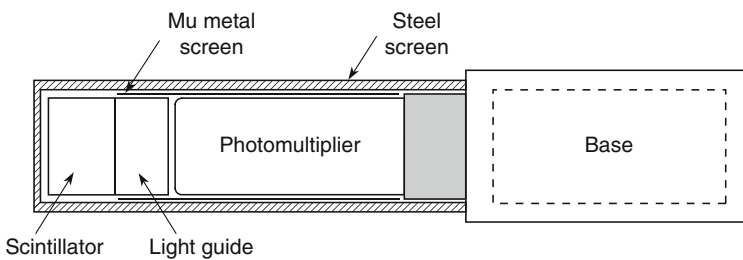


Fig. 2.12 Scheme of a scintillation counter

²In this case, one speaks about *fluorescence*; when the light is emitted in a relatively long time, one speaks about *phosphorescence*; the term *luminescence* includes both fluorescence and phosphorescence.

Table 2.4 Characteristics of some commercial scintillators: Density, refraction index n , luminous efficiency (mean energy to produce a light photon), decay constant, wavelength to which the maximum emission is obtained, ratio atoms of H/atoms of C, characteristic uses

Scintillator	Type	Density (g cm ⁻³)	n	Luminous efficiency (eV/ γ)	Decay constant (ns)	λ_{max} (nm)	H/C	Uses
NE 110	Plastic	1.032	1.580	36	3.3	434	1.104	γ, α, β, n
NE 220	Liquid	1.036	1.442	39	3.8	425	1.669	Dosimetry
NE 311	With 5%B, Liq.	0.91	1.411	39	3.8	425	1.701	n
Anthracene	Crystal	1.25	1.620	60	30.	447	0.715	γ, α, β, n
NaI(Tl)	Crystal	3.67	1.775	138	230.	413	—	γ, X
LiI(En)	Crystal	4.06	1.955	45	1200.	475	—	n
BGO	Crystal	7.1		300	300.	480	—	γ
CeF ₃	Crystal	6.16		240	10.	320	—	

Organic scintillators. They are formed from aromatic compounds containing chemical ring structures, for example, benzene. These scintillators emit light with decay times of a few nanoseconds. The light is produced in transitions that involve valence electrons of molecules. Organic scintillators of various types exist: *organic crystals* (for example, the anthracene), *organic liquids* in liquid solutions of one or more scintillating materials and *plastic ones* formed as those from liquid solutions, though now at the solid state. The greatest advantage of plastic scintillators is due to their manufacturing flexibility.

Inorganic scintillators. Inorganic scintillators are crystals, often of alkaline type with a small amount of activator impurities. The widely used type is the sodium iodide doped with thallium, NaI (Tl). Others are Bi₄Ge₃O₁₂ (bismuth germanate, BGO) and BaF₂ (barium fluoride). These scintillators have a high luminous efficiency, though they are one or two orders of magnitude slower than the organic scintillators (see Table 2.4).

Luminous efficiency ϵ (“light output”). It is defined as the energy necessary to produce a light photon. It is important because the scintillator energy resolution depends on it. Within ample limits, the quantity of light emitted by a scintillator is proportional to the energy lost by the particle that crosses it. Saturation effects happen only for very high lost energies. At room or close to room temperatures (i.e., from -10°C to 80°C), the quantity of emitted light barely depends on the temperature; the dependence only becomes important for temperatures considerably outside this interval.

Photomultipliers. Figure 2.13a shows the scheme of a photomultiplier. It is formed with a photocathode where the light photons are converted into electrons (the so-called *photoelectrons*), a focusing system of the electrons, the first dynode where the first electron multiplication (by a factor 3–10) happens and finally the other dynodes (from 8 to 12) at positive increasing voltages (up to about 2,000 V), where other multiplications occur up to a total factor of 10^5 – 10^7 .

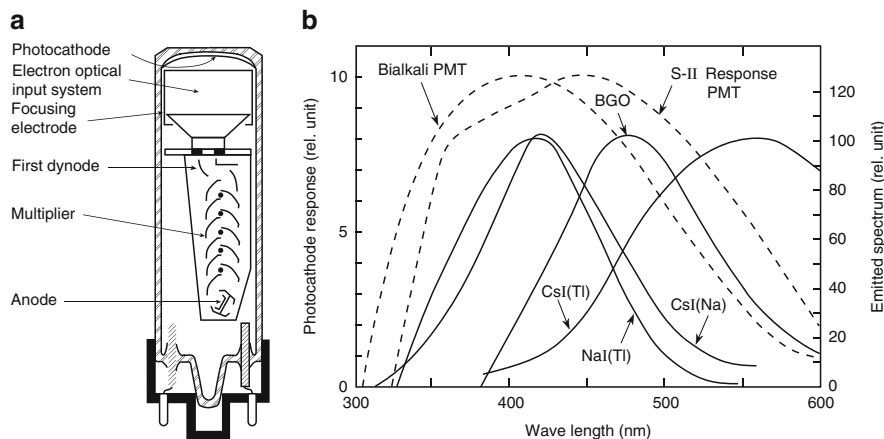


Fig. 2.13 (a) Scheme of a photomultiplier (from the Philips catalogue); (b) Luminous spectrum emitted by some inorganic materials (full lines) and the response curve of some photomultiplier photocathodes (dashed lines) (From the Harshaw Chemical Company catalogue)

In the nuclear and subnuclear physics experiments, the photomultipliers are used in pulsed regime, which means that they respond to a fast luminous signal producing a fast electronic output signal which sometimes must be subsequently amplified.

The photocathode *quantum efficiency* and its *spectral response* to luminous radiation of different wavelengths are important parameters. The quantum efficiency is the probability that a single incident photon on the photocathode produces an electron that contributes to the detector electric current. If, as it happens, more than a photon is present, the quantum efficiency is defined as the ratio between the number of the produced electrons (photoelectrons) and the number of incident photons. The most widely used cathodes are made of semiconductor material formed by antimony and by one or two alkaline metals, with which quantum efficiencies up to 26% and usable response curves for wavelengths from 320 to 580 nm may be reached (see Fig. 2.13b). To obtain higher position resolutions, segmented scintillators with very small pixels, namely, multianode photodetectors with very small anodes, can be used.

The statistical error on the energy loss measurement is connected to the number of photoelectrons. For this reason, it is necessary to collect the largest possible fraction of the emitted light on the photocathode, sometimes making use of good light guides and covering the scintillator and the light guides with reflecting or diffusing material; besides, it is necessary to use a photomultiplier with high photocathodic efficiencies. In order to be able to observe a single photoelectron, it is also required to have a high sensitivity.

It is important that the luminous spectrum emitted by the scintillator be contained in a bandwidth of equal wavelengths to that of the photocathode response. This is the case in Fig. 2.13b for NaI (Tl) and BGO, but not for CsI (Tl). In case of a mismatch between the emitted spectrum and that of the photocathode response, a *wavelength*

shifter may be used in the scintillator. This is practically possible for scintillators made from different materials.

The electric output signal of a photomultiplier used with a plastic organic scintillator is a pulse about 0.5 V high, with a rise time of 2–4 ns and a fall time of 10–20 ns.

To maintain the gain stability, it is necessary to have high voltage generators that are well stabilized both for short and long time terms. A photomultiplier is very sensitive to external magnetic fields: indeed, only a small field may cause the electrons to deflect inside the photomultiplier, especially in the first stage. For this reason, it is necessary to mask the photomultiplier with a magnetic screen of mu-metal.

2.10 Semiconductor Detectors

The *semiconductor detectors*, also called *solid state* detectors, are built with crystalline semiconductor material such as silicon and germanium. The basic principle of these detectors is analogous to that of the ionization gas detectors, with the difference that the medium is solid. The passage of an ionizing particle creates *electron-hole* pairs (instead of electron-positive ion pairs) that can be collected and multiplied through an appropriate electric field. The advantage of a semiconductor is due to the small energy necessary to create an electron-hole pair, namely, 3.6 eV in silicon and 3.0 eV in germanium, that is, about an order of magnitude smaller than that necessary for the gases used in ionization detectors (see Table 2.3). The ionization is therefore ten times larger and better resolutions in energy can be obtained. Also, note that the number of photoelectrons in a scintillation counter is about 100 times worse. The first applications of the semiconductor detectors have been radioactivity measurements with high energy resolutions. The main use in the high energy field regards the silicon microstrip detectors with the primary goal to obtain vertex and track detectors with high position resolution (5–10 μm).

Most semiconductor detectors, with the exception of the silicon and the gallium arsenide detectors, have to be operated at low temperatures in order to reduce thermal effects. Another difficulty is due to the possible damage caused by high radiation doses; therefore, material usable at room temperature and less sensitive to radiation doses have been found (for example, Ga and As).

The semiconductor detectors used in high energy physics are thin (thicknesses of 200–300 μm) and are composed of high purity crystalline (silicon) materials; however, material doped with impurities pentavalent or trivalent (with respect to the tetravalence of Si) are also used. The obtained signals are linear in the sense that the electric output signal is directly proportional to the deposited energy.

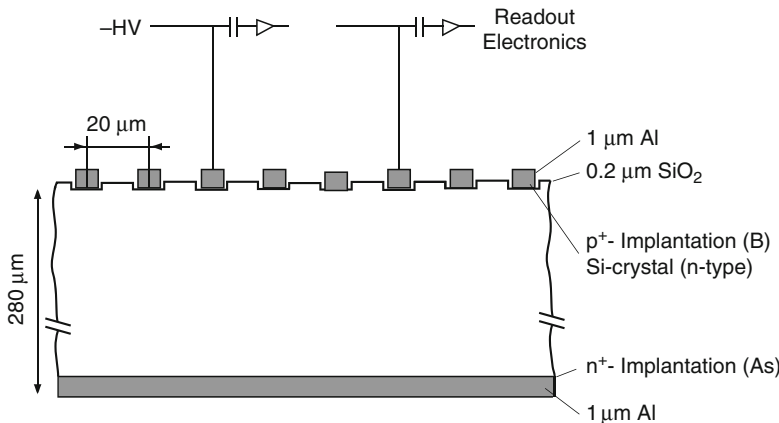


Fig. 2.14 Silicon microstrip detector scheme

In conclusion, the main characteristics of a semiconductor detector are:

1. Low energy necessary to create an electron-hole pair;
2. Linear response;
3. Presence of a dark current due to minority carriers of thermal type and to superficial contributions;
4. The signals must be preamplified with low noise charge amplifiers; the output signals must undergo proper shaping.

Figure 2.14 shows the scheme of a *microstrip detector*. It is composed of readout strips spaced by $20 \mu\text{m}$. The strips of p^+ type (i.e., constituted from a p type material with a high doping) with contacts in aluminum are implanted on n type silicon (with a $2,000 \Omega \text{ cm}$ resistivity). An electrode of n^+ type (n type material with high doping) is installed on the other side. The detector thickness is $\sim 300 \mu\text{m}$ and is operated with voltages of the order of 40 V.

For the detection of γ rays with energies of the order of MeV, the most used detector is that with Germanium ($Z_{Ge} = 32$) at the liquid nitrogen temperature. The dimension of a typical counter are $5 \text{ cm} \times 5 \text{ cm} \times 5 \text{ cm}$. They provide high detection efficiencies and excellent energy resolutions.

2.11 Cherenkov Counters

The electric field produced by an electric charge Ze moving with a speed $v = \beta c$ in a medium with refractive index n propagates with a speed $v_E = c/n$. If the speed of the particle is larger than that of the field, $v = \beta c > v_E = c/n$, one has a phenomenon similar to that of the generation of a shock wave.

The angle θ_c of the emitted radiation relative to the particle direction is $\cos \theta_c = (1/n\beta)$; the number of emitted photons per unit energy and per unit path length of a particle is

$$\frac{d^2N}{dE_\gamma dx} = \frac{\alpha Z^2}{\hbar c} \sin^2 \theta_c = \frac{\alpha^2 Z^2}{r_e m_e c^2} \left(1 - \frac{1}{\beta^2 n^2}\right) \xrightarrow{Z=1} 370 \sin^2 \theta_c \text{ eV}^{-1} \text{cm}^{-1} \quad (2.27)$$

where $(\alpha^2/r_e m_e c^2) = 370 \text{ eV}^{-1} \text{cm}^{-1}$, $Z = 1$, r_e = classical electron radius $= e^2/m_e c^2 = 2.82 \cdot 10^{-13} \text{ cm}$. The number of photons per unit wavelength is

$$\frac{d^2N}{d\lambda dx} = \frac{2\pi\alpha Z^2}{\lambda^2} \left(1 - \frac{1}{\beta^2 n^2}\right). \quad (2.28)$$

Note that the index of refraction is a function of the emitted photon energy, $n = n(E_\gamma)$. Remembering the relationship between energy and wavelength, $E = hc/\lambda$, one knows that the emitted photons with a wavelength between 300 and 600 nm are no more than 1/100 of the photons produced in a process of energy loss through ionization and excitation.

In a *threshold Cherenkov counter*, the total light emitted above threshold is collected. It gives a *yes/no* decision based on whether the particle speed is above or below threshold, $\beta_t = 1/n$. Instead, the *imaging Cherenkov counters* make use of the dependence of the fast particle speed β from the photon emission angle θ . These detectors make use of focusing lenses and pinholes to select the photons emitted at a certain angle. With such a detector, it is indeed possible to select, in a monochromatic particle beam, the light emitted by a certain type of particle, for example, π mesons. It is also possible to select another type of particle, for example, K mesons, by varying the counter gas pressure and therefore its index of refraction. In Cherenkov counters with a 4π geometry used in apparatuses covering the full solid angle, a gas with index of refraction $n = 1.0017$ (C_5F_{12}) has been used. Photons are optically focused with mirrors onto particular phototransducers, for example, wire chambers.

Some large underground water detectors are used as Cherenkov counters. In the Superkamiokande detector (see Chap. 12), about 20% of the external surface of the cylindrical vessel containing 50,000 t of water is covered with a large photomultiplier (PMT). This detector has obtained fundamental results on atmospheric and solar neutrino oscillations.

2.12 The Bubble Chamber

The bubble chamber is a detector that is no longer used. However, it was very important because it allowed one to visualize the interactions between particles and the production of new ones through photos. The bubble chamber allowed the visualization of trajectories of high energy particles exploiting the ionization

process; it therefore belonged to the ionization detector category. A bubble chamber contained a liquid that, during the passage of particles, was in a metastable condition. An example of this particular state could be water at a temperature of 110°C and at atmospheric pressure: water should boil, though it actually does not for a small fraction of a second.³ The liquid begins to boil where impurities are present, for example, at the edges of the vessel, and also around a group of negative and positive electric charges.

A fast charged particle that crosses a bubble chamber ionizes many atoms and molecules of the liquid. In each of these interactions, the fast charged particle loses a small part of its energy and is not deflected in an appreciable way. Along the path of the particle, free electrons (negative ions) and atoms without an electron (positive ions) are created around which the liquid begins to boil. This means that around groups of ions, little bubbles of vapor are formed that dimensionally increase until eventually they fill the whole chamber. If one takes a photo at the moment in which the little bubbles have a diameter of slightly less than a millimeter, the trajectory of the particles is visualized through a series of little bubbles.

To be able to again use the bubble chamber, one needs to increase the pressure (in the example of water at 110°C, the pressure could be brought to four atmospheres) to force the liquid to stop boiling. At the right moment, the pressure is again lowered (to one atmosphere) and the chamber is again ready. This moment must be synchronized because it must precede the arrival of fast charge particles by a few milliseconds.

A bubble chamber is usually surrounded by a big magnet that produces a strong magnetic field in the whole space of the chamber (typically $B = 2$ Tesla). The charged particles that cross the chamber are deflected by the magnetic field along a circular trajectory whose radius depends on the particle momentum. Then, analyzing the tracks, information can be obtained on the mass of the particles and on their momentum. Large bubble chambers have been used in experiments studying muon neutrinos; in this case, intense neutrino beams are needed in order to have a reasonable number of interactions.

Bubble chambers were built with operational liquids, for example, hydrogen, deuterium, neon plus hydrogen, helium and others. Hydrogen bubble chambers offer the advantage of allowing the study of collisions on protons that can be considered as free. The density of liquid hydrogen is low ($\rho \simeq 0.06 \text{ g cm}^{-3}$); therefore, the quantity of matter on the trajectory of every particle is small. The probability of interaction is low: well defined tracks can be seen, but interactions of γ rays are not observed. In a bubble chamber with heavy liquid, for example, a mixture of hydrogen and neon, there are many interactions of beam particles; besides, the probability of the interaction of γ rays is elevated (due to the neon high density and high atomic number).

³Water is actually not suited to be used as a liquid in a bubble chamber; it is only used here as an illustrative example.

Fig. 2.15 BEBC, the Big European Bubble Chamber, with a cylindric shape of 3.7 m diameter during its installation (the chamber is now in disuse). The main part is the cylindrical vessel visible at the top; the beam line was perpendicular to the cylinder axis (CERN archive photo)

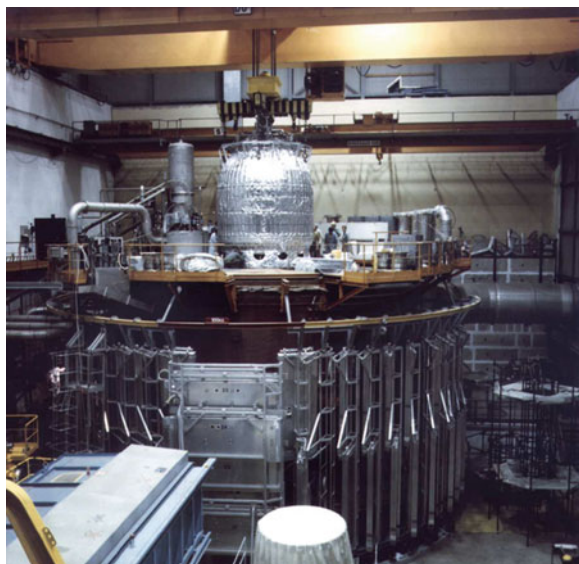


Figure 2.15 shows the Big European Bubble Chamber (BEBC) used at CERN in the 1970s until the end of 1983. A similar chamber was used at Fermilab until 1986. The bubble chamber, invented in 1952 by Glaser (Nobel laureate in 1960), played a crucial role from the 1960s to the 1980s. One of the reasons for its decline is the impossibility of building an “electronic” bubble chamber, that is, a chamber able to directly send signals to a computer. In the following chapters, we shall often use, for didactic purposes, photos produced by bubble chambers.

2.13 Electromagnetic and Hadronic Calorimeters

With an always increasing colliding energy of large accelerators (discussed in the next chapter), larger and more complex detectors have become even more important. In particular, the role of the *electromagnetic calorimeters*, *ECAL* and of the *hadronic calorimeters*, *HCAL* is becoming decisive. A *calorimeter* is a detector that absorbs all the kinetic energy of a particle and provides an electronic signal proportional to the deposited energy.

In a given medium, a γ ray and an electron of high energy produce an *electromagnetic cascade* through successive processes of e^+e^- pair production and bremsstrahlung. In a medium with high Z , such a cascade has limited longitudinal and transversal dimensions, as illustrated in Fig. 2.16a. An *electromagnetic calorimeter* measures the total energy produced through ionization (and excitation) due to e^+ , e^- , γ ; usually its longitudinal thickness is of 20–25 radiation lengths. Typical values of radiation lengths X_0 for some materials are listed in Table 2.5.

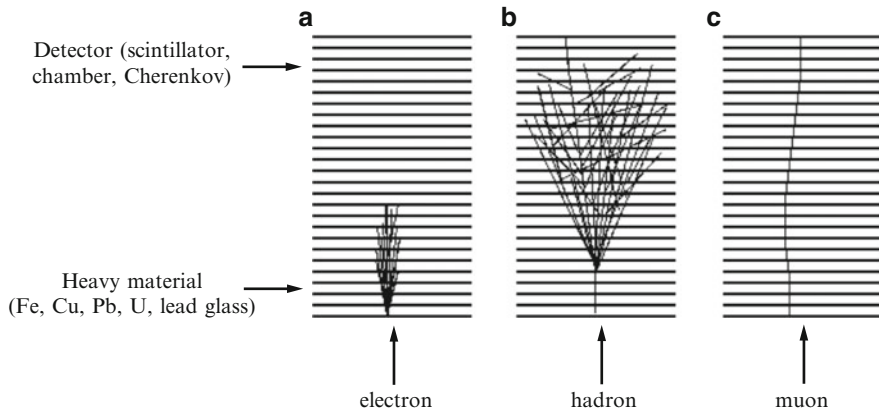


Fig. 2.16 Behavior (a) of an electromagnetic cascade, (b) of a hadronic and (c) of a muon when traversing a sampling calorimeter constituted of interleaved detector and absorber layers of heavy material. An ECAL measures the total energy deposited by the electrons/positrons that cross it. A HCAL measures the energy deposited by the charged hadrons. In both calorimeters, the muon behaves as a minimum ionizing particle and can be easily identified. In a multipurpose detector, an ECAL is usually installed first, followed by a HCAL, both with cylindrical symmetry with respect to the vacuum pipe where beams circulate

Table 2.5 Main characteristics of detectors and absorber materials used in ECAL and HCAL

Material		X_0 (cm)	λ_0 (cm)	ϵ (MeV)
Active detectors	NaI	2.6	41	12.5
	BGO	1.1	23	7
	Lead glass	2.36		15.8
Passive absorbers	Fe	1.7	17	28
	Pb	0.56	17	9.5
	U	0.32	10.5	9

X_0 radiation length, λ_0 interaction length, ϵ critical energy = energy to which energy loss through radiation is equal to that through ionization and excitation

The hadrons deposit energy in matter through a series of collisions due to the strong interaction and therefore through ionization/excitation from the produced charged hadrons (the primary strong interaction produces many π mesons which successively interact through the strong interaction). The hadronic cascade is wider and longer than that electromagnetic (see Fig. 2.16b), and therefore a *hadronic calorimeter* (HCAL) must have larger dimensions than the ECAL ones; typically, it has a thickness of six nuclear interaction lengths λ_0 . Some typical values of interaction lengths are given in Table 2.5.

However, there are strong fluctuations in the hadronic cascade because of various effects. The π^0 mesons immediately decay in 2γ , producing an electromagnetic cascade in which the energy is deposited in a narrow space. The π^\pm mesons

decay instead in $\mu\nu$; the neutrino interacts so little that they always leave without interacting in the hadronic calorimeter. This causes missing energy (about 30%) and momentum. For the most part, the muons also leave the hadronic calorimeter, as illustrated in Fig. 2.16c; the muons produce a signal at the minimum of ionization in both calorimeters and can be sometimes measured in specific muon chambers installed in the most external layers of the detector.

The calorimeters are divided into *homogeneous* and *sampling* calorimeters. The first ones are made of only one material, for example, lead glass in the case of electromagnetic calorimeters. The second calorimeters are made of active detectors (e.g., scintillation counters) interleaved with absorber layers (e.g., lead in electromagnetic calorimeters and iron in hadronic calorimeters) (see Fig. 2.16 and Table 2.5). The best segmentations are usually half a radiation length for ECAL and 0.25–0.5 interaction lengths for HCAL. The homogeneous calorimeters usually have better performances with respect to the sampling ones, though they are more expensive. Practically, all hadronic calorimeters are sampling calorimeters.

The important quantity for the energy resolution is the number N of track segments (N cm in a homogeneous calorimeter, N samplings in a sampling calorimeter). The energy E to be measured is the energy of the primary particle that induces the cascade and is indeed proportional to the number of secondary particles produced (particularly at the maximum, see (2.26)). The number of measured secondary particles is proportional to the number N of track segments and the energy resolution therefore has a percentage error, that is,

$$\frac{\sigma_E}{E} \simeq \frac{\Delta E}{E} \approx \frac{\Delta N}{N} \simeq \frac{\sqrt{N}}{N} \approx \frac{1}{\sqrt{E}}. \quad (2.29)$$

Typical energy resolutions for ECAL and sampling HCAL (with many individual channels) are respectively about $\Delta E/E \simeq 0.2/\sqrt{E}$ and $1.0/\sqrt{E}$ with E in GeV.

In experiments at large accelerators (as we shall see in Chap. 9), electrons/positrons are identified (and energies measured) in ECAL and hadrons in HCAL.

Chapter 3

Particle Accelerators and Particle Detection

3.1 Why Do We Need Accelerators?

Our knowledge regarding the structure of matter has been reached using optical microscopes, electronic microscopes, radioactive sources and, finally, particle accelerators. The possibility of continuously investigating the subatomic world is related to the construction of consistently larger and more sophisticated accelerators.

One reason for which the use of particles accelerated to high energy is necessary is connected to the wave-particle duality and to the uncertainty principle. In the framework of wave-particle duality, a particle exhibits wave-like properties and a wave exhibits particle-like properties. A wave is characterized by its wavelength; a particle is characterized by its energy or its momentum. The larger the particle energy, the smaller the associated wavelength. Quantitatively, the relation between the wavelength λ associated to a particle and the momentum p of the particle is given by the de Broglie relation $\lambda = h/p = 2\pi\hbar c/pc$, where h is Planck's constant, $\hbar = h/2\pi$. Numerically, one has (see Appendix 5)

$$\lambda(\text{cm}) = \frac{6.626 \cdot 10^{-27}(\text{erg s})}{p} = \frac{1.24 \cdot 10^{-10}(\text{MeV s})}{p (\text{MeV/c})} \quad (3.1)$$

that is $\lambda(\text{fm}) = 1.24/p$ (GeV/c). Sometimes, $\lambda = \lambda/2\pi = \hbar/p$ is used.

Intuitively, the wave-particle can be seen as a probability “cloud” with dimension comparable to the associated wavelength. In this representation, the particle is not an object with the dimension of the cloud: the particle is intrinsically smaller and it can be found in any point within the cloud. The cloud volume can be reduced by decreasing the wavelength which is equivalent to increasing the particle momentum (and therefore its energy). In conclusion, the larger the particle energy, the smaller associated wavelength is. Consequently, it is possible to study smaller objects possessing finer details. At high energies, the wave-like aspects can often be ignored; the particle can be considered to be a little ball (or a “spinning top” if its spin is considered). In this case, accelerators are comparable to large microscopes.

Table 3.1 Orders of magnitude of the minimum energy needed and tools used to explore distances of the order of Δx

Δx (cm)	E	Tool
10^{-5}	2 eV	Microscopes
10^{-8}	2 keV	X rays
10^{-11}	$2 \text{ MeV} \simeq 4m_e$	γ rays
10^{-14}	$2 \text{ GeV} \simeq 2m_p$	Accelerators
10^{-16}	$200 \text{ GeV} \simeq 2m_{W,Z}$	Accelerators
10^{-17}	2 TeV	Accelerators



Fig. 3.1 Illustration of a collision in the center-of-mass (c.m.) system and in the laboratory system (Lab.)

The *uncertainty principle* states that position x (with uncertainty Δx) and momentum p_x (with uncertainty Δp_x) cannot simultaneously be known to a precision better than $\Delta x \Delta p_x \simeq \hbar/2$, where Δx , Δp_x are root mean squared errors (standard deviations). A relation for the energy is obtained by multiplying c , $\Delta x \Delta E \simeq \hbar c/2$, which gives numerically, $\Delta E(\text{MeV}) \simeq 1.973 \cdot 10^{-11}(\text{MeV cm}) / 2\Delta x(\text{cm})$. To explore dimensions of the order of Δx , an energy of $E(\text{MeV}) \simeq 2\Delta E(\text{MeV}) \simeq \hbar c/\Delta x \simeq 1.973 \cdot 10^{-11}(\text{MeV cm}) / \Delta x(\text{cm})$ is needed. The orders of magnitude of the minimum energy needed to explore dimensions of the order of Δx are summarized in Table 3.1.

The second reason why particle accelerators are built is related to the “creation of particles.” This is a process of converting energy into mass based on the Einstein equation $E = mc^2$: the energy available in a collision between two particles can be transformed into the mass of the created particles. This creation occurs according to certain rules, obeying precise conservation laws. Typical particle masses are also listed in Table 3.1. In particular, the mass of 100 GeV approximately corresponds to the heaviest particle observed thus far (W^+ , W^- and Z^0). In March of 2010, LHC successfully started at a center-of-mass (c.m.) energy of 7 TeV (the world maximum available c.m. energy); the design luminosity and the maximum energy of 14 TeV should be reached within 2014.

The creation process allows one to study the characteristics of new and unstable particles; many particles are indeed unstable, with a lifetime in the range from 10^{-23} (for the so called “strong resonances”) to 10^3 s (for the neutrons). Besides, some stable particles, for example, the neutrinos, are produced through the decays of unstable particles.

Let us consider a simple reaction in which a new particle is produced:

$$pp \rightarrow pp\pi^0. \quad (3.2)$$

In this reaction, the electric charge and the baryonic number are conserved. We now consider the same process in the lab system (lab) and in the center-of-mass system (see Fig. 3.1).

3.1.1 The Center-of-Mass (c.m.) System

In the c.m. system, the four-momenta¹ of the two particles (1 and 2) are denoted as $p_1^* = (E_1^*, \mathbf{p})$, $p_2^* = (E_2^*, -\mathbf{p})$. It should be recalled that a four-vector squared is a relativistic invariant; in the four-momentum case, the invariant quantity is the rest mass of the particle (e.g., $p_1^{*2} = E_1^{*2} - \mathbf{p}_1^2 = m_1^2$). The squared sum of the two particles four-momenta is also a relativistic invariant representing the total energy squared denoted as s ; in the c.m. system, and with $\hbar = c = 1$, one has

$$s = (p_1^* + p_2^*)^2 = (E_1^* + E_2^*, \mathbf{p} - \mathbf{p})^2, \quad (3.3)$$

from which one can write

$$\sqrt{s} = E_{cm} = (E_1^* + E_2^*). \quad (3.4)$$

For a collider (Sect. 3.3) with identical colliding particles, as for the process (3.2), one has $E_1^* = E_2^*$ and the energy of each particle is equal to the rest mass plus the c.m. kinetic energy: $E_1^* = m_1 + T^{c.m.}$. In this case, Eq. 3.4 becomes ($m_1 = m_2 = m_p$)

$$\sqrt{s} = E_{cm} = 2T^{c.m.} + 2m_p. \quad (3.5)$$

The reaction (3.2) is only possible if the energy available in the final state is at least the rest mass of the three present particles, that is,

$$s_{thr} = (2m_p + m_{\pi^0})^2. \quad (3.6)$$

It is evident from (3.5) that the *minimum* kinetic energy (the so-called *threshold energy*) needed to form the π^0 in the c.m. is equal to

$$\sqrt{s_{thr}} = (2m_p + m_{\pi^0}) = 2T_{thr}^{c.m.} + 2m_p, \quad (3.7a)$$

from which

$$T_{thr}^{c.m.} = m_{\pi^0}/2 = 67.5 \text{ MeV}. \quad (3.7b)$$

3.1.2 The Laboratory System

We now denote $p_1 = (E_1, \mathbf{p}_1)$ and $p_2 = (m_2, 0)$ the four-momenta of the particles in the laboratory system in which particle one is moving and particle two is at rest.

¹Bold characters are used to indicate vectors.

Since a four-vector squared is a relativistic invariant, the total energy calculated in (3.3) must be equal to that computed in the laboratory system, that is,

$$s = [(E_1 + m_2)^2 - (\mathbf{p}_1 + 0)^2] = m_1^2 + m_2^2 + 2E_1m_2. \quad (3.8)$$

Also, in the laboratory system, the energy can be divided into a mass term and a kinetic energy term, that is, $E_1 = T^{lab} + m_1$. We can write (3.8) as (assuming again that particles 1 and 2 are protons, $m_1 = m_2 = m_p$)

$$s = (m_1 + m_2)^2 + 2T^{lab}m_2 = 4m_p^2 + 2T^{lab}m_p. \quad (3.9)$$

The kinetic energy necessary to form the state (3.2) must be larger than the process threshold (3.6)

$$T_{thr}^{lab} = (s_{thr} - 4m_p^2) / 2m_p. \quad (3.10a)$$

Using (3.6), we can calculate, in the laboratory system, the kinetic energy of particle one in order to satisfy the condition on the threshold energy for the production process of (3.2). The threshold kinetic energy ($m_p = 938 \text{ MeV}$, $m_\pi^0 = 135 \text{ MeV}$) is

$$T_{thr}^{lab} = [(2m_p + m_{\pi^0})^2 - 4m_p^2] / 2m_p = 280 \text{ MeV}, \quad (3.10b)$$

which can be compared with the kinetic energy of 67.5 MeV needed in the c.m. system (see Problem 3.5).

3.1.3 Fixed Target Accelerator and Collider

The above example is not only didactic, but it corresponds to the two experimental methods used to produce new particles: those with *fixed target accelerators* in which a particle is accelerated and the target is at rest in the laboratory system; and those with *colliders*, namely, accelerating devices in which both particles (in general, electrons and positrons, or protons and protons, or protons and antiprotons) collide with equal momenta of opposite sign.

The most important parameter of an accelerator is its *energy*: the larger the energy, the better the possibility is to investigate phenomena at smaller dimensions; besides, a larger energy allows the production of more massive particles. Another important parameter is the beam *intensity*: the larger the number of accelerated particles, the larger the number of collisions that can be observed, and consequently, the measurements that can be performed are more precise. Moreover, rarer phenomena can be searched for.

The construction and operation costs of these large accelerators has become so high that it can no longer be sustained by a single university or state. Therefore, large laboratories of international dimensions have been created. A well known example is the CERN, the European Centre for Elementary Particles Physics near

Geneva (Switzerland) which has actually become a world laboratory. The number of accelerators operating at the “frontiers” of high energy and high intensity is inevitably always growing smaller.

The increase in energy has been obtained not only by increasing the accelerator dimensions, but also by inventing new acceleration methods. The proton or electron energies in accelerators have increased by about a factor of ten every 5 years since 1930. Every “jump” in energy was realized thanks to the application of some new idea. The electrostatic accelerators allowed one to obtain protons with energies in the lab system from 1 to 10 MeV, synchrocyclotrons up to 700 MeV, protonsynchrotrons up to 1,000 GeV, and the storage rings allowed one to reach energies up to 2,000 GeV ($=2\text{TeV}$) in the c.m. system. At LHC, 14 TeV will be reached. It should be recalled that the energies involved in nuclear physics are of the order of the MeV, while high energy physics deals with energies of the order of at least the GeV.

The incident particles are characterized by their energy rather than their velocity because in high energy physics, the relativistic effects are dominant (remember $E = \gamma m_0 c^2$).

3.2 Linear and Circular Accelerators

Electrically charged particles (usually protons or electrons) are accelerated through electric and magnetic fields which may be constant or varying in time and space. An accelerator is schematically constituted by an *ion source*, an *accelerating field* and a *guide field* that forces the particles to move on well defined orbits. The acceleration takes place in high vacuum in order to reduce the collisions with molecules of the residual gas and therefore to minimize energy loss.

The ion source can be schematized as a small cavity at low pressure where a discharge ionizes in continuation gaseous hydrogen. Electric fields then carry the electrons or the protons towards the next accelerator.

Accelerators can be classified as *linear* or *circular*. In linear accelerators, particles are accelerated in a straight line by electric fields. In circular accelerators, a magnetic field forces the particles to move on circular orbits; the acceleration is performed through radio-frequency electric fields (or through increasing magnetic fields). Let us briefly illustrate the principle of accelerator operation.

3.2.1 Linear Accelerators

Low energy **proton** linear accelerators consist of a set of cylindrical electrodes connected to either side of an oscillating voltage with constant frequency. As shown in Fig. 3.2, the protons move from left to right inside a structure made of successive tubes. Inside the tubes, the protons are in a field-free region and therefore move with a constant velocity while they are accelerated by an electric field between two

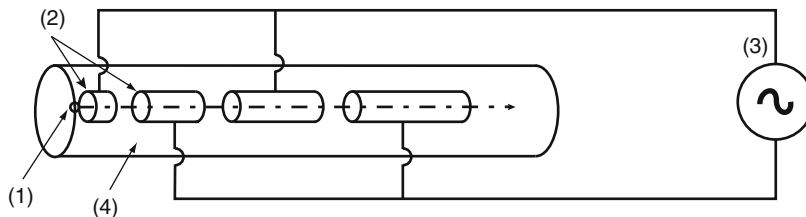


Fig. 3.2 Layout of a linear proton accelerator. The various components indicated are (1) ion source, (2) accelerating cylindrical electrodes, (3) radio-frequency and (4) vacuum pipe

neighboring tubes. If the tube length is chosen in such a way that the time needed to cross it is equal to half the oscillator period, the protons are accelerated a second time when passing from one tube to the next one, and so forth. The length of the tubes must therefore increase in order to take into account the increase in proton velocity.

In the case of an **electron** accelerator, the electrodes are all of the same length because the electrons, even of low energy, travel at the speed of light. The acceleration is performed by the electromagnetic wave traveling along the axis of the pipe with a phase velocity equal to the electron velocity. Only electrons in phase with the accelerator field (a *bunch* with a transverse dimension of a few centimeters and a length of some decimeters) are *accelerated*. We can imagine that the electron bunch rides the crest of the electromagnetic wave produced by the radio-frequency system.

The electron or proton beam produced by an electrostatic accelerator is constant in time. In linear accelerators (and in others that will be described in the following), accelerated particles instead arrive in *bunches*.

3.2.2 Circular Accelerators

Synchrotrons (schematized in Fig. 3.3) have supplanted other types of circular accelerators such as the *cyclotrons* and *synchrocyclotrons*. In synchrotrons, the use of big and expensive magnets is avoided and particles are accelerated through electric fields on an orbit of constant radius. The magnetic field necessary to deflect the particles is produced by a set of magnets placed along the circumference. Before being injected in the orbit, the protons are preaccelerated with an electrostatic accelerator followed by a linear accelerator. The particles are accelerated through radio-frequency electric fields (RF) in resonant cavities placed along the accelerator circumference; the particles are forced to stay on the same orbit thanks to the contemporaneous increasing magnetic field B . This allows the “bunches” of particles to move inside a large torus (the synchrotron *vacuum chamber*).

The *electron-synchrotrons* nearly have a constant RF since the e^- travel at a constant speed, approaching the light speed in vacuum.

Fig. 3.3 Layout of a proton synchrotron. The preaccelerator is an electrostatic accelerator (1) followed by a linear accelerator (2). In the main ring one finds (3) the magnets, (4) an accelerating cavity and (5) the “straight sections” in which (6) the targets are installed, from which (7) the secondary beam lines are produced for the experiments

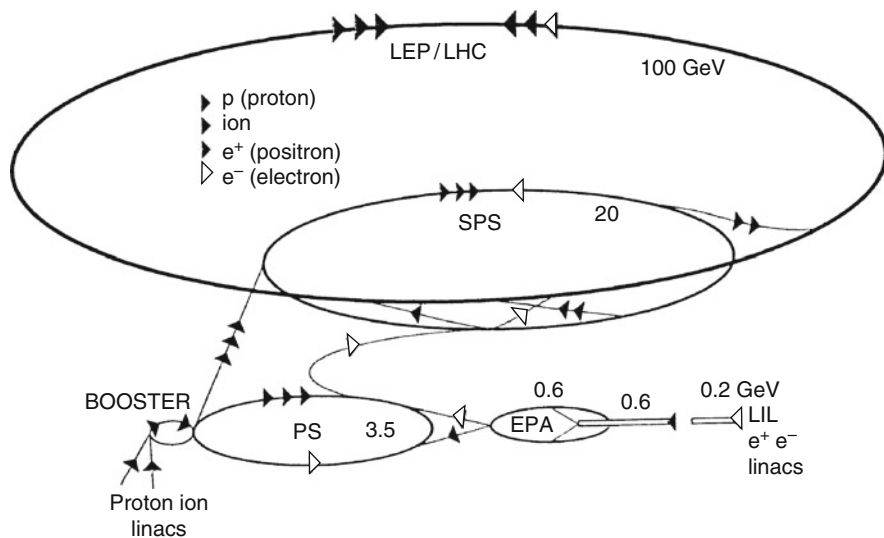
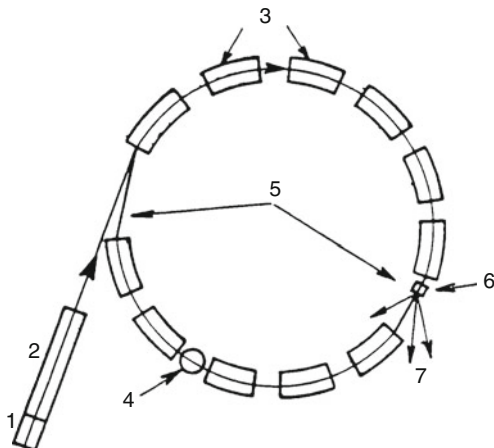


Fig. 3.4 Layout of the CERN accelerator complex in use with the e^+e^- LEP and pp ($E_{cm} = 7$ TeV) LHC colliders; the maximum energy obtained per beam is indicated for the various accelerators. (When the accelerator complex is used for the pp LHC, every accelerator energy per beam is higher). The SPS has also been used as a $p\bar{p}$ collider

All accelerators currently in operation with energies larger than the GeV are synchrotrons (for protons or electrons) or linear accelerators for electrons. These accelerators can be defined as *conventional*. More “advanced” accelerators use superconducting magnets, superconducting RF cavities or new methods of acceleration. A modern high energy accelerator is made of a succession of accelerators. Every accelerator increases the particle energy by about an order of magnitude (Fig. 3.4).

3.3 Colliders and Luminosity

In *storage rings (colliders, accelerators with intersecting beams)* beams of particles circulating in opposite directions are accumulated and then deflected in order to make them collide in one or more well defined interaction points. To obtain high energies, it is essential to use a circular accelerator (*collider*). In collisions produced with storage rings the laboratory system is almost coincident with the center-of-mass system; therefore, the energy in the c.m. system is equal to the sum of the energies of the two beams (for beams of particles with identical mass). For example, in the CERN proton-antiproton collider, collisions between antiprotons of 315 GeV with protons of 315 GeV were produced. It was equivalent, in terms of collision energy, to an accelerator of antiprotons of 201,000 GeV sent against protons at rest (verified using (3.10)). Such an accelerator would be currently impossible to build. Due to relativistic effects, an even better advantage is obtained when using electrons. Particle accelerators represent one of the more direct verifications of the validity of the special relativity theory: if nonrelativistic formulas were used to design them, they would not work.

The colliders have the disadvantage, with respect to the fixed target accelerators, of being less versatile and capable of producing a smaller number of interactions per unit of time. A collider *luminosity* \mathcal{L} is defined as the number that, multiplied by the total cross-section of a given process σ , gives the total number N of collisions per unit of time, that is,

$$N = \mathcal{L}\sigma. \quad (3.11a)$$

The luminosity can be expressed in terms of the collider parameters. Let us consider an accelerator with radius R ; number of particles per bunch circulating in one direction (i.e., protons or electrons) n_p and number of circulating bunches N_p ; number of particles per bunch circulating in the opposite direction (in most cases, antiprotons or positrons) n_a and the number of circulating bunches N_a ; average transverse radius of each bunch r . Then,

$$\mathcal{L} = \frac{fn_p n_a N_p N_a G}{4\pi r^2}, \quad (3.11b)$$

f is the beam revolution frequency $f = 1/\tau$, τ is the period $\tau = 2\pi R/c$. The factor G (usually ~ 1) takes into account the finite length of a bunch.

The first proton storage ring (up to 31 GeV per beam) was the ISR at CERN (1970s) where luminosities of $2 \cdot 10^{31} \text{ cm}^{-2} \text{ s}^{-1}$ have been reached. Since the total proton-proton cross-section at the ISR energy is $5 \cdot 10^{-26} \text{ cm}^2$, about 10^6 interactions per second were produced in every interaction region. Most of the events produced in the interactions were not very interesting (the so-called *minimum bias* events). It was therefore needed to select potentially interesting events (as for the experiments at successive, more advanced and more complicated accelerators). This is mainly done with an electronic logic of the data acquisition system (the *trigger*).

At the CERN and Fermilab proton-antiproton colliders, luminosities of the order of $(6 - 10) \cdot 10^{30} \text{ cm}^{-2}\text{s}^{-1}$ have been obtained. The Fermilab Tevatron, after some technical improvements, has reached luminosities about ten times larger. The PEP2 and KEKB e^+e^- colliders, in operation since 2000, and the pp LHC collider have a design luminosity of $10^{33}-10^{34} \text{ cm}^{-2}\text{s}^{-1}$.

3.3.1 Example: the CERN Accelerator Complex

A high energy accelerator is made of a succession of accelerators, each increasing the accelerated particle energy by roughly an order of magnitude. The SPS complex at CERN is composed of five consecutive accelerators. Actually, the CERN system is a complex of versatile accelerators that can be used for various purposes.

At LEP (Large Electron Positron Collider, Fig. 3.4), e^+e^- collisions were produced at an energy in the c.m. of about 91 GeV, corresponding to the mass of the Z^0 boson, one of the weak force mediators; in a second phase (LEP2), the c.m. energy was raised to 209 GeV.

To operate such an accelerator, it was necessary to produce adequate bunches of electrons and positrons, and to accelerate them at the various requested energies. In the first phase, a linear accelerator (LIL), designed to accelerate electrons and positrons (up to 200 MeV in its first part to produce e^+ ; up to 600 MeV in the second part) and the “Electron Positron Accumulator,” (EPA) (600 MeV) were built. In a second phase, the existing accelerators were modified, for example, the PS and SPS, in order to make them able to accelerate electrons and positrons in opposite directions (up to 3.5 GeV for the PS, up to 20 GeV for the SPS). In the third phase, the new large ring measuring 27 km in circumference was put into operation; at LEP, usually four “trains,” each consisting of four bunches of electrons and four positrons were accelerated. After acceleration, the particle bunches were circulating in the collider for a few hours. The particle bunches were deflected in eight regions; in four regions, they were kept vertically separated; in the other four regions, they were brought into collisions. Before making them collide, the beams were focused in order to reduce the transverse dimensions as much as possible in order to obtain the highest possible luminosity. Large detectors were installed around each of the four interaction points, allowing for the detailed studies of the positron-electron collisions (Chap. 9).

To reduce the energy loss through bremsstrahlung, the LEP magnetic field was very low, 0.2–0.4 Tesla. Such a field was obtained with low cost special magnets made of iron and concrete. Normal accelerating radio-frequencies were used in the first phase, while superconducting RF cavities were used in the LEP2 phase which reached c.m. energies of 130–209 GeV.

Starting in 2000, the LEP was dismantled in order to use the tunnel for the LHC (Large Hadron Collider) installation. The LHC is designed to study pp and *nucleus-nucleus* collisions. The LHC uses superconducting magnets with a magnetic field of 8.3 T. For the time being, protons are accelerated up to 3.5 TeV with a total c.m.

energy of 7 TeV. In the future, when a completely safe operation will be insured, the LHC will accelerate protons up to the design value of 7 TeV, reaching an energy in the c.m. of 14 TeV. The luminosity should reach values up to $10^{34} \text{ cm}^{-2} \text{ s}^{-1}$. The main reason for such a collider is to “understand the origin of the particle masses” (Chap. 11), that is, the search for the Higgs boson and possibly other new particles. Besides, at the LHC, heavy ions can be accelerated ($Pb + Pb$ collisions) with the main purpose of searching for and studying quark-gluon plasma.

High energy physics has contributed by bringing together scientists from around the world. Even during the Cold War, scientists from both sides collaborated in European, Russian and American research centers. As already mentioned, this type of research is today extremely expensive, and no country could afford the management of completely national laboratories or experiments. Besides the CERN European laboratory, other large accelerator complexes are:

- The Fermilab accelerators in Batavia, Illinois, USA. In particular, the Tevatron is a proton synchrotron with superconducting magnets which accelerates protons and antiprotons up to 1 TeV (hence the name)
- The SLAC accelerator complex in Stanford, California. The main accelerator is a 2 miles (about 3.2 km) long linear accelerator that can accelerate e^+ and e^- beams up to 50 GeV. The laboratory is now converting the original linear accelerator to a light source facility: the Linac Coherent Light Source (LCLS) is a free electron laser facility which can deliver extremely intense X-ray radiation for research in a number of areas. It achieved the first lasing in April 2009
- The Brookhaven National Laboratory on Long Island near New York
- The DESY laboratory in Hamburg where a new light source facility, the European X-ray free electron laser (European XFEL), is being built
- The Institute for High Energy Physics (IHEP) in Protvino, Serpukhov, Moscow region
- The Japanese laboratory KEK
- The INFN National Frascati Laboratory, close to Rome, Italy

3.4 Conversion of Energy into Mass

In a collision of a high energy proton with a proton at rest, a fraction of the available energy may be transformed into mass (Sect. 3.1); new particles can therefore be produced, most of them being unstable. In every reaction, besides the electric charge, other quantum numbers (which will be described later), for example, the baryonic number, the strong isospin, the leptonic numbers, etc., must be conserved. See, for instance, Problems 3.6 and 3.7, for the discovery of the antiproton. Examples of reactions due to the strong interaction are:

$$\left\{ \begin{array}{l} pp \rightarrow pp\pi^+\pi^- \\ pn \rightarrow pp\pi^- + \text{neutral particles} \\ pp \rightarrow pp\bar{p}p + \text{neutral particles, etc.} \end{array} \right. \quad (3.12)$$

Similar reactions due to the electromagnetic interaction, followed by the strong one, are:

$$\begin{cases} e^- p \rightarrow e^- p \pi^+ \pi^- \pi^0 \\ e^- p \rightarrow e^- n \pi^+ \\ \gamma n \rightarrow \pi^- p \\ e^+ e^- \rightarrow \pi^+ \pi^- \pi^0, \text{etc.} \end{cases} \quad (3.13)$$

For the weak interaction, one has, for example, $\nu_\mu p \rightarrow \mu^- p \pi^+$.

3.4.1 Use of Fixed Target Accelerators

We shall now describe how a proton beam may be used in a fixed target experiment. At the end of the acceleration cycle, the accelerated protons are extracted from the accelerator: they constitute the primary beam which is sent onto a target, for example, a beryllium cylinder (see Fig. 3.5). In the collision of a proton with a beryllium nucleus, various types of particles are produced, some of them with a short or very short lifetime. Secondary beams can be produced with long lifetime particles emitted at a certain angle, as illustrated in Fig. 3.5b. The target acts as a “source;” magnetic quadrupoles act as focusing magnetic lenses. Magnetic dipoles have the same function as optical prisms, separating by “color” (in momentum), thus allowing one to select monoenergetic particle beams.

With 450 GeV incident protons, about ten charged and five neutral particles are produced on average in one collision. Because of relativistic effects, most of these particles are preferably emitted in a small cone in the forward direction and each transports a fraction of the incident proton momentum. With protons of 25–30 GeV (as those coming from the PS of CERN and from the AGS of Brookhaven), the mean number of charged particles produced (the mean *charged multiplicity*) is much lower. Such particles have an average momentum of the order of a few GeV and are produced in a larger angular cone.

A set of “collimators” is used to define the solid angle and the beam monochromaticity. Such a beam is monoenergetic, though it contains particles of different mass (e.g., electrons, mesons, protons, etc.). It is possible to obtain beams containing a single type of particle performing a separation in mass on the monoenergetic beam using an *electrostatic separator*, that is, an apparatus that produces an electric field besides the magnetic one.

It is important that secondary particle beams have high intensity and relatively long temporal duration (a few seconds for every acceleration cycle) to be profitably used in experiments with counters and electronic devices. When these secondary beams were used with bubble chambers, they had to instead have low intensity (10–20 particles) and brief temporal duration (maximum of a few milliseconds). The lifetime of the particles of the secondary beams must be sufficiently long in order to travel tens or hundreds of meters.

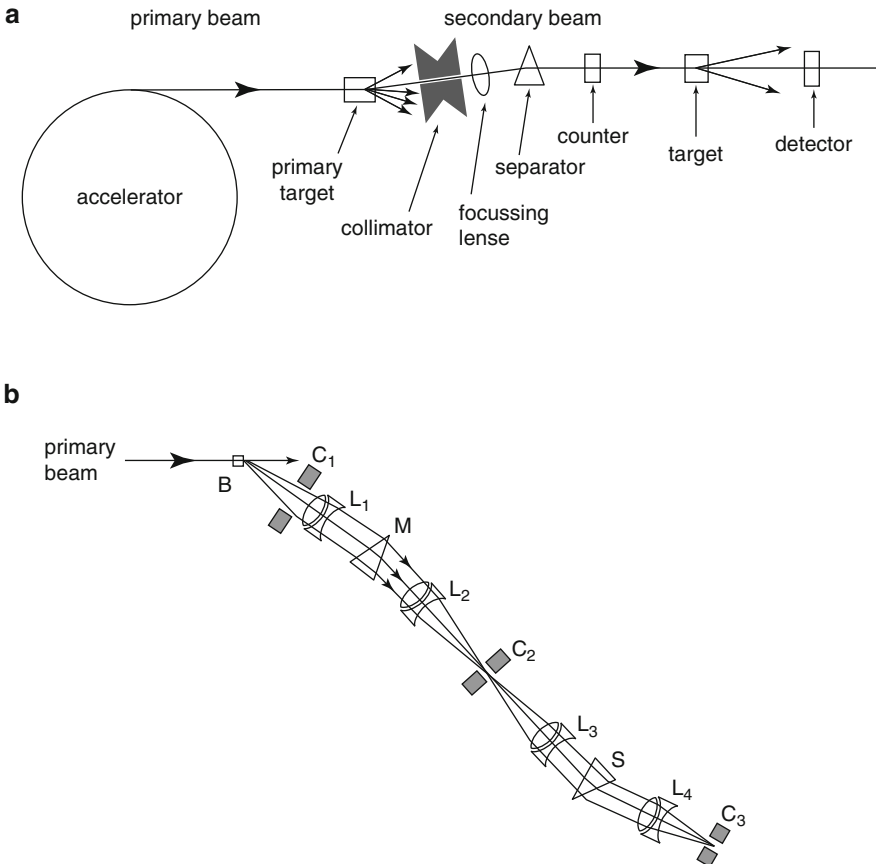


Fig. 3.5 (a) Layout of a fixed target experiment at a proton synchrotron: once accelerated, the protons are extracted in order to form the primary beam. The primary beam is then sent onto a target where many new hadrons are produced in the collision. The electrically charged hadrons of interest are collimated, focused and separated in momentum. In this way, one or more secondary beams are obtained: the one sketched here was used for a measurement of total hadron-hadron cross-sections. (b) Optical layout of a secondary beam. C_1, C_2, C_3 are collimators; L_1, L_2, L_3 , and L_4 are quadrupole lenses (magnetic quadrupoles); M, S are dipolar magnets

In the following paragraphs, the technique of a time-of-flight system in a magnetic spectrometer and the method used to measure the mass composition of a secondary beam will be introduced; the procedure for recognizing particles produced in interactions in a bubble chamber will also be presented.

The layout shown in Fig. 3.5 is valid for any fixed target experiment. In proton-antiproton storage rings, the two beams travel in almost circular orbits in opposite directions and are deflected in order to make them intersect in one or more interaction points. Collisions occur between protons and antiprotons moving in

opposite directions. In this case, it is not possible to directly measure the number of particles before they interact. Instead, the number of collisions per unit of time can be measured thanks to a system of detectors that surrounds the interaction zone. These techniques will be discussed later. For example, in Chap. 9, electron-positron interactions will be reviewed.

3.4.2 Baryonic Number Conservation

The proton and the particles that decay into a final state containing a proton are called *baryons*. In terms of subconstituents (Chap. 7), a baryon is formed by three quarks. The *baryonic number* +1 is attributed to baryons. The antifermions that contain a \bar{p} in the final state of the decay chain are *antibaryons*; they have the baryonic number equal to −1. All the other particles have a baryonic number equal to zero. It has been verified that until now, the total baryonic number is conserved in any reactions and decays. A good example comes from the Λ^0 decay: $\Lambda^0 \rightarrow p\pi^-$. The total baryonic number is +1 before the decay (since the Λ^0 is made of three quarks) and +1 in the final state (after the decay): the baryonic number conservation is satisfied and the reaction is possible, at least as long as this conservation law is concerned.

The proton is the lightest known baryon. Due to the baryonic number conservation, the proton should not decay and therefore should be rigorously stable. However, Grand Unified theories (GUT) of the interactions (Chap. 13) foresee the possibility of the proton decay, and therefore the violation of the baryon number conservation. Until now, no reliable evidence for proton decay has been found; the measured proton lifetime is much longer than the age of the Universe.

3.5 Particle Production in a Secondary Beam

3.5.1 Time-of-Flight Spectrometer

Charged particles in a secondary beam may be identified using a time-of-flight system in a magnetic spectrometer (see Fig. 3.6). The electrically charged particles produced in proton-proton collisions and emitted at a given angle are counted by the counter C_1 and separated in momentum by the magnet M . The magnet M acts on charged particles as an optical prism acts on light, i.e., by deflecting the particles of an angle β . In the case of light, the angle β depends on the wavelength of the light (the prism separates the light in its various colors); in the case of particles with electric charge q and momentum p , the angle β depends on p/q . The particles with a given momentum selected by the magnet reach the counter C_2 . The distance $C_1MC_2 = \ell$ and the time t employed by the particles to go from

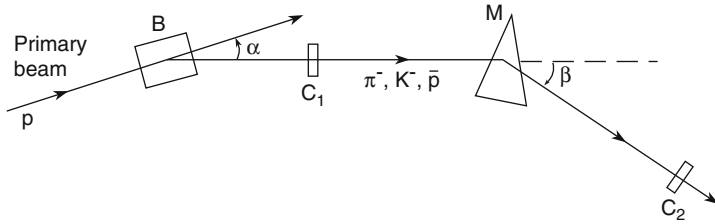


Fig. 3.6 A primary proton beam interacts with the neutrons and protons of the target B; the charged particles emitted at an angle α are counted with the counter C_1 , separated in momentum with the magnet M and again counted with the counter C_2 . The time used by every particle to travel the distance $\ell = C_1 M C_2$ is measured. (In real experiments, it is necessary to add collimators, quadrupole lenses and a first stage momentum separation)

C_1 to C_2 are measured; the measurements of p, ℓ, t allow one to determine the mass m . Nonrelativistically, one has

$$\begin{cases} p = mv \\ t = \ell/v \end{cases} \quad (3.14)$$

from which

$$m = p/v = pt/\ell \quad \rightarrow \quad t = m\ell/p. \quad (3.15)$$

With a given momentum p and a given distance ℓ , the time of flight t between C_1 and C_2 only depends on the particle mass which can therefore be obtained from the measurement of t . Practically, the particles have a very high velocity, comparable to the light velocity; it is therefore necessary to modify the first equation of (3.14) according to the special relativity formulas. Therefore, the momentum becomes $p = mv\gamma$, $\beta = v/c = \ell/tc$ and one has

$$m = \frac{p}{v\gamma} = \frac{pt}{\ell} \sqrt{1 - \frac{\ell^2}{t^2 c^2}} \rightarrow t = \frac{\ell}{p} \sqrt{(m^2 + p^2/c^2)}. \quad (3.16)$$

The time needed to cover the distance ℓ with respect to the time needed to cover the same distance by a particle traveling at the light speed is

$$\Delta t = \frac{\ell}{v} - \frac{\ell}{c} = \frac{\ell}{c} \left(\frac{1}{\beta} - 1 \right) = \frac{\ell}{c} \left(\frac{\sqrt{1 + \eta^2}}{\eta} - 1 \right) \quad (3.17)$$

where $\eta = p/mc$ ($\Rightarrow p/m$ if one sets $c = 1$). Indeed,

$$\beta = \frac{v}{c} = \frac{m_0 v \gamma c}{m_0 c^2} = \frac{pc}{E} = \frac{pc}{\sqrt{p^2 c^2 + m^2 c^4}} = \frac{p/mc}{\sqrt{1 + p^2/m^2 c^2}} = \frac{\eta}{\sqrt{1 + \eta^2}}. \quad (3.18)$$

Numerical example. Let us assume that the beam analyzed by the magnet M contains positive electrons ($m_{e^+} = 0.911 \cdot 10^{-27} g = 0.511 \text{ MeV}$), π^+ mesons ($m_{\pi^+} = 139.6 \text{ MeV} = 273 m_e$), K^+ ($m_{K^+} = 493.7 \text{ MeV} = 966 m_e$) and protons ($m_p = 938.3 \text{ MeV} = 1,836 m_e$) in equal proportions. Suppose also that the momentum of these particles is $p = 1 \text{ GeV}/c$ and that $\ell = C_1 MC_2 = 10 \text{ m}$. By calculating η , t and Δt for every particle, one has

$$\left\{ \begin{array}{ll} e^+ : & \eta = 1.957 \cdot 10^3 \quad t_e = \ell/c = 33.3 \text{ ns} \quad (\Delta t_e \simeq 0) \\ \pi^+ : & \eta = 7.16 \quad t_\pi = t = \frac{\ell}{c} \frac{\sqrt{1+\eta^2}}{\eta} = 33.6 \text{ ns} \quad (\Delta t_\pi = 0.3 \text{ ns}) \\ K^+ : & \eta = 2.03 \quad t_K = 37.2 \text{ ns} \quad (\Delta t_K = 3.9 \text{ ns}) \\ p : & \eta = 1.066 \quad t_p = 45.7 \text{ ns} \quad (\Delta t_p = 12.4 \text{ ns}) \end{array} \right. \quad (3.19)$$

($1 \text{ ns} = 1 \text{ nanosecond} = 10^{-9} \text{ s}$). The time zero is defined as the time employed by massless particles traveling at the light speed. Positrons cover the distance $\ell = 10 \text{ m}$ almost at the light speed. The additional time with respect to the time zero is given by (3.17).

Note that Δt only depends on $\eta = p/m$. The π^+ mesons take an additional time $\Delta t_\pi = 0.3 \text{ ns}$, the K^+ take an extra $\Delta t_K = 3.9 \text{ ns}$ and the protons take an extra $\Delta t_p = 12.4 \text{ ns}$. Figure 3.7 shows the time distribution (and therefore the mass distribution) observed if the four types of particles are produced in equal proportions. It should be noted that the relation between the time of flight and mass is not linear; it is therefore difficult to separate peaks due to small mass particles (electrons, pions, muons if they would be present). With common electronic systems, it is easy to distinguish time differences of the order of $0.1\text{--}0.5 \text{ ns}$. π^+ mesons can therefore be easily separated from protons for momenta up to a few GeV.

Figure 3.8 shows the results of an analysis in mass of a positive beam of about $2 \text{ GeV}/c$ at the CERN PS in the 1960s. The mass spectrometer using a time-of-flight system allows one to measure the *charge* and the *mass* of new particles; there is no information on other quantum numbers. In Fig. 3.8, some peaks corresponding to already known particles are present; they are peaks due to electrons (e^-), positrons (e^+) and protons (p). Besides, peaks due to new particles directly produced in the proton-nucleon interaction can be observed: they are peaks due to π^+ , π^- mesons with a mass of 139.6 MeV ; K^+ , K^- mesons with mass of 493.7 MeV and antiprotons, having the same mass as the proton, i.e., 938.3 MeV . Particles not directly produced in the proton-nucleon interaction are also visible; these particles come from the π and K meson decays and are, for example, the muons (μ^+ , μ^-) with a mass of $105.7 \text{ MeV} = 207 m_e$; these particles can also be

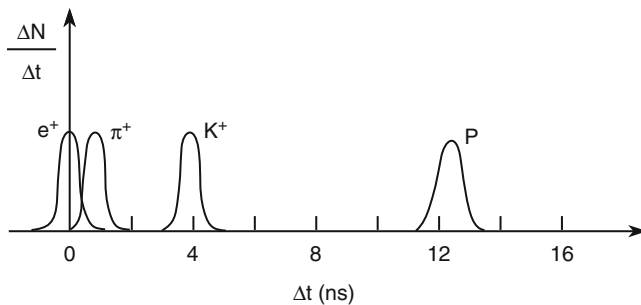


Fig. 3.7 Time distribution foreseen for particles analyzed with the time-of-flight system described in Fig. 3.6, assuming that the beam is composed of e^+ , π^+ , K^+ and p in equal proportions. The peak width is only due to the experimental resolution

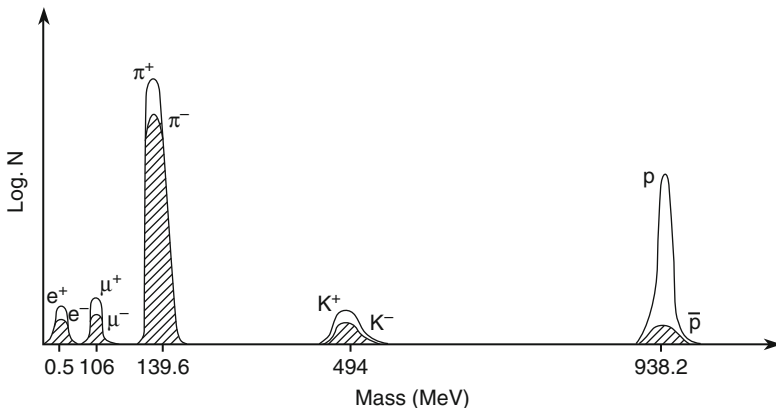


Fig. 3.8 Mass distribution of particles produced in the forward direction in pN collisions at 26 GeV and analyzed with a time-of-flight spectrometer. Muons and electrons are not directly produced in the pN collisions. The y-coordinate is an arbitrary logarithmic scale

produced in secondary interactions (electrons and positrons). Moreover, the following comments can be made:

1. The particles more abundantly produced are π mesons, followed by K mesons (about 10–100 times less) and finally by the antiprotons (1,000 times less).
2. The positive particles are more abundant than the negative. This is only partly due to the electric charge conservation (the initial state can be pp with charge +2, or pn with charge +1). The K^+ mesons are at least twice as abundant than the K^- mesons: strange particles as the K mesons are produced in pair (K^+K^-), but the K^+ can also be produced in association with a strange baryon² (see Sect. 8.14).
3. Particles and antiparticles rigorously have the same mass.

²This is the reason why positively charged secondary cosmic rays (see Chap. 13) on the Earth's surface are more abundant than the negatively charged ones.

4. The peak width in Fig. 3.8 is due to the experimental resolution and is not an intrinsic width.
5. The peaks due to electrons and muons can vary in intensity (height) according to the beam composition. This is due to the fact that electrons and muons are not secondary particles produced in the proton-nucleon interaction, but are at least tertiary particles.
6. Electrons and muons can be separated from pions only using a spectrometer with an extraordinary time resolution.

3.6 Bubble Chambers in Charged Particle Beams

3.6.1 Conservation Laws

It is quite instructive to analyze bubble chamber photographs. Each photo contains a wealth of information and it is sufficient enough to qualitatively analyze a few carefully chosen photos in order to verify the existence of new particles and to establish some of their properties. A quantitative analysis can also be done by performing measurements on the photos. This obviously requires the appropriate measurement tools. Before starting such analyses, we shall recall some formulas of relativistic mechanics, concepts on conservation laws, practical formulas, measurement units and orders of magnitude (see Appendix A.2).

Relativistic Mechanics Formulas

(for $c = 1$)

Momentum	$\mathbf{p} = m_0 \mathbf{v} \gamma$	$\mathbf{p} = m_0 \mathbf{v} \gamma$
Kinetic energy	$T = (\gamma - 1)m_0 c^2$	$T = (\gamma - 1)m_0$
Mass energy	$E_m = m_0 c^2$	$E_m = m_0$
Total energy	$E = T + E_m = \gamma m_0 c^2$ $= \sqrt{p^2 c^2 + m_0^2 c^4}$	$E = \gamma m_0$ $= \sqrt{p^2 + m_0^2}$

where m_0 is the particle rest mass, \mathbf{v} its velocity, c is the light speed in vacuum, $\beta = v/c$, $\gamma = 1/\sqrt{1 - \beta^2}$.

Conservation laws. In any interaction, the following quantities must be conserved:

1. The momentum
2. The total energy (and the kinetic energy in an elastic collision)
3. The electric charge
4. The baryonic number
5. Separately, the electron, muon and tau leptonic numbers. In the reactions due to the strong interaction, parity, strangeness, charm quantum number and other quantum numbers (see Chap. 7) must also be conserved

Lorentz force. A particle with an electric charge q and momentum \mathbf{p} moving in a magnetic field \mathbf{B} perpendicular to its velocity \mathbf{v} , is subject to the Lorentz force having an intensity $F = qvB$; the particle curves following a circumference arc with radius R such that

$$p = qRB \quad (3.20a)$$

(this is a classical formula which is also valid relativistically; in the cgs system, one has $F = qvB/c$, $p = qRB/c$). This equation allows one to determine the ratio p/q through the measurement of the curvature radius R , when the value of the magnetic field B is known. In practical units, one has (for $q = |e|$ = proton charge)

$$p(\text{GeV}/c) = 0.30R(\text{m})B(\text{T}). \quad (3.20b)$$

The momentum expressed in (GeV/c) is equal to the product of a constant (0.30) by the curvature radius R expressed in meters and by the magnetic field B expressed in Tesla. In the cgs system, one has $p(\text{MeV}/c) \simeq 0.30R(\text{cm})B(\text{kG})$.

Energy unit. Expressing an energy in electron Volt multiples, one has

$$\begin{aligned} 1J &= 1/(1.6022 \cdot 10^{-19}) \text{ eV} = 1/(1.6022 \cdot 10^{-13}) \text{ MeV} \\ &= 6.241 \cdot 10^{18} \text{ eV} = 6.241 \cdot 10^9 \text{ GeV}. \end{aligned} \quad (3.21)$$

Mass unit. A mass can be expressed in energy units using the formula $E = m_0c^2$. For the proton,³ one has $m_p = 1.6726 \cdot 10^{-27}(2.9979 \cdot 10^8)^2/(1.6022 \cdot 10^{-13}) = 938.27 \text{ MeV}/c^2$; with $c = 1$, one has $m_p = 938.27 \text{ MeV}$. As an order of magnitude, one can write $m_p \simeq 1 \text{ GeV}$.

Momentum unit. Expressing mass and momentum in energy units and using $c = 1$, one has

$$E^2 = p^2c^2 + m_0^2c^4 \xrightarrow{c=1} p^2 + m_0^2. \quad (3.22)$$

Energy and momentum. In chemical reactions, the involved energies are of the order of a few eV/atom. In nuclear reactions, the energies are of the order of the binding energy of a nucleon inside a nucleus, that is, of the order of a few MeV. In high energy physics, particles used as projectiles have an associated wavelength given by the de Broglie equation. This wavelength can be smaller than the proton (or neutron) size, that is, $\lambda = h/p < 1 \text{ fm}$. If $\lambda = 1 \text{ fm} = 10^{-15} \text{ m}$:

$$p = \frac{h}{\lambda} \rightarrow \frac{hc}{\lambda} = \frac{(4.136 \cdot 10^{-21} \text{ MeV s})(3 \cdot 10^{10} \text{ cm/s})}{10^{-15} \text{ cm}} = 1.24 \text{ GeV}/c. \quad (3.23)$$

³ $m_p = 1.6726 \cdot 10^{-27} \text{ kg}$, $c = 2.9979 \cdot 10^8 \text{ m/s}$.

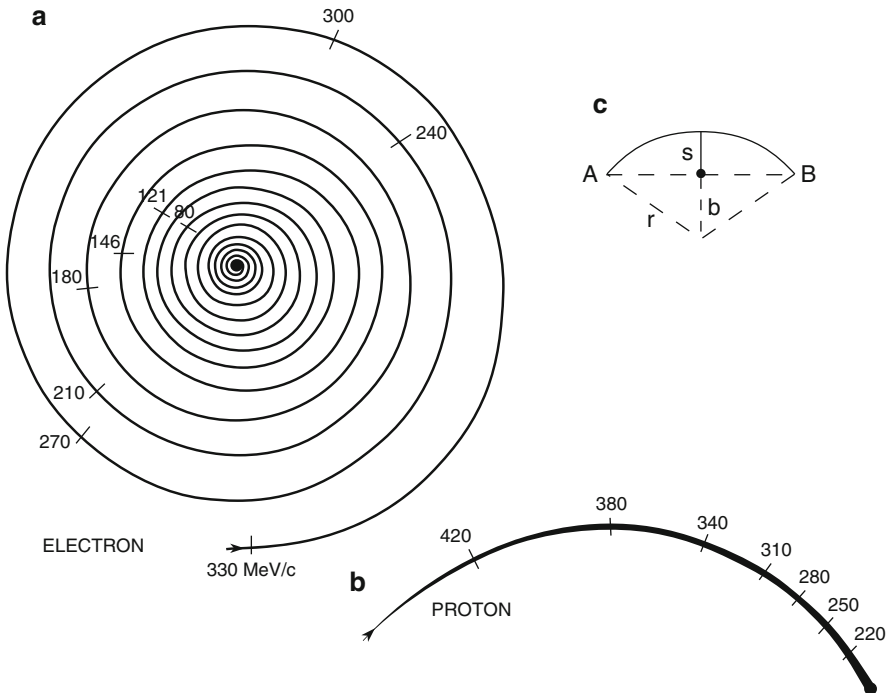


Fig. 3.9 Simulation of a particle trajectory (track) in a hydrogen bubble chamber inside a 2 T magnetic field due to (a) a 330 MeV/c electron; (b) a 470 MeV/c proton (dark track in the bottom part). (c) Definition of sagitta s and curvature radius r

Practical considerations. From formula (3.20b), a particle with 1 GeV/c momentum in a 2T magnetic field describes a circumference having 1.67 m radius. If the trajectory is measured for a path $AB = 50$ cm (see Fig. 3.9c), it corresponds to a sagitta⁴ of length $s \simeq \overline{AB}^2/8R = 50^2/(8 \cdot 167) = 2$ cm, which can be easily measured. For a particle with 10 GeV/c momentum, the sagitta becomes 2 mm, which is more difficult to measure. For didactic purposes, it is therefore better to use photos with particles having momenta of the order of 1 GeV/c or smaller. In addition, it is important to choose photos where the trajectories are in a plane perpendicular to the optical axis of the flash-camera system, with such an axis parallel to the magnetic field. Otherwise, we should make a tridimensional spatial reconstruction using at least two photos taken with different cameras. In the general case, a particle trajectory is a helix (having the direction of the magnetic field as an axis), not a circumference. One should also take into account that usually,

⁴For an arc of circumference of radius R and a chord length y , the sagitta length s is given by $R = \frac{y^2}{8s} + \frac{s}{2} \simeq \frac{y^2}{8s}$.

the photos are not of natural size; there is an enlargement factor g (generally smaller than one). The curvature radius R is determined through the measurement of many points along the trajectory which is then reconstructed using computer programs.

Energy loss. A fast charged particle constantly interacts through the Coulomb interaction with the atoms of the crossed medium ionizing and exciting them. Energy loss through ionization per path length unit depends on the atomic number Z of the crossed medium and on the square of the electric charge of the fast particle (2.10). At velocities much smaller than c , the dependence on the velocity in the Bethe–Block formula is of the type $1/v^2$; at larger velocities, the curve reaches a minimum followed by a slight relativistic rise. Such an energy loss is small in comparison to the kinetic energy of the fast particle. As a result of the energy loss, positive and negative ions are produced through ionization in the crossed medium along the trajectory of the particle. Around these ions, little bubbles may form and can be photographed. A relativistic charged particle produces 5–10 bubbles per centimeter in a bubble chamber; a slower particle loses more energy, producing a “black” track which may even stop in the bubble chamber. An electron always has a velocity close to that of light and loses little energy through ionization (thus producing a small number of bubbles per centimeter); however, it loses energy through radiation in a discontinuous way. Consequently, the radius of curvature of an electron track quickly decreases. The number of bubbles per cm of track are only roughly measured. However, it is possible to obtain estimates on the mass of heavy particles measuring the curvature radius and the number of bubbles per cm. In a liquid hydrogen bubble chamber, the energy loss is $dE/dx \simeq 0.27 \text{ MeV/cm}$, that is, about $4 \text{ MeV cm}^2/\text{g}$; in a material different from hydrogen, it is about $2 \text{ MeV cm}^2/\text{g}$. Let us now analyze a few photos, beginning with the simplest cases.

3.6.2 *The Electron “Spiral”*

The photo of Fig. 3.10 shows a series of bubbles (the so-called “track”) produced by an *electron* in a bubble chamber: it is a typical track with a spiral form. Tracks produced by electrons are easily recognizable because no other particle can leave a track with a small number of bubbles per cm describing a circumference with a small radius of curvature. The small number of bubbles indicates that the electron velocity is high, very close to the speed of light in vacuum. The small radius of curvature of the trajectory tells us that the particle rest mass is very small. The electron constantly loses energy; therefore, its energy and momentum, and consequently the radius of curvature continuously decreases. Figure 3.9a shows theoretical tracks calculated by only using the energy loss through ionization for a proton with a momentum of 470 MeV/c , and for an electron with a 330 MeV/c momentum in a bubble chamber immersed in a 2 T magnetic field. Notice that the proton (which produces a track with a large number of bubbles per cm, a “black” track) stops in the chamber.

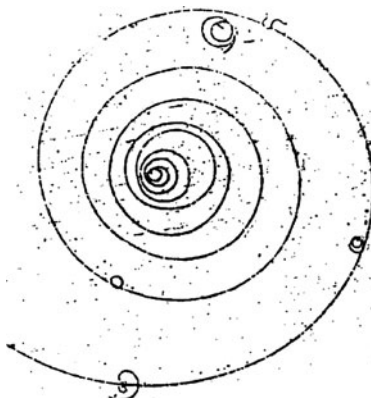


Fig. 3.10 Spiral track produced by an electron in a bubble chamber. The chamber is immersed in a magnetic field $B = 0.12 \text{ T}$ whose direction is perpendicular to and going out of the sheet plane. The moving electron is subject to a centripetal force, constraining it to describe a circumference whose radius of curvature is related to the electron momentum. In this picture, the initial electron momentum (p , in MeV/c) is $p = 3.6 R$ with R expressed in cm. The energy loss decreases the curvature radius of the trajectory which becomes a spiral (Photo: Harvard project, Elementary Particles)

The trajectory of the electron in Fig. 3.10 is different from that of Fig. 3.9; the electron loses energy in a discontinuous way also through bremsstrahlung; therefore, it loses more energy than predicted in Fig. 3.9. In conclusion, we can state that the track in Fig. 3.10 is surely due to an electron.

3.6.3 Electron-Positron Pair

In Fig. 3.11, besides the beam particle tracks, two spiral tracks starting from the same point are visible. The top one on the right is due to an electron as in Fig. 3.10. However, another spiral that rotates in opposite direction is also present. Accurate measurements establish that this spiral is due to the motion of a particle with a mass exactly equal to that of the electron and with the same electric charge but of opposite sign: it is the track produced by a *positron*. The presence of the two spirals with origin in a single vertex indicates that the following reaction took place:

$$\gamma + \text{nucleus} \rightarrow e^+ e^- + \text{nucleus}. \quad (3.24)$$

An $e^+ e^-$ pair was created by a high energy photon in the Coulomb field of a nucleus. In a bubble chamber, neutral particles such as the photon are not visible and the recoil nucleus travels too small of a distance to be observed. For high energy γ , the pair creation process dominates over the photoelectric and Compton effects.

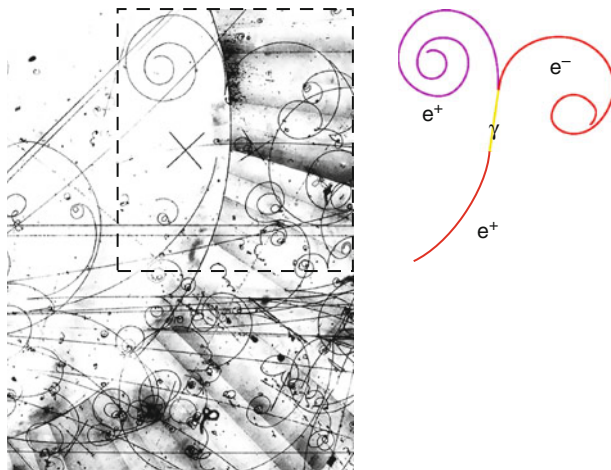


Fig. 3.11 e^+e^- pairs produced by a photon in the Coulomb field of a nucleus in a bubble chamber filled with heavy liquid. From the magnetic field, we know that the e^- spiral track on the right rotates clockwise. The e^+ track rotates on the left. The pair is produced by a photon coming from the annihilation of a positron (track at the bottom) with an electron of the medium filling the bubble chamber. Being neutral, the γ does not leave any track. The recoil nucleus involved in the interaction travels too small of a distance to be observed (Adapted from a CERN photo [3w1])

Sometimes, in addition to the tracks due to the e^+e^- pair, a third negative track, similar to that produced by an energetic electron, is present. It corresponds to the production of an e^+e^- pair in the Coulomb field of an atomic electron, that is,

$$\gamma e^- \rightarrow (e^+e^-)e^- \quad (3.25)$$

The γ -nucleus collision is more probable than the collision on an electron or a proton because the process cross-section is proportional to the square of the electric charge of the target.

3.6.4 An Electron-Positron “Tree”

In the collisions of particles with nuclei of the medium in a bubble chamber, many charged particles and some neutral particles (mainly π^0 mesons not visible in the chamber) are created. The π^0 mesons decay in gamma rays ($\pi^0 \rightarrow 2\gamma$). These gamma rays produce electron-positron pairs when interacting with the nuclei of the liquid which fills the bubble chamber. Many electrons and positrons are slowed down in the Coulomb field of the medium nuclei (the probability is proportional to the square of the atomic number). In these slowing down processes, an electron loses energy, emitting a photon; this photon successively produces an electron-positron

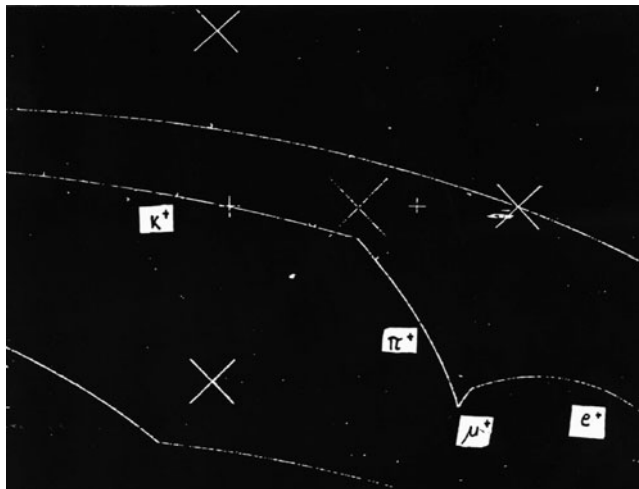


Fig. 3.12 Decay chain: $K^+ \rightarrow \pi^+ \rightarrow \mu^+ \rightarrow e^+$ (see text, where every decay is called an “event”) (BGRT experiment; CERN photo, Geneva [2w1])

pair, and so on. A rapid multiplication of electrons and positrons (an *electromagnetic cascade*) takes place. This cascade is sometimes visible in the photos with a typical “tree” structure, and well visible in bubble chambers filled with a heavy liquid.

Electron-positron pairs are produced abundantly. It is very easy to observe them. The production of $p\bar{p}$ pairs happens much less frequently; the production probability increases with the energy of the interacting particles, and it becomes relatively large for very high energies.

Besides proving the easy transformation of energy in matter, the photos also show that *in the collisions between high energy particles, the positrons and electrons are produced in equal numbers*: the laws of nature do not express preference towards matter or antimatter, as required by special relativity and quantum mechanics theories. This happens every time that the kinetic energies of the interacting particles are much larger than the rest mass energy of the created particle and antiparticle. For an e^+e^- pair, this happens for energies larger than a few MeV. For a $p\bar{p}$ pair, much larger energies would be needed.

3.6.5 Charged Particle Decays

Figure 3.12 shows a hydrogen bubble chamber photograph containing an interesting track; it is composed of three successive events: the positive incident track (a K^+ meson in a beam obtained with electrostatic separators) gives origin to a second positive track (referred to as π^+) which in turn gives origin to a third positive track (μ^+) and finally to an e^+ track.

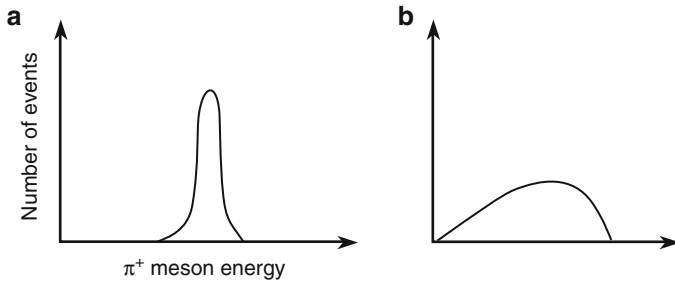


Fig. 3.13 Energy distribution of (a) π^+ mesons produced in the decay of monoenergetic K^+ and (b) e^+ emitted in the decay (3.29), as detected with hypothetical detectors with finite energy resolution

Let us analyze the first “event” at the point where the K^+ gives origin to a π^+ . We can suppose that the incident particle (a K^+ meson) is subjected to a collision. In hydrogen, the collision can occur with a proton or an electron. If the collision occurs with a proton, we should have two positive particles in the final state. In the photo, only one appears; this event cannot result from a glancing collision where the target proton would recoil by an imperceptible quantity because the deflection angle of the second charged particle is too large (which would correspond to an almost head-on collision). Therefore, this event cannot be due to a collision with a proton. In a similar way, it can be verified that this event cannot result from a collision with an electron.

From precise measurements of the momentum and velocity of the second positive track, one can deduce that the mass of this second particle is about 140 MeV. We can therefore think that the K^+ meson has disappeared, contemporarily producing a π^+ (*positive pion*). The first event is therefore classified as a *decay*:



To contemporarily conserve momentum and energy, at least one neutral particle must be present in the final state (a particle cannot decay into a single new particle, but at least into two particles). Analyzing many decays of the type shown in Fig. 3.12, it is observed that the π^+ meson has an energy distribution similar to that shown in Fig. 3.13a: the π^+ meson is monoenergetic; the width of the curve is due to detector resolution. Therefore, it can be concluded that this is a two-body decay: the K^+ meson gives origin to a π^+ plus a single neutral particle. Indeed, the decay is



where the π^0 meson has almost the same mass as the π^+ meson.

In the second event of Fig. 3.12, the π^+ positive track gives origin to a third positive track. Also, in this case, one has a decay. Analyzing many events of this

type, it is observed that the resulting positive tracks have very similar lengths, and thus the same energy. With the same arguments as above, one can conclude that one has a two-body decay, that is,

$$\pi^+ \rightarrow \mu^+ + \text{one neutral particle}. \quad (3.28)$$

The positive *muon* (μ^+) has a mass of 105.7 MeV; the neutral particle is the *muon neutrino* (ν_μ).

Finally, one can analyze the last event which consists of a decay of the type

$$\mu^+ \rightarrow e^+ + \text{two neutral particles}. \quad (3.29)$$

The final state of this event must contain more than one neutral particle; indeed, analyzing many events of the same type, it is observed that the electron is emitted with different energies (see Fig. 3.13b). As a consequence, the decay cannot be a two-body decay; the presence of only two neutral particles in the final state is deduced from other conservation laws. The two neutral particles are an electron neutrino (ν_e) and a muon antineutrino ($\bar{\nu}_\mu$). The decay chain is $\mu^+ \rightarrow e^+ \nu_e \bar{\nu}_\mu$.

In a single bubble chamber photo, we have seen four new particles that do not exist in ordinary matter: K^+ , π^+ , μ^+ , e^+ . Besides, we know that there must also be neutral particles.

We have observed a μ as an intermediate decay product. The muon, being a lepton, interacts electromagnetically and not strongly. The muon mass (105.7 MeV) is much higher than that of the electron, but only slightly smaller than that of the pion (139.6 MeV); therefore, in the decay $\pi^+ \rightarrow \mu^+ \nu_\mu$, the kinetic energy available for the μ^+ and the ν_μ is small; since the muon kinetic energy is small, the muon has a short “range” (Sect. 2.2.2).

Fermi has shown first that the electron emitted in the decay of radioactive nuclei in general and in the decay of the neutron, in particular, did not exist inside the nucleus, but is created at the time in which the decay occurred. A decay is a process in which an unstable particle disappears and is replaced by two or more new particles with smaller mass. The energy conservation in the $K^+ \rightarrow \pi^+ \pi^0$ decay in the K^+ rest frame gives

$$m_K c^2 = (m_{\pi^+} c^2 + m_{\pi^0} c^2) + (T_{\pi^+} + T_{\pi^0}). \quad (3.30)$$

The sum of the rest masses of the final state particles must be smaller than the decaying particle rest mass.

Three-prong decay. Figure 3.14 shows a positive track (again a K^+ meson) which gives origin to three charged particle tracks, two positive and one negative. Each of them in turn produces a *one-prong decay* (decay with one charged track) similar to the decay analyzed in the previous paragraph. Applying the electric charge conservation principle, we can state that the event producing three charged tracks is not an interaction, but a decay (for instance, the interaction with a single proton

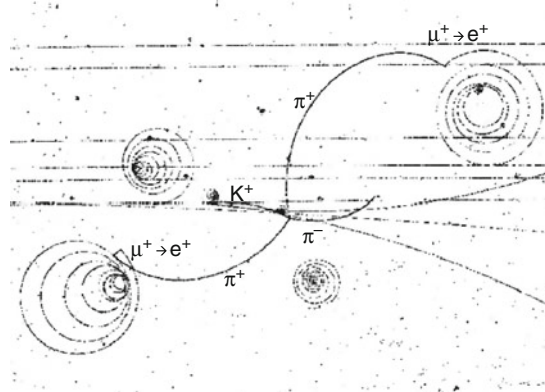


Fig. 3.14 K^+ meson decay in 3π ($K^+ \rightarrow \pi^+\pi^+\pi^-$) and successive decays of every π meson. It should be noted that in the $\pi^+ \rightarrow \mu^+ \rightarrow e^+$ decay, the length of the tracks due to μ^+ are extremely small. The μ^- is not visible in the photo view plane. At the bottom of the photo, one can also observe an electron which seems to appear from nowhere: it is an electron extracted by a high energy photon from a medium nucleus through the Compton effect (BGRT experiment; adaptation from a CERN photo, Geneva)

would have two tracks in the final state). Analyzing the momenta and the number of bubbles per cm, one can conclude that the decay is of the type

$$K^+ \rightarrow \pi^+ \pi^+ \pi^- \quad (3.31)$$

where the π^- meson has the same mass but opposite charge of the π^+ meson. The successive one-prong decays are

$$\pi^+ \rightarrow \mu^+ + 1 \text{ neutral particle} = \mu^+ \nu_\mu \quad (3.32)$$

$$\pi^- \rightarrow \mu^- + 1 \text{ neutral particle} = \mu^- \bar{\nu}_\mu . \quad (3.33)$$

However, in the photo, the π^- goes outside the view plane and the decay in μ^- is not visible. The positive muon, μ^+ , has the same mass (but opposite charge) than the μ^- . One has

$$\mu^+ \rightarrow e^+ + \text{two neutral particles} = e^+ \nu_e \bar{\nu}_\mu \quad (3.34)$$

$$\mu^- \rightarrow e^- + \text{two neutral particles} = e^- \bar{\nu}_e \nu_\mu \quad (3.35)$$

(obviously, the μ^- also decays outside the photo view plane). Finally, after three successive decays, the K^+ meson has disappeared and has been replaced by (2 positrons +1 electron) + (3 neutral particles associated to the muons) + (6 neutral particles associated to the $\mu \rightarrow e$ decays). The K^+ meson has generated in total 12 particles, nine of which are neutral and three are charged. As explained in the previous paragraph, the K^+ is not composed of 12 particles, though these are created at the time in which the decays occur.

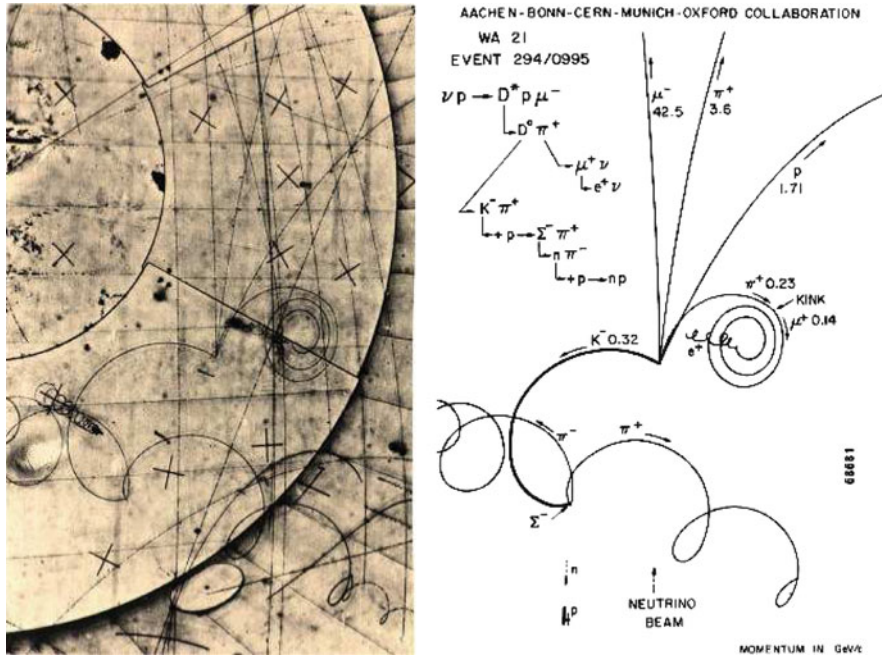


Fig. 3.15 A rather complicated photo containing a lot of information resulting from the interaction of an incident muon neutrino on a target proton in the Big European Bubble Chamber (BEBC) filled with hydrogen. (1) In the reaction (weak interaction, WI), a D^{*+} is created. In terms of quarks (between parentheses), one has $\nu_\mu p(uud) \rightarrow D^{*+}(cd)p(uud)\mu^-$. The charged current WI of the neutrino occurs with a quark d and produces a *charm* quark ($\nu_\mu d \rightarrow \mu^- c$); a $u\bar{u}$ pair is created in the hadronization of the final state through strong interaction. (2-a) The D^{*+} is a *resonance* which decays through strong interaction in a very short time ($\sim 10^{-23}$ s) and with the formation of a $u\bar{u}$ pair: $D^{*+}(cd) \rightarrow D^0(c\bar{u})\pi^+(u\bar{d})$; it is therefore not visible in the photo. The π^+ is however visible (spiral track on the right). A *kink* (change in the curvature radius) indicates the $\pi^+ \rightarrow \mu^+ \nu_\mu$ decay, and the final very small spiral indicates the μ^+ decay in the positron. (2-b) The D^0 decays and its decay products are visible: $D^0(c\bar{u}) \rightarrow K^-(s\bar{u})\pi^+(u\bar{d})$. This decay is not due to the strong interaction because the strong interaction conserves the flavor; this is not the case here where a quark c disappears. This decay is therefore due to the weak interaction; the lifetime is about $\sim 10^{-13}$ s, corresponding to a decay length of a few tens of μm ; for this reason, the D^0 is not visible in the photo. The produced π^+ has a high energy and travels away to the top without decaying before going out of the viewing plane of the photo. (3) The strange meson K^- has a sufficiently long lifetime to interact with a proton of the medium: $K^-(s\bar{u})p(uud) \rightarrow \Sigma^-(dds)\pi^+(u\bar{d})$. The Σ^- decays (WI) in $\Sigma^-(dds) \rightarrow n(ddu)\pi^-(d\bar{u})$. The π^+ of the K^- decay and the π^- of the Σ^- decay are both visible as helicoidal tracks at the bottom of the photo (WA21 experiment (BEBC); CERN photo, Geneva [3w2])

Multi-prong decay. Figure 3.15 shows an event due to the interaction of an incident neutrino on a target proton; in the interaction, a *charm* meson (i.e., composed of a c quark, see Chap. 7) is produced and decays in other particles made of lighter quarks. As explained in the figure caption, this decay chain involves the strong interaction (Chap. 7) as well as the weak interaction (Chap. 8).

Chapter 4

The Paradigm of Interactions: The Electromagnetic Case

Electromagnetic (EM) theory is one of the most successful paradigms of classical physics. From Maxwell's original formulation, the EM equations were easily adapted to a relativistic representation and then to a quantized field theory. The success of the EM theory is due to the precise knowledge of the analytic form of the interaction potential between charged particles.

The quantum electrodynamics (QED) theory includes the spin of particles (within the framework of the Dirac theory) and describes the interaction between charged particles through the exchange of a quantum field (the photon). Using QED, it is possible to calculate with great precision many physics quantities (cross-sections, particle lifetimes, magnetic moments, and so on) over a wide range of energies. The success of the QED formulation (in particular, in the perturbative version of Feynman diagrams) has allowed the extension to the weak and (partially) to the strong interactions. For this reason, some useful concepts of quantum mechanics and perturbative theory are presented in this chapter. Particular emphasis is given to the description of the *transition probability* quantity which allows the comparison of theoretical predictions with experimental measurements.

Over the past 50 years, it was first hypothesized and then experimentally verified that the electromagnetic and the weak interactions are different manifestations of a single interaction, the *electroweak interaction*. The unification of the two interactions occurs at an energy larger than the W^+ , W^- , and Z^0 boson masses, i.e., for center-of-mass (c.m.) energies above ~ 90 GeV. At lower energies, the electromagnetic and weak interactions are separate and different, as discussed in Chap. 11. At much larger energies, the electroweak and strong interaction unification (the so-called *Grand Unification Theory*, Chap. 13) can be hypothesized.

4.1 The Interaction Between Electric Charges

The electromagnetic interaction can be considered as a unification of the electrostatic and magnetic forces which were thought to be distinct until the middle of the nineteenth century. The electrostatic force is ruled by Coulomb's law:

$$\mathbf{F} = K \frac{q_1 q_2}{r^2} \hat{\mathbf{r}} \quad (4.1)$$

where q_1 e q_2 are the point-like particle electric charges, r is the distance between them, $\hat{\mathbf{r}}$ is a unit vector directed from q_1 to q_2 and K is a proportionality constant. The spatial dependence is similar to that of Newton's law. The electric charges q_1 and q_2 do not depend on the inertial mass and can assume positive and negative values. The electrostatic force can attract or repel particles, depending on the relative sign of the charges.

A law similar to that of Coulomb, commonly considered for magnetic charges during the nineteenth century, allowed one to introduce the magnetic induction \mathbf{B} . This situation was only formally valid because isolate free magnetic charges (*magnetic monopoles*) were never observed. The \mathbf{B} field was without "sources." Today, we know that each magnetic field is generated by electric charges in motion, and that the field is a relativistic effect of such a motion. In the relativistic theory, the electric and magnetic fields are so interrelated that an unique interaction, the *electromagnetic interaction*, must be considered (see Appendix A.3). The force acting on a moving charge q with velocity \mathbf{v} in an electric field \mathbf{E} and a magnetic field \mathbf{B} is (in the International System):

$$\mathbf{F} = q\mathbf{E} + q\mathbf{v} \times \mathbf{B}. \quad (4.2)$$

The representation of *Feynman diagrams* has been very successful for describing the EM interaction in quantum mechanics. The Feynman diagrams represent a visual method which provides both an intuitive representation of the interaction and a rigorous way to obtain numerical quantities through a perturbative calculation method. Let us first consider the Feynman diagram of Fig. 4.1 for the interaction between two electrons. Experimentally, it is observed that the two electrons repel each other. It is conceivable that the interaction occurs through the exchange of a particle, the photon. It may be useful to make the following analogy: if two people aboard two different boats at rest (= the electrons) exchange a ball (= the photon), the boats slowly start moving away from each other (but do not expect too much from the intuitive validity of this model; for instance, how does it explain an attractive force? Perhaps by sending the ball into the opposite direction and waiting until it makes it around the world and hits the second person?). An electron at rest cannot, however, emit a "real" photon because this would violate the energy conservation law (Problem 4.2):

Process	Initial state	Final state	
$e \rightarrow e\gamma$	$m_e c^2$	$m_e c^2 + \frac{p_e^2}{2m_e} + E_\gamma$	(4.3)

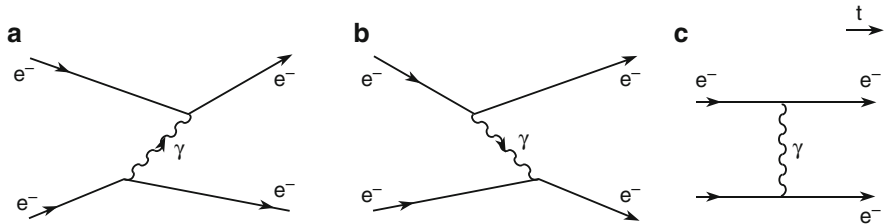


Fig. 4.1 Lowest order Feynman diagrams for the elastic electron–electron collision due to the EM interaction. The time is in abscissa (from *left* to *right*). In (a), the electron in the bottom part emits a “virtual” photon which is then absorbed by the electron at the *top*; (b) shows the other way around. The diagram (c) represents the interaction without specifying the time direction

E_γ is the total energy of the emitted photon, p_e is the (nonrelativistic) momentum acquired by the electron, m_e is the electron mass. According to Heisenberg’s uncertainty principle, if energy is measured with an uncertainty of ΔE , the uncertainty on the time measurement is

$$\Delta t \geq \hbar / (\Delta E). \quad (4.4)$$

Suppose that a photon is emitted from the first electron violating the energy conservation (by a quantity ΔE). Now, suppose that the photon is absorbed by the second electron within a time Δt , resulting in a second violation of energy conservation by a value of $-\Delta E$. If all this occurs within the time interval defined in (4.4), none of the two violations can be observed: they are “hidden” by the uncertainty principle. Such a process would therefore be considered as possible. The net effect is an exchange of energy and momentum between the two electrons, and is therefore a way in which two electrons, and more generally two charged particles, can interact. Since an unperturbed free particle with defined energy remains in the same state for a time $\Delta t = \infty$, its energy uncertainty is zero, $\Delta E = 0$.

An alternative way to consider the process is to assume that both the energy and momentum are conserved at the interaction vertex, but that the relation $E^2 = m^2 c^4 + p^2 c^2$ does not hold for the “virtual” particle (which propagates within the interval Δt). In quantum theory, it is believed that the EM interaction takes place in this way, i.e., by exchanging a virtual, nonobservable, photon. The electron quantum numbers, particularly its spin, must remain unchanged. As a consequence, the exchanged particle must have integer spin and is therefore a *boson* (we shall see in Chap. 5 that all the force mediators have spin 1, except the graviton that has spin 2). Assuming that the boson is moving at the light speed and has no rest mass, it travels in the time interval Δt at a distance of $\Delta r = c \Delta t$. Placing this quantity in the uncertainty relation, one obtains $\Delta E \geq \hbar / (\Delta t) \simeq \hbar c / (\Delta r)$. Since the interaction energy V is of the order of ΔE (for a single exchange process), one has

$$\Delta E \simeq V = \alpha_i \hbar c / r. \quad (4.5)$$

The dimensionless constant α_i characterizes the interaction intensity. Equation 4.5 is obtained, assuming the exchange of a massless boson. As a consequence, the forces due to the exchange of virtual massless particles decrease with the distance r as $F \sim dV/dr \sim 1/r^2$.

From the opposite approach, i.e., assuming a force dependence $1/r^2$, one knows that the exchanged virtual particle in the EM interaction is massless. The exchanged virtual particle can therefore be identified with the *photon*, the real quantum of the EM field.

Since the gravitational force has a similar dependence in $1/r^2$, the *graviton* should also be massless.

4.1.1 The EM Coupling Constant

In quantum mechanics, the emission of a photon by an electron means that the electron *creates* a field; when the electron absorbs a photon, it *destroys* a field. An interaction should therefore be considered as a sequence of two processes: the creation and the destruction of a field represented by the two diagrams of Fig. 4.1a,b. Since the virtual field (the photon) is not observable, and since the final states are identical, we do not know if the photon is created (destroyed) by the electron at the top or at the bottom of the diagram: the two processes are indistinguishable. This situation is represented in the diagram of Fig. 4.1c in which the timeline is not specified.

The dimensionless parameter characteristic of the EM interaction is the *fine structure constant* (also called *electromagnetic coupling constant*) already known from atomic physics. It can be derived by equating (4.5) with the Coulomb energy potential: $\alpha_i \hbar c / r = Kq^2 / r$, from which one finds ($q = e$ is the electric charge of the electron): $\alpha_i = \alpha_{EM} = Ke^2 / \hbar c$; numerically, one has

$$\alpha_{EM} = \frac{e^2}{4\pi\epsilon_0\hbar c} = \frac{(1.602 \cdot 10^{-19})^2}{4\pi \cdot 8.85 \cdot 10^{-12} \cdot 1.05 \cdot 10^{-34} \cdot 3 \cdot 10^8} = \mathbf{1/137.1} \quad \text{S.I.} \quad (4.6a)$$

$$\alpha_{EM} = \frac{e^2}{\hbar c} = \frac{(4.803 \cdot 10^{-10})^2}{1.0546 \cdot 10^{-27} \cdot 3 \cdot 10^{10}} = \mathbf{1/137.1} = 7.294 \cdot 10^{-3} \quad \text{cgs;} \quad (4.6b)$$

$$\alpha_{EM} = e^2 \quad (\hbar = c = 1) \quad \text{cgs.} \quad (4.6c)$$

Since α_{EM} is smaller than unity, EM processes can be treated in a perturbative theory with a good approximation already at the lowest orders. As discussed below, the Feynman diagrams are a graphical representation of the terms of the perturbative expansion. The order of the approximation is given by the number of vertices; in the calculation of the process amplitude probability, a factor $\sqrt{\alpha_{EM}}$ (i.e., the electric charge e , in the cgs system of units with $\hbar = c = 1$, see Appendix A.2) is present for each vertex. We shall see that the probability that a particular

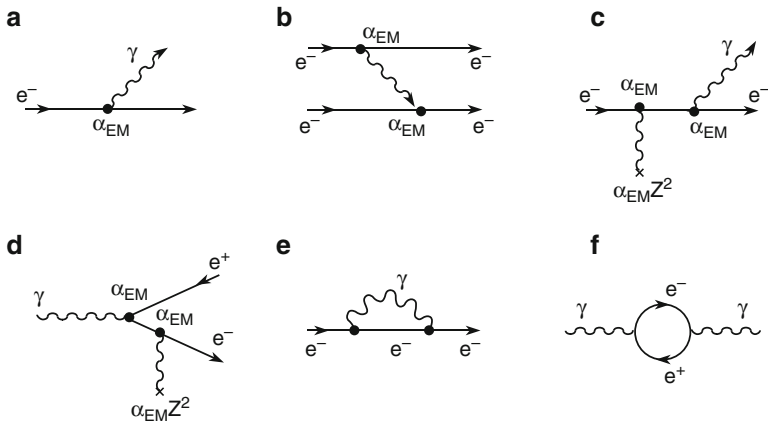


Fig. 4.2 Feynman diagrams of some of the most important processes due to the EM interaction. (a) emission of a photon by an electron (this fundamental vertex cannot occur if the electron is isolated; the corresponding contribution to the amplitude squared is proportional to α_{EM}); (b) elastic e^-e^- collision; (c) bremsstrahlung; (d) pair creation; (e) emission and absorption of a virtual photon by an electron; (f) creation of a virtual e^+e^- pair and subsequent annihilation (these last two diagrams give rise to closed lines, with virtual particles not directly observed, see text)

process takes place (experimentally measured through the process *cross-section*) is described by the process *matrix element*. This quantity remains the same if an incident electron with momentum \mathbf{p} is replaced by an outgoing antielectron with momentum $-\mathbf{p}$; there is clearly a relation between the cross-sections of different processes.

Figure 4.2 shows the Feynman diagrams for the most important processes due to the electromagnetic interaction. Figure 4.2a represents the emission of a photon by an electron (see also Problem 4.2). The photon couples to the electron with an amplitude proportional to $\sqrt{\alpha_{EM}}$. It is a first order process since only one vertex is present. The elastic collision between two electrons, shown in Fig. 4.2b, is a second order process with two vertices. The virtual photon contributes with a term $1/q^2$, called *propagator*, where q is the momentum transferred from an electron to another. Figure 4.2c shows a *bremsstrahlung* process, i.e., the emission of a photon by an incident electron accelerated in the Coulomb field of a nucleus, indicated as x. Because three vertices are present (including the nucleus x), it corresponds to a third order process and the cross-section is proportional to $Z^2\alpha_{EM}^3$. Figure 4.2d shows the e^+e^- pair creation by a photon interacting with the Coulomb field of a nucleus. This is also a third order process. The diagrams (c) and (d) are similar: (d) can be deduced from (c) by replacing the incoming electron line with that of the outgoing positron and by changing the photon γ from outgoing to incoming.

4.1.2 The Quantum Theory of Electromagnetism

The experiments carried out at the beginning of the 1900s on the emission of, for example, blackbody radiation, photoelectric effect, Compton effect, showed that the electromagnetic field is quantized; the quantum of the EM field is the photon, with energy $E = h\nu$, momentum $p = h\nu/c$, spin $s = 1\hbar$. Because it always moves at the light speed c , the photon only has two polarization states (e.g., right-handed or left-hand circular polarization). Classically, this is equivalent to the fact that only transverse EM waves propagate in vacuum. A virtual photon (by definition, the relation $E^2 = p^2 + m^2$ does not hold for a *virtual* particle with a rest mass m) can have a mass different from zero and a third polarization state, the longitudinal one. Classically, this occurs with electromagnetic waves moving in a waveguide.

The theory of quantum electrodynamics (QED) developed in the 1940s and 1950s by Feynman, Schwinger, Tomonaga (Nobel laureate in 1965) and others, describes the interaction of charged Dirac fields (= charged fermions) with the quantized electromagnetic field (*second quantization*). The theory predicts, in a large energy range and with high precision, many phenomena, such as, the cross-sections and transition probabilities.

One of the most important QED properties is its *renormalizability*. This means that terms producing infinite quantities (e.g., the so-called “self-energy” terms due to the diagrams shown in Fig. 4.2e,f) may be all included in the electron mass m_0 and electric charge e_0 . Mass and charge can then be overridden by the experimentally measured values.

A second important property of QED is the *gauge invariance*. To intuitively understand the meaning, remember that in electrostatic, the interaction energy (experimentally measurable) depends on the electrostatic potential difference, and not on its absolute value. The interaction energy is therefore invariant under any change of scale (or “*gauge*”) of the potential (the potential is known but an additive constant, the “*global gauge*”). We shall discuss in Sect. 6.9 the *local gauge invariance*, which leads to the electric charge conservation. It is believed that the theories of fundamental interactions should be renormalizable local gauge theories.

The “constant” α_{EM} is known with high accuracy from experiments at low energy. We shall see in Chap. 11 that α_{EM} is not really constant, but increases logarithmically with the c.m. energy; for example, it is equal to 1/137 at “zero” energy and to 1/128 at $E_{cm} = \sqrt{s} = 91.2 \text{ GeV}$.

4.2 Some Quantum Mechanics Concepts

In this section, we shall recall some quantum mechanics concepts. A few simple rules were established to go from classical equations to quantum equations through the substitution of energy E and momentum \mathbf{p} with the corresponding operators:

$$\boxed{E \rightarrow i\hbar \frac{\partial}{\partial t}, \mathbf{p} \rightarrow -i\hbar \nabla} \quad (4.7)$$

where ∇ is the gradient operator. The operators $\partial/\partial t$ and ∇ are applied on wave functions. In the covariant form, one has $p^\mu \rightarrow +i\hbar\partial/\partial x_\mu = +i\hbar\partial^\mu$, where the coordinates of the space-time four-vector x_μ are indicated as $x_0 = ct, x_1 = -x, x_2 = -y, x_3 = -z$.

4.2.1 The Schrödinger Equation

Classically, a free particle kinetic energy is $E = p^2/2m$. Applying the substitution (4.7), one obtains the nonrelativistic Schrödinger equation:

$$i\hbar \frac{\partial \psi}{\partial t} + \frac{\hbar^2}{2m} \nabla^2 \psi = 0. \quad (4.8a)$$

The Schrödinger equation describes the time evolution of the wave function ψ ; it can also be written as

$$i\hbar \frac{\partial \psi}{\partial t} = H\psi \quad (4.8b)$$

where H is the system Hamiltonian. For steady states (i.e., not time dependent), the equation used to derive the energy eigenvalues E is

$$H\psi = E\psi. \quad (4.8c)$$

The probability density flux is defined as

$$\mathbf{j} = -\frac{i\hbar}{2m}(\psi^* \nabla \psi - \psi \nabla \psi^*), \quad (4.9)$$

satisfying the continuity equation

$$\frac{1}{c} \frac{\partial \rho}{\partial t} + \nabla \cdot \mathbf{j} = 0 \Rightarrow \partial_v J^v = 0 \quad (4.10)$$

where $\rho = |\psi|^2$ is the probability density to find the particle in a unit volume ($|\psi|^2 dV$ is the probability to find the particle in a volume dV).

The solution of the Schrödinger equation:

$$\psi = N e^{(i\mathbf{p}\cdot\mathbf{r}-iEt)/\hbar} \quad (4.11)$$

describes a free particle with energy E and momentum \mathbf{p} , with $\rho = |N|^2$ and $\mathbf{j} = \mathbf{p}|N|^2/m$.

4.2.2 Klein–Gordon Equation

Let us consider the relativistic relation between energy and momentum, $E^2 = p^2 c^2 + m^2 c^4$. Using the substitution (4.7), one obtains the Klein–Gordon equation:

$$\left(\frac{1}{c^2} \frac{\partial^2}{\partial t^2} - \nabla^2 \right) \phi + \frac{m^2 c^2}{\hbar^2} \phi = 0 \quad (4.12)$$

which describes the propagation of a relativistic free particle of mass m . In covariant notation and using the definition $\square = \partial_\mu \partial^\mu = \partial^\mu \partial_\mu$, one has

$$\square \phi + \frac{m^2 c^2}{\hbar^2} \phi = 0, \quad \left(\frac{\partial^2}{\partial x_\mu \partial x^\mu} + \frac{m^2 c^2}{\hbar^2} \right) \phi = 0. \quad (4.13)$$

If $m = 0$, it corresponds to the equation describing the propagation of an electromagnetic wave; ϕ is now interpreted as the potential U in the coordinate space, or as the wave amplitude of associated photons which propagate the interaction.

For a static potential in (4.12), the time dependence disappears and by replacing $\phi(r, t) \rightarrow U(r)$, one obtains

$$\nabla^2 U = \frac{m^2 c^2}{\hbar^2} U. \quad (4.14)$$

For a spherically symmetric potential generated by a point source, $U = U(\mathbf{r}) = U(r)$, one has $\nabla^2 U(r) = \frac{1}{r^2} \frac{\partial}{\partial r} (r^2 \frac{\partial U}{\partial r})$; r is the distance from the point source placed in the origin of the system reference frame. It can be verified that the solution is of the type

$$U(r) = \frac{g}{4\pi r} e^{-r/R} \quad (4.15)$$

where $R = \hbar/mc$ is a quantity with the dimensions of a length, g is an integration constant and is interpreted as the “intensity strength” of the point source. The potential (4.15) was initially considered as the “strong” interaction potential between nucleons in the Yukawa model (see Sect. 7.1.1). The mediators of a Yukawa interaction have a mass m . The EM case instead corresponds to $m = 0$, so that $\nabla^2 U(r) = 0$ with a solution $U = Q/r$, where Q is the electric charge at the origin. By analogy, the constant $g/4\pi$ in the case of the “strong” potential (4.15) can be considered as the “charge” of the particle that generates the strong field. The factor R in (4.15), related to the mass m of the interaction mediator boson, is interpreted as the *interaction range*. According to the original Yukawa model and since $R \simeq 1.2 \text{ fm}$ for a static interaction between two hadrons, one has $mc^2 = \hbar c / R \simeq 100 \text{ MeV}$ (remember $\hbar c = 197.327 \text{ MeV}\cdot\text{fm}$). The predicted boson was identified as the π meson. The fact that hadrons are composite objects complicates this simple interpretation.

4.2.3 Dirac Equation

The next conceptual step occurred in 1928 when Dirac introduced the quantum equation which describes the relativistic behavior of point-like particles (as the electron) with semi-integer spin $s = \frac{1}{2}\hbar$:

$$(i\hbar\gamma^\mu \frac{\partial}{\partial x^\mu} - mc)\psi = 0. \quad (4.16)$$

Dirac formulated Eq. 4.16 assuming that it was the quantum analogous of the relation $E = \pm \sqrt{p^2c^2 + m^2c^4}$. In this way, (4.16) contains, contrary to the Klein–Gordon equation, only first derivatives with respect to space and time. The γ^μ matrices are defined in Appendix A.4 where the derivation of the Dirac equation, its general properties and solutions are also presented in details. The Dirac equation solutions are four component wave functions ψ called *spinors*. They can be considered as the “Dirac field,” in analogy with the “electromagnetic field” (the photon) for the Maxwell equations. The Dirac theory explains all the electron properties known from atomic physics, in particular, the value of the gyromagnetic ratio between the spin s and the electron magnetic moment $\mu_e = g\mu_B s$, in units of the Bohr magneton μ_B .

The “Dirac sea.” The Dirac equation admits solutions with negative energy. The states with positive energy and those with negative energy are symmetric with respect to zero. The existence of negative energy states would destabilize matter. The hydrogen atom would lose its electron, which would immediately fall in a negative energy state by emitting a photon of positive energy, in this way respecting the energy balance. Dirac solved the problem by assuming that all the negative energy states were filled, forming the so-called Dirac sea. The Pauli exclusion principle ensures the stability of the hydrogen atom: the electron cannot move into a negative energy state because all levels are already occupied.

In the Standard Model (Chap. 11), the wave functions of all “elementary” spin $s = 1/2$ particles obey Eq. 4.16. Here, “elementary” means a particle without a known internal structure. For example, the proton is not an elementary particle, and the correct value of its magnetic dipole moment is not directly obtained from the Dirac equation (see Sect. 7.14.4).

The application of the Dirac theory to the neutrino is currently not verified by any experimental evidence. In 1937, E. Majorana obtained a relativistic wave equation for neutral particles different from that of Dirac. This suggests that neutrinos could either be Majorana or Dirac particles. The determination of the neutral particle nature (Dirac or Majorana particle) [Be08] is nowadays one of the most interesting open experimental questions [4A08].

4.3 Transition Probabilities in Perturbation Theory

In this section, we shall use a perturbation theory in nonrelativistic quantum mechanics¹ [P87] to calculate the *transition probability* (denoted W) from an initial to a final state. As discussed in the next chapters, this quantity is used to compare theoretical predictions with experimental data not only for the electromagnetic case, but also for the weak and strong interactions.

Let us consider the transition probability in a *decay process* of a particle, or an interaction (collision) between particles. In the latter case, the *cross-section* is the key experimental parameter used to describe the process. The system initial state is assumed to be well defined: it is, for instance, described by a stationary wave function ψ , with defined energy E_m . This wave function (valid for $t < 0$) is one of the possible eigenstates of the free Hamiltonian system H_0 . Factorizing the wave function (4.11) in a time-dependent term and a time-independent part ϕ_m , one can write

$$\psi(t < 0) = \phi_m e^{-iE_m t/\hbar}. \quad (4.17)$$

The set of ϕ_m functions represents a complete set of eigenfunctions (orthonormal to each other) of the H_0 Hamiltonian system, i.e.,

$$H_0 \phi_m = E_m \phi_m. \quad (4.18)$$

The transition to one of the allowed possible final states (some can be excluded by the conservation law) is caused by the action of an energy potential term V , which starts to be effective for $t \geq 0$. V is linked to a potential U by a constant: $V = g_0 U$. In the electromagnetic case, g_0 is the electric charge of the particle described by the wave function ψ . When the potential V “turns on,” the particle has a finite probability to move to a different allowed quantum state ϕ_n . At the time $t \geq 0$, the total wave function can be expressed as a superposition of possible states, that is,

$$\psi(t) = \sum_{n=0}^{\infty} c_n(t) \phi_n e^{-iE_n t/\hbar}. \quad (4.19)$$

The square of the coefficient $c_n(t)$ represents the probability amplitude of finding the system in the ϕ_n state. At $t = 0$, $c_m(0) = 1$ and $c_n(0) = 0$ for $n \neq m$. At $t \geq 0$, the wave function (4.19) must satisfy the nonrelativistic Schrödinger equation for the Hamiltonian $H = H_0 + V$:

$$H\psi = (H_0 + V)\psi = i\hbar\partial\psi/\partial t. \quad (4.20)$$

¹The student unfamiliar with the formalism can consider only the calculation final results, Eqs. 4.28 and 4.29.

Placing Eqs. 4.19 and 4.18 in Eq. 4.20, one obtains

$$i\hbar \sum_{n=0}^{\infty} \left(\frac{dc_n}{dt} \right) \phi_n e^{-iE_n t/\hbar} = \sum_{n=0}^{\infty} V c_n(t) \phi_n e^{-iE_n t/\hbar} \quad (4.21)$$

(the term coming from the time partial derivative of the function ψ is canceled since $H_0\psi = \sum_n c_n E_n \phi_n e^{-iE_n t}$). Multiplying Eq. 4.21 by the complex conjugate function ψ_k^* (where k is a generic eigenstate of H_0) and using the normalization property $\phi_k^* \phi_n = 0$ for $n \neq k$, one gets

$$i\hbar \left(\frac{dc_k}{dt} \right) = \sum_{n=0}^{\infty} c_n(t) M_{nk} e^{-i(E_n - E_k)t/\hbar}, \quad (4.22)$$

where the quantity M_{nk} is the matrix element for the transition probability from the state n into the state k , induced by the potential V , that is,

$$M_{nk} = \int \phi_k^* V \phi_n d\tau. \quad (4.23)$$

Note that M_{nk} has the **dimension of an energy** since V (as H) is an operator with the dimension of an energy, $d\tau = d^3x = d\mathbf{v}$ is the volume element, and the wave functions ϕ have the dimension of a *volume* $^{-1/2}$.

In perturbation theory, the potential U is assumed to be so weak and the transition probabilities so small that during the considered time t , the coefficients are such that $c_m(t) \simeq 1$ and $c_n(t) \simeq 0$ for $n \neq m$. In other words, this means that the possibility of two or more transitions is extremely unlikely and therefore negligible. This condition is expressed as

$$M_{nk} \simeq 0 \quad \text{for } n \neq m. \quad (4.24)$$

Integrating (4.22) over time, assuming a time-independent potential V ,

$$\begin{aligned} c_k(t) &= \frac{1}{i\hbar} \int_0^t M_{km} e^{-i(E_k - E_m)t/\hbar} dt = M_{km} \left[\frac{1 - e^{-i(E_k - E_m)t/\hbar}}{E_k - E_m} \right] \\ &= 2i M_{km} e^{-i(E_k - E_m)t/\hbar} \left[\frac{\sin[(E_k - E_m)t/2\hbar]}{E_k - E_m} \right]. \end{aligned} \quad (4.25)$$

The square of the coefficient $c_k(t)$ represents the probability amplitude of finding the system in the state ϕ_k . In general, the experimentally observed final state is a superposition of different final states. This is the case, for example, of a particle decaying in three particles (three-body decay e.g., the neutron, Chap. 8). The total energy E_0 available in the final state is a constant, but the three particles can share

the total energy in an extremely large number of ways, provided that the sum is E_0 . The total transition probability per time unit towards one of the possible allowed states is the sum of all the probability amplitudes (4.25), that is,

$$W = \frac{1}{t} \sum_i |c_i(t)|^2 \longrightarrow \frac{1}{t} \int_{-\infty}^{+\infty} |c_k(t)|^2 \cdot \frac{dN}{dE} \cdot dE. \quad (4.26)$$

The sum over discrete states is replaced by an integral on continuous energy states, as indeed we shall do when examining the above mentioned three-body decay. This is justified by the fact that the final state system can be represented by the superposition of a large number of quantized states with a tiny energy difference between contiguous levels allowed by energy conservation. The quantity dN/dE is the *density of states per energy interval unit*.

Equation 4.26 can be integrated with some approximations; by defining the quantity $x = (E_k - E_m)t/2\hbar$, and placing Eq. 4.25 in (4.26), one obtains

$$W = \frac{2}{\hbar} |M_{km}|^2 \int_{-\infty}^{+\infty} \left(\frac{dN}{dE} \right) \frac{\sin^2 x}{x^2} dx. \quad (4.27)$$

The function $\sin^2 x/x^2$ is already known from basic physics studies (diffraction of electromagnetic waves). This is not surprising since we are also analyzing a superposition of waves. The function has a main maximum at $x = 0$ and vanishes at the first minimum at $x = \pm\pi$. The contribution to the integral for $|x| > \pi$ is small (of the order of 10%). Practically, Eq. 4.27 can be further simplified by assuming that dN/dE does not vary dramatically in the range $[-\pi; \pi]$ (where $\sin^2 x/x^2$ is not negligible) and extracts this term from the integral. Using the fact that

$$\int_{-\infty}^{+\infty} \frac{\sin^2 x}{x^2} dx = \pi,$$

the transition probability W becomes

$$W = \frac{2\pi}{\hbar} \cdot |M_{if}|^2 \frac{dN}{dE_f}$$

(4.28)

where the index i represents the initial state and f represents the final states. From the dimensional analysis, W has the dimension of $[\text{time}]^{-1}$ and is measured in (s^{-1}) . The Plank's constant has the dimension of $[\text{Energy} \cdot \text{Time}]$, M has the dimension of $[\text{Energy}]$ and dN/dE has the dimension of $[\text{Energy}]^{-1}$ (see Appendix A.2). The matrix elements for the transition between the states i and f is given by

$$M_{if} = \int \phi_i^* V \phi_f d\tau$$

(4.29)

where ϕ_i and ϕ_f are respectively the spatial part (time-independent) of the initial and final wave functions. dN/dE_f is the final state energy density (in the literature, it is sometimes referred to as ρ_f).

Equation 4.28 is also called the *second Fermi golden rule*. In the next section, we shall see its application for a particular potential, which is of great importance for both EM and weak interactions (Chap. 8).

4.4 The Bosonic Propagator

Let us consider a free particle with a defined energy which is scattered by a potential of the form (4.15). Note that if the parameter $g/4\pi$ coincides with the electric charge Ze and if $m = 0$ (i.e., $R = \hbar/mc = \infty$), the potential (4.15) is exactly the Coulomb potential of a point-like electric charge. The transition occurs between the defined initial state to a stationary final state. The spatial part of the initial free particle wave function is $\phi_i = e^{i\mathbf{p}_i \cdot \mathbf{r}/\hbar}$ and $\phi_f = e^{i\mathbf{p}_f \cdot \mathbf{r}/\hbar}$ for the final state. The matrix element (4.29) becomes²

$$\begin{aligned} M_{if} &= \int \phi_i^* V(r) \phi_f d\tau = g_0 \int U(r) e^{-i\mathbf{p}_i \cdot \mathbf{r}/\hbar} e^{i\mathbf{p}_f \cdot \mathbf{r}/\hbar} d\tau = \\ &= g_0 \int U(r) e^{i(\mathbf{p}_f - \mathbf{p}_i) \cdot \mathbf{r}/\hbar} d\tau = g_0 \int U(r) e^{i\mathbf{q} \cdot \mathbf{r}/\hbar} d\tau \end{aligned} \quad (4.30)$$

where $\mathbf{q} = \mathbf{p}_f - \mathbf{p}_i$, $V(r) = g_0 U(r)$, and g_0 is a constant describing the coupling of the particle with the potential $U(r)$ (in the case of the Coulomb potential, it coincides with the electric charge of the incident particle). For the considered potential $U(r)$, the matrix element (4.30) is called the *bosonic propagator*. The name sounds strange, but it actually (as we shall see in the following paragraphs with the Feynman diagrams) simply expresses the idea that the interaction (i.e., a momentum exchange) takes place through the exchange of a *bosonic* particle, which *propagates* between the two fermions. The probability that this exchange occurs is described by the bosonic propagator and depends on the transferred momentum. The boson propagator is indicated as

$$f(\mathbf{q}) = g_0 \int U(\mathbf{r}) e^{i\mathbf{q} \cdot \mathbf{r}} d\tau. \quad (4.31)$$

For the central potential (4.15), one has

- $U(\mathbf{r}) = U(r) = \frac{g}{4\pi r} e^{-r/R}$
- $\mathbf{q} \cdot \mathbf{r} = qr \cos \theta$

²To be rigorous, we should also consider the spinor part of the fermion wave functions. As we shall see later, this changes the final result by a multiplicative factor, depending on the fermion spin.

- $d\tau = r^2 d\varphi \sin \theta d\theta dr$
- $\int_0^\pi \sin \theta e^{iqr \cos \theta} d\theta = (2 \sin qr)/qr$

For a complex number z , one has $\sin z = (e^{iz} - e^{-iz})/2i$ and Eq. 4.31 can be written as

$$f(\mathbf{q}) = f(q) = 4\pi g_0 \int_0^\infty U(r) \frac{\sin qr}{qr} r^2 dr = g_0 g \int_0^\infty e^{-r/R} \frac{e^{iqr} - e^{-iqr}}{2iq} dr.$$

Using the relation $R = \hbar/mc$, integrating the above equation and using $\hbar = c = 1$, one obtains

$$f(q) = \frac{g_0 g}{q^2 + m^2}.$$

(4.32)

This formula describes in the *momentum space* the same law as that expressed by the potential (4.15) in the *coordinate space*. Equation 4.32 can be interpreted as the term describing the probability that a boson be exchanged between the two interacting particles (fermions). The point where the exchanged boson is emitted or absorbed is called the *vertex*. The vertices are characterized by the corresponding *vertex factors*, i.e., the coupling constants g_0, g ; the vertex factors weigh the probability that the boson couples to each fermion. The *propagator* is the quantity $(q^2 + m^2 c^2)^{-1}$.

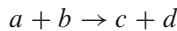
In Chap. 10, we shall extend the validity of (4.32) to the case where both energy and momentum are transferred; the variable q^2 will have a slightly different meaning (it will represent a relativistic invariant).

4.5 Cross-Sections and Lifetime: Theory and Experiment

In this section, we enter into the heart of the problem of how to compare *theoretical predictions* with *experimental data*. Amongst the experimentally accessible quantities, the particle *lifetime* and the *cross-section* are of fundamental importance.

4.5.1 The Cross-Section

Consider a reaction of the type



with two particles (a, b) in the initial state and two (c, d) in the final state. In an elastic collision, (c, d) are identical to (a, b) . If n_a is the density (cm^{-3}) of incident

particles with a velocity v_i relative to the target particle b , the flux Φ ($\text{cm}^{-2} \text{s}^{-1}$) of particles incident on the target is

$$\Phi = n_a v_i. \quad (4.33)$$

(If only one particle a , moving with a velocity v_i and described by the wave function ψ is considered, the flux is given by $\Phi = v_i |\psi|^2$, whose dimensional units are the same as in Eq. 4.33). The probability that a beam particle interacts with a target particle in the time unit is given by the quantity W defined in the previous section. It depends on Φ through a constant σ which has the dimensions of an area

$$W = \sigma \Phi = \sigma n_a v_i \quad [\text{cm}^2][\text{cm}^{-3}][\text{cm s}^{-1}]. \quad (4.34)$$

($W = \sigma |\psi|^2 v_i = \sigma v_i$ in the case of only one incoming particle. Remember that $|\psi|$ has the dimensions of $[\text{volume}]^{-1/2}$). If the interaction potential is unknown, information on the quantity W can be obtained from the cross-section measurement. This is the case for the *strong interaction between hadrons*, (discussed in Chap. 7) and for the *weak interaction* (described in Chap. 8). In both cases, information on the unknown interaction potential are inferred from lifetime and cross-section measurement.

On the opposite side, when the interaction potential is known (as for the *electromagnetic interaction*), the quantity W can be computed. In the case of a single incoming particle, from (4.34), one has

$$\boxed{\sigma = \frac{W}{v_i}}. \quad (4.35)$$

This relation is exactly true if all the involved particles are spinless. As it shall be shown below, when spins are considered, the number of possible final states given by (4.35) is multiplied by a factor $g_f = (2s_c + 1) \cdot (2s_d + 1)$, where s_c and s_d are respectively the spins of the particles c and d .

To obtain information on the quantity W (4.28), it should be connected to easily accessible experimental parameters. In the phase space expressed in Cartesian coordinates, the number of states of a particle is given by $dN = dx dy dz dp_x dp_y dp_z / \hbar^3$. In spherical coordinates, the number of states in a unit volume v and in the momentum range between p and $(p + dp)$ in the laboratory frame given by

$$dN = \frac{d\Omega}{(2\pi)^3 \hbar^3} p^2 dp \quad (4.36)$$

where $d\Omega$ is the differential solid angle; in spherical coordinates (θ, φ) one has $d\Omega = \sin \theta d\theta d\varphi$. Therefore, the number of available states corresponding to the total energy E_0 is (using the natural system of units, with $\hbar = c = 1$)

$$\frac{dN}{dE_0} = \frac{d\Omega}{(2\pi)^3} \cdot g_f \cdot p^2 \frac{dp}{dE_0}. \quad (4.37)$$

Let us now develop the calculation for the particular situation in which a heavy particle of mass M undergoes a negligible momentum variation as a result of an impact process (as is the case for a heavy nucleus in a Coulomb collision). Indicating respectively with E , p , m , the energy, momentum and mass of the scattered particle, the total energy in the final state is

$$E_0 = M + \sqrt{p^2 + m^2} \quad \text{from which} \quad dE_0 = \frac{p}{E} dp. \quad (4.38)$$

Making use of the relativistic relations $E = mc^2\gamma$, $p = mv\gamma$, one obtains (again using natural units) $p/E = v$ and

$$\frac{dp}{dE_0} = \frac{E}{p} = \frac{1}{v} \quad (4.39)$$

where v is the velocity of the particle scattered from the diffusion center at rest. It can be shown (e.g., in [P87]) that (4.39) is also valid in the c.m. system, where v is the relative velocity between the particles c , d . Equation 4.35 can be rewritten in a more general form as

$$d\sigma(a + b \rightarrow c + d) = \frac{1}{(2\pi)^2} |f(q)|^2 \frac{g_f}{v_i v} p^2 d\Omega. \quad (4.40)$$

We shall use (4.40) in the next section to obtain the differential cross-section when $f(q)^2$ is known; it shall also be used in the following chapters to obtain information on the interaction potential through the measurement of $d\sigma/d\Omega$.

4.5.2 Particle Decay and Lifetime

Particle decay is the spontaneous process in which one particle transforms itself into other lighter particles. Amongst charged particles, only the proton and the electron are stable (or at least have a lifetime much longer than the age of the universe, see Chap. 13). A *radioactive decay* is a process in which an unstable atomic nucleus disintegrates into a smaller nucleus together with the emission of particles or radiation (Chap. 14). Particle decays can be described by a simple law with only one free parameter, that is, the *lifetime* τ . This parameter varies from particle to particle. The lifetime spans from ∞ for stable particles, to billions of years for some nuclei, to $\tau \sim 900$ s for the neutron, down to $\tau \sim 10^{-23}$ s for most of the particles made of quarks (hadrons).

The decay law can be determined as follows. The probability $P(\Delta t)$ that a particle at time t decays in the following time interval Δt is equal to the product of Δt by a constant $1/\tau$, which depends on the particle

$$P(\Delta t) = \frac{\Delta t}{\tau}.$$

For a large number N of identical particles, the number of those decaying in the time interval Δt is $NP(\Delta t)$. These decays decrease the number of initial particles by an amount of $-\Delta t(dN/dt)$, that is,

$$NP(\Delta t) = \frac{N\Delta t}{\tau} = -\Delta t \frac{dN}{dt} \quad \rightarrow \quad \frac{dN}{dt} = -\frac{N}{\tau}. \quad (4.41)$$

Indicating with N_0 the number of particles present at the initial time, the solution of Eq. 4.41 is

$$N(t) = N_0 e^{-t/\tau}. \quad (4.42)$$

Equation 4.42 is the *law of radioactive decay*. Since $\frac{\int t \cdot N(t) dt}{\int N(t) dt} = \tau$, the constant τ is called the *lifetime*. It is conventionally defined in the *reference system in which the decaying particle is at rest*. Equation 4.42 is a phenomenological law in agreement with experimental observations and quantum mechanics theory. The objective of a fundamental interaction theory is to *predict* the value of τ . A decay process is nothing more than a transition from a defined physics state into one of the possible final states with a smaller mass, taking into account conservation laws. During this process, an intermediate particle (such as the photon in EM decays or the W^\pm, Z^0 bosons in weak decays) is exchanged between the initial and final states. If the transition probability W (units: s^{-1}) is large, the particle lifetime is small, and vice versa. Therefore, the transition probability W and the particle lifetime are related as

$$W = \frac{1}{\tau}$$

(4.43)

4.5.2.1 Decay Fraction and Branching Ratio

In general a particle has several decay modes. The *decay fraction* is the fraction of particles which decay through a particular decay mode with respect to the total number of possible decays; the decay fraction is measured by the relative amount of this decay Γ_i with respect to the total amount of decays: Γ_i/Γ . This ratio is also called *branching ratio* (BR). Obviously, $\sum_i \Gamma_i/\Gamma = 1$. A given *decay mode* of a particle usually has a characteristic lifetime, i.e., the average time between decays in the same specific channel. For example, the muon decay from the *Particle Data Book* [P10] (the biennial report on progress in particle physics and on particle properties) gives:

Particle	Mass (MeV)	Lifetime (s)	Decay Mode	Decay Fraction (Γ_i/Γ)
μ^\pm	105.65837(± 1)	$2.19703(\pm 4) \times 10^{-6}$	$e\nu\bar{\nu}$	100%

From the table, we learn that the μ decays into an electron plus two neutrinos in 100% of the cases. The number in brackets represents the uncertainty on the last significant digit. In the case of the pion, one instead has

Particle	Mass (MeV)	Lifetime (s)	Decay Mode	Decay Fraction (Γ_i/Γ)
π^\pm	139.5702(± 4)	$2.6033(\pm 5) \times 10^{-8}$	$\mu\nu$	$\simeq 99.98770\%$
			$e\nu$	1.230×10^{-4}
			$\mu\nu\gamma$	2.0×10^{-4}
			$e\nu\gamma$	7.39×10^{-7}
			$\pi^0 e\nu$	1.036×10^{-8}
			$e\nu e^+ e^-$	3.2×10^{-9}

This means that the pion has a main decay mode (into $\mu\nu$), but there are other more unique decays, each measured by a given decay fraction Γ_i/Γ . We shall explain in Sect. 8.10 the reason why the pion decay into νe is suppressed by a factor $\sim 10^4$ compared to the decay into $\nu\mu$.

Different decay channels Γ_i/Γ are often caused by different interaction mechanisms (only the weak interaction is involved in the pion case, as a neutrino is always present in the final state); each decay channel lifetime τ_i is obtained from Eq. 4.43 and is given by

$$W_i = \frac{(\Gamma_i/\Gamma)}{\tau}. \quad (4.44)$$

4.6 Feynman Diagrams

The Feynman diagrams are graphical representations of a perturbation contribution to the transition amplitude. They represent mathematical expressions defined by a set of well-defined rules which are not discussed in detail here. A thorough description of the rule codification can be found in theoretical physics texts (see, for instance, the review on the CERN website [4T73]). Feynman diagrams offer a simple visualization of the interaction mechanism between particles and provide rules for calculating the transition amplitude. A physics quantity is expressed as a series development of terms with increasing power of a dimensionless parameter (α_{EM} in the EM case). As the parameter is < 1 , the sum is composed of terms decreasing with increasing order. The first order approximation gives a better approximation if the coupling constant of the considered interaction is small.

Let us consider the EM interaction of electrons e^- and positrons e^+ with the presence of both *real* and/or *virtual* photons γ ; these particles are represented (see Fig. 4.3) respectively by

- e^- : a solid line with an arrow pointing in the same direction as the time (always assumed from left to right);

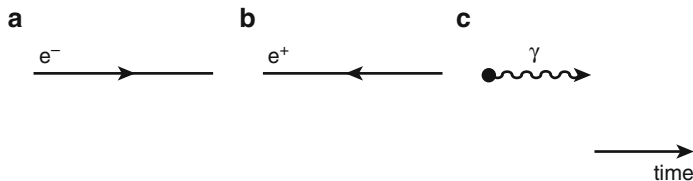


Fig. 4.3 Representation of free particles in Feynman diagrams. (a) The electron e^- moves with constant velocity $v < c$ and is denoted by an arrow in the same direction as the time arrow; (b) the positron e^+ moves with constant velocity $v < c$ in the direction opposite to the direction of time; (c) the photon moves with speed c

Fig. 4.4 Basic vertex of quantum electrodynamics. The *solid line* with an *arrow* represents an electron and the *wavy line* represents a photon

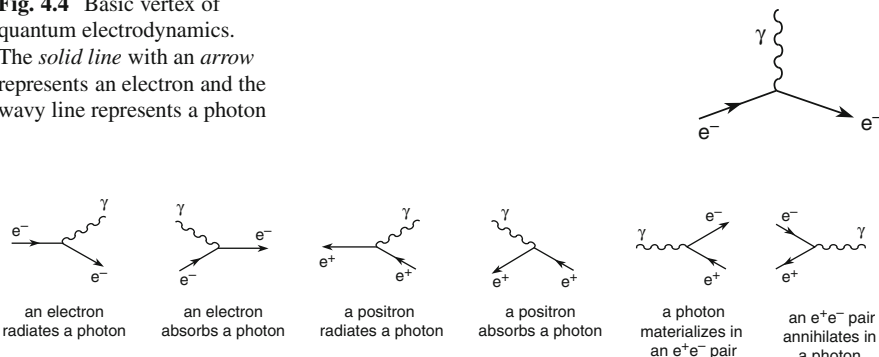


Fig. 4.5 Six examples of vertex diagrams oriented in time in order to describe six different basic QED processes

- e^+ : a solid line with an arrow opposite to the time direction;
- γ : a wavy line (sometimes indicated by an arrow, if the photon is real).

The particle is **real** or *on mass shell* if the relation $E^2 = m^2 c^4 + p^2 c^2$ is valid. For a **virtual** particle (or *off mass shell*), this energy-momentum relation is not verified. Particles connecting two interaction vertices are virtual (see below). In particular, a real photon has $m_\gamma = 0$; a virtual photon can have $E > pc$ (a *time-like* photon), or $E < pc$ (a *space-like* photon). A virtual particle cannot become free, it exists only for a time allowed by the uncertainty principle. The virtual photon is the messenger of the interaction between electrically charged particles (see Fig. 4.1).

The basic element of Feynman diagrams is the *vertex* (consisting of two fermionic lines plus one bosonic line), as shown in Fig. 4.4. The time is assumed on the horizontal axis. If the “legs” of the diagram are rotated in various ways with respect to the vertex point, the six diagrams of Fig. 4.5 are obtained. Each of them represents six different basic QED processes.

At each vertex, the energy, momentum, electric charge and other quantities (e.g., the baryon and lepton numbers introduced in the next chapter) must always be

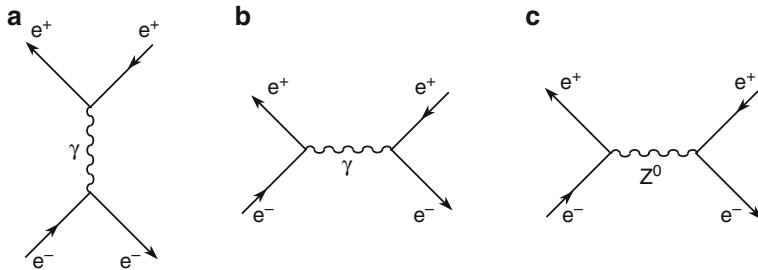
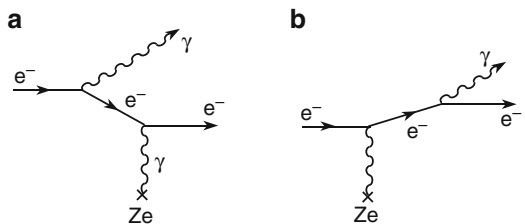


Fig. 4.6 (a, b) Feynman diagrams contributing to the lowest order elastic collision $e^+e^- \rightarrow e^+e^-$ due to the EM interaction only. (c) Contribution of the Z^0 boson of the weak interaction

Fig. 4.7 Lowest order Feynman diagrams for the emission of a photon by an electron in the Coulomb field of a nucleus (*bremsstrahlung*)



conserved. As discussed in Eq. 4.3, not one of the six processes shown in Fig. 4.5 is possible if the three particles are all real.

Let us use the basic QED vertex to build more complicated diagrams. For example, the diagram of Fig. 4.1 for the elastic $e^-e^- \rightarrow e^-e^-$ collision (*Møller scattering*) is obtained using twice the vertex of Fig. 4.4. Note that electrons are real, while the photon is virtual. This diagram is actually composed of two diagrams, each specifying which electron emits or absorbs the exchanged photon, as shown in Fig. 4.1a,b. These diagrams are the simplest combinations of the vertex of Fig. 4.4 (the *leading order* diagrams). Other examples of the lowest order diagrams are shown in Fig. 4.6a,b for the elastic $e^+e^- \rightarrow e^+e^-$ collision (*Bhabha scattering*). Note that the diagram of Fig. 4.6a is similar than that of Fig. 4.1c (and should be treated as Fig. 4.1a,b), while that of Fig. 4.6b (the *annihilation diagram*) is typical of an annihilation process. Figure 4.6c shows the contribution of the Z^0 boson (a neutral current weak interaction which is discussed later).

Figure 4.7 shows the emission of a photon by an electron in the Coulomb field of a nucleus of charge Ze (*bremsstrahlung*). Compared to the diagrams of Figs. 4.5 and 4.6, there is an additional vertex represented by the nucleus connected by the virtual photon. In addition to the real photon and the initial and final electrons, a virtual electron is also present (the e^- line between the two vertices).

The calculation of the transition probability and of the cross-sections is based on the use of the perturbation expansion. The bosonic propagator (4.32) can be interpreted as the exchange of a boson between two particles connected by two vertices and with a probability proportional to $(q^2 + m^2c^2)^{-1}$. Each vertex is

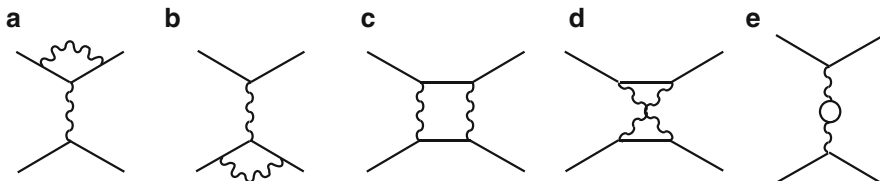


Fig. 4.8 Second order Feynman diagrams for the elastic collision $e^-e^- \rightarrow e^-e^-$

characterized by the presence of a *vertex factor* g_0, g describing the coupling of the boson with the particles. The cross-section (4.40) is the product of $|f(q)|^2$ with quantities depending on the phase space and on factors related to the particle spins. For the exchange of a photon (which is massless), one has $m = 0$ and the propagator is $1/q^2$; therefore, the cross-section is proportional to $1/q^4 = 1/t^2$ where ($t = q^2$).

The addition of higher order diagrams slightly changes the results obtained with lower order calculation. In terms of Feynman diagrams, in addition to the lowest order diagram (*leading order*), other diagrams with additional lines and vertices are added. The next order (*next-to-leading-order*) involves two more vertices, as shown in Fig. 4.8 in the case of the elastic $e^-e^- \rightarrow e^-e^-$ collision. Since each vertex contributes with $\sqrt{\alpha_{EM}}$ to the matrix element $|M_{if}|$, their contribution is about α_{EM} times lower (~137 times lower).

The Feynman diagrams are important for high precision calculations of QED processes (see specialized texts for details, e.g., [A89]). The diagrams are more easily interpretable in the momentum space than in the coordinate space (see comment after (4.32)).

4.7 A Few Examples of Electromagnetic Processes

4.7.1 Rutherford Scattering

The interaction between two particles is described in terms of a *cross-section*, that is, a quantity representing the likelihood that a reaction occurs. Let us consider the simple case of particles that collide against a single massive target particle at rest in the origin of a Cartesian reference frame. In the following, the description is limited to the specific case of the elastic scattering of point-like and spinless particles (the kinetic energy of the incident particles is conserved, the momentum changes), assuming that the collision takes place through a spherically symmetric potential (independent from the azimuth angle φ).

As shown in Fig. 4.9a, the diffusion angle is determined by the value of the *impact parameter* b . Particles with an impact parameter between b and $b + db$ reach the annular region between $(b, b + db)$ and are scattered within the angular region $(\theta, \theta - d\theta)$, corresponding to a solid angle $d\Omega$. For a larger impact parameter b ,

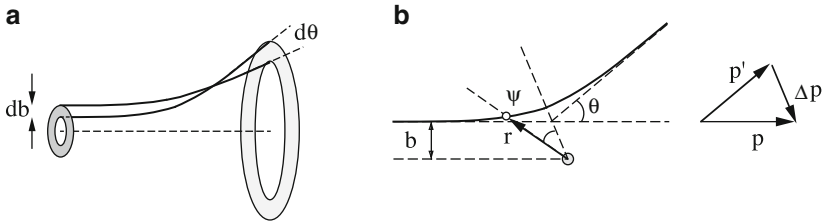


Fig. 4.9 Elastic scattering of charged particles reaching the region of surface $2\pi b db$ around a fixed massive center of diffusion (generally, a heavy nucleus) which produces a Coulomb type potential. (a) The incident particles are elastically scattered in the angular range $(\theta, \theta - d\theta)$. (b) Relation between the impact parameter b and the deflection angle in the Coulomb elastic scattering

the diffusion occurs at a smaller angle θ . For this reason, a negative $d\theta$ corresponds to a positive db . The number of incident particles elastically scattered per time unit in the interval $(\theta, \theta - d\theta)$ is

$$dN = 2\pi N_0 b db = N_0 d\sigma \quad (4.45)$$

where N_0 is the number of incident particles per area and time units and $d\sigma = 2\pi b db$ is the surface of the annular ring crossed by the incident particles scattered in the angular range $(\theta, \theta - d\theta)$. Note that if one considers dN as the difference between the number of initial and final particles, the variation of the number of beam particles is written as a negative term. The elastic differential cross-section $d\sigma/d\Omega$ is defined as

$$d\sigma(\theta) = \frac{d\sigma}{d\Omega} d\Omega = \frac{d\sigma}{d\Omega} 2\pi \sin \theta d\theta = -2\pi b db, \quad (4.46)$$

($d\Omega = 2\pi \sin \theta d\theta$ is the differential solid angle) from which one gets

$$\frac{d\sigma}{d\Omega}(\theta) = -\frac{b}{\sin \theta} \frac{db}{d\theta}. \quad (4.47)$$

In the general case, without assuming spherical symmetry, Eq. 4.46 is

$$d\sigma(\theta, \varphi) = b db d\varphi = -\frac{d\sigma}{d\Omega}(\theta, \varphi) d\Omega = -\frac{d\sigma}{d\Omega}(\theta, \varphi) \sin \theta d\theta d\varphi. \quad (4.48)$$

The *total elastic cross-section* is obtained by integrating Eq. 4.47 in θ :

$$\sigma_{tot}^{el} = \int \frac{d\sigma}{d\Omega}(\theta) d\Omega = -2\pi \int_0^\pi \sin \theta \frac{d\sigma}{d\Omega}(\theta) d\theta \quad (4.49)$$

as $\int d\varphi = 2\pi$. We can consider that the total cross-section represents the actual size of the target, or rather the “transverse” area offered by the diffusion center to the

incident particles. This is only qualitatively true: the effective area depends on the considered process and the incident particle energy. The cross-section $(d\sigma/d\Omega)_{el}$ is the fraction of cross-section due to elastic scattering at an angle in the range $(\theta, \theta + d\theta)$.

Classical calculation. The calculation can be applied to the elastic Coulomb scattering. For example, Rutherford used α particles (that is, ${}^4\text{He}$ nuclei) with a few MeV of energy, colliding against heavy gold ($Z = 79$) nuclei. The Coulomb potential of the nucleus with charge Ze is

$$U(r) = \frac{Ze}{r}. \quad (4.50)$$

If ze is the charge of the incident particle ($z = 2$ for helium nuclei), the Coulomb energy potential is $V(r) = zeU(r)$.

Classically (see Fig. 4.9b), the relation between the scattering angle θ , the incident particle kinetic energy $E_c = (p^2/2m)$ and the impact parameter b is given by (see Problem 4.3)

$$\tan \frac{\theta}{2} = \frac{zZe^2}{2E_c b} = \frac{\text{Potential energy at a distance } 2b}{\text{Kinetic energy}}, \quad (4.51)$$

from which one has

$$b = \frac{Zze^2}{2E_c} \cot \frac{\theta}{2}. \quad (4.52)$$

Then, it follows $(d(\cot x) = -(\sin x)^{-2} dx)$:

$$\frac{db}{d\theta} = -\frac{Zze^2}{2 \cdot 4E_c} \frac{1}{\sin^2 \theta/2}. \quad (4.53)$$

Placing this relation into Eq. 4.47, one obtains

$$\frac{d\sigma}{d\Omega}(\theta) = -\frac{b}{\sin \theta} \frac{db}{d\theta} = \frac{(Zze^2)^2}{(4E_c)^2} \frac{1}{\sin^4(\theta/2)}. \quad (4.54)$$

This corresponds to Rutherford's classical formula for elastic scattering between two spinless charged particles. The integral of (4.54) gives the total elastic cross-section,

$$\sigma_{tot}^{el} = \int \frac{d\sigma}{d\Omega}(\theta) d\Omega = 8\pi \left(\frac{Zze^2}{4E_c} \right)^2 \int_0^1 \frac{d(\sin(\theta/2))}{\sin^3(\theta/2)}. \quad (4.55)$$

Equation 4.55 diverges for $\theta \rightarrow 0$. This typical divergence of the Coulomb interaction is due to the potential spatial dependence in $(1/r^2)$, corresponding to an infinite range of the force. For very large r , a very small deflection is allowed.

To allow a comparison with experimental data, Eq. 4.55 can be integrated up to an angle $\theta = \theta_0 > 0^\circ$, representing, for example, the angular resolution of the experimental apparatus. A second effect should be considered: the target scattering centers are affected by the screening action of the atomic electrons. Incoming particles with impact parameters larger than the distance between the nucleus and the inner electrons of the gold atom *feel* an “effective” charge smaller than Ze .

The quantity e^2/E_c in (4.55) has the dimensions of a length; in particular, $e^2/m_e c^2 = 2.8 \times 10^{-13} \text{ cm} = r_e$ represents the *classical* electron radius. The term $(e^2/4E_c)^2$ in (4.55) at $E_c = 1 \text{ MeV} \simeq 2m_e$ corresponds to $r_e^2/64$.

Calculation in perturbation theory. It is instructive to consider the same process in the context of perturbation theory, using the bosonic propagator. As seen in Sect. 4.4, the matrix element $|M| = f(q)$ is given by Eq. 4.32 which includes the special case of the photon ($m = 0$). The matrix element for the transition probability of a particle with “charge” $g_0 = (ze)$ on a nucleus with charge $g/4\pi = (Ze)$ is

$$f(q) = 4\pi \frac{Zze^2}{q^2} \quad (4.56)$$

where q is the transferred momentum between the initial and final states in the interaction (Fig. 4.9b)³

$$q^2 = (\mathbf{p} - \mathbf{p}')^2 = p^2 + p'^2 - 2\mathbf{p} \cdot \mathbf{p}' \simeq 2p^2(1 - \cos\theta) = 4p^2 \sin^2 \theta/2. \quad (4.57)$$

From Eq. 4.40, assuming relativistic velocities before and after the collision and using $\hbar = c = 1$, one has

$$d\sigma = \frac{1}{(2\pi)^2} |f(q)|^2 \frac{p^2}{v_i v} d\Omega \quad (4.58)$$

that is, as $\frac{p^2}{v_i v} \simeq m^2$:

$$\frac{d\sigma}{d\Omega} = \left[4\pi \left(\frac{Zze^2}{4p^2 \sin^2 \theta/2} \right) \right]^2 \cdot \frac{m^2}{(2\pi)^2}. \quad (4.59)$$

In the approximation of a nucleus with very high mass, spinless and non-relativistic incident particles ($p^2/(2m) = E_c$), one finally has

$$\left(\frac{d\sigma}{d\Omega} \right)_R = \frac{Z^2 z^2 e^4 m^2}{4p^4 \sin^4 \theta/2} = \frac{Z^2 z^2 e^4}{(4E_c)^2 \sin^4 \theta/2} \quad (4.60)$$

³The quantity q^2 defined above is not relativistically invariant. In Sect. 10.3.1, it shall be redefined to make it independent of the choice of the reference system.

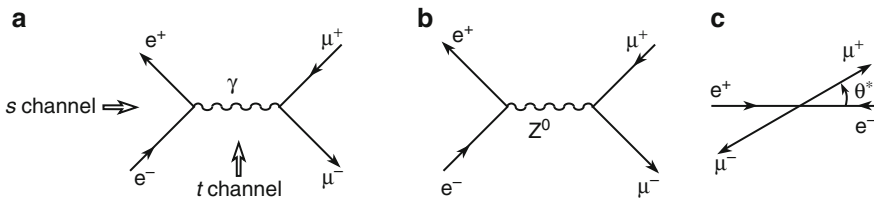


Fig. 4.10 Feynman diagrams for the reaction $e^+e^- \rightarrow \mu^+\mu^-$ caused by (a) electromagnetic interaction and (b) through the weak neutral current. Note that the reaction in the s channel is $e^+e^- \rightarrow \mu^+\mu^-$ while in the t channel, it is $e^-\mu^+ \rightarrow e^-\mu^+$. (c) Illustration of the collision $e^+e^- \rightarrow \mu^+\mu^-$ in the c.m. system

coinciding with Eq. 4.54 obtained with the classical calculation, see also problem 4.6. This equation is valid for any electric charge, assuming a target particle much heavier than the incident one. For example, this is the case for the e^-p scattering ($Z = z = 1$). The study of this process shall be extended in Chap. 10 in order to include the finite mass of the interacting particles, their spin and the finite size of the proton. Note that Eq. 4.60 depends on E_c^{-2} : the probability of a particle to be elastically scattered through the electromagnetic interaction decreases quadratically with increasing kinetic energy of the incident particle.

4.7.2 The $e^+e^- \rightarrow \mu^+\mu^-$ Process

(This and the following subsections are more advanced, and can be skipped during the first reading). The annihilation of an electron–positron pair with the creation of a muon–antimuon pair is a typical example of an electromagnetic process whose cross-section can be calculated with Feynman diagrams. The result of the calculation is used in Sect. 9.3 which describes the discovery of heavy quarks.

The electromagnetic cross-section for the reaction $e^+e^- \rightarrow \mu^+\mu^-$ can be obtained from the lowest order Feynman diagram of Fig. 4.10a. The cross-section is proportional to α_{EM}^2 (because two vertices are present). The e^+e^- annihilation generally occurs in colliders where particle and antiparticle have momentum equal in magnitude and opposite in direction. In this case, the relativistically invariant q^2 coincides (in natural units) with the c.m. energy s . Using $p^2 = s$, one obtains an equation similar to (4.59), that is,

$$\sigma \sim \alpha_{EM}^2 \frac{(\hbar c)^2}{s}. \quad (4.61a)$$

The resulting angular distribution for nonpolarized e^+, e^- beams is given by

$$\frac{d\sigma}{d\Omega} = \frac{\alpha_{EM}^2}{4s} (1 + \cos^2 \theta^*) \quad (4.61b)$$

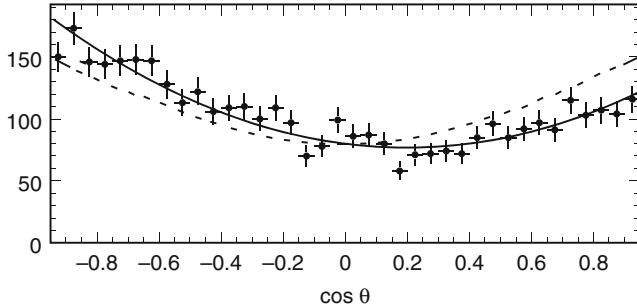


Fig. 4.11 Angular distribution in the c.m. system of the μ^- , from the process $e^+e^- \rightarrow \mu^+\mu^-$ at $\sqrt{s} \simeq 89$ GeV. The *dashed line* represents the $(1 + \cos^2 \theta^*)$ shape predicted by the EM interaction; the *solid line* is the optimization of experimental data in which a small effect due to weak interactions (diagram of Fig. 4.10b) is included

where θ^* is the emission angle of the muon in the c.m. system (see Fig. 4.10c). The term $(1 + \cos^2 \theta^*)$ comes from the e^+, e^- total angular momentum: $J = 0$ or $J = 1$ if their spin are antiparallel or parallel. For $J = 0$, as discussed in Sect. 7.5.1, the differential cross-section has no angular structure; for $J = 1$, angular momentum conservation requires $\frac{d\sigma}{d\Omega} \propto \cos^2 \theta^*$.

The integration on the solid angle of (4.61b) for energies well above the muon mass (this process has a threshold of $\sqrt{s} = 2m_\mu c^2$) leads to

$$\sigma(e^+e^- \rightarrow \mu^+\mu^-) = \frac{4\pi\alpha_{EM}^2(\hbar c)^2}{3s} = \frac{86.8}{s} \text{ nb} \quad \text{if } s \text{ in GeV}^2, \quad (4.62)$$

where $s = (2E_0)^2$ with E_0 = energy of the colliding electron and positron in the c.m. system. The factor $4\pi/3$ is derived from the integration over the solid angle.

The experimental angular distributions at relatively low energies are in agreement with the $(1 + \cos^2 \theta^*)$ shape of (4.62), but at higher energies, for example, $\sqrt{s} > 20$ GeV, a disagreement is clearly visible in Fig. 4.11. The $e^+e^- \rightarrow \mu^+\mu^-$ can also occur through the exchange of a Z^0 , as shown in Fig. 4.10b. This process is a pure weak interaction process (neutral current). It becomes more important with increasing c.m. energy, reaching a maximum at energies corresponding to the Z^0 boson mass. This topic shall be discussed in Chap. 9. We shall see in Chap. 11 that at high energy, the electromagnetic and weak interactions give rise to a unified electroweak interaction.

4.7.3 Elastic Scattering $e^+e^- \rightarrow e^+e^-$ (Bhabha Scattering)

The two EM diagrams of Fig. 4.6a,b contribute to this process. The s channel diagram shown in Fig. 4.6b produces a result similar to that obtained with the graph of Fig. 4.10a for $e^+e^- \rightarrow \mu^+\mu^-$. The diagram of Fig. 4.6a is similar to that for the

elastic scattering and produces a term which dominates at small diffusion angles. The corresponding cross-section rapidly increases with decreasing angle. The two vertices contribute to the matrix element M_{if} , each with a $\sqrt{\alpha_{EM}}$; the photon propagator contributes with a term $1/q^2$. Therefore, the cross-section is proportional to $\frac{d\sigma}{dq^2} \approx M_{if}^2 \approx \frac{q_{EM}^2}{q^4}$. The correct formula for relativistic electrons (obtained using the full QED procedure [H84]) is

$$\frac{d\sigma}{dq^2} = \frac{4\pi\alpha_{EM}^2(\hbar c)^2}{q^4c^2} \cos^2 \frac{\theta^*}{2}. \quad (4.63)$$

The weak interaction diagram shown in Fig. 4.6c must be added to the two EM diagrams. The result provides a complicated angular distribution, in which the behavior can be roughly described by two contributions: at small angles, the cross-section has a dependence in $1/\theta^4 \approx 1/q^4$ due to the EM terms; at large angles, the situation is similar to that of the process $e^+e^- \rightarrow \mu^+\mu^-$ (see Fig. 4.11).

The total cross-section for the Bhabha scattering has a $1/s$ energy dependence, as the $e^+e^- \rightarrow \mu^+\mu^-$ process. This is a characteristic of the EM interaction. The large cross-section at small angles is only due to the EM interaction and is calculated with a precision better than 1%. Electron–positron colliders (for example, the LEP at CERN) use the measurement of the Bhabha cross-section at small angles to derive the collider luminosity. An accurate luminosity measurement is necessary for precise measurements of the cross-sections of other processes (Chap. 10).

4.7.4 $e^+e^- \rightarrow \gamma\gamma$ Annihilation

The production of a photon pair in an e^+e^- annihilation offers the possibility to check the QED validity at the highest available energies. At the lowest order, the process takes place through the exchange of an electron, as shown in the Feynman diagram of Fig. 4.12a; therefore, this process only involves the EM interaction and the terms due to the weak interaction are negligible. The cross-section due to this diagram is

$$\sigma_T = \frac{2\pi\alpha^2}{s} \ln \left(\frac{s}{m_e^2} \right). \quad (4.64)$$

Experimental results on the total cross-section are in good agreement with the predictions of Eq. 4.64 (see Fig. 4.12b).

4.7.5 Some QED Checks

Checks of the QED have been made with great precision in many fields of particle physics. The most accurate test arises from the measurement of the electron and muon magnetic moments. The lowest order Dirac theory predicts that the magnetic moments of both particles are equal to one Bohr magneton $\mu_{Bohr} = e\hbar/2m$

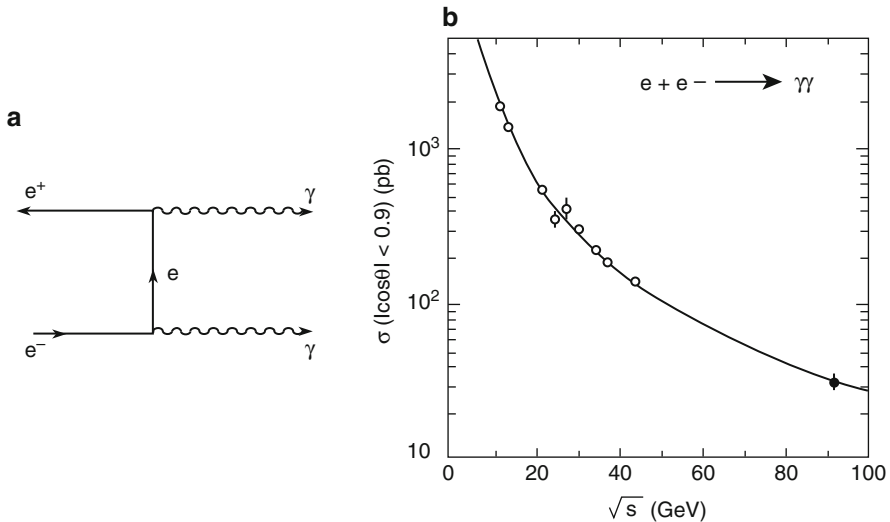


Fig. 4.12 $e^+e^- \rightarrow \gamma\gamma$ process: (a) first order Feynman diagram and (b) total cross-section as a function of c.m. energy (LEP data)

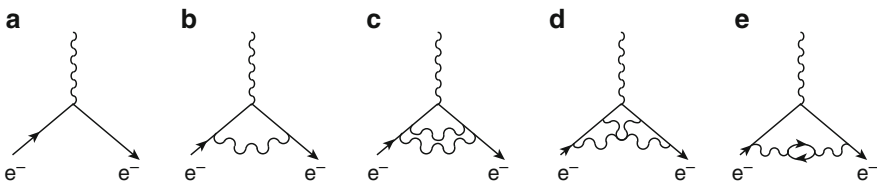


Fig. 4.13 Feynman diagrams for the interaction between the magnetic moment of the electron with an external \mathbf{B} field. (a) lowest (leading) order, (b) next-to-leading order, (c–e) next-to-next-to-leading order [W91]

(with $m = m_e, m_\mu$). The radiative corrections accounts for the interaction of the electron (muon) with the magnetic field needed to make the measurement (see Fig. 4.13). The radiative corrections modify the ratio as ($\alpha = \alpha_{EM}$):

$$\frac{\mu_e}{\mu_{Bohr}} = 1 + \frac{1}{2} \frac{\alpha}{\pi} - 0.32848 \left(\frac{\alpha}{\pi} \right)^2 + 1.1765 \left(\frac{\alpha}{\pi} \right)^3 - 0.8 \left(\frac{\alpha}{\pi} \right)^4 = 1.001159652307(11). \quad (4.65)$$

The experimental value is 1.001 159 652 193 (10) (the last two numbers in the bracket represents the experimental uncertainty). The theoretical error is due to the uncertainty on higher order diagrams.

An agreement experiment-theory of the same order of magnitude is also obtained for the magnetic moment of the muon. Note that one often refers to the value of $(g - 2)$ where g is the gyromagnetic ratio expected to be equal to two with the lowest order diagram. Other QED precision tests will be discussed in Chap. 9.

Chapter 5

First Discussion of the Other Fundamental Interactions

5.1 Introduction

In the last chapter, we learned that the electromagnetic interaction between particles occurs through momentum exchange. Classically, this exchange is due to a *field*: a particle is a source of one or more fields through which it modifies the properties of the surrounding space. A second particle within the range of the first particle field and which generates the same field is subject to a force. Due to the field created by the second particle, the first particle “feels” the same force but in the opposite direction (third principle of dynamics). A field can only be measured through its effects on another source of the same field.

In terms of quantum mechanical laws and in analogy with QED, any interaction between two fermionic particles is seen as the process of emission/absorption of a *virtual bosonic particle*. These virtual bosonic particles are “carriers” of the field. Virtual particles cannot be directly observed because they are “hidden” by the uncertainty principle.

Presently, four types of interactions are known: the *gravitational*, *weak*, *electromagnetic* and *strong* interactions. The electromagnetic interaction was presented in the previous chapter. Here, we will give a semiquantitative introduction of the remaining three. The gravitational interaction is negligible at the submicroscopic level (except for the first moments of the universe, as we shall see in Chap. 13) and will no longer be considered in the remainder of the book.

5.2 The Gravitational Interaction

From a historical point of view, the gravitational force (the first known interaction) can be regarded as the “unification” of two interactions. Until the formulation of Newton (*Philosophiae Naturalis Principia Mathematica*, 1687), the attraction force between the sun and the planets, and the weight of objects on Earth’s surface were

considered as two distinct forces. Newton realized that the force that ties the planets to the sun, and the moon to the earth is the same force as that responsible for the fall of bodies on earth. The gravitational force is expressed by

$$\mathbf{F} = -G_N \frac{m_1 m_2}{r^2} \hat{\mathbf{r}} \quad (5.1)$$

where m_1 and m_2 are the gravitational masses of the two interacting bodies, r is the distance between them, $\hat{\mathbf{r}}$ is a unit vector directed from m_1 to m_2 , and G_N is the gravitational constant

$$G_N = 6.672 \cdot 10^{-8} \text{ cm}^3 \text{ g}^{-1} \text{ s}^{-2} = 6.672 \cdot 10^{-11} \text{ N m}^2 \text{ kg}^{-2} .$$

The gravitational mass is always positive and therefore, the gravitational force is always attractive.

It is an experimental fact and a principle of general relativity that the ratio between the inertial mass (m_i) and the gravitational mass (m_g) is constant for all bodies. In our metric system, m_i and m_g are dimensionally and numerically equal.

Each interaction can be characterized by a dimensionless parameter expressed in terms of universal constants; these *coupling constants* (similar to α_{EM}) characterize the intensity of the interactions (see Table 5.1). For gravity, taking the proton mass as the fundamental mass, the corresponding dimensionless quantity is

$$\alpha_G = G_N \frac{m_p^2}{\hbar c} = 6.673 \cdot 10^{-11} \frac{(1.67 \cdot 10^{-27})^2}{1.05 \cdot 10^{-34} \cdot 3.00 \cdot 10^8} = 5.90 \cdot 10^{-39} . \quad (5.2)$$

In terms of universal constants, two other quantities related to the gravitational interaction can be constructed. The first is the *Planck mass*

$$M_{Pl} = \sqrt{\hbar c / G_N} = \sqrt{3.1638 \cdot 10^{-26} / 6.673 \cdot 10^{-11}} = 1.221 \cdot 10^{19} \text{ GeV} \quad (5.3)$$

which is a huge mass compared to the most massive particles known today, i.e., ~ 100 GeV for the weak vector bosons and ~ 170 GeV for the *top* quark. The second quantity is the *Planck length*

$$\ell_{Pl} = \frac{\hbar c}{M_{Pl} c^2} = 1.616 \cdot 10^{-35} \text{ m} . \quad (5.4)$$

Note that the Planck length is $\sim 10^{20}$ smaller than the proton size.

A satisfactory quantum theory of gravitation still does not exist. It is expected that the particle carrier of the gravitational field, the *graviton*, should have spin two, and zero mass (the mass is inversely proportional to the range of the force, which is infinite). The gravitational force plays a fundamental role in the macrocosm. At the subatomic level, the gravity is completely negligible compared to the other three interactions: if the hydrogen atom was held together by only the gravitational force,

its size would be larger than that of the universe. It is assumed that the gravitational interaction becomes important for distances of the order of the Planck length and energy (and mass) above the Planck mass.

5.3 The Weak Interaction

The weak interaction (WI) was initially investigated while studying the radioactive decays of atomic nuclei (Chap. 14). The β decay of a nucleus $A(Z, N)$ with mass number A , with Z protons and N neutrons, occurs in the following such that

$$A(Z, N) \rightarrow A(Z + 1, N - 1)e^- \bar{\nu}_e . \quad (5.5a)$$

This process corresponds to a neutron decay

$$n \rightarrow p e^- \bar{\nu}_e \quad (5.5b)$$

which, at the fundamental level, corresponds to the decay of a d quark

$$d \rightarrow u e^- \bar{\nu}_e . \quad (5.5c)$$

The nucleons (protons and neutrons) in (5.5a) and quarks in (5.5b), which do not participate in the decay, are called “spectators.”

At the level of the ultimate constituents of matter, the weak interaction takes place between two quarks, two leptons and between a lepton and a quark. Quarks and leptons can be thought of as having a *weak charge*. The weak interaction is less intense than strong and EM interactions. In most cases, it is “overwhelmed” by the strong and EM interactions, unless these cannot act due to some conservation law.

The weak interaction is responsible for all processes in which neutrinos are involved. Neutrinos have neither a strong charge (*color charge*) nor an electric charge. Examples of neutrino interactions on protons and electrons are

$$\left\{ \begin{array}{ll} \text{High energy } \bar{\nu}_\mu \text{ interaction} & \bar{\nu}_\mu p \rightarrow \mu^+ n \\ \text{High energy } \bar{\nu}_e \text{ interaction} & \bar{\nu}_e p \rightarrow e^+ n \\ (\text{Charged Current interaction}) & \\ \text{Elastic scattering } \nu_\mu e^- & \nu_\mu e^- \rightarrow \nu_\mu e^- \\ (\text{Neutral Current interaction}). & \end{array} \right. \quad \begin{array}{l} (a) \\ (b) \\ (c) \end{array} \quad (5.6)$$

The β decay of a neutron (5.5b) is an example involving a neutrino. Note that the neutron cannot have other types of decay because of baryon and lepton number conservation (Sect. 5.5.3): a proton and an e^- , $\bar{\nu}_e$ pair must be present in the final state. Neutron decay into $p\mu^- \bar{\nu}_\mu$ or $p\tau^- \bar{\nu}_\tau$ are energetically forbidden.

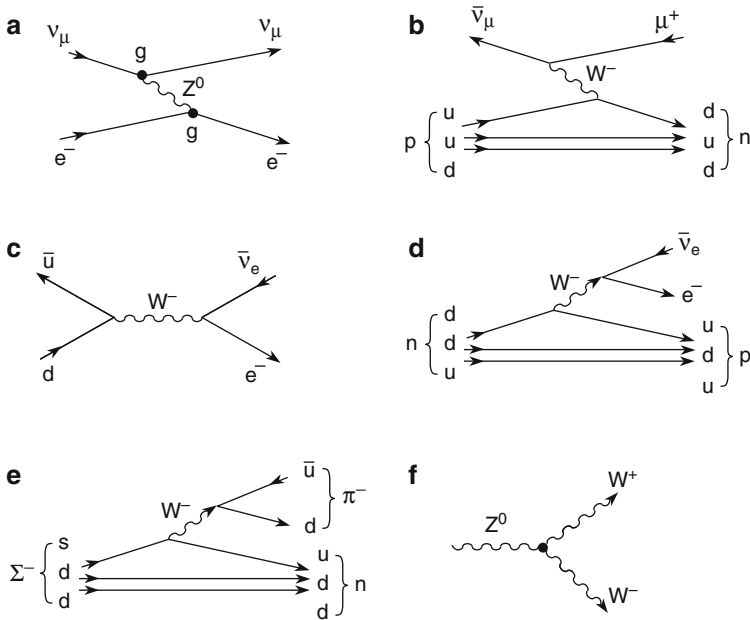


Fig. 5.1 Weak interaction Feynman diagrams. (a) Elastic scattering $v_\mu e^- \rightarrow v_\mu e^-$, mediated through a Z^0 boson (neutral current weak interaction); g represents the coupling constant. (b) $\bar{v}_\mu p \rightarrow \mu^+ n$ interaction mediated through a W^- boson (charged current interaction). The elementary process is $\bar{v}_\mu u \rightarrow \mu^+ d$, with the remaining u, d quarks acting as “spectators.” (c) Charged current $\bar{u}d \rightarrow \bar{v}_e e^-$ interaction involving quarks, mediated through a W^- boson. (d) Neutron decay, $n \rightarrow p e^- \bar{v}_e$; quarks d, u act as “spectators,” the basic process is similar to that shown in (c), with the transformation of the incoming d quark into an outgoing u . (e) $\Sigma^- \rightarrow n \pi^-$ decay. (f) Triple vertex between Z^0, W^+ and W^- bosons

Quark interactions and decay processes involving a quark *flavor* change (see Chap. 7) with a variation in strangeness S or charm C quantum numbers ($\Delta S \neq 0$, $\Delta C \neq 0$) are forbidden in strong and EM interactions. Those processes can therefore be used to study the weak interaction. The nonleptonic decay of the Σ^- hyperon (Fig. 5.1e) is an example of a decay with a flavor change:

$$\begin{array}{c} \Sigma^- \longrightarrow n + \pi^- \\ S \quad -1 \quad 0 \quad 0 \end{array} \quad (5.7a)$$

which involves the transformation of a strange quark s ($S = -1$) into a nonstrange quark u ($S = 0$). Similarly to the neutron decay, one has at the quark level (Fig. 5.1d):

$$\Sigma^- \left\{ \begin{array}{l} s \rightarrow u W^- \rightarrow u(d\bar{u}) \rightarrow u\pi^- \\ dd \quad dd \quad dd \quad dd \end{array} \right\} \rightarrow n\pi^- \quad (5.7b)$$

with the two dd quarks of the initial Σ^- acting as spectators.

The weak interaction is mediated through the massive vector bosons, W^\pm and Z^0 , respectively with a mass of 80.3 and 91.2 GeV. The processes with a W^+ or W^- exchange are called *Charged Current interactions*. They involve the transformation of a lepton into another lepton of the same family (see reactions (5.6a,b)) and of a quark into a different flavor quark. The processes with a Z^0 exchange are called *Neutral Current interactions* (see reaction (5.6c)). Figure 5.1 illustrates the interpretation of processes such as (5.6) in terms of quarks and leptons exchanging a W^+ , W^- or Z^0 vector boson. Note that the leptonic weak vertices involve only members of the same family (= generation). The emission (or absorption) of a W boson by a lepton transforms a member of the family into the other, and vice versa ($e^- \leftrightarrow \nu_e; \mu^- \leftrightarrow \nu_\mu; \tau \leftrightarrow \nu_\tau$). As discussed in Chap. 8, transitions between different families are allowed in the quark sector. “Spectator” quarks present in weak processes with hadrons are later involved in the hadronization process (Chap. 10).

An estimate of the intensity of the weak interaction with respect to the EM one can be obtained by comparing the lifetimes of decays involving particles with similar masses, but due to different interactions, that is,

$$\begin{aligned} \text{Weak interaction} \quad & \pi^- \rightarrow \bar{\nu}_\mu \mu^- \quad \tau_{WI} = 2.6 \cdot 10^{-8} \sim 10^{-8} s \\ \text{Electromagnetic interaction} \quad & \pi^0 \rightarrow \gamma \gamma \quad \tau_{EM} = 8.4 \cdot 10^{-17} \sim 10^{-16} s. \end{aligned}$$

The ratio between the two lifetimes is related to the inverse of the ratio between transition amplitudes: ($\tau_{WI}/\tau_{EM} \propto W_{EM}/W_{WI}$), (4.43). The “weak” diagram of Fig. 5.1e can be interpreted in a similar manner to that of the EM interaction of Fig. 4.1. The contribution of the two vertices to the scattering amplitude is $W_{WI} \propto \alpha_W \alpha_W = [gg]^2$, where g may be thought of as the “weak” equivalent of the electric charge. For the electromagnetic interaction, one has $W_{EM} \propto \alpha_{EM} \alpha_{EM} = [e^2]^2$. It follows that

$$\frac{\alpha_W}{\alpha_{EM}} \propto \left(\frac{\tau_{EM}}{\tau_{WI}} \right)^{-1/2} \simeq \left(\frac{10^{-16}}{10^{-8}} \right)^{1/2} \simeq 10^{-4}. \quad (5.8)$$

This is a rough estimate, which neglect some factors, but sufficient to show that the weak interaction is much weaker than the electromagnetic one. The “magic” of being able to estimate the particle lifetimes when the coupling constant is known shall be discussed in detail in Chap. 8.

The weak interaction bosonic propagator must take into account the fact that the (W^\pm, Z^0) masses are large. According to (4.32), the transition probability for the weak interaction W_{WI} (Sect. 4.4) becomes

$$W_{WI}^{1/2} \propto f(q^2) = \frac{g^2}{q^2 + m_{W,Z^0}^2} = \frac{\alpha_W}{q^2 + m_{W,Z^0}^2}. \quad (5.9)$$

At low energies, one has $q^2 \ll m_{W,Z^0}^2$ and therefore $f(q^2) \simeq g^2/m_{W,Z^0}^2 = \text{constant}$, independent of q^2 . Because the Fourier transform of a constant in momentum space is a Dirac delta function in the coordinate space, the interaction is practically point-like, as Fermi postulated in 1935. For $q^2 \ll m_{W,Z^0}^2$, one can write

$$\frac{G_F}{\sqrt{2}} = \frac{g^2}{8m_W^2} \quad (5.10)$$

where G_F is the Fermi coupling constant, $G_F/(\hbar c)^3 = 1.1664 \cdot 10^{-5} \text{ GeV}^{-2}$. The dimensionless constant of the weak interaction can be constructed using, for example, the proton mass m_p as the reference mass

$$\alpha_W = (m_p c^2)^2 \frac{G_F}{(\hbar c)^3} = (0.932827)^2 \cdot 1.1664 \cdot 10^{-5} = 1.027 \cdot 10^{-5}. \quad (5.11)$$

The weak coupling $g = \sqrt{\alpha_W}$ is not constant, but increases with energy with a dependence stronger than that of α_{EM} (Chap. 11).

The weak interaction violates a number of conservation laws. For example, it violates the conservation of parity (Sect. 6.4). Assuming that neutrinos are massless,¹ the weak couplings of right-handed neutrinos and left-handed antineutrinos are null. Therefore, neutrinos are always left-handed, that is, the neutrino spin (\Leftarrow) is antiparallel to the momentum (\rightarrow): $\nu = (\overleftarrow{})$. The antineutrinos are always right-handed, i.e., with parallel spin and momentum: $\bar{\nu} = (\overrightarrow{})$.

A “triple” vertex involving the vector bosons Z^0 , W^+ and W^- (see Fig. 5.1f) is also theoretically allowed. Due to the high mass of the Z^0 , W^\pm bosons, the contribution of this vertex is negligible at low energy. It becomes important in $e^+e^- \rightarrow Z^0 \rightarrow W^+W^-$ collisions, for $\sqrt{s} \geq 2m_W \simeq 161 \text{ GeV}$ (Chap. 9).

5.4 The Strong Interaction

At the fundamental level, the strong interaction takes place between quarks and gluons (Fig. 5.2). It controls the collisions between two quarks, the interaction between three quarks to form a baryon, or between a quark and an antiquark to form a meson.

It can be assumed that the force between two nucleons (Chap. 14) is a “residual” strong force, similar to the electromagnetic force between two atoms to form

¹Recent experimental results on neutrino oscillations demonstrate that neutrinos have a very small, but nonzero, mass (Sect. 12.6).

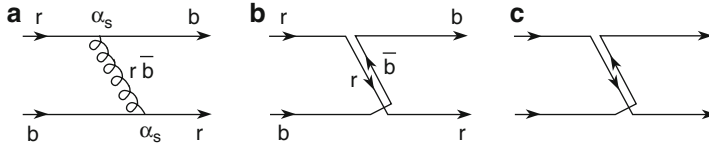


Fig. 5.2 (a) Illustration of the strong force between a red (r) quark and a blue (b) quark through the exchange of a red-antiblue ($r\bar{b}$) gluon (α_S represents the squared amplitude of the process). (b), (c) Illustration of the same process with color lines. Note that the line that goes back in time represents the (\bar{b}) anticolor. The black and white figure does not affect the representation. It would be difficult to draw the *antired* or the *antiblue*. The three colors, in fact, have no relation to the ordinary colors in the visible electromagnetic spectrum

a molecule. Indeed, the fundamental electromagnetic force occurs between protons and electrons to form the hydrogen and heavier atoms. The force between atoms (neutral objects) is a “residual” EM force.

The source of the EM interaction is the electric charge and the interaction is mediated by the photon. There is only one type of electric charge, and that of the opposite sign. The theory of strong interaction is *quantum chromodynamics* (QCD). It is modeled by analogy to quantum electrodynamics (QED). The source of the strong force is the *color charge*. Three degrees of freedom are necessary to describe the dynamics: the *red* (r), *blue* (b) and *green* (g) colors for quarks and three anticolors *antired* (\bar{r}), *antiblue* (\bar{b}) and *antigreen* (\bar{g}) for the corresponding antiquarks. The color choice is purely conventional.

The strong interaction is mediated by eight massless gluons. Each gluon carries a color and an anticolor charge: $r\bar{b}$, $r\bar{g}$, $b\bar{r}$, $b\bar{g}$, $g\bar{r}$, $g\bar{b}$, plus two linear combinations. The Feynman diagram shown in Fig. 5.2 describes the interaction between a red and a blue quark, with the exchange of a “colored” gluon (red, antiblue). Note that the color line has a continuous arrow in the same direction as the time; the arrow directed from right to left corresponds to the anticolor. The strong interaction changes the quark color, though not the quark flavor (a u or d quark remains unchanged in the strong interaction). A flavor variation is only possible in weak interaction processes.

Similarly to what was done with the weak interaction, one can obtain an estimate of the relationship between the strong and the EM coupling constants using the lifetimes of strong and EM decays involving two particles with similar masses. Hadrons decaying via the strong interaction (e.g., $N^* \rightarrow N\pi$) have lifetimes $\tau_S \sim 10^{-23}$ s, while particles that decay via the electromagnetic interaction (e.g., $\Sigma^0 \rightarrow \Lambda^0\gamma$) have lifetimes of the order of 10^{-19} s. This yields

$$\frac{\alpha_S}{\alpha_{EM}} \simeq \left(\frac{\tau_{EM}}{\tau_S} \right)^{1/2} \simeq \left(\frac{10^{-19}}{10^{-23}} \right)^{1/2} \simeq 100 \text{ which leads to } \alpha_S \sim 1. \quad (5.12)$$

The fact of the matter is, $\alpha_S \sim 1$ has an important consequence, that is, **the condition for the validity of the perturbation theory fails**. A perturbation diagram

Fig. 5.3 (a) Illustration of a three-gluon vertex and (b) its simplest interpretation in terms of color lines

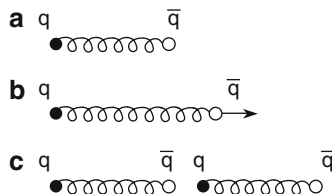
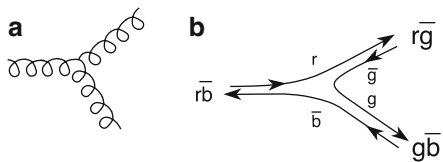


Fig. 5.4 (a) The interaction between a quark and an antiquark in a meson at a relatively large distance can be thought of as an elastic force (the spirals of the illustration represent an elastic, not gluons). (b) An attempt to elongate the elastic to free the quark-antiquark pair results in the creation (formation) of a new quark-antiquark pair (c)

with the exchange of one gluon, like the one shown in Fig. 5.2, can no longer be the dominant diagram. The diagrams with the exchange of many gluons are equally important. The calculation of quantities at low transferred momentum squared (q^2) processes is impossible. For high q^2 , i.e., for short distance collisions, it can be shown (Chaps. 9 and 11) that α_S decreases to a value of the order of $\simeq 0.1$ ($\alpha_S \simeq 0.12$ at $q^2 = m_Z^2$). In this case, diagrams with a single gluon exchange are a good approximation for high q^2 processes.

Since the gluons carry one color and one anticolor charge, the interaction amongst gluons through three-gluon vertices, as shown in Fig. 5.3a, is possible. Figure 5.3b shows the interpretation in terms of color lines. The presence of a vertex with three gluons with a very high probability at low q^2 qualitatively distinguishes the strong interaction from the other interactions. A vertex with four gluons is also foreseen. The EM interaction has no vertex with two or more photons.

The quasistatic potential between two quarks within a hadron can be parameterized in the following form:

$$V_S = -\frac{4}{3} \frac{\alpha_S}{r} + Kr . \quad (5.13)$$

The Coulomb-type term dominates at small distances; it is not divergent, as α_S is not constant, but decreases with decreasing distance (*asymptotic freedom*). This makes the radius of hadrons finite, as an equilibrium position is reached. The second term, which linearly increases with the distance r between the two quarks, gives rise to an elastic-type force. It is related to the interaction between gluons

Table 5.1 Main properties of the four fundamental interactions at low energy

Force	Strength (adimensional constant)	Range (cm)	Subjected particles	Exchanged (boson) particle	Mass of the exchanged bosons	Spin ^{Parity} of the exchanged bosons
Strong	0.1 { <i>short distances</i>	10^{-13}	Quarks, gluons	8 gluons	0	1^-
	1 { <i>large distances</i>					
Electro- magnetic	$1/137$	∞	Charged particles	Photon	0	1^-
Weak	$1.027 \cdot 10^{-5}$	$<10^{-15}$	Leptons, quarks	Vector intermediate bosons (W^\pm, Z^0)	80.6 GeV 91.2 GeV	$1^+, 1^-$ ^a
Gravitation	$5.9 \cdot 10^{-39}$	∞	All	Graviton	0	2^+

^a In weak interaction, parity is violated

and manifests itself by the confinement of quarks within hadrons. The effect of this term is illustrated in Fig. 5.4: trying to free quarks, extending the elastic “spring of gluons” that keeps them tied together, leads to the rupture of the elastic with the creation of a quark-antiquark pair (a system which is more stable from the energetic point of view).

The three “coupling constants” of the electromagnetic, weak and strong interactions are slightly energy dependent. In Chap. 13, we shall see that at extremely high energies, of the order of $\sqrt{s} \sim 10^{15}$ GeV, the “constants” are believed to have approximately the same value. This corresponds to the unification of fundamental interactions. Table 5.1 summarizes the main properties of the four fundamental interactions.

5.5 Particle Classification

Each particle is subject to one or more fundamental interactions. All fermions interact through the weak interaction; electrically charged particles “feel” the EM interaction and particles made of quarks (hadrons) are subject to the strong interaction through their *color* charge. From an experimental point of view, it is useful to classify particles in several categories.

5.5.1 Classification According to Stability

A first classification of particles with masses below 3 GeV can be done in terms of their *stability*.

Stable particles are: the photon (γ), the electron (e^-) and the corresponding antiparticle; in the Standard Model (SM), neutrinos and antineutrinos are also stable. Among hadrons, only the proton and the antiproton are stable. In models beyond the Standard Model, the proton and the neutrinos may be unstable.

Many particles are unstable and can be classified according to their lifetime. Remember that the initial number N_0 of unstable particles at the time $t = 0$ is reduced after a time t to $N = N_0 \exp(-t/\tau)$, where τ is the *lifetime measured at rest* ($t_{1/2} = \tau \ln 2 = 0.693\tau$ is the *half-life*).

Particles with masses in the range $0.1\text{--}3\,\text{GeV}/c^2$ and with lifetimes ranging from 10^{-6} to $10^{-12}\,\text{s}$ decay via the weak interaction. This group includes the μ^\pm, τ^\pm , the d, s, c, b quarks and the $\pi^\pm, K^\pm, K^0, \bar{K^0}, \Lambda^0, \Sigma^\pm, \Xi^-, D, F, \Lambda_c, B, \dots$ hadrons.

Particles with lifetimes ranging from 10^{-16} to $10^{-20}\,\text{s}$ decay via the electromagnetic interaction; these are, for instance, the hadrons π^0, η^0, Σ^0 .

Hadrons with lifetimes of the order of $10^{-23}\,\text{s}$ decay via the strong interaction. These are the so-called *resonances*, e.g., $\rho, \omega, K^*, N^*, \Delta, Y^*$, etc.

The W^+, W^-, Z^0 bosons, which are the mediators of the weak interaction, have lifetimes of the order of $10^{-25}\,\text{s}$. These lifetimes are very short due to the vector boson large masses with respect to the relatively small mass of the final state particles. The phase space factor dN/dE_0 (4.37) is huge and the decay is very rapid, even if it is caused by the weak interaction.

In most cases, particles with lifetimes longer than about $10^{-8}\,\text{s}$ are considered to be “almost stable” since they can be used in an accelerator as secondary beams of particles.

5.5.2 Classification According to the Spin

One of the most important quantum numbers is the *spin*, that is, the intrinsic angular momentum of each particle.

Elementary particles are classified in *bosons* and *fermions* depending on whether they have integer or semi-integer spin, respectively. Fermions follow the *Fermi-Dirac statistics* and the *Pauli exclusion principle*. A system of identical fermions is described by an antisymmetric wave function for the exchange of any fermion pair. Bosons follow the *Bose-Einstein statistics* and the wave function of a system of identical bosons is symmetric for the exchange of any two bosons. As a result, identical bosons produced in high energy collisions tend to assume the same quantum numbers and have similar energies and momenta, similar to lasers.

Bosons are divided into *fundamental* bosons, mediators of interactions, and *mesons*, which are hadrons. Fermions are divided into *baryons*, which feel the strong interaction, and *leptons*, which are not subject to the strong interaction.

5.5.3 Classification According to the Baryon and Lepton Numbers

We have already seen that one can assign a *baryon number* $B = +1$ to hadrons as the proton and neutron, $B = -1$ to antibaryons and $B = 0$ to mesons. We shall see in Chap. 7 that baryons are made of three quarks, and mesons consist of a quark-antiquark pair. The *conservation of the baryon number* means that a baryon cannot decay into a system without baryons. It is equivalent to state that an *unstable baryon* is a hadron that, after a series of decays, ends up as the lightest baryon, that is, a proton. Proton decay into lighter particles, such as, mesons or leptons, has been searched for, but it has never been experimentally observed.

As for the baryon number, a *lepton number* can be defined. Its conservation prohibits the conversion of leptons into bosons or baryons. Three types of lepton numbers, corresponding to the three known families of leptons, can be defined as the *electron lepton number* $L_e = +1$ is attributed to the electron, e^- , and to its neutrino ν_e ; $L_e = -1$ for their antiparticles (e^+ , $\bar{\nu}_e$). $L_e = 0$ for the leptons and antilepton of the other two families. The *muonic lepton number* is $L_\mu = +1$ for μ^- and ν_μ . The *tau lepton number* $L_\tau = +1$ for the τ^- lepton and its neutrino, ν_τ .

The baryon and lepton numbers are always conserved in any process resulting from any kind of interaction.² Other quantum numbers are conserved only in strong interaction processes, or in electromagnetic and strong interactions. These quantum numbers are related to approximate conservation principles.

²For the family lepton number, this is not completely true since the discovery of neutrino oscillations, Chap. 12.

Chapter 6

Invariance and Conservation Principles

6.1 Introduction

Two important aspects in physics are the *invariance* (or *symmetry*) of the equations describing the behavior of a system under a given transformation (for example, a translation of the system frame) and the *conservation* of some physical quantities (e.g., the momentum). The invariance properties are abstract features of the mathematical formalism. These invariance properties are intimately connected to conservation laws. For example, the conservation of angular momentum is related to the invariance under spatial rotations; the conservation of the linear momentum is related to the homogeneity of space. *Noether's theorem* formally expresses the fact that a physical conserved quantity corresponds to each invariant, and vice versa.

The equations which rule the dynamic evolution of a system (e.g., the Schrödinger or the Lagrange equations) are first order differential equations in time and second order in space coordinates. Every first integral of motion gives rise to a conservation law. Each fundamental interaction (as the electromagnetic one described by Maxwell's equations) obeys various conservation laws. The formalism of the considered interaction must obey several invariance requirements, which limit its mathematical description.

Transformations can be *continuous* or *discrete*. In the first case, the transformation can be achieved by applying successive infinitesimal transformations. This is not possible for a discrete transformation. A rotation is an example of continuous transformation; the mirror reflection in space is an example of discrete transformation. The conservation laws related to these transformations are respectively *additive* and *multiplicative*.¹

¹A given quantum number q is *additive* if in a reaction the sum of the q -values of the interacting particles is the same before and after the reaction. Most conserved quantum numbers, as the electric charge, are additive in this sense. Instead, for a *multiplicative* quantum number q , the corresponding product, rather than the sum, is conserved

In this chapter, we shall discuss invariance principles and conservation laws in classical and quantum mechanics. Some examples will then be presented and analyzed.

6.2 Invariance Principle Reminder

6.2.1 Invariance in Classical Mechanics

Lagrange equations. In classical mechanics, the state of a system with n degrees of freedom is described by a *Lagrangian* $L = T - V$ – kinetic energy – potential energy. The Lagrangian contains n *generalized coordinates* q_i from which n *conjugated momenta* $p_i = \partial L / \partial \dot{q}_i$ are derived. The motion of a system is described, for each degree of freedom, by the *Lagrange equation*:

$$\frac{dp_i}{dt} - \frac{\partial L}{\partial q_i} = 0. \quad (6.1)$$

Suppose that for a particular system, the Lagrangian L does not depend on the q_k coordinate. In this case, L is independent (or symmetric) with respect to any transformation of this coordinate, which is called *ignorable*. If L does not depend on q_k , one has $\partial L / \partial q_k = 0$ and then, from (6.1), one has $dp_k / dt = 0$, i.e., the conjugated momentum p_k is constant. The momentum p_k , conjugated to the ignorable variable q_k , is therefore conserved.

Translation along x . Let us consider the system Lagrangian $L = T - V = (1/2)m\dot{x}^2$. In this case, L does not depend on x and is invariant under translations along the x axis. From the Lagrange Eq. 6.1, one has $p_x = \partial L / \partial \dot{x} = m\dot{x} = \text{constant}$, i.e., the linear momentum along x ($p_x = m\dot{x}$) is conserved.

Rotations. The Lagrangian $L = T - V = (1/2)m\dot{\phi}^2r^2$ where $\dot{\phi}r = v$, does not depend on ϕ ; this implies that L is invariant under spatial rotations. From (6.1) follows that $p_\phi = \partial L / \partial \dot{\phi} = m\dot{\phi}r^2 = mvr = \text{constant}$, i.e., that the angular momentum is conserved.

Noether's theorem. The conservation laws considered above are examples of Noether's Theorem: *in a Lagrangian field theory, a conserved quantity is associated to a continuous symmetry (and vice versa)* [G91]. A symmetry condition constrains the Lagrangian equation (note that the Lagrangian density $\mathcal{L} = L/v$ where v is the volume is sometimes used). For example, the assumption of time-translation invariance requires that the Lagrangian does not depend on t . The hypothesis of *Poincare invariance* (that is, the invariance under Lorentz transformation and space-time translations) requires that the Lagrangian relativistically transforms as a scalar. The inverse is also true: the symmetries of the motion equations can be deduced from the Lagrangian analysis.

Hamilton equations. The motion of a classical system can also be described in terms of the *Hamilton equations*:

$$\dot{q}_i = \partial H / \partial p_i \quad ; \quad \dot{p}_i = -\partial H / \partial q_i \quad (6.2)$$

where the *Hamiltonian* H is given by $H = T + V$. In this description, an additional relation exists between the invariance principles and the conservation laws: *invariance* means that H does not change under a given transformation.

Space translations. Consider an infinitesimal translation along the x axis, i.e., a transformation $x \rightarrow x + dx$. In this case, the Hamiltonian varies by the quantity $dH = dx(\partial H / \partial x) = -dx \dot{p}_x$. If p_x remains constant during the transformation, we have $\dot{p}_x = 0$ and then $dH = 0$. In other words, if p_x is constant, the Hamiltonian is invariant for space translation along the x axis.

Similarly, it can be shown that the energy conservation implies time-translation invariance and that the angular momentum conservation implies invariance under space rotations.

6.2.2 Invariance in Quantum Mechanics

In quantum mechanics, the state of a system is described by a wave function ψ . The average of the results of a measurement on the system corresponds to the average value $\langle q \rangle$ of an operator Q associated with the observable quantity, which acts on the wave function ψ . The average value (or the *expectation value*) is given by ($\tau = v$ is the volume)

$$\langle q \rangle = \int_{\tau} \psi^* Q \psi d\tau \equiv \langle \psi | Q | \psi \rangle . \quad (6.3)$$

In the last equality, the Dirac notation, using the state vector “ket” $|\psi\rangle$ and its conjugate transpose “bra” $\langle\psi|$, is introduced. The operator Q should be *Hermitian*, i.e., $Q^+ = Q$. This condition ensures that the average values (6.3) are real numbers corresponding to measurable quantities. If Q is represented by a matrix with elements Q_{ij} , the operator Q^+ has elements Q_{ji}^* .

The time evolution of $\langle q \rangle$ can be described by either the time evolution of ψ , $\psi = \psi(t)$, or by the time evolution of Q , $Q = Q(t)$. The first case is the *Schrödinger representation*; the second is the *Heisenberg representation*.

Schrödinger representation. The Schrödinger equation describes the time evolution of the wave function ψ_S :

$$i\hbar \frac{\partial}{\partial t} \psi_S(t) = H_S \psi_S(t) \quad (6.4)$$

where H is the Hamiltonian and the status ψ_S is known. For stationary states, the eigenvalue equation is $H\psi = E\psi$. The time development of ψ_S can also be described in terms of an operator U applied to ψ_S

$$\psi_S(t) = U(t, t_0) \psi_S(t_0) \quad (6.5)$$

where U must be a *unitary operator*, i.e., $U^{-1} = U^+$, since only this condition allows one to maintain the normalization of $\psi_S(t)$. A unitary operator can be written as

$$U(t, t_0) = e^{-i(t-t_0)H/\hbar}. \quad (6.6)$$

For the complex conjugated wave function, one has

$$\psi_S^*(t) = \psi_S^*(t_0)U^{-1}(t, t_0). \quad (6.7)$$

Heisenberg representation. The Heisenberg equation describes the time evolution of Q :

$$-i\hbar \frac{dQ}{dt} = i\hbar \frac{\partial Q}{\partial t} + [Q, H]. \quad (6.8a)$$

The *commutation parenthesis* is defined as $[Q, H] = QH - HQ$. Note that if $\partial Q / \partial t = 0$, one has:

$$-i\hbar \frac{dQ}{dt} = [Q, H]. \quad (6.8b)$$

If $[Q, H] = 0$, then $dQ/dt = 0$, and therefore Q is constant. The quantity corresponding to the Q operator is *conserved* (and consequently, the corresponding quantum numbers are conserved) if Q commutes with H .

Let us now derive a relation between the two representations. A mean value ($\langle q \rangle$) (eigenvalue) must be the same in the two representations, i.e., one must have

$$\langle q \rangle = \int_{\tau} \psi_S(t_0)^* Q \psi_S(t_0) d\tau = \int_{\tau} \psi_S(t)^* Q_0 \psi_S(t) d\tau \quad (6.9)$$

Heisenberg Schrödinger

where $d\tau = dv$ is the volume element. As the volume τ is arbitrary, the equation is always true only if the two integrands are equal, that is,

$$\psi_S(t_0)^* Q \psi_S(t_0) = \psi_S(t)^* Q_0 \psi_S(t). \quad (6.10)$$

Since $\psi_S(t)^* = \psi_S(t_0)^* U^{-1}$ and $\psi_S(t) = U\psi_S(t_0)$, the second member of Eq. 6.10 can be written as

$$\psi_S(t_0)^* U^{-1} Q_0 U \psi_S(t_0).$$

which is equal to the left side of (6.10) if

$$Q = U^{-1} Q_0 U. \quad (6.11)$$

The time derivative of (6.11), multiplied by $i\hbar$, gives (if $\partial Q_0/\partial t = 0$)

$$-i\hbar \frac{dQ}{dt} = i\hbar \frac{dU^{-1}}{dt} Q_0 U + i\hbar U^{-1} Q_0 \frac{dU}{dt}.$$

Using the form (6.6) for U , one has

$$\begin{aligned} -i\hbar \frac{dQ}{dt} &= i\hbar \frac{iH}{\hbar} e^{i(t-t_0)H/\hbar} Q_0 U + i\hbar \left(-\frac{iH}{\hbar}\right) U^{-1} Q_0 e^{-i(t-t_0)H/\hbar} \\ &= -HU^{-1}Q_0U + U^{-1}Q_0UH \\ &= -HQ + QH = [Q, H], \end{aligned} \quad (6.12)$$

that is, $i\hbar \frac{dQ}{dt} = [Q, H]$. This is the Heisenberg equation when Q does not explicitly depend on time. We obtained the Heisenberg equation starting from (6.9) and using the transformations of the wave function (6.5 and 6.7). Equation 6.12 can then be generalized to Eq. 6.8a.

6.2.3 Continuous Transformations: Translations and Rotations

Translations. Let us consider an infinitesimal translation dx along the x axis: $x' = x + dx$. Its effect on the wave function $\psi(x)$ is

$$\psi(x') = \psi(x + dx) = \psi(x) + dx \frac{\partial \psi(x)}{\partial x} = \left(1 + dx \frac{\partial}{\partial x}\right) \psi(x) = dD_x \psi(x) \quad (6.13)$$

where the operator $dD_x = 1 + dx\partial/\partial x$ is the operator which generates an infinitesimal translation. Recall that the linear momentum operator is $p_x = (\hbar/i)\partial/\partial x$. The operator dD_x can therefore be written in the form

$$dD_x = 1 + (i/\hbar)p_x dx. \quad (6.14)$$

A finite translation Δx can be thought of as a series of infinitesimal translations, $\Delta x = n dx$, with $n \rightarrow \infty$; it follows that ($dx = \Delta x/n$)

$$D_x = \lim_{n \rightarrow \infty} \left(1 + \frac{i}{\hbar} p_x dx\right)^n = \exp\left(\frac{i}{\hbar} p_x \Delta x\right). \quad (6.15)$$

D_x is a unitary operator, i.e., $D_x^+ D_x = 1$. The momentum p_x is the generator of the operator D_x , which in turn is associated with spatial translations along x . If the Hamiltonian H is invariant under space translation along the x axis, one has $[D_x, H] = 0$. From Eq. 6.14, it follows that p_x commutes with H , i.e., $[p_x, H] = 0$. The momentum p_x is a Hermitian operator; from Eq. 6.12, one finds that $\dot{p}_x = 0$ and consequently, p_x is conserved. One can therefore conclude that the following statements are equivalent:

1. The Hamiltonian is invariant under space translations
2. The operator \mathbf{p} commutes with the Hamiltonian
3. The momentum \mathbf{p} is conserved

Rotations in space. Proceeding as in the case of translations, let us define an infinitesimal rotation around the z axis, i.e., $\varphi' = \varphi + d\varphi$; the operator dR_z associated with these rotations is

$$dR_z = 1 + d\varphi \frac{\partial}{\partial \varphi}. \quad (6.16)$$

Recalling that $L_z = (\hbar/i)\partial/\partial\varphi$ corresponds to the z component of the orbital angular momentum operator, one has

$$dR_z = 1 + (i/\hbar)L_z d\varphi. \quad (6.17)$$

A finite rotation $\Delta\varphi$ can be obtained as a series of infinitesimal rotations ($d\varphi = \Delta\varphi/n$):

$$R_z = \lim_{n \rightarrow \infty} \left(1 + \frac{i}{\hbar} L_z d\varphi \right)^n = \exp \left(\frac{i}{\hbar} L_z \Delta\varphi \right). \quad (6.18)$$

It follows that the invariance of the Hamiltonian under a rotation around the z axis implies that $[L_z, H] = 0$ and therefore corresponds to the conservation of the z component of the orbital angular momentum L_z .

6.3 Spin-Statistics Connection

The spin-statistics connection is one of the most important in the submicroscopic world. Particles with half-integer spin ($1/2, 3/2, \dots$), in units of \hbar , follow the Fermi–Dirac statistics and are called *fermions*. Particles with integer spin ($0, 1, 2, \dots$) follow the Bose–Einstein statistics and are called *bosons*. Statistics fix the symmetry properties of the wave function for a pair of identical particles with respect to their exchange.

Consider a pair of identical particles, denoted by (1,2), and consider the operator I which reverses the positions of two particles:

$$I(1, 2) \rightarrow (2, 1). \quad (6.19a)$$

For the wave function describing two identical particles, one has

$$I\psi(1, 2) = \psi(2, 1). \quad (6.19b)$$

Applying twice the operator I , the initial situation is obtained, that is,

$$I^2\psi(1, 2) = I[\psi(2, 1)] = \psi(1, 2). \quad (6.19c)$$

An eigenvalue equation exists for I^2 , with eigenvalue +1. The possible eigenvalues for the I operator are ± 1

$$I\psi(1, 2) = \pm\psi(1, 2). \quad (6.19d)$$

Comparing (6.19b) and (6.19d), we obtain $\psi(2, 1) = \pm\psi(1, 2)$. It is assumed that

1. The wave function for two identical bosons must be **symmetric** under the exchange $1 \leftrightarrow 2$: $\psi(1, 2) = \psi(2, 1)$
2. The wave function for two identical fermions must be **antisymmetric** under the exchange $1 \leftrightarrow 2$: $\psi(1, 2) = -\psi(2, 1)$

The total wave function can be expressed as the product of a spatial function, α (space), and a spin function, β (spin). The spatial part describes the orbital motion of a particle with respect to the other, and it is given (as already known from atomic physics) by spherical harmonics $Y_\ell^m(\theta, \varphi)$ functions (see Sect. 6.4). The exchange of two particles corresponds to an inversion of coordinates which introduces the factor $(-1)^\ell$. If ℓ is even (odd), the wave function α is symmetric (antisymmetric) under the exchange operation.

From the Dirac theory, the function describing the spin status β is symmetric if the two spins are parallel, and antisymmetric if the two spins are antiparallel. Identical bosons must therefore have both α and β symmetric or antisymmetric, while identical fermions must have α symmetric and β antisymmetric, or vice versa.

6.4 Parity

The inversion of spatial coordinates ($x, y, z \rightarrow -x, -y, -z$), or $\mathbf{r} \rightarrow -\mathbf{r}$, or “exchange of the right with the left” is an example of a *discrete* transformation. The inversion is generated by the parity operator P , which reverses the spatial coordinates (Fig. 6.1), that is,

$$P\mathbf{r} = -\mathbf{r}. \quad (6.20)$$

Its application on a wave function gives

$$P\psi(\mathbf{r}) = \psi(-\mathbf{r}). \quad (6.21)$$

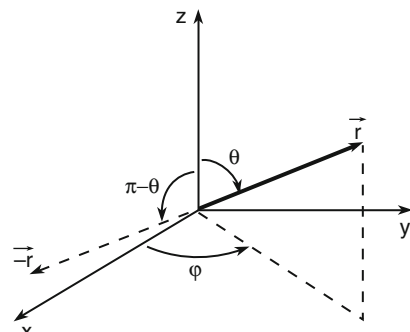


Fig. 6.1 Angles θ, φ for the vector \mathbf{r} and angles $(\pi - \theta), (\varphi + \pi)$ for $-\mathbf{r}$

The parity operator applied two times gives

$$P^2\psi(\mathbf{r}) = PP\psi(\mathbf{r}) = P\psi(-\mathbf{r}) = \psi(\mathbf{r}). \quad (6.22)$$

This implies $P^2 = 1$. The eigenvalue equation

$$P\psi = p\psi = \pm\psi \quad (6.23)$$

has eigenvalues $p = \pm 1$ (assuming that it admits eigenvalues). The parity of the system is positive or negative. An example of a wave function with positive (even) parity is the function $\psi(x) = \cos x$

$$P\cos x = \cos(-x) = \cos x, \text{ that is } p = +1, \text{ positive.} \quad (6.24)$$

An example of a wave function with negative (odd) parity is $\psi(x) = \sin x$

$$P\sin x = \sin(-x) = -\sin x, \text{ } p = -1, \text{ negative.} \quad (6.25)$$

A wave function with undefined parity is $\psi(x) = \sin x + \cos x$

$$P(\sin x + \cos x) = \sin(-x) + \cos(-x) = -\sin x + \cos x. \quad (6.26)$$

$\psi(x) = \sin x + \cos x$ is not a P eigenfunction and the parity is not defined.

In a physics process, the parity of the system is a conserved quantity if the parity operator commutes with the Hamiltonian, $[H, P] = 0$. For example, any potential with spherical symmetry has the properties $H(-\mathbf{r}) = H(\mathbf{r}) = H(r)$. In this case, one has $[H, P] = 0$ and the bound states of the system have defined parity. Familiar examples are the atomic bound states described by (neglecting the spin)

$$\psi(r, \theta, \varphi) = \chi(r)Y_\ell^m(\theta, \varphi). \quad (6.27)$$

The angular functions $Y_\ell^m(\theta, \varphi)$ are the *spherical harmonics*

$$Y_\ell^m(\theta, \varphi) = \sqrt{\frac{(2\ell+1)(\ell-m)!}{4\pi(\ell+m)!}} P_\ell^m(\cos \theta) e^{im\varphi} \quad (6.28)$$

where $P_\ell^m(\cos \theta)$ are the *Legendre polynomials*. The space inversion $\mathbf{r} \rightarrow -\mathbf{r}$ is equivalent to $\theta \rightarrow \pi - \theta, \varphi \rightarrow \pi + \varphi$ (see Fig. 6.1). The application of the parity operator to the functions $e^{im\varphi}$ and P_ℓ^m gives

$$\begin{aligned} Pe^{im\varphi} &= e^{im(\varphi+\pi)} = e^{im\pi} e^{im\varphi} = (-1)^m e^{im\varphi} \\ PP_\ell^m(\cos \theta) &= (-1)^{\ell+m} P_\ell^m(\cos \theta) \end{aligned} \quad (6.29a)$$

(ℓ, m are the orbital and azimuthal quantum numbers); finally, one has

$$PY_\ell^m(\theta, \varphi) = (-1)^\ell Y_\ell^m(\theta, \varphi). \quad (6.29b)$$

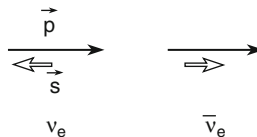


Fig. 6.2 Momentum \mathbf{p} and spin \mathbf{s} for an electron neutrino and an antineutrino. The momentum is indicated by the simple arrow at the *top* and the spin by the arrow at the *bottom*

The parity of the spherical harmonic functions Y_ℓ^m is then $(-1)^\ell$; states with $\ell = 0, 2, \dots$ have parity $p = +1$, while those with $\ell = 1, 3, \dots$ have parity $p = -1$. The so-called electric dipole transitions between two states are characterized by the selection rule $\Delta\ell = 1$. In an electric dipole transition, the parity of the atomic (nuclear) state changes, while the parity of the entire system, which consists of the final state photon + atom (nucleus) is conserved. The parity of the emitted electromagnetic radiation (the photon) must be $p = -1$ in order to conserve the total parity of the system. The spin-parity assignment for the photon is $J^P = \text{Spin}^{\text{parity}} = 1^-$: the photon is a vector particle. All observed electromagnetic processes conserve parity.

The conservation of parity gives rise to a multiplicative law and *parity is a multiplicative quantum number*. The parity of a system described by $\psi = \psi_1\psi_2$ is given by $P = P_1P_2$.

Because the parity operator corresponds to a mirror reflection, it was believed until 1956 that Nature laws are symmetric under parity transformations. Mathematically, it corresponds to the fact that the parity operator gives rise to eigenvalues that are conserved in each transition. It is an experimental fact that parity is conserved in all transitions due to electromagnetic and strong interactions. The wave functions describing the particles have definite parity for (6.24) or (6.25). Parity is instead violated in weak interaction transitions (Chap. 8).

Parity violation in weak interactions. Let us anticipate an example of parity violation in the weak interaction. The electron neutrino has spin $s = 1/2$ and it may therefore have two polarization states, $s_z = \pm 1/2$. It is experimentally found by only the neutrino with polarization antiparallel to the momentum ($s_z = -1/2$): the neutrino is said to be *left-handed*). Likewise, the antineutrino has only $s_z = +1/2$, and it is *right-handed* (see Fig. 6.2).

Consider an electron neutrino and apply the parity operator. This operation changes the neutrino momentum, $\mathbf{p} \rightarrow -\mathbf{p}$, but not its spin \mathbf{s} . The application of the parity operator to a left-handed neutrino gives rise to a right-handed neutrino, i.e., a state which is not observed (schematically: $P(\overleftarrow{\nu}_e) = (\overleftarrow{\nu}_e)$). The neutrino is subject only to the weak interaction: this interaction is thus not invariant under spatial inversion, meaning that it does not conserve parity.

6.5 Spin-Parity of the π Meson

As in the case of the photon, most particles have defined spin and parity which must be experimentally determined. In this section, the important case of the spin and parity determination of the charged pion is reviewed. Pions are abundantly produced in strong interactions, and their spin and parity values are used in other parts of the book. The reader can skip this section during the first reading.

6.5.1 Spin of the π Meson

The spin of the π^+ meson was determined by applying the “*principle of detailed balance*” to the reaction $pp \rightarrow \pi^+ d$ and to its reverse reaction, $\pi^+ d \rightarrow pp$. The deuteron d is a bound pn state, its ground state is 3S_1 (the notation is ${}^{2s+1}l_j$). The orbital angular momentum between p and n is zero ($l_{pn} = 0$, S wave); therefore, the total angular momentum corresponds to the spin of the deuteron, $s_d = 1$. This means that the spin states of n and p are aligned and that the state corresponds to a spin triplet ($2s_d + 1 = 3$).

The cross-section for the direct reaction is given by (4.40):

$$\sigma(pp \rightarrow \pi^+ d) = \frac{|M_{if}|^2}{\text{matrix element}} \frac{\frac{(2s_\pi+1)(2s_d+1)}{\pi v_i v_f} p_\pi^2}{\text{phase space and flux factors}} \quad (6.30)$$

where the flux term contains the dependence on the relative speed of the initial state $v_i = v_p - v_{p'}$, and that of the final state $v_f = v_d - v_{\pi^+}$.

The cross-section is averaged over initial spins, and it is summed over all orbital angular moments ℓ . The element M_{if} contains the dependence on the interaction dynamics, and is unknown for the strong interaction. The *density of final states* (= phase space) gives the terms $(2s_\pi + 1)(2s_d + 1)p_\pi^2/v_f$, where p_π = is the pion momentum in the c.m.

The cross-section for the reverse reaction is given by

$$\sigma(\pi^+ d \rightarrow pp) = \frac{1}{2} |M_{fi}|^2 \frac{(2s_p + 1)^2}{\pi v'_f v'_i} p_p^2. \quad (6.31)$$

The factor 1/2 is due to the fact that in the final state, there are two identical fermions. Assuming that the strong interaction is invariant under time reversal (Sect. 6.7) and parity, it can be formally assumed that

$$|M_{if}|^2 = |M_{fi}|^2. \quad (6.32)$$

This relation is called *detailed balance principle*. If the cross-section for the direct and the reverse reaction are measured at the same c.m. energy, one has $v_i v_f = v'_f v'_i$.

Using the ratio between the cross-sections of the direct and reverse reactions, one obtains

$$\frac{\sigma(pp \rightarrow \pi^+ d)}{\sigma(\pi^+ d \rightarrow pp)} = 2 \frac{(2s_\pi + 1)(2s_d + 1)}{(2s_p + 1)^2} \frac{p_\pi^2}{p_p^2} = \frac{3}{2}(s_\pi + 1) \frac{p_\pi^2}{p_p^2}. \quad (6.33)$$

The measurements of the direct (6.30) and of the inverse (6.31) cross-sections have been carried out since the early 1950s, with proton and pion beams of different momenta (typically a few tens of MeV in the c.m. system). Once the ratio ($\frac{p_\pi^2}{p_p^2}$) between the momentum of the particles in the final state was calculated and the ratio between the cross-sections was measured, it was possible to determine the factor $\frac{3}{2}(s_\pi + 1)$; it was found to be compatible with the value $s_\pi = 0$. It was therefore concluded that **the spin of the π^+ meson was zero**.

The spin of the π^- and π^0 mesons are determined with a simpler and qualitative reasoning. In e^+e^- , $\bar{p}p$ and pp collider at high energy ($E_{c.m.} > 10$ GeV) π^+, π^-, π^0 are abundantly produced in equal numbers. This suggests that the three π mesons must have the same spin and isospin (see Sect. 7.2), otherwise they could not be produced with the same abundance. Therefore, the spin of the π^- and π^0 mesons must be zero as the spin of the π^+ .

6.5.2 Parity of the π Meson

The intrinsic parity of the π^- meson was determined by observing low-energy π^- absorption in deuterium. The process is due to the strong reaction (capture):

$$\pi^- d \rightarrow nn. \quad (6.34)$$

Initial π^-d state. The deuterium nucleus (deuteron) has spin $s_d = 1$, the π^- has spin 0. The orbital angular momentum between the π^- and deuteron is zero ($\ell_{\pi d} = 0$) because the pion is captured at very low energies. The total angular momentum of the initial π^-d state is then $|\mathbf{J}_i| = |\mathbf{S}_\pi + \mathbf{S}_d + \mathbf{L}_{\pi d}| = 1$.

Final nn state. The angular momentum $|\mathbf{J}_f| = |\mathbf{L}_{nn} + \mathbf{S}_{nn}|$ must be equal to that of the initial state. \mathbf{L}_{nn} is the orbital angular momentum between the two neutrons; \mathbf{S}_{nn} is their total spin, respectively denoted here as ℓ and S .

Let us make some considerations on the symmetry of the system before considering the consequences of the conservation of \mathbf{J} . The wave function describing the system of two neutrons can be written as the product of a space coordinates term and a spin term, that is,

$$\psi_{tot} = \alpha(\text{space}) \cdot \beta(\text{spin}). \quad (6.35)$$

As the two neutrons are identical fermions, their wave function ψ_{tot} must be antisymmetric under their exchange. The product of the symmetries $\alpha(\text{space})$ and $\beta(\text{spin})$ is considered separately and must be antisymmetric.

$\alpha(\text{space})$ is described by spherical harmonic functions, $Y_\ell^m(\theta, \varphi)$. The exchange of the two neutrons is equivalent to the transformation $\theta \rightarrow \pi - \theta, \varphi \rightarrow \pi + \varphi$, for which one has

$$Y_\ell^m(\theta, \varphi) \xrightarrow{1 \leftrightarrow 2} (-1)^\ell Y_\ell^m(\theta, \varphi). \quad (6.36)$$

The factor $(-1)^\ell$ gives the symmetry of the space function α under the exchange of the two particles.

The functions **$\beta(\text{spin})$** for the combination of two spin 1/2 particles are written as

$$\begin{cases} \text{the first neutron is described by } & \beta_1 \text{ with } S_1 = 1/2, S_{1z} = \pm 1/2 \\ \text{the second neutron is described by } & \beta_2 \text{ with } S_2 = 1/2, S_{2z} = \pm 1/2. \end{cases}$$

If S_1 and S_2 are parallel, we have $S_{nn} = S = S_1 + S_2 = 1, S_z = 0, \pm 1$. If S_1 and S_2 are antiparallel one has $S = 0, S_z = 0$. In the first case, the three states with $S = 1$ and $S_z = 0, \pm 1$ represent a spin triplet, which is symmetric under the exchange of neutron 1 with neutron 2. The wave functions β for the three states of the triplet (the second number in parentheses refers to the third component) are written as

$$\begin{cases} \beta(1, 1) = & \beta_1(1/2, +1/2)\beta_2(1/2, +1/2) \\ \beta(1, 0) = & (1/\sqrt{2})[\beta_1(1/2, +1/2)\beta_2(1/2, -1/2) + \beta_2(1/2, +1/2)\beta_1(1/2, -1/2)] \\ \beta(1, -1) = & \beta_1(1/2, -1/2)\beta_2(1/2, -1/2). \end{cases} \quad (6.37)$$

The state with $S = 0, S_z = 0$ is an antisymmetric singlet:

$$\beta(0, 0) = (1/\sqrt{2})[\beta_1(1/2, +1/2)\beta_2(1/2, -1/2) - \beta_2(1/2, +1/2)\beta_1(1/2, -1/2)]. \quad (6.38)$$

The symmetry of the spin wave function is therefore $(-1)^{S+1}$. It follows that the symmetry of the final state wave function ψ_{tot} under the exchange of the two n is $(-1)^{\ell+S+1}$; this quantity should be equal to -1 because the two n are identical fermions: $\psi_{tot} \xrightarrow{1 \leftrightarrow 2} (-1)^{\ell+S+1}\psi_{tot} = -\psi_{tot}$. In conclusion, $(\ell + S + 1)$ must be odd, and $(\ell + S)$ must be even. The final state must be such that

1. $\ell + S = \text{even}$ for symmetry arguments;
2. $|\mathbf{J}| = 1$ for angular momentum conservation.

The possible combinations of ℓ and S for $|\mathbf{J}| = 1$ are

$$\begin{cases} \ell = 0 & \begin{cases} \ell = 1 & \begin{cases} \ell = 1 & \begin{cases} \ell = 2 & \\ S = 1 & \end{cases} \\ S = 0 & \ell + S = \text{odd} & S = 1 & \end{cases} \\ \ell + S = \text{odd} & \ell + S = \text{odd} & \ell + S = \text{even} & \end{cases} \\ S = 1 & \end{cases} \quad \begin{cases} \ell = 1 & \begin{cases} \ell = 1 & \begin{cases} \ell = 2 & \\ S = 1 & \end{cases} \\ S = 0 & \ell + S = \text{odd} & S = 1 & \end{cases} \\ \ell + S = \text{odd} & \ell + S = \text{even} & \ell + S = \text{odd}, & \end{cases}$$

among these, only the combination $\ell = 1, S = 1$ has $\ell + S = \text{even}$ and one can conclude that the two neutrons are in a state 3P_1 . (The notation is as follows: $P \rightarrow P$ wave, $\ell = 1$; index $= 1 \rightarrow J = 1$; superscript $= 3 \rightarrow 2S + 1 = 3$.)

The parity of the final state is $P(2n) = P(n) \cdot P(n) \cdot (-1)^\ell = -1$. The parity of n and p is conventionally taken to be equal to $+1$. Note that in all interactions, the baryon number is conserved. Accordingly, the absolute value of the nucleon parity is irrelevant because it cancels out in each reaction.

Let us assume that parity is conserved in the strong interaction. No experimental indication is reported so far to sustain the contrary. The parity of the initial state is equal to that of the final state, i.e., $P(\pi^- d) = P(nn) = -1$. On the other hand, one has $P(\pi^- d) = P(\pi^-) \cdot P(d) \cdot (-1)^{\ell=0}$; since $P(d) = P(p) \cdot P(n) \cdot (-1)^0 = +1$, one has $P(\pi^- d) = P(\pi^-)$. The reaction (6.34) can therefore occur through the strong interaction only if $P(\pi^-) = -1$. It can be concluded that **the π^- has negative parity**. One can show that $P(\pi^+) = P(\pi^0) = P(\pi^-)$. Systems with n pions have parity $P(n\pi) = (-1)^n$.

The π mesons have spin-parity $J^P = 0^-$, and are called *pseudoscalar mesons*. Bosons with $J^P = 0^+$ are called *scalar*, those with $J^P = 1^-$ *vector mesons* and those with $J^P = 1^+$ are *axial mesons*.

6.5.3 Particle–Antiparticle Parity

The intrinsic parity of the proton is defined by convention. The Dirac theory predicts opposite parity for fermion–antifermion, and the same intrinsic parity for boson–antiboson (for example, $\pi^+ - \pi^-$ and $K^+ - K^-$).

It is possible to make a precise experimental assignment of the intrinsic parity of the π because the π can be individually produced. Similarly, a relative parity can be assigned to the $p - \bar{p}$ pair because it can also be produced individually, for example, in the reaction

$$pp \rightarrow pp(p\bar{p}). \quad (6.39)$$

The parity of the particle–antiparticle system was found to be equal to -1 . The intrinsic parity of strange mesons that are produced in association, for example, in $\pi^- p \rightarrow K^+ K^- n$, cannot be individually measured. For instance, in the reaction

$$pp \rightarrow \Lambda K^+ p, \quad (6.40)$$

only the relative parity of the ΛK^+ pair (which is found to be odd) with respect to the proton can be determined. Conventionally, the same even parity of the proton is assigned to the Λ and the same odd parity of the π is assigned to the K^+ .

6.6 Charge Conjugation

The charge conjugation operator was originally defined through its action on an electric charge q , that is,

$$Cq = -q \quad (6.41\text{a})$$

$$C\psi(q) = \psi(-q). \quad (6.41\text{b})$$

As with parity, the charge conjugation is a discrete operator. Applying the charge conjugation twice, one has

$$C^2q = CCq = C(-q) = q \quad (6.42\text{a})$$

$$C^2\psi(q) = C\psi(-q) = \psi(q). \quad (6.42\text{b})$$

Equation 6.42b is an eigenvalue equation with $c^2 = 1$; it follows that the only possible eigenvalues are $c = \pm 1$.

Generalizing, the operator C transforms a particle, even if it is electrically neutral, in the corresponding antiparticle. After the application of this operator to a particle wave function, the baryon and lepton numbers are not conserved and no real physical process corresponds to this transformation. It follows that after a transformation due to the operator C , an arbitrary phase φ appears in the wave function, that is, $C\psi(q) = \psi(\bar{q}) \exp(i\varphi)$. The phase can be chosen at our convenience.

Let us analyze the effects of the C operator on some characteristic parameters of a particle (see Table 6.1). Applying C to a proton, one obtains an antiproton, which has electric charge, baryon number and *magnetic dipole moment* opposed to those of the proton; instead, the spin remains unchanged. Note that a positive magnetic dipole moment means that it has the same direction and orientation of the spin. This occurs for the proton and the positron; spin and magnetic dipole are opposite for the

Table 6.1 Effect of the charge conjugation operation C applied to a proton and to an electron. The magnetic moment μ is in units $[e\hbar/(2mc)]$, the spin s in units \hbar . μ and s are parallel and in the same direction for the proton and the positron

	Electric charge q	Baryonic number B	Magnetic moment $(e\hbar/2m_p c)$	Spin (\hbar)
Proton p	$+e$	$+1$	2.793	$1/2$
$Cp = \bar{p}$	$-e$	-1	-2.793	$1/2$
	Electric charge q	Electronic number L_e	Magnetic moment $(e\hbar/2m_e c)$	Spin (\hbar)
Electron e^-	$-e$	$+1$	-1.0012	$1/2$
$Ce^- = e^+$	$+e$	-1	$+1.0012$	$1/2$

antiproton and the electron. A neutron is different from the antineutron because the magnetic dipole moment of the neutron is directed in the opposite direction to that of the spin, while it has the same direction as the spin for the antineutron.

6.6.1 Charge Conjugation in Electromagnetic Processes

Applying the C operator to a π^+ meson, a π^- is obtained:

$$C|\pi^+\rangle = |\pi^-\rangle.$$

Note that the Dirac notation ket introduced in Eq. 6.3 is used for states such as $|\pi^+\rangle$. It is obvious that for π^+ and π^- charged mesons, an eigenvalue equation cannot be written since the application of the operator C transforms the particle in a different one. Instead, the application of C to π^0 does not change the state and an eigenvalue equation can be written as

$$C|\pi^0\rangle = \eta|\pi^0\rangle \quad (6.43)$$

with $\eta = +1$ or -1 . To assign the correct sign, let us consider the π^0 electromagnetic decay into two photons; since the electromagnetic interaction conserves C , the effect of C on the photon must be examined.

Photons are emitted by accelerated charged particles. A charge changes sign when the operator C is applied. The application of C to a photon must keep track of this effect, suggesting that

$$C|\gamma\rangle = -|\gamma\rangle. \quad (6.44)$$

Since C is a multiplicative operator, for a system of n photons, one therefore has

$$C|n\gamma\rangle = (-1)^n|n\gamma\rangle. \quad (6.45)$$

For the considered electromagnetic decay of the π^0 into two photons, $\pi^0 \rightarrow 2\gamma$, the application of C to the π^0 is equivalent to the application of C to the system of the two photons. Assuming that the EM interaction conserves C , one can write

$$C|\pi^0\rangle = C|2\gamma\rangle = (-1)^2|2\gamma\rangle = |2\gamma\rangle = +|\pi^0\rangle. \quad (6.46)$$

As the decay $\pi^0 \rightarrow 2\gamma$ exists, and represents 99% of all π^0 decays, we can conclude that the π^0 is an eigenstate of C with even *C-parity*. The decay $\pi^0 \rightarrow 3\gamma$ would lead to a state of odd *C-parity*; this decay must therefore be prohibited if the EM interaction is invariant under C . Experimentally, the decay $\pi^0 \rightarrow 3\gamma$ has never been observed. The upper limit $(\pi^0 \rightarrow 3\gamma)/(\pi^0 \rightarrow 2\gamma) < 3.1 \cdot 10^{-8}$ represents one of the strong confirmations of charge conjugation conservation in the electromagnetic interaction. For neutral mesons, for example, the π^0 , the notation $J^{PC} = 0^{-+}$ is often used.

Another test of the conservation of C can be done in reactions that involve particles and antiparticles which are exchanged under C . By applying the charge conjugation operation in a typical reaction due to strong and/or electromagnetic interaction at high energy, one has

$$C(p\bar{p} \rightarrow \pi^+\pi^-\pi^+\pi^-...) = (\bar{p}p \rightarrow \pi^-\pi^+\pi^-\pi^+...) \quad (6.47a)$$

$$C(e^+e^- \rightarrow \pi^+\pi^-\pi^+\pi^-...) = (e^-e^+ \rightarrow \pi^-\pi^+\pi^-\pi^+...). \quad (6.47b)$$

This implies that the average number and energy spectra of π^+ and π^- must be equal. This was experimentally verified with an accuracy of about 1%.

In the microcosm, at very high energy, one has always observed a symmetry between particles and antiparticles. These are produced in equal number if the energies involved are well above given thresholds, such as, very large energies compared to the masses of the produced particles. In the macrocosm, however, this particle–antiparticle symmetry is not observed: the universe seems to only contain matter and not antimatter. This is one of the most fascinating topics of research interconnecting particle physics, astrophysics and cosmology (see Chaps. 12 and 13).

6.6.2 Violation of C in the Weak Interaction

The strong and electromagnetic interactions are invariant under the C operation, and C eigenvalues are conserved quantum numbers, while weak interaction processes are not invariant under C . To check the violation of C in the weak interaction, we proceed as we did for parity. Applying C to a neutrino, an antineutrino with the same momentum \mathbf{p} and the same spin \mathbf{S} is obtained. This state corresponds to a non-observed left-handed antineutrino:

$$C(\overleftrightarrow{} v_e) = (\overleftrightarrow{} \bar{v}_e).$$

One can conclude that the weak interaction involving neutrinos does not conserve parity nor charge conjugation. By applying to a neutrino the C and P operators in sequence (e.g., P first and then C or vice versa), an existing right-handed antineutrino is produced, that is,

$$CP(\overleftrightarrow{} v_e) = (\overleftarrow{} \bar{v}_e). \quad (6.48)$$

It follows that the weak interaction may conserve CP (see Fig. 6.3).

6.7 Time Reversal

The time reversal operator T reverses the time coordinate t :

$$Tt = -t \quad (6.49a)$$

$$T\psi(\mathbf{r}, t) = \psi(\mathbf{r}, -t). \quad (6.49b)$$

In classical mechanics, the systems are invariant under time reversal. For example, the time reversed condition for a planet moving on a circular orbit around the sun corresponds to the planet following the same orbit, though in opposite direction. This is a meaningful situation; the fact that the planet moves in one way depends on the initial conditions. Similarly, the application of T to a two body scattering process would reverse the reaction:

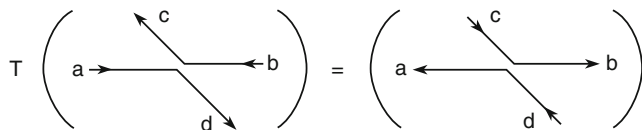


Table 6.2 summarizes the effects of application of P and T on some physical quantities. To check the conservation of P and/or T , it is necessary to experimentally study the product of variables given in Table 6.2. One example is the electron momentum \mathbf{p} with respect to its spin σ . Some studied quantities and their transformation properties under parity and time reversal are listed in Table 6.3.

If the parity P (or T) is conserved in a process due to a specific interaction, the Hamiltonian of the interaction **must not contain** terms that change sign after application of the parity or time reversal operators. Referring to Table 6.3, *elementary particles* with spin σ may have a magnetic dipole moment, but not a static electric dipole moment (as in ordinary matter) because the term $\mu_E^n \propto \sigma \cdot \mathbf{E}$ is not invariant under T . For this reason, the search for a nonzero electric dipole moment of the neutron (which can be measured with great precision) is historically

Table 6.2 Effect of the application of the parity (P) and time reversal (T) operators on some basic physics quantities

Quantity	Transformation		
	P	T	
\mathbf{r}	$-\mathbf{r}$	\mathbf{r}	Polar vector
\mathbf{p}	$-\mathbf{p}$	$-\mathbf{p}$	Polar vector
σ	σ	$-\sigma$	Axial vector (like $\mathbf{L} = \mathbf{r} \times \mathbf{p}$)
\mathbf{E}	$-\mathbf{E}$	\mathbf{E}	Remember that $\mathbf{E} = -\partial\phi/\partial\mathbf{r}$
\mathbf{B}^a	\mathbf{B}	$-\mathbf{B}$	\mathbf{B} is similar to σ

^aWe can think of \mathbf{B} as being due to the current in a coil. Reversing T means to invert the current direction and therefore the magnetic field direction.

Table 6.3 Effect of the application of the parity and time reversal operators on the products of some fundamental physical quantities

Quantity	Transformation		Physics quantity
	P	T	
$\sigma \cdot \mathbf{B}$	$+\sigma \cdot \mathbf{B}$	$+\sigma \cdot \mathbf{B}$	Magnetic dipole moment
$\sigma \cdot \mathbf{E}$	$-\sigma \cdot \mathbf{E}$	$-\sigma \cdot \mathbf{E}$	Electric dipole moment
$\sigma \cdot \mathbf{p}$	$-\sigma \cdot \mathbf{p}$	$+\sigma \cdot \mathbf{p}$	Longitudinal polarization
$\sigma \cdot \mathbf{p}_1 \times \mathbf{p}_2$	$+\sigma \cdot \mathbf{p}_1 \times \mathbf{p}_2$	$-\sigma \cdot \mathbf{p}_1 \times \mathbf{p}_2$	Transverse polarization
$\mathbf{p}_1 \cdot \mathbf{p}_2 \times \mathbf{p}_3$	$-\mathbf{p}_1 \cdot \mathbf{p}_2 \times \mathbf{p}_3$	$-\mathbf{p}_1 \cdot \mathbf{p}_2 \times \mathbf{p}_3$	

very important. A μ_E^n different from zero would imply the violation of both T and P . Similarly, it is expected that the interaction Hamiltonian does not contain terms which depend on the longitudinal polarization of the particles (a term $\sigma \cdot \mathbf{p}$). As we shall see in Chap. 8, this term is present in the weak interaction Hamiltonian. Table 6.4 summarizes some invariance properties of fundamental interactions.

Time Reversal in Macroscopic Processes. At the microscopic level, all processes (except those that violate CP , Sect. 6.8) are reversible and therefore invariant under time reversal. For complex systems at the macroscopic level, a well defined arrow for the time exists. The time reversal applied to a human being does not make sense: the person should die first, then rejuvenate and finally is born. The time arrow is also established for a gas in a container under pressure, which expands through a hole into a second empty container. The system evolves increasing its entropy, as in all irreversible processes. A movie of the gas expansion gives us a realistic situation; if the film is shown in reverse, it gives us an unrealistic view.

The time reversal symmetry is valid for microscopic systems, though not for complex systems. Let us better understand the situation by considering a man smoking a pipe (though it is a serious detriment to health). In the “normal” time direction, the smoke exits the pipe; in the “reverse” direction, it enters the pipe. The movie seems realistic in the normal direction, while in the reverse direction, it seems absurd. Suppose we can do an incredible zoom that allows us to view the individual collisions of the molecules of smoke. At that level, we observe molecules moving and colliding; the situation is invariant under time reversal and when we reverse the film, the situation seems completely normal. Let us decrease the zoom to see aggregates of smoke particles: also in this case, the dynamics of the aggregates do not appear strange when the film is shown in reverse. By gradually decreasing the magnification, we can begin to see puffs of smoke forming clots, that is, something that condenses rather than expands. Finally, we have a situation where it becomes clear if the molecules are expanding or condensing.

Changing from the microscopic to the macroscopic scale, i.e., from molecules to large sets of molecules (by removing the motion of individual

Table 6.4 Conservation laws and their validity in strong, weak and electromagnetic processes. The quantum numbers N may be additive (A) or multiplicative (M)

Conservation of	Interaction			N
	Strong	Electromagnetic	Weak	
Energy–Momentum $E; \mathbf{p}$	yes	yes	yes	A
Angular momentum \mathbf{J}	yes	yes	yes	A
Parity P	yes	yes	no	M
Baryonic number B	yes	yes	yes	A
Leptonic numbers ^b L_e, L_μ, L_τ	yes	yes	yes	A
Electric charge Q	yes	yes	yes	A
Charge conjugation C	yes	yes	no	M
Time reversal T	yes	yes	yes ^a	M
CP	yes	yes	yes ^a	M
CPT	yes	yes	yes	M
Strong isospin I	yes	no	no	A
3 rd isospin component I_z	yes	yes	no	A
Strangeness S	yes	yes	no	A
Lifetime	$\sim 10^{-23}$ s	$\sim 10^{-20}$ s	$\sim 10^{-12}$ s	—
Interaction range	$\sim 10^{-13}$ cm	infinite	$< 10^{-15}$ cm	—

^aExcept for some meson decays, such as, $K^0, \overline{K^0}$ and $(B^0, \overline{B^0})$

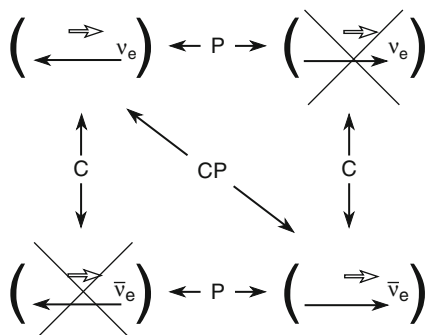
^bExcept for neutrino oscillations, Sect. 12.6

molecules), we lose information. By averaging the microscopic description and eliminating details, we get a situation that is not symmetric with respect to time and violates the invariance under time reversal. Probably, it is our exact request of a macroscopic description that introduces the arrow of time. However, why do we need to perform averages? This is probably associated to the process of biological evolution, and to the fact that organisms develop sensors that receive average quantities, for example, the temperature. Biological selection leads to the development of more adapted organisms. Evolution is dependent on success, which is nothing but a mechanism of variations, of trials and errors, based on sensitivity to averaged properties.

6.8 CP and CPT

Although the weak interaction violates C and P , it was believed that it conserves CP . Figure 6.3 illustrates the effect of applying C , P and CP to the electron neutrino. In 1964, Christenson and other physicists discovered a rare decay of the K_L^0 meson that violated the conservation of CP (Chap. 12). The violation of CP is a small effect which only involves a small part of the weak interaction. It was initially

Fig. 6.3 The application of the operator C , or P to the electron neutrino state generates a state that does not exist in nature. The application of CP generates the antineutrino with the correct helicity



only found in the neutral kaon system, which acts as a very sensitive interferometer. Recently, it was also found in other mesons.

The CP violation probably played an important role in the earliest moments of the Universe. It is believed that at the beginning, all quantum numbers of the Universe were equal to zero, with an equal number of particles and antiparticles. Probably after $t \simeq 10^{-35}$ s, a phase transition took place. After this transition, the particles began to decay with a small CP violation, producing a slight predominance of particles with respect to antiparticles less than one part per billion). When later particle–antiparticle annihilated, that little excess of particles produced the matter-dominated Universe which we observe today. The small amount of CP violation observed in the weak interaction therefore seems not enough to fully explain this scenario.

The CP violation involves a violation of T as well because all interactions are invariant under CPT in any order the three transformations are applied. The CPT invariance is one of the fundamental properties of quantum field theories. It is often called *CPT theorem* (from C. Lüders): *any quantum theory that (1) obeys the postulates of special relativity, (2) admits a state with minimum energy and (3) respects the microcausality is invariant under CPT*. The microcausality requires that the fields obey commutation or anticommutation relations, implying the correct statistics according to the spin of the particles (the Fermi–Dirac statistics for fermions, the Bose–Einstein statistics for bosons).

The consequence of the *CPT theorem* is that a particle and its corresponding antiparticle must have the same mass and lifetime; the magnetic moments must be equal, but with opposite sign. Let us check this: if CPT is conserved, one has $[CPT, H] = 0$; on the other hand, one has $(CPT)^2 = 1$. If the particle state $|a\rangle$ is an eigenstate for the Hamiltonian (mass m and lifetime τ):

$$\langle a | H | a \rangle = \langle a | H(CPT)^2 | a \rangle = \langle a | CPT H CPT | a \rangle = \langle \bar{a} | H | \bar{a} \rangle \rightarrow m_a = m_{\bar{a}}.$$

The mass, lifetime and magnetic moment equality is experimentally well verified [P08] for particle and antiparticle. For example,

$$\left| \frac{q_{\bar{p}}}{m_{\bar{p}}} \right| / \left| \frac{q_p}{m_p} \right| < 0.99999999991 \pm 0.00000000009 \quad (6.50a)$$

$$[m_{e^+} - m_{e^-}] / m_e < 8 \cdot 10^{-9} \quad (6.50b)$$

$$\tau_{\mu^+} / \tau_{\mu^-} < 1.00002 \pm 0.00008 \quad (6.50c)$$

$$[|\mu_{e^+}| - |\mu_{e^-}|] / |\mu_e| < (-0.5 \pm 2.1) \cdot 10^{-12}. \quad (6.50d)$$

6.9 Electric Charge and Gauge Invariance

The last subject presented in this chapter refers to a particular invariance of quantum field theories called *gauge invariance*. This invariance was discovered in the EM interaction and was found to be deeply correlated to electric charge conservation. The gauge invariance mechanism can be extended in quantum mechanics to a “local invariance,” as discussed in Chap. 11.

In classical electrostatics, the potential φ is defined up to an arbitrary constant. Measurable quantities (as the electric field \mathbf{E}) depend on potential difference, and not on its absolute value. The fields \mathbf{E} , \mathbf{B} can be expressed in terms of a scalar and a vector potential (see Appendix A.3). \mathbf{E} , \mathbf{B} are invariant under a transformation of the scalar and vector potential of the type:

$$A_\mu \rightarrow A'_\mu(x'_\mu) = A_\mu(x_\mu) + \frac{\partial \Lambda}{\partial x_\mu} \quad \begin{cases} \mathbf{A}' = \mathbf{A} + \nabla \Lambda \\ \varphi' = \varphi - \frac{1}{c} \frac{\partial \Lambda}{\partial t} \end{cases}$$

defining the gauge invariance. The existence of this symmetry is linked to the absence of a mass term in the electromagnetic field equations (Chap. 11). As a consequence, the photon mass is zero.

The conservation of electric charge leads to the invariance for a local group of gauge transformations. An electromagnetic field A_μ , also called gauge field, with many massless quanta (photons) coupled to the electric charge is needed. In this way, it is clear how a gauge invariance became the basis of electromagnetism and of its quantization.

The success of this procedure suggests that other forces may have a similar origin with a different gauge invariance.

Chapter 7

Hadron Interactions at Low Energies and the Static Quark Model

7.1 Hadrons and Quarks

The current vision of the submicroscopic world is based on a relatively small number of constituents that interact through three fundamental interactions: the electromagnetic, the weak and the strong interactions. The behavior of matter at the smallest distances currently accessible (about 10^{-17} m) is explained in terms of fundamental point-like and indivisible fermions (quarks and leptons) and of vector bosons which mediate the interactions between fermions.

The list of “elementary particles” is much longer and not as well defined as the elementary constituents. In this chapter, some simple schemes for the classification of particles made of quarks is presented. As soon as the 1960s, the growing number of hadrons and the repetition of some characteristics led some to believe that hadrons were not “elementary particles,” but that they are made up of smaller objects, the quarks. Initially, it was thought that only three quark types (u, d, s) plus their antiquarks existed. Today, six quark *flavors* u, d, s, c, b, t , are known.

At the fundamental level, the strong interaction occurs between quarks. Nuclei (which are discussed in Chap. 14) are formed through the interaction between the constituent protons and neutrons (the *nucleons*); this interaction can be considered as a “residual” interaction of the strong interaction. The same occurs in atomic physics, where the force acting between atoms to form molecules is a “residual” electromagnetic interaction. The basic electromagnetic interaction occurs between the nucleus and electrons to form the atom. The interaction between nucleons inside nuclei is a complicated many-body problem.

A “normal” hadron is made of quarks and has dimensions of about 1 fm. Hadrons with integer spin are called *mesons*, those with semi-integer spin are called *baryons*. The *hyperons* are “strange” baryons, i.e., composed of at least one s quark. Hadron “spectroscopy” can be explained by using the simple *static quark model* of hadrons, which is described in this chapter with some experimental verifications and model limits.

The constituent quarks, i.e., the *valence quarks*, explain the regularities of the hadron spectra. At first, the quarks were considered as a mathematical fiction because *free quarks* have never been observed. The evidence for quarks occurred via lepton-hadron collisions with high transferred momentum (*deep inelastic scattering*), consisting of direct collision between two point-like constituents (the lepton and one of the quarks in the hadron). The *dynamic quark structure* of hadrons shall be presented in Chap. 10. Deep inelastic scattering experiments demonstrated that hadrons also contain other particles, namely, the *gluons* and virtual $q\bar{q}$ pairs, rapidly created and annihilated. These virtual $q\bar{q}$ pairs are called *sea quarks*.

7.1.1 The Yukawa Model

The first attempt to explain the interaction between nucleons in nuclei with a quantum mechanical model was developed by Yukawa in the 1930s. For each particle, particularly for a boson of mass m , the relation between its energy E and its momentum \mathbf{p} is $E^2 - p^2 c^2 = m^2 c^4$. The corresponding quantum equation is obtained by replacing E , \mathbf{p} with the corresponding operators, $E \rightarrow i\hbar\partial/\partial t$, $\mathbf{p} \rightarrow -i\hbar\nabla$, acting on a wave function ψ :

$$-\hbar^2 \frac{\partial^2 \psi}{\partial t^2} + \hbar^2 c^2 \nabla^2 \psi = m^2 c^4 \psi.$$

This is the *Klein–Gordon* equation, already presented in Sect. 4.2.2. In the static case (i.e., independent of time), the following solution is obtained:

$$\nabla^2 \psi = \left(\frac{mc}{\hbar}\right)^2 \psi \quad \rightarrow \quad \psi = \frac{K}{r} e^{-r/a} \quad (7.1)$$

with $a = \hbar/mc$. Yukawa applied Eq. 7.1 to the case of nucleon interactions in nuclei. He imagined that a nucleon could interact via a bosonic field with a dependence on the distance from the center of the nucleon within a range a . He required that the static potential $U(r)$ between two nucleons follows the same law, namely,

$$U(r) = \frac{K}{r} e^{-r/a} \quad ; \quad a = \hbar/mc. \quad (7.2)$$

If the range of the nuclear force is $a \simeq 2$ fm, the bosonic field must have $m \simeq 100$ MeV/c². It follows that the nuclear force mediator predicted by the Yukawa model is a boson with a mass of about 100 MeV/c². The mediator was later identified as the π meson, see Problem 7.1. For some time, it was believed that the muon¹ found in cosmic rays was the π meson. An important experiment performed in

¹The muon μ was originally called μ *meson*. However, it is not a meson according to the definition stating that a meson is a *particle made of a $q\bar{q}$ pair*; therefore, it is not correct to call “meson” the μ lepton.

Rome during World War II by Conversi, Pancini, and Piccioni proved that the μ does not interact strongly. Therefore, it could not be the meson predicted by Yukawa.

Today, we know that the strong interaction is much more complicated, and that at the fundamental level, the strong interaction occurs between quarks, and not between nucleons.

7.2 Proton-Neutron Symmetry and the Isotopic Spin

The neutron and proton behave similarly with respect to the strong interaction. In 1932, Heisenberg proposed to consider the neutron and the proton as two states of a single particle, the *nucleon N*. In analogy with spin 1/2 states, which can have two orientations along the third component, i.e., $s_z = +1/2$ and $s_z = -1/2$, the *strong isotopic spin* (or *isospin*) $I = 1/2$ is assigned to the nucleon, with the third component $I_z = +1/2$ for the proton and $I_z = -1/2$ for the neutron. The isotopic spin is denoted by I and the three components with I_x, I_y, I_z (or I_1, I_2, I_3). The isotopic spin can be visualized as a vector in the three-dimensional space of the isospin, a hypothetical space with axis I_x, I_y, I_z . The strong interaction depends on I , not on I_z : the third component of the strong isotopic spin behaves like the electric charge. The strong isotopic spin is not conserved in decays induced by weak and electromagnetic interactions (the latter conserves I_z).

The isotopic spin has the same mathematical behavior as the spin. The spin is a physical quantity measured in units of \hbar , and with the dimension [Energy · Time]. The isotopic spin is a dimensionless quantity. The introduction of the isotopic spin helps to classify the hadrons into multiplets. See Problems from 7.11 to 7.16.

If the Hamiltonian H is invariant for all operations in the abstract isospin space, the energy levels of the system are degenerate and can be classified according to the total isospin I . The eigenvalues of the operator $I^2 = I_x^2 + I_y^2 + I_z^2$ is $I(I+1)$. Possible values of I are integers or semi-integer $0, 1/2, 1, 3/2, \dots$ For each value of I , there is a multiplet with $(2I+1)$ eigenstates of H with the same energy but with different values of I_z . For a fixed value of I , the possible values of I_z are $I, (I-1), \dots, -I$.

Isospin in nuclear physics. In nuclear physics, the conservation of I is connected to the observation that nuclear states with the same number of nucleons but with a different number of protons have the same energy, spin and parity. The invariance of the Hamiltonian of nuclear interactions corresponds to the **nuclear interaction independence from the electric charge**.

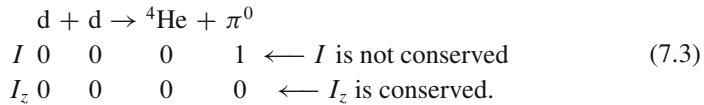
For example, the ground states of ${}^7\text{Be}$ and of ${}^7\text{Li}$ (which differ by the presence of a pp pair in the ${}^7\text{Be}$ state and a nn pair in the ${}^7\text{Li}$ state) have the same energy, spin

and parity. The value $I = 1/2$ can be attributed to these two states with $I_z = +1/2$ assigned to ${}^7\text{Be}$, and $I_z = -1/2$ to ${}^7\text{Li}$. Excluding electromagnetic effects, this implies the equality of forces between the nn and pp pairs.

A second example of the nuclear interaction independence from the nucleon electric charge comes from the observation that the three nuclei with $A = 14$ have $J^P = 0^+$ and practically the same energy:

$$\begin{cases} {}^{14}\text{C}, \quad I_z = -1, \text{ with a } nn \text{ pair} \\ {}^{14}\text{N}, \quad I_z = 0, \text{ with a } np \text{ pair} \\ {}^{14}\text{O}, \quad I_z = +1, \text{ with a } pp \text{ pair.} \end{cases}$$

A third example comes from the reaction



This reaction is prohibited for the strong interaction, though it is allowed for the electromagnetic one. The process (7.3) must therefore occur with a production cross-section typical of the electromagnetic interaction. Under similar kinematic conditions, it was experimentally confirmed that the measured cross-section was almost one hundred times smaller than a typical “strong interaction” cross-section, confirming the hypothesis that the process is indeed due to the electromagnetic interaction.

Isotopic spin of the π meson. The three π^+, π^0, π^- mesons have almost identical properties, with the exception of the electric charge. For the strong interaction, it can be hypothesized that the triplet corresponds to a single particle, the π meson. This is similar to the case of the nucleon, with the difference that there are three instead of two degenerate states. Since the number of degenerate states associated with the isotopic spin I is $N_I = (2I + 1)$, the value $I_\pi = 1$ is attributed to the pion, so that $2I_\pi + 1 = 3$. The three pions form an isospin triplet with $I_z = +1, 0, -1$, respectively for the π^+, π^0, π^- .

Conservation of isotopic spin in strong interaction. The relation between electric charge Q , isospin I and baryon number B ($B = 0$ for the π meson, $B = 1$ for the nucleon) is

$$Q = I_z + B/2. \quad (7.4)$$

Let us generalize the above observations with the two following assumptions:

1. The strong interaction involving mesons and nucleons depends only on the total isospin I and is independent of I_z and Q .
2. The total isotopic spin I is conserved in strong interaction processes.

The conservation of the isospin leads to selection rules and precise relations between the production cross-sections of related processes. Consider for example

the two reactions $pp \rightarrow d\pi^+$ and $pn \rightarrow d\pi^0$. The isospin composition of the initial and final states is

$$I \underbrace{p + p}_{1} \rightarrow \underbrace{d + \pi^+}_{0 \quad 1} \quad (7.5)$$

$$I \underbrace{p + n}_{0,1} \rightarrow \underbrace{d + \pi^0}_{0 \quad 1}. \quad (7.6)$$

The initial states are a pure state of isospin 1 for (7.5) and a mixed state, 50% of isospin 0 and 50% of isospin 1, for (7.6). Both reactions have final states with total isospin equal to one and occur via strong interaction, which conserves isospin. The first reaction is allowed, while the second is allowed only for the 50% of the cases with initial isospin $I = 1$. It follows that $\sigma(pp \rightarrow d\pi^+)/\sigma(pn \rightarrow d\pi^0) = 2$, as experimentally observed.

Isospin for quarks. As anticipated, p and n are not fundamental objects, and are made of (u, d) quarks. The symmetry in terms of *isospin* should be reflected in symmetry in terms of quarks. The (u, d) quarks can be regarded as members of a strong isospin doublet ($I = 1/2$, with $I_z(u) = +1/2$, $I_z(d) = -1/2$) similarly to the neutron and proton. As we shall see in Sect. 7.14.5, the masses of the u and d quarks are almost equal and very small in comparison to the nucleon mass. The mass of hadrons made of the lighter (u, d) quarks receive a dominant contribution from the energy of the strong interaction field to which quarks are subjected. This interaction mechanism is described by *Quantum Chromodynamics (QCD)*, Sect. 11.9. The isospin independence of strong interaction reflects the fact that **color forces are independent of the quark flavor**. The s, c, b, t quarks are strong isospin singlets, with $I = 0$; their mass is significantly larger than that of u, d quarks and the mass of hadrons made of heavier quarks is highly dependent on the quark flavor.

7.3 The Strong Interaction Cross-Section

As discussed in Chap. 4, one way to obtain information on the interaction potential comes from the measurement of the cross-section. In the case of a short-range potential, that is negligible for $r > R_0$ (in the case of the Yukawa potential $R_0 \sim a$), we expect a purely *geometric* cross-section. The geometric cross-section corresponds to the effective area of the target, namely,

$$\sigma = \pi R_0^2. \quad (7.7)$$

This is valid when *the size of the projectile is negligible compared to that of the target*. The projectile particle wave length is given by the de Broglie length (3.1)

$\lambda = \hbar/p = 1.24 \text{ fm}/2\pi p (\text{GeV}/c)$. Only projectiles with momentum $p \gg 1 \text{ GeV}/c$ can be considered as *point-like* with respect to targets with nuclear dimensions ($\sim 1 \text{ fm}$).

The *elastic collisions* occur when the projectile and the target remain unchanged before and after the collision, and have the same energy in the center of mass (c.m.) system. At high energy, the *inelastic collisions* are dominant; it is therefore possible that the incident particle (or the target) be excited, and that new particles are produced. These new possibilities are accounted for by the inelastic cross-section, σ_{inel} . The total cross-section is the sum of the elastic and inelastic ones, namely, $\sigma_{tot} = \sigma_{el} + \sigma_{inel}$.

The hypothesis that the nuclear forces are short-range can be qualitatively checked by observing Figs. 7.1 and 7.2. The former shows the measurements of pion-proton cross-sections and the latter the measurements of proton–proton (and $\bar{p}p$) cross-sections as a function of the momentum p_{lab} of the incoming projectile particle. For $p_{lab} \gg 1 \text{ GeV}/c$, the cross-sections vary only slowly with energy, with a mean value of $\sigma_{pp} \simeq 40 \text{ mb}$ and $\sigma_{\pi p} \simeq 25 \text{ mb}$ over a wide momentum range. The quantity $R_0 \simeq 1.1 \text{ fm}$ and 0.9 fm can be derived from Eq. 7.7 for the two cases. They correspond respectively to the $p - p$ and $\pi - p$ interaction ranges.

In the following, we shall see how this assumption is valid only in a first approximation. We shall also need to change the description at low energy, where the condition of negligible size of the projectile is no longer satisfied.

7.3.1 Mean Free Path

The *mean free path* is a useful quantity for the study of long-lived particles (Table 7.3) propagating in a given medium. Consider a beam of nuclei or long-lived hadrons with intensity $I (\text{cm}^{-2}\text{s}^{-1})$ colliding on a target containing N_n (nuclei cm^{-3}). A target layer dx contains $N_n dx$ (nuclei cm^{-2}). Due to the collisions with the target nuclei, the incident beam is attenuated by the quantity

$$-dI = I\sigma N_n dx \quad (7.8)$$

where σ is a proportionality factor with the dimensions of an area. One can interpret this parameter as an estimate of the geometric size of the target nucleus. By integrating Eq. 7.8 over a finite thickness x , one obtains

$$I(x) = I(0) e^{-N_n \sigma x} = I(0) e^{-\mu x} = I(0) e^{-x/\lambda} \quad (7.9)$$

where $I(0)$ is the intensity of the incident beam before the target; the quantity $\mu = N_n \sigma$ is the *absorption coefficient*, while its inverse,

$$\lambda = 1/\mu = 1/N_n \sigma \quad (\text{cm}), \quad (7.10)$$

is the *mean free path* or the *collision length*. Sometimes, the mean free path is multiplied by the density of the medium, and is expressed as

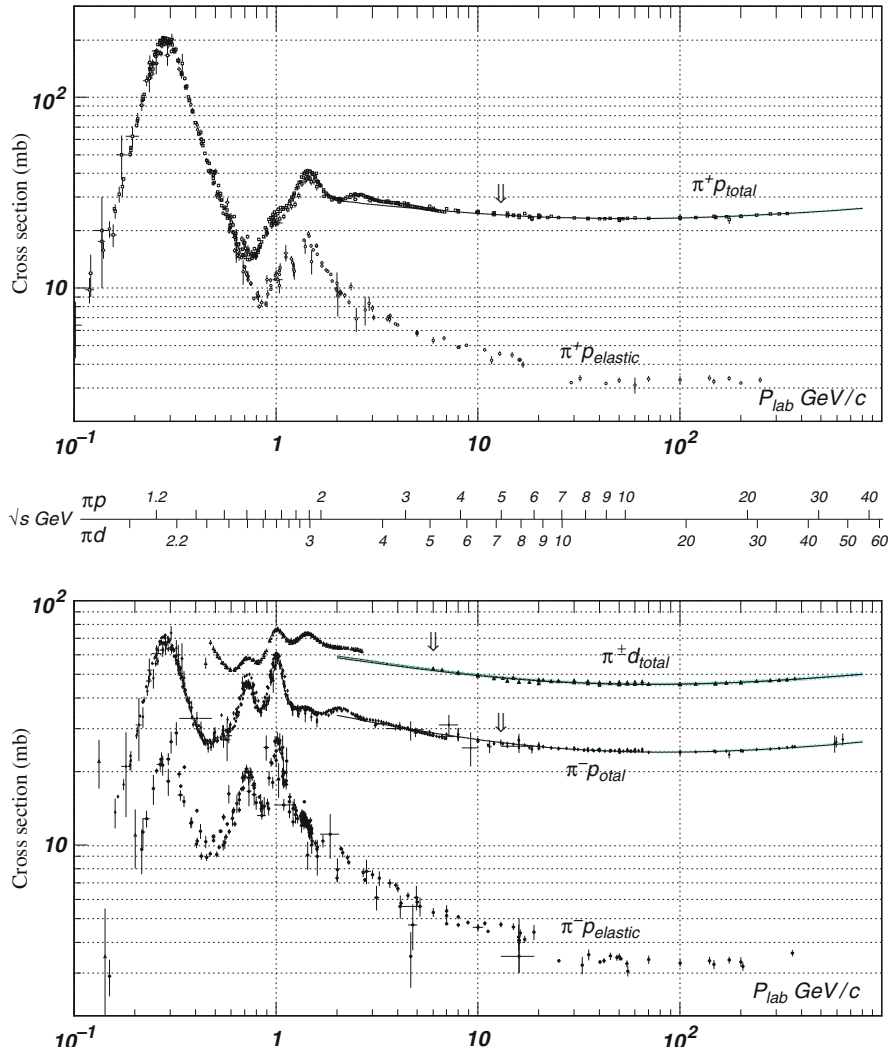


Fig. 7.1 Measurements of the total and elastic cross-sections for $\pi^+ p$ (upper plot), $\pi^- p$, $\pi^\pm d$ (bottom plot) collisions [P08]

$$\lambda = \rho/\mu = \rho/N_n\sigma \quad (\text{g cm}^{-2}). \quad (7.11)$$

In this case, it corresponds to a path (in cm) in a medium with the density of the water. Equations 7.10 and 7.11 differ only in the units, and both are used to define the mean free path. The ratio $I(x)/I(0) = e^{-N_n\sigma x}$ is called *attenuation*. The integration of Eq. 7.8 is possible only if there is no “shadowing effect” of the target nuclei. This is true in practice because the nuclear size is small (\sim few fm, see Problem 7.10) compared to the distance between nuclei.

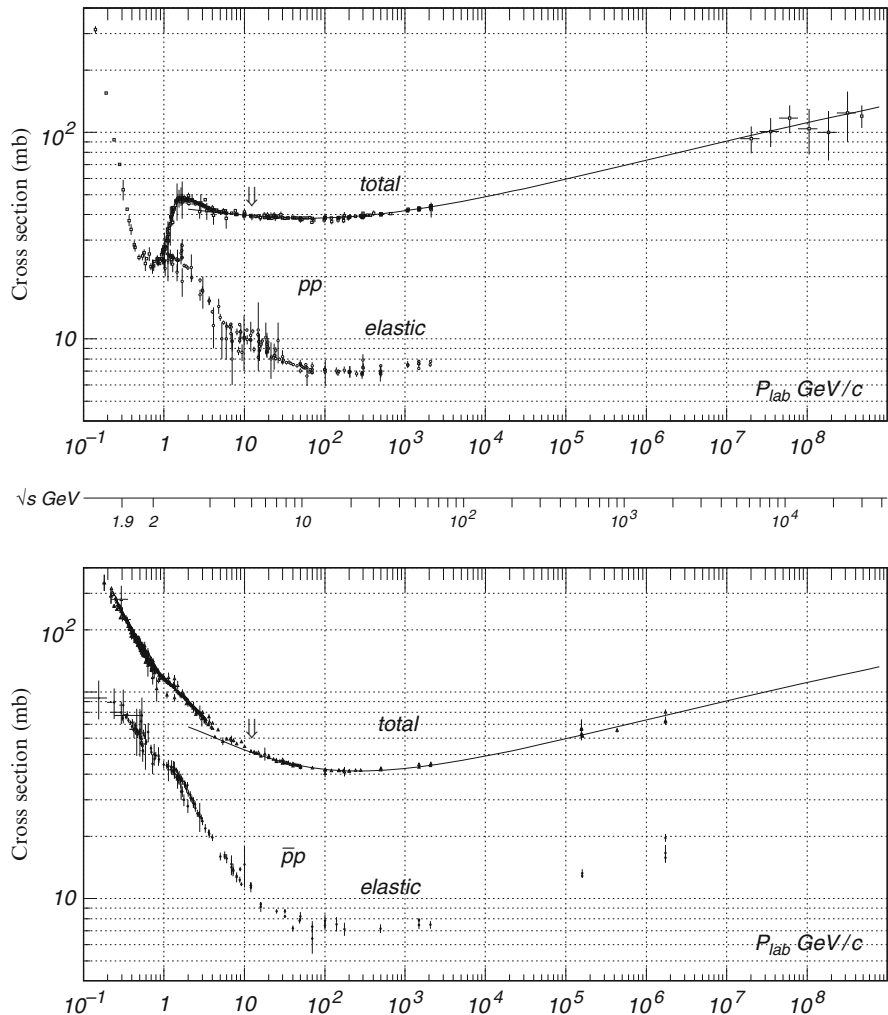


Fig. 7.2 Measurements of the total and elastic cross-sections for pp (upper plot) and $\bar{p}p$ (lower plot) collisions [P08]

7.4 Low Energy Hadron-Hadron Collisions

The study of pion-nucleon collisions at low energy (up to a few GeV) has been historically important in establishing the existence of *hadronic resonances* and for the measurements of their masses and quantum numbers.

A qualitative idea of the features of hadron-hadron collisions [7G76] can be obtained by analyzing the measurements of the total and elastic cross-sections of charged hadrons on hydrogen and deuterium, shown in Figs. 7.1–7.3. For

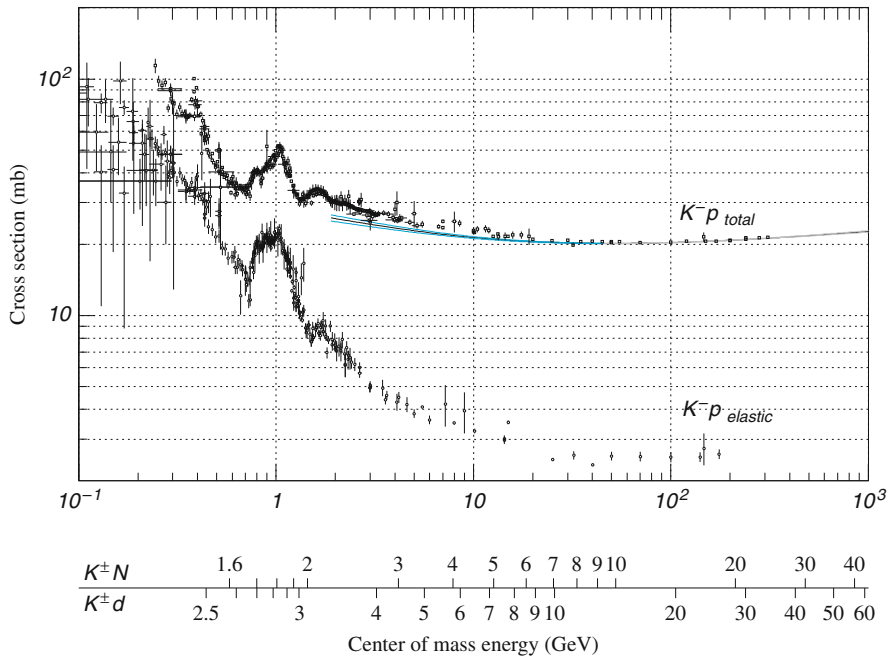


Fig. 7.3 Measurements of the total and elastic cross-sections for $K^- p$ collisions [P08]

c.m. energies smaller than ~ 3 GeV, the total $\pi^\pm p$, $K^- p$, $K^- n$ cross-sections are characterized by peaks and structures, whose heights decrease with increasing energy. The $K^+ p$, $p p$ and $\bar{p} p$ cross-sections do not have large peaks, and only present minor structures.

The quantum mechanical formalism used for the study of cross-sections at low energies is developed in terms of amplitudes and phases of matter waves, in analogy with the description of optical waves. A fairly detailed description of the formalism can be found in [P87]. The mathematical function that describes the increases of the cross-section is derived in Sect. 7.5.

7.4.1 *Antibaryons*

Baryons, as protons, neutrons and hyperons, are semi-integer spin particles. According to the Dirac theory, the corresponding charge conjugated states must exist. These states correspond to *antibaryons* with opposite fermionic number, electric charge, magnetic moment and strangeness. The theory is confirmed by the existence of antileptons, such as the *positron* (e^+), the μ^+ lepton and the antineutrinos. To test the Dirac prediction in the hadron system, O. Chamberlain and E. Segrè (with Wiegand and Ypsilantis) managed, in 1955, to produce antiprotons with the Bevatron accelerator at the Lawrence Radiation Laboratory in Berkeley. For this discovery, Segrè and Chamberlain earned the Nobel Prize in 1959.

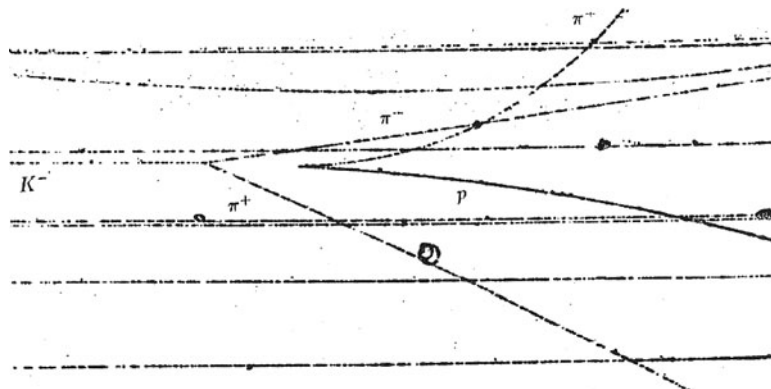


Fig. 7.4 Interaction of a K^- meson of 4.2 GeV/c momentum, in a bubble chamber filled with liquid hydrogen. Two charged pions and a Λ^0 are produced in the interaction. The Λ^0 decays shortly afterwards into a proton and a negative pion (From R.T. Van de Walle, Photo CERN, Geneva)

An antiproton (\bar{p}) can be produced in interactions of protons on nuclei through the reactions $p\bar{p} \rightarrow \bar{p}ppp$ or $p\bar{n} \rightarrow \bar{p}ppn$ that conserve the baryon number and the electric charge. The reactions only occur if the beam kinetic energy is larger than $6m_p = 5.6$ GeV (Sect. 3.1). The \bar{p} production is indicated by the presence in the final state of a particle with the same mass as that of the proton but with an opposite electric charge. At this energy, many π^- mesons are produced with a much higher probability. Particles with mass $= m_p$ must then be selected by measuring both the momentum and the speed of the produced particles. The experiment was done using bending magnets to select negative charged particles and both time-of-flight and Cherenkov detectors to measure the speed.

Once the method to produce a secondary beam of antiprotons was known, it was used to produce other antibaryons in $p\bar{p}$ annihilations through the reactions $p\bar{p} \rightarrow \text{baryon} + \text{antibaryon}$. In 1957, Cork, Lamberston and Piccioni discovered the antineutron (\bar{n}) in this way. Shortly after, the Λ^0 was observed in the \bar{p} annihilation with liquid hydrogen nuclei in a bubble chamber, $\bar{p}p \rightarrow \Lambda^0\bar{\Lambda}^0$. Other antibaryons were then discovered in the same way: for every baryon, the corresponding antibaryon was observed. The antibaryons have negative baryon number, and decay in the charged conjugated states of the corresponding baryons. For instance, the antineutron decays as $\bar{n} \rightarrow \bar{p}e^+\nu_e$.

7.4.2 Hadron Resonances

Figure 7.4 shows an event recorded in a hydrogen bubble chamber. An incident K^- meson interacts with a proton of the liquid inside the bubble chamber. The K^- beam was selected with the techniques described in Chap. 3. The final state consists of two

charged and one neutral particle. The neutral one decays into two charged particles. The event is consistent with the following hypothesis:

$$\begin{aligned} K^- p &\rightarrow \Lambda^0 \pi^+ \pi^- \\ &\hookrightarrow \pi^- p. \end{aligned} \quad (7.12)$$

This first reaction corresponds to the production of two charged pions and a Λ^0 ; the Λ^0 then decays into a proton and a π^- meson.

However, one can imagine that the reaction (7.12) proceeds through an intermediate process, with a much higher probability (i.e., cross-section). In this second hypothesis, two new resonant states (each of which represents a new **particle**) are formed. These resonant states are called $\Sigma^{\pm*}$. The $\Sigma^{\pm*}$, depending on the sign, decay into $\Lambda^0 \pi^+$ or $\Lambda^0 \pi^-$; these new reactions yield the same final state as in (7.12) through the sequence

$$\begin{aligned} K^- p &\rightarrow \Sigma^{+\ast} \pi^- \quad \text{or} \quad K^- p \rightarrow \Sigma^{-\ast} \pi^+ \\ &\hookrightarrow \Lambda^0 \pi^+ \quad \hookrightarrow \Lambda^0 \pi^- \\ &\hookrightarrow p \pi^- \quad \hookrightarrow p \pi^-. \end{aligned} \quad (7.13)$$

If this is indeed the case, the mass of the system $\Lambda^0 \pi^+$, obtained in (7.13) “peaks” at a value corresponding to the mass of the new $\Sigma^{+\ast}$ resonant state (the same for the $\Sigma^{-\ast}$). To test the hypothesis, many events, for example, the one shown in Fig. 7.4, must be found and measured. It is necessary to have several photos similar to this (it is not difficult since this process is governed by the strong interaction, and the production is abundant). The kinematic variables which can be measured (assuming that the proton and pion masses are known) are the charged particle momentum and the emission angles between them.

The “effective mass” of the $(\Lambda^0 \pi^+)$ system in the final state is ($c = 1$)

$$m_{\Lambda^0 \pi^+}^2 = E_{\Lambda^0 \pi^+}^2 - p_{\Lambda^0 \pi^+}^2 \quad (7.14)$$

$$\begin{aligned} &= (E_{\Lambda^0} + E_{\pi^+})^2 - (\vec{p}_{\Lambda^0} + \vec{p}_{\pi^+})^2 \\ &= E_{\Lambda^0}^2 + E_{\pi^+}^2 + 2E_{\Lambda^0}E_{\pi^+} - p_{\Lambda^0}^2 - p_{\pi^+}^2 - 2\mathbf{p}_{\Lambda^0}\mathbf{p}_{\pi^+}. \end{aligned} \quad (7.15)$$

Remember that $E_{\Lambda^0}^2 - p_{\Lambda^0}^2 = m_{\Lambda^0}^2$, $E_{\pi^+}^2 - p_{\pi^+}^2 = m_{\pi^+}^2$. In addition, one has $\mathbf{p}_{\Lambda^0} \cdot \mathbf{p}_{\pi^+} = p_{\Lambda^0} p_{\pi^+} \cos \vartheta_{\Lambda\pi}$, where $\theta_{\Lambda\pi}$ is the angle between the emission directions of the Λ^0 and of the π^+ . From (7.15), one obtains

$$m_{\Lambda^0 \pi^+}^2 = m_{\Lambda^0}^2 + m_{\pi^+}^2 + 2E_{\Lambda^0}E_{\pi^+} - 2p_{\Lambda^0}p_{\pi^+} \cos \theta_{\Lambda\pi}. \quad (7.16)$$

The Λ^0 and π^+ momenta are measured by the curvature radius of the particle in the magnetic field. The energies E_{Λ^0} and E_{π^+} are obtained from the masses and the measured momenta, $E_{\Lambda^0}^2 = m_{\Lambda^0}^2 + p_{\Lambda^0}^2$, $E_{\pi^+}^2 = m_{\pi^+}^2 + p_{\pi^+}^2$.

A “trick,” due to Dalitz (1953), helps to demonstrate the existence of a resonant $\Sigma^{\pm*}$ state, quickly decaying into $\Lambda^0 \pi^+$ or $\Lambda^0 \pi^-$. The invariant mass (7.15)

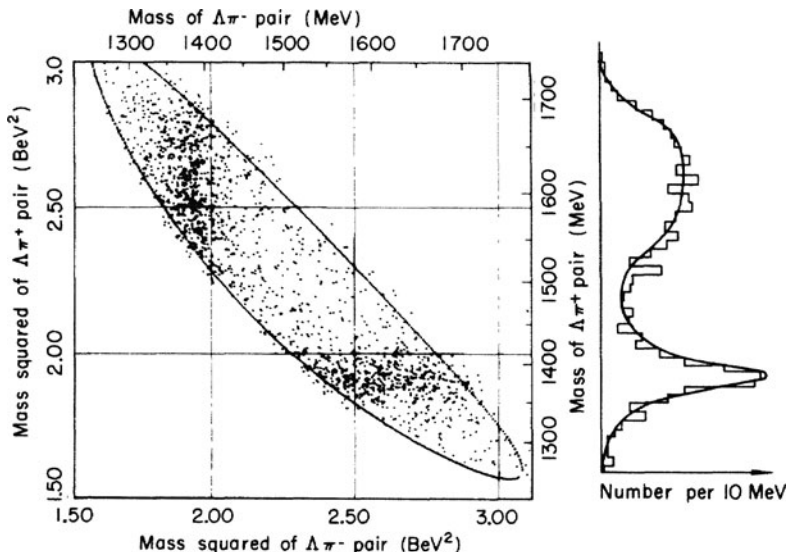


Fig. 7.5 Two-dimensional diagram (called Dalitz plot) of $K^- p \rightarrow \Lambda^0 \pi^+ \pi^-$ events for incident K^- of 1.22 GeV/c momentum. Each measured event is represented with a dot in the plot. The solid line delineates the available phase space, that is, the region of values allowed by the energy conservation. The mass distribution of the $\Lambda^0 \pi^+$ is also shown as a projection along the y -axis: note the peak at 1,385 MeV corresponding to the Σ^{+*} particle mass. The structure near 1,600 MeV is a “reflection” of the $\Lambda \pi^-$ resonance, peaking at the mass 1,385 MeV along the x -axis (not shown) [7S63]

measured on each of many recorded events is plotted along one axis of a two-dimensional graph (*scatter plot*). For the second axis, the value of the similar invariant mass of the $\Lambda^0 \pi^-$ system is used. If a resonance is formed (i.e., a particle with defined mass and quantum numbers), one would expect to find a clustering of points in the plot.

Figure 7.5 shows the Dalitz diagram (Dalitz Plot) for $K^- p \rightarrow \Lambda^0 \pi^+ \pi^-$ events. A horizontal concentration of events corresponding to $m_{\Lambda \pi^+} = 1,385$ MeV and a vertical concentration corresponding to $m_{\Lambda \pi^-} = 1,385$ MeV are clearly visible. The projection along the y axis is also shown. Note the peak at $m_{\Lambda \pi^+} \simeq 1,385$ MeV and a broader peak at $\simeq 1,600$ MeV. The latter is caused by the presence of the clustering of the $m_{\Lambda \pi^-} \simeq 1,385$ MeV (it is a so-called “reflection”). The structure at $m_{\Lambda \pi^+} = 1,385$ MeV corresponds to the $\Sigma^{+*}(1385)$.

From Fig. 7.5, it can be deduced that about half of the events of reaction (7.12) produces $\Lambda^0 \pi^+$ pairs with a peak at mass 1,385 MeV; this means that in 50% of the cases, the reaction occurs through $\Sigma^{+*}(1385)$, giving rise to the chain of events described in (7.13). In the bubble chamber, the state $\Sigma^{+*}(1385)$ cannot be seen because it has a very short lifetime, of the order of 10^{-23} s, typical of a hadron which decays through the strong interaction.

The lifetime of the state can be estimated using the peak width shown in the projection along the y -axis in Fig. 7.5. The typical width of these states is $\Gamma \approx 100 \text{ MeV}$. From the uncertainty principle, one can write

$$\tau \simeq \frac{\hbar}{\Gamma} = \frac{6.6 \cdot 10^{-22} \text{ MeV s}}{100 \text{ MeV}} = 6.6 \cdot 10^{-24} \text{ s} \sim 10^{-23} \text{ s.}$$

The $\Sigma^{+*}(1385)$ is a state with well defined mass, electric charge, spin and others quantum numbers. However, because of the short lifetime, it seemed difficult to call them “a particle.” For this reason, and because of the mathematical form of the cross-section as a function of energy described in the next paragraph, these short-lived particles were called *resonances*.

Clarifications regarding the uncertainty principle. The uncertainty principle tells us that in Nature, a limit exists on our possible knowledge of the submicroscopic world, e.g., regarding the dynamics of a particle. For pairs of conjugated physics variables, for example, energy and time, momentum and position, there are limitations in the precision of their measurements. For example, if we measure the position x of an electron with a precision Δx , we cannot simultaneously measure the p_x component of its momentum with unlimited precision. According to the uncertainty principle, an uncertainty Δp_x related to the uncertainty Δx exists. Similarly, ΔE and Δt are related through the uncertainty principle. In the literature, different numerical expressions for the uncertainty principle are used, that is,

$$\begin{aligned}\Delta E \Delta t &\geq \frac{\hbar}{2}, \quad \geq \hbar, \quad \geq h \\ \Delta p_x \Delta x &\geq \frac{\hbar}{2}, \quad \geq \hbar, \quad \geq h.\end{aligned}$$

From a theoretical point of view, the first expression is better justified ($\Delta E \Delta t \geq \hbar/2$, $\Delta p_x \Delta x \geq \hbar/2$), because it can be directly derived from (1) the commutator algebra, (2) the analysis of the wave functions structure, (3) the quantum harmonic oscillator ground state. This implies that the uncertainties ΔE , Δt , Δx , Δp_x have the meaning of standard deviation, i.e., the mean squared error at the 67% probability. In the case of the energy (mass) width of a resonance, we can consider that $\Delta E = \Gamma/2$, i.e., the half-width at half-maximum, as coinciding with one standard deviation. For this reason, the quantity Γ is expressed in MeV (the quantity Γ_i/Γ is dimensionless, and expresses the decay probability in the i th channel). For decay processes, one uses $\Delta t = \tau = \text{lifetime of the particle at rest}$. Finally, one can write

$$\Delta E \Delta t \simeq \frac{\Gamma}{2} \tau \geq \frac{\hbar}{2} \Rightarrow \Gamma \tau \geq \hbar. \quad (7.17)$$

In the considered hadronic resonance, $\Gamma \simeq 100$ MeV, yielding to $\tau \simeq 0.66 \cdot 10^{-23}$ s. For a resonance of mass m produced with kinetic energy E , the lifetime is relativistically increased by a factor of $\gamma = E/m$, and $\tau = \gamma \tau_{rest}$.

7.5 Breit–Wigner Equation for Resonances

Consider the collision between two hadrons: the incident particle corresponds to a wave function with de Broglie length λ , the second hadron is at rest in the laboratory system. The energy of the incident particle can be varied. If, at some value of λ and for a particular value of the relative angular momentum ℓ between the two hadrons, the cross-section passes through a maximum, one can say that there is a *hadronic resonance*. The resonance is characterized by

- Defined angular momentum $J = \ell$ (for spinless particles).
- Defined parity.
- Defined value of the isospin I .
- Defined mass, equal to the total energy in the center of mass at which there is the resonance maximum.
- Defined lifetime, as determined by the width at half-maximum (Γ) of the curve.

A resonance implies an increase of the formation probability W (4.28). Figure 7.5 shows a concentration of events in the energy region around 1,385 MeV. An enhancement of the number of produced events, and consequently of W , with a bell-shaped distribution as that seen along the y -axis projection of the figure, involves a similar increase in the production cross-section ($\sigma \simeq W$). In the following, we shall derive the equation of the curve, called the *Breit–Wigner (BW) equation*. The typical BW shape is plotted in Fig. 7.6. Note that the resonance energy E_R , which corresponds to the *mass of the resonance*, coincides with the peak of the function. However, the width Γ is defined as the difference in energy between the two points where $\sigma = \sigma_{max}/2$ (full width at half-maximum).

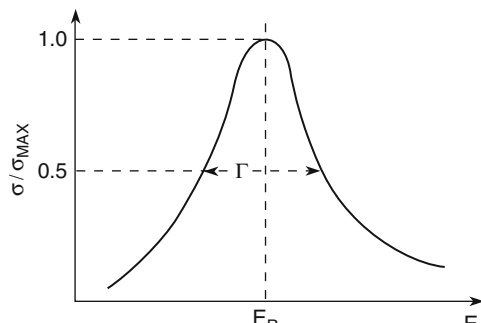


Fig. 7.6 Shape of the Breit–Wigner equation. Γ is the width of the curve at the ordinate point where $\sigma = \sigma_{max}/2$

The shape of the BW curve can be obtained from the formalism of the amplitudes and phases of matter waves. However, it is instructive to derive it from the general property that the resonance is an unstable particle, with lifetime τ , and that time and energy are variables correlated by the uncertainty principle. The energy dependence of the amplitude of Fig. 7.6 is the Fourier transform of a wave function that describes a survival probability decreasing exponentially over time, with lifetime τ .

Let us imagine the elastic formation process of a generic resonance R , which decays with lifetime τ into the same initial particles. The presence of a interaction process is demonstrated by the different directions and momenta of the particles in the final state, that is,

$$a + b \rightarrow R \rightarrow a' + b'. \quad (7.18)$$

The unstable resonance R is described by the free particle wave function (4.11) multiplied by a real function describing its decay probability as a function of time, that is,

$$\psi(t) = \psi(0)e^{-i\omega_R t} e^{-\frac{t}{2\tau}} = \psi(0)e^{-\frac{iE_R}{\hbar}t} e^{-\frac{\Gamma}{2\hbar}t}, \quad (7.19)$$

where the relations $\omega_R = E_R/\hbar$ and $\tau = \hbar/\Gamma$ have been inserted in the last equality. The probability of finding the particle at a time t is

$$I(t) = \psi^* \psi = \psi(0)^2 e^{-t/\tau} = I(0)e^{-t/\tau}, \quad (7.20)$$

corresponding to the radioactive decay law (Sect. 4.5.2). The Fourier transform of (7.19), in the natural unit system ($\hbar = c = 1$), is

$$\begin{aligned} \chi(E) &= \int \psi(t) e^{iEt} dt = \psi(0) \int e^{-t[(\Gamma/2) + iE_R - iE]} dt = \\ &= \frac{K}{(E_R - E) - i\Gamma/2}. \end{aligned} \quad (7.21)$$

The constant K must be determined with the normalization properties of wave functions. Since the square of the wave function $\chi(E)$ represents the probability of finding the particle in the energy state E , it must be proportional to the process cross-section, that is,

$$\sigma(E) = \sigma_0 \chi^*(E) \chi(E) = \sigma_0 \frac{K^2}{[(E_R - E)^2 + \Gamma^2/4]}. \quad (7.22)$$

Since Eq. 7.22 presents a maximum at $E = E_R$, one can determine K as

$$1 = \chi^*(E_R) \chi(E_R) = 4K^2/\Gamma^2 \quad \longrightarrow \quad K^2 = \Gamma^2/4. \quad (7.23)$$

The proportionality constant σ_0 must be related to the wavelength of the incident particle, as mentioned at the beginning of the paragraph. From a dimension analysis, one has $\sigma_0 \simeq \pi\lambda^2$. Detailed calculations [P87] show that

$$\sigma_0 = \pi(2\lambda)^2 = 4\pi\lambda^2. \quad (7.24)$$

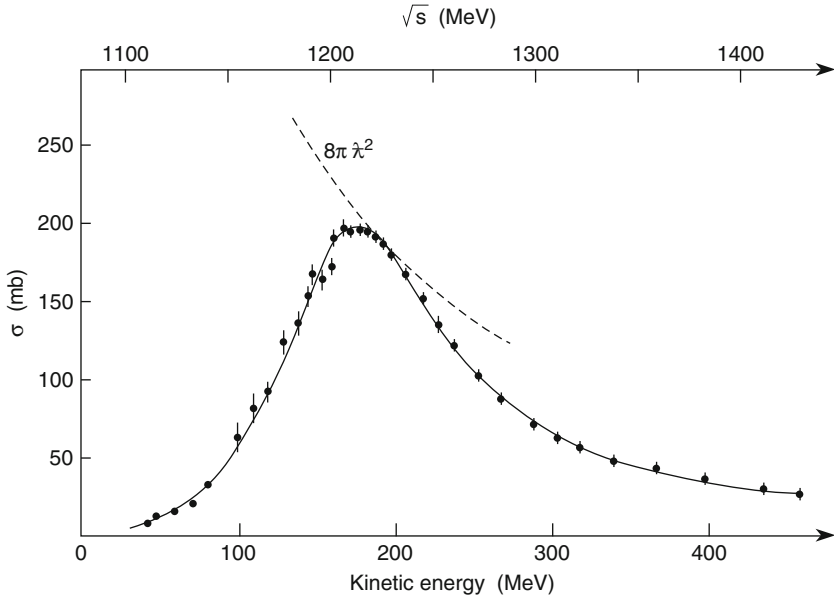


Fig. 7.7 Total cross-section $\pi^+ p$ as a function of the kinetic energy of the incident pion (the scale indicated below the x -axis) in the region of the $\Delta^{++}(1,232)$ resonance. The maximum value of the cross-section is consistent with the value $8\pi\lambda^2$ predicted for an elastic resonance with spin 3/2. The abscissa scale at the top refers to the c.m. energy, corresponding to the effective mass of the π p system

Let us now consider the formation and decay of a resonance of total angular momentum J by the collision of two particles a, b , with spin s_a, s_b . In this case, the cross-section must be averaged over the number of spin states of the incoming particles and multiplied (Sect. 4.5) by a factor $(2J + 1)$. Taking this into account, from Eqs. 7.23 and 7.24, the elastic cross-section (7.22) as a function energy becomes

$$\boxed{\sigma_{el}(E; J) = 4\pi\lambda^2 \frac{(2J + 1)}{(2s_a + 1)(2s_b + 1)} \left[\frac{\Gamma^2/4}{(E_R - E)^2 + \Gamma^2/4} \right].} \quad (7.25)$$

This equation corresponds to the Breit–Wigner equation. The formula must be further modified to describe the production of nonelastic resonances (see Sect. 9.3.2).

7.5.1 The $\Delta^{++}(1232)$ Resonance

The total cross-section $\pi^+ p$ at low energy, see Figs. 7.1 and 7.7, shows a large peak at the kinetic energy of the incident pion $T_{\pi lab} = 191$ MeV. This is equivalent to a total energy in the c.m. system E_{cm} :

$$E_{cm} = 1232 \text{ MeV} \quad \Gamma = 120 \text{ MeV}. \quad (7.26)$$

The width Γ at half-maximum of the peak is obtained from the data shown in Fig. 7.7. This resonance peak corresponds to the $\Delta(1232)$ which is the most famous baryonic resonance. Because it is produced in $\pi^+ p$ interactions, it is a baryon state ($B = +1$), with isospin $I = 3/2$ and total angular momentum $J = 3/2$ (the “spin” of the resonance).

The momentum corresponding to the c.m. energy value $mc^2 = E_{cm} = 1232 \text{ MeV}$ is $p_{\pi_{lab}} = 300 \text{ MeV}/c$ in the laboratory system and $p_{\pi_{cm}} = 228 \text{ MeV}/c$ in the c.m. system. The corresponding total and kinetic energies in the laboratory system are

$$\begin{aligned} E_{\pi_{lab}} &= \sqrt{p_\pi^2 + m_\pi^2} = \sqrt{300^2 + 139.6^2} = 330.9 \text{ MeV} \\ T_{\pi_{lab}} &= E_{\pi_{lab}} - m_\pi = 330 - 139.6 = 191.3 \text{ MeV}. \end{aligned}$$

Let us check the resonance spin assignment using the experimental values (7.26). Recalling that $s_p = 1/2$ and $s_\pi = 0$, the Breit–Wigner (7.25) for the $\Delta^{++}(1232)$ resonance can be written as (energy in GeV)

$$\begin{aligned} \sigma_{el}(E; J) &= 4\pi\lambda^2 \left(\frac{(2J+1)}{(2s_p+1)(2s_\pi+1)} \right) \frac{\Gamma^2/4}{(E_R - E)^2 + \Gamma^2/4} \\ &= 2\pi\lambda^2(2J+1) \frac{0.120^2/4}{(1.232 - E)^2 + 0.120^2/4}. \end{aligned} \quad (7.27)$$

At the maximum of the cross-section $E = E_R$ and assuming $J = 3/2$, the formula gives

$$\sigma_{max} = \sigma_{el}(E = E_R; J = 3/2) = 8\pi\lambda^2 = \frac{8\pi}{p_{\pi_{cm}}^2} = \frac{8\pi(\hbar c)^2}{(0.228 \text{ GeV})^2} \simeq 188 \text{ mb}$$

(recall that $1 \text{ mb} = 10^{-27} \text{ cm}^2$; $\hbar c = 197 \text{ MeV fm}$, $(\hbar c)^2 = 0.388 \text{ GeV}^2 \text{ mb}$; $1 \text{ fm} = 10^{-15} \text{ m}$). The computed value of σ_{max} corresponds to that experimentally shown in Fig. 7.7. It is also worth stressing that any other assignment of the particle spin different from $J = 3/2$, leads to a different value of σ_{max} . For example, for $J = 1/2$, one would obtain $\sigma_{el}(E = E_R; J = 1/2) = 94 \text{ mb}$, which is half of the measured value.

7.5.2 Resonance Formation and Production

The $\Delta^{++}(1232)$ resonance as studied in elastic $\pi^+ p \rightarrow \pi^+ p$ collisions corresponds to the process of *resonance formation in the s-channel*, see Fig. 7.8a. For the s-channel shown in Fig. 7.8a, it is assumed that time runs from left to right, corresponding to the reaction $\pi^+ p \rightarrow \Delta^{++} \rightarrow \pi^+ p$; in the t-channel, time

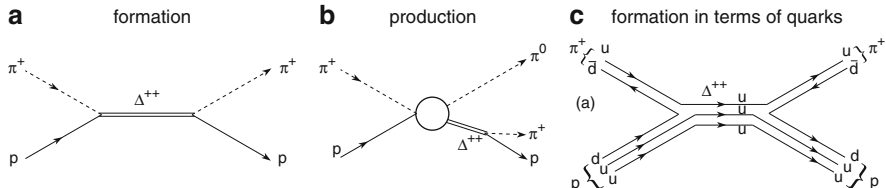


Fig. 7.8 Illustration of the (a) $\Delta^{++}(1232)$ resonance formation in the s -channel from $\pi^+ p$ interactions; (b) $\Delta^{++}(1232)$ production in inelastic collisions: $\pi^+ p \rightarrow \Delta^{++} \pi^0 \rightarrow \pi^+ p \pi^0$. In (c), the Δ^{++} resonance formation is shown in terms of constituent quarks

goes from the bottom to the top of the same figure, corresponding to the reaction $\bar{p}p \rightarrow \pi^+ \pi^-$.

The resonance can also be produced through reactions of the type

$$\pi^+ p \rightarrow \Delta^{++} \pi^0 \rightarrow \pi^+ p \pi^0. \quad (7.28)$$

This process is called *resonance production*, see Fig. 7.8b. The case of the Σ^* (1385) discussed in Sect. 7.4.2 corresponds to a resonance production. The $\Delta^{++}(1232)$ lifetime is so short ($\sim 10^{-23}$ s) that the resonance remains confined in the interaction region. Its traveling distance is of the order of $c\tau = 3 \times 10^8 \cdot 10^{-23} = 3 \times 10^{-15}$ m = 3 fm.

In terms of constituent quarks, the proton consists of three quarks ($p = uud$), the meson π^+ is made of a quark and an antiquark pair ($\pi^+ = u\bar{d}$), and the Δ^{++} of three quarks ($\Delta^{++} = uuu$). The formation of the Δ^{++} resonance in elastic $\pi^+ p$ collisions in terms of constituent quarks is illustrated in Fig. 7.8c.

7.5.3 Angular Distribution of Resonance Decay Products

In this subsection, which can be skipped during an initial reading, the Clebsch-Gordan coefficients [P08], known from the spin combinations in atomic physics, are used. Our primary interest is based on the experimental fact that the angular distribution of emitted particles can be used to determine the spin of the resonance. For example, the assignment $J = 3/2$ to the Δ^{++} may be confirmed by the study of the angular distribution of the outgoing π^+ meson at the resonance energy.

Consider the situation in the c.m. system before the collision, as shown in Fig. 7.9. Taking the quantization z axis in the direction of the incident pion, one has $m_\ell = 0$. The spin of the proton can be directed towards the z axis or in the opposite direction. The initial state has a wave function with $J = 3/2$; since the π is spinless and $m_\ell = 0$, the third component of m_j depends on the proton polarization:

$$\psi_i(J = 3/2, m_i = \pm 1/2) = \psi(\ell, 0) \cdot X(1/2, \pm 1/2). \quad (7.29)$$

$\psi(\ell, 0)$ is the orbital wave function of the πp system and $X(1/2, \pm 1/2)$ is the proton spin wave function. To obtain $J = 3/2$, ℓ must be equal to one or two. Let us assume $\ell = 1$ and $m = +1/2$.

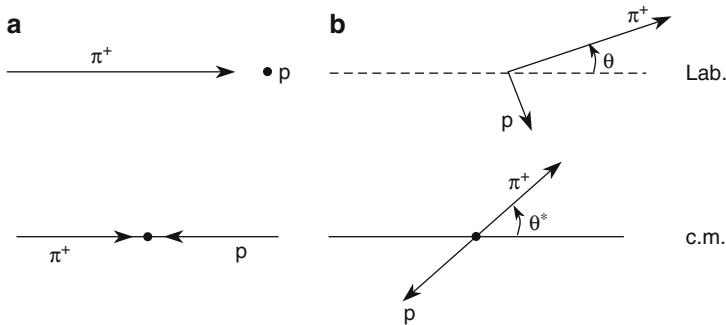


Fig. 7.9 Elastic π^+ p collision: (a) before and (b) after the collision in the laboratory and in the center-of-mass system

Two options are possible for the final state wave function; the first one corresponds to the configuration in which the proton spin is oriented as before the collision; in the second one, the spin is flipped with respect to its original orientation. Since the orbital wave functions are the spherical harmonic functions $Y(\ell, m)$, and using the Clebsch–Gordan coefficients (the radial wave function does not contribute to the angular distribution), one has

$$\psi_f(3/2, +1/2) = \sqrt{2/3} Y(1, 0) X(1/2, +1/2) + \sqrt{1/3} Y(1, 1) X(1/2, -1/2) \quad (7.30)$$

(the notation $X(1/2, +1/2) = X_\uparrow$, $X(1/2, -1/2) = X_\downarrow$ is also used). Note that, due to the choice of the reference system, the scattering angle coincides with the zenith angle θ^* that appears in Y_ℓ^m . The spherical harmonic functions are

$$\begin{cases} Y(1, 0) = \sqrt{3/4\pi} \cos \theta^* \\ Y(1, +1) = -\sqrt{3/8\pi} \sin \theta^* e^{i\varphi^*} \end{cases} \quad (7.31)$$

The angular distribution of the pion, $I(\theta^*)$, is given by the probability density $\psi_f^* \psi_f$. The spin part of the wave functions are orthonormal functions: $X_\uparrow^2 = X_\downarrow^2 = 1$, $X_\uparrow \cdot X_\downarrow = 0$. Therefore, one has

$$\begin{aligned} I(\theta^*) &= \psi_f \psi_f^* = \frac{2}{3} |Y(1, 0)|^2 \langle X_\uparrow | X_\uparrow \rangle + \frac{1}{3} |Y(1, 1)|^2 \langle X_\downarrow | X_\downarrow \rangle \\ &= \frac{2}{3} \frac{3}{4\pi} \cos^2 \theta^* + \frac{1}{3} \frac{3}{8\pi} \sin^2 \theta^* = \frac{1}{2\pi} \cos^2 \theta^* + \frac{1}{8\pi} \sin^2 \theta^* \\ &= \frac{1}{8\pi} (1 + 3 \cos^2 \theta^*). \end{aligned} \quad (7.32)$$

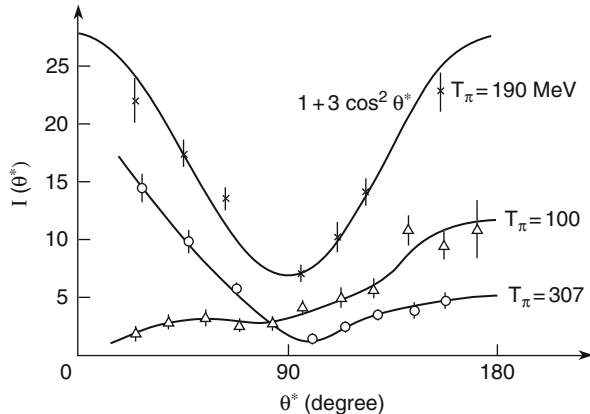


Fig. 7.10 Angular distribution in the c.m. system of the scattered pion with respect to the incident pion direction in the elastic $\pi^+ p$ collision at the $\Delta^{++}(1232)$ resonance energy and two nearby energies. Note that the shape of the distribution $I(\theta^*)$ continuously changes with energy

Figure 7.10 shows the experimental angular distribution of the scattered pion with respect to the incident pion direction in the c.m. system. The results for $\pi^+ p$ elastic collisions at the energy of the $\Delta^{++}(1232)$ resonance and at two nearby energies are shown. At the Δ^{++} energy, the angular distribution follows (7.32), confirming the assignment of $J = 3/2, \ell = 1$ to the resonance. The value $\ell = 2$ would produce a different angular distribution.

7.6 Production and Decay of Strange Particles

In this section, we introduce the so-called *strange particles*. This term does not mean that these particles are strange in the etymological sense of the word. It means that when they were discovered their behavior seemed strange. These particles were produced abundantly, which means that their production was through the strong interaction. As subjected to strong interaction, one would have expected a very short lifetime ($\sim 10^{-23} \text{ s}$). Instead, they had relatively long lifetimes of the order of $10^{-8}\text{--}10^{-13} \text{ s}$, corresponding to typical lifetimes of weak interaction decays. Why are their lifetimes so long even though they are abundantly produced? In addition, why are they produced in pairs? The name “strange” particles was derived from these very dilemmas. The solution was to invent the conservation of a new quantum number: the “strangeness.” Due to their long lifetimes yielding path lengths up to several centimeters, the bubble chamber was well suited to study the strange particle properties. In Fig. 7.11, an incoming π^- meson from the left reaches the liquid hydrogen bubble chamber. In addition to the π^- , two pairs of tracks are visible. Each pair has a V-shape. The two arms of the V correspond to two opposite sign

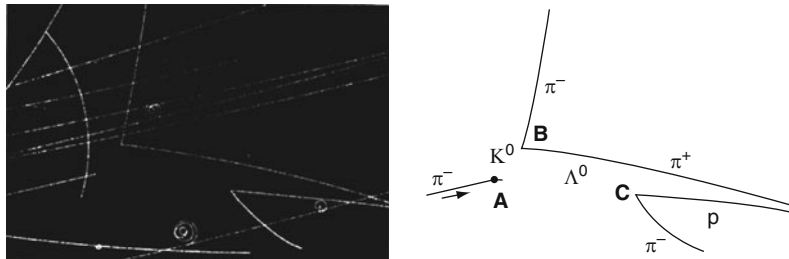


Fig. 7.11 Example of a bubble chamber picture showing an associated production of two strange particles (the K^0 meson and the Λ^0 baryon) and their decay products. The associated production $\pi^- p \rightarrow \Lambda^0 K^0$ occurs in A. The K^0 meson travels from A to B, where it decays into two charged particles ($K^0 \rightarrow \pi^+ \pi^-$); the Λ^0 baryon travels from A to C, where it decays into two charged particles ($\Lambda^0 \rightarrow p \pi^-$)

charged tracks starting from a single point, called the *vertex*. In A, the π^- interacts with a proton, giving rise to:

$$\pi^- p \rightarrow \text{two strange neutral particles}. \quad (7.33)$$

Because of electric charge conservation, neither the π^- collision on an electron nor a π^- decay can be considered. The process $\pi^- + e^-$ would produce *two negatively charged particles*. The π^- decay would produce an odd number of visible charged tracks. Two neutral particles are then originated from the π^- interaction on proton in A. Each unknown neutral state was originally denoted by the symbol V^0 .

If at the vertex B or C, one of the two V^0 interacts with a proton, only one charged particle track would be visible. As a pair of charged particles can be seen at each vertex, the simplest interpretation is that each pair corresponds to the decay of both the neutral V^0 particle, with conservation of the electric charge:

$$V^0 \rightarrow \text{positively charged particle} + \text{negatively charged particle}. \quad (7.34)$$

The explanation of the series of events in the three vertices of Fig. 7.11 is as follows: in A, two neutral strange particles are produced, the K^0 meson and the Λ^0 baryon according to the reaction

$$\pi^- p \rightarrow K^0 \Lambda^0. \quad (7.35)$$

The K^0 meson (with mass $m_{K^0} = 497.7 \text{ MeV}$) travels from A to B. In B, it decays into two charged π mesons:

$$K^0 \rightarrow \pi^+ \pi^-. \quad (7.36)$$

The Λ^0 baryon ($m_\Lambda = 1115.7 \text{ MeV}$) travels from A to C; in C, it decays into p and π^- :

$$\Lambda^0 \rightarrow p \pi^-. \quad (7.37)$$

These statements can be verified by measuring all the parameters in the bubble chamber pictures and using conservation principles.

The “strange” production of associated particles is explained assuming that the Λ^0 and the K^0 produced in A have opposite strangeness quantum number; the strangeness must be conserved in strong and electromagnetic interactions, but can be violated in weak interaction processes.

The strangeness quantum number is explained in terms of the constituents of hadrons, the quarks. An “ordinary” (not strange) hadron is made of u, d quarks. A “strange” hadron contains at least one strange s quark; a “strange” antihadron contains at least one strange antiquark \bar{s} . A hadron with one strange quark has strangeness -1 (e.g., $\Lambda^0 = sdu$), those with two strange quarks have strangeness -2 (e.g., $\Xi^- = ssd$), those with three strange quarks have strangeness -3 (e.g., $\Omega^- =sss$).

The production of Λ^0, K^0 is abundant and caused by the strong interaction, which conserves strangeness

$$\begin{array}{c} \pi^- + p \rightarrow K^0 + \Lambda^0 \\ \text{strangeness } 0 \quad 0 \quad +1 - 1. \end{array} \quad (7.38)$$

The associated production phenomenon (strange particles are produced in pairs) is explained by the conservation of strangeness. Λ^0 and K^0 have relatively long lifetimes, typical of the weak interaction. The strangeness is not conserved in weak interaction decays, that is,

$$\begin{array}{c} \Lambda^0 \rightarrow p + \pi^- \\ \text{strangeness } -1 \quad 0 \quad 0 \quad . \end{array} \quad (7.39)$$

The system of K mesons has the following strangeness assignment: the K^- and \bar{K}^0 have $S = -1$; the K^+ and K^0 have $S = +1$. Another example of production and successive decay of strange particles is

$$\begin{array}{c} K^- + p \rightarrow \Omega^- + K^+ + K^0 \\ \text{strangeness } -1 \quad 0 \quad -3 \quad +1 \quad +1 \quad . \end{array} \quad (7.40)$$

7.7 Classification of Hadrons Made of u, d, s Quarks

Before quarks were hypothesized, the increasing number of discovered hadronic particles led one to suspect the existence of some inner symmetry law that could explain the particle proliferation. The quark model solved the problem of hadron classification. Until the discovery of the heaviest quarks (the c, b and t , see Chap. 9), only the quarks u, d and s were known. From the regularity of discovered hadrons (including many *resonances* with lifetime of the order of 10^{-23} s), it was derived that quarks have fractional electric charge with respect to that of the proton.

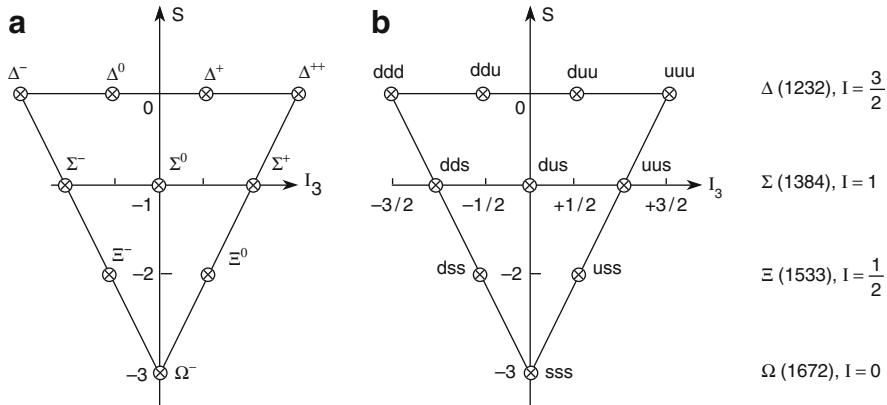


Fig. 7.12 The $J^P = 3/2^+$ baryonic decuplet. (a) Assignment of the observed baryons and (b) interpretation in terms of quarks. The isotopic spin and the average mass of each observed baryon multiplet are indicated on the right. The third component of isospin is indicated as I_3

It was found that hadrons having the same spin and parity could be grouped in families, graphically represented in a S , I_z diagram. The charge Q is in units of the proton charge and the baryon number is $B = +1/3$ for each quark. According to the static model, quarks are grouped in order to form particles with *integer* electric charge in two different ways:

- The **baryons** are made of three quarks (called *valence quarks*), the antibaryons of three antiquarks.
- The **mesons** are made of a quark and an antiquark.

Ordinary matter only consists of u, d quarks ($p = uud, n = ddu$). The *valence quarks* explain the hadron spectroscopy. Hadrons are considered eigenstates of a system of quarks interacting via the strong interaction in a similar way as the hydrogen atom energy levels are eigenstates of the $p - e$ system in the Coulomb field.

Here, the hadrons are classified on the basis of the static quark model. Originally, the formalism of group theory was used. The unitary group of matrices with three rows and three columns in the u, d, s space of quarks was called SU(3) (sometimes written as $SU(3)_{uds}$ or $SU(3)_f$, where f stands for *flavor*).

After the discovery that the strong interaction dynamic is ruled by the “color” quantum number, this classification became obsolete. However, it is still useful (with its extension to four and five quarks) for the nomenclature of particles made of quarks.

The *baryons* (and similarly, the *antibaryons*) can either have the three quark spins aligned ($\uparrow\uparrow\uparrow$), or one quark with a spin opposite to that of the other two quarks ($\uparrow\uparrow\downarrow$). In the first case, the baryons have spin^{parity} $J^P = 3/2^+$ and form a decuplet, graphically represented by a triangle, see Fig. 7.12. If one quark has its spin in the opposite direction of the two others, the baryons have $J^P = 1/2^+$ and form an octet (which includes protons and neutrons), as shown in Fig. 7.14.

The *mesons* may be formed either with two quarks with spins in opposite directions ($\uparrow\downarrow$) or with two spins aligned in the same direction ($\uparrow\uparrow$). In the first case, the mesons have spin zero and negative parity, $J^P = 0^-$, forming a nonet graphically represented by the hexagon of Fig. 7.15a. In the case of spin aligned in the same direction, the mesons form the nonet of particles shown in Fig. 7.15b.

All the multiplets would be degenerate states for the strong interaction if the masses of all quark flavors were the same. The strong interaction depends on an inner quark quantum number, the *color*. The color force is independent of the flavor. The mass of the hadrons made of the u, d, s quarks is larger than the sum of the masses of their quarks. Notably $m_u \simeq m_d$, very small mass in comparison to the nucleon mass. The masses of the nonstrange hadrons consist predominantly of the color field energy. This explains why isotopic spin is a good symmetry. Particles with the same J^P and differing only by the presence of a u or d quark have almost the same characteristics. They are *isospin multiplets* indicated with the same letter (the only notably known exception is that of p and n). Small differences in mass between members of a multiplet are due to the electromagnetic interaction. The case of neutral mesons in the center of the hexagon of Fig. 7.15 is more complicated. The larger mass m_s of the strange quark with respect to m_u, m_d corresponds to a larger mass of the particles obtained from the substitution of a u, d quark with a s .

In the following sections, these multiplets are illustrated in detail.

7.8 The $J^P = 3/2^+$ Baryonic Decuplet

Consider the particles that have $J^P = 3/2^+$; they form a decuplet. Figure 7.12a shows the ten baryon with $J^P = 3/2^+$ and lower masses (states with higher orbital angular momentum have higher masses). These baryons are

- The $\Delta(1232)$ with isospin $I = 3/2$. It has four different charged states Δ^{++} , Δ^+ , Δ^0 , Δ^- .
- The hyperon $\Sigma(1385)$ with strangeness -1 , (namely $\Sigma^*(1385)$), with $I = 1$ and the three states Σ^+ , Σ^0 , Σ^- .
- The hyperon $\Xi(1533)$ with strangeness -2 , (namely, $\Xi^*(1533)$), with $I = 1/2$ and the two states Ξ^0 , Ξ^- .
- The hyperon $\Omega^-(1672)$ with strangeness -3 , with $I = 0$.

The masses given in the figure are the average mass of each isospin multiplet. The graph shows the third component of isospin along the x-axis, and the strangeness S along the y-axis. The ten baryons are arranged in a regular pattern forming an inverted triangle. The mass difference between two neighboring isospin multiplets is $m_\Sigma - m_\Delta = 152 \text{ MeV}$, $m_\Xi - m_\Sigma = 149 \text{ MeV}$, $m_\Omega - m_\Xi = 139 \text{ MeV}$, a difference that is almost constant, with an average of about 147 MeV. One can recall the empirical relation $m = a + bY$, where $Y = B + S$ is the *strong hypercharge*.

Table 7.1 Additive quantum numbers of the six quark “flavors.” S, c, b, t represent the strangeness, charm, bottom and top quantum numbers, respectively. Antiquarks have the same quantum numbers of quarks, but with opposite sign, except for the spin and isospin which are the same. The table rows are in order of increasing mass, except for u, d

Flavor	I	I_3	S	c	b	t	Q/e
d	$1/2$	$-1/2$	0	0	0	0	$-1/3$
u	$1/2$	$+1/2$	0	0	0	0	$+2/3$
s	0	0	-1	0	0	0	$-1/3$
c	0	0	0	$+1$	0	0	$+2/3$
b	0	0	0	0	-1	0	$-1/3$
t	0	0	0	0	0	$+1$	$+2/3$

The mass of the Ω^- was predicted before being discovered on the basis of this simple mass formula.²

The multiplet regularity are interpreted in terms of three quarks (u, d, s) with the quantum numbers shown in Table 7.1. Quarks (u, d) form an isospin doublet with $S = 0, I = 1/2$ and $I_3 = +1/2, -1/2$ respectively. The quark s with strangeness $S = -1$ has $I = 0$. The baryon number B of each quark is $B = 1/3$. Gell-Mann and Nishijima had shown in the early 1950s that the electric charge Q , the baryon number B , the strangeness S and the third component of isotopic spin I_z were related through the equation

$$Q = (B + S)/2 + I_z = Y/2 + I_z. \quad (7.41)$$

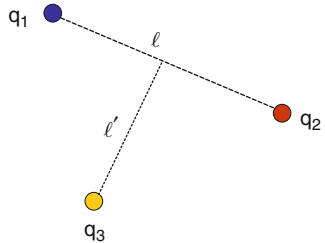
It follows that quarks must have fractional charge, namely, $Q(u) = +2/3, Q(d) = Q(s) = -1/3$.

The composition in terms of quarks of the ten baryons of the $3/2^+$ decuplet is shown in Fig. 7.12b. The regular mass increase with increasing $|S|$ may be explained, assuming that the mass of the strange quark is about 150 MeV larger than the masses of the u, d quarks. Free quarks have never been observed, and it is assumed that they remain confined within hadrons. Within the hadron, a quark can be regarded as a nearly free particle. Quarks u and d should have a momentum of the order R_0^{-1} , where $R_0 \simeq 1$ fm is the size of a hadron. In natural units $\hbar = c = 1$, one has $R_0 \simeq \frac{1}{200} \text{ MeV}^{-1}$; it follows that the Fermi momentum is $R_0^{-1} \simeq 200 \text{ MeV}$.

The three quarks inside baryons of the $J^P = 3/2^+$ decuplet have zero orbital angular momenta, i.e., $\ell = \ell' = 0$ and $L = \ell + \ell' = 0$, see Fig. 7.13. This corresponds to a symmetric state in space coordinates. The total angular momentum $J = 3/2$ (the particle *spin*), is obtained assuming that the spins of the three quarks are aligned: $q_{\uparrow} q_{\uparrow} q_{\uparrow}$. The positive parity (+) comes from the intrinsic positive parity

²The symbol Ω , which corresponds to the last letter of the Greek alphabet was chosen because, according to $SU(3)_f$, it was supposed to be the last fundamental particle that remained to be discovered! Only three of the six existing quarks were known at that time, and $SU(3)_f$ is only an approximate symmetry.

Fig. 7.13 Relative orbital angular momentum ℓ, ℓ' of a system made of three quarks



of each quark and from $\ell = \ell' = 0$. The decuplet is described by a wave function symmetric in the space of the spin.

The third component m_j of the total angular momentum and the parity P of a baryon of the $3/2^+$ decuplet are then

$$m_j = m_L + m_{s1} + m_{s2} + m_{s3} = 0 + 1/2 + 1/2 + 1/2 = +3/2 \rightarrow J = 3/2 \quad (7.42a)$$

$$P = (-1)^\ell (-1)^{\ell'} P_{q_1} P_{q_2} P_{q_3} = +. \quad (7.42b)$$

7.8.1 First Indications for the Color Quantum Number

Some symmetry considerations are now necessary because of an apparent difficulty to explain the $J^P = 3/2^+$ baryons in terms of quarks. Since a baryon is made of three quarks, and since only the three u, d, s flavors are considered, there are $3^3 = 27$ possible combinations. However, only ten states were experimentally identified. A symmetry principle must be found in order to justify such a selection. Baryons consisting of three quarks of the same flavor, uuu, ddd, sss , have a symmetric wave function under a quark exchange. This suggests that both the term describing the space coordinates and that describing the flavor of all the $J^P = 3/2^+$ baryon wave function are symmetric under the exchange of a quark pair. The states ddu, duu, uss , etc., must therefore be symmetrized. For instance, the state udd in Fig. 7.12b represents a symmetric state under the exchange of any pair of quarks. It can be written as $(udd + dud + ddu)/\sqrt{3}$; the factor $1/\sqrt{3}$ is the normalization factor.

Similarly, for the other states, the following ten combinations are obtained:

$$\begin{aligned} \Delta^- &= (ddd) \quad \Delta^0 = \frac{(ddu + udd + dud)}{\sqrt{3}} \quad \Delta^+ = \frac{(duu + udu + uud)}{\sqrt{3}} \quad \Delta^{++} = (uuu) \\ \Sigma^{*-} &= \frac{(dds + sdd + dsd)}{\sqrt{3}} \quad \Sigma^{*0} = \frac{(dsu + uds + sud + sd़u + usd + dus)}{\sqrt{6}} \\ \Sigma^{*+} &= \frac{(uus + suu + usu)}{\sqrt{3}} \\ \Xi^{*-} &= \frac{(dss + sds + ssd)}{\sqrt{3}} \quad \Xi^{*0} = \frac{(sus + ssu + uss)}{\sqrt{3}} \\ \Omega^- &= sss. \end{aligned} \quad (7.43)$$

They are the only ten completely symmetric combinations under the exchange of any quark pair.

This result presents a problem with the spin-statistics connection. Baryons are fermions and their wave function must globally be *antisymmetric* under the exchange of any two of three quarks. However, the $[\psi(\text{space}) \psi(\text{spin}) \psi(\text{flavor})]$ wave function is *symmetric* under this exchange! If one postulates that quarks have an additional degree of freedom, the *color*, and that the wave function corresponding to the color degree of freedom is antisymmetric, the total baryon wave function acquires the desired antisymmetry

$$\psi = \psi(\text{space}) \psi(\text{spin}) \psi(\text{flavor}) \psi(\text{color}). \quad (7.44)$$

The *color charge* of a quark has three possible values, *red* (r), *blue* (b) and *green* (g). Antiquarks have an *anticolor*. It is then assumed that the interactions between quarks are invariant under color exchange. The strong interaction is described by the symmetry group $SU(3)_C$ (C stands for color), which represents an exact symmetry, unlike the case of the *flavor* symmetry $SU(3)_f$.

There are eight symmetry generators; they correspond to the eight ways in which the colors of the quarks can interact (see Fig. 5.2 for an intuitive sketch)

$$\begin{aligned} r\bar{b} &\quad b\bar{g} & g\bar{r} &\quad (r\bar{r} - b\bar{b})/\sqrt{2} \\ b\bar{r} &\quad g\bar{b} & r\bar{g} &\quad (r\bar{r} + b\bar{b} - 2g\bar{g})/\sqrt{3}. \end{aligned}$$

The colors of the quarks are the sources of the strong interaction and the interaction is transmitted through eight bosonic fields named *gluons*. The name originates from the nature of the interaction: quarks are glued inside hadrons.

The $SU(3)_C$ symmetry assumes that *all hadrons are colorless*; this means that they are *color singlets* or *white*. The analogous electromagnetic is the Bohr atom: although it is electrically neutral, it consists of positively charged protons and negatively charged electrons. If this *white* condition is not fulfilled, hadronic states would be colored and the color degree of freedom would be a measurable quantity. The simpler states without color are the bound states $q\bar{q}$ (color, anticolor) for mesons and qqq for baryons ($\bar{q}\bar{q}\bar{q}$ for antibaryons). Each baryon consists of one red, one blue and one green quark. In such a way, the baryon is without color, the three quarks are not identical and the Pauli exclusion principle is satisfied.

The color is probably an unfortunate name (it has nothing to do with what we commonly mean by color) that indicates a new property of quarks, namely, their strong charge, similar to the electric charge for the EM interaction. Clear experimental evidence in favor of the color derived from the $[\sigma(e^+e^- \rightarrow \text{hadrons})/\sigma(e^+e^- \rightarrow \mu^+\mu^-)]$ measurements, Sect. 9.3, and from the decay probability of $\pi^0 \rightarrow 2\gamma$. Everything is formalized in the theory of strong interaction, the *quantum chromodynamics* (QCD).

7.9 The $J^P = 1/2^+$ Baryonic Octet

Now, consider all the possible combinations of the u, d, s quarks with one spin not aligned with the other two. The spin of the resulting particle is $1/2$. Figure 7.14 illustrates the $1/2^+$ baryon octet, which includes

- An isospin doublet: neutron, proton.
- An isospin triplet: Σ^- , Σ^0 , Σ^+ (symmetric under the exchange of u, d quarks).
- An isospin singlet: Λ^0 (antisymmetric under the exchange of u, d quarks).
- Another isospin doublet: Ξ^-, Ξ^0 .

The mass regularities observed in the $3/2^+$ decuplet are absent in this case ($m_\Lambda - m_N = 177$ MeV, $m_\Xi - m_\Lambda = 203$ MeV; it would be expected $m_\Lambda = m_\Sigma$, instead $m_\Sigma = 1,193$ MeV, considerably different from $m_\Lambda = 1,116$ MeV).

With the $J^P = 1/2^+$ assignment, states symmetric under the simultaneous exchange of spin and flavor of each pair can be built. These states are antisymmetric with respect to the exchange of spin or flavor only. Let us build the quark structure of the members of the $J^P = 1/2^+$ baryonic octet, assuming

- A symmetric space coordinate wave function $\ell = \ell' = 0$, $L = \ell + \ell' = 0$
 - Spin wave function in antisymmetric combinations $\uparrow\downarrow\uparrow$
 - Flavor wave function in antisymmetric combinations
- Color wave function in antisymmetric combinations.

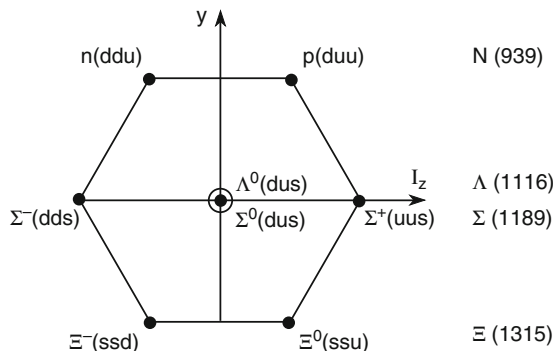


Fig. 7.14 The baryon family with $J^P = 1/2^+$ and the interpretation in terms of quarks. The proton, p , and the neutron, n , consist of three quarks of two different flavors (u, d), each quark with a different color (red, green or blue). The other baryons of the octet require the presence of the s quark. $Y = S + B$ is the hypercharge

Consider the proton (uud) and let us build the spin wave function starting with two quarks. First, we place them in an antisymmetric spin singlet state

$$(\uparrow\downarrow - \downarrow\uparrow)/\sqrt{2}.$$

Next, we construct the corresponding antisymmetric flavor state with the two u, d quarks (the combination uu cannot be antisymmetric):

$$(ud - du)/\sqrt{2}.$$

Finally, we combine the two conditions for spin and flavor in order to have a symmetric wave function under the simultaneous exchange of spin and flavor (for the moment, we neglect the normalization factor):

$$A = u_\uparrow d_\downarrow - u_\downarrow d_\uparrow - d_\uparrow u_\downarrow + d_\downarrow u_\uparrow$$

and finally, we add the third quark in the combination: Au_\uparrow . The expression A is already symmetric under the exchange of spin and flavor. The three quark system becomes symmetric through a cyclic permutation. For the proton, one has the following 12 term expression:

$$\begin{aligned} (p, J_z = +1/2) = & (2u_\uparrow u_\uparrow d_\downarrow + 2d_\downarrow u_\uparrow u_\uparrow + 2u_\uparrow d_\downarrow u_\uparrow \\ & - u_\downarrow d_\uparrow u_\uparrow - u_\uparrow u_\downarrow d_\uparrow - u_\downarrow u_\uparrow d_\uparrow \\ & - d_\uparrow u_\downarrow u_\uparrow - u_\uparrow d_\uparrow u_\downarrow - d_\uparrow u_\uparrow u_\downarrow)/\sqrt{18}. \end{aligned} \quad (7.45)$$

The multiplication of (7.45) by the color antisymmetric function (as we did for the members of the $3/2^+$ decuplet) leads to the global antisymmetric wave function. The quark composition of the baryonic $1/2^+$ octet members is shown in Fig. 7.14 (the octet baryons are listed simply as uud , ssu , etc., meaning a symmetric combination, for example, (7.45)).

In the baryonic octet $J^P = 1/2^+$, graphically represented by a hexagon, the symmetric combination uuu , ddd , and sss observed in the baryonic decuplet (vertices of the triangle) are absent. This fact is easily explained by symmetry arguments. For these states, the flavor wave function is necessarily symmetric (three identical quarks) and the color wave function must be antisymmetric. It follows that the spin wave function must be symmetric ($\uparrow\uparrow\uparrow$). This is impossible for the $J^P = 1/2^+$ baryonic octet, for which the spin wave function must be ($\uparrow\downarrow\uparrow$).

7.10 Pseudoscalar Mesons

Figure 7.15a shows the nine pseudoscalar mesons $J^P = 0^-$ with lower masses. They form an octet plus a singlet. The isospin singlet is the $\eta'(958)$ meson; the octet includes the nonstrange π^+ , π^0 , π^- , $\eta(547)$ mesons, the strange (K^0 , K^+) mesons with $S = +1$ and the strange (K^- , \bar{K}^0) mesons with $S = -1$.

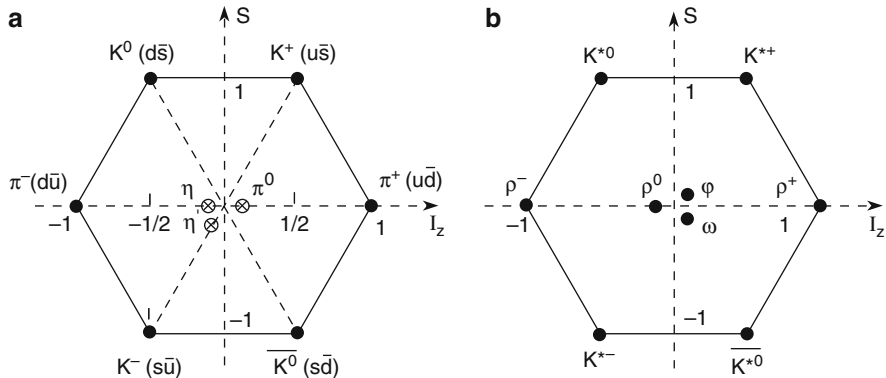


Fig. 7.15 (a) Nonet of mesons with spin parity $J^P = 0^-$ and its quark content. (b) Nonet of mesons with $J^P = 1^-$ (the structure is similar to (a) in terms of constituent quarks)

In terms of the quark model, mesons are made of a quark-antiquark pair. Limiting ourselves to the three u, d, s quarks, $3 \times 3 = 9$ states are possible, that is, a nonet of mesons. The $q\bar{q}$ combinations of the pseudoscalar meson nonet have

$$J = 0 \quad \left\{ \begin{array}{l} \text{orbital angular momentum } \ell = 0 \\ \text{opposite spin } \uparrow\downarrow \end{array} \right. \quad (7.46)$$

$$P = - \left\{ \begin{array}{l} P = (-1)^\ell P_q P_{\bar{q}}; \quad P_q = -P_{\bar{q}}, \text{ (opposite } q, \bar{q} \text{ parity).} \end{array} \right.$$

The nonstrange d, u quarks can be combined to form the following $2^2 = 4$ combinations:

$$\left\{ \begin{array}{ll} I=1 & \left\{ \begin{array}{ll} I_3 = +1 & \pi^+ = u\bar{d} \\ I_3 = 0 & \pi^0 = (d\bar{d} - u\bar{u})/\sqrt{2} \\ I_3 = -1 & \pi^- = -u\bar{d} \end{array} \right. \\ \text{isospin triplet} & m = 139.6 \text{ MeV} \\ I=0 & 135.0 \text{ MeV} \\ \text{isospin singlet} & 139.6 \text{ MeV} \\ & I_3 = 0 \quad \eta_4 = (d\bar{d} + u\bar{u})/\sqrt{2}. \end{array} \right. \quad (7.47)$$

With the addition of the s quark, there are five additional combinations (for a total of $3^2 = 9$ pseudoscalar mesons):

$$\text{octet } \begin{cases} I = 1 & \pi^+, \pi^-, \pi^0 \\ I = 1/2 & I_3 = +1/2 \quad S = +1 \quad K^+ = u\bar{s} \quad m = 494 \text{ MeV} \\ & I_3 = -1/2 \quad S = +1 \quad K^0 = d\bar{s} \quad m = 498 \text{ MeV} \\ I = 1/2 & I_3 = +1/2 \quad S = -1 \quad \bar{K}^0 = \bar{d}s \quad m = 498 \text{ MeV} \\ & I_3 = -1/2 \quad S = -1 \quad K^- = \bar{u}s \quad m = 494 \text{ MeV} \\ I = 0 & I_3 = 0 \quad S = 0 \quad \eta_8 = \frac{(d\bar{d} + u\bar{u} - 2s\bar{s})}{\sqrt{6}} \quad m_\eta = 547 \text{ MeV} \end{cases} \quad (7.48)$$

$$\text{singlet } I = 0 \quad I_3 = 0 \quad S = 0 \quad \eta_1 = (d\bar{d} + u\bar{u} + s\bar{s})/\sqrt{3} \quad m_{\eta'} = 958 \text{ MeV}.$$

The state denoted as η_8 and the isospin singlet η_1 have the same I, I_3, S but differ in the symmetry properties of the wave function. The η_8 and η_1 mesons are not directly observed. The observed states are their linear combinations, denoted as η and η' , obtained from η_8 and η_1 with a mixing angle of $\theta \simeq 11^\circ$. The question of the flavor composition of the η and η' pseudoscalar neutral mesons is highly nontrivial. The reason is that the color interaction induces continuous transitions between $q\bar{q}$ pairs and the particles acquire large masses. The correct description of these complicated mixtures of quark-antiquark pairs and gluons can be achieved only within the QCD theory and cannot be given at an elementary level.

7.11 The Vector Mesons

Figure 7.15b shows the nonet of vector mesons $J^P = 1^-$ with lower masses. It can be considered as an octet plus a singlet state. The octet includes the K^{*0} , K^{*+} meson pair, the K^{*-} , \bar{K}^{*0} pair and the triplet ρ^-, ρ^0, ρ^+ . The ω and ϕ are obtained from the mixing of the octet singlet φ_8 with the singlet of the nonet φ_1 (see Eq. 7.50). Mass values are $\rho(770)$, $K^*(892)$, $\omega(782)$, $\phi(1,020)$.

The $q\bar{q}$ combinations of the vector meson nonet have

$$J = 1 \begin{cases} \text{angular orbital momentum } \ell = 0 \\ \text{spin } \uparrow\uparrow \end{cases} \quad (7.49)$$

$$P = -\{\text{opposite } q, \bar{q} \text{ parity}\}.$$

The $q\bar{q}$ combinations are similar to those of the $J^P = 0^-$ multiplet (see Fig. 7.15).

As for the pseudoscalar mesons, the observed neutral states are a mixture. Here, the mixing between the two central states of the octet and singlet is more pronounced than for the pseudoscalar mesons. The mixing between particles is an important quantum phenomenon that shall be further discussed in Chap. 12. Formally, one can write

$$\begin{cases} \phi = \varphi_1 \sin \theta - \varphi_8 \cos \theta \\ \omega = \varphi_1 \cos \theta + \varphi_8 \sin \theta. \end{cases} \quad (7.50)$$

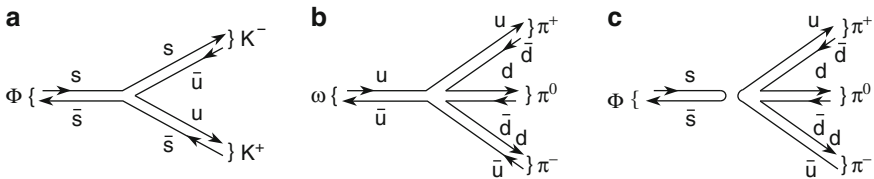


Fig. 7.16 (a, b) Diagrams for ϕ and ω decays. These diagrams are not real Feynman diagrams, but only show the flow of quarks. Note that in the diagram (c), the lines between the initial and final states are not connected; it is believed that the contribution of this type of diagram is severely suppressed (Zweig rule)

The mixing angle has to be determined experimentally (see Sect. 14. Quark model of [P10]); it is found to be $\theta \simeq 35^\circ$. The formulae of quark composition for the vector mesons, similar to (7.48), are

$$\begin{cases} \varphi_1 = (d\bar{d} + u\bar{u} + s\bar{s})/\sqrt{3} \\ \varphi_8 = (d\bar{d} + u\bar{u} - 2s\bar{s})/\sqrt{6} \end{cases} \quad (7.51)$$

from which, one obtains

$$\begin{cases} \phi = s\bar{s} \\ \omega = (u\bar{u} + d\bar{d})/\sqrt{2}. \end{cases} \quad (7.52)$$

It can therefore be assumed that the ϕ meson is an $s\bar{s}$ pair, while the ω does not contain strange quarks. This explains the observed decay fractions:

$$\begin{aligned} \phi(1,020) \rightarrow & K^+ K^- \left. \right\} 83.4\% \\ & \rightarrow K^0 \overline{K^0} \\ & \rightarrow \pi^+ \pi^- \pi^0 2.5\% \\ & \rightarrow \rho \pi \left. \right\} 12.9\% \left. \right\} 15.4\%. \end{aligned} \quad \begin{aligned} \omega(782) \rightarrow & \pi^+ \pi^- \pi^0 88.8\% \\ & \rightarrow \pi^+ \pi^- 2.2\% \\ & \rightarrow \pi^0 \gamma \quad 8.5\% \end{aligned}$$

The phase space factor favors the decay of the ϕ into 3π . The available energy is $E_0 = m_\phi - 2m_{\pi^+} - m_{\pi^0} = 1,020 - 2 \cdot 139.6 - 135 \simeq 606$ MeV, to be compared with $E_0 = m_\phi - 2m_{K^0} \simeq 1,020 - 2 \cdot 498 = 24$ MeV for $\phi \rightarrow K\bar{K}$. In addition, see Problem 7.6, as it explains why the ϕ cannot decay into two π^0 . Experimentally, it was found that the decay channel $\phi \rightarrow K\bar{K}$ is dominant. The explanation is related to the quark composition of the ϕ meson and to the decay diagrams shown in Fig. 7.16. The diagram for the $\phi \rightarrow 3\pi$ decays involve nonconnected lines between the initial and final states. It is believed that, in this case, the contribution of this channel to the decay is severely suppressed (Zweig rule).

7.12 Strangeness and Isospin Conservation

According to the quark model, the strange particles contain at least one s quark, while strange antiparticles contain at least one \bar{s} antiquark. The strangeness quantum number S is -1 for particles with one s quark and $S = +1$ for one \bar{s} . All remaining quarks have $S = 0$. The known particles have

$$\begin{aligned}
 S = 0 & \quad \text{for } \gamma, \pi^0, \pi^+, \pi^-, p, n, N^*, \Delta \\
 S = +1 & \quad \text{for } K^+, K^0, \overline{\Lambda}^0, \overline{\Sigma}^+, \overline{\Sigma}^-, \overline{\Sigma}^0 \\
 S = -1 & \quad \text{for } K^-, \overline{K}^0, \Lambda^0, \Sigma^+, \Sigma^-, \Sigma^0 \\
 S = -2 & \quad \text{for } \Xi^-, \Xi^0 \\
 S = -3 & \quad \text{for } \Omega^-.
 \end{aligned} \tag{7.53}$$

The strangeness quantum number is conserved in strong and electromagnetic interactions, while it is violated in weak interactions. This means that the quark s remains unchanged in strong and EM interactions, while it changes flavor in weak processes (as in the case $s \rightarrow ue^-\bar{\nu}_e$ which shall be discussed in the next chapter). Isospin and strangeness are useful in the classification of processes due to the strong, electromagnetic and weak interactions, as shown in the following examples.

Strong interaction. I and S are conserved, as shown in the following example:

$$\begin{array}{ccc}
 I & \overset{K^- + p}{\xrightarrow{\substack{1/2 \ 1/2 \\ 0,1}}} & \overset{\Lambda^0 + \pi^0}{\xrightarrow{\substack{0 \ 1 \\ 1}}} \rightarrow \Delta I = 0 \text{ active only } I = 1 \\
 I_z & \overset{-1/2 + 1/2}{\xrightarrow{\substack{-1/2 + 1/2 \\ 0}}} & \overset{0 \ 0}{\xrightarrow{\substack{0 \ 0}}} \rightarrow \Delta I_z = 0 \\
 S & \overset{-1 \ 0}{\xrightarrow{\substack{-1 \\ -1}}} & \overset{-1 \ 0}{\xrightarrow{\substack{-1 \\ -1}}} \rightarrow \Delta S = 0.
 \end{array}$$

Electromagnetic interaction. Electromagnetic interaction conserves parity, but not the isospin. An example is the following decay of a baryon of the octet:

$$\begin{array}{ccccc}
 & \Sigma^0 & \rightarrow & \Lambda^0 & + \quad \gamma \\
 I & 1 & & 0 & 0 \rightarrow \Delta I \neq 0 \\
 I_z & 0 & & 0 & 0 \rightarrow \Delta I_z = 0 \\
 S & -1 & & -1 & 0 \rightarrow \Delta S = 0
 \end{array} \tag{7.54}$$

(I, I_z, S are zero for the photon). The electromagnetic interaction is responsible for the mass differences between hadrons of an isospin multiplet. Many experimental indications converge to assign almost the same small mass (between 5–10 MeV) to

the u and d quarks. The strong interaction depends on many factors, but not on the quark flavor and electric charge. For this reason, the proton and the neutron masses are expected to be identical. The small difference (less than 0.14%) is due to the electromagnetic interactions, which depends on the quark electric charge. This is also true for other particles of the same isospin multiplet. All mass differences in percentages are of the order of 10^{-3} – 10^{-2} :

Hadrons	Δm (MeV)	\bar{m} (MeV)	$\Delta m/\bar{m}$	
$n - p$	1.293	938.9	$1.4 \cdot 10^{-3}$	
$\Sigma^- - \Sigma^+$	8.07	1193.4	$6.8 \cdot 10^{-3}$	
$\Sigma^- - \Sigma^0$	4.88	1195.0	$4.1 \cdot 10^{-3}$	
$K^0 - K^+$	4.00	495.7	$8.1 \cdot 10^{-3}$	
$\pi^+ - \pi^0$	4.59	137.3	$3.3 \cdot 10^{-2}$	

(7.55)

Weak interaction. Weak interaction processes conserve neither strangeness nor isospin, as in the following example:

$$\begin{array}{ll}
 \Lambda^0 \rightarrow p + \pi^- & \\
 I \quad 0 \quad \underbrace{1/2, 1}_{1/2, 3/2} \rightarrow \Delta I \neq 0 & \\
 I_z \quad 0 \quad \underbrace{+1/2 - 1}_{-1/2} \rightarrow \Delta I_z \neq 0 & \\
 S \quad -1 \quad \underbrace{0 + 0}_0 \rightarrow \Delta I_z \neq 0. &
 \end{array}
 \quad (7.56)$$

7.13 The Six Quarks

In summary, various hadron classifications were introduced in the 1950s. These classifications suggested a composite nature of hadrons. The two u, d quarks form a strong isospin doublet, yielding a small mass difference between the two quarks. The strong interaction is independent of the quark flavor, and there is an almost complete symmetry between the two members of the doublet (broken only by the EM interaction). The independence from flavor is a consequence of the QCD invariance principles. The rotational invariance in isospin space is a consequence of this symmetry.

The strangeness S is a quantum number introduced to describe particles with a “strange” connection between their production cross-section and lifetime. S is conserved by strong and EM interactions and violated by the weak interaction.

The three lower mass quarks (u, d, s) follow a $SU(3)_f$ symmetry, which is only approximate since the s quark mass is about 150 MeV higher than that of the u, d quarks. Since the 1970s, three additional quark flavors were discovered (see Chap. 9 for the discovery of the c, b quarks). The addition of quark c leads to an extension

of the symmetry from $SU(3)_f$ to $SU(4)_f$, which is heavily broken since the quark c mass is much larger than that of the first three quarks. On the other hand, this symmetry is sufficient to determine the approximate number of baryons and mesons containing one or more c quarks.

Figure 7.17 shows the $J^P = 1/2^+$ and $J^P = 3/2^+$ baryons made of u, d, s, c quarks. The representations are obtained inserting on the third axis (vertical) the charm quantum number c . The baryons are grouped in 20-plets. The $3/2^+$ 20-plet contains the known baryon decuplet of Fig. 7.12 (at $c = 0$), a sextuplet of baryons containing one c quark, a triplet with two c quarks and a ccc singlet. The $1/2^+$ 20-plet contains the octet of Fig. 7.14, a sextuplet with one c quark, and a triplet with two c quarks.

Figure 7.18 shows the 0^- and 1^- mesons 16-plet. Both are made with the u, d, s quark nonet, two triplets with a c or a \bar{c} quark, and a $c\bar{c}$ singlet with the total charm quantum number c equal to zero. This singlet state can interfere with the other η, η' singlet of the 16-plet.

The addition of the b quark leads to the $SU(5)_f$ symmetry, which is even more broken than $SU(4)_f$ due to the very large mass of the b quark.

Table 7.1 summarizes the quantum numbers of the six quark *flavors*. These quantum numbers are constrained by the relation

$$Q = I_3 + \frac{B + S + c + b + t}{2} = I_3 + \frac{Y}{2}, \quad (7.57)$$

which is an extension of Eq. 7.41. The definition of strong hypercharge Y is extended from $Y = B + S$ to $Y = B + S + b + c + t$. The letters c, b, t denote, respectively, the *charm, bottom* and *top* quantum numbers.

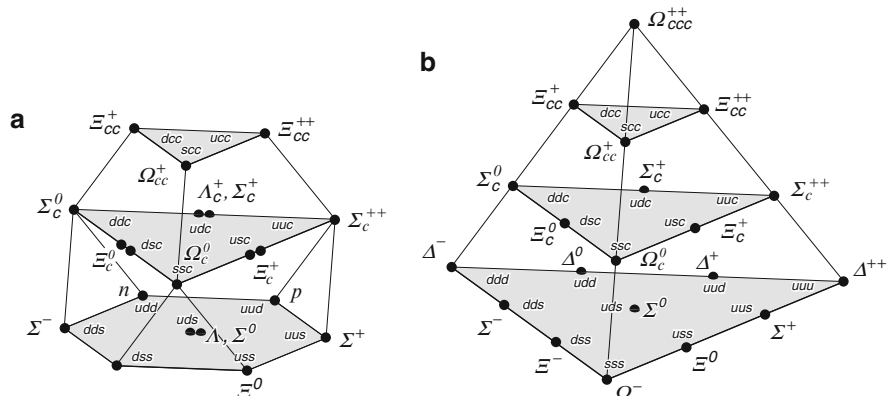


Fig. 7.17 The $SU(4)_f$ symmetry for baryonic states made of u, d, s and c quarks. On the x, y, z axes, one has, respectively, the third component of isospin, the strangeness and the charm quantum number. (a) 20-plet with $J^P = 1/2^+$ containing the known $SU(3)_f$ octet in the *bottom plane* ($c = 0$). (b) 20-plet with $J^P = 3/2^+$, which contains the known $SU(3)_f$ decuplet in the *bottom plane* [P08]

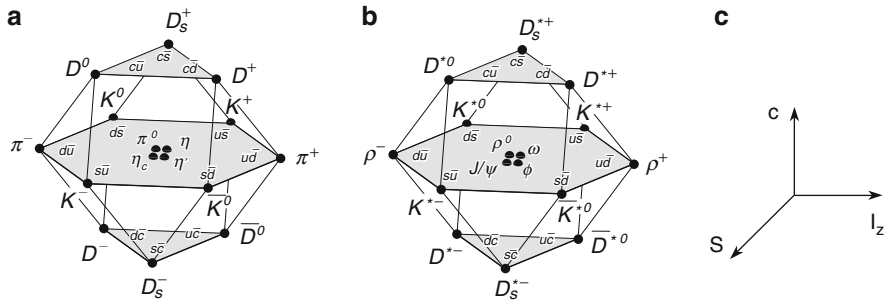


Fig. 7.18 The $SU(4)_f$ 16-plet symmetry for (a) the pseudoscalar ($J^P = 0^-$) mesons and (b) the vector ($J^P = 1^-$) mesons made of the d, u, s, c quarks. (c) On the x, y, z axes, one has, respectively, the third component of isospin, the strangeness and the charm quantum number. In the middle plane at $c = 0$, one finds the known nonet consisting of the light u, d, s quarks, to which the $c\bar{c}$ state is added. The mixed neutral mesons made of $u\bar{u}, d\bar{d}, s\bar{s}$ and $c\bar{c}$ are located in the center [P08]

7.14 Experimental Tests on the Static Quark Model

There are many possible direct and indirect tests on the static quark model and on the hadron composition in terms of quarks. Note that the static quark model is appropriate for explaining the hadron classification, but is not adequate for representing the quark dynamics, which need the contribution of gluons and $q\bar{q}$ pairs (sea quarks) inside the hadrons. The dynamic quark model shall be presented in Chap. 10. In this section, some experimental evidence for quarks are presented.

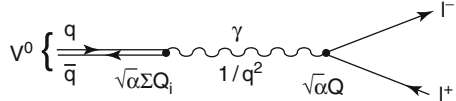
7.14.1 Leptonic Decays of Neutral Vector Mesons

In the static quark model, the ρ^0 , ω^0 and ϕ^0 neutral vector mesons have the following structure:

$$\begin{aligned} \rho^0 &= (u\bar{u} - d\bar{d})/\sqrt{2} & m &= 769.9 \pm 0.8 \text{ MeV} \\ \omega^0 &= (u\bar{u} + d\bar{d})/\sqrt{2} & & 781.94 \pm 0.12 \text{ MeV} \\ \phi^0 &= s\bar{s} & & 1019.413 \pm 0.008 \text{ MeV}. \end{aligned} \quad (7.58)$$

In the following, the three considered vector mesons are indicated with the generic symbol V^0 . The decay of a V^0 vector meson in a charged lepton–antilepton pair, $V^0 \rightarrow \ell^- \ell^+$, proceeds through the exchange of a virtual photon, as shown in Fig. 7.19. The transition probability W for this decay can be calculated since it is an electromagnetic decay (see Problem 7.17). This relation is known as the *Weisskopf formula* ($\hbar = c = 1$)

Fig. 7.19 Leptonic decay of a generic V^0 neutral vector meson



$$W(V^0 \rightarrow \ell^+ \ell^-) = \frac{16\pi\alpha_{EM}^2 (\Sigma_i Q_i)^2}{m_V^2} |\psi(0)|^2, \quad (7.59a)$$

which can be factorized as

$$W = 16\pi \left| \begin{array}{cccc} \text{coupling} & \text{photon} & \text{coupling phase} & \text{wave function} \\ q\bar{q}\gamma & \text{propagator} & \ell^+\ell^-\gamma & q\bar{q} \text{ at the origin,} \end{array} \right|^2 q^2 |\psi(0)|^2 \quad (7.59b)$$

with Q = charge of the ℓ lepton = ± 1 , Q_i = fractional charge of the quarks, $\alpha_{EM} = 1/137$. Assuming (for simplicity) that the three vector mesons have the same mass m_V and the same $\psi(0)$ (the wave function of the $\bar{q}q$ system at the origin) and assuming that $q^2 \simeq m_V^2$, $|\psi(0)|^2/m_V^2$ is expected to be roughly constant; it follows that $W \approx |\Sigma_i Q_i|^2$. From the quark composition given in (7.58), the following values for $(\Sigma_i Q_i)^2$ are obtained:

$$\begin{aligned} \rho^0 &= (u\bar{u} - d\bar{d})/\sqrt{2} \rightarrow \left[\frac{1}{\sqrt{2}} \left(\frac{2}{3} - \frac{(-1)}{3} \right) \right]^2 = \frac{1}{2} \\ \omega^0 &= (u\bar{u} + d\bar{d})/\sqrt{2} \rightarrow \left[\frac{1}{\sqrt{2}} \left(\frac{2}{3} - \frac{1}{3} \right) \right]^2 = \frac{1}{18} \\ \phi^0 &= s\bar{s} \rightarrow \left(-\frac{1}{3} \right)^2 = \frac{1}{9}, \end{aligned} \quad (7.60)$$

from which, one finds that

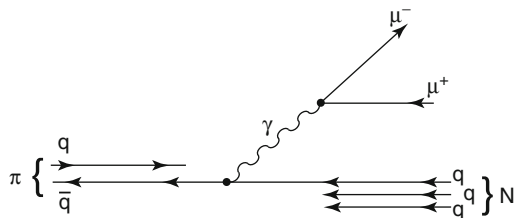
$$\begin{aligned} W(\rho^0) : W(\omega^0) : W(\phi^0) &= 9 : 1 : 2 && \text{theory} \\ &= (8.8 \pm 2.6) : 1 : (1.70 \pm 0.4) && \text{experiment.} \end{aligned} \quad (7.61)$$

The experimental data confirm the predictions of the static quark model of hadrons.

7.14.2 Lepton Pair Production

A second test of the quark model is given by the production of lepton pairs, especially muons, in pion-nucleon collisions. The mechanism is illustrated in Fig. 7.20: the antiquark of the π meson annihilates with a quark of the nucleon, giving rise to a virtual photon that becomes a $\mu^- \mu^+$ pair (*Drell-Yan model*). The

Fig. 7.20 Illustration of the lepton pair production in a pion-nucleon collision. The basic mechanism is the quark-antiquark annihilation into a virtual photon which gives rise to the lepton-antilepton pair



noninteracting quarks act as spectators. The process cross-section is proportional to the square of the quark charges.

In particular, consider the $\pi^- (= \bar{u}d)$ interaction with the isoscalar nucleus ^{12}C ($= 6p + 6n = 18u + 18d$). An isoscalar nucleus contains the same number of protons and neutrons. Only the $u\bar{u}$ annihilation can occur in this case; the cross-section is proportional to the square of the quark charges and

$$\sigma(\pi^- \text{C} \rightarrow \mu^- \mu^+ \dots) \propto 18Q_u^2 = 18 \cdot 4/9 = 8. \quad (7.62)$$

On the other side, in the interaction of a $\pi^+ (= \bar{d}u)$ with ^{12}C , only the $d\bar{d}$ annihilation can occur, that is,

$$\sigma(\pi^+ \text{C} \rightarrow \mu^- \mu^+ \dots) \propto 18Q_d^2 = 18 \cdot 1/9 = 2. \quad (7.63)$$

Outside the energy region corresponding to resonances, one must have

$$\sigma(\pi^- \text{C} \rightarrow \mu^- \mu^+ X) / \sigma(\pi^+ \text{C} \rightarrow \mu^- \mu^+ X) = 4,$$

which was experimentally verified, thus confirming the validity of the quark model and especially the electric charge assignment of u, d quarks.

7.14.3 Hadron-Hadron Cross-Sections at High Energies

Let us assume that in the interaction of two high energy hadrons, the collision occurs between a quark of the first hadron and a quark of the second hadron, independently of the other quarks. This is, of course, an approximation that does not take into account gluons and sea quarks within hadrons. Let us further assume that at high energies, one has $\sigma(uu) = \sigma(ud) = \sigma(dd)$ (corresponding to the isospin invariance) and even $\sigma(q\bar{q}) = \sigma(qq)$, and finally that the collisions between different quarks are additive. Under these conditions it follows that the ratio of the total πN and NN cross-sections is given by the ratio of the numbers of possible combinations between quark pairs, that is,

$$\frac{\sigma(\pi N)}{\sigma(N N)} = \frac{2 \cdot 3}{3 \cdot 3} = \frac{2}{3},$$

which is experimentally verified (see Figs. 7.1 and 7.2). For example, at $E_\pi = 60 \text{ GeV}$, one has $\sigma(\pi^+ p) \simeq \sigma(\pi^- p) \simeq 24 \text{ mb}$, and $\sigma(pp) \simeq \sigma(pn) \simeq 38 \text{ mb}$; the cross-section ratio is therefore $[\sigma(\pi N)/\sigma(NN)]_{exp} \simeq 24/38 \simeq 2/3$.

7.14.4 Baryon Magnetic Moments

In the Dirac theory, a point-like fermion with electric charge q , mass m and spin $1/2$ has a magnetic dipole moment. The magnetic dipole operator is defined as

$$\boldsymbol{\mu} = \frac{q\hbar}{2mc} \boldsymbol{\sigma} \xrightarrow{\hbar=c=1} \frac{q}{2m} \boldsymbol{\sigma}, \quad (7.64a)$$

where $\boldsymbol{\sigma}$ are the Pauli matrices (see Appendix A.4). The value of the magnetic dipole moment of a fermion f is the expectation value (defined by Eq. 6.3) of the operator (7.64a):

$$\mu_f \equiv \langle f | \boldsymbol{\mu} | f \rangle. \quad (7.64b)$$

In the case of the electron and the muon, the comparison between prediction and measurement of the magnetic dipole moment is one of the successes of the Dirac theory and of QED. Moreover, it is a clear confirmation that leptons are really “elementary particles.” Following the same argument, the proton and neutron are not “elementary” because their magnetic dipole moments are very different from those predicted by the Dirac theory. In particular, since the neutron is electrically neutral, the theory predicts $\mu_n = 0$.

Now, assume that each quark is a Dirac particle with an expectation value for the magnetic moment $\boldsymbol{\mu}$ given by (7.64b). In an explicit form for the for u and d quarks,

$$\mu_u = \langle u | \boldsymbol{\mu} | u \rangle = \frac{q_u}{2m_u} \quad ; \quad \mu_d = \langle d | \boldsymbol{\mu} | d \rangle = \frac{q_d}{2m_d}. \quad (7.64c)$$

Since $m_u \simeq m_d$ and $q_u = -2q_d$, one obtains

$$\mu_u \simeq -2\mu_d. \quad (7.64d)$$

We can now assume that the baryon magnetic moment is equal to the vector sum of quark magnetic moments, and that there is no contribution from orbital angular moments, i.e., $\ell = \ell' = 0$. Furthermore, gluons and sea quarks are not taken into account.

The proton consists of uud in antisymmetric combination of spin and flavor. In this case, because the flavor antisymmetry is irrelevant, we can rewrite (7.45), avoiding to report the permutations amongst flavors:

$$|p\rangle = |2u_\uparrow u_\uparrow d_\downarrow - u_\uparrow u_\downarrow d_\uparrow - u_\downarrow u_\uparrow d_\uparrow\rangle / \sqrt{6}. \quad (7.65)$$

Table 7.2 Predicted and observed [P10] magnetic moments of “stable” baryons of the $J^P = 1/2^+$ octet, in units of nuclear magnetons (n.m.) $\mu_N = e\hbar/2m_p c$. The p and n magnetic moments are measured with a relative precision of better than 10^{-7}

Baryon	Magnetic moment (quark model)	Prediction (n.m.)	Observed (n.m.)
p	$\frac{4}{3}\mu_u - \frac{1}{3}\mu_d$	2.793	2.793
n	$\frac{4}{3}\mu_d - \frac{1}{3}\mu_u$	-1.913	-1.913
Λ	μ_s	-0.613	-0.613 ± 0.004
Σ^+	$\frac{4}{3}\mu_u - \frac{1}{3}\mu_s$	2.68	2.46 ± 0.01
Σ^0	$\frac{2}{3}(\mu_u + \mu_d) - \frac{1}{3}\mu_s$	0.791	
Σ^-	$\frac{4}{3}\mu_d - \frac{1}{3}\mu_s$	-1.09	-1.160 ± 0.003
Ξ^0	$\frac{4}{3}\mu_s - \frac{1}{3}\mu_u$	-1.43	-1.250 ± 0.014
Ξ^-	$\frac{4}{3}\mu_s - \frac{1}{3}\mu_d$	-0.49	-0.651 ± 0.003

The corresponding magnetic dipole moment is obtained from the calculation of the expectation value (7.64b) applied to the $|p\rangle$ state:

$$\begin{aligned} \mu_p &= \langle p | \boldsymbol{\mu} | p \rangle = \frac{[4(\mu_u + \mu_u - \mu_d) + (\mu_u - \mu_u + \mu_d) + (-\mu_u + \mu_u + \mu_d)]}{6} \\ &= \frac{(8\mu_u - 2\mu_d)}{6}. \end{aligned} \quad (7.66)$$

The signs in the calculation take into account the relative orientation of the spin of the quarks. Recalling (7.64d), one has

$$\mu_p \simeq [4\mu_u - (-\mu_u/2)]/3 = (3/2)\mu_u. \quad (7.67)$$

Similarly, for the neutron, one has

$$|n\rangle = |2d_\uparrow d_\uparrow u_\downarrow - d_\uparrow d_\downarrow u_\uparrow - d_\downarrow d_\uparrow u_\uparrow\rangle / \sqrt{6}, \quad (7.68)$$

and thus

$$\mu_n = [4(\mu_d + \mu_d - \mu_u) + \mu_u + \mu_u]/6 = (4\mu_d - \mu_u)/3 \simeq -\mu_u. \quad (7.69)$$

The model predicts $\mu_n/\mu_p = -2/3$, which is in reasonable agreement with the observed value ($= -0.685$). Table 7.2 shows all the magnetic moments predicted by the static quark model and those measured for the hadrons of the $J^P = 1/2^+$ baryonic octet.

The static quark model predicts with some accuracy the μ_n/μ_p ratio. The predicted values of the hadron magnetic moments (in units of nuclear magnetons (n.m.) $\mu_N = e\hbar/2m_p c$) can be expressed in terms of μ_u, μ_d, μ_s . The computation of the quark magnetic moments resulting from (7.64c) requires the quark mass and electric charge values. Using the “bare” quark masses ($m_d \simeq m_u \simeq 5$ MeV;

Table 7.3 Quark contents of “quasi-stable” hadrons (i.e., not decaying through the strong interaction with a lifetime $\sim 10^{-23}$ s). The masses are in MeV. * See Sect. 12.2

Mesons			Baryons		
Quark	Mass(MeV)	τ (s)	Quark	Mass(MeV)	τ (s)
$u\bar{d}$	$\pi^+(139.57)$	2.6×10^{-8}	uud	p (938.272)	stable
$u\bar{u}, d\bar{d}$	$\pi^0(134.97)$	8.4×10^{-17}	udd	n (939.566)	886
$d\bar{u}$	$\pi^-(139.57)$	2.6×10^{-8}	uds	Λ^0 (1115.63)	2.6×10^{-10}
$u\bar{u}, d\bar{d}, s\bar{s}$	$\eta(548.8)$	$\Gamma = 1.18$ keV	uus	$\Sigma^+(1189.37)$	0.8×10^{-10}
$u\bar{u}, d\bar{d}, s\bar{s}$	$\eta'(957.5)$	$\Gamma = 2.2$ MeV	uds	$\Sigma^0(1192.55)$	7.4×10^{-20}
$u\bar{s}$	$K^+(493.65)$	1.2×10^{-8}	dds	$\Sigma^-(1197.43)$	0.8×10^{-10}
$d\bar{s}$	$K^0(497.67)$	*			
$s\bar{d}$	$\overline{K}^0(497.67)$	*	uss	$\Xi^0(1314.9)$	2.9×10^{-10}
$s\bar{u}$	$K^-(493.65)$	1.2×10^{-8}	dss	$\Xi^-(1321.3)$	1.6×10^{-10}
$c\bar{d}$	$D^+(1869.3)$	1.0×10^{-12}	sss	$\Omega^-(1672.4)$	0.82×10^{-10}
$c\bar{u}$	$D^0(1864.5)$	4.1×10^{-13}	udc	$\Lambda_c^+(2285.0)$	2.0×10^{-13}
$u\bar{c}$	$\overline{D}^0(1864.5)$.1 $\times 10^{-13}$	usc	$\Xi_c^+(2467)$	1.4×10^{-13}
$d\bar{c}$	$D^-(1869.3)$	1.0×10^{-12}	udb	$\Lambda_b^0(5500)$	1.2×10^{-12}
$c\bar{s}$	$D_s^+(1969)$	4.9×10^{-13}			
$s\bar{c}$	$D_s^-(1969)$	4.9×10^{-13}			
$u\bar{b}$	$B^+(5278)$	1.7×10^{-12}			
$d\bar{b}$	$B^0(5279)$	1.5×10^{-12}			
$b\bar{d}$	$\overline{B}^0(5279)$	1.5×10^{-12}			
$b\bar{u}$	$B^-(5278)$	1.7×10^{-12}			

$m_s = m_d + 150$ MeV), the values computed using the formulae given in the second column of Table 7.2 completely disagree with the measured values. Using the “effective” quark masses ($m_d \simeq m_u = m_p/3$; $m_s = m_d + 150$ MeV), the values of quark magnetic moments are $\mu_u = 2\mu_N$; $\mu_d = -1\mu_N$; $\mu_s = -0.67\mu_N$; these values are in much better agreement with the observed ones. If the measured p, n and Λ moments are used as input, the quark moments are $\mu_u = +1.852\mu_N$; $\mu_d = -0.972\mu_N$; $\mu_s = -0.613\mu_N$ [P10], from which the predicted values inserted in the table are derived.

The static quark model, although it qualitatively reproduces some observed features of hadron magnetic moments, fails to give precise agreements with experimental data. This can only be achieved through a “dynamics” description of the hadron constituents which includes gluons and quark of the sea, as discussed in Chap. 10.

7.14.5 Relations Between Masses

Quark masses cannot really be measured because quarks are never free; they can only be determined indirectly through their influence on the hadron properties (Table 7.3). The mass differences between hadrons of the same isospin multiplet

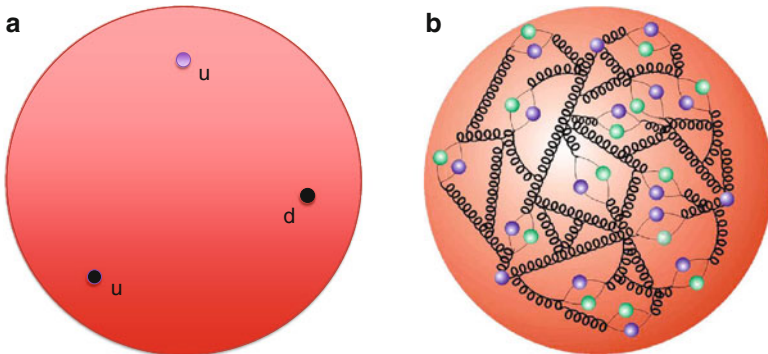


Fig. 7.21 (a) In the simplest static quark model of hadrons, the proton is made of three valence quarks (u, u, d) which are much lighter and smaller than the global proton mass and size. (b) In the dynamic quark model of hadrons, in addition to the three valence quarks, many gluons and many quark-antiquark pairs contribute to the proton mass

are attributed both to the $m_u - m_d$ mass difference and to the electromagnetic interaction. The latter introduces mass differences of a few MeV. The mass differences between particles of different isospin multiplets are mainly due to the mass difference between quarks.

It is often assumed that $m_u \simeq m_d \simeq$ few MeV and $m_s \simeq m_u + 150$ MeV. Mass differences between u, d and s quarks explain many of the mass differences of normal and strange hadrons. They are however not sufficient enough to explain the observed mass differences between the members of the $1/2^+$ baryonic octet and the members of the $3/2^+$ decuplet. These must be interpreted in terms of differences between quark-quark interaction, with the largest contribution given by the part of the strong interaction which depends on the spin (Chaps. 11 and 14).

The masses of heavier quarks are $m_c \simeq 1,550$ MeV and $m_b \simeq 4,300$ MeV. Hadrons and mesons made of the t quarks cannot be formed for the reasons explained in Sect. 10.2. The quark t is free for a very short time.

Atomic energy levels and electromagnetic properties are derived from QED. The calculation of the hadron mass spectrum and of the basic hadron properties from fundamental QCD principles is a fundamental theoretical problem. The dynamic range of strong interaction between quarks when forming hadrons made of u, d and s quarks corresponds to large values of the α_S coupling constant (Sect. 11.9.4). As a consequence, the contributions of the diagrams of increasing order do not decrease and a perturbation development is not possible. The problem is now studied with numerical methods (lattice QCD): powerful theoretical techniques using large computer farms have been developed. The proton mass is the sum of the small masses of the constituent quarks, plus the work that must be done on the system to bring the constituents into this minimum energy configuration. The sum of the proton valence quark masses is less than 2% of the proton mass: the rest must come from the gluons and virtual particles, Fig. 7.21. The scale of the energy

corresponding to a quark confined within 1 fm is 200–300 MeV (see Sect. 7.8); this is the order of magnitude of the work needed to bring one quark into a noninteracting configuration. For three quarks, it corresponds to ~ 1 GeV.

A second nontrivial problem is connected to the nucleon radius. Fundamental fermions (as quark and leptons) are point-like particles to a distance $< 10^{-16}$ cm [7B79]. Hadrons have dimensions of the order of 10^{-13} cm because of the QCD properties. As for the case of the electrons in the atomic system, the three quarks choose their average distances in order to minimize the energy.

7.15 Searches for Free Quarks and Limits of the Model

Quarks were introduced in order to explain the *regularity* and the *symmetry* properties of hadron spectroscopy. In Chap. 10, we shall study the inelastic lepton-nucleon and nucleon-nucleon collisions at high energies. These reveal a spatial structure for the proton and neutron that is easily explainable in terms of point-like constituents (quarks, gluons and quark-antiquark pairs). The hadron production in high energy e^+e^- collisions is also explained in terms of quarks and gluons.

Since the first formulation of Gell-Mann and Zweig in 1964, the question regarding the possible existence of free quarks fuels continuing interest. Many searches for free quarks have been performed [7P04], all without success (although some have indicated possible, but not confirmed, signals). QCD is consistent with the hypothesis of quark confinement within hadrons. However, the search for free quarks continues at increasing levels of precision. The research is based on the fact that any free quark or quark tied in nuclei corresponds to a fractional charge. Two research lines are followed: (1) the search for free quarks in terrestrial and extraterrestrial stable matter and (2) the search for fractional charged particles produced in high energy collisions or in the penetrating cosmic radiation.

Examples of the type (1) method are experiments like that used by Millikan for the measurement of the electron q/m ratio or experiments dealing with magnetic levitation. These experiments use microscopic samples of matter. The best limits obtained are less than one free quark over 10^{22} nucleons of stable matter.

Particles with fractional electric charge were searched for amongst the products of hadron-hadron, lepton-nucleon and e^+e^- inelastic collisions. The searches are based on the fact that particles with $\pm 1/3$ and $\pm 2/3$ electric charge ionize 1/9 and 4/9 compared to a muon with the same momentum. The best limits obtained are at the level of less than one quark for many millions of ordinary particles. Some studies were devoted to the search for free quarks after a possible deconfinement phase in nucleus–nucleus collisions at high energies.

In addition to the presented multiplets, other baryon multiplets with higher spin were observed. They can be interpreted as combinations of the three u, d, s quarks with orbital angular momenta ℓ, ℓ' different from zero, in order to obtain the observed spin of baryons. Remember that the separate quantization of spin and orbital angular momentum is possible only in the nonrelativistic approximation.

The spin internal structure of the nucleons was studied through the inelastic collisions of polarized electrons and muons on polarized targets. An electron (or muon) only interacts with one of the quarks (valence or sea) of a proton by exchanging a virtual photon. If the electron is polarized, also photon the is polarized, and it interacts differently with quarks of different polarization. The photons do not interact directly with gluons. Therefore, the information obtained from the study of the deep inelastic electron and muon collisions with the proton constituents only refer to the spin of the quark and antiquark. Measurements show that less than half of the spin of the proton is due to the valence quarks and sea quarks, the other half would be due to the gluons (Chap. 10).

No resonances were observed in $\pi^+\pi^+$, $\pi^+\pi^+\pi^+$, K^-K^- meson states. If existing, they would be *exotic meson resonances*. In the static quark model, they would require an exotic $qq\bar{q}\bar{q}$ structure. Similarly, baryon states of the form K^+N would be *exotic baryon states* which require a quark composition of the type $qqq\bar{q}\bar{q}$. Resonant states of di-baryons, like pp , were also hypothesized; this would require a more complex quark composition.

There could also be resonant states composed of only gluons (the *glueballs*) with spin parity of the type 0^+ (scalar mesons), 2^+ (tensor mesons), etc. There are some tentative experimental indications not confirmed, regarding their existence. There may also exist *hybrid states* made, e.g., of a quark, an antiquark and an “effective” gluon; they would have spin parity of the type 1^{-+} , etc. [P10].

Chapter 8

Weak Interactions and Neutrinos

8.1 Introduction

In this chapter, the *weak interactions*, WI¹ will be described. The history of weak interactions is closely connected with that of the neutral lepton called the *neutrino* by Fermi. We shall focus on the phenomena that led to hypothesize the existence of that particle, its experimental discovery and the discovery of different neutrino *flavors*. These new experimental facts were first mathematically included in the theoretical framework developed by Fermi himself. In particular, we shall see that:

1. Particles decaying through WI have relatively long lifetimes (typically of the order of 10^{-10} s, to be compared with 10^{-19} s for decays due to the electromagnetic interaction and 10^{-23} s for those due to the strong interaction).
2. Weak interaction processes have very small cross-sections, although increasing linearly with energy. At 1 MeV, the cross-section is of the order of 10^{-43} cm²; at 1 GeV, it is of the order of 10^{-38} cm². At this energy, it is about 10^{12} times smaller than the cross-sections for strong interaction processes.
3. Neutrinos are subject only to the weak interactions; charged leptons are subject both to the electromagnetic and weak interactions.
4. Weak interactions do not conserve some quantum numbers which are instead conserved in the electromagnetic and/or strong interactions. For example, the parity P , the charge conjugation C , the strangeness S (with the selection rule $\Delta S = \pm 1$) are violated in WIs.
5. Weak interactions do not play any role in binding submicroscopic systems; however, they are responsible for radioactive β decays and have an important role in astrophysical systems. For example, the nuclear chain reactions inside the Sun critically depend on the $pp \rightarrow de^+ \nu_e$ reaction, which is a WI process.

¹Weak interaction or interactions? The standard is defined by the Particle Data Group [P10], which indicates the plural. Initially, it seemed that the WIs amongst quarks and leptons slightly differed. Today, the plural indicates that charged currents (CC) and neutral currents (NC) are known. We shall often use the singular form to highlight the universality of the WI between quarks and leptons.

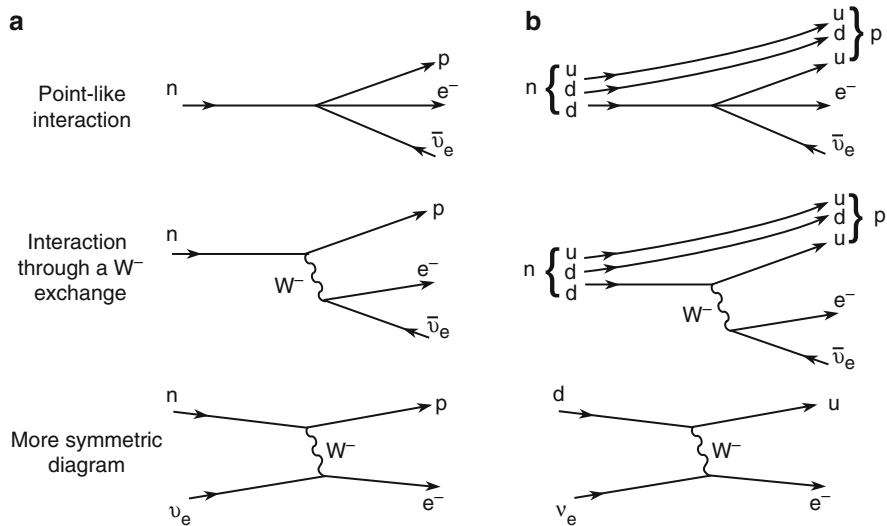


Fig. 8.1 Feynman diagrams for the neutron decay (a) considering the neutron as an elementary particle and (b) of its quark constituents. The more symmetric diagrams shown at the bottom are obtained by rotating the antineutrino line which now becomes a neutrino. Since the time direction does not change the amplitude probability in Feynman diagrams, these last two diagrams are equivalent to the two central ones

At the end of the chapter, the mathematical formalism shall be extended, taking into account that at a fundamental level, the WIs occur through the exchange of W^+ , W^- bosons (charged current (CC) weak interaction). The neutral current (NC) weak interaction which occurs through the exchange of a Z^0 boson is included in the theory described in Chap. 11 where the deep connection between electromagnetic and WI is presented. Since the W^\pm and Z^0 masses are large (80.3 and 91.2 GeV respectively), WIs have a short range $R = (\hbar c / m_W c^2) \simeq 0.197 \text{ GeV fm}/80.3 \text{ GeV} \simeq 2 \cdot 10^{-18} \text{ m}$. At low energy (in fact, at low transferred momentum), it can be assumed that the WI are actually point-like interactions which can be approximated by the Fermi theory (see Figs. 8.1a and 8.3a).

8.2 The Neutrino Hypothesis and the β Decay

8.2.1 Nuclear β Decay and the Missing Energy

The nuclear beta decay (see Chap. 14) is a transmutation of a (Z, N) element (Z is the number of protons and N represents the number of neutrons in the nucleus) to a nucleus with $Z + 1$ protons (β^- decay), or $Z - 1$ protons (β^+ decay). It was known from the beginning of the last century that in the case of *negative beta* transitions, an

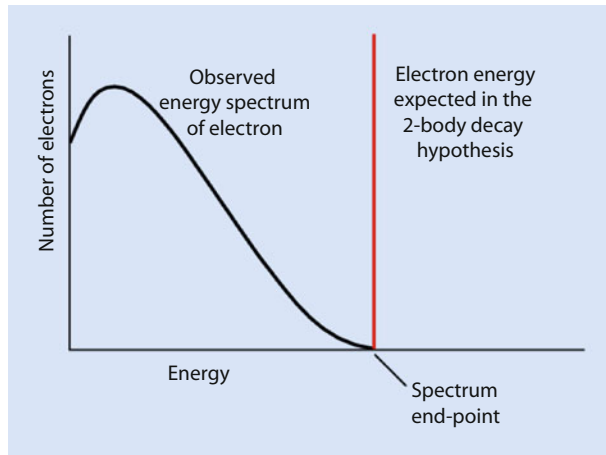


Fig. 8.2 Distribution of the energy carried by the electron in the nuclear β decay. The expected spectrum for a two-body decay coincides with a line, the value that corresponds to the end of the spectrum of the measured continuous curve

electron is emitted from the nucleus. The electron energy is typically several MeV, which is higher than the electron rest mass (0.511 MeV).

If a nucleus at rest decays into two bodies, that is,

$$(Z, N) \rightarrow (Z + 1, N - 1) + e^-, \quad (8.1)$$

the energy and momentum conservation requires that the two particles recoil back-to-back in the same direction, though with opposite momentum. Since the nucleus has a mass a thousand times larger than that of the electron, its recoil velocity (i.e., its kinetic energy) is negligible compared to that of the electron. Consequently, the emitted electron is expected to have a constant energy which coincides with the total energy released in the decay, Fig. 8.2.

However, the experimental results (using any β -emitting nucleus) were in complete disagreement with the above conclusion. This was known since 1914, from the early measurements made by Chadwick. The measured electrons had a continuous energy spectrum, up to the expected maximum value. Since no other particle was observed, the decay (8.1) **seemed to violate** the energy conservation law.

8.2.2 *The Pauli Desperate Remedy*

In 1930, Wolfgang Pauli formulated the hypothesis of a *desperate remedy* in a letter (reported below) addressed to colleagues attending a physics conference in Tübingen. This letter, midway between the courtly and the burlesque, hypothesized

the existence of a new particle called the *neutron*. In fact, two years later, Chadwick discovered the particle that we now know as the neutron, and Enrico Fermi baptized Pauli's particle, the *neutrino* (which, in Italian, means “the small neutral one”). Pauli's idea was that an elusive neutral particle associated with the electron was present in the β decay. The neutral particle was not subject to strong interaction, and its presence allowed the energy and momentum conservation:

$$(Z, N) \rightarrow (Z + 1, N - 1) + e^- + \nu. \quad (8.2)$$

(Note that no index appears within the symbol ν in the above equation). The question was, however, how such a particle could possibly be detected?

December 4, 1930

Gloriastr., Zürich

Physical Institute of the Federal Institute of Technology (ETH) Zürich

Dear radioactive ladies and gentlemen,

As the bearer of these lines, to whom I ask you to listen graciously, will explain more exactly, considering the “false” statistics of N -14 and Li -6 nuclei, as well as the continuous β -spectrum, I have hit upon a desperate remedy to save the “exchange theorem”² of statistics and the energy conservation. Namely [there is] the possibility that there could exist inside the nuclei electrically neutral spin 1/2 particles that I wish to call neutrons, which obey the exclusion principle, and additionally differ from light quanta in that they do not travel with the velocity of light: The mass of the neutron must be of the same order of magnitude as the electron mass and, in any case, not larger than 0.01 proton mass. The continuous β -spectrum would then become understandable by the assumption that in β decay a neutron is emitted together with the electron, in such a way that the sum of the energies of neutron and electron is constant. Now, the next question is what forces act upon the neutrons. The most likely model for the neutron seems to me to be, on quantum mechanics grounds (more details are known by the bearer of these lines), that the neutron at rest is a magnetic dipole of a certain moment m . Experiment probably required that the ionizing effect of such a neutron should not be larger than that of a γ -ray, and thus m should probably not be larger than $10^{-13} \text{ cm} \cdot \text{e}$. But I don't feel secure enough to publish anything about this idea, so I first turn confidently to you, dear radioactives, with a question as to the situation concerning experimental proof of such a neutron, if it has something like about ten times the penetrating capacity of a γ -ray. I admit that

²In a late 1957 lecture, Pauli explained: “This reads: exclusion principle (Fermi statistics) and half-integer spin for an odd number of particles; Bose statistics and integer spin for an even number of particles”.

*my remedy may appear to have a small *a priori* probability because neutrons, if they exist, would probably have long ago been seen. However, only those who wager can win, and the seriousness of the situation of the continuous β -spectrum can be made clear by the saying of my honored predecessor in office, Mr. Debye, who told me a short while ago in Brussels, One does best not to think about that at all, like the new taxes. Thus one should seriously discuss every way of salvation. So, dear radioactives, put it to test and set it right. Unfortunately, I cannot personally appear in Tübingen since I am indispensable here on account of a ball taking place in Zürich in the night from 6 to 7 of December.*

With many greetings to you, also to Mr. Back, your devoted servant,

W. Pauli (From [8B78])

Pauli feared that the experimental proof of his hypothesis could never be achieved. Unfortunately, in those years, aggressive military and totalitarian regimes were developing in Europe which would have indirectly accelerated the possibility of experimentally verifying the Pauli neutrino hypothesis.

8.2.3 How World War II Accelerated the Neutrino Discovery

Immediately after Pauli's assumption, Enrico Fermi formulated the mathematics of the β decay theory which is presented in the next section. The Fermi model postulates a new fundamental interaction and includes, in addition to Pauli's hypothesis, the Dirac theory of particle-antiparticle pair creation and the Heisenberg principle of symmetry between the proton and neutron in nuclear interactions.

Even if the Fermi theory is *predictive*, deducing the lifetime of nuclear β decays and the energy spectrum of emitted electrons from the energy available in the final state, the apparent impossibility to detect neutrinos still persists. Fermi's theory suggests a reaction in which the neutrinos could interact with matter. In 1936, Bethe and Bacher stated, "it seems almost impossible to detect free neutrinos, i.e., after they are emitted by radioactive atoms. There is one reaction that neutrinos can cause: the β -inverse process, namely, the capture of a neutrino by a nucleus, accompanied by the emission of an electron (or positron)." This is the reaction in which, almost 25 years after Pauli's letter, neutrinos were effectively detected.

World War II caused disasters around the world, though also in physics. The Italian government, following Nazi Germany, issued the infamous racial laws discriminating Jews. Fermi, who was awarded the Nobel Prize in 1938, sailed directly from Stockholm to the United States with his Jewish wife. Fermi, with many other European physicist refugees in the America, played a significant role in the Manhattan Project. This famous project (at the Los Alamos laboratory) led to the production of the so-called *atomic bombs* used by the U.S. military during the

attack on Hiroshima and Nagasaki in August of 1945. The understanding of nuclear phenomena, however, led to the development of nuclear reactors in order to produce energy for peaceful purposes. Precisely one of these reactors, a source of a large neutrino flux, was used for their discovery.

8.3 Fermi Theory of Beta Decay

In Sect. 4.3, the transition probability W was obtained from the perturbation theory. For the new interaction causing the β decay, there is no information regarding the potential. Fermi's theory was developed in 1934 by analogy with the electromagnetic one [8F84]. It initially involved a point-like interaction of four fermions. From the mathematical point of view, this implies an infinite potential in a dimensionless point; the Fourier transform of such a potential (the boson propagator of Sect. 4.4) is a constant. Considering the neutron decay as a prototype of this interaction, Fermi then simply assumed that

$$W = \frac{2\pi}{\hbar} G_F^2 |\mathcal{M}|^2 \frac{dN}{dE_0} \quad (8.3)$$

where G_F is an universal numerical constant which should be determined, $|\mathcal{M}|^2$ is a dimensionless numerical constant of the order of unity, a characteristic of the considered decay process (a different symbol, \mathcal{M} , is used to distinguish it from the matrix element (4.29)). As a first approximation, Fermi assumed $|\mathcal{M}|^2 = 1$. We shall derive the correct value in Sect. 8.16.

The problem of the theory was the determination of G_F . Fermi used a physical process, namely, the lifetime of neutron decay, from which G_F could be obtained. Once G_F is determined, it may be used to calculate the transition probability of other WI processes. The particle lifetime is the inverse of the transition probability per time unit (Sect. 4.5.2), that is,

$$\frac{1}{\tau} = W = \frac{2\pi}{\hbar} G_F^2 |\mathcal{M}|^2 \frac{dN}{dE_0} \quad (8.4)$$

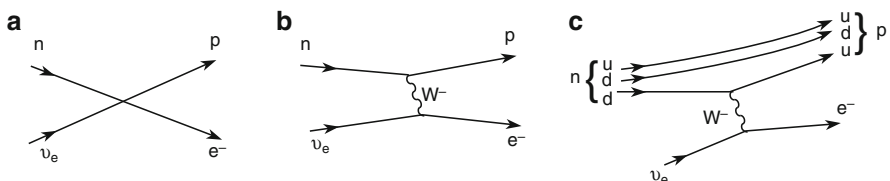
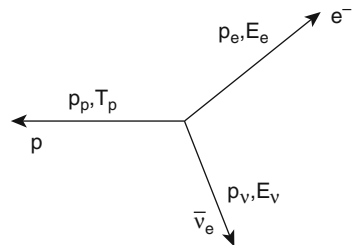


Fig. 8.3 Feynman diagrams for the reaction $\nu_e n \rightarrow p e^-$ (a) considered as a point-like interaction of four fermions, (b) through a W^- boson exchange and (c) taking the neutron and proton quark structure into account

Fig. 8.4 Illustration of the kinematics of the final state particles in the neutron decay at rest, $n \rightarrow pe^-\bar{\nu}_e$



where E_0 is the available energy in the final state; dN/dE_0 is the final state density, that is, the number of ways the available energy in the interval $E_0 \rightarrow E_0 + dE$ can be divided between the final state particles ($p, e^-, \bar{\nu}_e$).

8.3.1 Neutron Decay

Figure 8.4 illustrates the kinematics of the final state in the decay

$$n \rightarrow pe^-\bar{\nu}_e \quad (8.5)$$

in the center-of-mass system. Energy and momentum conservation requires that

$$\begin{cases} \mathbf{p}_p + \mathbf{p}_e + \mathbf{p}_{\bar{\nu}} = 0 \\ T_p + E_e + E_{\bar{\nu}} = E_0 \end{cases}$$

where the available energy in the final state is

$$E_0 = [m_n - m_p]c^2 = 939.566 - 938.272 = 1.294 \text{ MeV}. \quad (8.6)$$

The proton kinetic energy is negligible ($T_p \simeq p_p^2/2m_p \simeq 10^{-3} \text{ MeV}$): the proton is “needed” for the momentum conservation, and E_0 is shared between the electron and the antineutrino: $E_0 \simeq E_e + E_{\bar{\nu}}$. Using Cartesian coordinates, the number of states in the phase space is $dN_e = dx dy dz dp_x dp_y dp_z / h^3$. In spherical coordinates for an electron in a volume v and in the momentum range ($p + dp$), one has

$$dN_e = \frac{vd\Omega}{h^3} p_e^2 dp_e \xrightarrow[\Omega=4\pi]{v=1} \frac{p_e^2 dp_e}{2\pi^2 \hbar^3}. \quad (8.7a)$$

Similarly, for ν_e , one has $dN_{\bar{\nu}} = p_{\bar{\nu}}^2 dp_{\bar{\nu}} / 2\pi^2 \hbar^3$. Since there are no correlations, one has

$$dN = dN_e dN_{\bar{\nu}} = \frac{1}{4\pi^4 \hbar^6} p_e^2 p_{\bar{\nu}}^2 dp_e dp_{\bar{\nu}}. \quad (8.7b)$$

For fixed p_e , E_e and neglecting T_p , one has $p_v = E_v/c = (E_0 - E_e)/c$, $dp_v = dE_0/c$, yielding

$$\frac{dN}{dE_0} = \frac{1}{4\pi^4\hbar^6c^3} p_e^2 (E_0 - E_e)^2 dp_e. \quad (8.8)$$

This equation can be easily integrated (Exercise 8.16):

$$\int_0^{E_0/c} p_e^2 (E_0 - E_e)^2 dp_e = \frac{E_0^5}{30c^3}. \quad (8.9)$$

The integral of (8.8) over all possible electron momenta provides the phase space factor

$$\frac{dN}{dE_0} = \frac{E_0^5}{30 \times 4\pi^4\hbar^6c^6}. \quad (8.10)$$

Inserting Eq. 8.10 in (8.4) and assuming $|\mathcal{M}|^2 = 1$, one obtains

$$\frac{1}{\tau} = \frac{2\pi G_F^2 |\mathcal{M}|^2}{\hbar} \frac{E_0^5}{30 \times 4\pi^4\hbar^6c^6} = \left(\frac{G_F}{\hbar^3 c^3} \right)^2 \frac{E_0^5}{60\pi^3\hbar}. \quad (8.11)$$

The *Fermi coupling constant* is defined as the quantity $\frac{G_F}{\hbar^3 c^3}$; as can be easily verified from the above equation, it has the dimension of $[Energy]^{-2}$ (see Appendix A.5). Note that if we use natural units ($\hbar = c = 1$), we have

$$G_F \leftrightarrow \frac{G_F}{\hbar^3 c^3}. \quad (8.12)$$

The constant G_F must have the dimension of $[Energy]^{-2}$.

The proton is stable in Fermi's theory: its rest mass is lower than that of the neutron, and a free proton decay is impossible. However, β positive (β^+) nuclear decays, where a positron is emitted, are known. In β^+ decays, a fraction of the nuclear binding energy (Sect. 14.8) is used to make the decay of a proton inside a nucleus possible.

Today, we know that “neutrinos” emitted in the β^+ and β^- decays are different. In the β^+ decay, a *neutrino* is emitted: it always produces an electron when it interacts. In the β^- decay, an *antineutrino* is emitted: it always produces a positron when it interacts.

8.3.2 The Fermi Coupling Constant from Neutron β Decay

The Fermi coupling constant G_F can be determined from (8.11) using the measured value of the neutron lifetime $\tau_n = 885.7$ s. The second parameter needed for the

calculation is the value of the free available energy given in Eq. 8.6, corresponding to $E_0 \sim 1.2$ MeV. With these numerical values, one obtains

$$G_F^{n \text{ decay}} = \left(\frac{60\pi^3 \hbar}{\tau E_0^5} \right)^{1/2} \simeq 2 \times 10^{-5} \text{ GeV}^{-2}. \quad (8.13)$$

This value is a good estimate, though it does not coincide with the value of G_F reported in Appendix A.5. Additionally, calculated using the muon lifetime (Sect. 8.4.1),

$$G_F \equiv G_F^\mu = (1.16639 \pm 0.00001) \cdot 10^{-5} \text{ GeV}^{-2}. \quad (8.14a)$$

The decay of the neutron is actually a mixed Fermi plus Gamow–Teller transition (Sect. 8.6). By taking into account some neglected correction factors and considering that in nature there are no neutrons completely at rest (see [Be08] for the description of the experimental techniques used in the measurement), the Fermi constant obtained from the neutron β decay is

$$G_F^{n \text{ decay}} = (1.140 \pm 0.002) \cdot 10^{-5} \text{ GeV}^{-2}. \quad (8.14b)$$

This value is smaller than (8.14a) obtained from a process only involving leptons. It seemed initially that the interactions involving leptons and quarks were *slightly* different. However, we will see in Sect. 8.12 that this is not the case.

8.3.3 The Coupling Constant α_W from Fermi Theory

As described in Chap. 5, it is convenient to define a dimensionless constant for the coupling of interacting particles (in this case, the weak interaction). The dimensionless constant of the weak interaction can be derived from G_F using a reference mass; if the proton mass m_p is used, one has

$$\alpha_W = (m_p c^2)^2 G_F = 0.932827^2 \cdot 1.1664 \cdot 10^{-5} = 1.027 \cdot 10^{-5}. \quad (8.15)$$

Note that α_W is about three orders of magnitude smaller than α_{EM} .

8.4 Universality of Weak Interactions (I)

8.4.1 Muon Lifetime

The muon is a charged lepton discovered in cosmic rays (CRs). CRs are mainly protons and heavier nuclei accelerated by astrophysical sources which remain confined in the Galaxy for a long time due to its magnetic field. A continuous CR

flux bombards the top of the atmosphere; many secondary unstable particles, mainly pions, are produced in CR interaction with atmospheric nuclei [G90]. A charged pion decays into a muon and a muon neutrino: $\pi^- \rightarrow \mu^- \bar{\nu}_\mu$, $\pi^+ \rightarrow \mu^+ \nu_\mu$. The muon (and its antiparticle, the μ^+) decays in

$$\mu^- \rightarrow e^- \bar{\nu}_e \nu_\mu, \quad \mu^+ \rightarrow e^+ \nu_e \bar{\nu}_\mu. \quad (8.16)$$

The measurements of the atmospheric muon flux and of the muon lifetime are currently one of the laboratory experiments carried out by undergraduate particle physics students. The flux of muons at sea level is of the order of $\sim 100 \text{ m}^{-2} \text{ s}^{-1} \text{ sr}^{-1}$, and the muon lifetime is $\tau_\mu \simeq 2.2 \times 10^{-6} \text{ s}$.

The charged lepton (e^+, e^-) energy spectrum indicates that in muon decay, there must be two invisible particles: it is a decay with three particles in the final state (three-body decay). In the case of a two-body decay, the emitted electron would be monoenergetic (see Fig. 8.2). Neutrinos now have an index (e, μ) for reasons that will become clear later.

The neutron lifetime $\tau_n \simeq 10^3 \text{ s}$ and that of the muon $\tau_\mu \simeq 2 \times 10^{-6} \text{ s}$ differ by nine orders of magnitude. This is larger than the difference between the lifetime of a π^\pm (which decays through weak interactions in $\sim 10^{-8} \text{ s}$), and that of a π^0 (which decays electromagnetically in 10^{-16} s). Was it possible that the muon (a lepton) and the neutron (a hadron) were subject to *different* weak interactions? The strong point of the Fermi theory was the ability to explain these different phenomena within the same model.

In the lifetime prediction given in Eq. 8.11, not only the *strength* of the interaction, which depends on G_F , is significant, but also the *phase space factor*. For a three-body decay (such as that of a muon or a neutron), the phase space factor given in (8.10) depends on the fifth power of the available energy E_0 in the final state. In the case of a neutron, $E_0^n = m_n - m_p - m_e \sim 1 \text{ MeV}$. For the muon decay, the particles in the final state have negligible masses, and $E_0^\mu \sim m_\mu \sim 100 \text{ MeV}$. Because of the dependence on the fifth power of E_0 , the ratio between the muon and neutron lifetimes scales as

$$\frac{\tau_\mu}{\tau_n} \sim \left(\frac{E_0^n}{E_0^\mu} \right)^5 \sim (10^{-2})^5 = 10^{-10},$$

in qualitative agreement with the measured value of the ratio.

From an experimental point of view, the best measurement of the Fermi constant is obtained using muon decay. The process is exactly as described for neutron decay, but with a more complicated phase space calculation (see below). The result published in [8B84] is

$$G_F = \sqrt{\frac{192\pi^3 \hbar}{m_\mu^5 \tau_\mu}} = \sqrt{\frac{192\pi^3 (6.582122 \cdot 10^{-25})}{(0.1056584)^5 (2.197 \cdot 10^{-6})}} = 1.16639(1) \cdot 10^{-5} \text{ GeV}^{-2}. \quad (8.17)$$

8.4.2 The Sargent Rule

Three particles are present in the final states of neutron and muon decay; in both cases, the integral on the number of final states in phase space is proportional to the fifth power of the available energy E_0 : $dN/dE_0 \sim KE_0^5$, where K is an integration constant. In the neutron case, some approximations (negligible recoil energy of the proton, electron assumed massless) simplify the analytic calculation of K . In other cases (including the muon), the integral is analytically more difficult, or it must be solved by numerical methods. Nevertheless, for a three-body decay, the dependence on E_0^5 is always present. The available energy E_0 can be approximated as Δm , the difference between the decaying particle mass and the sum of the final state particle masses: $E_0 \simeq \Delta m = m_i - \sum_f m_f$.

If τ is the lifetime of a particle and Γ_i/Γ is its branching ratio (Sect. 4.5.2) in a particular weak decay into three-bodies in the final state, then the *Sargent rule* states that the transition probability W corresponds to

$$W = \frac{(\Gamma_i/\Gamma)}{\tau} \simeq G_F^2 E_0^5 \simeq G_F^2 \Delta m^5. \quad (8.18)$$

8.4.3 The Puppi Triangle

With G_F known from one weak decay process, Fermi's theory allows the calculation of the lifetimes of other weak decays involving nuclei, leptons and hadrons.³ In addition, the cross-section for the neutrino capture process (the β inverse decay) could be computed (Sect. 8.6.1).

It was soon recognized that the neutron β decay, the muon capture by a nucleus, the muon decay and other weak decays all had similar coupling constants; this led to the development of the *weak coupling universality* concept. Historically, the formulation of this universality has taken various forms. The first was the *Puppi triangle* shown in Fig. 8.5a, where the coupling constants between the particles placed at the triangle vertices are assumed to be the same. The transitions between the vertices correspond to $n \rightarrow pe^{-}\bar{\nu}_e$ (A side), $\mu^- \rightarrow e^-\bar{\nu}_e\nu_\mu$ (C side), and $\mu^- p \rightarrow n\nu_\mu$ capture (B side). We will come back to the weak interaction universality in Sect. 8.12.

³This was true until the discovery of the strange particles. The decays with a strangeness variation $\Delta S = 1$ are treated in Sect. 8.11.

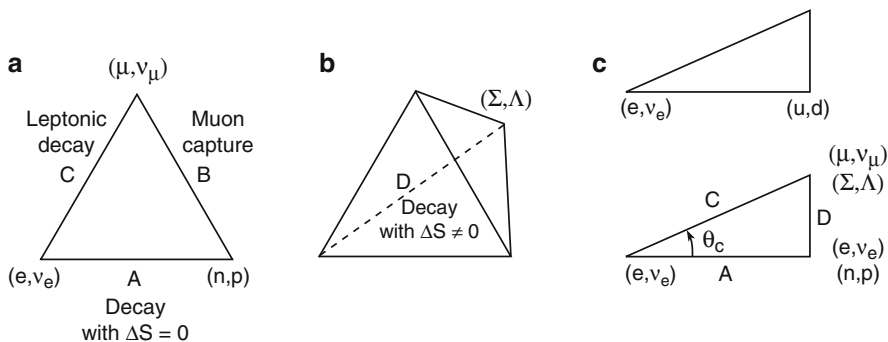


Fig. 8.5 (a) The Puppi triangle. Fermions at the triangle vertices interact through weak interaction with the same “strength.” Side A represents the decay $n \rightarrow pe^{-\bar{\nu}_e}$, C represents muon decay, $\mu^- \rightarrow e^-\bar{\nu}_e\nu_\mu$, and B represents the muon capture by a nucleus, $\mu^- p \rightarrow nv_\mu$. (b) Dallaporta Tetrahedron. Compared to the Puppi triangle, a fourth vertex was added to include strange particles. (c) Cabibbo triangle, which takes into account the different “strengths” of the weak interaction due to mixing of quark states. Sides A and C are the same in (a), and the D side is also shown in (b). The top triangle of (c) shows the interpretation in terms of quarks and leptons

8.5 The Discovery of the Neutrino

As suggested by Bethe and Baker, it was clear from Fermi’s theory that the possibility to detect neutrinos was related to the inverse- β reaction:

$$\bar{\nu}_e p \rightarrow e^+ n. \quad (8.19)$$

The main problem is that the cross-section of the process (8.19) is so small that a very high $\bar{\nu}_e$ flux is needed to have a chance to reveal some interactions. In addition, the neutron in (8.19) is difficult to detect. In this case, it is not possible to discriminate the positron produced by the inverse- β reaction from electrons/positrons emitted by nuclear β decays which produce a signal that *fakes* the neutrino interaction. Particle detectors are composed of materials (glass, metals, gases, liquids, etc.) that have small contaminations of radioactive elements. The β decays represent an *irreducible background* for reaction (8.19). Two circumstances solved both problems.

8.5.1 The Poltergeist Project

On August 6, 1945, the first nuclear bomb exploded over Hiroshima, followed a few days later by a second bomb over Nagasaki, dramatically ending World War II. As we shall see in Sect. 14.9, the capture of a thermal neutron by the ^{235}U

uranium isotope triggers nuclear fission, producing energy plus two or three free neutrons. These free neutrons can multiply the fission process. If this basic process is uncontrolled, a bomb is obtained; otherwise, one has a peaceful reactor producing energy. Each neutron produced in a fission process, if not captured by another uranium nucleus, decays producing antineutrinos.

During the war, the research center in Los Alamos in the United States existed as a secret military laboratory where the Manhattan project was developed. After the war, it became a center of excellence for research in nuclear and particle physics. In particular, F. Reines and C. Cowan initiated a research project to detect neutrinos in 1951 (Cowan died in 1974; Reines was honored with the Nobel Prize in 1995). It was called the *Poltergeist Project*.

As explained before, a large neutrino flux and a method of discriminating the signal from the background were needed. The initial project, which solved both of these problems, was to use the explosion of a nuclear bomb to detect neutrinos. The bomb would produce:

- An intense neutrino flux calculated from the explosion power
- An impulsive neutrino flux in such a small time interval that the signal to noise ratio would have been very large. The *noise*, in this case, would be due to the detected environmental radioactivity

The explosion of a 20-kiloton bomb would generate an antineutrino flux high enough to be detected with an apparatus located about 50 m underground below the explosion point. The bomb would be placed on a tower about 30 m high, and the experiment control room would be (of course) placed at a remote distance. The possible detector was a huge container filled with a liquid scintillator, which was called “El Mostro” (the monster).

In 1952, it became clear that a better way was offered by the steady $\bar{\nu}_e$ flux (less intense with respect to the flux produced by a bomb) from a nuclear reactor. The remaining problem was to detect the reaction (8.19) over the background due to environmental radioactivity. The new idea was to measure not only the annihilation of the positron, but also the possible capture of the neutron. The neutron, once moderated (i.e., slowed down by elastic collisions with other nuclei) can be captured with high probability by some nuclei (for instance, Cadmium). After neutron capture, the nuclear isotope is unstable and emits a γ -ray. The experimental technique is illustrated in Fig. 8.6. As Cowan said, “instead of detecting a burst of neutrinos in a second or two coming from the fury of a nuclear explosion, we would now be able to watch patiently near a reactor and catch one ν every few hours or so. And there are many hours available for watching in a month—or a year!”

The Savannah River nuclear reactor, with a power of 150 MW, was chosen for the experiment. It was possible to install the detector (shown in Fig. 8.7) at about 11 m from the reactor core, and about 12 m deep. The detector consisted of two containers of 2001 of water placed between three liquid scintillator containers, each with a capacity of 1,4001. This is a small detector compared to the scale of the current experiments: today, Super-Kamiokande (Sect. 12.8) uses 50,000 tons of water!

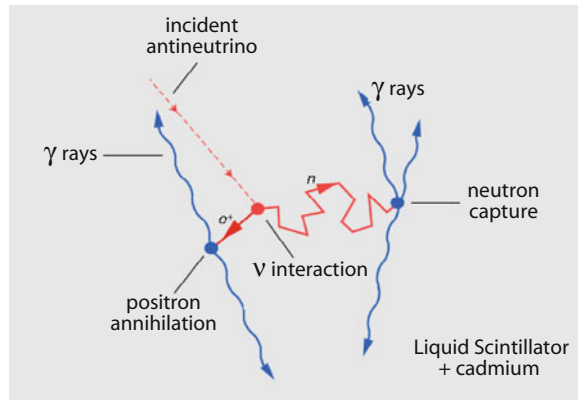


Fig. 8.6 To detect an $\bar{\nu}_e$ interaction through the inverse- β reaction (8.19), one needs to detect both the e^+ annihilation and the n capture. The interaction may take place either in a tank filled with water or liquid scintillator: both materials have many hydrogen atoms whose nuclei serve as a target. The e^+ , once produced, immediately annihilates with an e^- of the medium, releasing two 0.511 MeV γ -rays. Each γ -ray loses about half its energy each time it undergoes Compton scattering, see Sect. 2.3. The resulting electromagnetic cascade quickly produces large numbers of ultraviolet and visible photons. The scintillator is a liquid highly transparent to visible light, and thus the visible photons can be collected by the PMTs covering the scintillation counter walls. The neutron (with a kinetic energy below one MeV) is slowed down (or *moderated*) by many scatterings with the light nuclei of the material, as schematized by the dashed line. The moderation time lasts up to a few tens of μs , which is a very long time compared to the time resolution of the detector (of the order of a few ns). If a cadmium salt is dissolved in the liquid, there is a higher probability that the moderated neutron be captured by a Cd nucleus. The excited Cd^* state returns to the ground state with the emission of a 9 MeV γ -ray. This sequence of two flashes of light separated by a few μs is the basic signature of inverse- β decay and confirms the $\bar{\nu}_e$ capture by the proton. This experimental technique is called *delayed coincidence*, and is frequently used for $\bar{\nu}_e$ detection (see Sect. 12.7). The logic of the data acquisition had a decisive role in the experiment

A sufficiently high flux of antineutrinos (emitted by the reactor) was reaching the detector; this flux can be estimated from the electric power P produced by the reactor. If $P = 0$, obviously $\Phi_{\bar{\nu}} = 0$ and possibly measured counts are due to spurious coincidences. In the case of maximum power $P = 150 \text{ MW}$, one should take into account that an antineutrino is emitted, on average, every $\bar{E} \simeq 10 \text{ MeV}$. Given the conversion factor $1 \text{ MeV} = 1.6 \times 10^{-13} \text{ J}$, the number R of antineutrinos emitted per second by the reactor corresponds to

$$R = 150 \text{ MW} / \bar{E} = \frac{1.5 \times 10^8 \text{ J/s}}{\bar{E}} \simeq \frac{10^{21} \text{ MeV/s}}{\bar{E}} \simeq 10^{20} \nu/\text{s}.$$

At the distance $D \simeq 10 \text{ m} = 10^3 \text{ cm}$ from the reactor, the expected flux is

$$\Phi_{\nu} = R / 4\pi d^2 \simeq 10^{13} \text{ cm}^{-2} \text{ s}^{-1}.$$

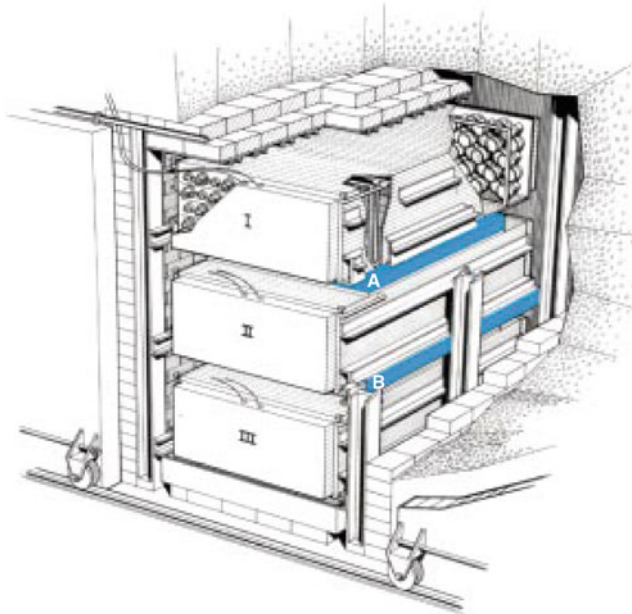


Fig. 8.7 The detector at Savannah River was in a cavity about 11 m from the nuclear reactor core; it was surrounded by a lead shield. Two plastic tanks (*A* and *B*) each contained 200 l of water. 40 kg of cadmium chloride salt was dissolved in the water to increase the probability of neutron capture. Three tanks (each 1,400 l) of liquid scintillator were placed above and below those of water. On each tank, 110 photomultiplier tubes were arranged to collect scintillation light and produce electronic signals. The total mass, including the lead screen, was about 10 tons. The experiment took data for 5 months (~ 900 h with the nuclear reactor on and ~ 250 h with reactor off). The number of target protons in 200 kg of water is $N_T = 0.6 \times 10^{28}$ protons. The data acquisition was able to record the signal due to positron annihilation, and the delayed signal due to the γ -rays emitted a few μs later from the cadmium nucleus after neutron capture. The rate of delayed coincidences was five times larger when the reactor was on than when it was off

Many tests were carried out to ensure that the signal was really due to antineutrinos rather than to background reactions. One of the key points was to estimate the efficiency ϵ with which the e^+ annihilation and the delayed n capture were *both* measured. The detection probability of the first signal (annihilation) was relatively high; on the contrary, the efficiency of detecting the neutron capture was estimated to be $\epsilon \simeq 10\%$; this low efficiency arises from the fact that neutrons could leave the region with the cadmium salt during the moderation process. In this case, the delayed signal would be missed.

The Savannah experiment not only demonstrated the existence of the neutrino, but also allowed the measurement of the cross-section for the reaction (8.19). The measured number of interactions (about three events per hour) is proportional to the flux Φ_ν of antineutrinos from the reactor times the number N_T

of protons in the detector target, the detection efficiency ϵ and the unknown cross-section:

$$N(\text{interactions/s}) = \Phi_\nu (\text{cm}^{-2}\text{s}^{-1}) \cdot \sigma (\text{cm}^2) \cdot N_T \cdot \epsilon. \quad (8.20)$$

The cross-section for an antineutrino energy $E_\nu \sim \text{MeV}$ is

$$\sigma = \frac{N(\text{interactions/s})}{\Phi_\nu \cdot N_T \cdot \epsilon} = \frac{(3/3600)}{10^{13} \cdot 0.6 \times 10^{28} \cdot 0.1} = 1.3 \times 10^{-43} \text{ cm}^2. \quad (8.21)$$

The estimated error associated with the measurement was about 25%. The cross-section measurement reported in the first published article in 1956 was about two times smaller due to an erroneous overestimation of ϵ . In a second paper in 1960, the analytical procedures were checked and a new efficiency was estimated. As will be discussed in the next paragraph, the cross-section value (8.21) is in good agreement with the value expected from the Fermi theory.

8.6 Different Transition Types in β Decay

Most of the information on the weak interaction at low energy is derived from the study of the β decay of a free neutron [$n \rightarrow pe^- \bar{\nu}_e$]; from the β^- decay of a neutron bound in nuclei [$(A, Z) \rightarrow (A, Z + 1) + e^- + \bar{\nu}_e$]; from β^+ decays [$(A, Z) \rightarrow (A, Z - 1) + e^+ + \nu_e$] and from the capture of an electron by a proton [$pe^- \rightarrow nv_e$] in a nucleus [$(A, Z) + e^- \rightarrow (A, Z - 1) + \nu_e$]. These processes can be described in terms of nuclei and interpreted at the particle level or at the level of quarks and leptons, see table below.

	of elementary particles	of point-like particles (quarks and leptons)
At the nuclear level		
$(A, Z) \rightarrow (A, Z + 1) + e^- + \bar{\nu}_e$	$n \rightarrow pe^- \bar{\nu}_e$	$d \rightarrow ue^- \bar{\nu}_e$
$(A, Z) \rightarrow (A, Z - 1) + e^+ + \nu_e$	$p \rightarrow ne^+ \nu_e$	$u \rightarrow de^+ \nu_e$
$(A, Z) + e^- \rightarrow (A, Z - 1) + \nu_e$	$pe^- \rightarrow nv_e$	$ue^- \rightarrow dv_e$

Note that for energy considerations, a free proton cannot spontaneously decay into $ne^+ \nu_e$, while it can occur for protons bound in a nucleus. Similarly, the reaction $pe^- \rightarrow nv_e$ does not occur for free protons at rest, though it can happen with a proton bound in a nucleus. In terms of Feynman diagrams, the neutron decay is described in Fig. 8.1. The nuclear β decays are more difficult to interpret in a quantitative way because of the presence of nucleons not directly involved in the

Table 8.1 β decays are classified as Fermi, Gamow–Teller (GT) and mixed. The lifetimes, the factor $f\tau$ and the constant value $G_F^2|\mathcal{M}|^2$ are reported. The matrix element $|\mathcal{M}|$ depends on the n and p wave functions in the nucleus: in particular, it takes into account the Pauli exclusion principle that prevents a $n \rightarrow p$ transition towards an already occupied nuclear state. The calculation should consider in each case the isospin multiplicity $m_{i,s}$ of the newly formed state and the multiplicity of nuclear spin states. For example, $m_{i,s} = 2$ in the Fermi decay of $^{14}_8 O$; $m_{i,s} = 6$ in the case of the GT decay of $^6_3 He$

Decay	Transition J^P	τ s	E_0 MeV	$f\tau$	$G_F^2 \mathcal{M} ^2$ $MeV^2 fm^6$
$^{14}_8 O \rightarrow ^{14}_7 N^* e^+ \nu$	$0^+ \rightarrow 0^+$	102	2.26	4.51×10^3	1.52×10^{-8}
$^{34}_{17} Cl \rightarrow ^{34}_{16} S e^+ \nu$	$0^+ \rightarrow 0^+$	2.21	4.94	4.54×10^3	1.51×10^{-8}
$^6_2 He \rightarrow ^6_3 Li e^- \bar{\nu}$	$0^+ \rightarrow 1^+$	1.15	3.99	1.17×10^3	7.45×10^{-8}
$^{13}_5 B \rightarrow ^{13}_6 C e^- \bar{\nu}$	$\frac{3}{2}^- \rightarrow \frac{1}{2}^-$	2.51×10^{-3}	13.4	1.11×10^3	6.17×10^{-8}
$n \rightarrow p e^- \bar{\nu}$	$\frac{1}{2}^+ \rightarrow \frac{1}{2}^+$	890	1.18	1.61×10^3	4.25×10^{-8}
$^3_1 H \rightarrow ^3_2 He e^- \bar{\nu}$	$\frac{1}{2}^+ \rightarrow \frac{1}{2}^+$	5.6×10^8	0.14	1.63×10^3	4.20×10^{-8}

decay. It is conceivable that a difficulty of the same type is also present in a free neutron decay which can be interpreted as due to a d -quark decay, while the two remaining quarks are spectators.

The nuclear transitions have been classified on the basis of the change in the nucleus total angular momentum (spin) before and after the decay. This variation is related to the spin of the two leptons e^- , $\bar{\nu}_e$ (or e^+ , ν_e). As both particles have spin 1/2, the change in the nuclear spin may be zero (for neutrino and electron spins antiparallel to each other) or ± 1 (for parallel spins). The calculation of the transition probability takes into account the number of states allowed by angular momentum through the quantity $|\mathcal{M}|^2$ that in (8.13) was considered equal to one. The product $G_F^2|\mathcal{M}|^2$ is inversely proportional to the lifetime τ of the particle through the relation $G_F^2|\mathcal{M}|^2 = \frac{\text{constant}}{f\tau}$, where $f \sim E_0^5$.

Measurements on some β decays are presented in Table 8.1 [8B83]. Note that despite the large variation in lifetime due to the strong dependence of f on E_0^5 , the product $G_F^2|\mathcal{M}|^2$ is approximately the same. There is however a dependence on the nuclear spin variation in the transition probability. It is assumed that the electron and neutrino are emitted in a state of orbital angular momentum $\ell = 0$. In this case, the variation of the nuclear spin is equal to the sum of the spins of the electron and of the neutrino. According to this variation, the transitions are classified as follows: (i) for nuclear $0 \rightarrow 0$ transitions, the electron/neutrino spins are antiparallel (singlet state); (ii) for nuclear $0 \rightarrow 1$ transitions, the lepton spins are parallel (triplet state); (iii) for nuclear $\frac{1}{2} \rightarrow \frac{1}{2}$ transitions, the lepton spins are antiparallel (the spin of the nucleus does not change) or parallel (the spin of the nucleus changes direction). The transitions of the first type are called Fermi transitions, those of the second type are Gamow–Teller transitions; in both cases, the parity P does not change. The third case corresponds to the more complex mixed transitions.

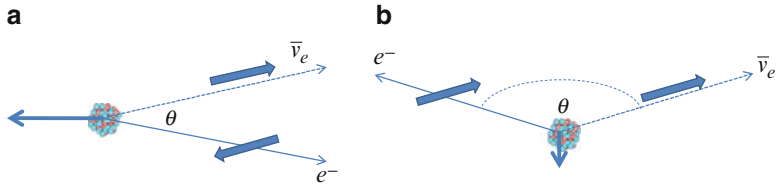
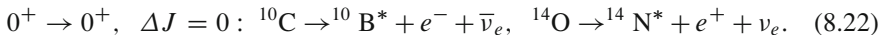


Fig. 8.8 (a) In Fermi transitions ($\Delta J = 0$), the measured nucleus momentum is high. The two leptons must then be emitted almost parallel to each other (θ small). (b) In GT transitions ($\Delta J = 1$), the measured nucleus momentum is small. The two leptons must then be emitted almost back-to-back (θ large). In both cases, the \bar{v}_e spin (the large arrow) is aligned along its momentum; the e^- spin is almost antiparallel to its momentum. The projection of the spin along the direction of the momentum is called *helicity* (defined in Appendix A.4). As all experiments involving leptons, nuclear β decays show that the \bar{v}_e helicity is +1 while the e^- prefers to have negative helicity. It is easy to verify that (keeping the \bar{v}_e helicity = +1) in a Fermi (GT) transition with large (small) angle θ , the electron helicity would be positive. It will be shown in Sect. 8.16 how the theory takes into account the lepton helicity preferences (including that the v_e helicity is -1 while the e^+ prefers to have positive helicity)

Fermi transitions: ΔJ (nuclear spin) = 0, singlet leptonic spin state ($\uparrow\downarrow$). Example of a Fermi transition:

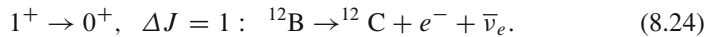


In the case of Fermi transitions (Fig. 8.8a), the angular momentum conservation requires that the spins of the e^- , \bar{v}_e or e^+ , v_e pair are antiparallel. Here, $|\mathcal{M}|^2 \equiv |\mathcal{M}_F|^2 = m_{i,s} g_V^2$ (the quantity $g_V \simeq 1$ will be defined in Sect. 8.16). The electron momentum can be easily measured, while that of the neutrino can only be estimated by the (not easy) measurement of the recoil nucleus momentum and by applying the momentum conservation law. Experiments carried out since the late 1950s have shown that the sum of the electron and neutrino momenta is *large*; they are emitted predominantly parallel to each other. Defining θ the relative angle between the directions of the electron and of the neutrino, the experiments show that for Fermi transitions, the angular distribution of the electron is described by

$$f(\theta) = 1 + \frac{v}{c} \cos \theta \quad (8.23)$$

which presents a maximum for $\theta = 0^\circ$.

Gamow–Teller (GT) transitions: ΔJ (nuclear spin) = 1, triplet leptonic spin state ($\uparrow\uparrow$). Example of Gamow–Teller transitions:



For Gamow–Teller transitions, $|\mathcal{M}|^2 \equiv |\mathcal{M}_{GT}|^2 = m_{i,s} g_A^2$ (g_A will be defined in Sect. 8.16). The angular distribution of the relative e^- , \bar{v}_e (or e^+ , v_e) emission

angle θ can also be studied in these GT transitions (Fig. 8.8b). As before, it is necessary to measure the nuclear recoil momentum and apply the angular momentum conservation law. In this case, it was found that the momentum of the nuclei is *small*, and that the two leptons are emitted mostly antiparallel to each other. The measured angular distribution is:

$$f(\theta) = 1 - \frac{1}{3} \frac{v}{c} \cos \theta \quad (8.25)$$

and the angle of emission has a maximum probability at $\theta = 180^\circ$. The constants g_V, g_A were measured in pure Fermi and GT transitions. The absolute value of the ratio between the two constants can be derived from experimental data (Problem 8.8), that is,

$$\left| \frac{g_A}{g_V} \right| = 1.26. \quad (8.26)$$

The constant g_A related to GT transitions is larger than the g_V of Fermi transitions. The relative sign (as discussed in Sect. 8.16) is discordant.

8.6.1 The Cross-Section of the β -Inverse Process

The cross-section (in natural units) for the β -inverse decay $\bar{\nu}_e p \rightarrow e^+ n$ can be obtained from the general formula (8.3)

$$\sigma(\bar{\nu}_e p \rightarrow ne^+) = \frac{W}{c} = 2\pi G_F^2 |\mathcal{M}|^2 \frac{dN}{dE} = \frac{G_F^2}{\pi} |\mathcal{M}|^2 E^2. \quad (8.27)$$

In the last equality (assuming the kinetic energy transferred to the neutron to be negligible), we used the number of phase space states for the electron given by (8.7a). For neutrino energies above the MeV, the rest mass of the electron can also be neglected and $E = p_e$. In this case, $dN/dE = E^2/2\pi^2$.

Reaction (8.19) corresponds to a mixed transition; the contribution from the Fermi transition is $\mathcal{M}_F^2 \simeq 1$, and that of the Gamow–Teller transition is $\mathcal{M}_{GT}^2 \simeq 3$, and thus $|\mathcal{M}|^2 \simeq 4$. Inserting this value in (8.27), one obtains

$$\begin{aligned} \sigma(\bar{\nu}_e p \rightarrow ne^+) &= \frac{4}{\pi} G_F^2 E^2 (\hbar c)^2 \\ &= \frac{4}{\pi} \times (1.16 \times 10^{-5})^2 [\text{GeV}^{-2}] \times 0.389 [\text{GeV}^2 \text{ mb}] \times E^2 [\text{GeV}^2] \\ &= 0.67 \times 10^{-37} [\text{cm}^2] \times E^2 [\text{GeV}^2]. \end{aligned} \quad (8.28)$$

The factor $(\hbar c)^2 = 0.389 \text{ (GeV}^2 \text{ mb)}$ with the dimensions of $[\text{Energy Length}]^2$ was inserted. In the case of $\sim 1 \text{ MeV}$ ($= 10^{-3} \text{ GeV}$) neutrinos, one obtains

$$\sigma(1 \text{ MeV}) \simeq 7 \cdot 10^{-44} \text{ (cm}^2)$$

in agreement with the experimental result (8.21). This is a very small cross-section, corresponding to a ν mean free path (or interaction length) of

$$\lambda(\text{g cm}^{-2}) = (1/N_A \cdot \sigma) \simeq [(6 \times 10^{23})(7 \times 10^{-44})]^{-1} \simeq 2 \cdot 10^{19} \text{ g cm}^{-2}, \quad (8.29)$$

equivalent to $2 \cdot 10^{19} \text{ cm}$ of water. A neutrino of 1 MeV can travel a distance of $\simeq 20$ light-years of water (7 parsec) before interacting.

8.7 Lepton Families

In 1963, a second neutrino type was identified in an experiment led by Lederman, Schwartz and Steinberger (Nobel laureate in 1988). This second neutrino was closely related to the muon, just as the neutrino from the β decay is connected with the electron. The experiment was conceptually very simple: a beam of charged pions (positive or negative) was selected by a device similar to the one shown in Fig. 8.9. The selected positive (for example) pions decay in a vacuum tunnel, that is,

$$\pi^+ \rightarrow \mu^+ \nu. \quad (8.30)$$

After the vacuum tunnel, the emitted charged particle was easily identified as a positive muon. If the ν in (8.30) is the same particle emitted in nuclear β decays, it could likely produce, with equal probability, a muon or an electron when interacting with a nucleon N : $\sigma(\nu N \rightarrow e^- X) = \sigma(\nu N \rightarrow \mu^- X)$. If the ν in (8.30) is different from that associated with the electron in the β decay, only μ^- are expected in the final state after the interactions.

The experiment consisted of a massive apparatus placed at the end of the vacuum tunnel. There, neutrinos produced by pion decay could interact with matter. The charged lepton in the final state was always identified as a muon, and electrons were never detected.

It was therefore necessary to define a new neutrino *type*, or more correctly *flavor*, called the *muon neutrino*, and symbolically denoted as ν_μ . Similarly, in the case of a π^- decay, the neutral particle produced in association with the negative muon always generated a positive muon when interacting with matter. It was identified as the muon antineutrino ($\bar{\nu}_\mu$).

As a result of the Lederman et al. experiment, the *lepton number conservation* needed to be revised: in each reaction, not only the total lepton number is conserved, but the number of leptons of each family must also be separately conserved

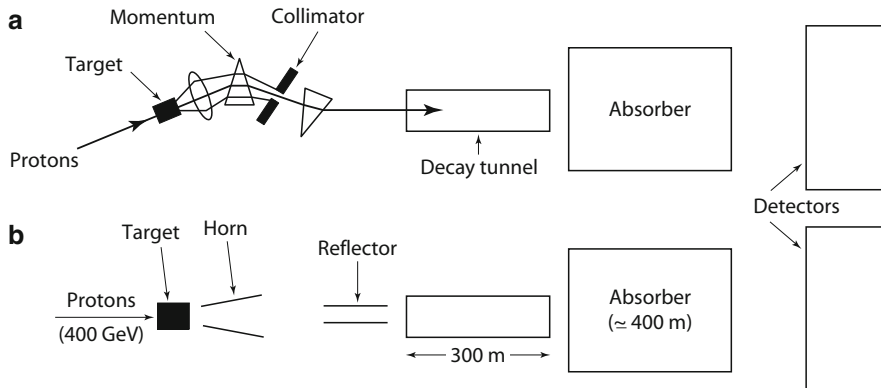


Fig. 8.9 Layout of neutrino beams at the CERN SPS: (a) narrow-band beam and (b) broad-band beam

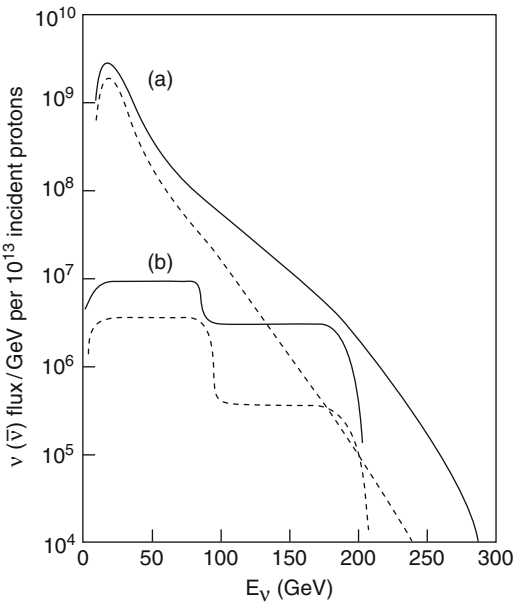
(Sect. 5.5.3). The electron and electron neutrino, as with the muon and muon neutrino, have been grouped into different lepton families. A third family (the tau and tau neutrino) was successively identified. As we shall see in Sect. 9.7, from the precision measurements obtained in the LEP experiments, we know that there are only three families of leptons.

The *flavor lepton number conservation* is respected in every decay or interaction process in Nature (and in all equations presented in this book). In Chap. 12, we shall discover a new phenomenon which involves neutrino flavor changes during their propagation, the *neutrino oscillations*. This imposes a modification in the application of the flavor lepton number conservation law.

Muon neutrino beams and experiments. Many experiments were carried out with ν_μ beams: they were used to test the quark composition of protons and neutrons (Chap. 10), or to study particle flavor oscillations (Chap. 12). To produce intense beams of high energy muon neutrinos, protons from a synchrotron are accelerated to the maximum available energy (for example, 450 GeV at CERN SPS and 900 GeV at the Fermilab Tevatron). At the end of the acceleration cycle, the protons are extracted and sent against a beryllium target about one meter long where they produce π and K mesons. The mesons are collimated and pass in a 300 m long vacuum tube where they decay (Fig. 8.9). After the vacuum tube, there is a region with absorbing material. In the absorber, photons and electrons are stopped first, followed by hadrons and finally muons. Only neutrinos proceed and reach the experimental area where different detectors are installed.

The neutrino beam is not monochromatic; it can be either narrow-band or broad-band, depending on the focusing of the charged hadrons produced in

Fig. 8.10 Typical neutrino (full line) and antineutrino (dashed lines) flux for 10^{13} incident 400 GeV protons at the CERN SPS:
(a) broad-band beam and
(b) narrow-band beam, after selection of 200 GeV/c π and K



the primary collision. To obtain a narrow-band neutrino beam, quadrupole magnets and magnetic deflectors are placed immediately after the target. A beam of π and K mesons with selected momentum and wide enough bandwidth ($\Delta p/p \simeq 10\%$) is formed. The selected beam passes through a quadrupole system to form a collinear beam optimized for the decay in the vacuum tube (see Fig. 8.9a). In a broad-band neutrino beam, the focusing system is optimized to produce the maximum intensity of π and K mesons (see Fig. 8.9b). The narrow-band neutrino beam has an energy distribution with a “two boxes” shape, while the broad-band has a maximum at a few tens of GeV (see Fig. 8.10). The intensity of a narrow-band beam is obviously smaller than that of a broad-band beam.

Neutrino detectors. Since the neutrino cross-section is small, the target must be very massive to obtain a reasonable interaction rate. The mean free path in iron of 10 GeV neutrinos is $\lambda = 2.6 \cdot 10^9$ km. This means that only a very small fraction $\sim 3 \cdot 10^{-13}$ of 10 GeV neutrinos interact in a meter of iron. With a flux of 10^{12} neutrinos (for $\sim 10^{13}$ accelerated protons incident on the target), there are only 0.3 interactions in one meter of iron. In general, the target corresponds to the detector sensitive volume, particularly if one is interested in studying the hadronic system X produced in $\nu_\mu N \rightarrow \mu + X$ interactions. In the past, large bubble chambers were intensively used; alternatively, large sampling calorimeters are used as target and as electronic detectors, often

followed by a separated muon detector. It is important to identify muons to separate the charged current interactions from the neutral current ones. Electronic detectors used at the CERN SPS and Fermilab consisted of a target calorimeter (to measure the total energy of hadrons and photons) and of muon chambers (which also measured their momentum). These experiments (CDHSW, CHARM, CHORUS and others) were used to study the properties of neutrinos, the structure functions of nucleons (Sect. 10.5), and neutrino oscillations. As described in Sect. 12.6, neutrino oscillations can be observed if neutrinos travel a long distance L from the production point to the detection point. For this reason, there are (2011) three long baseline beams (see Sect. 12.8.1) where the neutrino is produced in a laboratory (CERN in Europe, Fermilab in USA, Jpark in Japan) and detected in distant experiments (OPERA at Gran Sasso for the CERN beam, MINOS at the Soudan laboratory for the Fermilab beam, both located ~ 730 km from the accelerator; Super-Kamiokande in Japan, which is 250 km away from Tsukuba).

8.8 Parity Violation in β Decays

The idea (quite original at that time) that parity was not conserved in weak interactions came up in 1955. It originated from the evidence that the K meson decays into two states of opposite parity. In 1956, T.D. Lee and C.N. Yang (Nobel prize in 1957) made a critical analysis of the results obtained from the study of weak processes and concluded that the dependence of the interaction on pseudoscalar terms was never experimentally studied. A pseudoscalar quantity changes sign under a parity transformation. Examples of pseudoscalar quantum mechanics operators are the *helicity* (Appendix A.4), that is, the scalar product of the spin with the particle momentum ($\sigma \cdot \mathbf{p}_e$) or with the electric field ($\sigma \cdot \mathbf{E}$). All the eigenvalues of these operators are pseudoscalar quantities.

Lee and Yang observed that the Hamiltonian of weak interaction processes was expressed as a superposition of Fermi and Gamow–Teller terms, which are separately invariant under parity.⁴ They proposed a more general formulation. The inclusion in the Hamiltonian of a term whose eigenvalues change sign under parity transformation (as, for instance, the terms $\sigma \cdot \mathbf{E}$, $\sigma \cdot \mathbf{p}$) would result in the violation of parity in the interaction (see Table 6.3). The term that Lee and Yang suggested was connected with the longitudinal polarization $\sigma \cdot \mathbf{p}$. They also proposed some experiments to evidence the possible parity violation in weak decays. Two of them, the decay of polarized nuclei and the decay of the muon, were performed

⁴The explanation of these concepts will be formalized in the theory presented in Sect. 8.16.

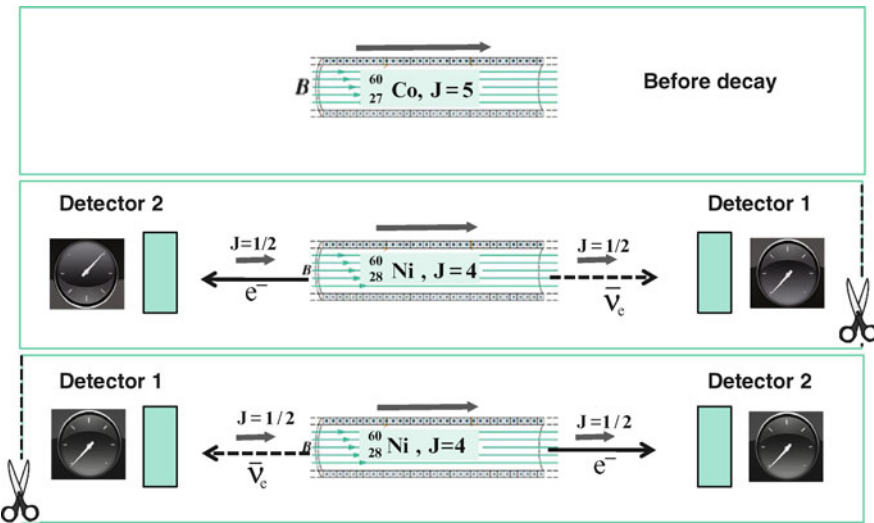


Fig. 8.11 Parity violation in β decay. Initially (*upper panel*), the ^{60}Co nucleus spin (indicated by the arrow) with $J = 5$ is aligned by the presence of a magnetic field along the solenoid axis. Two identical detectors are placed at the ends of the solenoid. In the middle panel, detector 2 counts events: they are electrons with spin aligned as shown. From momentum conservation, the antineutrinos travel to detector 1 (which of course does not count anything); from the angular momentum conservation, their spin is parallel to the direction of the momentum. The *bottom panel* represents what you would see in a mirror, cutting the middle panel along the dashed line on the right and approaching that side near the mirror. Unlike before, counter 2 now counts nothing! In fact, taking into account the properties of angular momentum in the reflection, the right-handed electrons should reach counter 2 because a left-handed antineutrino is going to counter 1. However, the left-handed antineutrinos have never been observed, and counter 2 counts nothing. The reflection in the mirror of this physical process gives a different result from the real experiment!

in the following months and clearly showed that parity is not conserved in weak interaction.

Here, we schematically describe the results obtained by Madame Wu and collaborators on the decay of polarized cobalt nuclei. In Sect. 8.10, we shall analyze the second experiment which involved the measurement of the $\pi - \mu - e$ decay at the Nevis cyclotron at Columbia University by R. L. Garwin, L. M. Lederman and M. Weinrich. The articles relating to both experiments were published in 1957 in the same issue of Physical Review Letters (Vol. 105, No. 4, pp. 1413–1414 and 1415–1417).

In the β decay of ^{60}Co (see Fig. 8.11), a term $\sigma_{\text{Co}} \cdot \mathbf{p}_e$ that changes sign under the application of the parity operator was considered [$P(\sigma_{\text{Co}} \cdot \mathbf{p}_e) = -(\sigma_{\text{Co}} \cdot \mathbf{p}_e)$]; it produces a pseudoscalar quantity. ^{60}Co polarization can be achieved by an experimental setup at a very low temperature (0.01 K). The nuclear magnetic moments of ^{60}Co , which are parallel to the nuclear spins, are oriented in a strong magnetic field \mathbf{B} . The emitted electrons were counted in the directions parallel and

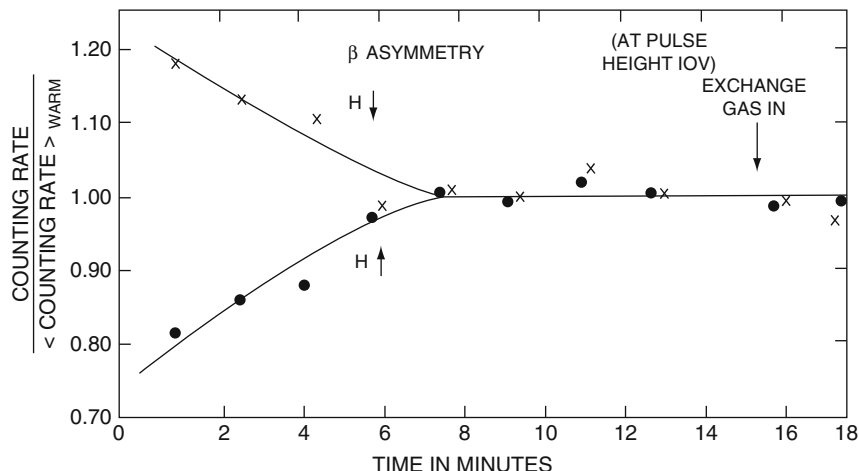
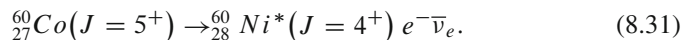


Fig. 8.12 Measured asymmetry of electrons emitted in ^{60}Co decay in the Wu et al. experiment. The upper counter measures different frequency counts when the magnetic field (denoted as H) is aligned towards the bottom (*upper curve*) or top (*lower curve*). As time (abscissa) increases, the Co sample warms up, the spins tend to lose alignment, and the asymmetry disappears

antiparallel to the nuclear magnetization: the two numbers were different, which unambiguously demonstrated that parity is violated in WI.

The ^{60}Co ($J = 5$) decays into an excited state of $^{60}\text{Ni}^*$ ($J = 4$) through a pure GT transition. The lifetime is seven and a half years, and the available energy is $E_0 = 0.32 \text{ MeV}$



From the angular momentum conservation law, the electron and antineutrino are emitted with spin parallel to the ^{60}Co spin, oriented in the direction of the magnetic field.

The intensity of the electrons emitted in the direction of the magnetic field and in the opposite direction (Fig. 8.11) was measured using scintillation counters. Counters 1 and 2 play a symmetric role: if Nature and its image in a mirror are the same (parity conservation), counter 1 should measure the same rate as counter 2, regardless of the orientation of the magnetic field (and thus of the orientation of the cobalt nuclear spin). The measurements have shown that when the magnetic field is inverted, the electron count changes. Electrons prefer to be emitted with momentum in the opposite direction of the nuclear spin, and with the spin oriented in the same direction of the nuclear spin. This corresponds to the same electron spin-momentum assignment in nuclear decays of Fig. 8.8b. The right-left asymmetry in the electron counts depends on the degree of the magnetization of the source (Fig. 8.12). The intensity of the emitted electrons as a function of the angle θ between the direction

of electron emission and the polarization of the sample (emitted electron angular distribution) has the form

$$I(\theta) = 1 + \frac{\alpha \sigma_{\text{Co}} \cdot \mathbf{p}_e}{E_e} = 1 + \alpha \frac{v_e}{c} \cos \theta \quad (8.32)$$

where \mathbf{p}_e , E_e are the momentum and energy of the electron, and σ_{Co} is the ^{60}Co spin. Data are consistent with $\alpha = -1$. The counts for the upward and downward ^{60}Co polarization are different and therefore parity is violated. In fact, in (8.32), under inversion of coordinates (parity P transformation), the pseudoscalar term $\sigma_{\text{Co}} \cdot \mathbf{p}_e$ changes sign: $P(\sigma_{\text{Co}} \cdot \mathbf{p}_e) = -\sigma_{\text{Co}} \cdot \mathbf{p}_e$.

This experiment showed for the first time that electrons are prevalently emitted longitudinally polarized in the opposite direction of its momentum (the electron has negative helicity, it is left-handed). The charged current weak processes involve left-handed e^- and right-handed e^+ . The helicity Λ (see Appendix A.4) is measured as the net longitudinal polarization of a set of particles. Using (8.32), one has

$$\Lambda = \frac{I_+ - I_-}{I_+ + I_-} = \alpha \frac{v}{c} \quad (8.33)$$

where I_+ ed I_- are the relative intensities of the component with spin parallel and antiparallel to the momentum \mathbf{p} . The value of α was found to be equal to -1 for e^- ($\Lambda = -v/c$) and equal to $+1$ for e^+ ($\Lambda = +v/c$).

8.9 The Two-Component Neutrino Theory

For a massless neutrino, $v = c$ and (8.33) implies that the particle must be completely polarized, i.e., $\Lambda = +1$ or $\Lambda = -1$. An experiment performed by M. Goldhaber et al. in 1958 demonstrated that the neutrino helicity is negative, i.e., the neutrino spin σ_ν is antiparallel to its momentum p_ν : schematically, $(\mathbf{p}_\nu \uparrow \downarrow \sigma_\nu)$. The antineutrino is right-handed ($\mathbf{p}_{\bar{\nu}} \uparrow \uparrow \sigma_{\bar{\nu}}$); for example, the spin pattern in polarized neutron decay is

$$\begin{array}{ccccccc} n & \longrightarrow & p & + & e^- & + & \bar{\nu}_e \\ & & \uparrow & & \uparrow & & \uparrow_{LH} \quad \downarrow_{RH} \end{array}$$

where LH means left-handed, i.e., with the spin antiparallel to the momentum direction ($\uparrow \downarrow$); RH stands for right-handed, which means that the spin and momentum are in the same direction ($\uparrow \uparrow$). As a result of many experiments, the helicity assignment of leptons and antileptons is (see also Appendix A.4)

particle	ν_e	$\bar{\nu}_e$	e^-	e^+		
helicity probability	-	1	+1	- v/c	+ v/c .	(8.34)

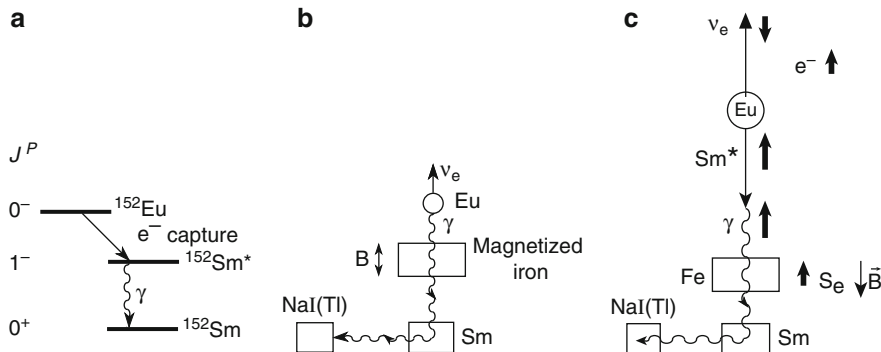
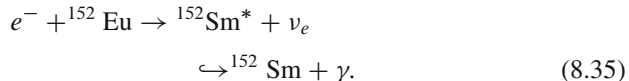


Fig. 8.13 (a) Diagram of energy levels in the ^{152}Eu and $^{152}\text{Sm}^*$ decays. (b) Schematic apparatus used to measure the neutrino helicity. (c) Spin directions

These considerations lead to the *two-component neutrino theory*, i.e., that the neutrino is left-handed while the antineutrino is right-handed.

Neutrino Helicity. [8G10] The process studied by Goldhaber was the electron capture in the ^{152}Eu nucleus, that is,



The excited samarium state decays with the emission of a 960 keV γ (see diagram of Fig. 8.13a). The γ rays are emitted in the same direction as the recoiling ${}^{152}\text{Sm}^*$ and are immediately detected after a 90° scattering in a samarium target. Only the γ emitted in the direction opposite to the ν_e have an energy slightly higher than 960 keV and therefore sufficient to give rise to a resonant scattering in the samarium target, i.e., $\gamma + \text{Sm} \rightarrow \text{Sm}^* \rightarrow \text{Sm} + \gamma$. For a neutrino with negative helicity, the spin configuration is shown in Fig. 8.13c. If the electrons in the magnetized iron are polarized in the same direction as the photon, the photon can go through; if the photon has spin opposite to that of the electron, it can be absorbed in an interaction that reverses the electron spin. The helicity of the photon is then measured by the scattering in magnetized iron (reverting \mathbf{B} , the polarization can be determined by the change in the counting rate). It can be concluded that the neutrino is left-handed (i.e., the spin has an opposite direction with respect to the momentum direction).

8.10 Charged Pion Decay

The second crucial experiment that confirmed the nonconservation of parity, the neutrino LH helicity and the antineutrino RH helicity is based on the study of π^\pm meson decays. Figure 8.14a shows the Feynman diagrams of the π^+ meson

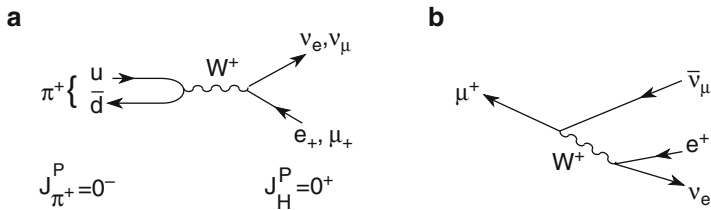


Fig. 8.14 Feynman diagrams (a) for the $\pi^+ \rightarrow \mu^+ \nu_\mu$ and $\pi^+ \rightarrow e^+ \nu_e$ decays, and (b) for the $\mu^+ \rightarrow e^+ \nu_e \bar{\nu}_\mu$ decay

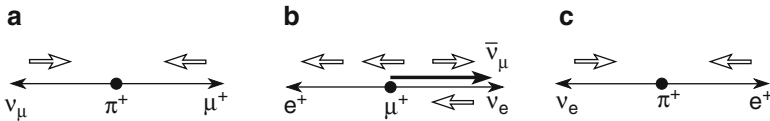


Fig. 8.15 Illustration of the momentum and spin of the particles in the decays (a) $\pi^+ \rightarrow \mu^+ \nu_\mu$, (b) $\mu^+ \rightarrow e^+ \nu_e \bar{\nu}_\mu$, and (c) $\pi^+ \rightarrow e^+ \nu_e$

decays: $\pi^+ \rightarrow \mu^+ \nu_\mu$, $\pi^+ \rightarrow e^+ \nu_e$. The π^+ meson is made of $u\bar{d}$ quarks; it annihilates into a virtual W^+ vector boson which then decays into $\mu^+ \nu_\mu$ or $e^+ \nu_e$. The momentum and spin assignments of the μ^+ and of the ν_μ in the π^+ rest frame is shown in Fig. 8.15a. The ν_μ and μ^+ have equal momentum with opposite directions: $|\mathbf{p}_{\nu_\mu}| = |\mathbf{p}_{\mu^+}| = |\mathbf{p}|$. If ν_μ is LH, that is, with helicity $\Lambda = -1$, its spin is antiparallel to the momentum, as shown in Fig. 8.15a. From angular momentum conservation, also the μ^+ must have negative helicity. In the following $\mu^+ \rightarrow e^+ \nu_e \bar{\nu}_\mu$ decay in the μ^+ rest frame, the momentum and spin configurations must be as shown in Fig. 8.15b for the limit case where the ν_e and $\bar{\nu}_\mu$ are emitted in the same direction. The experiments carried out in 1957 verified that the angular distribution of the positron is in agreement with that predicted by the two-component neutrino theory with the spin configuration shown in Fig. 8.15b.

In the following, we will study the ratio of branching ratios (see Sect. 4.5.2)

$$\Gamma(\pi^+ \rightarrow e^+ \nu_e) / \Gamma(\pi^+ \rightarrow \mu^+ \nu_\mu), \quad (8.36)$$

which gives important information on the mathematical structure of weak interaction currents. On the basis of the Sargent rule (8.18), the decay $\pi \rightarrow e\nu$ should be favored due to the larger energy available in the final state ($m_\mu \gg m_e$). However, the decay $\pi \rightarrow e\nu_e$ is disfavored by a factor $\sim 10^4$ compared to $\pi \rightarrow \mu\nu_\mu$. The reason is that the emitted charged lepton has, in both cases, the *wrong* helicity. Neutrinos have negative helicity ($\Lambda = -1$) and antineutrinos have positive helicity

($\Lambda = +1$); as a consequence, e^+, μ^+ must have helicity as shown in Fig. 8.15a, c. According to (8.34), antiparticles have spin parallel to the momentum with a probability $P_{RH} = v/c$ (Appendix A.4). The configurations of Fig. 8.15a,c with negative helicity both for the μ^+ and for the e^+ are disfavored configurations, corresponding to a probability $P_{LH} = (1 - v/c)$ since $P_{LH} + P_{RH} = 1$. The quantity P_{LH} is much smaller for the positron, as its mass is small and the velocity approaches c . The heavier μ^+ is rather nonrelativistic. In the case of $\pi^+ \rightarrow \mu^+ \nu_\mu$, the decay fraction is proportional to

$$\Gamma_{\pi \rightarrow \mu} \simeq (\text{helicity factor})(\text{phase space factor}) \simeq \left(1 - \frac{v_\mu}{c}\right) p^2 \frac{dp}{dE_0} \quad (8.37)$$

where p is the momentum of the μ^+ and of the ν_μ , and the total energy is $E_0 = m_\pi = p + \sqrt{p^2 + m_\mu^2}$ (units with $c = 1$). Consequently, one has

$$\begin{aligned} p &= \frac{m_\pi^2 - m_\mu^2}{2m_\pi} = \frac{E_0^2 - m_\mu^2}{2E_0}, \quad p^2 = \frac{(m_\pi^2 - m_\mu^2)^2}{4m_\pi^2}, \quad \frac{dp}{dE_0} = \frac{m_\pi^2 + m_\mu^2}{2m_\pi^2} \\ \frac{v_\mu}{c} &= \frac{p_\mu}{E_\mu}, \quad 1 - \frac{v_\mu}{c} = \frac{2m_\mu^2}{m_\pi^2 + m_\mu^2} \end{aligned}$$

and then

$$\begin{aligned} \Gamma_{\pi \rightarrow \mu} &\simeq \left(1 - \frac{v_\mu}{c}\right) p^2 \frac{dp}{dE_0} = \frac{2m_\mu^2}{m_\pi^2 + m_\mu^2} \frac{(m_\pi^2 - m_\mu^2)^2}{4m_\pi^2} \frac{m_\pi^2 + m_\mu^2}{2m_\pi^2} \\ &= \frac{m_\mu^2}{4} \left(1 - \frac{m_\mu^2}{m_\pi^2}\right)^2. \end{aligned} \quad (8.38)$$

In the case of $\pi^+ \rightarrow e^+ \nu_e$, the decay fraction $\Gamma_{\pi \rightarrow e}$ is similar to (8.38) with the change $m_\mu \rightarrow m_e$. The ratio R between the decay fractions is

$$R = \frac{\Gamma_{\pi \rightarrow e}}{\Gamma_{\pi \rightarrow \mu}} = \frac{m_e^2 \left(1 - \frac{m_e^2}{m_\pi^2}\right)^2}{m_\mu^2 \left(1 - \frac{m_\mu^2}{m_\pi^2}\right)^2} \simeq \frac{m_e^2}{m_\mu^2} \cdot \frac{1}{1 - \frac{m_\mu^2}{m_\pi^2}} \simeq 1.27 \cdot 10^{-4}, \quad (8.39)$$

which is in good agreement with the experimental results. The key ingredient of prediction (8.39) is the helicity assignments for the neutrinos and antileptons which is formalized in the so-called $V - A$ theory (Sect. 8.16).

8.11 Strange Particle Decays

Hadrons and leptons are both subject to weak interactions. WIs are usually classified as follows: (1) processes only involving leptons (*leptonic WI*) [8B84]; (2) processes involving only hadrons (*nonleptonic WI*) [8P84]; (3) processes involving hadrons and leptons (*semileptonic WI*) [8V84].

$$\text{leptonic : } \mu^+ \rightarrow e^+ \nu_e \bar{\nu}_\mu, \quad \nu_e e^- \rightarrow \nu_e e^- \quad (8.40)$$

$$\text{semileptonic : } \Delta S = 0 \begin{cases} n \rightarrow p e^- \bar{\nu}_e \\ \bar{\nu}_e p \rightarrow n e^+ \end{cases} \quad \Delta S = 1 \begin{cases} K^+ \rightarrow \pi^0 e^+ \nu_e \\ K^+ \rightarrow \mu^+ \nu_\mu \end{cases} \quad (8.41)$$

$$\text{nonleptonic : } \Delta S = 0 \quad \{ NN \rightarrow NN \} \quad \Delta S = 1 \begin{cases} \Lambda^0 \rightarrow p \pi^- \\ K^+ \rightarrow \pi^+ \pi^0 \end{cases}. \quad (8.42)$$

Furthermore, in semileptonic or nonleptonic processes, decays in which strange particles are not involved ($\Delta S = 0$), or strangeness violating decays with the selection rule $\Delta S = 1$ are observed. The weak decay of strange particles presents some anomalies, whether leptonic, semileptonic or nonleptonic processes are considered.

Leptonic decays. Let us examine the case of some purely leptonic decays:

Decay		Strangeness Change	Lifetime s	$BR = \Gamma_i / \Gamma$
$\pi^- \rightarrow \mu^- \bar{\nu}_\mu$	$\bar{u}d \rightarrow W^- \rightarrow \mu^- \bar{\nu}_\mu$	$\Delta S = 0$	2.6×10^{-8}	100%
$K^- \rightarrow \mu^- \bar{\nu}_\mu$	$\bar{u}s \rightarrow W^- \rightarrow \mu^- \bar{\nu}_\mu$	$\Delta S = 1$	1.27×10^{-8}	63.5%

The K^- lifetime calculation follows the same procedure as that presented in the previous paragraph. Using (8.37) and the Fermi constant G_F , the computed K^- lifetime is about 20 times smaller than the measured one.

To explain this new “strange” behavior, one can imagine that the effective WI coupling constant to be used depends on the quark flavor. In the case of π decay, the d quark is involved. The related weak coupling constant should be $G_d \simeq G_F$ since the π lifetime calculated with the Fermi constant G_F gives an almost correct result. In the case of K decay, the s quark is involved. The effective coupling constant to be used must be such that $G_s < G_d$ in order to obtain the measured K lifetime.

From the measurements of the π , K lifetimes, and from the calculation of the helicity and phase space factors, one obtains

$$\frac{G_s^2}{G_d^2} \simeq 0.05. \quad (8.43)$$

Semileptonic decays. Strange mesons and baryons are also subject to β decays. Examples of the semileptonic decay modes in which both leptons and hadrons are present in the final state are:

		Δm (MeV)	$BR = \Gamma_i/\Gamma$	τ (s)
$\Delta S = 0$	$n \rightarrow p e^- \bar{\nu}_e$	1.29	1	887
	$\Sigma^+ \rightarrow \Lambda^0 e^+ \nu_e$	73.7	0.20×10^{-4}	0.80×10^{-10}
	$\Sigma^- \rightarrow \Lambda^0 e^- \bar{\nu}_e$	81.7	0.57×10^{-4}	1.48×10^{-10}
$\Delta S = 1$	$\Lambda^0 \rightarrow p e^- \bar{\nu}_e$	177.4	8.32×10^{-4}	2.63×10^{-10}
	$\Sigma^- \rightarrow n e^- \bar{\nu}_e$	257.8	1.02×10^{-3}	1.48×10^{-10}
	$\Xi^0 \rightarrow \Sigma^+ e^- \bar{\nu}_e$	125.5	2.7×10^{-4}	2.90×10^{-10}
	$\Xi^- \rightarrow \Lambda^0 e^- \bar{\nu}_e$	205.6	5.63×10^{-4}	1.64×10^{-10}
	$\Xi^- \rightarrow \Sigma^0 e^- \bar{\nu}_e$	128.7	0.87×10^{-4}	1.64×10^{-10}

Antibaryons decay in the charge conjugate states. For all *semileptonic decays*, including those listed above, the relation $\Delta Q = \Delta S$ holds, where $\Delta Q = Q_f - Q_i$ and $\Delta S = S_f - S_i$ are the variation of charge and strangeness of hadrons in the final versus initial state. This implies that in terms of quarks, the process is

$$s \rightarrow W^- u \rightarrow (e^- \bar{\nu}_e) u.$$

Decays that do not satisfy the relation $\Delta Q = \Delta S$ are largely suppressed. Consider, for example, the β decays of Σ^- and Σ^+ and their interpretation in terms of quarks, that is,

$$\Sigma^- \rightarrow n e^- \bar{\nu}_e \quad dds \rightarrow ddu e^- \bar{\nu}_e \quad \Delta S = \Delta Q = 1 \quad (8.44a)$$

$$\Sigma^+ \rightarrow n e^+ \nu_e \quad uus \rightarrow udde^+ \nu_e \quad \Delta S = -\Delta Q = 1. \quad (8.44b)$$

The decay branching ratio of the process (8.44a) is $BR = 1.0 \times 10^{-3}$, while for the decay (8.44b), one has $BR = 5 \times 10^{-6}$. The second decay is therefore largely suppressed (by a factor 5×10^{-3}) compared to the first one. The reason is that in the decay (8.44b), two quarks must change flavor ($u \rightarrow d$, $s \rightarrow u$) and this can only occur through higher order weak interaction diagrams (see Fig. 8.16b).

The Sargent rule (8.18) provides a good approximation for the calculation of the lifetimes of all of these decays. The numerical results obtained using G_F are almost correct for $\Delta S = 0$ decays, but wrong by a factor ~ 20 for $\Delta S = 1$ decays. We can imagine again that in the case of decays without strangeness change, the appropriate constant is G_d , while it is G_s when $\Delta S = 1$. We can estimate the relationship between the two constants using the Σ^- decays

$$\frac{G_s^2}{G_d^2} = \frac{\Gamma(\Sigma^- \rightarrow n e^- \bar{\nu}_e)/\Delta m_{\Sigma n}^5}{\Gamma(\Sigma^- \rightarrow \Lambda^0 e^- \bar{\nu}_e)/\Delta m_{\Sigma \Lambda}^5} = 0.057. \quad (8.45)$$

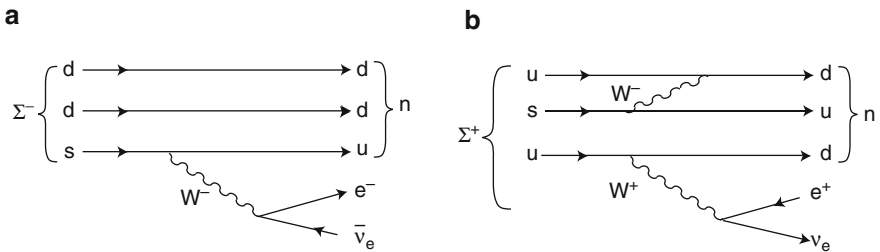


Fig. 8.16 Feynman diagrams for the semileptonic decays (a) $\Sigma^- \rightarrow n e^- \bar{\nu}_e$, (b) $\Sigma^+ \rightarrow n e^+ \nu_e$

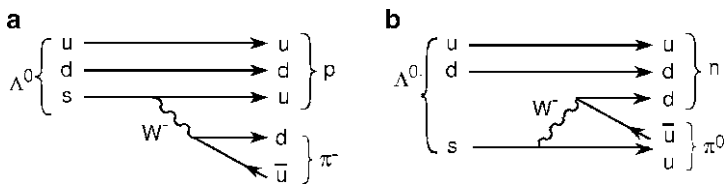


Fig. 8.17 Feynman diagrams for nonleptonic decays (a) $\Lambda^0 \rightarrow p \pi^-$, (b) $\Lambda^0 \rightarrow n \pi^0$, with the exchange of a W^- boson

Even in the case of semileptonic decays, the appropriate coupling constants to be used for $\Delta S = 1$, $\Delta S = 0$ transitions are different. The ratio $G_s^2/G_d^2 \simeq 0.05$ is independent from the transition type between hadrons: *this must therefore reflect a property of the constituent quarks.*

Nonleptonic decays. Strange particle *nonleptonic decays* are characterized by the selection rules $\Delta S = 1$ and $\Delta I = 1/2$ (ΔS is the variation in strangeness, ΔI is the variation in the strong isospin of the involved hadrons). This selection rule corresponds to the quark transition $s \rightarrow u$. Here, the appropriate coupling constant is G_s .

As an example, let us consider the Λ^0 decay shown in Fig. 8.17, for which $\Delta S = S_f - S_i = 1$. To verify that $\Delta I = 1/2$, we need to make some considerations on the branching ratio of the Λ^0 decays in $p\pi^+$ and $n\pi^0$:

$$\begin{aligned} \Lambda^0 &\longrightarrow p\pi^- & BR = (2/3 \cdot \text{phase space factor}) = 0.655, \text{ Exp} = 0.641 \pm 0.005 \\ &\longrightarrow n\pi^0 & BR = (1/3 \cdot \text{phase space factor}) = 0.345, \text{ Exp} = 0.367 \pm 0.005 \\ I = 0 &\longrightarrow I = 1/2. \end{aligned} \tag{8.46}$$

If the final state has $I = 1/2$, the respective branching ratios for the decays in $p\pi^-$ and $n\pi^0$ can be derived from the Clebsch–Gordan coefficients (if $I = 1/2$, one has 2/3 for $p\pi^-$ and 1/3 for $n\pi^0$; if $I = 3/2$, one has 1/3 for $p\pi^-$ and 2/3 for $n\pi^0$), and from a factor which takes into account the small difference in phase space

between $p\pi^-$ and $n\pi^0$. The assignment $I = 1/2$ to the final state is confirmed, and thus $\Delta I = 1/2$. The rule is not absolute since it is broken by the electromagnetic interaction; a small “contamination” of $\Delta I = 3/2$ shall be present in the final state.

This selection rule is explained by assuming that in terms of quarks, the following sequence of “processes” takes place:

$$\Lambda^0 \rightarrow p\pi^- \quad uds \xrightarrow{\text{WI}} udu W^- \xrightarrow{\text{WI+SI}} udu + \bar{u}d \xrightarrow{\text{SI}} p\pi^- \quad (8.47\text{a})$$

$$\Lambda^0 \rightarrow n\pi^0 \quad uds \xrightarrow{\text{WI}} udu W^- \xrightarrow{\text{WI+SI}} udd + \bar{u}u \xrightarrow{\text{SI}} n\pi^0. \quad (8.47\text{b})$$

The corresponding Feynman diagrams with a W^\pm boson exchange are shown in Fig. 8.17.

8.12 Universality of Weak Interactions (II). The Cabibbo Angle

The Puppi triangle (Fig. 8.5) which involves neutron and muon decays, and the μ^- capture by a proton expresses the universality of weak interactions. The extension to strange particles led to the *Dallaporta tetrahedron* where the semileptonic decays $\Sigma^- \rightarrow \Lambda^0 e^- \bar{\nu}_e$, $\Lambda^0 \rightarrow pe^- \bar{\nu}_e$, $\Sigma \rightarrow nev$, shown in Fig. 8.5b, are also included. The “universality” is only approximate because, as we have seen for the $K^+ \rightarrow \mu^+ \nu_\mu$ and $\pi^+ \rightarrow \mu^+ \nu_\mu$ decays, the coupling constants seem quite different, i.e., smaller for K decay. The same situation occurs for the semileptonic decays of strange baryons ($\Lambda^0 \rightarrow pe^- \bar{\nu}_e$, $\Sigma \rightarrow nev_e$, $\Xi \rightarrow \Lambda^0 ev_e$) compared to the neutron decay. Accurate measurements show that the coupling constant obtained from the neutron decay is slightly smaller than that obtained from the muon decay, as can be observed by comparing the values given in (8.14a, b). It should also be noted that various empirical selection rules, $\Delta S = \pm 1$, $\Delta I = 1/2$, $\Delta Q = \Delta S$, indicate some regularity in the decays of strange particles.

The above mentioned experimental facts were brilliantly interpreted by N. Cabibbo in 1964. The leptons are weak interaction eigenstates and quarks are eigenstates of the strong interaction. Cabibbo demonstrated that leptons and quarks are eigenstates of the WI with the following assumptions:

- The coupling of electrons with the weak interaction field is proportional to a *weak charge* g_{ev} ;
- The coupling of muons is proportional to $g_{\mu\nu}$ and is identical to that of electrons: $g_{ev} = g_{\mu\nu}$;
- The coupling of (u, d) quarks generates the transitions with $\Delta S = 0$ and is proportional to g_{ud} ;
- The coupling of (u, s) quarks generates transitions with $\Delta S = 1$ and is proportional to g_{us} .

In a Feynman diagram, the constant corresponding to the particles involved in a vertex must be inserted. The matrix elements of weak transitions (described by the Hamiltonian H_W) involving only leptons (i.e., $|i\rangle = |\nu e\rangle$; $\langle f| = \langle e \nu|$) are proportional to the Fermi constant

$$\langle f | H_W | i \rangle \propto g_{ev}^2 = G_F. \quad (8.48a)$$

The matrix elements of $\Delta S = 0$ semileptonic processes where $|i\rangle = |\bar{\nu}_e u\rangle$; $\langle f| = \langle e^+ d|$ or $|i\rangle = |\nu_e d\rangle$; $\langle f| = \langle e^- u|$ (as in Fig. 8.1b) are

$$\langle f | H_W | i \rangle_{\Delta S=0} \propto g_{ev} g_{ud} = G_d. \quad (8.48b)$$

For $\Delta S = 1$ processes (Fig. 8.16a) where $|i\rangle = |\nu_e s\rangle$; $\langle f| = \langle e^- u|$, one has

$$\langle f | H_W | i \rangle_{\Delta S=1} \propto g_{ev} g_{us} = G_s. \quad (8.48c)$$

The Cabibbo hypothesis (shown qualitatively in Fig. 8.5c) states that the weak interaction is truly universal, as thought before the discovery of strange particles. The universality is expressed by the fact that the WI depends on a single parameter, the Fermi constant G_F . The weak interaction couplings with quarks and leptons occur through the relation

$$G_F = g_{ev}^2 = g_{ud}^2 + g_{us}^2 \longrightarrow g_{ud} = g_{ev} \cos \theta_C; \quad g_{us} = g_{ev} \sin \theta_C. \quad (8.49)$$

In the Cabibbo model, this corresponds to the fact that the quarks involved in the weak interaction are not the flavor eigenstates u, d, s that characterize the strong interaction. The WI quark eigenstates are a linear combination of u, d, s which can be denoted as (u_c, d_c, s_c) . By convention, the quark u is not mixed, so u_c coincides with u . The other quark pair with charge $-1/3$ is mixed through an angle θ_c , compared to ordinary quarks. When Cabibbo wrote his paper, two lepton families and the three quarks u, d, s were known; the weak interaction involves the following “weak doublets:”

$$\begin{pmatrix} v_e \\ e^- \end{pmatrix}, \quad \begin{pmatrix} v_\mu \\ \mu^- \end{pmatrix}, \quad \begin{pmatrix} u \\ d_c \end{pmatrix} = \begin{pmatrix} u \\ d \cos \theta_c + s \sin \theta_c \end{pmatrix} \quad (8.50)$$

where $\theta_c = 0.235 \text{ rad} = 13.5^\circ$ is the *Cabibbo angle*. For each lepton doublet, the weak coupling is specified by the Fermi constant G_F . For transitions involving quarks $u \rightarrow d$ with $\Delta S = 0$, the equivalent constant corresponds to $G_F \cos \theta_c$; for transitions involving quark $s \rightarrow u$ ($\Delta S = 1$), the equivalent constant corresponds to $G_F \sin \theta_c$. **The different value of the effective coupling constants is only due to the quark mixing process to form the WI eigenstates, see Table 8.2.** Since $\sin \theta_c = 0.235$ and $\cos \theta_c = 0.972$, transitions with $\Delta S = 0$ have an effective coupling constant larger than those with $\Delta S = 1$. This explains why G_F^n (Eq. 8.14b) is smaller than G_F^μ (Eq. 8.14a): indeed, what is measured in the neutron decay is the quantity $G_F \cos \theta_c$.

Table 8.2 Couplings for different types of decay ($G_F = G_F^\mu$)

Decay	Quark transitions	Hadronic J^P	ΔS	Coupling
$n \rightarrow p e^- \bar{\nu}_e$	$d \rightarrow u e^- \bar{\nu}_e$	$1/2^+ \rightarrow 1/2^+$	0	$G_F^2 \cos^2 \theta_c$
$p \rightarrow n e^+ \nu_e$ (in ^{14}O)	$u \rightarrow d e^+ \nu_e$	$0^+ \rightarrow 0^+$	0	$G_F^2 \cos^2 \theta_c$
$\pi^- \rightarrow \pi^0 e^- \bar{\nu}_e$	$d \rightarrow u e^- \bar{\nu}_e$	$0^- \rightarrow 0^-$	0	$G_F^2 \cos^2 \theta_c$
$K^- \rightarrow \pi^0 e^- \bar{\nu}_e$	$s \rightarrow u e^- \bar{\nu}_e$	$0^- \rightarrow 0^-$	1	$G_F^2 \sin^2 \theta_c$
$\mu^+ \rightarrow e^+ \nu_e \bar{\nu}_\mu$	—	—	—	G_F^2

The second decay is relative to a proton in a ^{14}O nucleus since free protons do not decay

The value of the Cabibbo angle can be derived by comparing similar $\Delta S = 1$ and $\Delta S = 0$ semileptonic decays. For example, the decays $K^+ \rightarrow \mu^+ \nu_\mu$ ($\propto G_F^2 \sin^2 \theta_c$) and $\pi^+ \rightarrow \mu^+ \nu_\mu$ ($\propto G_F^2 \cos^2 \theta_c$) can be used. They are very similar, except for a quark \bar{s} in K^+ and a quark \bar{d} in π^+ . The ratio of decay fractions gives

$$\frac{\Gamma(K^+ \rightarrow \mu^+ \nu_\mu)}{\Gamma(\pi^+ \rightarrow \mu^+ \nu_\mu)} = \frac{m_K^2 [1 - (m_\mu^2/m_K^2)]^2}{m_\pi^2 [1 - (m_\mu^2/m_\pi^2)]^2} \tan^2 \theta_c. \quad (8.51)$$

Using the π , μ and K masses [P08], the value $\theta_c = (0.235 \pm 0.006)$ is obtained. Today, three different quark families are known (Sect. 8.14) and different methods are used to evaluate the mixing angles. The best value of the Cabibbo angle is $\theta_c = (0.2253 \pm 0.0007)$.

8.13 Weak Interaction Neutral Current

At a fundamental level, the decays and reactions considered thus far are mediated through the exchange of charged W^+ , W^- vector bosons: these processes are weak *charged current* (CC) reactions. The reactions

$$\begin{aligned} \nu_\mu e^- &\rightarrow \nu_\mu e^- \\ \bar{\nu}_\mu e^- &\rightarrow \bar{\nu}_\mu e^- \end{aligned} \quad (8.52)$$

can only occur through the exchange of a neutral boson, the Z^0 (see Fig. 8.18). These are the so-called *weak interaction neutral current* (NC) processes. A contribution due to the WI neutral current is also present in the reaction

$$e^+ e^- \rightarrow q\bar{q}(\ell\bar{\ell}) \quad (8.53)$$

shown in Fig. 8.18b; this will be discussed in detail in Chap. 9. Historically, the NC was introduced to remove mathematical divergences. For example, the lowest

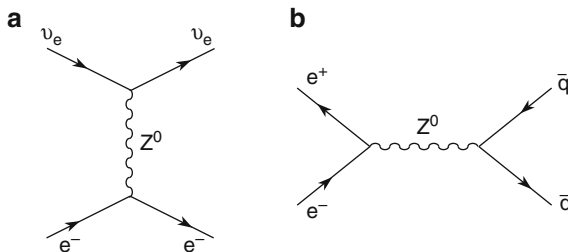


Fig. 8.18 Examples of weak interaction neutral current processes. (a) The Z^0 is exchanged in the t channel: the electric charge of the leptonic current does not change over time. (b) Exchange in the s channel: lepton and antilepton annihilate to form the neutral Z^0 boson which decays into a quark-antiquark pair

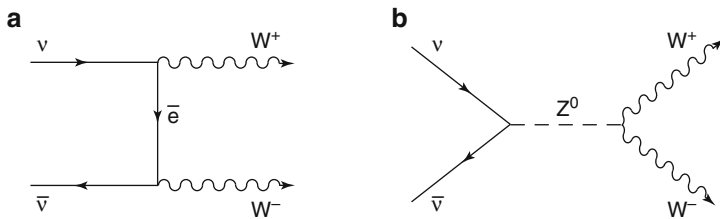


Fig. 8.19 Reaction $\nu\bar{\nu} \rightarrow W^+W^-$: (a) diagram with CC interaction; this diagram gives a divergence that is canceled by the introduction of the NC diagram (b)

order diagram of the reaction $\nu\bar{\nu} \rightarrow W^+W^-$ contains the exchange of an electron which gives rise to a divergence. The divergence is canceled by the introduction of a diagram with a Z^0 vector boson exchange (see Fig. 8.19).

The Z^0 , as the virtual γ , can be exchanged in the t channel (Fig. 8.18a), resulting in processes where the electric charge of interacting particles does not change. For example, NC neutrino-nucleon interaction takes place in the t channel through a Z^0 exchange with a quark (or antiquark) of the nucleon (see Fig. 10.1) which remains unchanged. The interaction can occur with any quark (or antiquark) flavor. If a neutral boson is exchanged in the s channel (Fig. 8.18b), one has an annihilation process $f\bar{f} \rightarrow Z^0$ followed by the creation of a $f'\bar{f}'$ pair. f, f' are fermions; f, f' are antifermions.

The neutral current interaction was discovered in 1977 using a heavy liquid bubble chamber (Gargamelle, CERN) exposed to a beam of high energy muon neutrinos. The following reactions were observed: (i) $\nu_\mu e^- \rightarrow \nu_\mu e^-$: scattering on atomic electrons. The electron in the final state is produced by an invisible particle track. (ii) $\nu_\mu N \rightarrow \nu_\mu + \text{hadrons}$: interactions on nuclei. Only charged particles in the final state are visible (hadrons or their decay products). In both cases, the characteristic signature of a CC interaction, i.e., the presence of a muon, is missing and therefore, the reactions could only proceed via NC.

The ratio between NC and CC cross-sections for high energy neutrinos is $\sigma_{\nu N}^{NC}/\sigma_{\nu N}^{CC} \simeq 0.25$, $\sigma_{\bar{\nu} N}^{NC}/\sigma_{\bar{\nu} N}^{CC} \simeq 0.45$. The neutral currents are not foreseen in the Fermi theory and represent one of the reasons for its extension.

8.14 Weak Interactions and Quark Eigenstates

8.14.1 The WI Hamiltonian and the GIM Mechanism

The K^0 , \bar{K}^0 are hadronic interaction eigenstates. In 1955, Gell–Mann and Pais found that it was possible to form two linear combinations of the neutral K mesons which are CP eigenstates; these correspond to particles which decay in two different CP states

$$|K_1^0\rangle = 1/\sqrt{2}(|K^0\rangle + |\bar{K}^0\rangle); \quad |K_2^0\rangle = 1/\sqrt{2}(|K^0\rangle - |\bar{K}^0\rangle). \quad (8.54)$$

K_1^0 and K_2^0 are two distinct states, that is, linear combinations of strong interaction eigenstates; they have different masses and decay in different ways, for example,

$$|K_1^0\rangle = \frac{1}{\sqrt{2}}(|d\bar{s}\rangle + |s\bar{d}\rangle) \quad CP = +1 \longrightarrow \pi\pi \quad (8.55)$$

$$|K_2^0\rangle = \frac{1}{\sqrt{2}}(|d\bar{s}\rangle - |s\bar{d}\rangle) \quad CP = -1 \longrightarrow \pi\pi\pi. \quad (8.56)$$

We will return to this subject in Sect. 12.2. For the moment, it is important to note that the K^0 e \bar{K}^0 mesons are charged conjugate states with the same mass. The linear combinations K_1^0 and K_2^0 are two different particles with different mass. The mass difference $\Delta m = |m_{K_2^0} - m_{K_1^0}|$ can be calculated in the framework of the quark model, and is proportional to the matrix element that describes the $K^0 \leftrightarrow \bar{K}^0$ transition probability. This is a second order transition, with $\Delta S = 2$: the K^0 has strangeness $S = 1$, while the \bar{K}^0 has $S = -1$. When computed considering only the u, d, s quark contributions, the obtained Δm is much larger than the experimental value. There must be some new phenomenon that prevents transitions *that change the quark flavor, but do not change the electric charge*. This was pointed out in 1970 by Glashow, Iliopoulos and Maiani in the so-called *GIM mechanism* where they proposed the existence of a fourth quark. According to this hypothesis, the properties of the fourth quark (called c , charm) are

1. Electric charge $2/3$, isospin $I = 0$, strangeness $S = 0$, baryon number $B = 1/3$
2. “Charm” quantum number $c = 1$. This is a new quantum number that, like strangeness, is conserved in strong interactions and violated in weak interactions

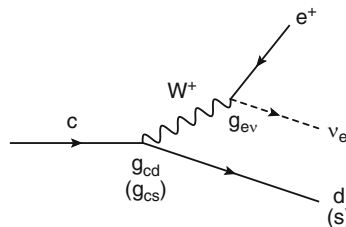
3. It is a weak interaction eigenstate and forms a second quark doublet with the second “rotated” state of the Cabibbo theory: $s_c = s \cos \theta_c - d \sin \theta_c$. With this assumption, a new doublet for the weak interactions is obtained, that is,

$$\begin{pmatrix} c \\ s_c \end{pmatrix} = \begin{pmatrix} c \\ s \cos \theta_c - d \sin \theta_c \end{pmatrix}. \quad (8.57)$$

Let us again consider the weak Hamiltonian H_W appearing in (8.48); it is an operator acting on particle wave functions and consisting of four terms:

- A universal dimensional constant G_F (the same for all particles)
- A combination of (dimensionless) operators O_i which assigns the helicity state preferences of the involved fermions and defines the behavior under the parity operator. The mathematical structure of the O_i operators present in H_W (described in detail in Sect. 8.16) is deduced from the experimental results described in previous sections
- A multiplicative term that takes into account the multiplicity of spin and isospin states available in the final state (the term $m_{i,s}$ defined in Sect. 8.6)
- A (dimensionless) term equal to one if the interaction is purely leptonic; if the interaction is nonleptonic, its value depends on the involved quark flavor

Using the same notations used in (8.48), the semileptonic c quark decay ($\Delta c = 1$, $\Delta Q = 1$) can be described using the GIM mechanism hypothesis:



$$\bar{s}c \equiv \langle (v_e e^+) s | H_W | c \rangle \propto g_{ev} g_{cs} = G_F \cos \theta_c \quad (8.58a)$$

$$\bar{d}c \equiv \langle (v_e e^+) d | H_W | c \rangle \propto g_{ev} g_{cd} = G_F \sin \theta_c. \quad (8.58b)$$

Note the shortening $\bar{s}c$ for the transition probability from a quark c to a quark s (8.58a) and $\bar{d}c$ for the transition from a quark c to d (8.58b). Up to Eq. 8.62c the symbol, e.g., c stands for the wave operator which **destroys** the quark c , while \bar{s} is the operator that **creates** the quark s , and similarly for other quarks. Here, do not confuse the object \bar{s} with the strange antiquark.

In $\Delta c = 1$ charmed meson decays, the $c \rightarrow s$ transitions with coupling $\propto \cos^2 \theta_c$ are dominant with respect to $c \rightarrow d$ transitions, with coupling $\propto \sin^2 \theta_c$.

Let us, for example, consider the transition from an initial d_c or s_c quark into a final \bar{u} or \bar{c} , plus a W^- state. With two quark families, the corresponding term in the Hamiltonian H_W can be written using (8.50) and (8.57) as

$$\begin{aligned}
(\bar{u}, \bar{c}) \begin{pmatrix} d_c \\ s_c \end{pmatrix} &= (\bar{u}, \bar{c}) \begin{pmatrix} d \cos \theta_c + s \sin \theta_c \\ s \cos \theta_c - d \sin \theta_c \end{pmatrix} = (\bar{u}, \bar{c}) \begin{pmatrix} \cos \theta_c & \sin \theta_c \\ -\sin \theta_c & \cos \theta_c \end{pmatrix} \begin{pmatrix} d \\ s \end{pmatrix} \\
&= (\bar{u}, \bar{c}) V_C \begin{pmatrix} d \\ s \end{pmatrix}. \tag{8.59}
\end{aligned}$$

For the first two quark families, the 2×2 V_C mixing matrix only contains one free parameter: the Cabibbo angle. Experimental data on weak transitions of u, d, s, c quarks are consistent with the same value of θ_c . The weak Hamiltonian H_W eigenstates of charge $-1/3$ quarks do not coincide with the d, s strong interaction eigenstates. The charge $2/3$ quarks are unchanged by convention.

8.14.2 Hints on the Fourth Quark from WI Neutral Currents

A fourth quark was also necessary to solve some problems associated with WI neutral currents. The observed NC processes are characterized by the selection rule $\Delta S = 0$. Neutral currents with $\Delta S = 1$ were never observed (Problem 8.18). However, assuming the existence of only the u, d, s quarks, the mechanism which rotates the (d, s) quarks in the NC includes a $\Delta S = 1$ term, that is,

$$\begin{aligned}
(\bar{u}, \bar{d}_c) \begin{pmatrix} u \\ d_c \end{pmatrix} &= (\bar{u}, \bar{d} \cos \theta_c + \bar{s} \sin \theta_c) \begin{pmatrix} u \\ d \cos \theta_c + s \sin \theta_c \end{pmatrix} \\
&= \underbrace{u\bar{u} + (d\bar{d} \cos^2 \theta_c + s\bar{s} \sin^2 \theta_c)}_{\Delta S=0} + \underbrace{(s\bar{d} + \bar{s}d) \sin \theta_c \cos \theta_c}_{\Delta S=1}.
\end{aligned}$$

Each term $u\bar{u}$, $d\bar{d}$, $s\bar{s}$ represents the probability density for the transition from a quark of a given flavor in the initial state toward the same quark flavor plus a Z^0 boson in the final state. Although $s\bar{d}$ and $d\bar{s}$ processes were never observed, the mechanism foresees their existence. With the new doublet (8.57), the neutral current can be rewritten in the form

$$\begin{aligned}
&(\bar{u}, \bar{d}_c) \begin{pmatrix} u \\ d_c \end{pmatrix} + (\bar{c}, \bar{s}_c) \begin{pmatrix} c \\ s_c \end{pmatrix} \\
&= \underbrace{u\bar{u} + c\bar{c} + (d\bar{d} + s\bar{s}) \cos^2 \theta_c + (s\bar{s} + d\bar{d}) \sin^2 \theta_c}_{\Delta S=0} \\
&\quad + \underbrace{(s\bar{d} + \bar{s}d - \bar{s}d - s\bar{d}) \sin \theta_c \cos \theta_c}_{\Delta S=1} \tag{8.60}
\end{aligned}$$

and the term with $\Delta S = 1$ is automatically canceled.

8.14.3 The Six Quarks and the Cabibbo–Kobayashi–Maskawa Matrix

Today, we are aware of six different quarks; the discovery of the heaviest quark is described in Chap. 9. The generalization of (8.59) leads to the following form of the weak interaction current in the quark sector, namely,

$$(\bar{u}, \bar{c}, \bar{t}) \cdot V_{CKM} \begin{pmatrix} d \\ s \\ b \end{pmatrix} \quad (8.61)$$

where the *Cabibbo–Kobayashi–Maskawa matrix* (CKM matrix) V_{CKM} is a 3×3 matrix. In the literature, several parametrizations of the CKM matrix can be found. The form originally proposed by Kobayashi and Maskawa is ($c_i = \cos \theta_i$, $s_i = \sin \theta_i$):

$$\begin{pmatrix} d_c \\ s_c \\ b_c \end{pmatrix} = V_{CKM} \begin{pmatrix} d \\ s \\ b \end{pmatrix}$$

$$V_{CKM} = \begin{pmatrix} c_1 & c_3 s_1 & s_1 s_3 \\ -c_2 s_1 & c_1 c_2 c_3 - s_2 s_3 e^{i\delta} & c_1 c_2 s_3 + c_3 s_2 e^{i\delta} \\ s_1 s_2 & -c_1 c_3 s_2 - c_2 s_3 e^{i\delta} & -c_1 s_2 s_3 + c_2 c_3 e^{i\delta} \end{pmatrix} \quad (8.62a)$$

where $\theta_1, \theta_2, \theta_3$ are three mixing angles and δ is a phase angle (note that some authors use the form $s_1 \rightarrow -s_1$). V_{CKM} can be regarded as a three-dimensional rotation matrix with three Euler angles. In the limit $\theta_2 \simeq \theta_3 \simeq 0$, the matrix only contains the Cabibbo angle. Another standard parametrization is

$$V_{CKM} = \begin{pmatrix} c_{12} c_{13} & s_{12} c_{13} & s_{13} e^{-i\delta_{13}} \\ -s_{12} c_{23} - c_{12} s_{23} s_{13} e^{i\delta_{13}} & c_{12} c_{23} - s_{12} s_{23} s_{13} e^{i\delta_{13}} & s_{23} c_{13} \\ s_{12} c_{23} - c_{12} s_{23} s_{13} e^{i\delta_{13}} & -c_{12} s_{23} - s_{12} c_{23} s_{13} e^{i\delta_{13}} + c_{23} c_{13} \end{pmatrix}. \quad (8.62b)$$

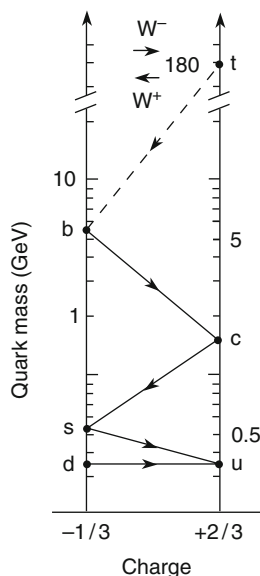
Experimentally, $s_{12} \simeq 0.23$, $s_{13} \simeq 0.003$, $s_{23} \simeq 0.04$. The phase angle δ_{13} , if different from zero, leads to the CP violation in the weak interaction (see Chap. 12). Nowadays, the following parametrization is preferred, that is,

$$\begin{pmatrix} d' \\ s' \\ b' \end{pmatrix} = \begin{pmatrix} V_{ud} & V_{us} & V_{ub} \\ V_{cd} & V_{cs} & V_{cb} \\ V_{td} & V_{ts} & V_{tb} \end{pmatrix} \begin{pmatrix} d \\ s \\ b \end{pmatrix} \quad (8.62c)$$

Table 8.3 Experimental measurements of the V_{ij} elements of the CKM matrix in the form (8.62c). To take into account the small CP violation, V_{ub} must be multiplied by the phase $e^{-i\gamma}$ and V_{td} by $e^{-i\beta}$ [P10]

$V_{CKM} = \begin{pmatrix} 0.97428 \pm 0.00015 & 0.2253 \pm 0.0007 & 0.00347 \pm 0.00016 \\ 0.2252 \pm 0.0007 & 0.97345 \pm 0.00015 & 0.041 \pm 0.001 \\ 0.0086 \pm 0.0003 & 0.040 \pm 0.001 & 0.99915 \pm 0.00005 \end{pmatrix}$

Fig. 8.20 Scheme of the decay chain
 $t \rightarrow b \rightarrow c \rightarrow s \rightarrow u$ and
 $d \rightarrow u$ ($t \rightarrow bW^+$,
 $b \rightarrow cW^-$, $c \rightarrow sW^+$,
 $s \rightarrow uW^-$, $d \rightarrow uW^-$).
Note that the mass of the d, u quarks is ~ 5 and 2.5 MeV,
that is, very small compared
to the other quark masses.
The mass of the t quark is
about 172 GeV [P10]



where d', s', b' are the weak interaction eigenstates; d, s, b are the mass eigenstates of the strong interaction (by convention, the u, c, t states are unchanged). The square of the matrix element V_{ud} gives the probability that an *up* quark turns into a *down* quark, and similarly for the other matrix elements.

Experimentally, the off-diagonal elements of the CKM matrix in the form (8.62c) are small (see Table 8.3); therefore, all mixing angles are small. This implies that the model predicts a specific sequence of decays: starting from the top quark t , the favored decay chain, shown in Fig. 8.20, is

$$t \rightarrow b \rightarrow c \rightarrow s \rightarrow u \quad (8.63)$$

More precisely, one has: $t \rightarrow bW^+$, $b \rightarrow cW^-$, $c \rightarrow sW^+$, $s \rightarrow uW^-$, $d \rightarrow uW^-$.

With the introduction of the CKM mixing, quarks and leptons have the same coupling for the weak interactions: this is the so-called *lepton-quark universality*. The CKM matrix elements cannot be derived from the theory: they are *free*

parameters in the Standard Model (Chap. 11). The CKM elements are experimentally determined [P10]: (1) V_{ud} from the ratio of the neutron decay with respect to the muon decay; (2) V_{us} from the $K^+ \rightarrow \pi^0 e^+ \nu_e$, $K_L^0 \rightarrow \pi^\pm e^\mp (\bar{\nu}_e)$ decays; (3) V_{cd} from charmed particle production in collisions with the d valence quark; (4) V_{cs} from the width of $\Gamma(D \rightarrow \bar{K} e^+ \nu_e)$ and from the hadronic decays of the W^\pm ; (5) V_{cb} from the decay rate of $B^0 \rightarrow D^{*+} \ell^- \bar{\nu}_\ell$.

8.15 Discovery of the W^\pm and Z^0 Vector Bosons

The CERN Large Electron Positron collider (LEP), which operated from 1989 to 2001 (Chap. 9), was originally designed and built for the discovery of the weak interactions W^\pm, Z^0 vector bosons. The LEP made many high precision measurements of weak and electromagnetic interactions (electroweak interaction, Chap. 11), including that of the vector boson masses. However, the discovery of the W^\pm, Z^0 was anticipated in 1983 by a phenomenal intuition of C. Rubbia, with the transformation of the CERN SPS into a collider machine (named $Spp\bar{p}S$). When protons and antiprotons interact at high energy, a $q\bar{q}$ annihilation takes place, generating real (on mass shell) W^\pm or Z^0 bosons. The problem of accumulating a large enough number of \bar{p} was solved by a technique (*stochastic cooling*) due to S. van der Meer (with C. Rubbia, Nobel laureate in 1994). The W^\pm and Z^0 bosons were observed through the following elementary processes:

$$u\bar{d} \rightarrow W^+ \rightarrow e^+ \nu_e, \rightarrow \mu^+ \nu_\mu \quad (8.64a)$$

$$d\bar{u} \rightarrow W^- \rightarrow e^- \bar{\nu}_e, \rightarrow \mu^- \bar{\nu}_\mu \quad (8.64b)$$

$$\left\{ \begin{array}{l} u\bar{u} \\ d\bar{d} \end{array} \right\} \rightarrow Z^0 \rightarrow e^+ e^-, \rightarrow \mu^+ \mu^- \quad (8.64c)$$

In these processes, a quark of the proton annihilates with an antiquark of the antiproton (Problem 10.6), producing a W^+ , a W^- or a Z^0 which are observed through their leptonic decays. These leptonic channels are relatively easy to experimentally observe, see Fig. 8.21. The energy necessary to produce a real W^\pm or Z^0 at rest is $\sqrt{s} \sim m_W, m_Z$. If proton-proton collisions were used, the annihilating antiquark must come from the “sea” (see Chap. 10).

Experimentally [8G84], the observed reactions were

$$p\bar{p} \rightarrow W^+ + X\dots, \quad W^+ \rightarrow e^+ \nu_e$$

$$p\bar{p} \rightarrow Z^0 + X\dots, \quad Z^0 \rightarrow e^+ e^-.$$

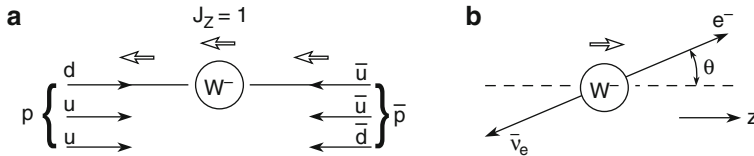


Fig. 8.21 Observation of the W^- vector boson at the CERN $S\bar{p}pS$ collider in 1983. At a fundamental level, the process is $\bar{u}d \rightarrow W^- \rightarrow e^-\bar{\nu}_e$. (a) $p\bar{p}$ collision with a \bar{u} quark of the antiproton that annihilates with a d quark of the proton producing a W^- boson almost at rest; (b) the W^- vector boson decays in $e^- + \bar{\nu}_e$

The resulting cross-sections were evaluated by integrating the cross-sections for the elementary $q\bar{q}$ processes, each described by a Breit-Wigner formula, see Sect. 9.3.2. For the production of a W^+ decaying into an $e^+\nu_e$ pair, one has

$$\sigma(\bar{u}d \rightarrow W^+ \rightarrow e^+\nu_e) = \frac{1}{N_c} \frac{4\pi\lambda^2 \Gamma_{\bar{u}d} \Gamma_{ev}/4}{(2s_d + 1)(2s_u + 1)[(E - M_W)^2 + \Gamma^2/4]} \frac{2J + 1}{3} \quad (8.65)$$

where λ is the de Broglie wavelength in the c.m. of colliding quarks; Γ , $\Gamma_{\bar{u}d}$, Γ_{ev} are the total and partial widths (for $W \rightarrow \bar{u}d$, $W \rightarrow ev$), and $s_d = s_u = 1/2$ are the quark spins. Only states with defined helicity are involved: left-handed fermions and right-handed antifermions. The spin multiplicity for the W is $(2J + 1)/3 = 3/3 = 1$. N_c is the color factor and $1/N_c = 1/3$ is the probability that a quark of the proton “matches” an antiquark of the antiproton. At the energy $E = M_W$, there is a maximum, that is,

$$\sigma_{max}(\bar{u}d \rightarrow W^+ \rightarrow e^+\nu_e) = \frac{4\pi\Gamma_{\bar{u}d}\Gamma_{ev}}{3M_W^2\Gamma^2} = \frac{\pi}{36M_W^2} \simeq 5.2 \text{ nb}, \quad (8.66)$$

using $M_W = (80.22 \pm 0.26) \text{ GeV}$, a color factor of three for $W \rightarrow \bar{u}d$, $c\bar{s}$, $t\bar{b}$ and one for $W \rightarrow ev_e$, $\mu\nu_\mu$, and $\tau\nu_\tau$ and $\Gamma_{\bar{u}d}/\Gamma = 1/4$, $\Gamma_{ev}/\Gamma = 1/12$.

The cross-section for the processes (8.64c) involves the weak neutral current which is (Chap. 11) about ten times smaller than the cross-sections of reactions (8.64a, b). Both the W^\pm , Z^0 production and leptonic decays are rare processes, at the level of 10^{-8} – 10^{-9} of the total number of events. The total proton-antiproton cross-section is $\sigma_t(p\bar{p}) \simeq 60 \text{ mb}$. These events (called *minimum bias events*) give rise to final state hadrons with a low transverse momentum, Sect. 10.7. The W^\pm and Z^0 leptonic decays are relatively easy to detect because the leptons have a high transverse momentum, $p_t \leq M_W/2 \simeq 40 \text{ GeV}/c$, without any appreciable background from minimum bias events.

The W vector bosons couple with fermions/antifermions having spin antiparallel/parallel to the momentum direction (e.g., left-handed electrons, e_L^- , or

right-handed positrons, e_R^+). The W bosons do not couple with either the e_L^- P -conjugate particle, the e_R^- , or with the C -conjugate particle, the e_L^+ . However, the vector bosons couple with the e_L^- CP -conjugate state, the e_R^+ .

8.16 The V-A Theory of CC Weak Interaction

The observation of the preferred W^\pm coupling with LH fermions (and RH antifermions) and of the parity violation in weak interactions imposes some conditions on the WI Hamiltonian. For spin 1/2 particles, the appropriate wave functions are four-component spinors that satisfy the Dirac equation. Below, we describe the weak interaction developed in 1957 by Feynman and Gell–Mann ($V - A$ theory) as an extension of the Fermi theory. The basic idea is formalized in analogy with the electromagnetic interaction: the amplitude of the process is proportional to the four-vector current density. The $V - A$ theory does not include the neutral currents, nor the finite masses of the vector bosons. These features are included in the electroweak theory of the Standard Model, presented in Chap. 11, which enlarges the $V - A$ theory.

8.16.1 Bilinear Forms of Dirac Fermions

Electromagnetic interaction [A89]. We need to extend the definition of the matrix element (4.29) obtained for the EM interaction without the assumption that fermions are described by Dirac 4-spinors (see Appendixes A.3 and A.4, which should be read before continuing with this section). When the Dirac theory is considered, the matrix element M_{if} for the transition probability can be represented as the product of two “electromagnetic currents.”

Consider, for instance, the $e^- \mu^- \rightarrow e^- \mu^-$ elastic scattering; the matrix element of this process can be written as

$$M_{if}(e^- \mu^- \rightarrow e^- \mu^-) \propto \frac{\alpha_{EM}}{q^2} (\bar{\psi}_e \gamma^\mu \psi_e)(\bar{\psi}_\mu \gamma^\nu \psi_\mu) = \frac{\alpha_{EM}}{q^2} J_\mu J^\mu. \quad (8.67)$$

The transition $e^- \rightarrow e^-$ (electron *current*) is described by $(\bar{\psi}_e \gamma^\mu \psi_e)$ and the muon *current* $\mu^- \rightarrow \mu^-$ by $(\bar{\psi}_\mu \gamma^\nu \psi_\mu)$. The electromagnetic interaction (EM) has a vector (V) nature and the operators which relate the initial, and the final 4-spinors ψ are the Dirac γ^μ matrices. The interaction between electric charges depends on α_{EM} and occurs through a virtual photon exchange; these, as we already know, introduce the propagator $\propto \frac{\alpha_{EM}}{q^2}$, where q is the transferred four-momentum. The particle currents can be now shortened by the symbol J^μ (where the index μ indicates that the quantity is a four-vector: $J^\mu = (J^0, \vec{J})$, with $\vec{J} = (J^1, J^2, J^3)$) regardless of

whether it is due to an electron or a muon; indeed, the EM interaction only depends on the electric charge.

In the case of electron scattering on a proton, the EM matrix element is

$$M_{if}(e^- p \rightarrow e^- p) \approx \frac{\alpha_{EM}}{q^2} J_\mu J_{baryonic}^\mu. \quad (8.68)$$

The current due to the proton is denoted by $J_{baryonic}^\mu$; the effect of the composite structure of the proton shall be taken into account.

The *vector* nature of the EM interaction should now be explicitly introduced. For this reason, we may indicate the vector current in (8.67) as $J_1^\mu = V_1^\mu$ and $J_2^\mu = V_2^\mu$:

$$M_{if}(e^- \mu^- \rightarrow e^- \mu^-) \propto \frac{\alpha_{EM}}{q^2} J_\mu J^\mu = \eta_{\mu\nu} \frac{\alpha_{EM}}{q^2} V_1^\mu V_2^\nu \quad (8.69)$$

where $\eta_{\mu\nu}$ is the metric tensor (Appendix A.3). The explicit form is

$$\eta_{\mu\nu} V_1^\mu V_2^\nu = V_1^0 V_2^0 - \vec{V}_1 \cdot \vec{V}_2. \quad (8.70)$$

Extension to the WI [8Pu84]. To extend the concept of *current* to weak interactions, it should be written in the more general form, that is,

$$J^\mu = \bar{\psi} O_i \psi. \quad (8.71)$$

$J^\mu = (J^0, \vec{J})$, where $\vec{J} = (J^1, J^2, J^3)$. O_i is the operator that defines the interaction type; it is a combination of Dirac γ^μ matrices. The bilinear form (8.71) behaves under Lorentz transformations as a scalar quantity (S), a pseudoscalar (P), a vector (V), an axial-vector (A) and a tensor (T) according to the chosen operator O_i , where the index i can assume the values $i = S, P, V, T, A$. The relativistic invariance properties (Problem 8.15) establish specific restrictions on the possible shape of the current, as shown in the following table:

	Current	Number of components	Behavior under Parity	Relative helicity of fermion and antifermion
S Scalar	$\bar{\psi} \psi$	1	+	Same
V Vector	$\bar{\psi} \gamma^\mu \psi$	4	Spatial part: -	Opposite
T Tensor	$\bar{\psi} \sigma^{\mu\nu} \psi$	6		Same
A Axial-vector	$\bar{\psi} \gamma^\mu \gamma^5 \psi$	4	Spatial part: +	Opposite
P Pseudoscalar	$\bar{\psi} \gamma^5 \psi$	1	-	-

The operator of an interaction which occurs through the exchange of spin 1 particles (like the photon or the massive vector bosons W^\pm, Z^0) may have a vector or axial-vector structure. We shall show below that if the interaction conserves

parity, it must be either purely vector or purely axial-vector. If parity is conserved, vector bosons equally couple with LH and RH particles.

Parity operator. In Appendix A.4, we show that under the parity operator P , the four-dimensional spinor ψ transforms as

$$\psi \xrightarrow{P} \gamma^0 \psi. \quad (8.72)$$

The matrix γ^0 allows the inversion of the spatial coordinates corresponding to the parity operation. For $\bar{\psi} = \psi^+ \gamma^0$, one has the transformation $\bar{\psi} \xrightarrow{P} (\gamma^0 \psi)^+ \gamma^0 = \psi^+ \gamma^0 \gamma^0 = \bar{\psi} \gamma^0$.

Vector current. The vector current, for example, the electromagnetic $V^\mu = \bar{\psi} \gamma^\mu \psi$, transforms under parity as

$$\bar{\psi} \gamma^\mu \psi \xrightarrow{P} (\bar{\psi} \gamma^0) \gamma^\mu (\gamma^0 \psi). \quad (8.73a)$$

For time and space coordinates separately, one has

$$\bar{\psi} \gamma^0 \psi \xrightarrow{P} (\bar{\psi} \gamma^0) \gamma^0 (\gamma^0 \psi) = \bar{\psi} \gamma^0 \psi \quad (8.73b)$$

$$\bar{\psi} \gamma^k \psi \xrightarrow{P} (\bar{\psi} \gamma^0) \gamma^k (\gamma^0 \psi) = -\bar{\psi} \gamma^k \psi \quad (8.73c)$$

with $k = 1, 2, 3$. The spatial components change sign; the time component does not: $(V^0, \vec{V}) \xrightarrow{P} (V^0, -\vec{V})$. Four-vectors V^μ which transform in this way are vector-like. Equation 8.70 transforms under parity as

$$V_1^0 V_2^0 - \vec{V}_1 \vec{V}_2 \xrightarrow{P} V_1^0 V_2^0 - (-\vec{V}_1) (-\vec{V}_2) = V_1^0 V_2^0 - \vec{V}_1 \vec{V}_2. \quad (8.74)$$

The matrix element of electromagnetic interaction does not change under the parity operator. QED is a vector theory (V) which conserves parity.

Axial current (pseudovector). Let us now consider an axial current of the form

$$A^\mu = \bar{\psi} \gamma^\mu \gamma^5 \psi. \quad (8.75)$$

Note that the γ^5 and γ^μ matrices anticommute: $\gamma^5 \gamma^\mu = -\gamma^\mu \gamma^5$. The A^μ current transforms under parity as

$$\bar{\psi} \gamma^\mu \gamma^5 \psi \xrightarrow{P} (\bar{\psi} \gamma^0) \gamma^\mu \gamma^5 (\gamma^0 \psi). \quad (8.76)$$

For time and space coordinates separately, one has

$$\bar{\psi} \gamma^0 \gamma^5 \psi \xrightarrow{P} (\bar{\psi} \gamma^0) \gamma^0 \gamma^5 (\gamma^0 \psi) = -\bar{\psi} \gamma^0 \gamma^5 \psi \quad (8.77a)$$

$$\bar{\psi} \gamma^k \gamma^5 \psi \xrightarrow{P} (\bar{\psi} \gamma^0) \gamma^k \gamma^5 (\gamma^0 \psi) = \bar{\psi} \gamma^k \gamma^5 \psi \quad (8.77b)$$

with $k = 1, 2, 3$. The time component changes sign, the spatial components do not: $(A^0, \vec{A}) \xrightarrow{P} (-A^0, \vec{A})$, where $\vec{A} = (A^1, A^2, A^3)$. The four-vectors A^μ which transform in this way are known as axial-vectors (see Table 6.2). The matrix element based on axial currents transforms under parity as

$$M_{if} \propto A_1^0 A_2^0 - \vec{A}_1 \vec{A}_2 \quad (8.78)$$

$$\xrightarrow{P} M_{if} \propto (-A_1^0)(-A_2^0) - \vec{A}_1 \vec{A}_2 = A_1^0 A_2^0 - \vec{A}_1 \vec{A}_2. \quad (8.79)$$

The dot product of two axial-vectors is still invariant under parity.

Vector axial current. An operator consisting of a mixture of V and A is not invariant under parity. The matrix element of a $V - A$ current is

$$M_{if} \propto \eta_{\mu\nu} (V_1^\mu - A_1^\mu) (V_2^\mu - A_2^\mu) \quad (8.80)$$

$$= (V_1^0 - A_1^0)(V_2^0 - A_2^0) - (\vec{V}_1 - \vec{A}_1)(\vec{V}_2 - \vec{A}_2). \quad (8.81)$$

Under parity, M_{if} transforms as

$$\begin{aligned} M_{if} &= (V_1^0 - A_1^0)(V_2^0 - A_2^0) - (\vec{V}_1 - \vec{A}_1)(\vec{V}_2 - \vec{A}_2) \\ \xrightarrow{P} M_{if} &= (V_1^0 + A_1^0)(V_2^0 + A_2^0) - (-\vec{V}_1 - \vec{A}_1)(-\vec{V}_2 - \vec{A}_2) \\ &= (V_1^0 + A_1^0)(V_2^0 + A_2^0) - (\vec{V}_1 + \vec{A}_1)(\vec{V}_2 + \vec{A}_2). \end{aligned}$$

Under parity, the matrix element transforms differently than a simple change of sign of the space or time components. An observable constructed from vector and axial-vector quantities (here, $V - A$) changes, i.e., it is not conserved under a parity transformation.

8.16.2 Current–Current Weak Interaction

The experimental data described in previous sections of this chapter unequivocally indicate that the weak interaction vertex (with variation of the lepton electric charge) is achieved through the exchange of a W^\pm vector boson and that it has a $V - A$ structure. The $V - A$ choice (for example, with respect to $V + A$ or T) was guided by experimental considerations, for example, the decay of charged pions.

For the reaction $\nu_e n \rightarrow e^- p$ (Fig. 8.3), we can apply the current-current formulation in order to write a matrix element with the same form as in the EM case (8.68); the weak current J^μ must be necessarily different. The $\nu_e n \rightarrow e^- p$ process is mediated by the W^\pm exchange and one can hypothesize that the process arises through a $n \rightarrow p$ transition (described by $J_{baryonic}$), and a $\nu_e \rightarrow e^-$ transition (described by $J_{leptonic}$). By analogy with (8.68c), the WI matrix element is

$$M_{if} = G_F \cdot J_{leptonic} J_{baryonic} = G_F \eta_{\mu\nu} J_l^\mu J_b^\nu. \quad (8.82)$$

The weak leptonic and hadronic currents can be written in the form

$$J_{leptonic} = \bar{\psi}_e O_i \psi_v; \quad J_{baryonic} = \bar{\psi}_p O_i \psi_n. \quad (8.83)$$

Let us analyze the leptonic current first.

Leptonic weak current. In the interaction vertex of the leptonic current of Fig. 8.3, an electron neutrino **disappears** and an electron **appears**. The most general form of the leptonic current must take into account its vector or axial-vector character; it can be written as

$$J_{leptonic} \equiv J_l^\mu = (c_V V_l^\mu + c_A A_l^\mu) \quad (8.84)$$

where V^μ, A^μ are respectively the vector and axial-vector currents, and c_V, c_A are two numerical constants. However, only the choice

$$c_V = -c_A = 1 \quad (8.85)$$

explains the observed phenomena described above, for example, the parity nonconservation in cobalt decay (Sect. 8.8), the helicity of the neutrino (Sect. 8.9) and the branching ratios of pion decay in muons and electrons (Sect. 8.10). Assuming the quoted values of c_V, c_A , Eq. (8.84) can be explicitly written as

$$J_l^\mu = \bar{\psi}_e \gamma^\mu \psi_v - \bar{\psi}_e \gamma^\mu \gamma^5 \psi_v = \bar{\psi}_e \gamma^\mu (1 - \gamma^5) \psi_v. \quad (8.86)$$

With the following property of the γ matrices:

$$\gamma^\mu (1 - \gamma^5) = \frac{1}{2} (1 + \gamma^5) \gamma^\mu (1 - \gamma^5), \quad (8.87)$$

Equation 8.86 can be written as

$$J_l^\mu = 2 \bar{\psi}_e \left(\frac{1 + \gamma^5}{2} \right) \gamma^\mu \left(\frac{1 - \gamma^5}{2} \right) \psi_v = 2 (\bar{\psi}_e)_L \gamma^\mu (\psi_v)_L. \quad (8.88)$$

In the latter form, the leptonic WI charged current is formally analogous to that for an EM photon exchange. The important difference is that **only left-handed**

fermions $(\psi)_L$ couple with the W^\pm vector bosons. It is easy to show that right-handed antifermions also couple with the W^\pm . In addition, ψ_v can be considered as the wave operator which **destroys** the neutrino, while $\bar{\psi}_e$ is the operator that **creates** the electron.

Weak baryonic current. Let us turn to the description of the baryonic part of (8.82). In principle, transitions that do not change the nuclear angular momentum ($\Delta J = 0$, Fermi transitions) can be associated with scalar (S) and vector (V) currents. T, A interactions may instead produce a nuclear spin variation $\Delta J = 1$, and can therefore describe the Gamow–Teller transitions. The P (pseudoscalar) interaction contains a term v/c where v is the nucleon velocity; in nuclear decay, one has $v \ll c$; thus, P does not give an important contribution to the transition probability. Moreover, in the case of the pion decay (Sect. 8.10), the P interaction would give a helicity factor equal to $(1 + v_\mu/c)$, which would lead to the ratio of branching ratios defined in (8.39) equal to $R = 5.5$, in complete disagreement with the experimental results.

In terms of elementary constituents, protons and neutrons are made of spin 1/2 fermions (quarks) which, regarding their spinorial nature, have characteristics similar to those of the leptons. One may assume that the baryonic weak current operators are composed of a linear combination of V, A terms. This was experimentally confirmed from radioactive decays, the analysis of the β decay spectra, the study of the correlations between the electron and neutrino momenta, and the nuclear lifetime measurements (see Sect. 8.6).

As shown in Fig. 8.3c, the baryonic current is actually considered as a transition from a quark d to a quark u (with a variation of one unit of electric charge), $d \rightarrow u$; by neglecting the spectator quark contribution, the baryonic current can be written in analogy to (8.86), that is,

$$J_{baryonic} \equiv J_b^\mu = g_V \bar{\psi}_u \gamma^\mu \psi_d + g_A \bar{\psi}_u \gamma^\mu \gamma^5 \psi_d \quad (8.89)$$

where g_V, g_A are vector and axial-vector coupling constants which can be written as

$$g_V = \cos \theta_C \cdot c_V \quad (8.90a)$$

$$g_A = \cos \theta_C \cdot \lambda \cdot c_A \quad (8.90b)$$

where θ_C is the Cabibbo angle (see Sect. 8.12) and c_V, c_A are the respective couplings with the vector and axial-vector components of the current. Assuming the universality of fermions, one has $c_V = -c_A = 1$ as in (8.85).

The constant λ appearing in (8.90b) can be calculated in the 4-spinors Dirac theory, and is $\lambda = -5/3$ [P95]. If we assume that there is no interference between the vector and axial-vector amplitudes, the total contribution to the transition probability (8.82) is

$$|\mathcal{M}|^2 \equiv |M_{if}|^2/G_F^2 = (g_V^2 + 3g_A^2) \quad (8.91)$$

where the factor three in the axial part takes into account the spin 1 state multiplicity (the factor is $m_{i,s}$ defined in Sect. 8.6). This is the exact term that should be included in the formula for neutron decay (8.11).

If we assume that the Fermi constant G_F is known from the muon decay, the quantity $(g_V^2 + 3g_A^2)$ can be determined from the neutron lifetime measurements (as the kinematic factors are known). To separate g_V from g_A , a second quantity must be independently measured. The asymmetry in the decay of polarized neutrons [P10] was chosen. The combination of these two measurements gives

$$\lambda \equiv \frac{g_A}{g_V} = -1.267 \pm 0.004. \quad (8.92)$$

This value should be compared with that of (8.26); it confirms (given the value of the Cabibbo angle θ_C) that $c_V = 1$. Note that the measured values of λ are not exactly those expected for point-like Dirac particles ($\lambda = -1.666$). This is due to the presence of strongly interacting spectator quarks that change the spin dependent part of the interaction. This induces some effects on the axial-vector component of the weak baryonic current.

In general, it is expected⁵ that in leptonic decays (e.g., that of the muon), one has $c_A/c_V = \lambda = -1$. In processes involving hadrons, the perturbation due to the strong interaction slightly changes the λ value: in the $\Delta S = 0$ $n \rightarrow pe^- \bar{\nu}_e$ decay, $\lambda = -1.27$, while in the $\Delta S = 1$ decay, $\Lambda^0 \rightarrow pe^- \bar{\nu}_e$, it is $\lambda = -0.69$.

⁵This part of the weak interaction theory is called PCAC, that is, Partially Conserved Axial-vector Current [8V84].

Chapter 9

Discoveries in Electron-Positron Collisions

9.1 Introduction

The first e^+e^- colliders were completed in the 1960s at the Italian National Laboratories of Frascati with the small storage ring AdA followed by Adone (i.e., “big AdA”) at $\sqrt{s} = 3\text{ GeV}$. A series of electron-positron colliders were successively built in the U.S., Europe, Japan, Russia and China. A major motivation for the construction of higher energy e^+e^- colliders came from the discovery of the J/ψ particle at SLAC (Stanford, USA) in 1974. This meson is made of a $q\bar{q}$ pair, where q is the fourth type of quark, that is, the *charm*. Previously, e^+e^- collisions provided the first experimental indication of the quark color quantum number. In 1977 the third lepton family (with the τ lepton) was discovered always at SLAC, immediately after the observation at Fermilab of the third family of quarks (with the *bottom* quark). In this chapter, we shall discuss this series of discoveries. Finally, high-precision measurements of the parameters of the electroweak theory and a thorough verification of the Standard Model have been performed since 1989 by the four LEP experiments at CERN (ALEPH, DELPHI, L3 and OPAL) and the SLD experiment at Stanford. These experiments, together with those at DESY and at the Fermilab $\bar{p}p$ collider, represented a new era in terms of the size, complexity, accuracy and the number of physicists participating in a single experiment. A further increase is now observed for the LHC experiments.

Apart from hadrons, which are made of subconstituent quarks, electron and positron are “fundamental” objects. For this reason, e^+e^- collisions are easier to analyze compared to hadron-hadron and lepton-hadron collisions. At high energies, the basic e^+e^- interactions are

$$e^+e^- \rightarrow f\bar{f} \quad (9.1a)$$

$$\rightarrow GG'. \quad (9.1b)$$

In (9.1a), the fermion-antifermion pair is either a charged lepton pair (e^-e^+ , μ^- , $\tau^-\tau^+$), a neutral lepton pair ($\nu_e\bar{\nu}_e$, $\nu_\mu\bar{\nu}_\mu$, $\nu_\tau\bar{\nu}_\tau$), or a quark-antiquark pair ($u\bar{u}$, $d\bar{d}$, $s\bar{s}$, $c\bar{c}$, $b\bar{b}$); the $t\bar{t}$ pair cannot be produced at current e^+e^- colliders. Each quark or antiquark *hadronizes* in a hadron jet which is better identified when the energy of the colliding e^+e^- is higher. The quark and/or the antiquark can radiate one (or more) energetic gluon, resulting in a third (or more) jet. The fermion-antifermion pair production proceeds through the exchange of a γ or a Z^0 in the so-called *s* channel (see Fig. 9.2).

In the process $e^+e^- \rightarrow GG'$, the Gauge boson G is either a γ , a W^\pm , or a Z^0 . Note that for $G = \gamma$ or Z^0 , $G = G'$. For $G = W$, one has $GG' = W^+W^-$.

At LEP, the case $G = \gamma$ and the processes $e^+e^- \rightarrow W^+W^-$, $e^+e^- \rightarrow Z^0Z^0$ have been studied in great detail. The weak interaction vertex $Z^0W^+W^-$ was studied for the first time at LEP2, i.e., the LEP operating phase in which the c.m. energy was increased to 209 GeV.

The processes involving the exchange of photons are well described by quantum electrodynamics (QED). The inclusion of the Z^0 exchange requires the weak interaction and the interference between the two forces. At energies close to m_{Z^0} , the electromagnetic and weak interactions are unified into the electroweak interaction (see Chap. 11).

Some processes are due to a single type of interaction. For example, the reaction

$$e^+e^- \rightarrow \gamma\gamma \quad (9.2a)$$

is only due to the *Electromagnetic Interaction* (“EM”), while the reaction

$$e^+e^- \rightarrow \nu\bar{\nu} \quad (9.2b)$$

is only due to the *Weak Interaction* (“WI”). For the process ($\ell = \text{lepton}$)

$$e^+e^- \rightarrow \ell^+\ell^-, \quad (9.2c)$$

both the weak and the EM interactions must be considered. For $e^+e^- \xrightarrow{\text{WI+EM}} q\bar{q} \xrightarrow{\text{SI}} \text{hadrons}$, the *Strong Interaction* (“SI”) must be added for the quark hadronization. The process $e^+e^- \rightarrow q\bar{q} \rightarrow \text{two hadronic jets}$ can be regarded as one of the best manifestations of quark existence; this is also true for the reaction $e^+e^- \rightarrow q\bar{q} \rightarrow q\bar{q}g \rightarrow \text{three hadronic jets}$ for the existence of gluons.

In the first part of the chapter, we shall analyze the e^+e^- collisions to explain the cross-sections shown in Fig. 9.1a up to a c.m. energy of about 30 GeV. Then, we shall focus on the e^+e^- collisions at energies close to the Z^0 peak, using mainly information from the LEP collider at CERN (LEP phase 1, LEP1). During this period, the c.m. energy of the colliding particles was around the Z^0 mass (i.e., below 100 GeV). With about 18 million recorded events, the Z^0 peak characteristics were optimally studied, yielding a systematic and high-precision study of the electroweak interaction. Finally, we shall present the results obtained in the second phase of LEP operation (LEP2) with c.m. energies up to 209 GeV.

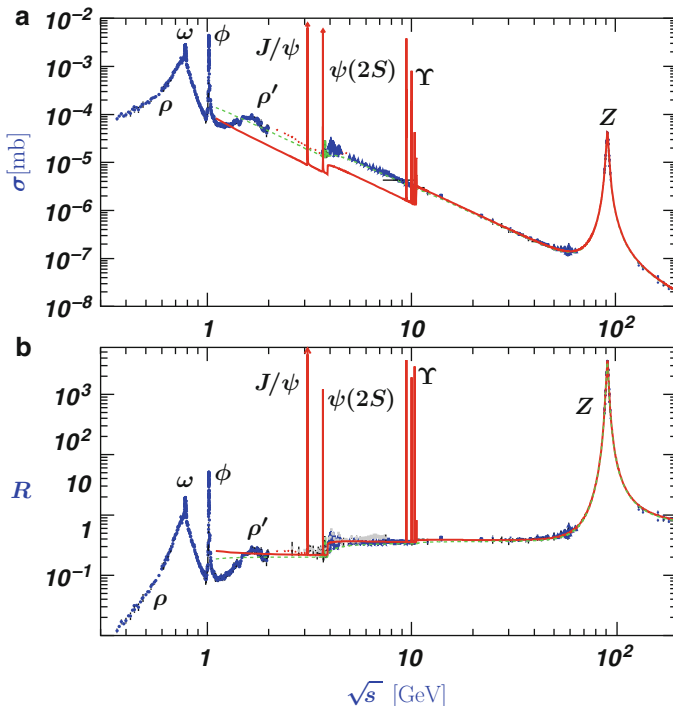


Fig. 9.1 (a) Cross-section of the process $(e^+e^- \rightarrow q\bar{q} \rightarrow \text{hadrons})$ as a function of the center-of-mass (c.m.) energy. (b) Ratio $R = [\sigma(e^+e^- \rightarrow \text{hadrons})]/[\sigma(e^+e^- \rightarrow \mu^+\mu^-)]$ as a function of the c.m. energy [P08]

9.2 Electron-Positron Cross-Section and the Determination of the Number of Colors

Figure 9.1a shows the cross-section for the process $e^+e^- \rightarrow \text{hadrons}$ as a function of the c.m. energy. The experimental points (drawn up to a c.m. energy of about 200 GeV) are the results of a large number of measurements made with different experiments at various e^+e^- colliders. The purely EM cross-section decreases regularly with increasing c.m. energy, as expected from the Coulomb interaction between point-like objects. The peaks are due to the reactions $e^+e^- \rightarrow \gamma \rightarrow \text{vector meson} \rightarrow \text{hadrons}$. The vector mesons made of quark-antiquark pair and with the same photon quantum numbers can be easily studied by analyzing the hadronic cross-section $\sigma(e^+e^- \rightarrow \text{hadrons})$.

The first two peaks are due to the ρ^0 , ω^0 meson resonances. In terms of quarks, they are resonances of the $u\bar{u}$ and $d\bar{d}$ type. The third peak is due to the $\phi = s\bar{s}$ resonance. The fourth peak is also a resonance, the $J/\psi = c\bar{c}$, due to a new quark flavor. Finally, the last peaks are due to a fifth quark flavor, forming the $\Upsilon = b\bar{b}$ and its excited states.

Fig. 9.2 Lowest order Feynman diagrams for $e^+e^- \rightarrow \mu^+\mu^-$, (a) with a virtual photon γ exchange, and (b) with a Z^0 boson exchange

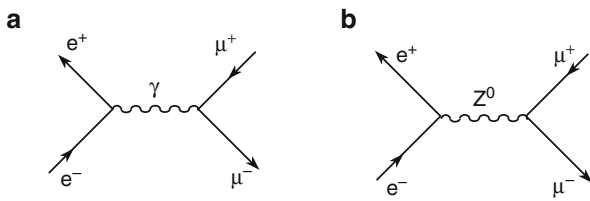


Figure 9.1b shows the ratio

$$R = \frac{\sigma(e^+e^- \rightarrow \text{hadrons})_{\text{measured}}}{\sigma(e^+e^- \rightarrow \mu^+\mu^-)_{\text{calculated}}} \quad (9.3)$$

as a function of the c.m. energy in the range from 0.3 to 200 GeV.

9.2.1 The Process $e^+e^- \rightarrow \gamma \rightarrow \mu^+\mu^-$

At the lowest order, the EM cross-section $\sigma(e^+e^- \rightarrow \mu^+\mu^-)$ is explained by the Feynman diagram of Fig. 9.2a: the e^+e^- pair annihilates into a virtual photon γ which materializes as a $\mu^+\mu^-$ pair. Outside resonances, the cross-section is given by Eq. 4.62, that is,

$$\sigma(e^+e^- \rightarrow \gamma \rightarrow \mu^+\mu^-) = \frac{4\pi\alpha_{EM}^2(\hbar c)^2}{3} \frac{1}{s} \quad (9.4)$$

where $\alpha_{EM} = 1/137$ and $s = E_{cm}^2$. Placing the numerical value of α_{EM} in (9.4), and using appropriate units (Appendix 2), one obtains

$$\sigma(e^+e^- \rightarrow \gamma \rightarrow \mu^+\mu^-) \simeq \frac{86.8 \text{ [nb]}}{s \text{ [GeV}^2\text{]}}. \quad (9.5)$$

The cross-section is expressed in [nb] = (10^{-33} cm 2) if $E_{cm}^2 = s$ is expressed in [GeV 2]. The contribution due to the weak interaction, with a Z^0 exchange as shown in Fig. 9.2b, is only important around $\sqrt{s} \sim m_Z \sim 90$ GeV.

9.2.2 The Color Quantum Number

The $e^+e^- \rightarrow \text{hadrons}$ process for $\sqrt{s} < 30$ GeV proceeds through the exchange of a virtual photon which subsequently produces a quark-antiquark pair, i.e., $e^+e^- \rightarrow \gamma \rightarrow q\bar{q}$ (see Fig. 9.3b). Since free quarks cannot be produced, the $q\bar{q}$ pair is thus a virtual pair: the quark and antiquark give rise to two jets of hadrons that are well

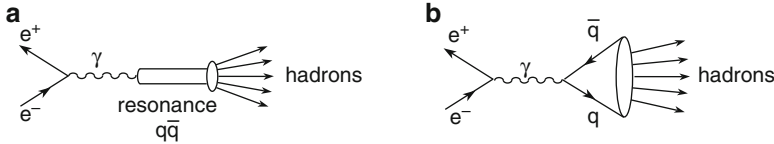


Fig. 9.3 For $\sqrt{s} < 30 \text{ GeV}$, the hadron production proceeds through the annihilation $e^+e^- \rightarrow \gamma$; (a) at the energy corresponding to a $q\bar{q}$ resonance, with spin-parity $J^P = 1^-$, the γ directly couples to the resonance which then decays in hadrons; (b) in the continuum regions of Fig. 9.1a, the γ gives rise to a $q\bar{q}$ pair which subsequently produces hadrons (two well defined jets at high energies)

defined and clearly visible at higher energies. For each type of quark “flavor” with charge Q_q , the cross-section outside the resonances is equal to (9.4) multiplied by the considered quark charge Q_q squared, that is,

$$\sigma(e^+e^- \rightarrow \gamma \rightarrow q\bar{q} \rightarrow \text{hadrons}) = \frac{4\pi\alpha_{EM}^2 Q_q^2}{3} \frac{(\hbar c)^2}{s}. \quad (9.6)$$

As seen in Sect. 7.8.1, Fermi statistics require that baryons are described by antisymmetric wave functions. This means the introduction in the wave function of a new quantum number, the so-called “color” quantum number. The first experimental confirmation came precisely from the study of (9.6): the theoretical prediction differed by a factor of three compared to experimental data. The quarks produced in the final state each have three different *degrees of freedom*, corresponding to the three colors. As a result, a multiplicative factor $N_C = 3$ must be introduced in (9.6). If there are N_f different types of quarks, i.e., N_f flavors, for energies higher than their production threshold, one has

$$\sigma(e^+e^- \rightarrow \gamma \rightarrow q\bar{q} \rightarrow \text{hadrons}) = N_C \frac{4\pi\alpha_{EM}^2}{3} \frac{(\hbar c)^2}{s} \sum_{n=1}^{N_f} Q_n^2. \quad (9.7)$$

Therefore, the expected ratio R is

$$R = \frac{\sigma(e^+e^- \rightarrow \gamma \rightarrow q\bar{q} \rightarrow \text{hadrons})}{\sigma(e^+e^- \rightarrow \gamma \rightarrow \mu^+\mu^-)} = N_C \sum_{n=1}^{N_f} Q_n^2, \quad (9.8)$$

where $\sigma(e^+e^- \rightarrow \mu^+\mu^-)$ is the predicted cross-section obtained in Eq. 9.5.

Let us study the expected ratio R (9.8) as a function of the c.m. energy:

- $1.5 < \sqrt{s} < 3 \text{ GeV}$. The three lower mass quarks are kinematically accessible, the quarks u with charge $+2/3$, d and s with charge $-1/3$; therefore,

$$R_{3q} = N_C(Q_u^2 + Q_d^2 + Q_s^2) = N_C \left[\left(+\frac{2}{3} \right)^2 + \left(-\frac{1}{3} \right)^2 + \left(-\frac{1}{3} \right)^2 \right] = \frac{2}{3} N_C. \quad (9.9)$$

The measured value is $R = 2$, as shown in Fig. 9.1b. The agreement between data and (9.9) is obtained only if $N_C = 3$, which confirms the existence of three different degrees-of-freedom (colors) for the quarks.

- $3 < \sqrt{s} < 9 \text{ GeV}$. After $\sqrt{s} \sim 3 \text{ GeV}$, the measured ratio R increases to $\sim 10/3$. This requires an additional term in (9.9). This is explained by the existence of a fourth quark (the charm c) and the fact that the $c\bar{c}$ pair production threshold is reached. The quark c has a charge $+2/3$; the value $3(2/3)^2 = 4/3$ must therefore be added to the value obtained in (9.9) which gives $2 + 4/3 = 10/3$.
- $9 < \sqrt{s} < 30 \text{ GeV}$. For $\sqrt{s} \sim 9.5 \text{ GeV}$, the $b\bar{b}$ (the fifth quark) production threshold is exceeded. Since $Q_b = -1/3$, there is an additional contribution of $+3(-1/3)^2 = 3/9 = 1/3$, which added to $10/3$ gives $11/3$, very close to the value measured for energies between 10 and 30 GeV.

Note that the process $e^+e^- \rightarrow f\bar{f}$ cannot be experimentally disentangled from $e^+e^- \rightarrow f\bar{f}\gamma$ for low energy γ . These radiative processes (which explain the small differences between experimental data and the values from Eq. 9.8) must therefore be included in the calculations.

We have explained the continuous behavior of the cross-section $\sigma(e^+e^- \rightarrow \gamma \rightarrow \text{hadrons})$ shown in Fig. 9.1a, and corresponding to the steps visible in Fig. 9.1b up to $\sqrt{s} \simeq 30 \text{ GeV}$. The peaks observed in $\sigma(e^+e^- \rightarrow \gamma \rightarrow \text{hadrons})$ of Fig. 9.1a must now be explained. These peaks are due to resonances in the $q\bar{q}$ systems, as shown in Fig. 9.3a.

9.3 The Discovery of Charm and Beauty Quarks

9.3.1 Mesons with c, \bar{c} Quarks

In 1974, a new vector meson ($q\bar{q}$ state with spin = 1) with a large mass was discovered at the Stanford Linear Accelerator Center (SLAC) e^+e^- collider. The vector meson with a mass of 3,097 MeV was observed by the research group headed by Burton Richter (who named the new particle ψ) through both leptonic decays $e^+e^- \rightarrow \psi \rightarrow e^+e^-, \mu^+\mu^-$ and hadronic decays $e^+e^- \rightarrow \psi \rightarrow \text{hadrons}$.

It was also independently observed in hadron-hadron collisions at the AGS proton accelerator at the Brookhaven National Laboratory (BNL) by a group headed by Samuel Ting (who named the new particle J): $p \text{ Be} \rightarrow JX, J \rightarrow e^+e^-$. Richter and Ting (Nobel laureate in 1976) announced their discoveries on the same day, and the new particle was named J/ψ . The J/ψ is regarded as a pure $c\bar{c}$ state as the $\phi(1,020)$ meson is considered to be a pure $s\bar{s}$ state. The c quark is the fourth quark predicted by the GIM mechanism (see Sect. 8.14). The J/ψ meson has a very small width ($\Gamma = 93 \text{ keV}$, see Problem 9.7) and thus a relatively long lifetime ($\tau = \hbar/\Gamma \simeq 10^{-20} \text{ s}$).

The excited state of the J/ψ were found at SLAC, and the first one was called ψ' . It is now called $\psi(2S)$ or $\psi(3686)$, respectively indicating its quantum state or

Table 9.1 Main characteristics and decay modes of the “charmed” J/ψ and $\psi(3686)$ vector mesons

State	Mass (MeV)	J^P, I	Γ_{tot} (keV)	Branching ratios	
$J/\psi(3100)$	$3,096.916 \pm 0.011$	$1^-, 0$	93.2 ± 2.1	hadrons [mostly $(2n + 1)\pi$] e^+e^- $\mu^+\mu^-$	88%
$\psi(3686)$	$3,686.09 \pm 0.04$	$1^-, 0$	317 ± 9	$J/\psi 2\pi$ $\chi\gamma$ e^+e^- $\mu^+\mu^-$	49.4% 26.5% 0.8% 0.8%

mass in MeV. Other $c\bar{c}$ vector mesons are denoted similarly with ψ and the quantum state (if known) or the mass. The name *charmonium* is used for the J/ψ and other charm-anticharm bound states, Sect. 9.4. This is analogous with *positronium*, which consists of a bound electron-positron state. Table 9.1 summarizes the main characteristics of the J/ψ and $\psi(3686)$ vector mesons.

9.3.2 The J/ψ Resonance Properties

Let us consider the cross-section $\sigma(e^+e^- \rightarrow \gamma \rightarrow q\bar{q} \text{ resonance} \rightarrow \text{hadrons})$ at energies close to a $q\bar{q}$ resonance, producing the peaks observed in Fig. 9.3a, b. Close to a resonance, the cross-section is given by the usual Breit–Wigner formula (7.25). We need to modify it in order to introduce the resonance parameters for a nonelastic process. In particular, the factor Γ^2 appearing at the numerator of (7.25) must be substituted with $\Gamma_{ee}\Gamma_h$ to take into account that the production takes place through a resonant annihilation of an electron-positron pair and a decay into hadrons. Γ_{ee} is the resonance formation width in $e^+e^- \rightarrow \text{resonance}$. It is equal to the decay probability $\text{resonance} \rightarrow e^+e^-$, which is proportional to the branching ratio BR, see Sect. 4.5.2. At the denominator, Γ represents the resonance total width (in MeV). Γ_h is the width (BR) for the hadronic decay $\text{resonance} \rightarrow \text{hadrons}$. The Breit–Wigner formula for the formation of a spin $J = 1$ resonance from (e^+, e^-) with spin $s_1 = s_2 = 1/2$ becomes

$$\sigma_{had} = 4\pi\hat{\lambda}^2 \frac{(2J+1)}{(2s_1+1)(2s_2+1)} \frac{\Gamma_{ee}\Gamma_h/4}{[(E - E_R)^2 + \Gamma^2/4]} \quad (9.10)$$

where $\hat{\lambda} = \hbar/p$ is the e^+, e^- de Broglie wavelength in the c.m.

Let us calculate the cross-section for the formation of the J/ψ resonance in $e^+e^- \rightarrow J/\psi \rightarrow \text{hadrons}$; the value obtained can be compared with the results shown in Fig. 9.1, that is,

$$\begin{aligned}\sigma(e^+e^- \rightarrow J/\psi \rightarrow \text{hadrons}) &= \frac{\pi\lambda^2(2J+1)\Gamma_{ee}\Gamma_h}{(2s_1+1)(2s_2+1)[(E-E_R)^2+\Gamma^2/4]} \\ &= \frac{3\pi\lambda^2\Gamma_h\Gamma_{ee}}{4[(E-3097)^2+\Gamma^2/4]}\end{aligned}\quad (9.11)$$

where $E_R = 3,097$ MeV is the energy corresponding to the resonance, λ is the de Broglie wavelength (in the e^+, e^- collider, $p \simeq E_e = \sqrt{s}/2 = 3,097/2 = 1548$ MeV):

$$\lambda = \hbar/p = \hbar c/pc \simeq 197 \text{ MeV fm}/1548 \text{ MeV} \simeq 0.127 \text{ fm}. \quad (9.12)$$

$\Gamma \simeq 93$ keV is the resonance total width. The ratio $\Gamma_{ee}\Gamma_h/\Gamma^2 \simeq (0.05) \times (0.88) \simeq 0.04$: in 5% of the cases, the J/ψ decays in (or it is formed by) an e^+e^- pair and 87.7% of the time, it decays in hadrons [P08]. At the resonance energy ($E = E_R = 3097$ MeV), the cross-section (9.11) is equal to

$$\sigma(e^+e^- \rightarrow J/\psi \rightarrow \text{hadrons}) = 3\pi\lambda^2 \left[\frac{\Gamma_{ee}\Gamma_h}{\Gamma^2} \right] = 0.07 \text{ mbarn}. \quad (9.13)$$

This value must be summed to the EM cross-section. At 3 GeV, the (9.7) gives a value of ~ 20 nb. The cross-section for the resonance production is about four orders of magnitude larger. The photon directly couples to resonance with J^P equal to that of the photon, $J^P = 1^-$. This explains the major peaks appearing in the hadron production cross-section for energies up to 12 GeV. Note that the vector meson resonances can decay into e^+e^- and $\mu^+\mu^-$ with more equal probability than in hadrons. Peaks are also therefore expected in the reactions $e^+e^- \rightarrow e^+e^-$, $\mu^+\mu^-$.

Finally, let us explain the structures observed in $\sigma(e^+e^- \rightarrow \text{hadrons})$ between 4 and 4.5 GeV and in the ratio R between 3.5 and 4.5 GeV. The structures around 4.1 GeV are connected to the energy threshold corresponding to $2m_c$. Above this threshold, the pair production of charmed D mesons¹, for example, $e^+e^- \rightarrow \gamma \rightarrow c\bar{c} \rightarrow D^+D^-$, is now kinematically accessible.

A situation similar to that of the charmed mesons was later observed in the region around 9–10 GeV.

9.3.3 Mesons with b, \bar{b} Quarks

In 1977, 3 years after the J/ψ discovery, the $\Upsilon(9880)$ and other similar vector mesons were observed. They were discovered by the Fermilab E288 experiment team headed by Leon M. Lederman in the reaction $p\text{Be} \rightarrow \Upsilon X \rightarrow \mu^+\mu^-X$. These mesons require a fifth quark, the *bottom/beauty* quark b , with a mass $m_b \simeq 4,300$ MeV ($\Upsilon = b\bar{b}$).

¹The composition in terms of the quark of these mesons is $D^+ = c\bar{d}$, $D^- = \bar{c}d$.

Table 9.2 Main parameters of the Υ vector mesons

	$\Upsilon(1^3S)$	$\Upsilon'(2^3S)$	$\Upsilon''(3^3S)$	$\Upsilon'''(4^3S)$
Mass (MeV)	$9,460.30 \pm 0.26$	$10,023.26 \pm 0.31$	$10,355.2 \pm 0.5$	$10,579.4 \pm 1.2$
$\Gamma_{e^+e^-}$ (keV)	1.340 ± 0.018	0.612 ± 0.011	0.443 ± 0.008	0.272 ± 0.029
Γ_{tot} (keV)	54.02 ± 1.25	31.98 ± 2.63	20.32 ± 1.85	$20,500 \pm 2,500$

The neutral vector mesons Υ are formed by a quark-antiquark $b\bar{b}$ pair and have masses of 9.46, 10.02, 10.35 and 10.58 GeV. The discovery was confirmed and the Υ mesons were analyzed in more detail in e^+e^- collisions. Table 9.2 gives the various states for the $b\bar{b}$ system (the mesons formed from a bottom quark and its antiquark with different total or orbital angular momentum are called “bottomonium”).

9.4 Spectroscopy of Heavy Mesons and α_S Estimate

Atomic physics: α_{EM} analogy. The discovery of the c and b heavy quarks, and of the particles they form, led to the possibility of studying all mesons made of the same quark-antiquark pair, but with different spin states. In analogy with the atomic system, which gives precise information on the EM interaction, a sort of “spectroscopy” of states composed of heavy quarks was used to obtain information on the potential energy that binds quarks and on the strong interaction coupling constant α_S [P95].

A positron and an electron at a relative distance r , under the Coulomb potential

$$V_{em} = -\alpha_{EM}/r, \quad (9.14)$$

can form bound states (*positronium*) similar to those of the hydrogen atom. The energy levels, as for the Bohr atom, are

$$E_n = -\frac{\alpha_{EM}^2 m_e c^2}{4n^2} \quad (9.15)$$

where n is the total quantum number (9.15) differs by a factor 1/2 with respect to the Balmer formula due to the fact that the electron reduced mass $m_e/2$ is introduced (in the hydrogen atom the proton mass is much higher than m_e). The spin-orbit interaction splits the levels: for each n , there are $\ell = 0, 1, \dots, n-1$ possible values (*fine structure*). The spin-spin interaction produces an additional splitting in a triplet ($\uparrow\uparrow$, with three sub-states) and in a singlet ($\uparrow\downarrow$) (*hyperfine structure*).

Figure 9.4a shows the positronium quantum numbers and energy levels. The lower level corresponds to the state $n^{2S+1}L_S = 1^1S_0$, with $n = 1, \ell = 0, J = 0, S = 0$ (spin singlet; *orthopositronium*). The first excited level is the state 1^3S_1 , with $n = 1, \ell = 0, J = 1, S = 1$ (spin triplet; *parapositronium*). The transition $1^3S_1 \rightarrow 1^1S_0$ produces photons with a frequency of 203,286 MHz, in good agreement with

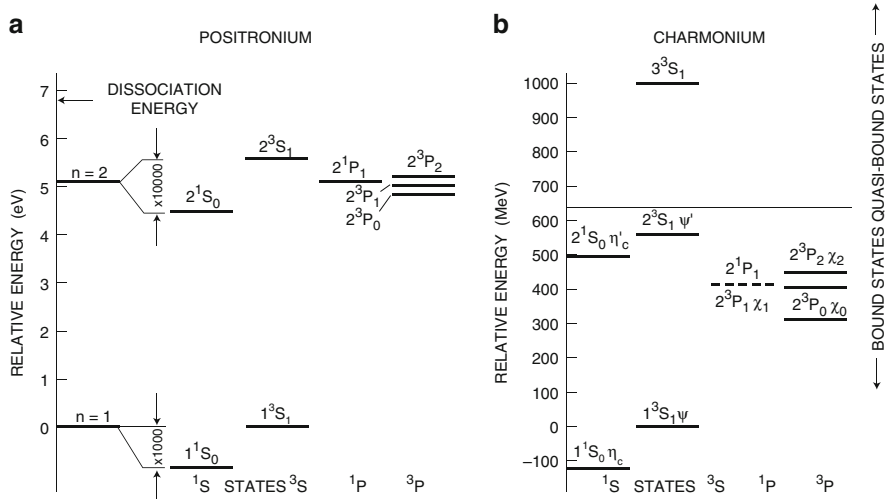


Fig. 9.4 Energy levels for (a) the *positronium* and (b) the *charmonium*. Note that the scale on the ordinate of the figure on the left is in eV, while it is in MeV for the figure on the right [9B82]

the theoretical prediction. The state 1^1S_0 has a charge conjugation $C = +1$ and gives rise to a fast annihilation ($\tau = 1.25 \cdot 10^{-10}$ s) into two photons. The state 1^3S_1 has $C = -1$ and produces a slower annihilation rate ($\tau = 1.4 \cdot 10^{-7}$ s) in three photons.

The coupling constant α_s . Figure 9.4b shows the energy levels of the “charmonium” ($c\bar{c}$ states). Note the great similarity between these levels and those of the positronium. The levels of the $q\bar{q}$ systems shown in Fig. 9.4b can be calculated with good approximation assuming that the potential produced by a quark (or by the antiquark) on the other is (natural units, $\hbar = c = 1$):

$$V_{QCD} = -\frac{4}{3} \frac{\alpha_s}{r} + Kr. \quad (9.16)$$

The factor $4/3$ is the *color factor*, see Sect. 11.9.3. At small r values ($r < 1$ fm), only the Coulomb-like potential plays a role. To reproduce the experimental sequence shown in Fig. 9.4, the strong coupling constant must be $\alpha_s \simeq 0.3$, see Problem 9.1. At large distances ($r > 1$ fm), the elastic-type potential Kr (with $K \simeq 1$ GeV/fm) is dominant.

9.5 The τ Lepton

The known charged leptons are the electron e^- , the muon μ^- and the tau τ^- , with respective masses of 0.5110, 105.66, and 1,777.1 MeV. The third lepton was first observed in a series of experiments between 1974 and 1977 by M.L.

Perl (Nobel laureate in 1995) and colleagues at the SPEAR colliding ring of SLAC. The magnetic apparatus detected and distinguished between leptons, hadrons and photons.

$\tau^+\tau^-$ pairs were produced through the reaction: $e^+e^- \rightarrow \gamma \rightarrow \tau^+\tau^-$. The cross-section $\sigma(e^+e^- \rightarrow \tau^+\tau^-)$ is zero for $\sqrt{s} < 3,700\text{ MeV}$; for $\sqrt{s} > 3,700\text{ MeV}$, the cross-section increases rapidly until it reaches the same value of $\sigma(e^+e^- \rightarrow \mu^+\mu^-)$ and then it follows the same trend with increasing energy. The equality of the cross-sections $\sigma(e^+e^- \rightarrow e^+e^-) = \sigma(e^+e^- \rightarrow \mu^+\mu^-) = \sigma(e^+e^- \rightarrow \tau^+\tau^-)$ at high energies represents a test of the *lepton universality*: the three leptons e^- , μ^- , τ^- behave in a similar way.

The τ lepton has a short lifetime, $\tau_\tau = 2.96 \cdot 10^{-13}\text{ s}$. In the first experiments performed at c.m. energies around 4 GeV, the τ were only observed through their decay products. Amongst these decays, the leptonic decay channels are easily identified; these leptonic decay modes are: $\tau^- \rightarrow \nu_\tau e^- \bar{\nu}_e$, $\tau^- \rightarrow \nu_\tau \mu^- \bar{\nu}_\mu$, each with a branching ratio of $\sim 18\%$ (in about 64% of the case, the τ decays in charged hadrons, plus the tau neutrino). The leptonic decays of $\tau^+\tau^-$ pairs give rise to e^+e^- , $\mu^+\mu^-$ pairs and to $e^+\mu^-$ or $e^-\mu^+$ combinations. The τ has been discovered through the observation of $e^\pm\mu^\mp$ in acoplanar configuration. These final states seem to produce an apparent violation of the conservation of the electron and muon lepton numbers (there is in fact no such violation because neutrinos and antineutrinos carrying the right lepton number are present in the final states in order to insure the conservation).

The tau neutrino is the most recently discovered particle in the Standard Model. It was first reported by the DONUT experiment at the Fermilab in July 2000.

9.6 LEP Experiments and Examples of Events at LEP

9.6.1 The LEP Detectors

At the LEP collider [9B00] at CERN, Sect. 3.3.1, in operation from 1989 until 2000, data were collected by four large detectors: ALEPH, DELPHI, L3 and OPAL. These detectors had a cylindrical structure, with dimensions of at least $\simeq 10\text{ m}$ in diameter, $\simeq 10\text{ m}$ in length. They consisted a set of subdetectors, most of them arranged in a concentric cylindrical structure with the axis coincident with the LEP beam pipe. The detectors were closed on each side by two *end-caps*. These multipurpose devices were able to detect, in any direction, any type of particle produced (except neutrinos) at the e^+e^- interaction point. Experiments of this type are sometimes called *4 π detectors* because they are able to detect particles emitted in almost the full solid angle. Figure 9.5 shows the general characteristics of a LEP detector.

The main features of the four LEP detectors are summarized in Table 9.3. Since the LEP detectors had a similar structure, we shall hereafter use the OPAL detector as an example.

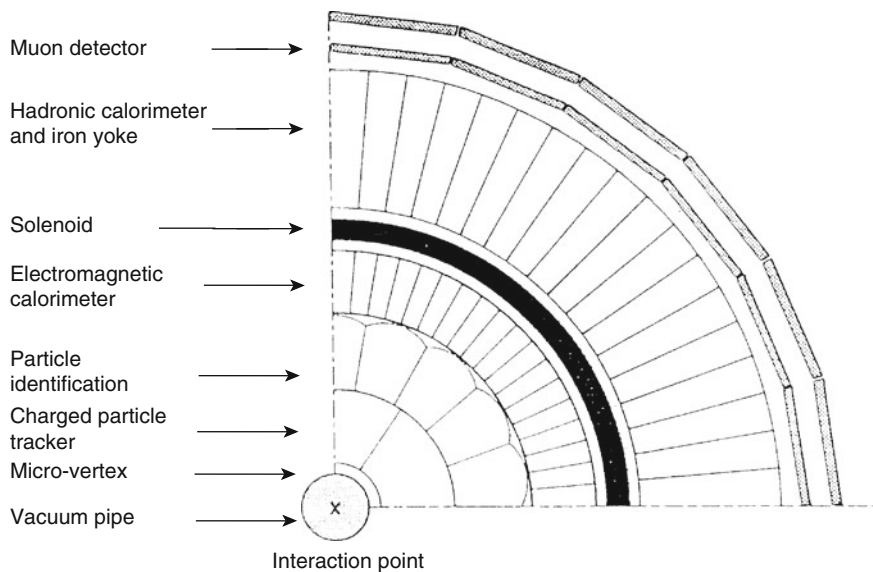


Fig. 9.5 Transverse view of an idealized LEP detector. The subdetector designed for particle identification is only present in some experiments (for example, the DELPHI Cherenkov detector)

The OPAL detector. The central detector consisted of a system of tracking chambers providing charged particle reconstruction over 96% of the full solid angle inside a 0.435 T uniform magnetic field. It consisted of a two-layer silicon microstrip vertex detector, a high-precision drift chamber, a large-volume JET chamber and a set of z-chambers measuring the track coordinates along the beam direction. The Central Jet chamber not only improved the measurement of the trajectory of the charged particles, but had an important role in particle identification by measuring the specific energy loss through ionization. The central tracking devices (except for the silicon detector) were enclosed in a cylindrical pressure vessel around which an aluminum conductor (solenoid) was wrapped; with a 7,000 A current passing through it, the solenoid generated the required magnetic field. The magnetic field was oriented along the axial direction and caused the charged particles to bend on a helical path around the magnetic field direction. The curvature of the track of the charged particle in the magnetic field was measured, making it possible to calculate the momentum of the tracked particle. A 1 m thick iron yoke was incorporated into the hadron calorimeter to provide magnetic flux return. The iron yoke served as the mechanical structure supporting the experimental apparatus. It was segmented into 10 cm thick iron layers used as a passive element for the hadron calorimeter. The electromagnetic calorimeter, segmented in more than ten thousand lead-glass

Table 9.3 Comparison of the main features of some subdetectors of the four experiments at LEP. Precision of the radial alignment of OPAL luminometer elements: $(\sigma_r)_{absolute} \simeq 200 \mu\text{m}$, $(\sigma_r)_{relative} \simeq 10 \mu\text{m}$

\Downarrow Sub-detector	Detector \Rightarrow	OPAL	L3	ALEPH	DELPHI
Tracker					
Microvertex					
Resolutions [μm]	$\sigma_{(r,\varphi)}$	5	7	12	8
	σ_z	15	14	10	
(for normal incidence)					
Vertex chamber					
External diameter [mm]		$\emptyset = 235$	$\emptyset = 180$	$\emptyset = 288$	
Length L [m]		1	1	2	
Resolutions $\sigma_{(r,\varphi)}$ [μm]		50	45	150	<150
Central chamber					
External diameter [m]		$\emptyset = 3.8$	$\emptyset = 0.9$	$\emptyset = 3.6$	$\emptyset = 1.2$
Length [m]		$L = 4.5$	$L = 1$	$L = 4.8$	$L = 2.8$
Resolutions [μm]		$\sigma_{(r,\varphi)} = 135$	$\sigma_{(r,\varphi)} = 45$	$\sigma_{(r,\varphi)} = 150$	$\sigma_{(r,\varphi)} = 250$
Resolution on track momentum					
$\left[\frac{\Delta p}{p^2} \cdot 10^3 (\text{GeV}/c)^{-1} \right]$		1.1		0.6	0.7
Obtained with		JET		$^{TPC}_{+VTX}$	$^{TPC}_{+VTX}$
z-chamber [μm]		$\sigma_z = 300$			
dE/dx (0.5 GeV/c π)		3.2%			
μ detection (barrel)					
Resolution on muon momentum					
$\left[\left(\frac{\Delta p}{p} \right)_{\mu\mu} \% \right]_{45 \text{ GeV}}$		5.5	2.5	3.0	3.5
$\sigma_{r\varphi}$ [mm]; σ_θ [mr]		1.5 ; 5			
Calorimeters					
Electromagnetic					
LGB		BGO	PWT	HPC	
11,704 blocks		7,680 blocks			
$Energy$ $resolution \left[\frac{\Delta E}{E} \% \right]_{45 \text{ GeV}}$		$\frac{6.3}{\sqrt{E}} \oplus 0.2$	$\frac{2}{\sqrt{E}} \oplus 0.9$	$\frac{19.5}{\sqrt{E}} \oplus 1$	$\frac{26}{\sqrt{E}} \oplus 4$
$Spatial$ $resolution [\Delta(r, \varphi); \Delta\vartheta]$		$2.3^\circ; 2.3^\circ$	$2.3^\circ; 2.3^\circ$	$1^\circ; 1^\circ$	$1^\circ; 0.1^\circ$
σ [cm]		1	1	3	9
Hadronic					
$\left[\frac{\Delta E}{E} \% \right]_{45 \text{ GeV}}$		$\frac{120}{\sqrt{E}}$	$\frac{55}{\sqrt{E}} \oplus 5$	$\frac{100}{\sqrt{E}}$	$\frac{120}{\sqrt{E}}$
$Spatial$ $resolution [\Delta(r, \varphi); \Delta\vartheta]$		$7^\circ; 7^\circ$	$2.5^\circ; 2.5^\circ$	$3.7^\circ; 3.7^\circ$	$3^\circ; 4^\circ$
Barrel diameter [m]		$\simeq 10$	16	$\simeq 10$	$\simeq 10$
Barrel length [m]		10	10	12	10
Magnetic field [T]		0.43	0.4	2	1
Time of flight [ns]		0.2			

TEC time expansion chamber, TPC time projection chamber, LGB lead glass block, BGO bismuth germanium oxide, PWT proportional wire tube, HPC high density projection chamber, RICH ring imaging Cherenkov, JET JET-CHamber, VTX VerTeX (vertex detectors), PRES PRESampler

blocks, was installed in the space located between the solenoid and the magnetic yoke. It was used for the identification and energy measurement of photons, electrons and positrons.

In addition to the subdetectors described above, the OPAL detector included others that will now be briefly described, starting from the innermost device and proceeding to the outermost one.

The first subdetector was located at the interaction point and immediately surrounding the vacuum pipe where the e^+ and e^- beams were circulating. It was a solid state silicon microvertex detector designed to give precise measurements regarding the position of the charged particle tracks. The accuracy of this detector allowed for the measurements with a resolution of the order of a few microns on the position of any secondary vertices resulting from decays of unstable particles produced in the primary e^+e^- interaction.

The microvertex detector was the first subdetector of the OPAL tracking system that allowed the detection of electrically charged particles produced at the e^+e^- interaction point. The second subdetector surrounding the microvertex detector was a set of high precision drift chambers, the vertex chambers. Just outside the vertex chambers, one had the large-volume JET chamber, followed by a set of drift chambers called the z-chambers designed to precisely measure the position of the tracks along the axial direction of the beams (z axis).

The central tracking system was enclosed in the solenoid that produced the magnetic field directed along the z axis. The Time-of-Flight (TOF) detector was installed on the outer surface of the solenoid. It was made of scintillation counters and designed to measure the transit time of particles traveling from the interaction region with a time resolution of about 0.4 ns.

The next detector was the electromagnetic calorimeter consisting of a presampler made of thin chambers arranged around the TOF, and the main calorimeter formed of lead-glass blocks. The electromagnetic calorimeter was composed of a central “barrel” and of two “end-caps.”

The following detector was the hadron calorimeter which served for the energy measurement of all hadrons produced in the e^+e^- collisions. This detector was a sampling calorimeter using limited streamer tubes as active elements interleaved with the magnet yoke iron layers as passive absorbing material. This detector was also used to track muons passing through it.

The outermost detector was the muon detector used to identify and track muons with energies above 3 GeV; indeed, only such muons managed to cross the entire thickness of the apparatus and be detected by the four layers of drift chambers mounted on the external surface of the magnetic yoke.

To determine the cross-section of each reaction considered, it was necessary to precisely measure the LEP luminosity in the OPAL interaction point. This was done by measuring the frequency of elastic positron-electron collisions in a small angular region at small angles, where the cross-section

is large and can be calculated with great precision. The detector used for measuring the elastic scattering at small angles was composed of two electromagnetic calorimeters mounted immediately around the beam pipe, both on the right and the left sides of the collision. Each of them was formed of two parts; the first one was made of silicon sensitive elements and tungsten absorbers. It covered a region at small angles and was called the luminometer. The second part was composed of scintillators as active elements plus passive lead absorbers; this part was called the forward detector. The luminometer allowed a luminosity measurement with a precision better than one per mil. This was very important for the precision measurements of the Z^0 boson parameters.

The choice of the various subdetectors was of course guided by considerations based on the LEP research programs.

9.6.2 Events in 4π Detectors at LEP

In the following, we shall discuss a few simple events observed with the OPAL detector. These events are interesting from an educational point of view in order to understand the techniques that were used as well as to illustrate various aspects of particle physics.

An elastic event. Figure 9.6a shows the “event display” of an $e^+e^- \rightarrow e^+e^-$ elastic collision. The positron and the electron beams are perpendicular to the page; they collide at the interaction point and are scattered. In the central detector, two tracks emitted in opposite directions are observed. Each track results from the combination of 18 positions (points) measured in the vertex chamber, 159 points in the JET chamber and six points in the z-chamber. The tracks, each 45.6 GeV, are slightly curved due to the 0.435 T magnetic field. The curvature can only be observed at a larger magnification. The curvature would be larger in the ALEPH and DELPHI detectors which had higher magnetic fields (respectively 2 and 1 T).

Inside the electromagnetic calorimeter, the electron and the positron each generate an electromagnetic shower. The graphic representation shown in Fig. 9.6a is a shaded trapezoid; it represents the analogue signal observed in each of the lead-glass blocks hit by the particles. The signal has a base equal to the size of a lead-glass block (10 cm) and a height proportional to the deposited energy (in this case 45.6 GeV per side).

This elastic event is a simple event, mainly characterized by the release of all the energy in two diametrically opposite sectors of the electromagnetic calorimeter. No signal is detected in the hadron calorimeter and in the muon detector, which is the evidence that the final state only contains one positron and one electron, each with an energy equal to that of the incident particles.

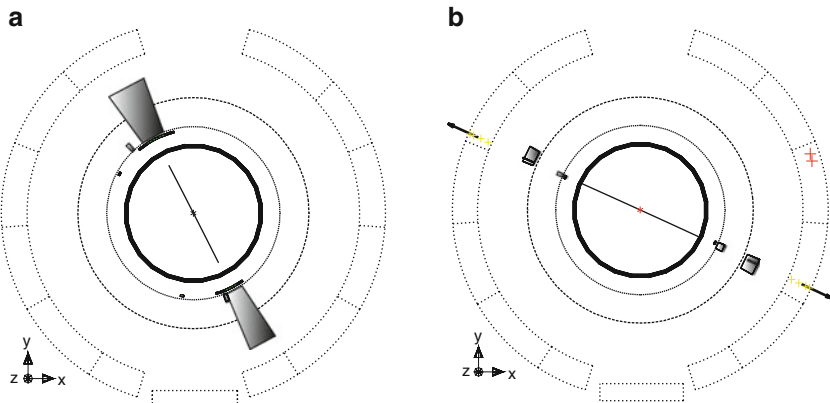


Fig. 9.6 (a) Transverse view of an elastic event $e^+e^- \rightarrow e^+e^-$ observed in the OPAL detector. The final state electron and positron are detected in the central tracking detector, the time-of-flight system and in the electromagnetic calorimeter. In the latter one, the electron and the positron release a large energy represented by two large gray shaded trapezoids. (b) Interaction $e^+e^- \rightarrow \mu^+\mu^-$: the μ^+ and the μ^- are detected in the central tracking detector, the time-of-flight system, the electromagnetic calorimeter (gray rectangles on each side) and in the muon detector (arrows on each side). The z axis is perpendicular to the page with its direction pointing out. The magnetic field is oriented along the z axis

The selection of these events is mainly based on the presence of an electronic signal into two diametrically opposite counters of the electromagnetic calorimeter, with the additional condition that each signal has an energy at least equal to half of that of each incident electron or positron. The number of elastic events, excluding the region of small angles, represents 3.3% of the total number of observable events.

The reaction $e^+e^- \rightarrow \gamma\gamma$ gives rise to only two signals in opposite sectors of the electromagnetic calorimeter since the photons are electrically neutral and do not leave any signal in the tracking chambers.

Interaction $e^+e^- \rightarrow \mu^+\mu^-$. Figure 9.6b shows an event due to an interaction $e^+e^- \rightarrow \mu^+\mu^-$. The two muons are represented by the two tracks, emitted in opposite directions in the central tracking detector and by the two small signals, also diametrically opposite, in the time-of-flight system. Thus far, there are no differences with respect to the elastic collision shown in Fig. 9.6a. The differences concern the signals deposited in the electromagnetic calorimeter. The presence of two very small gray trapezoids, diametrically opposite, indicates that the energy released by each muon in a lead-glass block is about 0.2 GeV.

The next detector hit by the muons is the hadronic calorimeter. The analogue signals recorded by its “tower structure” are illustrated by two small “towers;” the passage of a single muon that does not interact along its path produces relatively small signals. In the muon detector, the passage of two charged particles in the muon chamber is represented by arrows in opposite sectors. Such signals are due

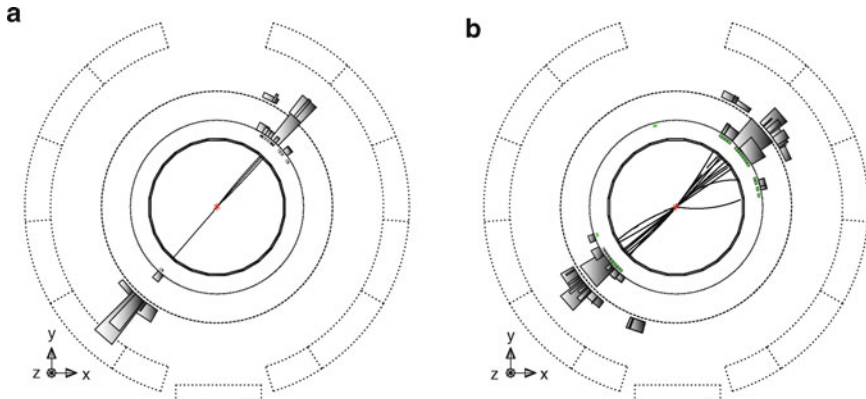


Fig. 9.7 (a) Interaction $e^+e^- \rightarrow \tau^+\tau^-$ in the OPAL detector. (b) Interaction $e^+e^- \rightarrow$ two particle jets (hadrons). The decay products are observed in the central tracking detector, the electromagnetic calorimeter and in the hadronic calorimeter

to particles that are able to cross the whole detector, including more than a meter of iron. Therefore, with no doubt, these two particles are muons. As for the elastic events, $\mu^+\mu^-$ pairs are produced at the 3.3% level of the total observable events.

Interaction $e^+e^- \rightarrow \tau^+\tau^-$ (Fig. 9.7a). The τ lepton is unstable and decays with a lifetime of $0.3 \cdot 10^{-12}$ s, corresponding to a mean decay length (distance between the production and decay points) of a few mm². Therefore, the decay occurs inside the LEP vacuum pipe and only the τ decay products are observed in the detector. Using the information provided by the silicon microvertex detector and the vertex chamber, charged particle tracks coming from secondary vertices can be reconstructed and the τ lepton lifetime can be measured.

In Fig. 9.7a, the τ^+ (track at the bottom left) decays in $\tau^+ \rightarrow \pi^+ \bar{\nu}_\tau$. A track is observed in the central tracking detector as well as a clear signal in the hadronic calorimeter (gray towers). The pion decays roughly in the same direction as the tau. The τ^- (track at the top right) decays in $\tau^- \rightarrow \pi^+\pi^-\pi^-\bar{\nu}_\tau$. Due to the high energy of the τ^- , the three pions produce a jet of three charged particles propagating approximately along the initial direction of the τ^- . No signal is observed in the muon detector because the final state charged particles are hadrons and the neutral ones are neutrinos (which almost do not interact).

As for the two previous cases, the $\tau^+\tau^-$ events amount for 3.3% of the total observable events. The equal production of e^+e^- , $\mu^+\mu^-$, $\tau^+\tau^-$ is representative of the “lepton universality.” It is also quite significant that no heavier charged leptons are observed.

²The decay length L is given by $L = \beta\gamma c\tau$ where $\beta\gamma = p/m$, c is the speed of light and τ is the lifetime of the considered particle. With $p \simeq 45$ GeV, $m_\tau = 1.7$ GeV and $\tau_\tau = 300 \times 10^{-15}$ s, one finds $L = \frac{p}{m}c\tau_\tau = 2.5$ mm.

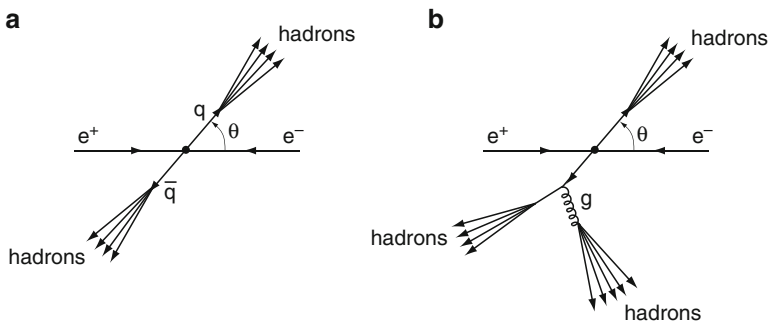


Fig. 9.8 Illustration of the formation process of two or more hadronic jets. The primary interaction is $e^+e^- \rightarrow q\bar{q}$. It is followed by (a) the quark and antiquark hadronization which gives rise to two hadronic jets emitted in opposite directions; (b) if the quark (or the antiquark) radiates a gluon g , three jets are present in the final state

Interaction $e^+e^- \rightarrow$ hadronic jets. Figure 9.7b illustrates the interaction $e^+e^- \rightarrow$ two hadronic jets (diametrically opposite). In the central detector, each jet is made of various charged tracks emitted in a rather small solid angle. The tracks are considerably bent by the magnetic field. Note that the jets contain tracks due to particles both with negative or positive electric charge.

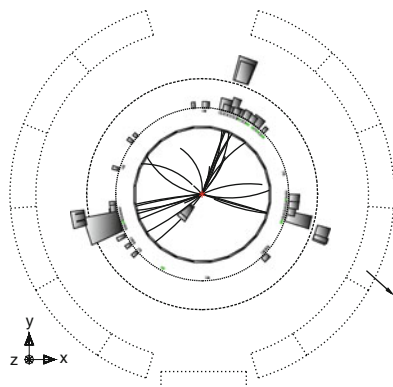
In the time-of-flight system and in the electromagnetic calorimeter, each jet of hadrons hits a number of counters. The overall energy released in the electromagnetic calorimeter is about 15 GeV per jet, a fraction is due to neutral particles that are unobserved in the central detector. In the hadronic calorimeter, each jet releases (10–15) GeV and produces a series of gray towers. These are typical signals for a hadronic shower which is concentrated in the first half of the calorimeter.

No signal is recorded in the muon detector, confirming the nature of the two hadronic jets of particles. The main characteristics of the two jets are: (1) they are emitted in diametrically opposite directions, (2) each jet deposits a high energy and there are strong indications in favor of the hadronic nature of the particles of the two jets, (3) each jet is contained in a cone with a small aperture angle.

These considerations suggest that the jet production does not result from direct electron-positron collisions, but rather that the process occurs in two steps: the incident electron and positron produce a quark-antiquark pair, each quark giving rise to a hadronic jet (each quark “hadronizes” in a jet): $e^+e^- \rightarrow q\bar{q}$, $q \rightarrow \text{jet 1}$, $\bar{q} \rightarrow \text{jet 2}$. The jets become more and more collimated with increasing c.m. energy: in this way, it is possible to determine the q and \bar{q} flight directions.

The processes involved in the jet production are illustrated in Fig. 9.8a. Two jet events are experimental evidence in favor of quark existence. Further confirmations come from more detailed analyses; these statistical studies also allow one to identify the type of quark involved and to measure its fractional charge. Events with two hadronic jets in the final state represent the majority of observable events, about 70%.

Fig. 9.9 An OPAL event with three jets of particles in the final state. The three jets are represented as three groups of tracks in the central detector and as rectangles in the electromagnetic calorimeter. The third jet of particles is due to the radiation of a gluon by the quark or antiquark



Interaction $e^+e^- \rightarrow 3$ hadronic jets.³ Figure 9.9 shows an inelastic interaction $e^+e^- \rightarrow 3$ hadronic jets. The tracks in the central detector are grouped into three jets.

To interpret three jet events, one must take into account the gluons, i.e., the bosons that mediate the strong interaction. The quark (or the antiquark) can radiate a gluon which also produces a jet of particles (Fig. 9.8b):

$$e^+e^- \rightarrow q\bar{q} \rightarrow q\bar{q}g, \quad q \rightarrow \text{jet 1}, \quad \bar{q} \rightarrow \text{jet 2}, \quad g \rightarrow \text{jet 3}.$$

The existence of multihadronic events with three jets in the final state was the first experimental evidence for the existence of gluons. The emission of a gluon by a quark is similar to “bremsstrahlung” radiation.

The gluon has usually low energy and produces a less energetic and not well defined jet (sometimes too small to be detectable). The gluon energy distribution has characteristics similar to that of bremsstrahlung photons. There are many low energy gluons. The number of observable jets is connected to the resolution of the apparatus and to the used jet reconstruction algorithm. Typically, the number of events with three well separated hadronic jets is about 15% of the total number of hadronic events. The ratio between the number of three jet events and that of two jet events provides information on the coupling of a gluon to a quark, and depends on the dimensionless “strong” coupling constant α_s .

Events with four or more jets were also observed; they are interpreted as being due to the radiation of two or more gluons and the subsequent quark and gluon hadronization.

³These events were first observed by the TASSO experiment at the PETRA accelerator at the DESY laboratory.

9.7 e^+e^- Collisions at $E_{cm} \sim 91$ GeV. The Z^0 Boson

In the following, we shall discuss the e^+e^- collisions at energies close to the Z^0 peak. A brief description of the formulas needed to explain the Z^0 physics, together with the experimental results, will be presented. The main physics results obtained in e^+e^- collisions at $\sqrt{s} \simeq 91$ GeV can be summarized as follows:

- The determination of the number of light neutrino families (three) and therefore of the number of families of quarks and leptons
- The precise determination of the Z^0 parameters and of various electroweak quantities and the determination below threshold of the t quark mass
- The demonstration that the strong coupling constant α_s decreases with increasing energy (“running”) and that it is independent of the quark flavor
- The verification that also α_{EM} increases with energy
- Systematic studies of the properties of the hadronic jets, in particular: the differences between jets initiated by quarks and jets initiated by gluons; the first evidence for the 4-gluon vertex; the demonstration that the theory of the strong interaction is nonabelian; the $\ln s$ dependence of the number of hadrons produced
- The spectroscopy of hadrons with quark b
- Precise measurements of the lifetimes of hadrons with quark c , b and of the τ lepton
- The determination of stringent limits on new particles, rare decays and on the Higgs (H^0) boson mass

9.7.1 The Z^0 Resonance

The measurement of the $e^+e^- \rightarrow Z^0/\gamma \rightarrow f\bar{f}$ cross-section as a function of the c.m. energy allows one to measure the Z^0 parameters such as its mass m_Z^0 and total width Γ_Z . The cross-section can be computed by considering the diagrams of Fig. 9.2. For each final state $f\bar{f}$, there are three different contributions:

- A term due to the electromagnetic interaction $e^+e^- \rightarrow \gamma \rightarrow f\bar{f}$. This is the dominant contribution for c.m. energy below the Z^0 mass. The EM term has a $1/s$ dependence typical of the electromagnetic annihilation
- A term due to the weak interaction $e^+e^- \rightarrow Z^0 \rightarrow f\bar{f}$. This contribution dominates at the Z^0 resonance, $\sqrt{s} = m_{Z^0}$, the so-called “ Z^0 peak”
- An EM/weak interference term vanishing at the Z^0 resonance

At the “ Z^0 peak,” the production of “real” (on mass shell) Z^0 can be studied. This means that in the diagram of Fig. 9.2b, the Z^0 is produced with energy and momentum such that $E^2 - p^2 = m_Z^2$.

Let us analyze in more detail the behavior of the cross-section around the Z^0 peak (omitting the purely electromagnetic term and terms due to radiative corrections).

This behavior is typical of a resonance with $J = 1$, described by the Breit–Wigner formula with a width depending on the number of channels kinematically accessible. From the experimental point of view, measurements were made (at LEP) through a series of scans around the Z^0 mass, at c.m. energies between 88 and 94 GeV. Similar measurements were performed at SLAC.

The cross-section $\sigma_{f\bar{f}}$ around the Z^0 peak is given by (7.25) with the same changes discussed in Sect. 9.3.2 for the formation of the J/ψ resonance. The quantity Γ_{ff} is the partial width corresponding to the Z^0 decay into $f\bar{f}$, $Z^0 \rightarrow f\bar{f}$ and Γ_Z is the Z^0 total width. Using the de Broglie wavelength (neglecting the electron mass) $\lambda = \hbar/p \rightarrow \hbar/E = \hbar/(\sqrt{s}/2)$ and defining $\sigma(s) \equiv \sigma(s)_{e^+e^- \rightarrow f\bar{f}}$, Eq. 7.25 becomes

$$\sigma(s) = \frac{4\pi}{(s/4)} \frac{3}{4} \left[\frac{\Gamma_{ee}\Gamma_{ff}/4}{(\sqrt{s}-m_Z)^2 + \Gamma_Z^2/4} \right] = \frac{12\pi}{m_Z^2} s \frac{\Gamma_{ee}\Gamma_{ff}}{(s-m_Z^2)^2 + s^2\Gamma_Z^2/m_Z^2} \quad (9.17)$$

in unit $\hbar = c = 1$; in the last equality we approximated $s \simeq m_Z^2$. To ensure correct dimensions, (9.17) must be multiplied by $(\hbar c)^2$. The factor $3/4 = (2J+1)/[(2s_a+1)(2s_b+1)]$ takes into account the Z^0 angular momentum and the spin $s_a = s_b = 1/2$ of the final state fermions. At $s = m_Z^2$, (9.17) becomes

$$\sigma^0 \equiv \sigma(s = m_Z^2) = \frac{12\pi}{m_Z^2} \frac{\Gamma_{ee}\Gamma_{ff}}{\Gamma_Z^2}. \quad (9.18)$$

9.7.2 Z^0 Total and Partial Widths

Since the Z^0 is unstable, the width of its peak has a finite value related to the number of species of fermions in which it can decay. Each kinematically accessible species (i.e., with a mass $< \frac{m_{Z^0}}{2}$) that couples to the Z^0 contributes to the width of the resonance.

The contribution of each fermion-antifermion pair may be estimated using the usual Feynman rules and considering the Z^0 as a real particle decaying into two bodies. The width Γ is connected with the lifetime (and to the transition probability W , Eq. 4.28) by the uncertainty principle $\Gamma = \hbar/\tau = \hbar W$. The transition probability can be estimated from dimensional considerations: the decay is due to the weak interaction, and hence is proportional to the Fermi constant G_F . Since the Fermi constant has dimension [Energy $^{-2}$], the width Γ (which has dimension of an energy) is obtained by multiplying by a factor with dimension [Energy 3]. The only physical quantity involved in the process that has dimension of an energy is the Z^0 boson mass; therefore, Eq. 4.44 can be expressed as $\hbar W = \Gamma \sim G_F m_Z^3$. The calculation of the numerical factor (which comes from the phase-space momentum integration) is beyond the difficulty level of this text (see [9M98]); the full calculation gives a factor equal to $1/6\sqrt{2}\pi$.

Table 9.4 Z^0 partial decay widths and branching ratios in various channels, as measured by several experiments and estimated by global *fits* as reported in [P08]. The Γ_{invis} is not directly measurable and refers to the decay into neutrinos. Γ_h is the total hadronic width, Γ_ℓ is the decay width in any charged lepton pair

Process ($f\bar{f}$)	Γ_{ff} (MeV)	BR (%)
e^+e^-	83.91 ± 0.12	3.363 ± 0.004
$\mu^+\mu^-$	83.99 ± 0.18	3.366 ± 0.007
$\tau^+\tau^-$	84.08 ± 0.22	3.370 ± 0.008
$\Gamma_\ell, \ell^+\ell^-$	83.984 ± 0.086	3.3658 ± 0.0023
Γ_h	$1,744.4 \pm 2.0$	69.91 ± 0.06
Γ_Z (total)	$2,495.2 \pm 2.3$	100
$\Gamma_{invis}, \sum_{\ell=e,\mu,\tau} \nu_\ell \bar{\nu}_\ell$	499 ± 1.5	20.0 ± 0.06

In addition to the numerical factor, for the computation of the decay fractions Γ_{ff} into fermion pairs, one should keep in mind that: (1) in the weak interaction, particles interact both through an axial part and through a vector part, (2) while the leptons do not have a color multiplicity, each quark has three degrees of freedom (one for each color quantum number). Finally, we can write

$$\Gamma_{ff} = \frac{G_F m_Z^3}{6\sqrt{2}\pi} (a_f^2 + v_f^2) N_C^f = 330(a_f^2 + v_f^2) N_C^f \text{ MeV} \quad (9.19)$$

where v_f and a_f are respectively the vector and axial coupling constants of the fermion f (they will be obtained from the Standard Model in Chap. 11, see Table 11.3). N_C^f is the color factor (three for the quarks and one for the leptons).

The partial width Γ_{ff} defined above represents the transition probability per time unit for the Z^0 boson decay to a given final state $f\bar{f}$. Table 9.4 summarizes the measurements of the partial widths and decay branching ratios for each channel. Note that the probability that the Z^0 decays into $\sum_\ell \nu_\ell \bar{\nu}_\ell$ ($\sim 20\%$) is significantly larger than that for the decay in a particular lepton pair $\ell\bar{\ell}$ ($\sim 3\%$). The Z^0 coupling with fermions is different and more complicated (as we shall see in Sect. 11.3) than that of the W^\pm , which couples only to left-handed fermions.

The hadronic width, Γ_h , is the sum of partial widths of quark-antiquark pairs kinematically accessible in the final state, that is,

$$\Gamma_h \equiv \Gamma_{uu} + \Gamma_{dd} + \Gamma_{ss} + \Gamma_{cc} + \Gamma_{bb}. \quad (9.20)$$

The top quark is excluded because it is too heavy to be produced at the Z^0 peak. Γ_{ee} , $\Gamma_{\mu\mu}$, $\Gamma_{\tau\tau}$, Γ_{vv} are the leptonic widths. The “invisible width,” Γ_{invis} , is not directly measurable and refers to the decay into neutrinos

$$\Gamma_{invis} \equiv N_v \Gamma_{v\bar{v}} \quad (9.21)$$

where N_ν is the number of light neutrino families. Γ_{invis} is obtained by subtracting the other known widths from the total width:

$$\Gamma_{invis} = \Gamma_Z - \Gamma_h - \Gamma_{ee} - \Gamma_{\mu\mu} - \Gamma_{\tau\tau} = \Gamma_Z - \Gamma_h - N_\nu \Gamma_{\ell\ell}. \quad (9.22)$$

We assume the *lepton universality*, that is, $\Gamma_{ee} = \Gamma_{\mu\mu} = \Gamma_{\tau\tau} = \Gamma_{\ell\ell}$.

The measured total width, Γ_Z , results from the sum of the partial widths, Γ_{ff} , of all known fermions, that is,

$$\Gamma_Z \equiv \Gamma_h + \Gamma_{ee} + \Gamma_{\mu\mu} + \Gamma_{\tau\tau} + N_\nu \Gamma_\nu = \Gamma_{vis} + \Gamma_{invis} \simeq 2.5 \text{ GeV}. \quad (9.23)$$

From Table 9.4, it is clear that the Z^0 predominantly decays into hadrons (about 70% of all decays).

The Z^0 lifetime can be estimated from the uncertainty principle: $\tau_Z \simeq \hbar / \Gamma_Z = 6.58 \cdot 10^{-22} / 2,495 = 2.7 \cdot 10^{-25}$ s; it is a very short lifetime. The decay is due to the weak interaction, but the phase space factor is very large.

9.7.3 Measurable Quantities, Γ_{invis} and the Number of Light Neutrino Families

Figure 9.10 summarizes the quantities which were accurately measured at e^+e^- colliders. For the Z^0 peak, they refer to

- The resonance mass, m_Z (GeV), obtained from the measurement of the cross-section. The mass corresponds to the position of the maximum of the Breit-Wigner curve
- The total width, Γ_Z (GeV), also obtained from the shape of the resonance curve
- The hadronic cross-section, σ_{had}^0 (nb), corresponding to the maximum of the resonance. The percentage of hadronic events is determined by the topology of events with jets (Fig. 9.8b). From (9.18) and using $\Gamma_{ff} = \Gamma_h$, the hadronic cross-section at the Z^0 peak (the so-called “pole” cross-section) is

$$\sigma_{had}^0 = \frac{12\pi \Gamma_{ee} \Gamma_h}{m_Z^2 \Gamma_Z^2}. \quad (9.24)$$

Inserting numerical values in the above equation, one obtains $\sigma_{had}^0 = 40.2$ nb. With the typical LEP luminosity, $\mathcal{L} \sim 10^{31} \text{ cm}^{-2} \text{ s}^{-1}$ (see Problems 9.4 and 9.5), the frequency of hadronic event production is 0.4 Hz

- The electron and muon pair production cross-sections measured in a similar way as the hadronic cross-section
- The partial widths, Γ_{ff} , Γ_{ee} , which are proportional to the peak cross-sections, $\Gamma_{ff}/\Gamma_{ee} = \sigma_f/\sigma_e$

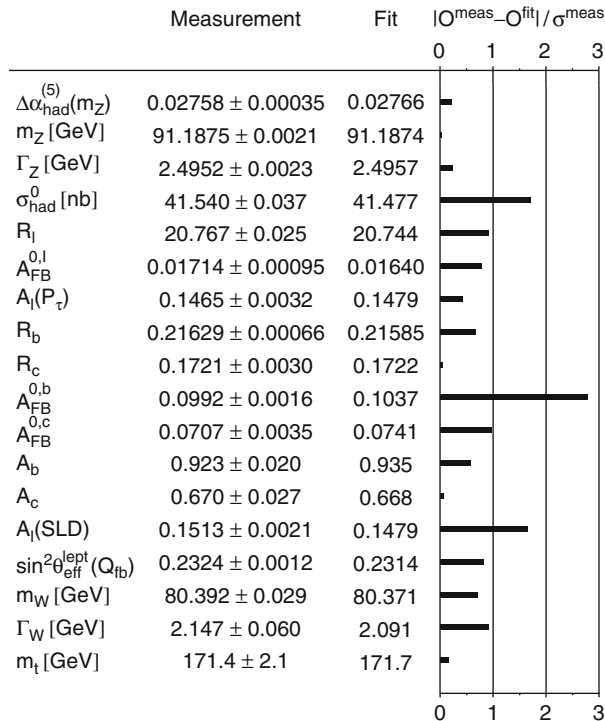


Fig. 9.10 Results [9w1] obtained by combining the measurements of the four LEP experiments at CERN (ALEPH, DELPHI, L3 and OPAL) and of the SLD experiment at SLC, in e^+e^- collisions around the Z^0 mass. The “pull” for each measurement is also presented; the “pull” is defined as the difference between the measured value and the expected value in the Standard Model in unit of uncertainty on the measurement

An important result from LEP and SLD was the determination of the number of lepton families and thus, of the number of N_ν families of “light neutrinos” with a mass smaller than half the Z^0 mass. If there was a fourth family of quarks and leptons with masses below half the Z^0 mass, the number of channels in which the Z^0 could decay, would be larger than expected from the Standard Model computation assuming three families. Experimentally, this would correspond to a larger Z^0 width (and to a smaller lifetime) and a smaller cross-section peak.

To determine N_ν , the ratios R_f^0 are defined as

$$R_e^0 \equiv \Gamma_h / \Gamma_{ee} \quad R_\mu^0 \equiv \Gamma_h / \Gamma_{\mu\mu} \quad R_\tau^0 \equiv \Gamma_h / \Gamma_{\tau\tau}. \quad (9.25a)$$

Assuming lepton universality, these three ratios are equal, that is,

$$R_l^0 \equiv \Gamma_h / \Gamma_{\ell\ell}. \quad (9.25b)$$

This quantity is measured using the ratio of the different event topologies (final states with hadronic jets or leptons). Using Eq. 9.23 and the lepton universality, we can now define the ratio as

$$R_{invis}^0 \equiv \frac{\Gamma_{invis}}{\Gamma_{\ell\ell}} = \frac{\Gamma_Z - \Gamma_h - 3\Gamma_{\ell\ell}}{\Gamma_{\ell\ell}}. \quad (9.26)$$

From (9.24), one obtains $\Gamma_Z = \sqrt{\frac{12\pi\Gamma_{ee}\Gamma_h}{m_Z^2\sigma_{had}^0}}$, and (9.25b) becomes

$$R_{invis}^0 = \sqrt{\frac{12\pi R_l^0}{\sigma_{had}^0 m_Z^2}} - R_l^0 - 3. \quad (9.27)$$

Using the experimental values of R_l^0 , σ_{had}^0 and m_Z given in Fig. 9.10, one obtains $R_{invis}^0 = 5.943 \pm 0.016$.

This value can be compared with the prediction of the Standard Model for the number of generations of light neutrinos, N_ν ,

$$R_{invis}^0 \equiv \frac{\Gamma_{invis}}{\Gamma_{\ell\ell}} = N_\nu \left(\frac{\Gamma_{\nu\bar{\nu}}}{\Gamma_{\ell\ell}} \right)_{SM}. \quad (9.28)$$

The value of the ratio $(\Gamma_{\nu\bar{\nu}}/\Gamma_{\ell\ell})_{SM}$ in the Standard Model is 1.99125 ± 0.00083 , which can be derived from (9.19). This result leads to the determination of the number of generations of light neutrinos, that is,

$$N_\nu = \frac{5.943 \pm 0.016}{1.99125 \pm 0.00083} = 2.984 \pm 0.008. \quad (9.29)$$

The dependence of the hadronic cross-section on the number N_ν is clearly visible in Fig. 9.11, which presents the cross-section for the process $e^+e^- \rightarrow \text{hadrons}$, for c.m. energies around 91 GeV. The precision achieved in this measurement places stringent limits on the possible contribution of any invisible decay of the Z^0 , other than the decays due to the three known generations of light neutrinos. In fact, the behavior is in perfect agreement with the existence of three families of neutrinos.

9.7.4 Forward–Backward Asymmetries A_{FB}

At energies below the resonance, the process $e^+e^- \rightarrow \gamma/Z^0 \rightarrow \mu^+\mu^-$ occurs either through the exchange of a photon (electromagnetic interaction with the cross-section in (9.5), or a Z^0 (weak interaction) and through an interference term between the two processes. At first order, the differential cross-section can be written (neglecting the fermion masses) as

$$\frac{d\sigma}{d\Omega} = \frac{\alpha^2}{4s} N_C^f [a(1 + \cos^2 \theta) + 2b \cos \theta] \quad (9.30)$$

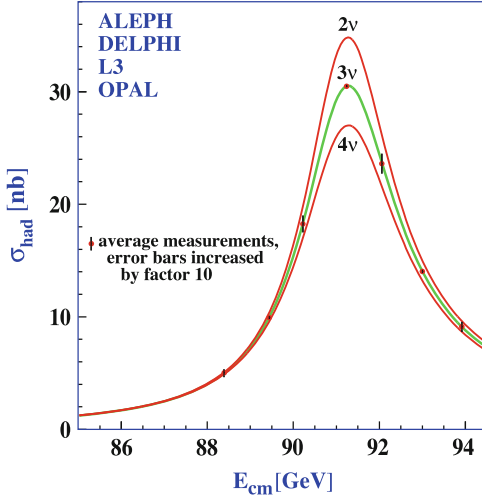


Fig. 9.11 Cross-section for the process $e^+e^- \rightarrow \text{hadrons}$ around a c.m. energy of 91 GeV. The points are the experimental data obtained with the four experiments at the LEP collider at CERN; the central curve is the theoretical prediction assuming that there are three different types of neutrinos, the upper (lower) corresponds to the prediction with two (4) types of neutrinos [P08]

where θ is the outgoing fermion scattering angle with respect to the e^- beam. The Standard Model predicts the value of the quantities a and b , see below. The integration of the term $(1 + \cos^2 \theta)$ of (9.30) provides the total cross-section for each type of final state ff . The linear term in $\cos \theta$ does not contribute to the total cross-section given that $\int_0^\pi \cos \theta d\theta = 0$, but contributes to the so-called forward-backward asymmetries.

Note that (9.17) and (9.18) apparently do not explicitly contain the parameter that characterizes the weak interaction, i.e., the Fermi constant. In fact, it is “hidden” in the partial widths (9.19). Recalling that $\Gamma_{ee} = \frac{G_F m_Z^3}{6\sqrt{2}\pi} (a_e^2 + v_e^2)$, Eq. 9.17 becomes

$$\sigma(s) = \frac{12\pi}{m_z^2} \cdot s \left[\frac{G_F^2 m_Z^6}{2 \cdot 6^2 \pi^2} (v_e^2 + a_e^2) \sum_f N_C^f (v_f^2 + a_f^2) \right] \frac{1}{(s - m_Z^2)^2 + s^2 \Gamma_Z^2 / m_Z^2}. \quad (9.31)$$

At the Z^0 peak ($s = m_Z^2$), one gets

$$\sigma^0 = \frac{G_F^2 m_Z^4}{6\pi \Gamma_Z^2} (a_e^2 + v_e^2) \sum_f (a_f^2 + v_f^2) N_C^f,$$

and the sum extends over all fermion f kinematically accessible, i.e., with a mass $m_f < \frac{m_{Z^0}}{2}$.

Equation 9.31 allows one to calculate, for example, the cross-section for the production of a muon pair in the final state. With $a_e = a_\mu = -1/2$ and neglecting v_e and v_μ (see Table 11.3), one finds

$$\sigma(e^+e^- \rightarrow Z^0 \rightarrow \mu^+\mu^-)_{m_{Z^0}} = \frac{G_F^2}{96\pi} \frac{s m_Z^4}{(s - m_Z^2)^2 + \Gamma_Z^2 m_Z^2}. \quad (9.32)$$

Equation 9.32 gives a cross-section of 1.6 nb at the Z^0 peak. The radiative corrections reduce it to ~ 1.2 nb. This value can be compared with the cross-section of 0.0105 nb due to the electromagnetic interaction.

For energies below 90 GeV, neglecting s with respect to m_Z^2 and since $\Gamma_Z \ll m_Z$, Eq. 9.32 is approximately

$$\sigma(e^+e^- \rightarrow Z^0 \rightarrow \mu^+\mu^-)_{E_{cm} < 90 \text{ GeV}} = \frac{G_F^2}{96\pi} (\hbar c)^2 s = 1.8 \cdot 10^{-7} s \text{ (GeV}^2\text{nb).} \quad (9.33)$$

Far from the Z^0 peak, the cross-section due to the weak interaction is much smaller than that due to the electromagnetic interaction given in (9.5). Below 50 GeV, the contribution due to the weak interaction can therefore be neglected (Fig. 9.1b).

Since the Z^0 coupling with fermions depends on both the vector and axial coupling constants, v_f and a_f , one can observe measurable asymmetries in the angular distributions of the final state fermions, as shown in Fig. 4.11. These asymmetries allow one to quantify the parity violation in the neutral current weak interaction.

The asymmetry in the angular distribution of the process $e^+e^- \rightarrow \gamma/Z^0 \rightarrow \mu^+\mu^-$ is relatively easy to measure:

$$A_{FB}^\mu = \frac{N_F^\mu - N_B^\mu}{N_F^\mu + N_B^\mu} = \frac{\sigma_F^\mu - \sigma_B^\mu}{\sigma_F^\mu + \sigma_B^\mu} \quad (9.34)$$

where “F” stands for “forward” and N_F^μ is the number of muons scattered in the forward hemisphere, i.e., with a diffusion angle θ such that $\cos \theta > 0$ with respect to the direction of the e^- beam. “B” stands for “backward” and N_B^μ is the number of muons scattered in the backward hemisphere, i.e., with a diffusion angle θ such that $\cos \theta < 0$. σ_F^μ and σ_B^μ are the corresponding cross-sections. Considering only the neutral current, the differential cross-section is given by [9M98]

$$\frac{d \sigma}{d \cos \theta} = \frac{3}{8} \sigma^0 [(1 + \cos^2 \theta) + 2 A_e A_f \cos \theta] \quad (9.35)$$

where

$$A_f = \frac{2v_f a_f}{v_f^2 + a_f^2} = 2 \frac{v_f/a_f}{1 + (v_f/a_f)^2}, \quad (9.36)$$

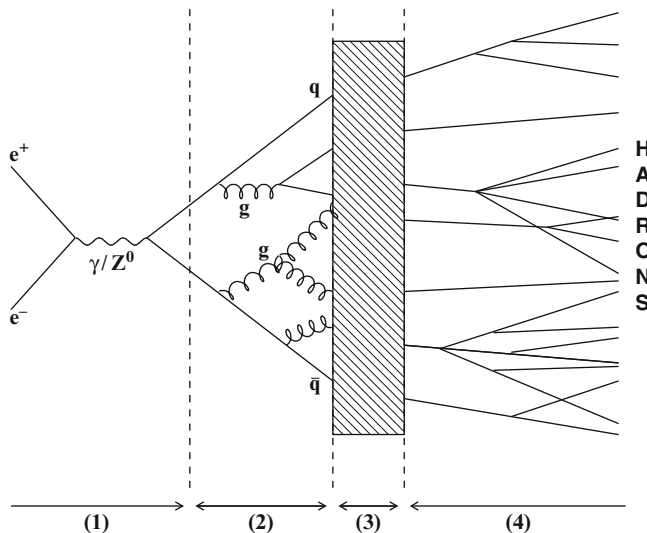


Fig. 9.12 Multihadronic production model

and similarly for A_e . The values of the axial and vector constants predicted by the Standard Model are given in Table 11.3. At the Z^0 peak, the forward–backward asymmetry for each $f\bar{f}$ channel is

$$A_{FB}^{0,f} = \frac{3}{4} A_e A_f. \quad (9.37)$$

Using other measurements of A_e , the parameters A_μ , A_τ , A_c and A_b can be measured using (9.37). A_c and A_b can be measured only if events where $c\bar{c}$, $b\bar{b}$ quark pairs are produced and identified with vertex detectors. At the Z^0 peak, the forward–backward asymmetry, for example, for channels with a charged lepton pair in the final state, $e^+e^- \rightarrow Z^0 \rightarrow l^+l^-$, is (Fig. 4.11)

$$A_{FB}^{0,l} = 0.01714 \pm 0.00095. \quad (9.38)$$

The fact that the value is statistically different from zero is significant: it provides further evidence of the parity violation in the weak interaction.

9.7.5 Multihadronic Production Model

In the annihilations $e^+e^- \rightarrow \gamma/Z^0 \rightarrow q\bar{q}$, the q and \bar{q} hadronize through the strong interaction. The multihadronic production proceeds through four distinct phases, as shown in Fig. 9.12.

1. In the first phase, the e^+e^- pair annihilates in a virtual γ or Z^0 , which give rise to the primary $q\bar{q}$ pair. Before the annihilation, the initial e^+ or e^- can radiate a γ . This reduces the total effective c.m. energy. The production of the primary $q\bar{q}$ pair is described by the perturbative electroweak theory which involves distances of the order of 10^{-17} cm.
2. In the second phase, the quark or the antiquark can radiate a gluon, which subsequently can radiate another gluon (producing, in this way, a three-gluon vertex), or produce a $q\bar{q}$ pair. This phase is described by the perturbative QCD and occurs at distances of the order of 10^{-15} cm.
3. In the third phase, the *colored partons* (quarks and gluons) fragment (*hadronize*) in colorless hadrons. The process (which occurs at distances of the order of the fm) cannot be treated with perturbation methods; in the absence of an exact analysis, the fragmentation is described by models.
4. In the fourth phase, the produced hadronic resonances decay rapidly into hadrons through the strong interaction (e.g., $\rho^0 \rightarrow \pi^+\pi^-$, $\tau_{\rho^0} \sim 10^{-23}$ s); other hadrons decay in hadrons via the electromagnetic interaction ($\Sigma^0 \rightarrow \Lambda^0\gamma$, $\pi^0 \rightarrow \gamma\gamma$, $\tau_{\pi^0} \sim 10^{-16}$ s). At this stage, the process is described with models that include experimental information about the branching ratios and lifetimes. At a longer time scale, most of the hadrons decay via the weak interaction. We will return to the hadronization process in Sect. 10.6.1.

There are several programs for Monte Carlo simulation, generating full multi-hadronic events. For example, the Monte Carlo JETSET includes the parton shower for phase (2) and the string fragmentation (also called Lund) for phase (3). The free parameters of the models are optimized by studying the shape variables of multihadronic events. Information on decays are “manually” introduced on the basis of experimental measurements. All Monte Carlos have the fact that the subsequent processes are independent from one another in common; for example, the decay of a hadron is independent of its production.

9.8 e^+e^- Collisions for $\sqrt{s} > 100$ GeV at LEP2

In this section, the processes produced in e^+e^- collisions with $\sqrt{s} > 100$ GeV (i.e., the second phase of LEP operation, the so-called LEP2 phase) are presented. The main results obtained at LEP2 are:

- The measurement of the triple vertex boson $Z^0W^+W^-$
- The accurate measurements of the W boson parameters and mass (m_W)
- The variation with energy of many hadronic parameters such as the number of charged particles produced in the collision (charged multiplicity)
- Limits on the existence of new particles

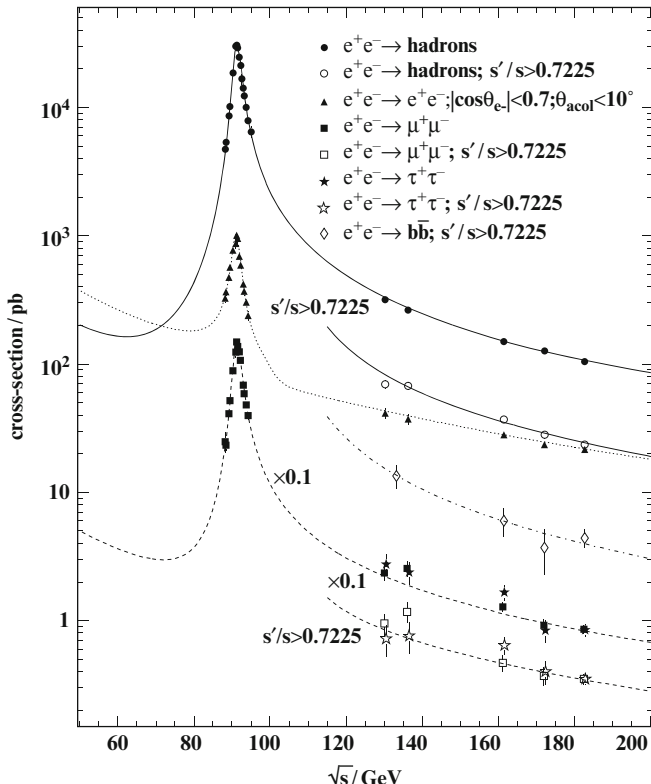


Fig. 9.13 Dependence as a function of the c.m. energy of the cross-sections $\sigma(e^+e^- \rightarrow \text{hadrons})$, $\sigma(e^+e^- \rightarrow \mu^+\mu^-)$ and $\sigma(e^+e^- \rightarrow \tau^+\tau^-)$ for $80 < \sqrt{s} < 183$ GeV. The production cross-sections for $\mu^+\mu^-$ and $\tau^+\tau^-$ are reduced by a factor 10. (The data for $s'/s > 0.7225$ exclude the radiative events)

9.8.1 $e^+e^- \rightarrow W^+, W^-, Z^0Z^0$ Cross-Sections

Cross-sections for the processes $e^+e^- \rightarrow e^+e^-$, $\mu^+\mu^-$, $\tau^+\tau^-$, hadrons (see Fig. 9.13) were measured for the first time at these high energies. The probability that the initial positron or electron radiates a photon is very large when the exchanged Z^0 is almost real. This phenomenon is the so-called “radiative return to the Z^0 :” the events are no longer collinear, but acollinear (see the topology shown in Fig. 9.14 to be compared with that shown in Fig. 9.6b). This implies that the reaction $e^+e^- \rightarrow \gamma + (\ell\bar{\ell}, q\bar{q}$ pair with the Z^0 mass), is almost twice as abundant than that in which the fermion pairs in the final state have an energy equal to twice the beam energy. In Fig. 9.13, radiative events are removed with the condition $s'/s > 0.7225$ where s' is the energy of the $\ell\bar{\ell}$, $q\bar{q}$ system and s is the c.m. energy.

Fig. 9.14 Radiative event $e^+e^- \rightarrow e^+e^-\gamma \rightarrow Z^0\gamma \rightarrow \mu^+\mu^-\gamma$ observed at $\sqrt{s} = 130$ GeV with a LEP detector. The event is shown in a longitudinal view which is perpendicular to that shown in Fig. 9.6

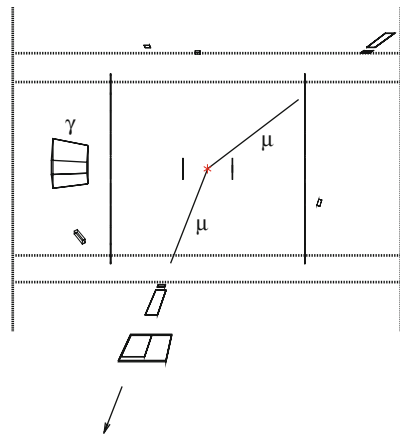
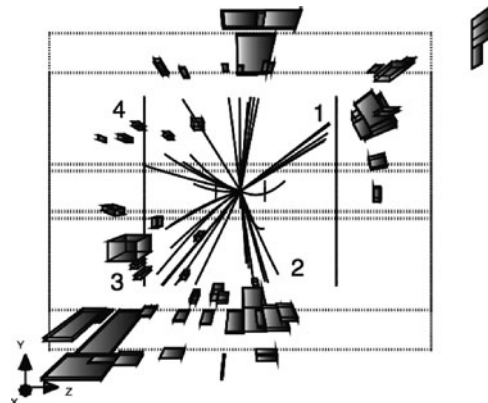


Fig. 9.15 Event display of the process $e^+e^- \rightarrow W^+W^- \rightarrow 4 \text{ quarks} \rightarrow 4 \text{ hadronic jets}$ observed at $\sqrt{s} = 161$ GeV with a LEP detector. The W^+ and W^- are produced almost at rest; the W^+ decays in the jets 1 and 3 ($W^+ \rightarrow \text{jet } 1 + \text{jet } 3$), while the W^- decays in the jets 2 and 4 ($W^- \rightarrow \text{jet } 2 + \text{jet } 4$)



LEP2 allowed one to explore the energy region $130 < E_{cm} < 209$ GeV. At such energies, it became possible to study the reactions

$$e^+e^- \rightarrow W^+W^- \quad (9.39a)$$

$$e^+e^- \rightarrow Z^0Z^0. \quad (9.39b)$$

The production thresholds are $E_{cm} = 2m_W = 160.7$ GeV and $2m_Z = 182.4$ GeV, respectively. Figure 9.15 shows an event display of the process $e^+e^- \rightarrow Z^0 \rightarrow W^+W^- \rightarrow 4q \rightarrow 4 \text{ jets}$ at the threshold energy $\sqrt{s} = 161$ GeV. The W^+W^- are produced almost at rest and each of them decays into two jets in opposite directions.

The cross-sections for the processes (9.39) can be calculated using the Feynman diagrams shown in Fig. 9.16. Amongst those, the most interesting is the diagram shown in Fig. 9.16c, which contains the triple boson vertex $Z^0W^+W^-$. The diagram with the Higgs boson (Fig. 9.16d) is also important to eliminate divergences.

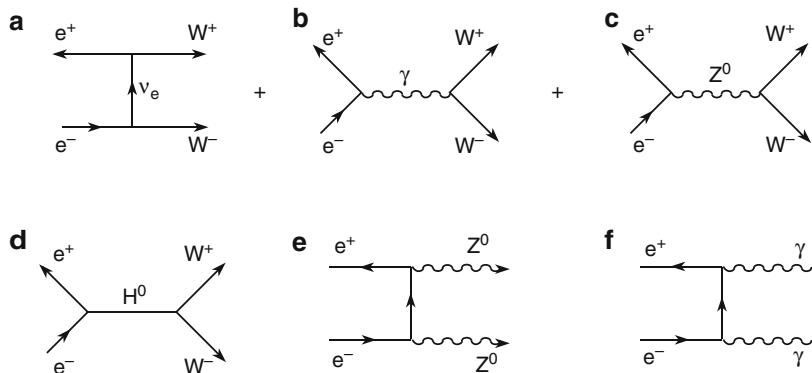


Fig. 9.16 Lowest order Feynman diagrams (a), (b), (c), and (d) for the process $e^+e^- \rightarrow W^+W^-$, (e) the Z^0Z^0 production and (f) the annihilation in two photons

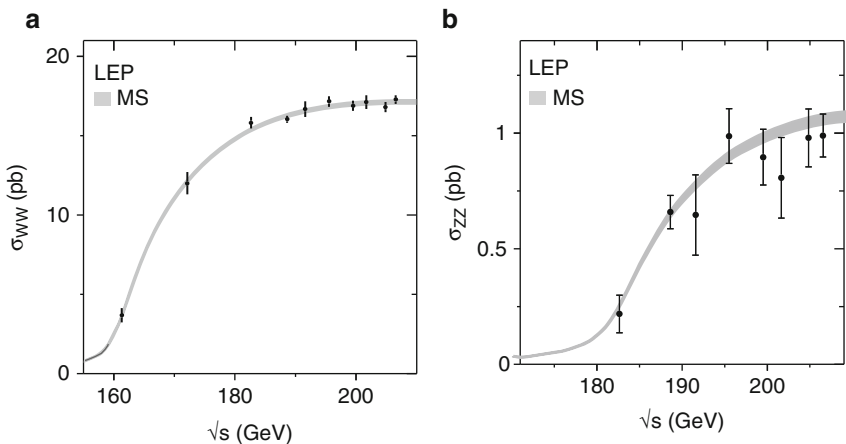


Fig. 9.17 Cross-section of (a) the process $e^+e^- \rightarrow W^+W^-$ and (b) of the reaction $e^+e^- \rightarrow Z^0Z^0$. The points are the combinations [9L03] of the experimental data of the four LEP experiments, compared with a prediction of the electroweak theory (shaded area)

Figure 9.17a shows the dependence as a function of \sqrt{s} of the cross-section of the process (9.39a): note that the cross-section starts to increase below the production threshold because of the large width of the W^+ , W^- bosons (Γ_W). Note also that the cross-section increases rapidly with increasing \sqrt{s} : this is a typical behavior for any “new” channel reaching the production threshold. The cross-section for the reaction (9.39b) shows a similar behavior (see Fig. 9.17b).

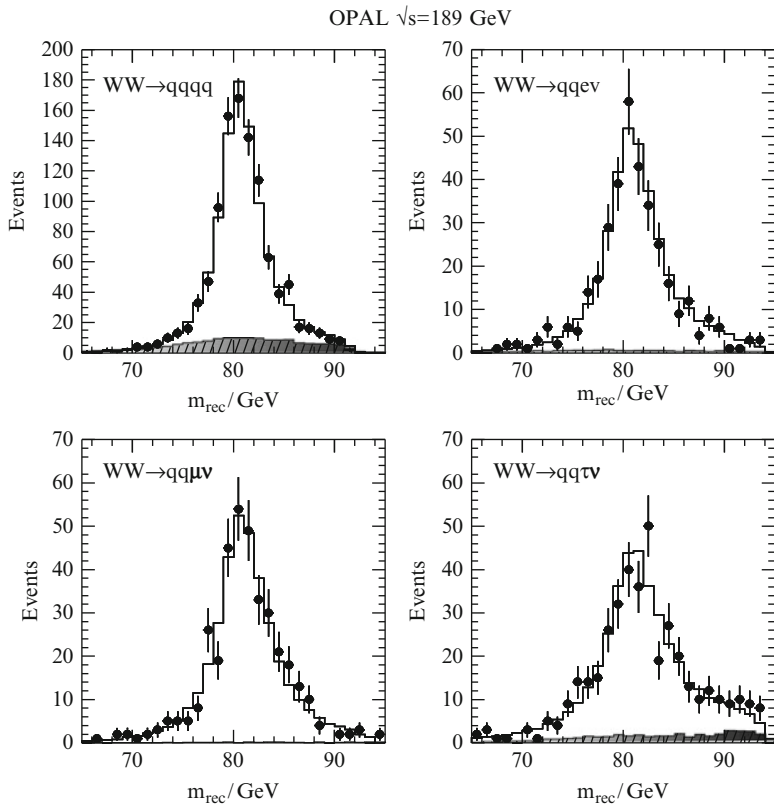


Fig. 9.18 Histograms [9A01] of the invariant mass reconstructed in the hadronic channel and in the three semileptonic channels. The *dots* correspond to the data. The contribution of non-WW background is shown as *shaded histograms*

9.8.2 The W Boson Mass and Width

The W boson mass was measured using the following channels:

- The hadronic channel, which represents 46% of the decays:

$$e^+e^- \rightarrow W^+W^- \rightarrow q\bar{q}' q''\bar{q}''' \quad (9.40a)$$

- The semileptonic channel, which represents 44% of the decays:

$$e^+e^- \rightarrow W^+W^- \rightarrow q\bar{q}' l\nu_l. \quad (9.40b)$$

The invariant mass of the W decay products is computed event by event. Figure 9.18 shows the invariant masses reconstructed in the hadronic channel and in the three semileptonic channels. Background events are mainly present in the hadronic

channel (four jets in the final state); they are mostly due to an incorrect assignment of jets to each W (“combinatorial background”). The invariant mass spectra are then used to reconstruct the mass of the W boson. A kinematic fit is performed, imposing the four constraints of energy and momentum conservation; it is also required that the masses of the two bosons be the same (fifth constraint).

The combination of the four LEP experiments gives the following results:

$$m_W = 80.376 \pm 0.033 \text{ GeV} \quad (9.41\text{a})$$

$$\Gamma_W = 2.196 \pm 0.083 \text{ GeV}. \quad (9.41\text{b})$$

9.8.3 Measurement of α_S

The LEP experiments have carried out many studies on the global properties of multihadronic final states, both at the Z^0 peak and at c.m. energies $\sqrt{s} > 100 \text{ GeV}$. In particular, the global structure of multihadronic events using “event shape” variables were studied in detail; the relative frequency of events with a given number of jets with respect to the total multihadronic production (“jet rate”); the hadronic charged multiplicity. The distribution of the hadronic charged multiplicity as a function of the c.m. energy \sqrt{s} is shown in Fig. 9.19 for e^+e^- , $p(\bar{p})p$ and ep colliders.

Various experimental methods based on these studies allowed the measurement of α_S and the verification of the QCD predictions (discussed in Sect. 11.9.4). For instance, the α_S “running” (i.e., the fact that α_S decreases with increasing E_{cm}) is rather interesting. Combining the results [9w2] from the four LEP experiments, one has

$$\alpha_S(\sqrt{s} = m_Z) = 0.1199 \pm 0.0052$$

$$\alpha_S(\sqrt{s} = 206 \text{ GeV}) = 0.1079 \pm 0.0014.$$

9.8.4 The Higgs Boson Search at LEP

Another motivation for the study of e^+e^- collisions above the Z^0 peak was the search for new particles and particularly for the Higgs boson (see also 10.10).

As we shall see in Chap. 11, the Higgs boson is an essential particle in the Standard Model. At least one neutral boson, the H^0 , should exist after the spontaneous symmetry breaking to give masses to the W^\pm and Z^0 bosons, while keeping the theory renormalizable. The model predicts the couplings of the Higgs boson, but not its mass. The H^0 production cross-section is expected to decrease rapidly with increasing M_{H^0} .

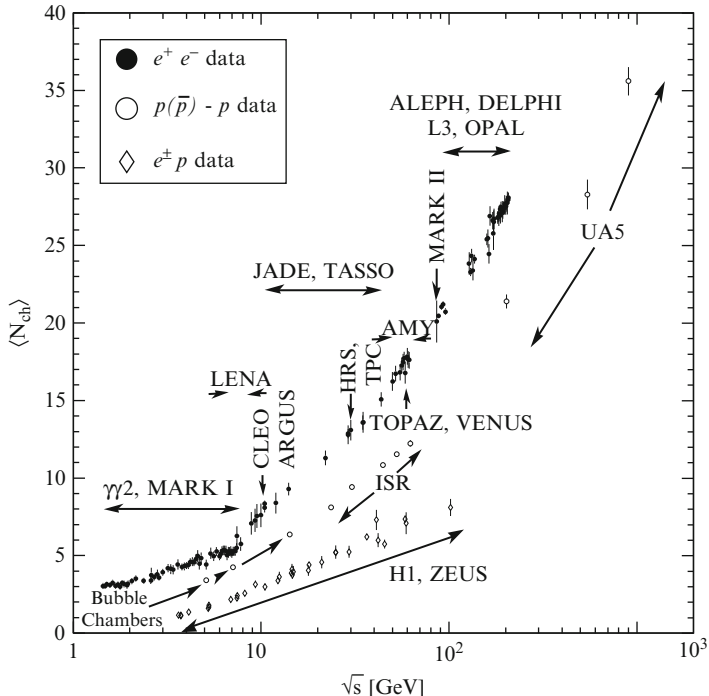


Fig. 9.19 Hadronic charged multiplicities measured by experiments at e^+e^- , $p(\bar{p})p$ and ep colliders as a function of \sqrt{s} [P10]. The indicated errors are statistical and systematic errors added in quadrature

At LEP, the Higgs boson search was made mainly through the “Higgsstrahlung” process $e^+e^- \rightarrow Z^* \rightarrow HZ$ (see Fig. 9.20a). The kinematic limit for this process is given by $M_H^{max} \simeq \sqrt{s} - m_Z$; since $m_Z = 91$ GeV, one obtains $M_H^{max} \simeq 115-116$ GeV for $\sqrt{s} = 206-207$ GeV. It is expected that a Higgs with a mass ~ 115 GeV would decay in $b\bar{b}$ pairs in 74% of the cases since the H coupling is proportional to the mass of the fermion to which it couples. The decays in τ pairs, gluon pairs ($\approx 7\%$ each) and in $c\bar{c}$ ($\approx 4\%$) are less important. The final state topologies are determined from these decays and those of the associated Z^0 boson.

At LEP, the H^0 boson was searched in the following channels:

1. Four hadronic jet channels: $e^+e^- \rightarrow H^0Z^0 \rightarrow b\bar{b}q\bar{q}$
2. Missing energy channel: $e^+e^- \rightarrow H^0Z^0 \rightarrow b\bar{b}\nu\bar{\nu}$
3. τ channel: $e^+e^- \rightarrow H^0Z^0 \rightarrow \tau^+\tau^-q\bar{q}, \rightarrow q\bar{q}\tau^+\tau^-$
4. Leptonic channels: $e^+e^- \rightarrow H^0Z^0 \rightarrow b\bar{b}e^+e^-, \rightarrow b\bar{b}\mu^+\mu^-$.

Figure 9.20b,c show the final state topology (in the plane transverse to the beam axis) in the missing energy channel and in the leptonic channel ($Z^0 \rightarrow e^+e^-$). The channels $Z^0 \rightarrow \nu\bar{\nu}$, $H^0 \rightarrow q\bar{q}$, $\tau^+\tau^-$ are characterized by an asymmetric topology

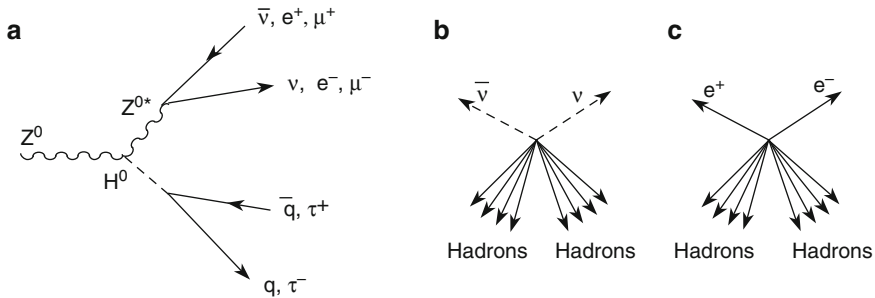


Fig. 9.20 (a) Feynman diagrams for the production and decay of a neutral Higgs boson, H^0 . (b) Sketch of a typical event predicted in the channel $Z^* \rightarrow \nu\bar{\nu}$ and $H^0 \rightarrow q\bar{q}$. (c) As in (b) for the channel $Z^0 \rightarrow e^+e^-$, $H^0 \rightarrow q\bar{q}$

with two hadronic jets in one hemisphere and a large missing energy in the opposite hemisphere. These are important channels because the branching ratio $Z^0 \rightarrow \nu\bar{\nu}$ is large ($\sim 20\%$). Also, the channels $Z^0 \rightarrow e^+e^-$, $\mu^+\mu^-$ and $H^0 \rightarrow q\bar{q}$, $\tau^+\tau^-$ have a simple and characteristic signature with a high detection efficiency; however, they have a smaller branching ratio. The background arises from Standard Model processes $e^+e^- \rightarrow Z^0Z^0$, W^+W^- , $f\bar{f} f'\bar{f}'$, which are very similar to the Higgs candidate events if the mass M_H is close to that of the m_Z . Such a background is reduced by applying selection criteria exploiting the kinematic differences with the signal (properties of the hadronic jets and of the event); these selections vary from experiment to experiment, and from channel to channel.

Combining the results of the four LEP experiments, a lower limit on the mass of the Standard Model Higgs boson was obtained: 114.4 GeV at the 95% confidence level. A small excess (2.1σ) on top of the SM background was observed, mainly in the data collected from ALEPH in the 4-jet channel at $E_{CM} > 206$ GeV.

Chapter 10

High Energy Interactions and the Dynamic Quark Model

10.1 Introduction

In the first part of this chapter, we study *deep inelastic scattering* (DIS) between leptons and nucleons. DIS experiments confirmed that quarks are not fictitious mathematical objects. DIS processes involve high transferred momentum from the lepton to the hadron constituents (the quarks). Quantum chromodynamics (QCD), the field theory describing the strong interaction between quarks and gluons, predicts a small value of the coupling constant α_s at large transferred momentum. Usually, such events have a large transverse momentum (high- p_t), which is the momentum perpendicular to the colliding beams. These high- p_t processes can be computed with perturbation methods.

In the second part of the chapter, we continue with a review of hadron-hadron interactions. These processes are characterized by large cross-sections, slowly varying with the energy available in the center of mass (c.m.) system. Most collisions have low transverse momentum (low- p_t processes). It can be hypothesized that low- p_t interactions involve hadrons as a whole and not only their subconstituents. Since α_s is large when the transferred momentum is small, perturbation theory cannot be used to describe low- p_t interactions. Experimental results must therefore be interpreted using various phenomenological models. At the end, the expected performances of the LHC collider in the search for the Higgs boson are discussed.

10.2 Lepton–Nucleon Interactions at High Energies

Deep inelastic lepton–nucleon collisions provided important information on proton and neutron structure. Historically, the first experimental study was the electron–nucleus elastic scattering, which allowed one to measure the distribution of electric charge inside nuclei (Chap. 14). They were followed, starting at the end of the 1960s by a series of experiments on deep inelastic scattering of electrons on nucleons,

which revealed the proton (and neutron) quark structure. Muon beams of ever increasing energy and quality and finally, high luminosity neutrino beams were used. The improved technology of producing ν_μ beams and the development of large detectors led to the detailed studies of neutrino-nucleon interactions. It should be remembered that it is easier to produce proton or electron beams than beams of muons or neutrinos which are decay products of secondary particles. In inelastic ep (μp) collisions, there are two structure functions related to the magnetic and electric interactions, and corresponding to the two helicity states of the exchanged photon. The inelastic $\nu_\mu + N \rightarrow \mu^- + X$ process depends on three nucleon structure functions related to the three helicity states of the W^\pm bosons. Finally, in the mid-1990s, the HERA collider at Hamburg, Germany, became operational. This accelerator allowed one to study the ep processes in a very large interval of kinematic variables. In each case, the studied reactions were

$$\ell + N \rightarrow \ell' + X, \quad (10.1)$$

where ℓ and ℓ' are charged or neutral leptons; N is the proton or neutron; the hadronic system X can be observed, unobserved or only partially observed.

The most important result was the discovery that inelastic ℓN collisions can be interpreted as the impact of the incident lepton with one constituent of the nucleon, a *parton*, a point-like fermion later identified as a quark or an antiquark. In the original parton model of the proton, the parton constituents were seen as noninteracting point-like particles. Lately, it became evident that partons are confined inside protons and must interact with each other. The parton model is a “naive” representation of the proton structure. The deep inelastic ℓN collision has a simple interpretation in a reference system (the *infinite momentum frame*) in which the proton has high momentum, each parton carries a fraction x of the proton momentum, and masses and transverse momenta of partons can be neglected.

The most studied deep inelastic reactions are

$$ep : e^\pm + p \rightarrow e^\pm + X^+ \quad (10.2a)$$

$$\mu p : \mu^\pm + p \rightarrow \mu^\pm + X^+ \quad (10.2b)$$

$$\nu_\mu p(CC) : \nu_\mu + p \rightarrow \mu^- + X^{++}, \bar{\nu}_\mu + p \rightarrow \mu^+ + X^0 \quad (10.2c)$$

$$\nu_\mu p(NC) : \nu_\mu + p \rightarrow \nu_\mu + X^+, \bar{\nu}_\mu + p \rightarrow \bar{\nu}_\mu + X^+. \quad (10.2d)$$

The X symbol represents a generic final state whose total electric charge is relevant. The first two reactions proceed through the exchange of a photon (the exchange of a Z^0 boson only gives an important contribution at high energies). The last two are weak interaction processes: the third reaction proceeds through the exchange of a W^\pm boson (charged current, CC); the last requires the exchange of the neutral massive Z^0 boson (neutral current, NC). The four reactions are shown in Fig. 10.1a at the level of elementary particles and in Fig. 10.1b in terms of the static quark model of hadrons, where only the so-called “valence quarks” are considered as partons.

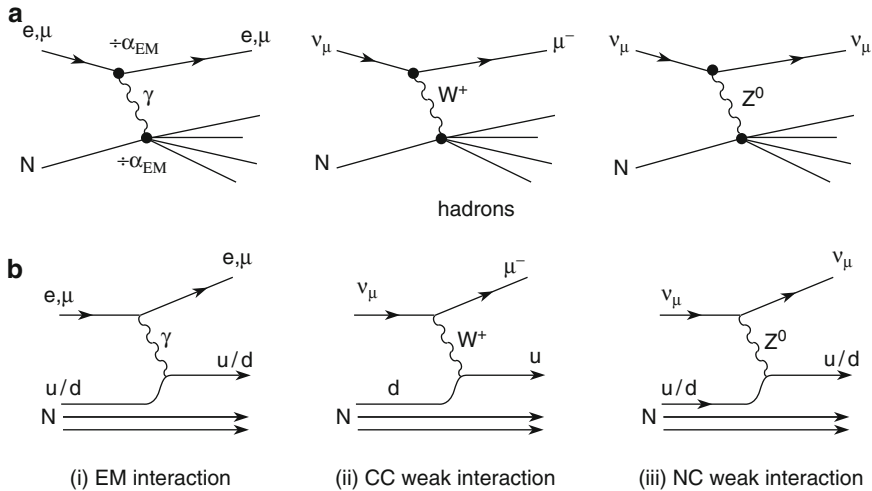


Fig. 10.1 Inelastic lepton–nucleon scattering at the level of (a) elementary particles and (b) in the simplest quark model. The two noninteracting quarks are “spectators” which hadronize (i.e., produce a large number of low p_t , hadrons) in a forward jet. The evolution of the static quark model will take into account the sea quarks and antiquarks, and the gluons present within the nucleon

Submicroscopic structures can be studied with real or virtual photons: the dimension scale that can be tested is inversely proportional to the transferred momentum. The internal structure of the nucleon can be studied with high energy inelastic collisions of charged leptons which occur via the exchange of a virtual photon, as shown in Fig. 10.1a. Deep inelastic collisions are characterized by a high transferred momentum squared, Q^2 . As Q^2 increases, smaller and smaller distances can be explored, according to the uncertainty relation $\Delta x \Delta pc \simeq \Delta x Q c \simeq \hbar c \sim 197 \text{ MeV fm}$; for $Q^2 = 400 \text{ GeV}^2/c^2$, one has $\Delta x \simeq 10^{-17} \text{ m}$; for $Q^2 = 40,000 \text{ GeV}^2/c^2$ (the maximum reached at the HERA collider), one has $\Delta x \sim 10^{-18} \text{ m}$.

Figures 10.1b and 10.2 illustrate some inelastic collision processes in the simplest quark model. The incident lepton interacts with a (valence) quark of the nucleon by emitting a high- Q^2 boson. Other constituents, such as gluons, “sea” quarks and antiquarks, are neglected. Figure 10.2 shows a two-stage process: the first stage is an almost elastic collision of the lepton with a quark, which carries a fraction x of the proton momentum; the virtual boson is absorbed by the quark. The corresponding *structure function* $F(x)$ describes the momentum distribution of the constituents within the proton. The photon (and also the massive W^+ , W^- , Z^0 bosons) does not interact directly with gluons, which are continuously exchanged to confine the quarks inside the proton.

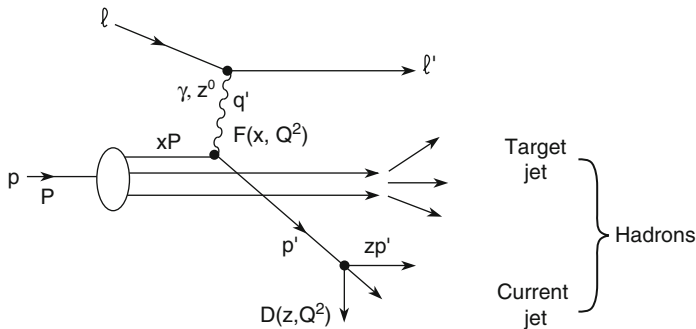


Fig. 10.2 Sketch of an inelastic lepton–nucleon scattering as a two-stage process. The parton interacting with the lepton carries a fraction x of the proton four-momentum P . The first stage involves the structure function $F(x, Q^2)$. In the second stage, the scattered parton, with four-momentum Q , gives rise to a jet of hadrons (current jet). The fragmentation function $D(z, Q^2)$ is defined for each hadron carrying a fraction z of the jet energy. The remaining two quarks are “spectators” and hadronize in a forward jet (target jet)

The second stage of the process is the parton *fragmentation* into two jets of hadrons. This is a complicated multistage strong interaction process, which “dresses” naked quarks to form hadrons in the final state. The first *hadron jet* comes from the parton interacting with the lepton and the second (denoted as *spectator jet* or *target jet*) comes from the spectator partons. Usually, the first jet is at large angles (high- p_t) and the second is emitted almost in the same direction of the incident proton (low- p_t). The energy distribution of each hadron type from the interacting parton is called the *fragmentation function*, $D(z, Q^2)$. It gives the probability that a given hadron carries a fraction z of the interacting parton energy. This energy is not experimentally measurable and must be estimated. In this second stage, the gluons play an important role. As illustrated in this chapter, the strong interaction amongst constituents modifies the structure function, making it dependent on Q^2 , $F(x, Q^2)$.

The γ_{virtual} -parton collision of the first phase occurs within a time $\Delta t_1 \sim \hbar/v$, where $v = E - E'$ is the transferred energy. The quark hadronization (or quark *dressing*) is characterized by a time $\Delta t_2 \sim \hbar/m_p c^2 \simeq 10^{-24} \text{ s}$ (m_p = proton mass). If $v \gg m_p$, one has $\Delta t_1 \ll \Delta t_2$ and the two subprocesses can be considered as distinct. In general, the hadronization occurs within

$$\Delta t_{\text{hadroniz}} \sim \hbar/Mc^2 \simeq 10^{-23} \div 10^{-24} \text{ s}, \quad (10.3)$$

where M is the mass of the formed hadron system. Note that the production of a top quark (t), whose mass is around 170 GeV, represents a special case. Due to its very high mass, the decay time through weak interaction (see Fig. 8.20) is smaller than the hadronization time. Unlike the other quarks, the t quark has no time to get dressed before decaying.

10.3 Elastic Electron-Proton Scattering

10.3.1 Kinematic Variables

Figure 10.3 illustrates the kinematics of an ep elastic scattering in the laboratory system using energy-momentum covariant four-vectors with $\hbar = c = 1$. The four-momenta of the involved particles are

$$P = (E, \mathbf{p}); P' = (E', \mathbf{p}') \quad \text{for the incident and scattered electron} \quad (10.4)$$

$$P_0 = (M, 0); W = (E'_0, \mathbf{p}'_0) \quad \text{for the proton before and after impact.} \quad (10.5)$$

M is the proton mass. The square of the four-momentum of the incident electron and of the proton at rest are

$$P^2 = (E^2/c^2 - \mathbf{p}^2) = m_e^2 c^2 \xrightarrow{c=1} m_e^2; \quad P_0^2 = M^2. \quad (10.6)$$

The four-momentum transferred by the e^- in the scattering is

$$q = P - P' = (E - E', \mathbf{p} - \mathbf{p}') = (v, \mathbf{q}) \quad (10.7)$$

and its square $t = q^2$ is

$$\begin{aligned} t = q^2 &= (P' - P)^2 = (E'/c - E/c)^2 - (\mathbf{p}' - \mathbf{p})^2 \\ &\xrightarrow{c=1} 2m_e^2 - 2E'E + 2\mathbf{p}'\mathbf{p} \cos\theta. \end{aligned} \quad (10.8)$$

At high energy, the electron mass can be neglected ($m_e = 0, p \simeq E$), that is,

$$q^2 = -Q^2 \simeq -2EE'(1 - \cos\theta) = -4EE' \sin^2(\theta/2). \quad (10.9)$$

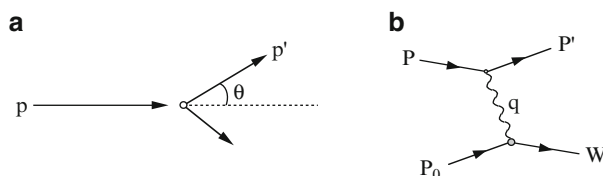


Fig. 10.3 (a) The kinematics of elastic $e^- p \rightarrow e^- p$ scattering in the laboratory system. \mathbf{p} e \mathbf{p}' are the electron momenta before and after collision; θ is the scattering angle. In (b), the corresponding Feynman diagram is shown: P, P' and P_0, W are, respectively, the energy-momentum four-vectors of the electron and of the hadronic system before and after collision. q is the transferred four-momentum

Since q^2 is negative, the quantity $Q^2 = -q^2$ is often used. For scattering at high energy and small angles, one has $p' \simeq p$, $\sin \theta \simeq \theta$ and $t = q^2 \simeq -p^2\theta^2$. In terms of the four-momentum transferred to the proton, one has

$$t = q^2 = (M - E'_0)^2 - (0 - \vec{p}')^2 = 2M^2 - 2MW = -2MT_p \quad (10.10)$$

where $T_p = W - M$ is the kinetic energy of the recoiling proton.
The total energy in the center of mass is

$$s = (P + P_0)^2 = p^2 + P_0^2 + 2PP_0 = m_e^2 + M^2 + 2EM \simeq M^2 + 2EM. \quad (10.11)$$

Finally, one has

$$P_0 \cdot q = Mv \quad \text{with} \quad v = E - E', \quad (10.12)$$

representing the condition for elastic scattering.

The numerical values of the squared four-vector, for example, q^2 and s , are the same in any reference system; they can be calculated in the laboratory system as shown here. For an elastic scattering, one has $q^2 < 0$; this condition is called *space-like*. In annihilation processes, one has $q^2 > 0$; this situation is called *time-like*. As shown below, the cross-section for elastic ep scattering can be calculated using successive approximations.

10.3.2 Proton Form Factors

Rutherford scattering. The simplest calculation concerns the elastic scattering of a spinless, point-like electron with mass m_e and charge $-e$ by a point-like infinitely massive nucleus of charge Ze (for the proton $Z = 1$). The elastic cross-section is described by the Rutherford formula seen in Sect. 4.7.1 (for $z = 1$), that is,

$$\left(\frac{d\sigma}{d\Omega} \right)_R = \frac{Z^2 e^4}{q^4} = \frac{Z^2 e^4}{t^2} = \frac{Z^2 e^4}{4E_0^2 \sin^4 \frac{\theta}{2}}. \quad (10.13)$$

The formula and the corresponding Feynman diagram are shown in the Box here below. Note that the wave line representing the exchanged photon ends (on the right) in the massive charge Ze .

Mott formula. The next approximation introduces the electron spin through the relativistic Dirac equation. The proton spin is still ignored. For relativistic electrons, the spin vector σ is aligned with the electron momentum \mathbf{p} . The *helicity* is the projection of the spin along the direction of the momentum (Appendix A.4). The electron helicity can be $\Lambda = \pm 1$. The electron is right-handed or left-handed if the helicity is $\Lambda = +1$ or $\Lambda = -1$, respectively. The *electromagnetic interaction conserves the helicity*. This implies constraints on the shape of the final state wave function [P87], which introduces a factor $\cos^2(\frac{\theta}{2})$ in the cross-section:

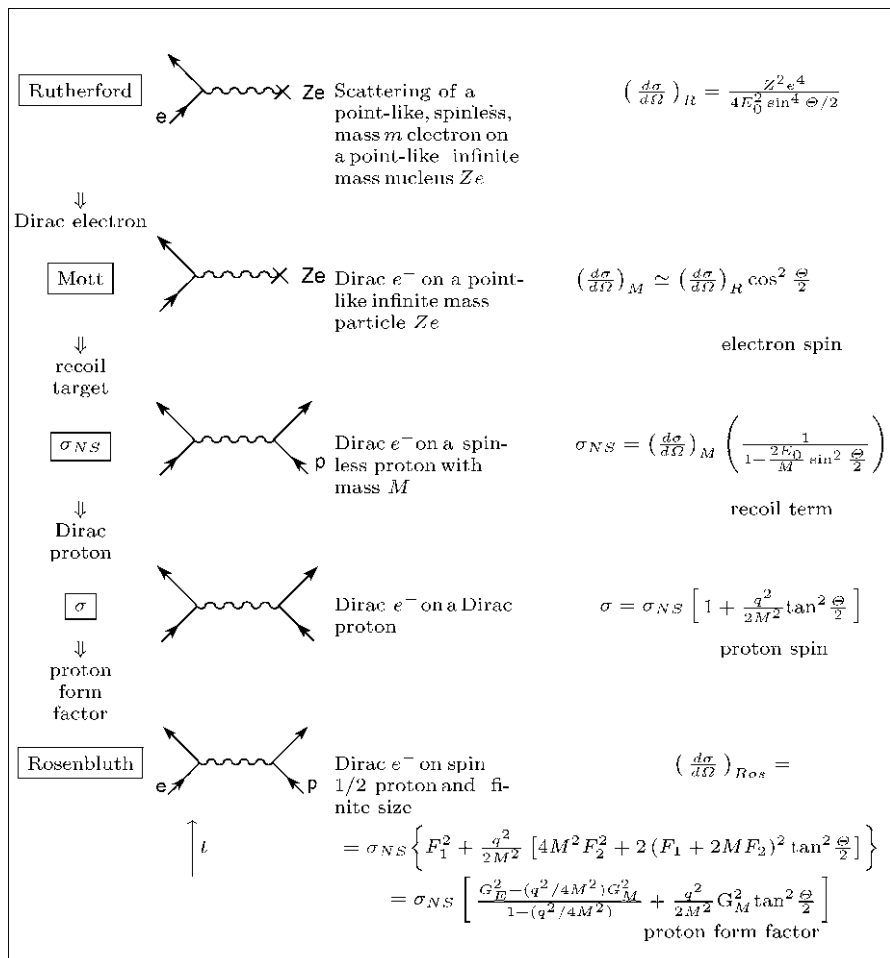
$$\left(\frac{d\sigma}{d\Omega}\right)_M = \left(\frac{d\sigma}{d\Omega}\right)_R (1 - \beta^2 \sin^2 \theta/2) \simeq \left(\frac{d\sigma}{d\Omega}\right)_R \cos^2(\theta/2). \quad (10.14)$$

Proton with mass M . In the previous formulas, the proton was considered as infinitely massive. The Feynman diagram must be modified (see Box) to include its finite mass M , leading to the following formula, that is,

$$\left(\frac{d\sigma}{d\Omega}\right)_{NS} = \left(\frac{d\sigma}{d\Omega}\right)_M \frac{1}{1 + (2E_0/M) \sin^2(\theta/2)}, \quad (10.15)$$

reducing to (10.14) for $M \rightarrow \infty$.

Box. Differential $e^- p$ cross-section with increasing accuracy in the description of the proton and electron structures. Note that in these Feynman diagrams, the time axis goes from bottom to top.



Proton with spin. The next approximation includes the spin of the proton, which is assumed to be point-like (Dirac proton). The introduction of the spin induces an additional term due to the magnetic dipole μ interaction between an electron and a proton at a distance r : $\frac{\mu_0}{4\pi} \frac{\mu \times \mathbf{r}}{r^3}$. The cross-section becomes

$$\left(\frac{d\sigma}{d\Omega} \right) = \left(\frac{d\sigma}{d\Omega} \right)_{NS} \left[1 + \frac{q^2}{2M^2} \tan^2(\theta/2) \right]. \quad (10.16a)$$

However, the magnetic moment of the proton (or neutron) is different from that predicted by the Dirac theory for spin 1/2 particles, i.e., $\mu_0 = e\hbar/2Mc$ (Sect. 7.14.4). In 1950, Rosenbluth obtained

$$\left(\frac{d\sigma}{d\Omega} \right) = \left(\frac{d\sigma}{d\Omega} \right)_{NS} \left\{ 1 + \frac{q^2}{4M^2} \left[2(1 + \kappa)^2 \tan^2(\theta/2) + \kappa^2 \right] \right\} \quad (10.16b)$$

for a “point-like” nucleus, where κ is the *anomalous* part of the magnetic moment, and equal to 1.79 for the proton and -2.91 for the neutron,

$$\mu_{p,n} = (1 + \kappa)\mu_0. \quad (10.17)$$

Formula (10.16b) can be extended to the case of a nucleon with an internal structure by introducing the so-called *form factors* $F_1(q^2)$ and $F_2(q^2)$.

Proton with finite size. Finally, the finite size of the proton ($\sim 10^{-15}$ m) must be taken into account. A *spatial form factor* $f(r)$ is introduced to remove the point-like approximation and to describe the electric charge spatial distribution, that is,

$$\varrho(r) = e f(r) \quad (10.18)$$

where $\varrho = dq/dv$, with the condition that $\int f(r)dv = 1$, that is, $\int \varrho(r)dv = e$.

In the simplest case, the distribution function $f(r)$ can be interpreted as the classical spatial distribution of electric charge, or the probability distribution of finding the charged point-like constituents in the proton volume. The *form factor* $F(\mathbf{q})$ is defined as the Fourier transform of the spatial distribution $f(r)$ and correspond to $f(r)$ in the momentum space

$$F(\mathbf{q}) = \int e^{i\mathbf{q}\cdot\mathbf{x}} f(r) d^3x. \quad (10.19)$$

Examples of some form factors are listed in Table 10.1 and shown in Fig. 10.4, assuming in all cases a spherically symmetric $f(r)$.

The Fourier transform (10.19) of the Yukawa potential has been explicitly derived in Sect. 4.4. This potential, except for numerical constants, has a similar dependence in r than that of the Yukawa charge spatial distribution given in Table 10.1. We may notice that $F(\mathbf{q})$ depends in this case only on the scalar quantity q^2 .

Table 10.1 Charge spatial distributions and corresponding form factors expressed as a function of the transferred four-momentum $q = \sqrt{|t|}$

Charge spatial distribution	Form factor	
Point-like	$f(r) = \delta(r - r_0)$	$F(q^2) = 1$ constant
Exponential	$f(r) = \frac{a^3}{8\pi} e^{-ar}$	$F(q^2) = \left[\frac{1}{1+q^2/a^2} \right]^2$ dipole
Yukawa	$f(r) = \frac{a^2}{4\pi r} e^{-ar}$	$F(q^2) = \frac{1}{1+q^2/a^2}$ pole
Gaussian	$f(r) = \left(\frac{a^2}{2\pi} \right)^{\frac{1}{2}} e^{-(a^2 r^2/2)}$	$F(q^2) = e^{-(q^2/2a^2)}$ Gaussian

The fact that $F(\mathbf{q}) = F(q^2)$ is true even if the charge distributions are exponential or Gaussian, as shown in the table. Hereafter, the form factor will always be referred to as $F(q^2)$.

Equation 10.16b can be generalized to take into account the proton (or neutron structure) due to charge distribution and magnetization, that is,

$$\left(\frac{d\sigma}{d\Omega} \right) = \left(\frac{d\sigma}{d\Omega} \right)_{NS} \left\{ F_1(q^2) + \frac{q^2}{4M^2} \left[2(F_1(q^2) + \kappa F_2(q^2))^2 \tan^2 \frac{\theta}{2} + \kappa^2 F_2^2(q^2) \right] \right\}. \quad (10.20)$$

The form factors are different for electron collisions on protons or neutrons: they will be listed in the following with a p or n superscript. The q^2 dependence indicates that the form factors are expected to vary with the square of the transferred four-momentum. For low q^2 , the form factors are normalized to

$$F_1^p(0) = F_2^p(0) = F_2^n(0) = 1; \quad F_1^n(0) = 0.$$

F_1^p , F_2^p and F_1^n , F_2^n (sometimes called Dirac and Pauli form factors) can be more conveniently expressed as a linear combination, producing the so-called electric and magnetic form factors. For the proton and the neutron, they are defined as

$$G_E^{p,n}(q^2) = F_1^{p,n}(q^2) - \frac{q^2}{4M^2} \kappa F_2^{p,n}(q^2) \quad (10.21a)$$

$$G_M^{p,n}(q^2) = F_1^{p,n}(q^2) + \kappa F_2^{p,n}(q^2). \quad (10.21b)$$

The *electric form factor* $G_E(q^2)$ describes the electric charge distribution inside the proton or the neutron. The *magnetic form factor* $G_M(q^2)$ describes the distribution of the magnetic dipole moment. It should be noted that the interpretation of form factors in terms of charge spatial distribution has no meaning in the high energy limit because the incident electron does not see a static charge distribution, but a

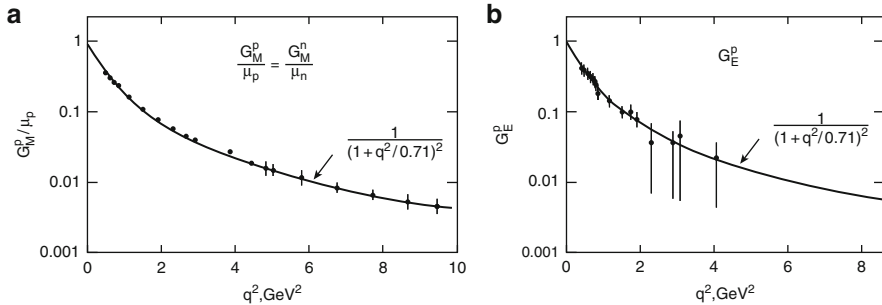


Fig. 10.4 Electric and magnetic form factors of the proton and magnetic form factor of the neutron. The *solid line* represents a fit with a dipole form factor (see Table 10.1), corresponding to a Yukawa-like charge spatial distribution

moving one. The electric and magnetic form factors are normalized to the electric charge and magnetic moment of each particle, for example,

$$\begin{aligned}
 G_E^p(q^2) \text{ is normalized to: } G_E^p(0) &= 1 \\
 G_M^p(q^2) &\quad " \quad G_M^p(0) = 2.79 \\
 G_E^n(q^2) &\quad " \quad G_E^n(0) = 0 \\
 G_M^n(q^2) &\quad " \quad G_M^n(0) = -1.91.
 \end{aligned} \tag{10.22}$$

With the introduction of form factors in (10.20), the Rosenbluth formula for the ep elastic scattering is obtained, namely,

$$\left(\frac{d\sigma}{d\Omega} \right)_{Ros} = \left(\frac{d\sigma}{d\Omega} \right)_{NS} \left[\frac{G_E^2 + (q^2/4M^2)G_M^2}{1 + (q^2/4M^2)} + \frac{q^2}{2M^2} G_M^2 \tan^2 \frac{\theta}{2} \right]. \tag{10.23}$$

Note that there is no interference between the electric and magnetic form factors. If the Rosenbluth cross-section is plotted at $q^2 = \text{constant}$ and for different energies and scattering angles, a linear dependence on $\tan^2(\theta/2)$ is obtained, namely,

$$\left(\frac{d\sigma}{d\Omega} \right)_{Ros} / \left(\frac{d\sigma}{d\Omega} \right)_{NS} = A(q^2) + B(q^2) \tan^2 \frac{\theta}{2}. \tag{10.24}$$

The experimental proof of such a linear dependence on $\tan^2(\theta/2)$ is evidence that the scattering is mediated by the exchange of a single photon.

Measurement of proton and neutron form factors are shown in Fig. 10.4. They were first obtained in the 1960s by R. Hofstadter for the proton. Because free neutrons are not available in nature, the neutron form factors were derived from

measurements on deuterium (the pn bound state) after subtracting the contribution of the proton. The results can be parameterized by the following empirical expression, the *scaling law* and the *dipole formula*. Scaling law:

$$G(q^2) = G_E^p(q^2) = \frac{G_M^p(q^2)}{\mu_p} = \frac{G_M^n(q^2)}{|\mu_n|} \quad (10.25a)$$

$$G_E^n(q^2) = 0. \quad (10.25b)$$

Dipole formula:

$$G(q^2) = \left(\frac{1}{1 + (q^2/0.71)} \right)^2 [q^2 \text{ in } (\text{GeV}/c)^2]. \quad (10.26)$$

The Fourier transform of the dipole form factor in the coordinate space gives (see Table 10.1, r in fm)

$$f(r)_{\text{dipole}} = 3.06 e^{-4.25r}. \quad (10.27)$$

For small transferred momentum, one has

$$G_E^p(q^2) \simeq f(0)[1 - (1/6)q^2\langle r^2 \rangle], \quad (10.28)$$

with $\sqrt{\langle r^2 \rangle} = 0.81$ fm. For high transferred momenta, the elastic form factors are very small and inelastic scattering of the incident electron becomes much more likely than elastic scattering.

10.4 Inelastic ep Cross-Section

If the reaction (10.1) is inelastic, the target fragments in a final state of mass $W > M$. The lepton energy and scattering angle in the final state are independent variables (Fig. 10.5). The mass of the system X is

$$W^2 = (P_0 + q)^2 = M^2 + q^2 + 2M\nu = M^2 - Q^2 + 2M\nu > M^2. \quad (10.29)$$

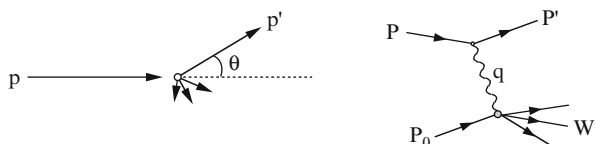


Fig. 10.5 Kinematics of inelastic scattering $e^- p \rightarrow e^- p'$ in the laboratory system and as a Feynman diagram. See Fig. 10.3 for a description of the variables

In this case,

$$2M\nu > Q^2. \quad (10.30)$$

For inelastic scattering, the squared transferred four-momentum q^2 and the transferred energy ν are independent variables. The elastic limit is characterized by the condition $W^2 = M^2$, i.e., $2M\nu = Q^2$. The inelastic cross-section can be expressed in terms of these two variables as

$$\frac{d^2\sigma}{dQ^2d\nu} = \frac{4\pi\alpha^2}{Q^4} \frac{E'}{E} \cos^2 \frac{\theta}{2} \left(W_2(Q^2, \nu) + W_1(Q^2, \nu) 2 \tan^2 \frac{\theta}{2} \right). \quad (10.31)$$

Equation 10.31 is similar to Eq. 10.16a for elastic scattering. The difference is that now W_1, W_2 are arbitrary *structure functions*, which generally depends on the two kinematic variables Q^2, ν .

Deep inelastic scattering (DIS) experiments were used to investigate the inner structure of protons and neutrons, and to test the quark hypothesis. The deep inelastic scattering conditions are defined by

$$Q^2 \gg M^2; \quad \nu = E - E' \gg M. \quad (10.32)$$

Deep inelastic interactions of *elementary* particles like electrons, muons or neutrinos with a nucleon will be the result of a superposition of elastic scattering with the constituents if the nucleon is composed of point-like particles. If these *partons* have mass m and if the transferred energy is much larger compared to their binding energy, the cross-section (10.31) will be the sum of the contributions of the *lepton elastic scattering on the different partons*, that is,

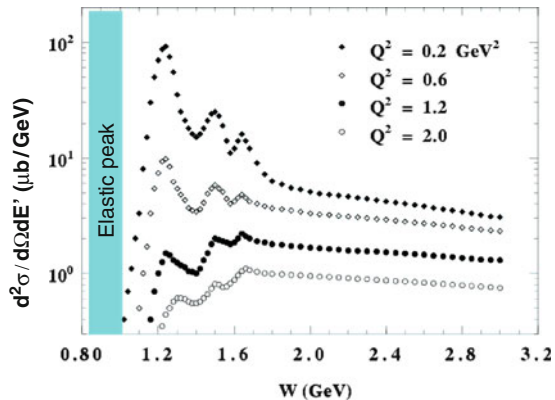
$$\left(\frac{d^2\sigma}{dQ^2d\nu} \right)_{ela} = \frac{4\pi\alpha^2}{Q^4} \frac{E'}{E} \cos^2 \frac{\theta}{2} \left(1 + \frac{Q^2}{4m^2} 2 \tan^2 \frac{\theta}{2} \right) \delta\left(\nu - \frac{Q^2}{2m}\right). \quad (10.33)$$

Note that (1) $\delta(\nu - Q^2/2m)$ expresses the condition that the impact is elastic ($W = m$) from (10.29); (2) since the collision with the parton is elastic, Eq. 10.33 has the same structure as the elastic ep cross-section (10.16a) after replacing M with the parton mass m ; (3) comparing Eq. 10.33 with Eq. 10.31, the following conditions on the structure functions can be written as

$$W_2(Q^2, \nu) \rightarrow \frac{1}{\nu} \delta\left(\nu - \frac{Q^2}{2m}\right); \quad W_1(Q^2, \nu) \rightarrow \frac{Q^2}{4m^2\nu} \delta\left(\nu - \frac{Q^2}{2m}\right). \quad (10.34)$$

In 1967, Bjorken showed that in deep inelastic scattering, the structure functions describing the nucleon depend on dimensionless variables. In particular, they do not depend on the transferred four-momentum Q^2 , on the transferred energy ν and on the nucleon size, as in the case of elastic scattering. This property was derived assuming that the collisions of electrons, muons and neutrinos on p and n occur with

Fig. 10.6 Differential cross-section for ep interactions as a function of the hadronic energy W



their point-like fermionic constituents; it is called the *Bjorken scaling law*. Bjorken scaling assumes that for $Q^2 \rightarrow \infty$, $v \rightarrow \infty$, the quantity

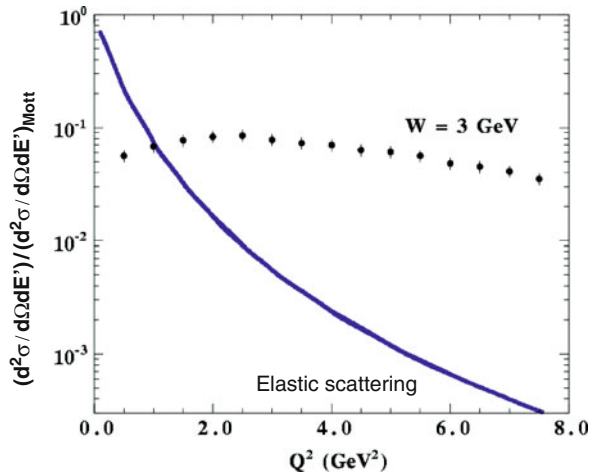
$$x = \frac{Q^2}{2Mv} \quad \text{remains finite.} \quad (10.35)$$

Let us assume that the elastic scattering condition $Q^2 = 2mv$, for a mass m parton at rest in the laboratory system, is valid. In this case, Eq. 10.35 becomes $x = m/M$. In this way, the variable x can be interpreted as the fraction of the nucleon mass carried by the parton interacting with the lepton. Consequently, the structure functions W_1, W_2 , in the high energy limit, do not separately depend on Q^2 and v , but only by the dimensionless ratio x , that is,

$$vW_2(Q^2, v) \xrightarrow{Q^2 \rightarrow \infty, v \rightarrow \infty} F_2(x); \quad MW_1(Q^2, v) \xrightarrow{Q^2 \rightarrow \infty, v \rightarrow \infty} F_1(x). \quad (10.36)$$

The proof of this hypothesis was obtained starting in 1968 with a series of experiments lead by Friedman, Kendall and Taylor (Nobel laureate in 1990) and collaborators at the Stanford University Linear Accelerator (SLAC) in California. In these experiments, a linear electron accelerator of approximately 3 km long produced electron beams up to 20 GeV that were directed on hydrogen and deuterium targets. The energy E' and the scattering angle θ of the electron in the final state were measured; from these measurements, Q^2, v and W were obtained. Figure 10.6 shows the differential cross-section $d\sigma^2/d\Omega dE'$ as a function of the hadronic energy W . The peak of the elastic scattering on the proton, at $W = M$, has been removed for clarity. At $W \sim 1.2 - 1.8$ GeV, the excitation of baryonic resonances (the first is the usual Δ with a mass of 1230 MeV) are visible; no excited states are present in the continuous distribution for $W > 1.8$ GeV. At a fixed W , the cross-section decreases rapidly with increasing Q^2 due to the form factor $F(Q^2)$: assuming that the scattering is elastic on the parton constituents, it is expected that the cross-section decreases with increasing Q^2 , similar to the elastic form factors (Fig. 10.4).

Fig. 10.7 ep interaction: ratio between the elastic (solid curve) and inelastic cross-sections (points) and the Mott cross-section (on a point-like and spinless target) as a function of the transferred four-momentum



With increasing transferred four-momentum Q^2 , the total electron-proton cross-section decreases: inelastic scattering becomes increasingly important compared to the elastic one. This is evident in Fig. 10.7, where the inelastic and elastic cross-sections are compared to a function of Q^2 . The inelastic cross-section becomes larger than the elastic one when Q^2 is larger than the values corresponding to the resonance formation ($Q^2 \sim O(1 \text{ GeV}^2)$). In addition, at fixed $W^2 = M^2 + 2Mv - Q^2$, the inelastic cross-section remains approximately constant and does not depend on Q^2 , as can be seen in Fig. 10.7 for $W = 3 \text{ GeV}$. The Bjorken scaling law is verified in the Q^2 region where the production of baryonic resonances is no longer important.

10.4.1 Partons in the Nucleons: Their Nature and Spin

The meaning of the Bjorken x variable (10.35) and of the functions $F_1(x)$ and $F_2(x)$ becomes more clear if the cross-section (10.31) is expressed as a function of x (the variable $x = Q^2/2Mv$ implies that $\frac{dx}{dv} = \frac{x}{v}$ and thus $\frac{d}{dx} = \frac{v}{x} \frac{d}{dv}$), that is,

$$\begin{aligned} \frac{d^2\sigma}{dQ^2dx} &= \frac{v}{x} \frac{d^2\sigma}{dQ^2dv} = \frac{4\pi\alpha^2}{Q^4} \frac{E'}{E} \frac{1}{x} \cos^2 \frac{\theta}{2} \left(vW_2(Q^2, v) + vW_1(Q^2, v)2\tan^2 \frac{\theta}{2} \right) \\ &= \frac{4\pi\alpha^2}{Q^4} \frac{E'}{E} \frac{1}{x} \cos^2 \frac{\theta}{2} \left(F_2(x) + \frac{vF_1(x)}{M} 2\tan^2 \frac{\theta}{2} \right) \\ &= \frac{4\pi\alpha^2}{Q^4} \frac{E'}{E} \frac{1}{x} \cos^2 \frac{\theta}{2} \left(F_2(x) + 2xF_1(x) \frac{Q^2}{4M^2x^2} 2\tan^2 \frac{\theta}{2} \right). \end{aligned} \tag{10.37}$$

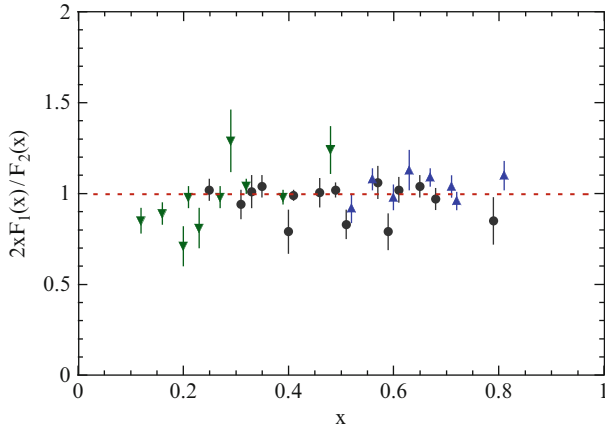


Fig. 10.8 Ratio $2xF_1(x)/F_2(x)$ as a function of the variable x for different Q^2 values. The figure refers to SLAC experimental data with (∇) $1.5 < Q^2 < 4 \text{ GeV}^2$; (\bullet) $5 < Q^2 < 11 \text{ GeV}^2$ and (\blacktriangle) $12 < Q^2 < 16 \text{ GeV}^2$

The two Bjorken structure functions F_1 and F_2 are not independent if the nucleon constituents are spin 1/2 fermions. Comparing the cross-section (10.38) with that of the elastic interaction of leptons on spin 0 particles (10.14) or on spin 1/2 particles with mass $m = Mx$ (10.16a), we deduce that

- For spin 0 constituents, one has $F_1(x) = 0$.
- For spin 1/2 constituents, one has

$$\boxed{F_2(x) = 2xF_1(x)}, \quad (10.38)$$

known as the *Callan-Gross relation*.

Figure 10.8 shows the value of the ratio $2xF_1(x)/F_2(x)$ measured at different Q^2 and v . The ratio is clearly different from zero and remains constant and approximately equal to one. Therefore, deep inelastic scattering experiments of electrons show that protons and neutrons *consist of spin 1/2 point-like constituents*.

Using the Callan-Gross relation, Eq. 10.38 can be written as

$$\frac{d^2\sigma}{dQ^2 dx} = \frac{4\pi\alpha^2}{Q^4} \frac{E'}{E} \frac{F_2(x)}{x} \cos^2 \frac{\theta}{2} \left(1 + \frac{Q^2}{4M^2 x^2} 2 \tan^2 \frac{\theta}{2} \right). \quad (10.39)$$

This relation has an attractive interpretation in the parton model introduced by Feynman in 1969. He considered the inelastic collision in a reference system in which the hadron target has high momentum ($|\mathbf{p}| \gg M$) so that the constituent masses and the transverse momenta can be neglected:

- The hadron consists of charged point-like particles called partons.
- The four-momentum P_o of the hadron is distributed among the partons.

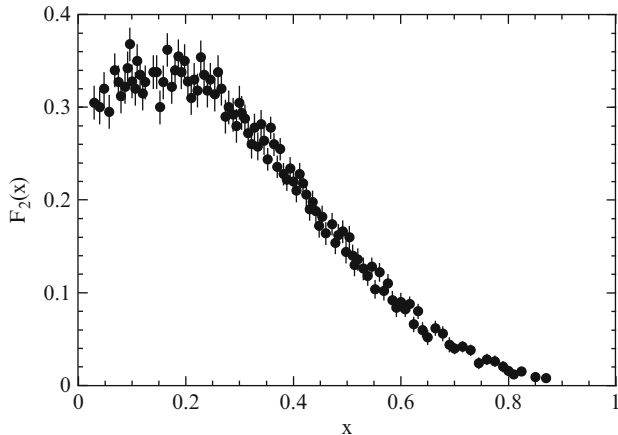


Fig. 10.9 Experimental measurements of the proton structure function $F_2^{ep}(x)$ as a function of the variable x . Note that $\int_0^1 F_2(x)dx \simeq 0.14$

- The inelastic interaction with transferred four-momentum Q and energy v is the result of elastic scattering on a parton with four-momentum xP_o .
- The structure function $F_2(x)/x$ represents the distribution function of partons in the nucleon.

This is the mechanism presented in Fig. 10.2. The square of the total electron-parton energy is

$$s = (P + xP_o)^2 = 2EMx + x^2M^2 + M^2 \simeq 2EMx \quad (E \gg M) \quad (10.40)$$

and the four-momentum Q is exchanged between the electron and the parton. The parton four-momentum after the interaction (recalling 10.35) is

$$(q + xP_o)^2 = -Q^2 + 2Mvx + x^2M^2 = -Q^2 + 2Mv\frac{Q^2}{2Mv} + (xM)^2 = m^2 \ll W^2 \quad (10.41)$$

and the hadron fragments into a final state with invariant mass W . The final state also contains the remaining partons carrying the residual four-momentum $(1-x)P_o$. The function $F_2(x)$ measured in electron-proton deep inelastic scattering is shown in Fig. 10.9.

10.4.2 Electric Charge of the Partons

The nucleon is made of point-like partons of spin 1/2. One may wonder if the partons can be identified with the quarks. Quarks have fractional electric charge, $e_u = 2/3$ and $e_d = e_s = -1/3$, in units of the elementary charge. The cross-section

for electromagnetic interactions is proportional to the electric charge squared: the interaction of an electron with a parton with a charge e_u has a larger probability to occur with respect to the interaction with a parton with a charge e_d by a factor $e_u^2/e_d^2 = 4$. Denoting with $f_k(x)$ the density in the nucleon of quarks of flavor k , the structure function $F_2(x)$ must take into account the different couplings with the parton electric charges through the constants $e_k = e_u, e_d, e_s$, that is,

$$F_2(x) = \sum_k e_k^2 \cdot x \cdot f_k(x). \quad (10.42)$$

Quark-antiquark pairs of the same flavor can also be produced in a deep inelastic interaction; the electromagnetic coupling constant has the same value for quarks and antiquarks. It is convenient to define the quarks that define the hadron quantum numbers as *valence quarks*: the proton $|p\rangle = |uud\rangle$ has two valence quarks u and a valence quark d ; the neutron $|n\rangle = |udd\rangle$ has a u quark plus two d valence quarks. The *sea quarks* are virtual quark-antiquark pairs of mass m_q , produced inside the nucleon through the strong interaction. Sea quark pairs are continuously created; they survive for a time interval Δt such that $\Delta t \cdot 2m_q < \hbar$, as the virtual e^+e^- pairs in Fig. 4.2f. The creation of c, b, t pairs is disfavored because of their high mass value.

Starting from (10.42), the proton and neutron structure functions may be measured using incoming electrons:

$$F_2^{ep} = x \left[\frac{4}{9}[(u_p(x) + \bar{u}(x)] + \frac{1}{9}[(d_p(x) + \bar{d}(x) + s(x) + \bar{s}(x))] \right] \quad (10.43a)$$

$$F_2^{en} = x \left[\frac{4}{9}[(u_n(x) + \bar{u}(x)] + \frac{1}{9}[(d_n(x) + \bar{d}(x) + s(x) + \bar{s}(x))] \right] \quad (10.43b)$$

$u_p(x), d_p(x)$ are respectively the densities of u and d quarks in the proton; $u_n(x), d_n(x)$ are those in the neutron. Sea pairs $u\bar{u}, d\bar{d}, s\bar{s}$ have approximately the same density in the proton and in the neutron (the indices n, p are not indicated) and the contribution of higher mass quarks is negligible. The isospin symmetry in hadronic interaction leads to the hypothesis that the density of u valence quarks in the proton is equal to the density of d valence quarks in the neutron. The role of u quarks in the proton corresponds to that of d quarks in the neutron, that is,

$$u_p(x) = d_n(x) = u_v(x); \quad d_p(x) = u_n(x) = d_v(x). \quad (10.43c)$$

With this hypothesis, the proton and neutron structure functions become

$$\begin{aligned} F_2^{ep} &= x \left[\frac{4}{9}(u_v + \bar{u}) + \frac{1}{9}(d_v + \bar{d} + s + \bar{s}) \right]; \\ F_2^{en} &= x \left[\frac{4}{9}(d_v + \bar{d}) + \frac{1}{9}(u_v + \bar{u} + s + \bar{s}) \right]. \end{aligned} \quad (10.44)$$

In a target with equal numbers of protons and neutrons (called *isoscalar target*), for example, deuterium, the numbers of u and d quarks are equal; a structure function averaged over the content of the valence and sea quarks is

$$\begin{aligned} F_2^{eN} &= \frac{F_2^{ep} + F_2^{en}}{2} = x \left[\frac{5}{18}(u_v + \bar{u}) + \frac{5}{18}(d_v + \bar{d}) + \frac{2}{18}(s + \bar{s}) \right] \\ &\simeq \frac{5}{18}x \left[q(x) + \bar{q}(x) \right] \end{aligned} \quad (10.45)$$

where $q(x)$ indicates the sum of quark densities, and $\bar{q}(x)$ that of the antiquarks.

The integral of $x[q(x) + \bar{q}(x)]$ over x must be equal to one since it represents the contribution to the interaction of all quarks and antiquarks. The measured value of the integral of F_2^{eN} in the region $1 < Q^2 < 10$ (GeV/c) 2 is about 0.14 (see Fig. 10.9). Therefore, one has

$$\int_0^1 x[q(x) + \bar{q}(x)]dx \simeq \frac{18}{5} \int_0^1 F_2^{eN}(x)dx \simeq (0.50 \pm 0.05). \quad (10.46)$$

This value was obtained with deep inelastic scattering of electrons and muons (the muons can reach higher energies) on different isoscalar targets (deuterium, carbon, etc.). The result is approximately independent of the transferred Q^2 and v . We conclude that the partons (spin 1/2 fermions) carry about 50% of the total nucleon momentum.

The above result can be explained if not all partons couple with the electromagnetic field, or if there are other objects, in addition to the quarks, inside the nucleon. It is possible to test these hypotheses by studying the neutrino-nucleon DIS; in this case, the interaction does not couple with the quark electric charge.

10.5 Cross-Section for CC $\nu_\mu N$ Interactions

ν_μ beams are produced via the decay of charged pions, as described in Sect. 8.7. A final state muon is generated through a ν_μ charged current interaction. The following deep inelastic scattering interactions were studied in detail, that is,

$$\nu_\mu p \rightarrow \mu^- + X^{++}, \quad \bar{\nu}_\mu p \rightarrow \mu^+ + X^0 \quad (10.47)$$

$$\nu_\mu n \rightarrow \mu^- + X^+, \quad \bar{\nu}_\mu n \rightarrow \mu^+ + X^-. \quad (10.48)$$

These weak interaction processes have very small cross-sections; therefore, the sensitive mass of the experiments should be very large in order to detect a reasonable number of events. The individual interacting neutrino energy cannot be measured, and only the neutrino flux per energy unit, $d\Phi/dE_\nu$, is known. The energy of the interacting neutrino is estimated by measuring both the direction and energy of the muon, and the direction and energy of the hadronic system X formed in the nucleon fragmentation.

The differential neutrino (or antineutrino) cross-sections in the laboratory system contain three functions, $W_1(Q^2, \nu)$, $W_2(Q^2, \nu)$ and $W_3(Q^2, \nu)$, that is,

$$\frac{d^2\sigma^{vp}}{dQ^2 d\nu} = \frac{G_F^2}{2\pi} \frac{E_\mu}{E_\nu} \left\{ \cos^2 \frac{\theta}{2} W_2 + 2 \sin^2 \frac{\theta}{2} W_1 \mp \frac{E_\nu + E_\mu}{M} \sin^2 \frac{\theta}{2} W_3 \right\}. \quad (10.49)$$

Comparing Eq. 10.49 with Eq. 10.31 obtained for the electromagnetic case, the replacement $4\pi\alpha^2/Q^4 \rightarrow G_F^2/2\pi$, where G_F is the Fermi constant, can be noted. For clarity, the energy of the incident particle E is replaced with E_ν , and that of the final lepton E' is replaced with E_μ . In the third addendum, the $-$ sign is valid for the ν_μ case, and the $+$ sign for the $\bar{\nu}_\mu$. Equation 10.49 contains three structure functions $W_i(Q^2, \nu)$ for the proton, and three others for the neutron. These correspond to the three helicity states of the W^+ or W^- massive bosons. There are four terms which correspond to amplitudes for which the nucleon changes the spin direction ($\propto \sin \frac{\theta}{2}$) or does not ($\propto \cos \frac{\theta}{2}$). Neutrinos and antineutrinos are helicity eigenstates with opposite eigenvalues and this gives rise to the difference in sign in the W_3 term.

The functions W_2 and $2W_1 \mp W_3(E_\nu + E_\mu)/M$ can be measured because the differential cross-section (10.49) has a dependence on the muon emission angle θ . W_1 and W_3 can be separated using both ν_μ and $\bar{\nu}_\mu$ beams. As in the case of the photon, the Bjorken scaling law predicts that for $Q^2 \gg M^2$ and $\nu \gg M$, the structure functions only depend on $x = Q^2/2M\nu$; thus, one has

$$\nu W_2(Q^2, \nu) \rightarrow F_2(x); M W_1(Q^2, \nu) \rightarrow F_1(x); \nu W_3(Q^2, \nu) \rightarrow F_3(x). \quad (10.50)$$

The differential cross-section (10.49) can be expressed in terms of two dimensionless variables. In addition to the Bjorken x , the *inelasticity* is a kinematic variable that sometimes replaces Q^2 , and it is defined as

$$y = \frac{\nu}{E}. \quad (10.51)$$

In an elastic collision, Eq. 10.9 provides the relation between Q^2 , the scattering angle θ and the initial and final energies. Using the definition (10.35) for x , one has $\nu = Q^2/2Mx$ and $y = Q^2/2MxE$. For this reason, at fixed x , one has $dQ^2 = 2MExdy$, that is, $\frac{d^2\sigma}{dxdy} = 2MxE \frac{d^2\sigma}{dx dQ^2}$. Hence, from (10.9), one obtains

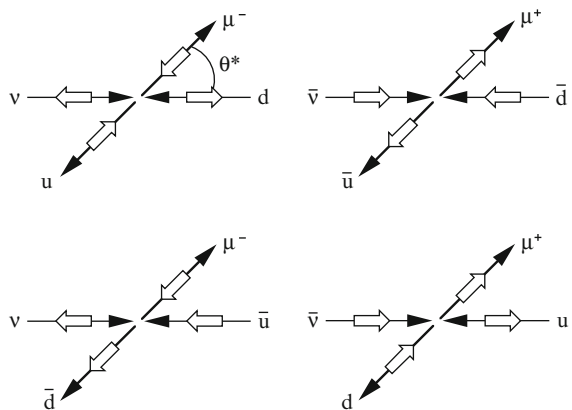
$$Q^2 = 2Mx\nu = 2E_\nu E_\mu (1 - \cos \theta) \quad (10.52a)$$

($E = E_\nu$, $E' = E_\mu$) from which:

$$\frac{\nu}{E_\nu} = \frac{E_\mu}{Mx} (1 - \cos \theta) \quad (10.52b)$$

$$y = \frac{E_\mu}{Mx} (1 - \cos \theta) = 2 \frac{E_\mu}{Mx} \sin^2 \frac{\theta}{2}. \quad (10.52c)$$

Fig. 10.10 Elastic scattering (anti)neutrino-(anti)quark in their center of mass system. The *black arrows* indicate the direction of the particle momentum, whereas the *white arrows* represent their spin direction



In terms of the dimensionless variables x and y , Eq. 10.49 becomes

$$\frac{d^2\sigma^{\nu,\bar{\nu}}}{dxdy} = \frac{G_F^2 ME_\nu}{\pi} \left\{ \left(1 - y - \frac{Mxy}{2E_\nu} \right) F_2 + xy^2 F_1 \mp xy \left(1 - \frac{y}{2} \right) F_3 \right\}. \quad (10.53)$$

For $E_\nu \gg M$, the term $Mxy/2E_\nu$ can be neglected. The numerical value of the constant at the beginning of the formula is

$$\begin{aligned} \sigma_0 &= G_F^2 M / \pi = [(1.1664 \cdot 10^{-5})^2 0.93827 / \pi] (\hbar c)^2 \text{cm}^2 \\ &= 1.58 \cdot 10^{-38} \text{cm}^2 \text{GeV}^{-1}. \end{aligned} \quad (10.54)$$

For spin 1/2 constituents, the Callan–Gross relation $F_2(x) = 2xF_1(x)$ can be used. Consequently, Eq. 10.53 can be rewritten as

$$\frac{d^2\sigma^{\nu,\bar{\nu}}}{dxdy} = \frac{\sigma_0}{2} E_\nu \left\{ \left[F_2(x) \mp xF_3(x) \right] (1-y)^2 + \left[F_2(x) \pm xF_3(x) \right] \right\}. \quad (10.55)$$

Note that the equation is of the type

$$\frac{d^2\sigma}{dxdy} = A(x)(1-y)^2 + B(x). \quad (10.56)$$

This relation takes a more explicit meaning in the neutrino-parton center of mass system. In this reference system, the quark (antiquark) coupling with the W vector boson must have negative (positive) helicity, assuming that quarks have negligible masses. Neutrinos and antineutrinos are helicity eigenstates. The only possible interactions between quarks and $\nu_\mu, \bar{\nu}_\mu$, shown in Fig. 10.10, are

$$\begin{aligned} \nu_\mu d &\rightarrow \mu^- u \iff J = 0 \\ \nu_\mu \bar{u} &\rightarrow \mu^- \bar{d} \iff J = 1 \end{aligned}$$

$$\begin{aligned}\bar{\nu}_\mu u &\rightarrow \mu^+ d \quad \Rightarrow \Rightarrow \quad J = 1 \\ \bar{\nu}_\mu \bar{d} &\rightarrow \mu^+ \bar{u} \quad \Rightarrow \Leftarrow \quad J = 0.\end{aligned}\tag{10.57}$$

The arrows represent the relative direction between the spins of incident particles, and thus the total angular momentum before collision. Remember that

- The total angular momentum is $J = 0$ if the two particles in the final state have opposite spins ($\Rightarrow \Leftarrow ; \Leftarrow \Rightarrow$). The angular distribution of the emitted particles in the c.m. system is isotropic: $F(\theta) = 1$. Thus, the cross-section angular distribution (also in terms of the *inelasticity* variable) does not contain any angular dependence, that is,

$$\frac{d\sigma}{d\Omega} = \frac{G_F^2}{4\pi^2} s; \quad \frac{d\sigma}{dy} = \frac{G_F^2}{\pi} s.\tag{10.58}$$

It is left as an exercise to show that using (10.52), one has $\frac{dy}{d\Omega} = \frac{1}{4\pi}$.

- The total angular momentum is $J = 1$ if the two particles have parallel spins in the final state ($\Rightarrow \Rightarrow ; \Leftarrow \Leftarrow$). The angular distribution of emitted particles is described by the eigenfunctions of the rotation matrix for spin 1 particles (as in the Δ^{++} case discussed in Sect. 7.5.1), and $F(\theta) = \left(\frac{1+\cos\theta}{2}\right)$. The cross-section angular distribution is

$$\frac{d\sigma}{d\Omega} = \frac{G_F^2}{4\pi^2} s \left(\frac{1 + \cos\theta}{2}\right)^2; \quad \frac{d\sigma}{dy} = \frac{G_F^2}{\pi} s(1 - y)^2.\tag{10.59}$$

Let us now transfer from the c.m. to the laboratory system. In the high energy limit, one obtains from Eq. 10.11 that the invariant variable s is $s \simeq 2ME_\nu$. For a collision with a parton of mass $m = xM$ and taking into account the coupling (10.57) of neutrinos and antineutrinos with quarks and antiquarks, one has

$$\frac{d^2\sigma^\nu}{dx dy} \simeq \frac{2G_F^2 ME_\nu}{\pi} [xq(x) + x\bar{q}(x)(1 - y)^2]\tag{10.60}$$

$$\frac{d^2\sigma^{\bar{\nu}}}{dx dy} \simeq \frac{2G_F^2 ME_\nu}{\pi} [xq(x)(1 - y)^2 + x\bar{q}(x)],\tag{10.61}$$

where $q(x)$ or $\bar{q}(x)$ are the quark or antiquark density distribution inside the nucleon. Comparing these two equations with (10.55), one obtains

$$\frac{1}{2}(F_2^\nu(x) - xF_3^\nu(x)) = 2x\bar{q}(x)\tag{10.62a}$$

$$\frac{1}{2}(F_2^{\bar{\nu}}(x) + xF_3^{\bar{\nu}}(x)) = 2xq(x),\tag{10.62b}$$

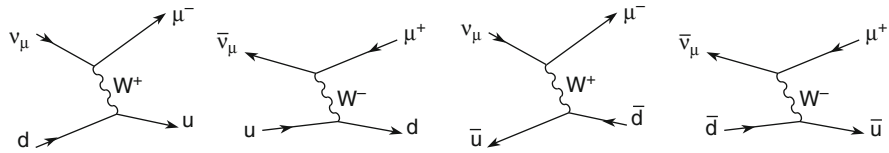
that is,

$$F_2^v(x) = 2x[q(x) + \bar{q}(x)] \quad (10.62c)$$

$$xF_3^v(x) = 2x[q(x) - \bar{q}(x)]. \quad (10.62d)$$

The structure functions F_2 and F_3/x describing the neutrino scattering on protons are proportional to the sum and difference of the parton/antiparton densities.

Identification of fermionic partons with the valence and sea quarks. If the partons are identified with the u , d , \bar{u} , \bar{d} quarks, the charged current interactions of neutrinos and antineutrinos on protons are expected to correspond to the elementary processes (10.57):



By only considering the first quark family, the v_μ interacts with a d quark, or with a \bar{u} ; the \bar{v}_μ interacts with a u quark or with a \bar{d} antiquark. Other combinations are not possible. If one defines $u(x)$, $d(x)$, $\bar{u}(x)$, $\bar{d}(x)$ the quark and antiquark distribution functions in the proton Eqs. 10.62c, d can be rewritten in the form

$$F_2^{vp}(x) = 2x[d(x) + \bar{u}(x)] \quad (10.63a)$$

$$xF_3^{vp}(x) = 2x[d(x) - \bar{u}(x)] \quad (10.63b)$$

$$F_2^{\bar{v}p}(x) = 2x[u(x) + \bar{d}(x)] \quad (10.63c)$$

$$xF_3^{\bar{v}p}(x) = 2x[u(x) - \bar{d}(x)]. \quad (10.63d)$$

Strange sea quark-antiquark pairs must be included in (10.63): the terms $+s(x)$, which couples with v_μ , and $+\bar{s}(x)$ for \bar{v}_μ , must be added.

Isoscalar targets. For isoscalar targets, taking into account (10.43c), we have $F_2^{vN} = F_2^{\bar{v}N}$ and $F_3^{vN} = F_3^{\bar{v}N}$. Only two structure functions are independent. Therefore, we choose F_2^{vN} e F_3^{vN} . Thus, one has

$$\begin{cases} F_2^{vN} = x(q + \bar{q}) = x[u(x) + d(x) + \bar{u}(x) + \bar{d}(x) + s(x) + \bar{s}(x)] \\ xF_3^{vN} = x(q - \bar{q}) = x[u(x) + d(x) + s(x) - \bar{u}(x) - \bar{d}(x) - \bar{s}(x)] \\ = x[u_v(x) + d_v(x)] \end{cases} \quad (10.64)$$

where u_v , d_v denote the valence quarks and s , \bar{s} refer to the strange sea quarks and antiquarks. The contribution of c , b , t quark flavors is negligible. F_2 depends on quarks and antiquarks; F_3 depends on the valence quarks only, assuming an equal contribution of the up and down sea quarks, and of the strange sea quarks and antiquarks, $s(x) = \bar{s}(x)$.

10.5.1 Comparison with Experimental Data

Number of Valence Quarks in the Nucleon. By integrating over the x variable, the second equation of (10.64) gives the number of valence quarks in the nucleon, that is,

$$n = \int_0^1 \frac{x F_3^{vN}}{x} dx = \int_0^1 [u_v(x) + d_v(x)] dx. \quad (10.65)$$

The measurements give $n \simeq 2.9$, in agreement with the three valence quarks.

Comparison between F_2^{vN} , F_2^{eN} and the gluons. In (10.45), the structure function F_2^{eN} was measured using electromagnetic probes (photons). The comparison of (10.45) with the analogous (10.64) for νN gives

$$F_2^{vN}(x) \simeq \frac{18}{5} F_2^{eN}(x) \quad (10.66)$$

where the equality is valid if the s quark contribution can be neglected. Neutrino experiments confirmed that the partons in the nucleon interacting via their electric and/or weak charges only carry half of the nucleon momentum. For this reason, it seemed that the quark model of the nucleon had to be abandoned. The problem was solved assuming the existence of other constituents not interacting with leptons through the weak or electromagnetic interactions. These constituents were identified with the *gluons* which interact among themselves and with the quarks through the strong interaction. Gluons are massless spin 1 bosons with no electric and weak charges, but carrying a “color” charge. There is no known reason as to why they are carrying about half of the proton momentum in the low- Q^2 region.

The “active” constituents in the nucleon are point-like, spin 1/2 particles, the valence quarks and sea $q\bar{q}$ pairs. They carry about 50% of the momentum of the nucleon while the remaining 50% is carried by the gluons, which give also a nonnegligible contribution to the nucleon mass.

Integral of the distribution functions. As shown in Eq. 10.62, F_2 depends on the quark and antiquark densities and F_3 depends only on $q - \bar{q} = q_{valence}$. From their measurements, one can extract the $q(x)$ and $\bar{q}(x)$ distributions shown in Fig. 10.11. By integrating the distribution of a certain type of $q(x), \bar{q}(x)$ in the range $0 \leq x \leq 1$,

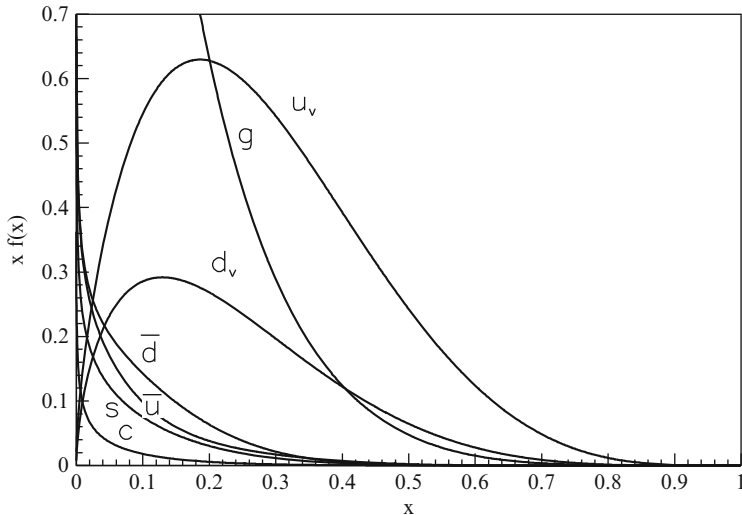


Fig. 10.11 Distributions of the quantity $xf(x)$ where $f(x)$ represents the parton density ($f = u_v; d_v; \bar{d}, \bar{u}; s, c, g$) obtained from a parameterization of the experimental results [10P02]. Color figures can be displayed on the web site of the Particle Data Group [P08]

the associated fraction of the proton momentum is obtained. The following relations are obtained as

$$\begin{aligned} \int dx xu_v &\simeq 0.2 \quad (a), \quad \int dx xd_v \simeq 0.1 \quad (b), \quad \int dx x(u_v + d_v) \simeq 0.3 \quad (c) \\ \int dx x\bar{q} &\simeq 0.06 \quad (d), \quad \int dx 2x\bar{s} \simeq 0.02 \quad (e), \quad \int dx 2x\bar{c} \lesssim 0.01 \quad (f) \\ \int dx F_2^{vN} &\simeq 0.5 \quad (g), \quad \int dx xg \simeq 0.5 \quad (h). \end{aligned} \quad (10.67)$$

As illustrated in Fig. 10.11, it can be observed that (1) $u_v(x) \simeq 2d_v(x)$; (2) the \bar{d}, \bar{u} antiquark distributions are not exactly equal; (3) the s, c antiquark contribution is of the order of a percent; (4) for $x < 0.2$, the gluon contribution is dominant.

10.5.2 The Neutrino-Nucleon Cross-Section

One of the simplest demonstrations of the validity of the nucleon parton model is the linear energy dependence of the total cross-section for charged current interactions:

$$\nu_\mu + N \rightarrow \mu^- + \text{hadrons}, \quad \bar{\nu}_\mu + N \rightarrow \mu^+ + \text{hadrons}. \quad (10.68)$$

Let us compute the total νN cross-section. The integration of (10.55) over the y variable implies the calculation of $\int_0^1 (1-y)^2 dy = 1/3$. This corresponds to a

reaction which occurs through an initial state with angular momentum $J = 1$. The conservation of the third component of the angular momentum allows the transition only to one of the possible $(2J + 1) = 3$ substates. The cross-section is thus suppressed by a factor of $1/3$ with respect to that of the $J = 0$ state. Integrating on y , one has

$$\frac{d\sigma^{\nu,\bar{\nu}}}{dx} = \frac{\sigma_0}{2} E_\nu \left\{ \frac{1}{3} \left[F_2(x) \mp x F_3(x) \right] + \left[F_2(x) \pm x F_3(x) \right] \right\}. \quad (10.69)$$

The integration on the variable x of the terms within the curly braces of (10.69) gives a constant. Thus, the total cross-section for ν (and $\bar{\nu}$) is linearly dependent on the energy E_ν . The proportionality constant is determined by the measurement of the structure functions F_2, F_3 . For neutrinos, one has

$$\sigma_{\nu_\mu N} = a_{\nu_\mu N} E_\nu = (0.667 \pm 0.014) \cdot 10^{-38} \left(\frac{\text{cm}^2}{\text{GeV}} \right) \cdot E_\nu (\text{GeV}). \quad (10.70)$$

For antineutrinos, one has:

$$\sigma_{\bar{\nu}_\mu N} = a_{\bar{\nu}_\mu N} E_\nu = (0.334 \pm 0.008) \cdot 10^{-38} \left(\frac{\text{cm}^2}{\text{GeV}} \right) \cdot E_{\bar{\nu}} (\text{GeV}). \quad (10.71)$$

Using relations (10.67c) and (10.67d), and the integral on the variable y , it can be shown that the ratio $\frac{\sigma_{\nu_\mu N}}{\sigma_{\bar{\nu}_\mu N}} = 2$. From (10.60, 10.61), one has

$$\begin{aligned} \int \frac{d^2\sigma^\nu}{dxdy} dx dy &= \sigma_0 \int [xq(x) + x\bar{q}(x)(1-y)^2] dx dy \\ &= \sigma_0 \left[0.3 + 0.06 \frac{1}{3} \right] = 0.32\sigma_0 \end{aligned} \quad (10.72a)$$

$$\begin{aligned} \int \frac{d^2\sigma^{\bar{\nu}}}{dxdy} dx dy &= \sigma_0 \int [xq(x)(1-y)^2 + x\bar{q}(x)] dx dy \\ &= \sigma_0 \left[0.3 \frac{1}{3} + 0.06 \right] = 0.16\sigma_0, \end{aligned} \quad (10.72b)$$

in good agreement with the experimental results. Figure 10.12 shows the dependence on E_ν of the ratio $\sigma_{tot}^{CC}/E_\nu = a_\nu$ for neutrinos and antineutrinos. These relations are constant up to $E_{\nu_{lab}} \simeq 250 \text{ GeV}$. It is believed that the cross-sections νN increases linearly with energy up to $\sqrt{s} \sim m_W$ in the c.m. system. For higher energies, the cross-sections must take into account the W vector boson mass in the bosonic propagator, as discussed in Chap. 11.

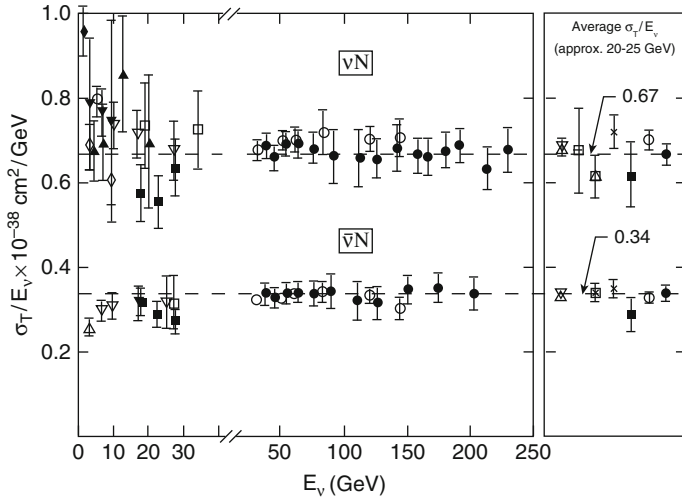


Fig. 10.12 Ratio between the total cross-section and E_ν for the processes $\nu_\mu N$ and $\bar{\nu}_\mu N$ as a function of the neutrino energy E_ν in the laboratory system. The ratios $a_{\nu_\mu N} = \sigma_{tot}^{CC}/E_{\nu_\mu}$ and $a_{\bar{\nu}_\mu N} = \sigma_{tot}^{CC}/E_{\bar{\nu}_\mu}$ are constant [P08]

10.6 “Naive” and “Advanced” Quark Models

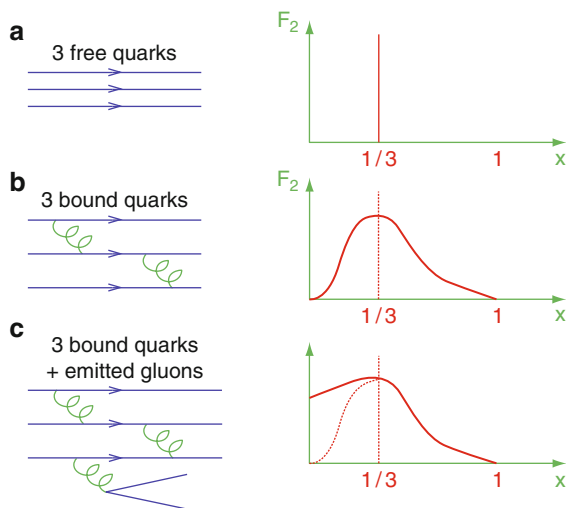
The structure functions have been measured with great precision in various experiments and in a wide range of parameters x, Q^2, W . In particular, the H1 and ZEUS experiments at the ep collider HERA at DESY produced an impressive series of results, whose importance can be appreciated by comparing the HERA $F_2(x)$ measurements shown in Fig. 10.16 and the earlier DIS measurements shown in Fig. 10.9.

In the static quark model (which assumes three noninteracting valence quarks), the structure function F_2 , as measured by an ideal experiment with infinite resolution, would be equal to the one shown in Fig. 10.13a. Each parton carries $1/3$ of the nucleon momentum. When interactions between quarks through the exchange of gluons are considered, each quark carries a larger or smaller fraction of the proton momentum compared to the previous *democratic* division. The $F_2(x)$ is similar to that in Fig. 10.13b. Finally, if the creation of $q\bar{q}$ virtual pairs by *soft gluons* radiated by each valence quark is included, a $F_2(x)$ similar to that sketched in Fig. 10.13c would be expected. The $q\bar{q}$ pairs carry a small fraction of the nucleon momentum.

10.6.1 Q^2 -Dependence of the Structure Functions

Early experiments indicated that the structure functions do not vary with Q^2 (*scaling invariance* or *Bjorken scaling*). The measurements performed in experiments at CERN and Fermilab in the late 1970s showed that $F_2(x)$ started to present a

Fig. 10.13 Schematic interpretation of the $F_2(x)$ function. From the top:
(a) Three noninteracting quarks carrying exactly $x = 1/3$ of the nucleon momentum;
(b) interactions between quarks produce variations of the fraction x of the carried momentum;
(c) quarks create, through gluon radiation, virtual $q\bar{q}$ pairs carrying a small x



dependence on Q^2 with gradually increasing energy. This violation of the scaling invariance (the *scale breaking effect*), shown in Fig. 10.14, was attributed to effects due to the strong interaction. In particular, $F_2(x)$ increases with Q^2 at low x , the region where the contribution of sea quarks is dominant. It decreases with Q^2 at large values of x , where the contribution of valence quarks is prevailing. When the transferred four-momentum Q^2 increases, the *resolving power* to study the nucleon structure improves. The contribution of partons with large momentum fraction ($x > 0.25$) and interacting through electromagnetic or weak interactions decreases, while the number of partons with small momentum ($x < 0.15$) increases. For $0.15 < x < 0.25$, the Bjorken scaling law is satisfied with a good approximation. In addition to the violation of Bjorken scaling, the “naive” parton model is unable to explain the production of hadrons with large transverse momentum with respect to the direction of the virtual boson, and events with multiple jets of hadrons.

The coupling constant α_S depends on Q^2 and can be determined from the Q^2 dependence of the structure functions. The scale breaking is explained in the “advanced” quark-parton model, where quarks are strongly interacting. For $Q^2 \gg \Lambda_{QCD}^2 \simeq (200 \text{ MeV})^2$ (see Sect. 11.9.2), α_S is small and perturbation expansions can be used to compute physical quantities, for example, cross-sections. For small Q^2 , α_S becomes large.

The dependence on the energy scale of the quark density functions has the following interpretation: when Q^2 increases, the spatial resolution of the virtual boson probing the proton improves. At high Q^2 , one can probe the cloud of partons surrounding each quark. The radiation of a high energy gluon gives rise to a jet of hadrons (as shown in Fig. 10.15c). This is an easily detectable event topology which is not explained in the simplest model of noninteracting quarks.

In $e p \rightarrow e + X$ collisions with small values of the Bjorken variable x ($x < 10^{-3}$), the main contribution to the inelastic cross-section is the interaction of the virtual photon with a sea quark. The structure functions at small x mainly depend on

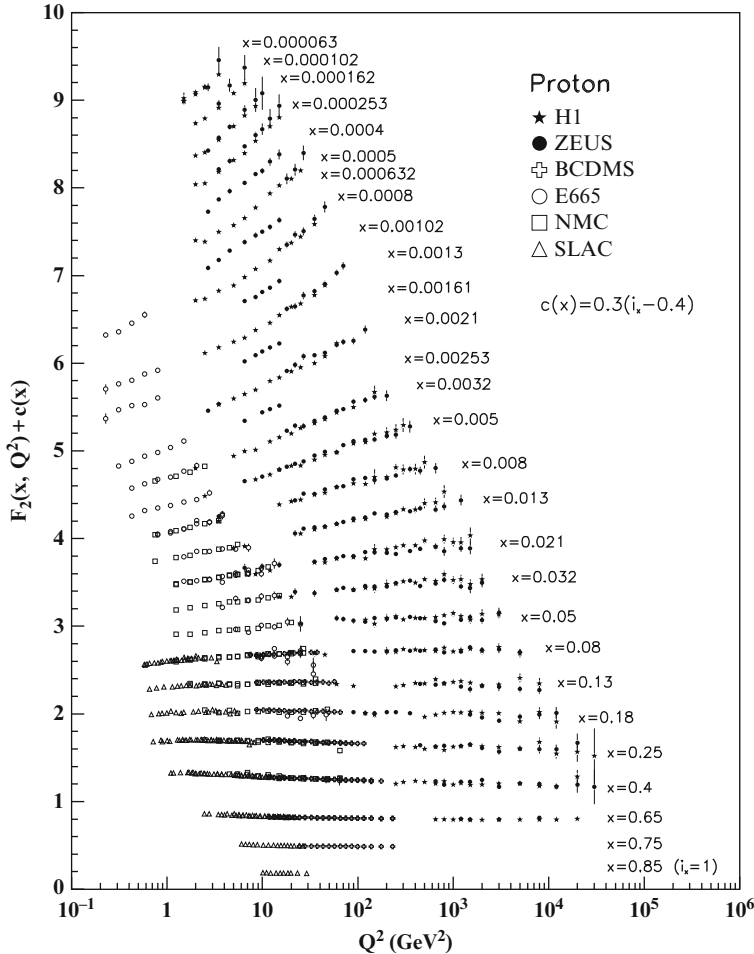


Fig. 10.14 The proton structure function F_2^p as a function of the transferred four-momentum squared Q^2 for fixed values of x . F_2^p was obtained from measurements of deep inelastic $e p$ scattering in the HERA kinematic domain ($x > 0.00006$) and for electron (SLAC) and muon scattering on a fixed target (BCDMS,E665,NMC). Note that the ordinate for each value of x are offset by a factor $c(x)$ for clarity [10P02]

sea quark and gluon distributions. The number of virtual pairs increases when the fraction x of the momentum that they carry decreases. This yields an increase of the function F_2 in the small x limit. The expected behavior for the gluon (xg) and sea quark ($x\bar{q}$) distributions is of the type $xg \simeq x^{-\lambda_1}$, $x\bar{q} \simeq x^{-\lambda_2}$ (see Fig. 10.16); this parametrization was confirmed by the data collected at HERA.

Fragmentation of the hadronic system. The single *inclusive* reaction $a + b \rightarrow c + X$ requires the presence of the specific c hadron in the final state, regardless of the remaining system X . Its cross-section is defined by the c.m. energy and by the

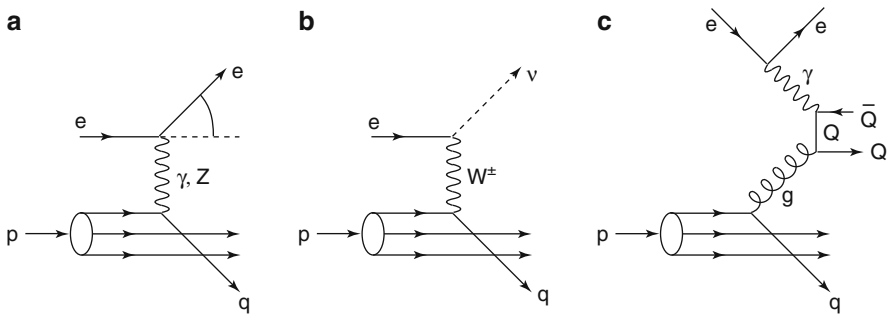


Fig. 10.15 Lowest order Feynman diagrams for the three basic processes of inelastic ep scattering: (a) NC scattering, (b) CC, (c) through photon–gluon fusion

kinematic variables x and Q^2 . If the two stages of the process are really independent, the cross-section for the inclusive single process can be factorized as

$$\frac{d^3\sigma}{dx dQ^2 dz} \simeq F(x, Q^2) D(z, Q^2) \quad (10.73)$$

with $F(x, Q^2) \simeq F(x)$, $D(z, Q^2) \simeq D(z)$ if the “scale breaking effect” is not considered. The properties of the hadronic system produced in lepton–nucleon collisions, are described by the *fragmentation function* $D(z, Q^2)$; they are related to the strong interaction hadronization process. The situation is very similar for high energy hadron-hadron and e^+e^- collisions. For example, the fragmentation function of a quark q into a pion π is defined as

$$D_q^\pi(z) = \frac{1}{N} \frac{dN}{dz} \quad (10.74)$$

where $z = E_\pi/v = E_\pi/E_q$ is the fraction of the energy transferred from the quark to the final pion. The variable z for the fragmentation function has a role similar to that of the variable x for the structure functions.

In the asymmetric HERA collider, 27.5 GeV electrons or positrons collided head-on with 820 GeV protons ($\sqrt{s} \simeq 300$ GeV). Between 1992 and 2000, HERA collected an integrated luminosity of about 130 pb^{-1} , producing detailed results on the proton structure functions, the production of heavy quarks, on diffraction and generally on QCD. After a major upgrade, the luminosity increased by a factor of ~ 5 and the lepton beams could be polarized longitudinally. The HERA collider was operated in this configuration from the end of 2003 until 2007. The collisions were recorded by two large 4π detectors: H1 and ZEUS. The beam asymmetry was reflected in the detector layout. Figure 10.17 shows the ZEUS detector. Schematically, it consisted

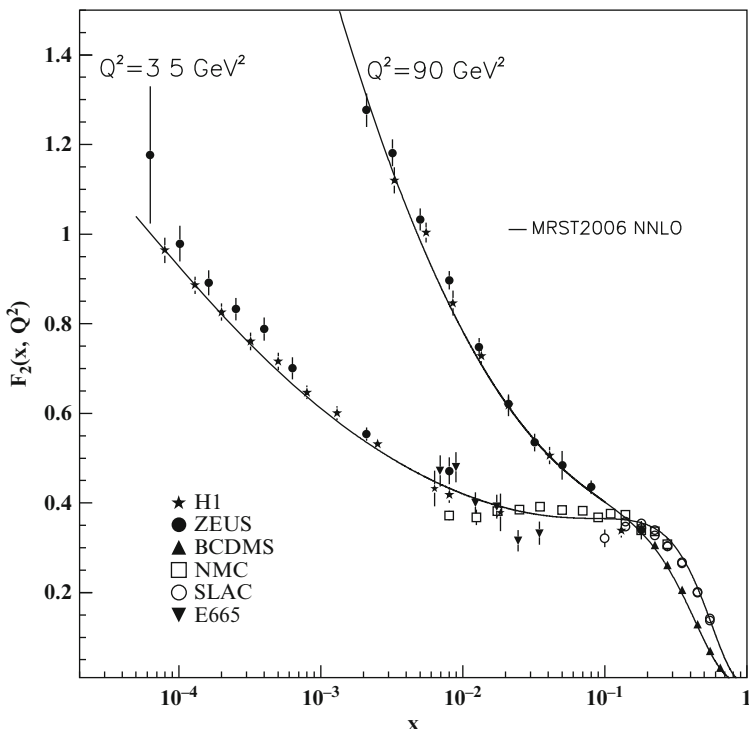


Fig. 10.16 The structure function F_2^p as a function of the variable x for two values of Q^2 (3.5 GeV^2 and 90 GeV^2), together with a parametrization obtained using a QCD-evolved model [10P02]

of (1) a set of detectors to measure the trajectory of charged particles in a magnetic field; (2) a sampling calorimeter with uranium-scintillator plates, serving as both electromagnetic (first part) and hadronic calorimeters; (3) an iron absorber (the return yoke of the magnetic field); (4) the muon detectors, before and after the iron absorber; (5) a forward detector, in the direction of the proton beam, to measure the “leading protons.” The luminosity monitor was a small angle radiation detector along the direction of the leptons, measuring the $e p \rightarrow e \gamma p$ bremsstrahlung. The cross-section for this process is linearly correlated with the total number of e^+ (e^-) crossing the interaction point.

10.6.2 Summary of DIS Results

Let us briefly recall the main results obtained on lepton–nucleon scattering. The elastic $e^- - nucleus$ scattering at relatively low energy probed the distribution

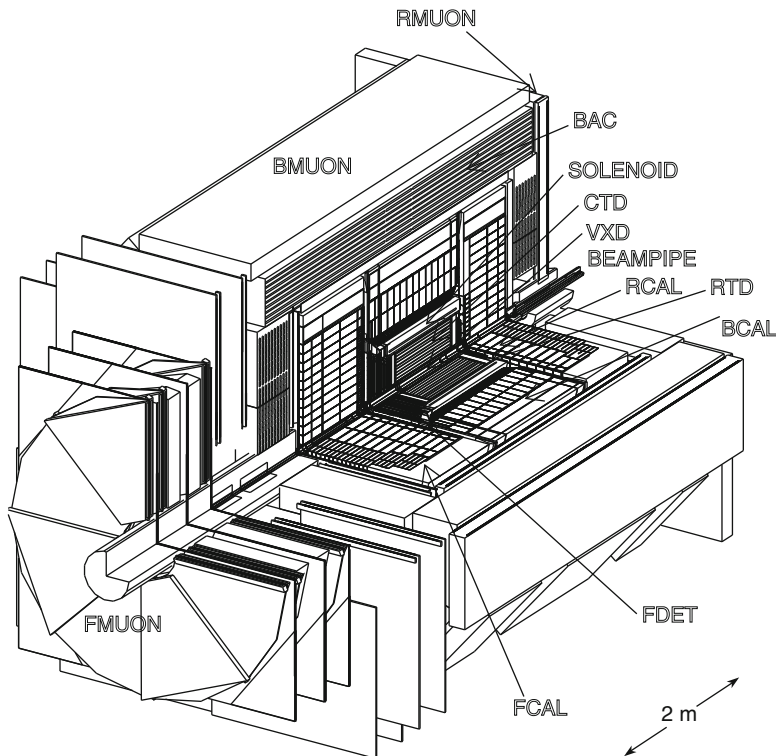
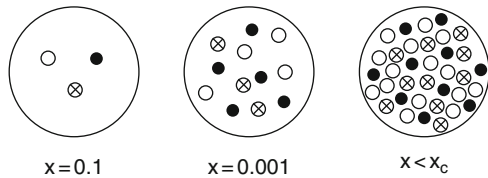


Fig. 10.17 Layout of the ZEUS detector operated at the HERA collider at DESY, Hamburg

of electric charge inside the nuclei, and revealed details of the nuclear structure. The observation of nearly elastic peaks in the inelastic electron-nucleus collision demonstrated the presence of constituents, the nucleons, inside the nuclei. High energy deep inelastic scattering in electron-, muon- and neutrino-nucleon interactions revealed that the proton and the neutron are composed of fractionally charged quarks, and that the neutron is not uniformly electrically neutral. Detailed analysis showed that the proton and the neutron contain, in addition to the valence quarks, sea quark-antiquark pairs. Finally, the nucleons must contain neutral constituents with integer spin, the gluons, carrying about half of the nucleon momentum.

With the HERA collider, an accurate study of structure functions at small x was performed. Figure 10.18 qualitatively illustrates what leptons “see” regarding the proton structure when increasing the resolving power. Take note that the increase of the parton number as x decreases. Amongst several other effects not discussed here, we can briefly mention the study of polarization effects performed with polarized muons and electrons colliding with polarized protons. These studies showed that the quarks contribute 25% to the proton spin and that the remaining contribution must come from the gluons.

Fig. 10.18 Qualitative illustration of the density of partons in the proton for different values of the variable x



10.7 High Energy Hadron-Hadron Collisions

In the following, we shall consider hadron collisions (mainly, pp and $\bar{p}p$) at c.m. energies above 10 GeV. For c.m. energies below ~ 3 GeV (Sect. 10.4), there is the resonance region. The total and elastic cross-sections vary rapidly and are characterized by peaks whose height decreases with increasing energy. For c.m. energies between 3 and 10 GeV, the cross-sections first decrease monotonically, reach a minimum and then increase, see Fig. 10.19. For $E_{cm} > 10$ GeV (20 GeV for $\bar{p}p$), the total cross-section increases logarithmically with energy. This was discovered in the early 1970s, first in $K^+ p$ interactions at Serpukhov, Russia, followed by pp interactions at the *Intersecting Storage Rings* (ISR) at CERN, and then with many other experiments at Fermilab in the United States. It is still not completely clear as to why the total hadron-hadron cross-sections increase with energy.

The differential elastic cross-section increases at low transferred momentum: this *elastic peak* becomes narrower with increasing energy. At high energies, inelastic processes are dominant and the *average charge multiplicity* (i.e., the average number of produced charged hadrons) increases logarithmically with c.m. energy.

Figure 10.20 schematically illustrates the various types of processes: elastic collision, single and double diffractive scattering, and inelastic collisions. The diffractive cross-section has characteristics similar to those of elastic scattering. The interpretation is that both the elastic and the diffractive scattering are mediated by the exchange of a *pomeron*, a pseudo-particle with the quantum numbers of the vacuum.

Low transverse momentum elastic, diffractive and inelastic scatterings are denoted as $\ln s$ processes. They are characterized by relatively large cross-sections varying slowly with energy, as $\ln s$. In contrast, the *high transverse momentum* processes ($high-p_t$ processes) discussed in the previous sections have relatively small cross-sections, rapidly varying with energy. It is conceivable that in $\ln s$ processes, hadrons in their entirety are involved, while $high-p_t$ collisions occur between the parton constituents. While perturbation methods can be used in $high-p_t$ strong interaction reactions, a different approach must be used for $low-p_t$ processes due to the large value of the strong coupling constant. For this reason, phenomenological models based on many-body QCD were developed. These models use interpolation/extrapolation of data and explain many important aspects of the secondary particle production, but sometimes have contradictory aspects. The $low-p_t$ models can be used to extrapolate predictions on the characteristics of secondary particles produced at LHC or by cosmic ray interactions in the atmosphere [G90].

Fig. 10.19 Total cross-section measurements in $\bar{p}p$ and $p\bar{p}$ collisions; data include high energy cosmic ray interactions

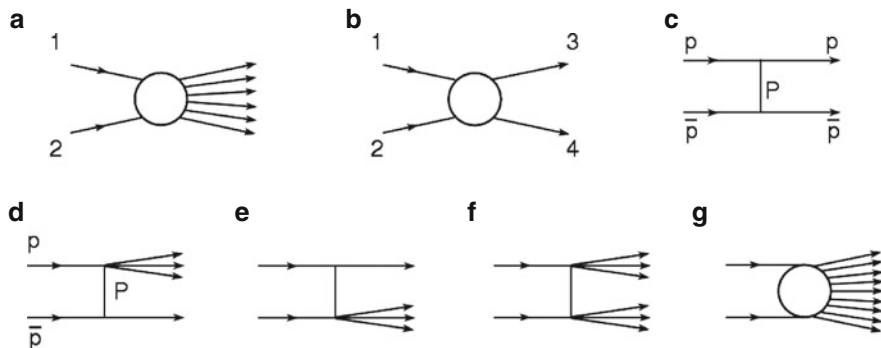
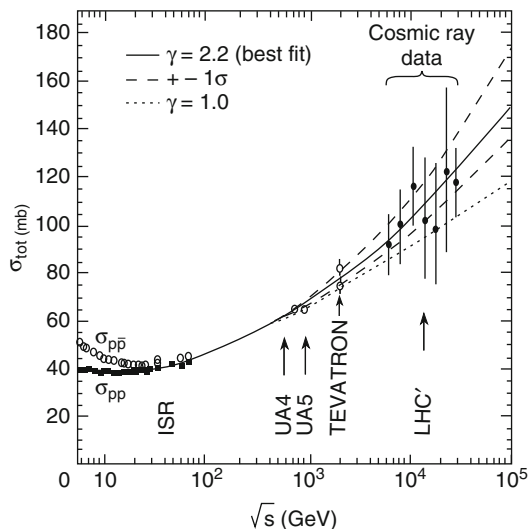


Fig. 10.20 Sketch of (a) inelastic and (b) two-body (if elastic, one has $1 = 3$ and $2 = 4$) processes. A further subdivision, considered in detail for $\bar{p}p$ collisions, is the (c) elastic collision with a Pomeron P exchange; (d) single-diffractive on proton; (e) single-diffractive on \bar{p} ; (f) double-diffractive; (g) inelastic as in (a)

Before 1975, the experimental apparatuses used to analyze the production of particles were very simple. Usually, they consisted of one or more layers of scintillation counters with one or more Cherenkov counters to measure the incident particle velocities and deduce their masses. Some experiments were also equipped to cover the solid angle region near the beam pipe. The first detector which covered almost the entire solid angle was the SFM (Split Field Magnet) at the CERN ISR. The c.m. energy was $\sqrt{s} \simeq 53$ GeV. After 1975, larger equipment and detectors were built, always covering almost the entire solid angle. The real “universal”

detectors were born at the CERN $Spp\bar{S}$ Collider ($\sqrt{s} \simeq 540$ GeV) with the UA1 and UA2 experiments. The history continued at the Fermilab collider ($\sqrt{s} \simeq 1,800$ GeV) with the Collider Detector Facility (CDF) and the D0 experiments. These detectors (similar to those used at the e^+e^- colliders discussed in Chap. 9) operate effectively in the c.m. system, and detect all secondary particles emitted in the full solid angle with a series of concentric subdetectors. Starting from the interaction point, one finds a tracking detector within a magnetic field, a time-of-flight system, an EM calorimeter, a hadron calorimeter, and finally a muon detector.

To observe every hadronic interaction without setting any condition, a *minimum bias trigger* requires that at least one charged track leave the interaction region. More selective triggers may require a high- p_t particle, a “jet” of particles, and so on.

The major result obtained in a hadron-hadron collider at high transverse momentum was discovered in 1983 regarding the W^\pm and Z^0 vector bosons (see Problem 10.6) at the CERN $Spp\bar{S}$, as described in Sect. 8.15. In the following, we shall mostly focus on the $\ln s$ process and on some interpretative models.

10.8 Total and Elastic Cross-Sections at High Energy

Figure 10.19 shows a compilation of total proton-proton cross-sections for $\sqrt{s} > 5$ GeV. The cross-sections for the six charged hadrons with long lifetime (π^\pm, K^\pm , as well as p, \bar{p}) decrease with increasing energy, reach a minimum and then increase with energy. For $\bar{p}p$ and pp , the increase is of the type $\ln^2 s$. Note that the argument of a logarithm must be dimensionless: $\ln^2 s$ means $\ln^2(s/s_0)$ with $s_0 = 1$ GeV 2 . The cross-sections for antiparticle-proton $\sigma_{tot}(\bar{x}p)$, with $\bar{x} = \pi^-, K^-, \bar{p}$, are larger than those for particle-proton $\sigma_{tot}(xp)$, with $x = \pi^+, K^+, p$.

The difference $\Delta\sigma = \sigma_{tot}(\bar{x}p) - \sigma_{tot}(xp)$ decreases with increasing energy, in agreement with the *Pomeranchuk theorem* which predicts that in the limit $s \rightarrow \infty$, $\sigma_{tot}(\bar{x}p) = \sigma_{tot}(xp)$. This theorem can be derived from the hypothesis that the number of available channels (i.e., the number of possible final states) increases with energy; the total cross-section remains finite and that the cross-section for each channel decreases asymptotically to zero with increasing energy. In this case, the annihilation channels, possible for $\bar{x}p$ and not for xp , are relatively few (in percent) and at high energy, they have a negligible cross-section compared to that of all other channels.

It is unclear why the total cross-sections increase with increasing energy. It is likely due to either the increase of the gluon contribution (responsible for the presence of “minijets”) or to the increase of diffractive-type phenomena.

10.8.1 Elastic Differential Cross-Sections

The elastic differential cross-section for a collision between two unpolarized hadrons depends on the c.m. energy and on a variable which depends on the

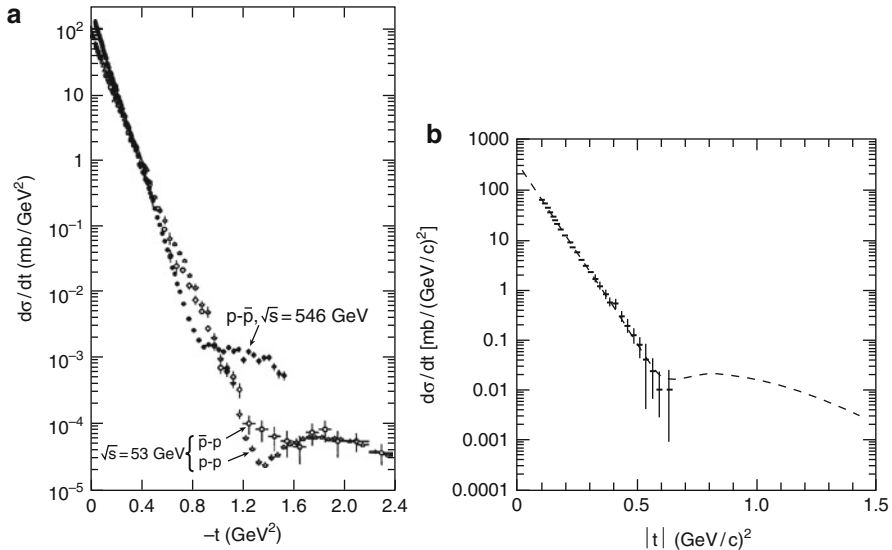


Fig. 10.21 Differential cross-section, $d\sigma/dt$ as a function of $|t|$, for elastic collisions (a) pp and $\bar{p}p$ at $\sqrt{s} = 53$ and 546 GeV; (b) $\bar{p}p$ at $\sqrt{s} = 1.8$ TeV [10G93]

scattering angle, for example, the transferred four-momentum squared, $Q^2 = |t|$. The elastic differential cross-section $d\sigma/dt$ for pp , $p\bar{p}$ reactions at the CERN ISR and $S\bar{p}\bar{p}S$, shown in Fig. 10.21, peaks at small angles ($t \simeq -p^2\theta^2$ at small θ). The distribution can be divided into four angular regions (of which only the last two are evident in the figure):

1. The *Coulomb* region $|t| < 0.001$ (GeV/c) 2 . The collision is due to the electromagnetic interaction and the cross-section can be explicitly calculated.
2. The *nuclear-Coulomb interference region* for $0.001 < |t| < 0.01$ (GeV/c) 2 .
3. The *nuclear diffractive region* $0.01 < |t| < 0.5$ (GeV/c) 2 . The interaction is basically due to the strong interaction only; the most important parameter is the slope b of the diffraction pattern. Here, the differential cross-section depends on t as

$$d\sigma/dt = Ae^{bt}. \quad (10.75)$$

With increasing energy, b increases according to the approximate formula $b \simeq 8 + 0.56 \ln s$, with a narrowing of the forward elastic peak. For a wider range of t , the dependence is of the type Ae^{bt+ct^2} .

4. The *large angles* region $|t| > 0.5$ (GeV/c) 2 . It is characterized by a very small elastic cross-sections and, for pp at $\sqrt{s} \simeq 53$ GeV, a valley-peak structure, similar to an optical diffraction pattern.

To measure the elastic differential cross-section, the number of interactions per unit of time and of transferred four-momentum t must be counted. For a collider, the

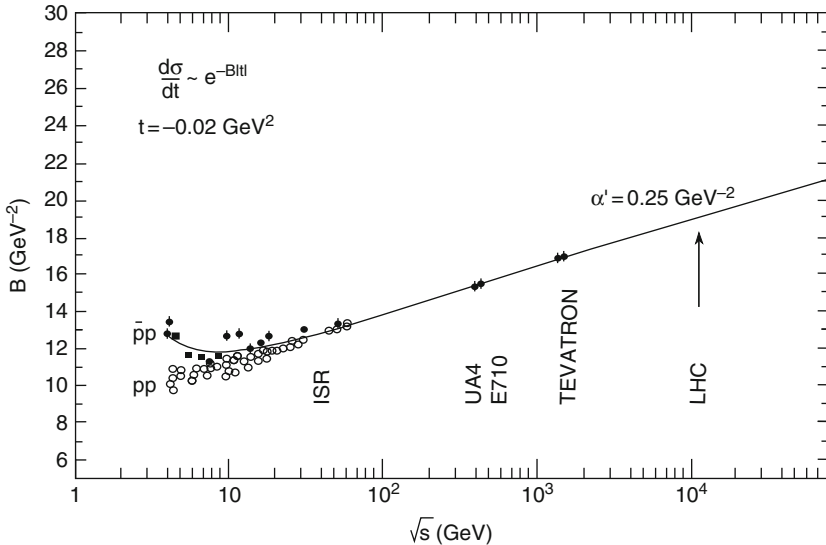


Fig. 10.22 Slopes $B = b_{pp}$ and $= b_{\bar{p}p}$ plotted as a function of the momentum in the laboratory system for elastic pp and $\bar{p}p$ collisions

luminosity \mathcal{L} (Sect. 3.3) is the number that, multiplied for the total cross-section σ , gives the total number N of interactions per time unit: $N = \mathcal{L}\sigma$. The *integrated luminosity* over a time interval dt is

$$L = \int \mathcal{L} dt \quad (10.76)$$

The integrated luminosity L is a fundamental quantity. By definition, its units are the inverse of the cross-section (for example, $\text{nb}^{-1}, \text{pb}^{-1}$). With an integrated luminosity of 1 pb^{-1} , one event is expected for a process that has a cross-section of $1 \text{ pb} = 10^{-36} \text{ cm}^2$.

Figure 10.22 shows the energy dependence of the elastic scattering slope b (10.75) measured at an average value $|t| \simeq 0.2 (\text{GeV}/c)^2$ in the interval $0.15 < |t| < 0.4 (\text{GeV}/c)^2$. Note that $b_{\bar{p}p}$ first decreases and then increases with \sqrt{s} , reaching the value b_{pp} . The data are consistent with a low- p_t model in which the hadron is basically an almost *black disk*. Using the analogy with classical optics, the diffraction pattern of an opaque disk of radius R and opacity a ($a = 0$ for a black disc, $a = 1$ for a completely transparent disk) is described by the order 1 (J_1) Bessel function:

$$\frac{d\sigma}{dt} \simeq (1-a)\pi R^2 \left| \frac{J_1(R\sqrt{|t|})}{R\sqrt{|t|}} \right|^2 \simeq (1-a)\frac{\pi R^4}{4} e^{-\frac{R^2|t|}{4}}. \quad (10.77)$$

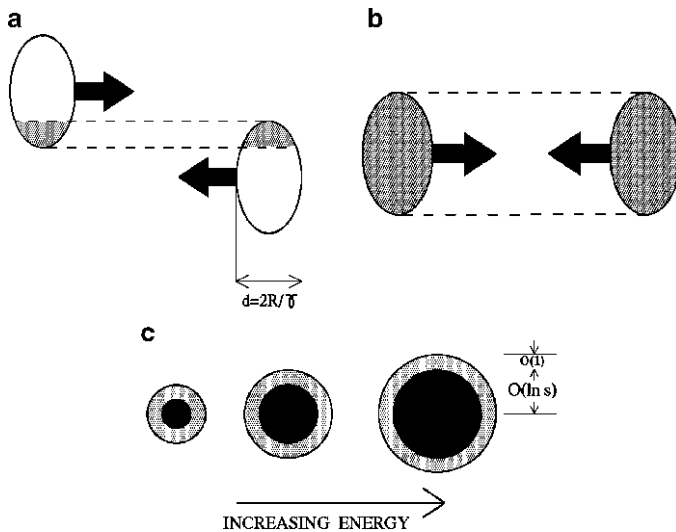


Fig. 10.23 Schematic representation of the status of two hadrons before collision for (a) peripheral and (b) central collisions. Due to relativistic effects, the two hadrons contract along the direction of motion. (c) Sketch of the increase with energy of the hadron size and opacity (the relativistic contraction is not shown)

The approximation is valid for $|t| < 0.2 (\text{GeV}/c)^2$; by comparing this expression with $d\sigma/dt \approx e^{bt}$ (10.75), one obtains $b = R^2/4$. From this relation, the disk radius R can be deduced, that is,

$$R \simeq 2\sqrt{b} (\text{GeV}^{-1}) \rightarrow 2\sqrt{b}(\hbar c) \simeq 0.4\sqrt{b} (\text{fm}). \quad (10.78)$$

The *apparent proton radius* increases with c.m. energy of the elastic reaction because $b \sim \ln s$, as schematically illustrated in Fig. 10.23.

10.8.2 Total Cross-Sections

In a model of the diffraction pattern of the incident particle wave on a target, similar to that of classical optics, the total cross-section σ_{tot} is related to the elastic differential cross-section at $t \rightarrow 0$ (optical theorem). The measurement of σ_{tot} may be made through the total number of collisions, both elastic and inelastic, and the integrated luminosity L

$$\sigma_{tot} = \frac{N_{tot}}{L} = \frac{N_{el} + N_{inel}}{L}. \quad (10.79)$$

Experiments at the CERN $S\bar{p}pS$ and at the Fermilab Tevatron collider measured σ_{tot} using a combination of both methods. Usually, the integrated luminosity L is not known with an accuracy better than 10%. The main results can be summarized as follows:

1. The total cross-section and the slope b of the elastic differential cross-section increase with energy: the proton radius (10.78) seems to become larger at high energy, Fig. 10.23.
2. The opacity $a = 2\sigma_{el}/\sigma_{tot}$ increases with energy, indicating that the proton becomes not only larger, but also “darker” with increasing energy, as shown in Fig. 10.23. At $\sqrt{s} = 1.8 \text{ TeV}$, one has $a \simeq 0.50$, which is lower by a factor of 2 than the value $a = 1$ for the diffraction on a black disk.
3. The shape of the “diffraction pattern for elastic collision,” Fig. 10.21 resembles that obtained in classical optics.
4. The interpretation of the elastic and total cross-section as a function of energy was made in terms of different, even contradictory, models. Within QCD, the growth of σ_{tot} with energy as $\sigma_{tot} \approx s^{\alpha_0}$ can be associated with the increasing contribution of soft gluon exchange (α_0 is a positive parameter). This behavior would be divergent at large s ; these divergences must be overcome with appropriate mathematical methods.

10.9 High Energy Inelastic Hadron Collisions at Low- p_t

In collisions between two high energy hadrons, particle production is mainly due to processes where the average transverse momentum p_t is small. At the beginning of the 1970s, it was believed that the basic characteristics of these processes were:

1. The number of charged particles produced, i.e., the *charge multiplicity*, increases logarithmically with the c.m. energy
2. The cross-section depends exponentially on the transverse momentum. The average transverse momentum of produced particles is $\langle p_t \rangle \simeq 350 \text{ MeV/c}$, roughly constant and independent from the energy and type of colliding hadrons

The increase in the charged multiplicity when the c.m. energy of the colliding hadrons increases is one of the main features of high energy collisions; this can be easily measured. Only a small fraction of the c.m. energy is converted into mass of the produced particles. Most of the energy remains in the form of kinetic energy of the outgoing particles. For example, at $\sqrt{s} = 62 \text{ GeV}$, the average multiplicity of charged hadrons (mostly pions) is 12, while the available energy would allow the production of several hundred pions.

The analysis of the charge multiplicity in hadron-hadron, lepton–nucleon and e^+e^- collisions shows that the average number of produced particles only depends on the available c.m. energy (\sqrt{s}) and that it is independent of the type of colliding particles (see Fig. 9.19). Table 10.2 gives the average number of hadrons produced

Table 10.2 Average numbers of particles (hadrons) produced in inelastic pp collisions at $\sqrt{s} = 53$ GeV and in $\bar{p}p$ collisions at $\sqrt{s} = 540$ and 1,800 GeV. At the higher energy, the number of neutral particles is equal to half of those charged. At LHC ($\sqrt{s} = 14$ TeV), the estimated number of charged hadrons per collision is ~ 80

Particle type \sqrt{s} (GeV)	pp 53	$\bar{p}p$ 540	$\bar{p}p$ 1,800
Charged	12.0	29.0	40
Neutral	6.0	14.5	20
π^+	4.7	{ } 23.9	
π^-	4.3		
π^0	4.5		12
K^\pm	0.46	{ } 2.24	
K^0	0.33		
$K^0 + \overline{K^0}$	0.79	2.24	
p	1.6	{ } 1.45	
\bar{p}	0.15		
$n + \bar{n}$	1.75	1.45	
$\Lambda + \overline{\Lambda} + \Sigma^0 + \overline{\Sigma^0}$	—	0.53	
$\Sigma^+ + \Sigma^- + \overline{\Sigma^+} + \overline{\Sigma^-}$	—	0.27	
$\Xi^- + \overline{\Xi^-} + \Xi^0 + \overline{\Xi^0}$	—	0.20	

in inelastic pp collisions at $\sqrt{s} = 53$ GeV and in $\bar{p}p$ collisions at $\sqrt{s} = 540$ and 1,800 GeV. At $\sqrt{s} = 1.8$ TeV, the average charged multiplicity is ~ 40 and the number of neutral hadrons is half of the charged ones. The dominance of pion production should also be noted.

The average transverse momentum ($\langle \bar{p}_t \rangle$) in a single event and the average transverse momentum in N events ($\langle \bar{p}_t \rangle$) are respectively defined as

$$\bar{p}_t = \frac{1}{n} \sum_{i=1}^n |p_t|_i; \quad \langle \bar{p}_t \rangle = \frac{1}{N} \sum_{j=1}^N \bar{p}_{tj}, \quad (10.80)$$

where n is the number of produced charged hadrons, each with momentum $|p_t|_i$. Figure 10.24 shows the average transverse momentum of charged hadrons produced in pp and $\bar{p}p$ high energy collisions as a function of \sqrt{s} . Although it remains small, it can be observed that $\langle \bar{p}_t \rangle$ increases slowly with \sqrt{s} .

10.9.1 Outline on High Energy Nucleus-Nucleus Collisions

High energy nucleus-nucleus collisions have been studied since the end of the 1980s using ${}^{80}\text{O}$, ${}^{16}\text{S}$ e ${}^{82}\text{Pb}$ ion beams of ~ 15 GeV/nucleon at Brookhaven and 200 (158 for ${}^{82}\text{Pb}$) GeV/nucleon at the CERN SPS. The results show that the

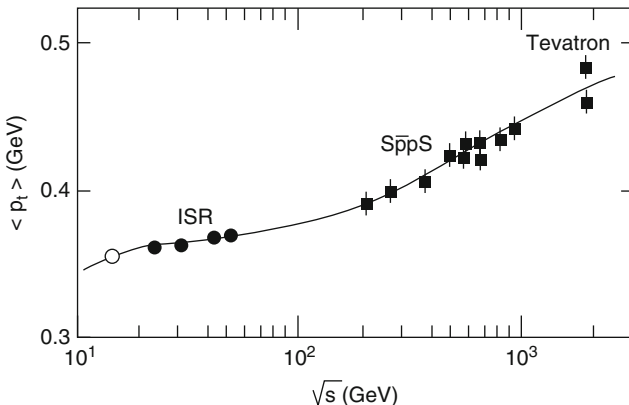


Fig. 10.24 Average transverse momentum of charged hadrons produced in high energy hadronic collisions as a function of the c.m. energy

nucleus-nucleus collision can be explained as a series of hadron–nucleus collisions (*superposition model*). Only few nucleons of the projectile (or target) interact inelastically, producing a heavy nuclear fragment, some light fragments and several spectator nucleons. About 20% of these nucleons reinteracts inside the target nucleus. The hadron–nucleus interaction is thus considered as a superposition of hadron-hadron interactions.

One of the most used models in Monte Carlo simulations of nucleus-nucleus interactions is the *Glauber model* of multiple nuclear scattering: a hadron crossing a nucleus can undergo multiple interactions; in each interaction, hadrons are produced which may in turn interact within the same nucleus, giving rise to a *intranuclear cascade*. The nucleus-nucleus interactions are important in the study of cascades induced by high energy cosmic rays (protons, helium nuclei and heavier nuclei) with nuclei in the upper atmosphere [G90].

Quark-gluon plasma. High energy nucleus-nucleus collisions are used to search for the possible state of matter denoted as *quark-gluon plasma*. The very high temperatures and densities achieved in the collisions should, for a very short time, allow quarks and gluons to exist in a free state, i.e., no longer confined in hadrons, in a kind of “soup” or plasma. It is believed that this state of matter has existed around 10^{-6} s after the Big Bang. The Brookhaven Relativistic Heavy Ion Collider (RHIC), devoted to these studies, became operational in June of 2000, with gold ions which collided at energies between 56–130 GeV/nucleon. They may have indications for a quark-gluon plasma which behaves more like a liquid than a gas [10w1]. At LHC, the ALICE experiment plans to study in detail the interactions between heavy nuclei at energies up to 5.5 TeV/nucleon. The study of the properties of

quark-gluon plasma can help to understand the origin of particles such as the proton and the neutron, and may also have important implications for our understanding of cosmology.

10.10 The LHC and the Search for the Higgs Boson

As shown in Chap. 9, the Standard Model of electroweak interactions has successfully gathered an impressive amount of experimental confirmations. Indeed, high-precision measurements and a thorough verification of the Standard Model were performed in 1989 by the four LEP experiments at CERN (ALEPH, DELPHI, L3 and OPAL) and the SLD experiment at Stanford. Nevertheless, the neutral Higgs boson which is an indispensable ingredient in the Standard Model, used to explain the origin of the masses, is still eluding experimental discovery. As described in Sect. 11.5, the Higgs boson is introduced through the spontaneous symmetry breaking mechanism responsible for generating masses of all known particles.

The advent of the Large Hadron Collider (LHC) at CERN (see Sect. 3.3), the highest-energy particle accelerator in the world, allows one to extend the search for the existence of the Higgs boson far beyond what was achieved by previous experiments. In addition, new particles predicted by extensions of the Standard Model, for example, the supersymmetric models (Sect. 13.2), are searched for at LHC.

On September 10, 2008, the proton beams were successfully circulated in the main LHC rings, but 9 days later, operations were halted due to a serious fault. After a long repair and test period, the LHC was restarted in March 2010, and each beam was accelerated up to 3.5 TeV (i.e., half of the design nominal beam energy). The first beam collisions at a center-of-mass energy (\sqrt{s}) of 7 TeV were immediately recorded by the detectors installed around the four LHC collision points; these detectors are ATLAS, CMS, ALICE and LHCb. The first two experiments are large omnipurpose detectors, while ALICE is mainly devoted to the search for the quark-gluon plasma state (Sect. 10.9.1); the LHCb experiment is instead designed for high statistic studies of CP violation (Sect. 12.5). LHC will likely continue to operate at this energy for a few years, but with an ever increasing instantaneous luminosity (in 2011, reaching $3.3 \times 10^{33} \text{ cm}^{-2} \text{ s}^{-1}$). LHC will not likely be operated at its design collision energy of 14 TeV until 2014.

On the experimental side, a proof of the high quality reached by the LHC detectors is, for instance, the invariant mass spectrum of opposite-sign muon pairs obtained with the CMS data, see Fig. 10.25. A muon pair can be produced by the combination of background events, or from a Drell–Yan process, see Sect. 7.14.2. Referring to Fig. 7.20, at the LHC c.m. energy, the exchange of a Z^0 , in addition to the γ , is also possible. In the case of the Drell–Yan mechanism, the $q\bar{q}$ vector meson resonances and the Z^0 on-mass shell are observed as peaks visible in Fig. 10.25.

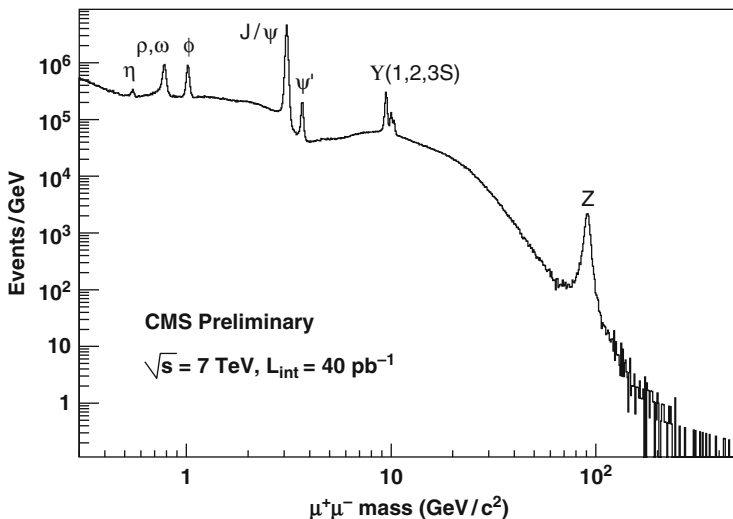


Fig. 10.25 Full invariant mass spectrum of opposite-sign muon pairs measured by the CMS experiment. Different subdetectors are involved in the measurement of the muon energy from the 100 MeV range to hundreds of GeV. The plot corresponds to an integrated luminosity of 40 pb^{-1} at the c.m. energy $\sqrt{s} = 7 \text{ TeV}$ [10C11]

10.10.1 Higgs Boson Production in pp Collisions

Within the Standard Model framework, the Higgs boson is characterized by a complete knowledge of its couplings to all quarks, leptons and gauge bosons, but a complete ignorance of its mass. This ignorance implies searches over a broad mass range. We need to consider various primary states that can produce a H^0 and different H^0 decay modes.

Direct Higgs boson searches at LEP (Sect. 9.8.4) relied on the “Higgsstrahlung” process $e^+e^- \rightarrow Z^* \rightarrow HZ$ shown in Fig. 9.20a. Combining the results of the four LEP experiments, a lower limit on the mass of the Standard Model Higgs boson was obtained: $M_H > 114.4 \text{ GeV}$ at the 95% confidence level. As a consequence, the LHC experiments must search for the Higgs boson in a broad mass interval: $100 \text{ GeV} < M_H < 1 \text{ TeV}$. Moreover, in a hadronic collider, the Higgs boson production mechanisms are completely different from those at LEP. At LHC, the dominant Higgs boson production mechanism are:

- The gluon fusion: $gg \rightarrow H$ shown in Fig. 10.26a.
- The vector boson fusion (VBF): $qq \rightarrow qqV^*V^* \rightarrow qqH$ shown in Fig. 10.26b.

It should be mentioned that searches for the Higgs boson are also performed at the Tevatron $p\bar{p}$ Collider at the Fermilab. Here, the second dominant Higgs production mechanism after the gluon fusion is due to quark-antiquark annihilation. In antiproton-proton colliders, antiquarks are available as valence quarks, carrying a

Fig. 10.26 Dominant Standard Model Higgs boson production mechanisms at LHC: (a) Gluon fusion and (b) Vector Boson Fusion (VBF)

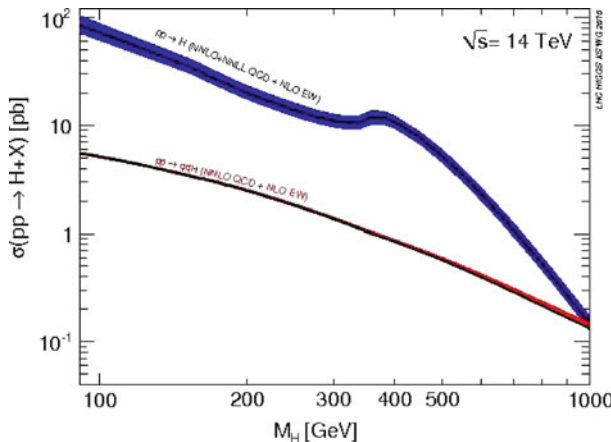
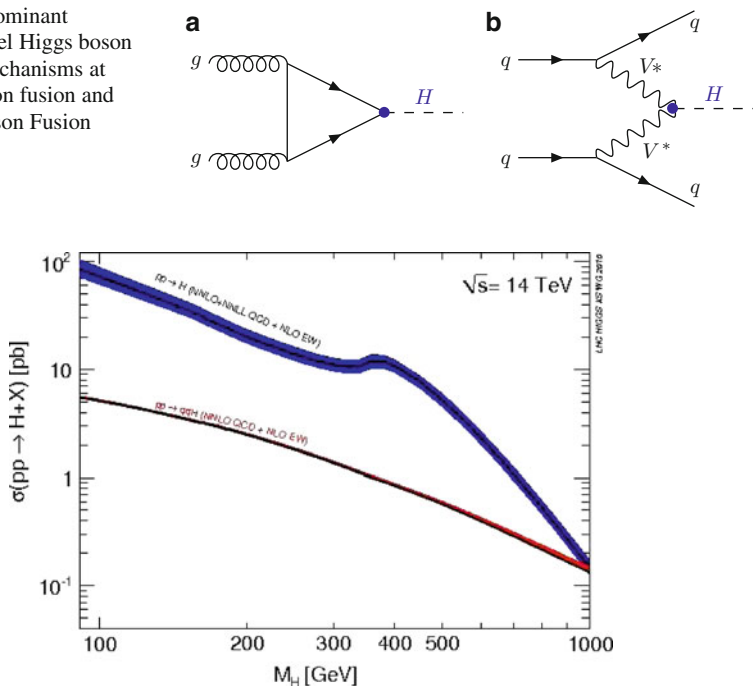


Fig. 10.27 Standard model Higgs boson production cross-sections with systematic uncertainties [10L11] (represented by the line thickness) for the two dominant processes at LHC: the gluon fusion ($pp \rightarrow H$) and the vector boson fusion ($pp \rightarrow qqH$)

large fraction of the total antiproton energy; at proton-proton colliders, such as, the LHC, sea antiquarks typically carry much less energy than the quarks (Fig. 10.11).

The cross-section dependence for the two dominant production mechanisms at LHC (the gluon fusion and the VBF) is shown in Fig. 10.27 as a function of the unknown Higgs mass, M_H , and at a c.m. energy $\sqrt{s} = 14 \text{ TeV}$. At $\sqrt{s} = 7 \text{ TeV}$, the gluon fusion cross-section is about a factor of 3, 5 and 10 smaller at $M_H = 100$, 400 and 1,000 GeV, respectively.

The gluon fusion $gg \rightarrow H$: the dynamics of the gluon fusion mechanism is controlled by strong interactions. Detailed studies of the effect of QCD radiative corrections are thus necessary to obtain accurate theoretical predictions [10L11]. In QCD perturbation theory, the leading order (LO) contribution to the gluon fusion cross-section is proportional to α_S^2 . The main contribution arises from the virtual top quark loop (see Feynman diagram in Fig. 10.26a), allowing the coupling of the Higgs boson to the massless gluons. Indeed, as seen in Sect. 9.8.4, the H^0 coupling is proportional to the mass of the fermion to which it couples. As expected, the lowest order cross-section has large corrections at the next-to-leading order (NLO) QCD diagrams, which represent one of the main sources of uncertainty.

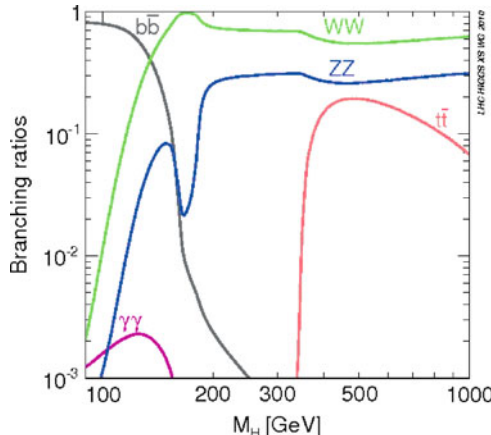


Fig. 10.28 SM Higgs boson decay branching ratios as a function of M_H [10L11]

They increase the LO cross-section by about 80–100%. Another uncertainty source is related to the knowledge of the gluon structure function in the low x region. Referring to Fig. 10.11, the contribution of the gluons to the structure function dominates at $x < 0.2$. It means that the energy available for the formation of the Higgs boson is in most cases smaller than $\sim 0.2^2 = 4\%$ of the c.m. energy of the pp collision. The decrease of the gluon structure function with increasing x is the main origin of the decrease of $\sigma(pp \rightarrow H)$ as M_H increases.

The vector boson fusion (VBF) $qq \rightarrow qqV^*V^* \rightarrow qqH$: the V^* can be either a W^\pm or a Z^0 . The * superscript (as in the following) means that the particle is *off-mass shell*, i.e., $E^2 \neq m^2c^4 + p^2c^2$ (see Sect. 4.6).

The calculation of the VBF cross-section needs the convolution with the structure functions of the incoming quarks. For all possible values of M_H , the VBF cross-section is smaller than that of the gluon fusion process (see Fig. 10.27). However, there is the additional topological signature of the two outgoing quarks participating in the process and forming *jets* whose identification could be easier in this production channel.

10.10.2 Higgs Boson Decays

Following its production, the Higgs boson may decay into a fermion–antifermion or a vector boson pair, respectively, with a coupling proportional to the fermion mass and to the boson mass squared. The main decay channels and their branching ratios (BR, Sect. 4.5.2) are shown in Fig. 10.28. The BRs change significantly across the considered range of M_H , yielding many different final states topologies. For this

reason and since the Higgs mass is unknown, different search strategies are needed to allow an efficient Higgs selection and identification in a broad mass interval. Note that the funny shape of the BR to Z^0 bosons for $130\text{ GeV} < M_H < 2M_Z$ is due to a threshold effect where the decay into two *on-mass shell* W bosons becomes possible.

As the Higgs couples to all fermions proportionally to their mass, the decay into top quarks is dominant. If $M_H < 2M_{top} \simeq 350\text{ GeV}$, the dominant fermionic decay will be to bottom quarks. The decays into $\tau^+\tau^-$, the heaviest charged leptons, is an order of magnitude below that of $b\bar{b}$. Above the WW and ZZ kinematic thresholds ($\sim 200\text{ GeV}$), the Higgs boson should mainly decay into a pair of massive gauge bosons. For large enough M_H , when the phase space factors can be ignored, the branching ratio into WW bosons is two times larger than the decay branching ratio into ZZ bosons.

Since the photon is massless, there is no coupling between the Higgs boson and the photon. However, the Higgs decay into $\gamma\gamma$ is possible through a virtual fermion or boson loop. As can be seen in Fig. 10.28, the $H \rightarrow \gamma\gamma$ branching ratio is at most 0.3% of the dominant $H \rightarrow bb$ channel. However, this is an important decay channel studied at the LHC because the two photon final state has a clean signature, especially in the low Higgs mass region.

Finally, it should be noted that the total width Γ_H is strongly dependent on M_H : it is $\Gamma_H = 3 \times 10^{-3}$, 0.1 and 200 GeV at $M_H = 120, 160$ and 400 GeV , respectively. This fact has important consequences on the search strategies, as discussed in Sect. 10.10.3.

10.10.3 Search Strategies at LHC

To estimate the number of expected signal Higgs events, the total cross-sections shown in Fig. 10.27 must be multiplied by the BRs of Fig. 10.28. To discover the Higgs boson at LHC, many different signatures are searched for, but lepton and photon final states are favored with respect to hadronic final states because of the large QCD background at hadron colliders. In addition, the lepton and photon energy is better measured than the energy of hadronic jets, and thus clearer signatures are expected.

Low Higgs mass ($M_H < 130\text{ GeV}/c^2$). Precision electroweak measurements at LEP and Fermilab seems to favor Higgs masses below $155\text{ GeV}/c^2$ [10A09]. The mass range $M_H < 130\text{ GeV}/c^2$ is particularly interesting, but it is the most difficult to explore. The dominant $H \rightarrow bb$ channel is overwhelmed by the background due to the huge QCD double-jet rate (more than six orders of magnitude higher).

The most promising channel is the decay $H \rightarrow \gamma\gamma$. The signal in this channel is represented by a resonant peak in the $\gamma\gamma$ invariant mass distribution. A very good photon resolution is required to discriminate the signal peak from the large $\gamma\gamma$ continuum from direct photon production and fake photons from hadron jets.

Since the Higgs boson width is small in this mass range (a few MeV for Higgs masses between 110 and 140 GeV), the measured mass peak is entirely dominated by the experimental resolution.

Intermediate mass ($130 \text{ GeV}/c^2 < M_H < 2M_Z$). In this mass region, the branching ratio for the Higgs decay into a vector boson pair becomes important (see Fig. 10.28). The fully leptonic decay $H \rightarrow ZZ^* \rightarrow \ell^+\ell^-\ell^+\ell^-$ has the cleanest experimental signature below $M_H \simeq 150 \text{ GeV}/c^2$, particularly in the four muon channel. Only one vector boson is on-mass shell. The signal selection is based on the reconstruction of the Z^0 mass from one of the lepton pairs. The main irreducible background arises from the ZZ continuum.

For $150 < M_H < 180 \text{ GeV}/c^2$, the most promising detection mode is represented by the leptonic decays of both W bosons: $H \rightarrow WW^* \rightarrow \ell^+\nu_\ell\ell^-\bar{\nu}_{\ell'}$. The $\text{BR}(W \rightarrow \ell\nu)$ is about 32%, where $\ell = e, \mu, \tau$ (68% into hadrons). The simultaneous leptonic decay of both W occurs in about 10% of the cases. Experimentally, a good detection of isolated high transverse momentum muons and electrons and an accurate calorimeter with hermetic coverage to measure the transverse energy of the missing neutrinos is needed. Since the Higgs mass cannot be reconstructed as a narrow mass peak (the energy resolution is poor in this channel and $\Gamma_H \sim \mathcal{O}(1 \text{ GeV})$ in this M_H range), the signal should be observed as an excess of events above backgrounds which therefore must be known as accurately as possible.

High Higgs mass ($M_H > 2M_Z$). If $M_H > 2M_Z$, the $H \rightarrow ZZ^* \rightarrow 4\ell$ provides a very clear signature, as a good mass peak can be reconstructed with the four leptons. The decay into electrons and muons is considered to be a “gold-plated” channel. Both lepton pairs will have a on-mass shell Z which makes it possible to reduce many types of backgrounds. The limitations for possibly detecting the Higgs boson in this decay channel are due to the reduced production rate (the $\text{BR}(H \rightarrow ZZ \rightarrow 4\ell) \sim 0.1\%$ for $\ell = e, \mu$) and to the large width of the Higgs boson in this mass range. For example, in 1 year at high luminosity ($10^{34} \text{ cm}^{-2}\text{s}^{-1}$), the production rate for a Higgs boson with $M_H = 700 \text{ GeV}/c^2$ and decaying into 4ℓ is of the order of 100 events. The large width Γ_H of heavy Higgs ($\Gamma_H = 200 \text{ GeV}$ for $M_H = 400 \text{ GeV}$) makes the observation of a mass peak very difficult.

For large M_H , the decays to vector bosons is dominant and the main detection channel is the $H \rightarrow WW \rightarrow \ell\nu jj$ where j denotes a jet originated from a quark. This WW decay has a $\sim 30\%$ branching ratio, yielding a rate ~ 50 times higher than the four lepton channel from $H \rightarrow ZZ$ decays.

Discovery expectations at the LHC. From March of 2010 to March 2011, the LHC delivered an integrated luminosity of $\sim 50 \text{ pb}^{-1}$ at $\sqrt{s} = 7 \text{ TeV}$. This luminosity is smaller by a factor of ~ 20 with respect to that planned in the first year of data taking. The detection mostly relies on the $gg \rightarrow H$ production mechanism with the subsequent decays $H \rightarrow \gamma\gamma, WW^*$ and ZZ^* . The value of the cross-section σ (Fig. 10.27) times the BR (Fig. 10.28) ranges from a few fb (for $H \rightarrow ZZ \rightarrow 4\ell$) to $\sim 1 \text{ pb}$ (for $H \rightarrow WW \rightarrow \ell^+\nu_\ell\ell^-\bar{\nu}_{\ell'}$ for a high Higgs mass). Including the detection efficiencies, and with a luminosity of a few fb^{-1} , only the

$gg \rightarrow H \rightarrow WW \rightarrow \ell^+ \nu \ell^- \bar{\nu}$ channel is accessible. While for other mass regions, some hints are possible. No signal evidence has been reported [10C11].

The SM Higgs boson is expected to be found at the LHC, provided that an integrated luminosity $L \sim 30 \text{ fb}^{-1}$ is collected and that the detectors perform as expected. For higher luminosities, more channels can be used, thus strengthening the signal and providing definite answers to the question if indeed a scalar Higgs boson exists.

Chapter 11

The Standard Model of the Microcosm

11.1 Introduction

The Standard Model (SM) of the microcosm describes the fundamental constituents of matter and the interactions amongst them. The Standard Model includes 12 fermionic fundamental constituents (see Tables 1.1 and 1.2):

$$\left. \begin{array}{l} 6 \text{ Leptons with Spin} = \frac{1}{2} \\ 6 \text{ Quarks with Spin} = \frac{1}{2} \end{array} \right\} \text{and their corresponding antiparticles.} \quad (11.1)$$

The fundamental fermions are classified into three families; each family is made of a quark doublet, a charged lepton and its associated neutrino plus their antiparticle counterparts. The six quarks each appear in three different colors. The fermions and the corresponding antifermions have quantum numbers of opposite sign. The total number of fundamental fermions is therefore equal to 24 fermions plus 24 antifermions.

An important problem in physics is to understand the ultimate constituents of matter and the fundamental interactions that occur amongst them; it is of equal importance to establish whether these interactions are, in reality, different manifestations of a single underlying (or unified) interaction which has yet to be discovered. The unification question was already addressed by Einstein at the beginning of the last century, though without reaching a conclusion. More recently, progress has been made. Four fundamental interactions have been identified at the common energy scale of our laboratories: weak, electromagnetic, strong and gravitational. The weak and electromagnetic interactions are unified in the electroweak theory of the Standard Model at an energy scale already attained at accelerators. The electroweak Standard Model and the Quantum ChromoDynamics (QCD), describing the strong interaction, together form the *Standard Model of the electroweak and strong interactions* (SM). The Standard Model of the microcosm refers to this definition.

The force fields are quantized and the force carriers correspond to 12 fundamental vector bosons: the photon γ , the intermediate gauge bosons W^+ , W^- , Z^0 , and 8 gluons.

Besides the ultimate fermionic constituents and the bosons that mediate the fundamental interactions, the electroweak SM predicts the existence of the *scalar Higgs boson*, with spin = 0, necessary for the spontaneous symmetry breaking mechanism through which fermions and W^+ , W^- , Z^0 bosons acquire mass. The symmetry is spontaneously broken through a scalar field. In the SM, the self-interacting Higgs field is chosen as a complex doublet. Massive particles acquire their mass through interaction with the Higgs field. Three of the four degrees of freedom connected to the complex doublet are “absorbed,” giving mass to the W^+ , W^- and Z^0 bosons, while the last degree of freedom gives origin to a new boson, the Higgs boson. The Higgs boson interacts with a fermion-antifermion pair, giving them masses. In total, there are 61 fundamental particles: 24 fermions +24 antifermions +12 vector bosons +1 Higgs boson.

It is rather likely that at much higher energies the electroweak and strong interactions unify in the framework of the Grand Unified Theories. At even higher energies, the gravitation should also enter this unification scheme. An intermediate energy scale corresponding to solutions beyond the SM, e.g., supersymmetry (see Sect. 13.2), may also exist.

In this chapter, we shall recall some considerations leading to the electroweak unification and the electroweak model will be described. A few concepts of QCD will then be presented. Some fundamental notions will be repeated even if they were already introduced in previous chapters.

11.2 Weak Interaction Divergences and Unitarity Problem

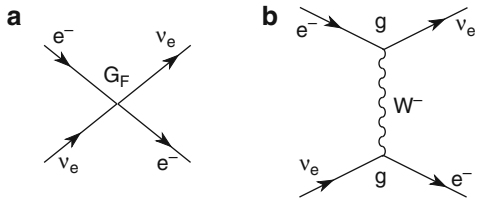
The theory of weak interactions described thus far works well at low energies and at the first order. At higher orders, it presents divergences that cannot be canceled without introducing an indefinitely large number of arbitrary constants; in this way, any predictive capacity of the theory is essentially lost. The $V - A$ theory is divergent. We recall that in the Fermi theory, the involved leptons are assumed to have a point-like interaction whose strength depends on the coupling constant G_F . Consider, for example, the process $\nu_e + e^- \rightarrow \nu_e + e^-$. The weak matrix element of the point-like interaction can be written as

$$M_{fi} = \frac{G_F}{\sqrt{2}} [\bar{\psi}_v \gamma^\mu (1 - \gamma^5) \psi_e] [\bar{\psi}_e \gamma^\mu (1 - \gamma^5) \psi_v]. \quad (11.2)$$

The cross-section of this elastic process is (for $E_{cm} \gg m_e$)

$$\sigma(\nu_e e^- \rightarrow \nu_e e^-) \simeq \frac{G_F^2}{\pi} q_{max}^2 = \frac{2G_F^2 m_e E_{lab}}{\pi} = \frac{G_F^2 s}{\pi} = \frac{4G_F^2 p^{*2}}{\pi}. \quad (11.3)$$

Fig. 11.1 Feynman diagrams of the $\nu_e e^- \rightarrow \nu_e e^-$ process:
(a) for the contact Fermi interaction and **(b)** for the charged current (CC) weak interaction with a W boson exchange



E_{lab} is the ν_e energy in the laboratory system, $q_{max}^2 = 2m_e E_{lab}$, $s = E_{cm}^2$ and p^* is the momentum of the ν_e (or of the e^-) in the center-of-mass system. The cross-section depends on G_F^2 and on the phase space factor. It increases with p^* squared and exceeds the unitarity limit (this limit is determined, in analogy with optics, from the condition that for any partial angular momentum wave function ℓ , the intensity of the scattered wave cannot be larger than that of the incident wave). For spin $s = 1/2$ particles, the wave analysis for the cross-section leads to

$$\sigma_{\ell=0} = \frac{\pi \lambda^2}{2} = \frac{\pi}{2 p^{*2}}. \quad (11.4)$$

The cross-section (11.3) exceeds (11.4) for $\frac{4G_F^2 p^{*2}}{\pi} > \frac{\pi}{2 p^{*2}}$, that is, for

$$p^* > \left(\frac{\pi^2}{8G_F^2} \right)^{1/4} = \left(\frac{\pi}{\sqrt{8}G_F} \right)^{1/2} = \left(\frac{\pi}{\sqrt{8} \cdot 1.17 \cdot 10^{-5}} \right)^{1/2} \simeq 300 \text{ GeV/c.}$$

Therefore, for $p^* > 300 \text{ GeV/c}$, the weak interaction Fermi cross-section (11.3) exceeds the unitarity limit.

The problem is solved by the introduction of the vector bosons W^\pm . Massive bosons lead to the presence of a propagator of the type $\frac{1}{q^2 + m_W^2}$ (see Fig. 11.1b). The matrix element becomes

$$M_{fi} = \left[\frac{g}{\sqrt{2}} \left(\bar{\psi}_v \gamma^\mu \frac{(1 - \gamma^5)}{2} \psi_e \right) \right] \frac{1}{q^2 + m_W^2} \left[\frac{g}{\sqrt{2}} \left(\bar{\psi}_e \gamma^\mu \frac{(1 - \gamma^5)}{2} \psi_v \right) \right]. \quad (11.5)$$

The change $G_F \rightarrow \frac{G_F m_W^2}{q^2 + m_W^2}$ modifies the cross-section (11.3) by

$$\sigma(\nu_e e^- \rightarrow \nu_e e^-) = \frac{4G_F^2 m_W^4 p^{*2}}{\pi(q^2 + m_W^2)^2}. \quad (11.6)$$

For $q^2 \sim p^{*2} \gg m_W^2$, one has

$$\sigma(\nu_e e^- \rightarrow \nu_e e^-) \simeq \frac{4G_F^2 m_W^4}{\pi p^{*2}}. \quad (11.7)$$

Therefore, the cross-section for $\nu_e e^- \rightarrow \nu_e e^-$ increases with p^* up to $p^* \sim 300 \text{ GeV}/c$, and then becomes almost constant and finally decreases with increasing p^{*2} . The unitarity limit violation is consequently solved.

In the limit of small q^2 ($q^2 \rightarrow 0$), the interaction through the exchange of a W boson gives the same result as the point-like Fermi interaction. For $q^2 \ll m_W^2$, the cross-section (11.6) reduces to the Fermi cross-section (11.3). Comparing matrix elements (11.2) and (11.5), one finds:

$$\lim_{q^2 \rightarrow 0} \frac{g^2}{8} \frac{1}{(q^2 + m_W^2)} \simeq \frac{g^2}{8m_W^2} = \frac{G_F}{\sqrt{2}}. \quad (11.8)$$

Even after introducing the W^\pm bosons, there are still divergences in the weak interactions, e.g., the t-channel diagram for the $\nu_e \bar{\nu}_e \rightarrow W^+ W^-$ process shown in Fig. 8.19a has a quadratically divergent cross-section. The divergence is precisely canceled by the s-channel diagram shown in Fig. 8.19b. The cancellation is due to the presence of Z^0 exchange neutral currents and a relationship between the $Z^0 \ell \bar{\ell}$ and the $W^\pm \ell \bar{\ell}$ coupling constants. Historically, this was one of the reasons for introducing the Z^0 boson.

The lowest order diagram for the electromagnetic process $e^+ e^- \rightarrow W^+ W^-$ shown in Fig. 9.16b is also divergent; in this case, the divergence is eliminated by adding the diagram shown in Fig. 9.16c where a Z^0 boson is exchanged. This cancellation occurs only if the weak coupling constant g is approximately equal to the electromagnetic constant, that is, if $g \simeq e$. This implies *the unification of weak and electromagnetic fields*.

The latter consideration can be applied to the $\nu_e e^- \rightarrow \nu_e e^-$ process described by the diagrams of Fig. 11.1. Placing $g \simeq e$ in (11.8), one obtains $m_W \simeq m_{Z^0} \simeq 100 \text{ GeV}$. This was the first estimate of the masses of the W^\pm, Z^0 bosons, that is, only such high masses can insure the unification with the same coupling constant and the reduction to the Fermi theory in the low energy limit.

11.3 Gauge Theories

The Standard Model includes the description of the electroweak and strong interactions. The electroweak and QCD theories are both gauge theories (see below), each with a symmetry group that characterizes the interaction [11A84].

Here, we show that in order to construct a gauge theory, it is necessary to:

- Choose the group describing the symmetry that characterizes the interactions in question
- Require local gauge invariance for the group symmetry transformations
- Choose the Higgs field that introduces the spontaneous symmetry breaking. This allows particles to acquire masses without explicitly breaking the gauge invariance

- Renormalize the couplings and the masses of the theory so that they correspond to the known experimental data. The study of renormalization leads to the concept of “running,” that is, the dependence on the energy scale of the coupling constants

11.3.1 Choice of the Symmetry Group

Some particles exhibit very similar properties; this suggests the existence of symmetries. For example, quarks appear in three colors and the properties of the weak interaction suggest the grouping of particles in doublets. These properties naturally lead to adopting the group structures $SU(2)$ and $SU(3)$ respectively for the weak and strong interactions. The electromagnetic interaction does not modify the quantum numbers of interacting particles and therefore can be described by the group $U(1)$.

The standard model for electroweak and strong interactions is based on the symmetry of unitary groups¹:

$$SU(3)_C \otimes [SU(2)_L \otimes U(1)_Y].$$

Historically, the necessity for the quarks to appear in three colors was introduced in order to maintain the Pauli exclusion principle in the case of hadrons made of three quarks (Sect. 7.8.1). Later, it became clear that the role of color was more important than what was originally thought; it was indeed understood afterwards that the “color charge” acts as the source of the strong interaction (the *color field*), just as the electric charge is the source of the electric field.

The “charge” for the weak interaction is the third component of the *weak isospin*, I_3 . The charged current weak interaction affects all left-handed particles, i.e., particles with spin antiparallel to the momentum (negative elicity). A weak isospin equal to $\pm 1/2$ is therefore assigned to left-handed particles, while right-handed particles are organized in isospin singlets (see Table 11.1). In the limit of zero mass, the $V - A$ nature of the charged current weak interaction only involves left-handed fermions. For massive particles, the interaction preferentially involves left-handed particles. Assuming that neutrinos have zero mass,² the weak couplings of right-handed neutrinos and left-handed antineutrinos would be equal to zero. Therefore, for every generation, we have 15 matter fields: 2 left-handed leptons and 1 right-handed, 2×3 left-handed quarks and 2×3 right-handed ones (the factor 3 takes color into account).

¹The unitary transformations rotate the vectors, but do not modify their length. The unitary symmetry groups $SU(N)$ are Special Unitary groups with a determinant equal to +1.

²Recent experimental results on neutrino oscillations favor the hypothesis that neutrinos have a very small nonzero mass (Sect. 12.6).

Table 11.1 Summary of fermion multiplets of the electroweak interaction. Left-handed weak isospin doublets are shown in parentheses; the right-handed singlets are shown separately. For left-handed quarks, the u, c, t quarks of the strong interaction and the “rotated” d', s', b' are used. The rotation is done according to the CKM matrix, that is, a generalization of the “Cabibbo rotation.” The electric charge Q of the two states of each doublet differs by one unit; the difference $Q - I_3 = Y_W/2$ is the same within each doublet ($-1/2$ for left-handed leptons, $+1/6$ for quarks)

	Fermion multiplets			I	I_3	Q	Y_W
Leptons	$\begin{pmatrix} v_e \\ e \end{pmatrix}_L$	$\begin{pmatrix} v_\mu \\ \mu \end{pmatrix}_L$	$\begin{pmatrix} v_\tau \\ \tau \end{pmatrix}_L$	1/2	+1/2	0	-1
	e_R	μ_R	τ_R	0	-1/2	-1	-1
					0	-1	-2
Quarks	$\begin{pmatrix} u \\ d' \end{pmatrix}_L$	$\begin{pmatrix} c \\ s' \end{pmatrix}_L$	$\begin{pmatrix} t \\ b' \end{pmatrix}_L$	1/2	+1/2	+2/3	+1/3
	u_R	c_R	t_R	0	-1/2	-1/3	+1/3
	d'_R	s'_R	b'_R	0	0	+2/3	+4/3

The electromagnetic interaction takes place through the exchange of both the neutral gauge boson of the $SU(2)_L$ group and that of the $U(1)_Y$ group; thus, the “charge” of the $U(1)_Y$ group cannot simply coincide with the electric charge; it instead corresponds to the weak hypercharge Y_W defined by the Gell–Mann–Nishijima relation

$$Q = I_3 + \frac{1}{2}Y_W. \quad (11.9)$$

Y_W is equal to $B - L$ for the left-handed doublets, and to $2Q$ for the right-handed singlets (B is the baryonic number equal to that $1/3$ for the quarks and to 0 for the leptons; L is the leptonic number equal to 1 for the leptons and to 0 for the quarks). Since I_3 and Q are both conserved, Y_W is a conserved quantum number.

11.3.2 Gauge Invariance

11.3.2.1 Gauge Invariance in QED

A *global gauge transformation* is a phase transformation (i.e., a phase rotation) of the material field ψ ; it can be written as

$$\psi_\mu \rightarrow \psi'_\mu = \psi_\mu e^{i\alpha/\hbar c} \rightarrow (1 + i\alpha/\hbar c)\psi_\mu \quad (11.10a)$$

$$\psi^*_\mu \rightarrow \psi'^*_\mu = \psi^*_\mu e^{-i\alpha/\hbar c} \rightarrow (1 - i\alpha/\hbar c)\psi^*_\mu, \quad (11.10b)$$

where the relations on the right are valid for infinitesimal transformations and α is a scalar that has the same value in each space-time point. The invariance for this transformation implies that the phase of the wave function is arbitrary and not

observable. The derivative of the wave function transforms as the wave function itself, $\partial\psi'/\partial x^\mu = \partial_\mu\psi' = e^{i\alpha}\partial_\mu\psi$.

The gauge transformation can be generalized considering α as a function of space-time, $\alpha = \alpha(x)$. In this case, one has a *local gauge transformation* that can be different from point to point. The electromagnetic theory is a local gauge invariant theory. If the wave function ψ and its derivative $\partial\psi/\partial x^\mu = \partial_\mu\psi$ transform in the same way, the Lagrangian is invariant under gauge transformations since it includes $[\psi^*(x)\partial_\mu\psi(x)]$ terms. The gauge transformation can be written in the form

$$\psi \rightarrow \psi' = e^{i\alpha(x)}\psi. \quad (11.11)$$

The derivative of $\psi(x)$ is then

$$\frac{\partial\psi'(x)}{\partial x^\mu} = \partial_\mu\psi'(x) = e^{i\alpha(x)}[\partial_\mu\psi(x) + i\psi(x)\partial_\mu\alpha(x)] \quad (11.12)$$

$$\neq e^{i\alpha(x)}\partial_\mu\psi(x). \quad (11.13)$$

The derivative does not transform as the wave function, and therefore the Lagrangian is not invariant under gauge transformation. The interaction of fermions with the electromagnetic field B_μ is introduced through the *covariant derivative* of the electromagnetic field³

$$\partial_\mu \rightarrow D_\mu = \partial_\mu + ieB_\mu. \quad (11.14)$$

Furthermore, to ensure the gauge invariance of the Lagrangian, the quadrivector potential of the electromagnetic field B_μ must transform as

$$B_\mu \rightarrow B'_\mu(x) = B_\mu(x) - \frac{1}{e}\partial_\mu\alpha(x). \quad (11.15)$$

With the transformations defined in (11.11), (11.14) and (11.15), the covariant derivative of the electromagnetic field transforms as

$$\begin{aligned} D_\mu\psi'(x) &= e^{i\alpha(x)}[\partial_\mu\psi(x) + i\psi(x)\partial_\mu\alpha(x) + ieB_\mu(x)\psi(x) - i\psi(x)\partial_\mu\alpha(x)] \\ &= e^{i\alpha(x)}D_\mu\psi(x). \end{aligned} \quad (11.16)$$

Thus, the term $[\psi^*(x)D_\mu\psi(x)]$ is invariant under local gauge transformations. The fact that we use the covariant derivative is connected to the nature of the interaction of an electric charge e with the field B_μ , i.e., eB_μ . The gauge invariance for the electromagnetic field leads to a conserved current (and therefore to the conservation of the electric charge). The infinite set of phase transformations (11.11) forms the *abelian* unitary group U(1). QED is invariant under gauge transformations of this group.

³The notation B_μ instead of A_μ is used to distinguish the electromagnetic field from the isovector field \mathbf{A}_μ introduced for the weak interaction in the next paragraph.

11.3.2.2 Gauge Invariance in SU(2)

Following the QED example, more complicated groups were proposed; these groups are specified by noncommutative operators in order to introduce other interactions from a local invariance principle. For the isotopic spin initially associated with the strong interaction, the SU(2) group was proposed. The conservation of weak isotopic spin implies invariance under rotation in the isospin space

$$\psi_j \rightarrow \psi'_j = e^{i\varepsilon^a \frac{\sigma_a}{2}} \psi_j \simeq \psi_j + i\varepsilon^a \frac{\sigma_a}{2} \psi_j \quad (a = 1, 2, 3) \quad (11.17)$$

where the index j represents each type of lepton, ε^a are infinitesimal arbitrary parameters and σ_a are the noncommutative Pauli matrices (Appendix 4) obeying

$$\left[\frac{\sigma_a}{2}, \frac{\sigma_b}{2} \right] = i \varepsilon_{abc} \frac{\sigma_c}{2} \quad (11.18)$$

where ε_{abc} is the totally antisymmetric tensor and $\psi(x)$ are SU(2) isospinors. Let us now require that ε^a be different in each space-time point, that is, $\varepsilon^a = \varepsilon^a(x)$. Proceeding as for QED, a gauge invariant description is obtained by introducing a massless *isovector field* \mathbf{A}_μ with charged and neutral components and with a coupling constant g similar to e . The invariance of the $\psi^* D_\mu \psi$ terms under the transformation (11.17) implies the introduction of the following covariant derivative:

$$\partial_\mu \rightarrow \nabla_\mu \equiv \partial_\mu + ig A_\mu^a \frac{\sigma_a}{2}. \quad (11.19)$$

The vector nature of these fields leads to the gauge transformation

$$A_\mu^a \rightarrow A_\mu^a - \frac{1}{g} \partial_\mu \varepsilon^a(x) - \varepsilon_{abc} \varepsilon^b(x) A_\mu^c. \quad (11.20)$$

The additional term, with respect to (11.15), is associated with the fact that the σ matrices do not commute. This also implies that there exists an interaction between \mathbf{A}_μ and all particles with isospin, including the \mathbf{A}_μ themselves. In this way, \mathbf{A}_μ are both sources and carriers of the isospin field. Notice that the hypothetical charged intermediate bosons of the isospin field are massless, just like the photon for the electromagnetic field.

11.3.2.3 Gauge Invariance in SU(3)

A generalization is obtained by requiring that the Lagrangian density be invariant under SU(N) rotations; in this case, one must have $\mathcal{L}(\psi') = \mathcal{L}(\psi)$, $\psi' = U\psi$, where U is an unitary matrix ($U^+ U = 1$) that can be written as

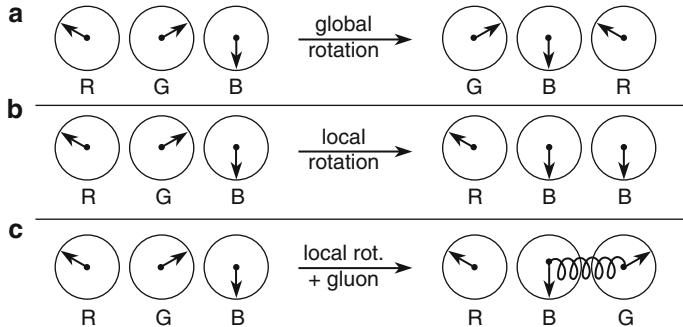


Fig. 11.2 Qualitative illustration of the difference between global and local rotations in the “color space.” The initial state on the left is a colorless baryon made of three quarks of different colors. (a) A global rotation changes the color of all three quarks at the same time, leaving the initial baryon colorless. (b) Local rotations, different for each quark, can locally change the color, thus changing the color of the initial baryon unless (c) the color is restored by the exchange of a gluon

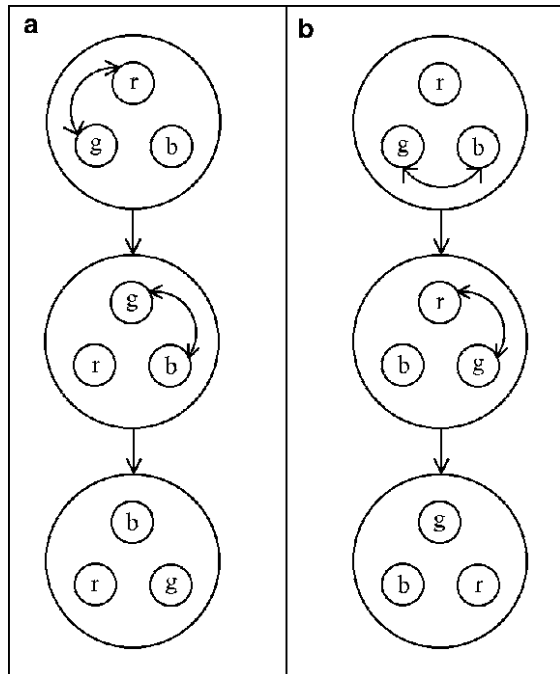
$$U = \exp \left(-i \sum_{K=1}^{N^2-1} \alpha_K \cdot F_K \right) \quad (11.21)$$

where α_K are the rotation parameters, F_K are the rotation matrices and $(N^2 - 1)$ is the number of degrees of freedom. For $SU(2)$, F_K are the three (2×2) Pauli matrices; for $SU(3)$, F_K are the eight (3×3) λ_a Gell–Mann matrices. The local gauge invariance is then introduced by replacing the derivative ∂_μ with the covariant derivative D_μ ($= \partial_\mu + ieB_\mu$, in QED), with the following property:

$$D'\psi' = UD\psi. \quad (11.22)$$

The covariant derivative transforms the material field ψ , unlike the usual derivative that transforms differently. We now require invariance under local (rather than global) transformations (rotations). The interactions should therefore be invariant under rotations of the symmetry group for each particle separately. The request of local gauge invariance leads to the introduction of intermediate vector bosons whose quantum numbers determine the interactions between the material fields, as shown first by Yang and Mills in 1957 for the isospin symmetry of the strong interaction. In the QCD framework, it is assumed that the interaction between two quarks is mediated by the exchange of massless gluons with spin 1. It is also assumed that the interaction between two quarks is invariant under the exchange of color. This implies that the three quarks of different colors are described by the symmetry group $SU(3)_C$, where C stands for color. The quark $SU(3)_C$ symmetry is considered exact. Figure 11.2 qualitatively shows the difference between global and local rotations in the “color space” for a colorless baryon consisting of three quarks

Fig. 11.3 Illustration of the non-abelian nature of SU(3) for a colorless baryon. Starting from the same hadron, (a) the quarks r and g are swapped first, exchanging a red-green gluon (more precisely $r\bar{g}$ or $\bar{g}r$); the quarks g and b are then swapped (exchanging a green-blue gluon). In (b) the order of the color swaps is inverted. The final results shown at the bottom are not the same; thus, these color swaps do not commute (non-abelian means that $A \cdot B \neq B \cdot A$)



of different colors. The color charges of gluons involve the non-abelian nature of SU(3): rotations in the “color space” do not commute, as shown in Fig. 11.3.

11.4 Gauge Invariance in the Electroweak Interaction

The covariant derivative of the Standard Model in the electroweak interaction can be written as

$$\nabla_\mu = \partial_\mu + \frac{ig'}{2} B_\mu \mathbf{1} + \frac{ig}{2} A_\mu^a \sigma_a \quad (11.23)$$

where B_μ is the massless mediator of the field of the U(1) group, with coupling constant g' . A_μ^a are the three massless quanta of SU(2) with coupling constant g . This covariant derivative can be extended to include the strong interaction; in this case, the covariant derivative can be written as

$$D_\mu = \nabla_\mu + \frac{ig_s}{2} G_\mu^a \lambda_a \quad (11.24)$$

where G_μ^a are the eight massless SU(3) quanta with coupling constant g_s . The treatment of the strong interaction will not be included here.

In (11.23), the term $A_\mu^a \sigma_a$ can be explicitly written as

$$\begin{aligned} A_\mu^1 \cdot \sigma_1 + A_\mu^2 \cdot \sigma_2 + A_\mu^3 \cdot \sigma_3 &= A_\mu^1 \begin{pmatrix} 0 & 1 \\ 1 & 0 \end{pmatrix} + A_\mu^2 \begin{pmatrix} 0 & -i \\ i & 0 \end{pmatrix} + A_\mu^3 \begin{pmatrix} 1 & 0 \\ 0 & -1 \end{pmatrix} \\ &= \begin{pmatrix} A_\mu^3 & A_\mu^1 - iA_\mu^2 \\ A_\mu^1 + iA_\mu^2 & -A_\mu^3 \end{pmatrix} \\ &= \begin{pmatrix} A_\mu^3 & \sqrt{2}W_\mu^+ \\ \sqrt{2}W_\mu^- & -A_\mu^3 \end{pmatrix} \end{aligned} \quad (11.25)$$

where

$$W_\mu^- = \frac{1}{\sqrt{2}}(A_\mu^1 + iA_\mu^2) \quad (11.26)$$

$$W_\mu^+ = \frac{1}{\sqrt{2}}(A_\mu^1 - iA_\mu^2). \quad (11.27)$$

Thus, the term $\frac{i}{2}(g'B_\mu \mathbf{1} + gA_\mu^a \sigma_a)$ in (11.23) explicitly becomes

$$\frac{i}{2} \begin{pmatrix} g'B_\mu + gA_\mu^3 & \sqrt{2}gW_\mu^+ \\ \sqrt{2}gW_\mu^- & g'B_\mu - gA_\mu^3 \end{pmatrix}. \quad (11.28)$$

The elements along the diagonal correspond to operators for transitions in which the fermion electric charge is not changed (neutral currents). The nondiagonal W_μ^+ , W_μ^- elements act as “raising” and “lowering” operators in the weak isospin space and transform, for example, an electron in its neutrino (or vice versa). The real fields γ , Z^0 and W^\pm are obtained from the gauge fields after spontaneous symmetry breaking (see Sect. 11.4.1).

11.4.1 Lagrangian Density of the Electroweak Theory

The procedure to construct a gauge invariant theory can be generalized to any symmetry group and particularly to the $SU(2) \times U(1)$ group in order to describe electromagnetic and weak interactions in a unified model. The Dirac Lagrangian density \mathcal{L} for a free fermion is

$$\mathcal{L} = i\bar{\psi}\gamma^\mu\partial_\mu\psi - m\bar{\psi}\psi = \bar{\psi}(x)(i\gamma^\mu\partial_\mu - m)\psi(x). \quad (11.29)$$

The first term represents the kinetic energy of the matter field ψ with a mass m ; the second term, bilinear in ψ , is the mass energy, proportional to the fermion mass m . For a massive Higgs, the Lagrangian density is given by the Klein–Gordon equation:

$$\mathcal{L} = (\partial_\mu\varphi^+)(\partial^\mu\varphi) - m^2\varphi^+\varphi. \quad (11.30)$$

In this case, the term bilinear in φ is proportional to m^2 , the Higgs mass squared. The Lagrangian density (11.29) must be invariant under SU(N) rotations, and therefore $\mathcal{L}(\psi') = \mathcal{L}(\psi)$, $\psi' = U\psi$, where U is a unitary matrix ($U^\dagger U = 1$). The invariance under rotations can be verified for the mass term

$$m\bar{\psi}'\psi' = m\bar{\psi}U^\dagger U\psi = m\bar{\psi}\psi, \quad (11.31)$$

given that $U^\dagger U = 1$. The kinetic term of (11.29) is invariant under global transformations (rotations), for which U is independent of x and can thus be treated as a constant, namely,

$$\mathcal{L}'_{kin} = \bar{\psi}U^\dagger\gamma^\mu\partial_\mu U\psi = \bar{\psi}U^\dagger U\gamma^\mu\partial_\mu\psi = \bar{\psi}\gamma^\mu\partial_\mu\psi = \mathcal{L}_{kin}. \quad (11.32)$$

The local gauge invariance is introduced by replacing the derivative ∂_μ with the covariant derivative of the $[SU(2)_L \times U(1)_Y]$ group $\nabla_\mu = \partial_\mu + \frac{i g'}{2}B_\mu\mathbf{1} + \frac{i g}{2}A_\mu^a\sigma_a$. The Lagrangian density (11.29)

$$\mathcal{L} = i\bar{\psi}\gamma^\mu\nabla_\mu\psi - m\bar{\psi}\psi \quad (11.33)$$

now transforms by

$$\mathcal{L}'(\psi') = i\bar{\psi}U^\dagger\gamma^\mu U\nabla\psi - m\bar{\psi}U^\dagger U\psi = i\bar{\psi}\gamma^\mu\nabla\psi - m\bar{\psi}\psi = \mathcal{L}(\psi). \quad (11.34)$$

The new Lagrangian density describes the interaction between particles of matter through the exchange of gauge bosons associated with the gauge fields, with the coupling constants g and g' . The resulting Lagrangian density $\mathcal{L}(\psi, \nabla_\mu)$ must be completed by adding the Yang–Mills Lagrangian density, \mathcal{L}_{YM} , describing the propagation of gauge fields:

$$\mathcal{L}_{YM} = -\frac{1}{4}F_{\mu\nu}^a(F^a)^{\mu\nu} - \frac{1}{4}G_{\mu\nu}G^{\mu\nu} \quad (11.35)$$

where

$$F_{\mu\nu}^a = \partial_\mu A_\nu^a - \partial_\nu A_\mu^a - g\varepsilon_{abc}A_\mu^b A_\nu^c \quad (11.36)$$

$$G_{\mu\nu} = \partial_\mu B_\nu - \partial_\nu B_\mu. \quad (11.37)$$

With a complete development of the Lagrangian density, it can be observed that it does not contain quadratic terms for the gauge fields, for example, $m^2 B_\mu B^\mu$ or $m^2 A_\mu^a (A^a)^\mu$, see also (11.30). Therefore, the gauge bosons associated with these gauge fields are massless. The real fields γ , Z^0 and W^\pm are obtained from the gauge fields after spontaneous symmetry breaking.

11.5 Spontaneous Symmetry Breaking. The Higgs Mechanism

The gauge theory of the electroweak interaction described above involves fields with massless propagators; but the vector boson mediators of the weak interaction, W^\pm and Z^0 , have a nonzero mass; their masses are actually large. Higgs proposed a mechanism that allows the mediators of the weak interaction to become massive while the mediator of the electromagnetic interaction (the photon) remains massless. This mechanism is the spontaneous symmetry breaking which keeps the Lagrangian density still invariant under the group of gauge transformations $[SU(2)_L \times U(1)_Y]$. This mechanism requires the introduction of a new scalar boson, the so-called Higgs boson and the corresponding Higgs field, whose self-interaction modifies the ground state (the state with minimum energy) so that it is no longer a hypercharge or a weak isospin eigenstate. The mass of the Higgs boson is not predicted by the theory. The masses of the intermediate weak bosons and fermions are dynamically generated through their interaction with the Higgs scalar field which is supposed to be present everywhere in the space-time where the interaction occurs.

The Higgs mechanism considers a gauge invariant Lagrangian density \mathcal{L}_H , corresponding to a self-interacting scalar isodoublet φ . This Lagrangian density is made of three terms and can be written in a symbolic way as

$$\mathcal{L}_H = \mathcal{L}_\nabla - \mathcal{L}_V + \mathcal{L}_{YM} \quad (11.38a)$$

where

$$\mathcal{L}_\nabla = (\nabla_\mu \varphi)^+ (\nabla^\mu \varphi) \quad (11.38b)$$

$$\mathcal{L}_V = V(\varphi^+ \varphi) \quad (11.38c)$$

$$\mathcal{L}_{YM} = -\frac{1}{4} F_{\mu\nu}^a (F^a)^{\mu\nu} - \frac{1}{4} G_{\mu\nu} G^{\mu\nu}. \quad (11.38d)$$

The theory of superconductivity was taken as a model for this essential part of the Standard Model of the microcosm. The Ginzburg–Landau potential in the theory of superconductivity is used for the Higgs potential, $\mathcal{L}_V = V(\varphi^+ \varphi)$:

$$V(\varphi^+ \varphi) = \mu^2 \varphi^+ \varphi + \lambda (\varphi^+ \varphi)^2 \quad (11.39)$$

where μ^2 and λ are complex constants. For $\mu^2 > 0$, the potential has a parabolic shape, while for $\mu^2 < 0$, it has the form of a “Mexican hat,” as shown in Fig. 11.4. In the latter case, the ground state with $\varphi = 0$ corresponds to a local maximum of the potential and therefore to an unstable equilibrium.

This system is still invariant under global rotations, though not under local rotations. The symmetry is broken by choosing φ as a complex doublet with a given hypercharge ($Y_W = 1$):

$$\varphi = \begin{pmatrix} \varphi^a \\ \varphi^b \end{pmatrix} \quad (11.40)$$

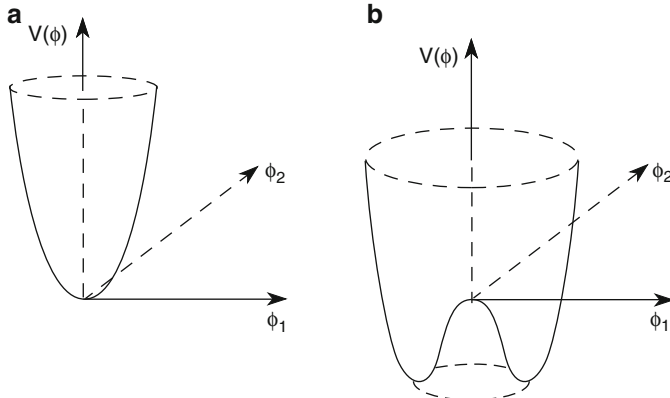


Fig. 11.4 Higgs potential (11.39), as a function of $\phi_1 = \text{Re}(\phi)$ and $\phi_2 = \text{Im}(\phi)$. (a) For $\mu^2 > 0$, $V(\phi)$ has a parabolic shape with a minimum for $V(\phi) = 0$ at $\phi_1 = \phi_2 = 0$. (b) For $\mu^2 < 0$, it has the form of a “Mexican hat”

where

$$\varphi^a = \frac{1}{\sqrt{2}}(\varphi_1 + i\varphi_2) \quad \varphi^b = \frac{1}{\sqrt{2}}(\varphi_3 + i\varphi_4). \quad (11.41)$$

Given that the Lagrangian density is invariant under gauge transformations and that the ground state is a neutral state, we can choose the shape of the field φ , and particularly φ_0 , in any space-time point x in order to have a down spinor of the form $\begin{pmatrix} 0 \\ v \end{pmatrix}$. With $\varphi_1 = \varphi_2 = \varphi_4 = 0$ and $\varphi_3 = \sqrt{\frac{-\mu^2}{2\lambda}}$, one has

$$\varphi_0 = \sqrt{\frac{1}{2}} \begin{pmatrix} 0 \\ v \end{pmatrix} \quad \text{with } v = \sqrt{\frac{-\mu^2}{\lambda}} \quad (11.42)$$

where v is the vacuum expectation value of the Higgs field. In choosing one particular minimum, the $SU(2)$ symmetry has been spontaneously broken. The ground state that is now different from zero is not isospin invariant. The Higgs field φ can be expanded around the ground state of the unitary gauge

$$\varphi = e^{i\xi(x)\cdot\sigma} \begin{pmatrix} 0 \\ v + h(x) \end{pmatrix}. \quad (11.43)$$

The real fields $\xi(x)$ are excitations along the minimum of the potential. In the case of global symmetry, they correspond to the so-called massless *Goldstone bosons*. In local gauge theories, they may be eliminated by an appropriate rotation

$$\varphi' = e^{-\xi(x)\cdot\sigma} \varphi(x) = \begin{pmatrix} 0 \\ v + h(x) \end{pmatrix}. \quad (11.44)$$

It follows that the fields ξ have no physical meaning as they disappear after a gauge transformation. Only the real field $h(x)$ can be interpreted as a real particle, the Higgs boson. The scalar field $\varphi(x)$ can now be introduced into the gauge invariant Lagrangian density (11.38) in order to determine the masses of the various bosons by collecting all terms which are of second order in the fields A_μ^a , B_μ and h . These bilinear terms can be extracted separately for the three Lagrangian densities defined in Eq. 11.38. Taking into account the second order terms in the fields A_μ^a , B_μ and h and neglecting higher order terms, the various contributions are:

1. The contribution from \mathcal{L}_∇ :

$$\begin{aligned}\mathcal{L}_\nabla = (\nabla_\mu \varphi)^+ (\nabla^\mu \varphi) &\xrightarrow{\text{2nd order}} \frac{1}{2} (\partial_\mu h) (\partial^\mu h) \\ &+ \frac{1}{2} \left(\frac{g^2 v^2}{4} \right) (A_\mu^1 A^{1\mu} + A_\mu^2 A^{2\mu}) \\ &+ \frac{1}{8} v^2 (g A_\mu^3 - g' B_\mu) (g A^{3\mu} - g' B^\mu).\end{aligned}\quad (11.45)$$

2. The contribution from \mathcal{L}_V :

$$\mathcal{L}_V = V(\varphi^+ \varphi) \xrightarrow{\text{2nd order}} \text{constant} + \frac{1}{2} (-2\mu^2) h^2. \quad (11.46)$$

3. The contribution from \mathcal{L}_{YM} :

$$\mathcal{L}_{YM} \xrightarrow{\text{2nd order}} -\frac{1}{4} A_{\mu\nu}^a A^{a\mu\nu} - \frac{1}{4} G_{\mu\nu} G^{\mu\nu} \quad (11.47)$$

where

$$A_{\mu\nu}^a \equiv \partial_\mu A_\nu^a - \partial_\nu A_\mu^a. \quad (11.48)$$

Since only second order terms are considered, $F_{\mu\nu}^a$ is simplified in $A_{\mu\nu}^a$.

Since (11.45) contains mixed products of the gauge fields A_μ^3 and B_μ , the corresponding bosons cannot appear with a physical mass. Two orthogonal combinations of A_μ^3 and B_μ must be defined, that is,

$$\mathcal{Z}_\mu = \cos \theta_w A_\mu^3 - \sin \theta_w B_\mu \quad (11.49)$$

$$\mathcal{A}_\mu = \sin \theta_w A_\mu^3 + \cos \theta_w B_\mu \quad (11.50)$$

where the so-called *Weinberg angle* θ_w is the weak mixing angle chosen in a way that the mixed products of \mathcal{Z}_μ and \mathcal{A}_μ disappear. Therefore,

$$\tan \theta_w = \frac{g'}{g}. \quad (11.51)$$

Finally, the free Lagrangian density for all fields can be written as

$$\begin{aligned} \mathcal{L}_H = & \frac{1}{2}(\partial_\mu h)(\partial^\mu h) - \frac{1}{2}(-2\mu^2)h^2 \\ & - \frac{1}{4}A_{\mu\nu}^1 A^{1\mu\nu} + \frac{1}{2}\left(\frac{g^2 v^2}{4}\right)A_\mu^1 A^{1\mu} \\ & - \frac{1}{4}A_{\mu\nu}^2 A^{2\mu\nu} + \frac{1}{2}\left(\frac{g^2 v^2}{4}\right)A_\mu^2 A^{2\mu} \\ & - \frac{1}{4}Z_{\mu\nu} Z^{\mu\nu} + \frac{1}{2}\left(\frac{g^2 v^2}{4\cos^2\theta_w}\right)\mathcal{Z}_\mu \mathcal{Z}^\mu \\ & - \frac{1}{4}A_{\mu\nu} A^{\mu\nu} + 0\mathcal{A}_\mu \mathcal{A}^\mu \end{aligned} \quad (11.52)$$

$$+ \mathcal{L}_{V VH}. \quad (11.53)$$

The term $\mathcal{L}_{V VH}$ described below (see (11.61) and (11.62)) contains mixed terms $hA_\mu^1 A^{1\mu}$, $hA_\mu^2 A^{2\mu}$, $h\mathcal{Z}_\mu \mathcal{Z}^\mu$ and $h\mathcal{A}_\mu \mathcal{A}^\mu$.

From the above equation, one sees that the Higgs mechanism allowed one to associate massive particles to some of the gauge fields without having explicitly introduced a mass term in the Lagrangian density (an operation which would not have maintained the required symmetry). Mass terms have appeared implicitly and the initial goal of describing the weak interaction via the exchange of massive vector bosons has been achieved. The three mass terms are

$$m_W^2 = \frac{g^2 v^2}{4} \quad \text{for } A_\mu^1 \text{ and } A_\mu^2 \quad (11.54a)$$

$$m_Z^2 = \frac{g^2 v^2}{4 \cos^2 \theta_w} = \frac{m_W^2}{\cos^2 \theta_w} \quad \text{for } \mathcal{Z}_\mu \quad (11.54b)$$

$$m_A^2 = 0 \quad \text{for } \mathcal{A}_\mu. \quad (11.54c)$$

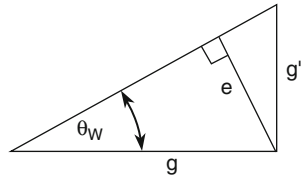
There is one additional massive scalar particle (the multiplicative term in front of the field h^2), the Higgs boson H^0 with mass

$$m_{H^0} = \sqrt{-2\mu^2} = \sqrt{2\lambda}v. \quad (11.55)$$

The gauge fields A_μ^1 and A_μ^2 can be replaced by the complex fields W_μ^+ and W_μ^- respectively defined in (11.26) and (11.27).

- W_μ^- and W_μ^+ are identified as the fields associated with the charged W^- and W^+ bosons;
- \mathcal{Z}_μ is identified as the field associated with the neutral Z^0 boson;
- The massless field \mathcal{A}_μ is identified as the electromagnetic field associated with the photon.

Fig. 11.5 Geometrical illustration of the relations between the electroweak coupling constants e, g, g', θ_w



Let us now consider the coupling constant of the massless field \mathcal{A}_μ . From Eqs. 11.49 and 11.50, one finds $A_\mu^3 = \mathcal{A}_\mu \sin \theta_w + \mathcal{Z}_\mu \cos \theta_w$ and $B_\mu = \mathcal{A}_\mu \cos \theta_w - \mathcal{Z}_\mu \sin \theta_w$. Extracting the terms along the diagonal of (11.28) and expressing them as functions of the fields \mathcal{A}_μ and \mathcal{Z}_μ as formulated above, we can write the following identity as

$$g A_\mu^3 \frac{\sigma_3}{2} + \frac{g'}{2} B_\mu \mathbf{1} = g \sin \theta_w Q \mathcal{A}_\mu + \frac{g}{\cos \theta_w} \left(\frac{\sigma_3}{2} - Q \sin^2 \theta_w \right) \mathcal{Z}_\mu, \quad (11.56)$$

defining $Q \equiv \frac{1+\sigma_3}{2}$. The coupling constant associated to the massless field \mathcal{A}_μ (the electric charge) is then identified to be $g \sin \theta_w$. It follows that

$$\boxed{g \sin \theta_w = e.} \quad (11.57)$$

Figure 11.5 shows a geometrical illustration of the relations between the electroweak coupling constants. The following important relations can therefore be written as

$$\boxed{\tan \theta_w = \frac{g'}{g}, \quad \sin \theta_w = \frac{g'}{\sqrt{g^2 + g'^2}}, \quad \cos \theta_w = \frac{g}{\sqrt{g^2 + g'^2}}, \quad e = \frac{gg'}{\sqrt{g^2 + g'^2}}.} \quad (11.58)$$

There is a deep connection between the coupling constants e, g and g' . The numerical value of the Weinberg angle was determined from: $v e$ scattering; the electroweak interference in $e^+ e^-$ collisions; the precision measurement of the Z^0 ; and the ratio between the masses m_{W^\pm} and m_{Z^0} . The most precise value of $\sin^2 \theta_w$ is obtained from the combination of all these measurements, obtaining $\sin^2 \theta_w = 0.2319 \pm 0.0005$. From (11.54a) and (11.54b), one also has

$$\boxed{m_W = m_Z \cos \theta_w, \quad \sin^2 \theta_w = 1 - \frac{m_W^2}{m_Z^2}.} \quad (11.59)$$

All these equations are valid at the fundamental level (“tree level”). They are substantially modified by the radiative corrections which strongly depend on the top quark mass and logarithmically on the Higgs boson mass.

Using Eqs. 11.8 and 11.54a, one can show that

$$v = (\sqrt{2} G_F)^{-\frac{1}{2}} = 246 \text{ GeV.} \quad (11.60)$$

From Eqs. 11.54a and 11.54b, the masses of the intermediate bosons W^\pm and Z^0 can be calculated using the experimental values of the Fermi coupling constant G_F and $\sin^2 \theta_w$. In 1984, the intermediate bosons W^\pm and Z^0 were discovered by the UA1 and UA2 collaborations and the measured masses agreed upon with the predicted masses. It should be noted that the value of λ in the Higgs potential (11.39) is not predicted and cannot be related to any measurable physics quantity. Therefore, the Higgs boson mass is not predicted in the theory and must be experimentally determined.

Let us now consider the Higgs boson (associated to the field h) couplings to the gauge bosons W^- , W^+ and Z^0 (respectively associated to the fields W_μ^- , W_μ^+ and Z_μ). We proceed as above and introduce the scalar field (11.43) in the gauge invariant Lagrangian density (11.38), collecting the terms $hA_\mu^1 A^{1\mu}$, $hA_\mu^2 A^{2\mu}$, $hZ_\mu Z^\mu$ and $hA_\mu A^\mu$. After some algebra, one obtains

$$\mathcal{L}_{VWH} = \frac{g^2 v}{4} h A_\mu^1 A^{1\mu} + \frac{g^2 v}{4} h A_\mu^2 A^{2\mu} + \frac{g^2 v}{4 \cos^2 \theta_w} h Z_\mu Z^\mu \quad (11.61)$$

where V denotes W and Z . Finally, by introducing in the Lagrangian density \mathcal{L}_{VWH} the complex fields W_μ^- (11.26) and W_μ^+ (11.27), one finds

$$\mathcal{L}_{VWH} = \frac{g^2 v}{2} h W_\mu^- W^{-\mu} + \frac{g^2 v}{2} h W_\mu^+ W^{+\mu} + \frac{g^2 v}{4 \cos^2 \theta_w} h Z_\mu Z^\mu. \quad (11.62)$$

It is important to notice that no term has survived for the Higgs coupling to the massless gauge field A_μ . As a result, that the Higgs boson does not directly couple to the photon. From Eq. 11.62, one can extract the Higgs coupling to the massive gauge bosons W^\pm and Z^0 . Using (11.54a) and (11.54b), one finds

$$g_{WWH} \equiv \frac{g^2 v}{2} = \frac{2 m_W^2}{v} \quad (11.63)$$

$$g_{ZZH} \equiv \frac{g^2 v}{4 \cos^2 \theta_w} = \frac{m_Z^2}{v}. \quad (11.64)$$

The Higgs boson coupling to the heavy vector bosons are proportional to their mass squared.

The gauge theory $SU(2) \times U(1)$ now has to be modified in order to take into account the ($V - A$) nature of the charged current weak interaction, as described in Sect. 8.16, and of the neutral current weak interaction.

11.6 The Weak Neutral Current

The electroweak interaction representation in terms of the symmetry group $SU(2)_L \times U(1)_Y$ requires (Sect. 11.3.1) for $U(1)$ the introduction of the *weak hypercharge* Y_W and for $SU(2)$, the *weak isospin* I ; all members of the same isospin multiplet have the same weak hypercharge, that is,

$$Y_W \equiv 2(Q - I_3) \quad (11.65)$$

(see Table 11.1). We have seen in Sect. 8.16 that the weak charged current is pure $V - A$ and therefore involves only left-handed leptons and correspondingly right-handed antileptons. This is taken into account by assigning, to the two left-handed leptons, the two possible values of the third component of the weak isospin doublet $I = 1/2$:

$$\begin{pmatrix} I_3 = +1/2 \\ I_3 = -1/2 \end{pmatrix} = \begin{pmatrix} \nu_{eL} \\ e_L^- \end{pmatrix} \begin{pmatrix} \nu_{\mu L} \\ \mu_L^- \end{pmatrix} \begin{pmatrix} \nu_{\tau L} \\ \tau_L^- \end{pmatrix}. \quad (11.66)$$

Contrary to the charged current interactions, the neutral currents (Sect. 8.13) also interact with the charged *right-handed* leptons, to which a weak isospin singlet state can therefore be assigned, namely,

$$(I = I_3 = 0) \quad (e_R^-) \quad , \quad (\mu_R^-) \quad , \quad (\tau_R^-). \quad (11.67)$$

The situation is similar for the quarks, provided that one considers the rotated states of the CKM matrix: the left-handed quarks of the same family are grouped into weak isospin doublets:

$$\begin{pmatrix} I_3 = +1/2 \\ I_3 = -1/2 \end{pmatrix} = \begin{pmatrix} u_L \\ d'_L \end{pmatrix} \begin{pmatrix} c_L \\ s'_L \end{pmatrix} \begin{pmatrix} t_L \\ b'_L \end{pmatrix} \quad (11.68)$$

and similarly for the singlet states,

$$(I = I_3 = 0) \quad (d'_R) \, , \, (u_R) \, , \, (s'_R) \, , \, (c_R) \, , \, (b'_R) \, , \, (t_R). \quad (11.69)$$

For antiparticles, the same considerations are valid, though the role of L particles must be exchanged with that of R particles.

A *neutral current* must be described by a bilinear form (similar to Eq. 8.71) where the fermion remains the same (e.g., $e \rightarrow e$, $\nu_e \rightarrow \nu_e$). In the case of a neutral current interaction between quarks, the quarks are assumed to maintain the same color: the Z^0 boson, similar to the W^\pm , does not carry *color charge*. Furthermore, experiments show that neutral currents do not have a $V - A$ space-time structure.

The symmetry group $U(2)_L \times U(1)_Y$ suggests, for the weak neutral current interaction, a Lagrangian density given by the sum of two fields A_μ^3 (with coupling g) and B_μ (with coupling g') defined along the diagonal of (11.28), that is,

$$\mathcal{L}_{NC} = -\bar{f} \gamma^\mu \left(g A_\mu^3 I_3 + \frac{1}{2} g' B_\mu Y \right) f. \quad (11.70)$$

Expressing A_μ^3 and B_μ in terms of \mathcal{A}_μ (defined in (11.50)) and \mathcal{Z}_μ (defined in (11.49)), one finds

$$\mathcal{L}_{NC} = -\bar{f} \gamma^\mu \left[g \sin \theta_w \mathcal{A}_\mu \left(I_3 + \frac{1}{2} Y \right) + \frac{g}{\cos \theta_w} \mathcal{Z}_\mu \left(I_3 - \sin^2 \theta_w \left(I_3 + \frac{1}{2} Y \right) \right) \right] f. \quad (11.71)$$

Table 11.2 Left-handed (C_L) and right-handed (C_R) coupling constants of the Z^0 to neutral and charged leptons, and to quarks

	ν	ℓ	u, c, t	d', s', b'
$C_L = I_3 - Q \sin^2 \theta_w$	$\frac{1}{2}$	$-\frac{1}{2} + \sin^2 \theta_w$	$\frac{1}{2} - \frac{2}{3} \sin^2 \theta_w$	$-\frac{1}{2} + \frac{1}{3} \sin^2 \theta_w$
$C_R = -Q \sin^2 \theta_w$	0	$+\sin^2 \theta_w$	$-\frac{2}{3} \sin^2 \theta_w$	$+\frac{1}{3} \sin^2 \theta_w$

The Lagrangian density is summed over all fermions and the states f can be a weak isospin doublet L or a singlet R . The electric charge is defined as $Q = I_3 + \frac{Y}{2}$ and using the projection properties (already used in Sect. 8.16), one can show that

$$\overline{f}_L \gamma^\mu f_L = \frac{1}{2} \bar{f} \gamma^\mu (1 - \gamma^5) f \quad (11.72a)$$

$$\overline{f}_R \gamma^\mu f_R = \frac{1}{2} \bar{f} \gamma^\mu (1 + \gamma^5) f \quad (11.72b)$$

where f_L e f_R are generic wave functions for left-handed and right-handed fermions.

Using these equations and the total Lagrangian density (11.71) for the neutral current interaction, the Lagrangian densities for the \mathcal{A}_μ and \mathcal{Z}_μ fields can separately be written as

$$\mathcal{L}_{NC}^{\mathcal{A}_\mu} = -e Q \mathcal{A}_\mu \bar{f} \gamma^\mu \left[\left(\frac{1 - \gamma^5}{2} \right) + \left(\frac{1 + \gamma^5}{2} \right) \right] f = -e Q \mathcal{A}_\mu \bar{f} \gamma^\mu f \quad (11.73)$$

$$\mathcal{L}_{NC}^{\mathcal{Z}_\mu} = -\frac{g}{2 \cos \theta_w} \mathcal{Z}_\mu \bar{f} \gamma^\mu \left[(I_3 - Q \sin^2 \theta_w)(1 - \gamma^5) - Q \sin^2 \theta_w (1 + \gamma^5) \right] f. \quad (11.74)$$

Note that the Lagrangian density (11.73) exactly corresponds to the electromagnetic one.

From (11.74), it can be observed that the effective neutral current weak interaction is not a pure $V - A$ interaction, but a superposition of $V - A$ and $V + A$ interactions. The left and right-handed coupling constants of the intermediate boson Z^0 to fermions are derived from (11.74)

$$C_L = I_3 - Q \sin^2 \theta_w \quad (11.75a)$$

$$C_R = -Q \sin^2 \theta_w. \quad (11.75b)$$

Explicitly, the left and right-handed coupling of the Z^0 to neutrinos, charged leptons, u and d' -type quarks is shown in Table 11.2.

Table 11.3 Axial and vector coupling constants calculated using $\sin^2 \theta_w = 0.232$. The last column shows $N_C^f (a_f^2 + v_f^2)$, the sum of the constants squared multiplied by the color factor $N_C^f = 3$ (for quarks) and 1 (for leptons) as in (9.19)

Fermion	a_f	v_f	$N_C^f (a_f^2 + v_f^2)$
e, μ, τ	$-\frac{1}{2}$	-0.040	0.252
ν_e, ν_μ, ν_τ	$+\frac{1}{2}$	$+\frac{1}{2}$	0.5
u, c, t	$+\frac{1}{2}$	0.193	0.861
d', s', b'	$-\frac{1}{2}$	-0.347	1.110

It is often convenient to specify these constants in terms of their so-called axial and vector components defined as

$$a_f \equiv C_L - C_R = I_3 \quad (11.76a)$$

$$v_f \equiv C_L + C_R = I_3 - 2Q_f \sin^2 \theta_w \quad (11.76b)$$

where Q_f is the electric charge Q of the fermion f . Table 11.3 provides the values of the axial and vector coupling constants using $\sin^2 \theta_w = 0.232$. The last column shows the quantity $N_C^f (a_f^2 + v_f^2)$ which is used to calculate the Z^0 partial decay widths listed in Table 9.4. These are obtained by multiplying by the constant $\frac{G_F m_Z^3}{6\sqrt{2}\pi} = 330 \text{ MeV}$.

Finally, the Lagrangian density (11.74) can be written in a more compact form using a_f e v_f :

$$\mathcal{L}_{NC}^{\mathcal{Z}_\mu} = -\frac{g}{2 \cos \theta_w} \mathcal{Z}_\mu \bar{f} \gamma^\mu (v_f - a_f \gamma^5) f. \quad (11.77)$$

11.7 The Fermion Masses

Fermions (leptons and quarks) are introduced in the theory with a mass equal to zero. The theory needs to be completed in order to confer a nonzero mass to fermions. As previously mentioned, the Higgs field solves the mass generation problem, namely, nonvanishing masses for the fermions are generated through the couplings of the Higgs field to the fermions. The Standard Model is thus completed by the introduction of the Yukawa Lagrangian density

$$\mathcal{L}_{\varphi-f_i} = -g_{si} \varphi \overline{\psi}_i \psi_i. \quad (11.78)$$

The index i stands for all types of fermions. The coupling constants are arbitrary and are chosen in a way to reproduce the known physical masses of the fermions.

If the Higgs field is expanded according to (11.43), we obtain symbolically for each fermion type i

$$\mathcal{L}_{\varphi-f_i} = -g_{si} \frac{v}{\sqrt{2}} \bar{\psi}_i \psi_i - g_{si} \frac{h}{\sqrt{2}} \bar{\psi}_i \psi_i. \quad (11.79)$$

The first term is the mass term for the corresponding fermion i . Thus, its mass is written as

$$m_{f_i} = g_{si} \frac{v}{\sqrt{2}} \rightarrow \frac{g_{si}}{\sqrt{2}} = \frac{m_{f_i}}{v}. \quad (11.80)$$

The second term expresses the coupling between the fermion fields and the Higgs field. The coupling is equal to $\frac{g_{si}}{\sqrt{2}}$ and from Eq. 11.80, one sees that **the coupling constants are proportional to fermion masses**. One can therefore conclude that the Higgs field would couple preferably to the heaviest fermion kinematically available. The decay rate in a given $f\bar{f}$ pair is proportional to the mass squared of the given fermion.

11.8 Parameters of the Electroweak Interaction

Quantum electrodynamics requires only one quantity which is determined experimentally as input, that is, the fundamental electric charge e , or a quantity associated with it, such as, the coupling constant α at zero energy (the fine structure constant): $\alpha = e^2/4\pi = 1/137.0359895(6)$. Note that the experimental uncertainty applies to the eighth decimal place.

The electroweak interaction theory requires three experimental parameters as input. Their choice is arbitrary and in the literature, different sets can be found, namely, (1) g, g', v ; (2) e, G_F, θ_w ; (3) e, G_F, m_Z ; (4) e, m_W, m_Z .

1. The first choice includes the isovector coupling constant g , the scalar coupling constant g' and the Higgs vacuum expectation value v . The two parameters, g and g' , are associated with the electroweak interaction invariance under two transformations: g is related to the weak isospin symmetry and g' is connected to the weak hypercharge symmetry. These quantities are very important from the theoretical point of view, but “far” from measurable quantities.
2. The second set contains the electric charge e , the Fermi weak interaction constant G_F and the Weinberg angle θ_w .
3. The third set uses e, G_F and the Z^0 mass.
4. The fourth choice is (e, m_Z, m_W) .

The last two correspond to the currently favorite choices. At the basic level (*tree level*), many relations between the above listed quantities are valid. From Eqs. 11.54a, 11.54b, 11.57 and 11.60, one finds

$$m_{W^\pm}^2 = \frac{\pi\alpha}{\sqrt{2}G_F \sin^2 \theta_w} \quad (11.81)$$

$$m_{Z^0}^2 = \frac{m_W^2}{\cos^2 \theta_w} = \frac{\pi \alpha}{\sqrt{2} G_F \sin^2 \theta_w \cos^2 \theta_w}. \quad (11.82)$$

Various relations, previously seen, are also valid, that is,

$$\sin^2 \theta_w = 1 - \frac{m_W^2}{m_Z^2} = \frac{\pi \alpha}{\sqrt{2} G_F m_W^2} = \frac{e^2}{g^2} = 1 - \frac{e^2}{g'^2} = \frac{g'^2}{g^2 + g'^2}. \quad (11.83)$$

The relations $e = g \sin \theta_w = g' \cos \theta_w$ are often called the *unification relations*. They suggest that the W^\pm and Z^0 couplings are the same as the electromagnetic one; the difference between weak and electromagnetic interactions is associated to the high masses of W^\pm and Z^0 bosons with respect to the massless γ .

The radiative corrections and the renormalization of the theory modify the relations obtained at the tree level; the simple formulation of (11.83) is no longer valid and must be modified with the introduction of a term Δr . As the coupling constants vary with energy, it is necessary to choose an appropriate *renormalization scheme* and to consider the *radiative corrections*. For the renormalization, one may choose the fundamental constants, being considerate of the energy scale at which the numerical values are measured. The electric charge, or the constant α , are measured at zero energy: $e(0)$ or $\alpha(0)$. At high energies, the values change because $\alpha = \alpha(Q^2)$ due to the vacuum polarization ($\alpha(m_Z) \simeq 1/128$), see Sect. 11.9.4.

The masses of the W^\pm and Z^0 bosons may be chosen to be equal to the experimentally measured masses. It is then possible to define $\sin^2 \theta_w = 1 - m_W^2/m_Z^2 = \text{constant}$ independent of the energy. For example, one can obtain:

$$G_F = \frac{\pi \alpha}{\sqrt{2} m_W^2} \frac{m_Z^2}{m_Z^2 - m_W^2} \frac{1}{1 - \Delta r} \quad (11.84)$$

where the first part is the formula at the tree level. The addition of the radiative corrections, incorporated within the term $(1 - \Delta r)^{-1}$, allows one to rewrite the formula (11.84) at the experimental level. Other different parameter choices are possible. For instance, one has

$$\sin^2 \theta_w = \frac{\pi \alpha}{\sqrt{2} G_F m_W^2 (1 - \Delta r)} \quad (11.85)$$

$$\sin^2 \theta_w \cos^2 \theta_w = \frac{\pi \alpha}{\sqrt{2} G_F m_Z^2 (1 - \Delta r)}. \quad (11.86)$$

The main contribution to Δr comes from two different sources, namely, the $\Delta \alpha$ correction and the $\Delta \rho$ correction. The $\Delta \alpha$ correction is due to a fermion loop in the photon propagator (see Fig. 11.6b) where the sum of all fermion pairs with a mass

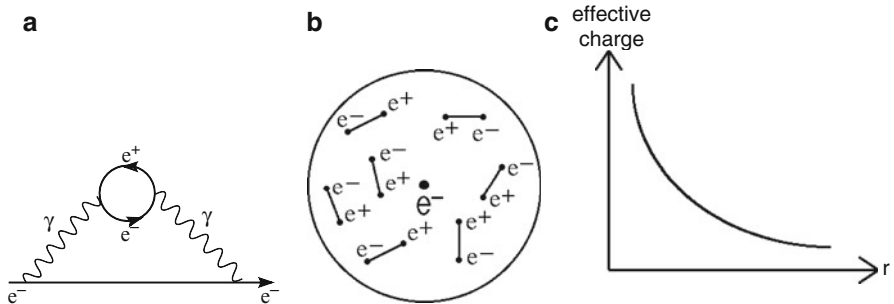


Fig. 11.6 (a) Simple Feynman diagram describing the production of virtual e^+e^- pairs around a free electron. (b) Illustration of the cloud of virtual e^+e^- charges around a free electron. (c) Electron effective charge as a function of the distance to its center. The measurement corresponds to the asymptotic value at large r

below m_Z are included. The $\Delta\rho$ correction describes the radiative corrections due to the top quark and the Higgs boson in the Z propagator.

11.8.1 Electric Charge Screening in QED

An isolated electric charge, for example, an electron placed in vacuum, can irradiate virtual photons which can give rise to virtual e^+e^- pairs. One can then think that the electric charge is surrounded by a cloud (or sea) of these pairs. Because of the electrostatic attraction, the virtual positrons tend to be closer to the electron than to the virtual electrons. The simplest Feynman diagram describing the production of virtual e^+e^- pairs around a free electron is shown in Fig. 11.6a; the resulting situation is schematized in Fig. 11.6b. If we measure the electron charge, for example, through a collision with another charged particle, the result depends on how deep the charged particle enters the cloud, i.e., it depends on r and thus on the four-momentum transfer Q^2 . For small distances (corresponding to high Q^2), a high electron charge is observed; for large distances (low Q^2), one observes a smaller charge (see Fig. 11.6c). In the high Q^2 limit, the electron charge tends to infinity. A finite value is algebraically obtained by an appropriate renormalization of the electron charge defined at an arbitrary scale $Q^2 = \mu^2$. The electric charge, and the electromagnetic coupling constant α , are not constant, but vary with Q^2 following the relation

$$\alpha(Q^2) = \frac{\alpha(\mu^2)}{1 - \frac{\alpha(\mu^2)}{3\pi} \ln\left(\frac{Q^2}{\mu^2}\right)}. \quad (11.87)$$

The numerical values found are $\alpha(m_e) \simeq 1/137$ and $\alpha(m_Z) \simeq 1/128$.

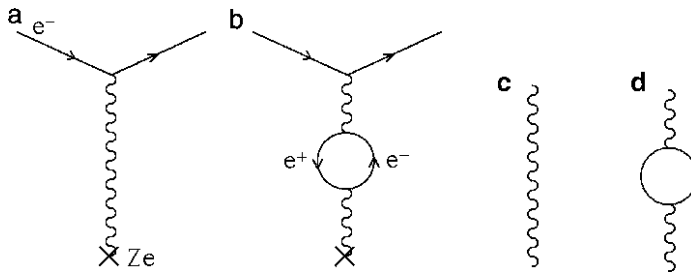


Fig. 11.7 Rutherford scattering (a) at the lowest order and (b) at the next order. The variation corresponds to the change of the photon propagator from (c) to (d)

$$\begin{array}{c}
 \text{Diagram c} \\
 = \\
 \text{Diagram d} \\
 = \\
 \left[1 - \frac{1}{e_0} + \left(\frac{1}{e_0} \right)^2 - \dots \right]
 \end{array}$$

Fig. 11.8 Elastic scattering involving the “effective charge” $e(Q^2)$, expressed in terms involving the “bare charge” e_0 and correction terms

11.8.2 Higher Order Feynman Diagrams, Mathematical Infinities and Renormalization in QED

Figure 11.7a shows the lowest order Feynman diagram for the Rutherford scattering between an electron and a nucleus with charge Ze . The next order diagram, shown in Fig. 11.7b, contains an (e^+e^-) “fermion loop.” This loop modifies the photon propagator of Fig. 11.7c into the propagator of Fig. 11.7d (*vacuum polarization*). Including higher orders, this change in the photon propagator produces a divergence for high Q^2 . This divergence can be eliminated by an appropriate *charge renormalization*, as shown in Fig. 11.8: e_0 is the *bare charge*, $e(Q^2)$ is the electric charge observed at a given Q^2 . This discussion explains the measured value of the *Lamb shift* and the *gyromagnetic ratio* of the electron and muon.

In addition to the photon propagator, the lowest order diagram of the electromagnetic vertex, shown in Fig. 11.9a, is modified at higher orders, as shown at the next order in Fig. 11.9b, c and d. It can be shown that the ∞ due to the vertex shown in Fig. 11.9b is precisely compensated by the sum of diagrams 11.9c and d. This cancellation occurs at all orders of the perturbation theory and is called *the Ward identity*.

Another way of looking at this problem is illustrated in Fig. 11.10: if we were to observe an electromagnetic vertex with increasing spatial resolution, i.e., with higher and higher momentum transfers Q^2 , the characteristics shown in the second and third diagrams would be observed. The experimental measurement is the

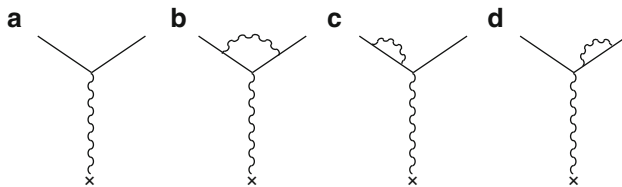


Fig. 11.9 Changes to the electromagnetic vertex (a) at the lowest order and (b), (c), (d) at the next order

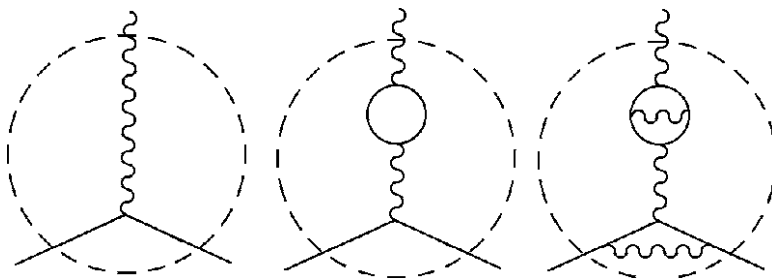


Fig. 11.10 Proceeding from left to right: “observation” of the QED vertex with microscopes of better and better spatial resolution, i.e., for higher and higher Q^2

combination of these diagrams. The coupling at the vertex of the first diagram is therefore modified by the following two diagrams.

11.9 The Strong Interaction

11.9.1 Quantum Chromodynamics (QCD)

In the static quark model of hadrons, quarks were introduced in order to explain the hadron spectrum; the three colors were then introduced to build an antisymmetric wave function for baryons made of three quarks of the same flavor (e.g., $\Delta^{++} = uuu$). The hypothesis was confirmed by the study of the ratio $R = [\sigma(e^+e^- \rightarrow \text{hadrons})/\sigma(e^+e^- \rightarrow \mu^+\mu^-)]$. Quarks should be introduced in three different colors in order to explain the experimental value of R (see Sect. 9.3).

One can therefore conclude that, both statically and dynamically, quarks must have different colors (*red, green, blue; r, g, b*) and a fractional electric charge. Antiquarks appear in three anticolors.

In the study of inelastic lepton-nucleon collisions, it has been observed (Sect. 10.4) that only half of the nucleon momentum is due to quarks (valence and sea quarks); the other half is transported by point-like objects with no electric charge

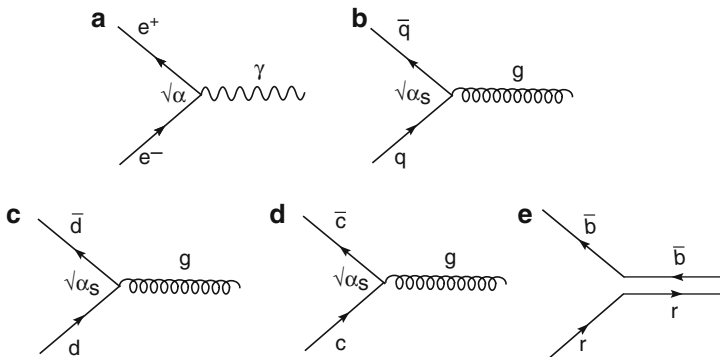


Fig. 11.11 (a) Electromagnetic vertex eey : the probability amplitude for a photon emission is proportional to $\sqrt{\alpha}$. (b) QCD vertex qqg ; q is the colored quark and g is a gluon, mediator of the color force; the probability amplitude for the emission of a gluon is proportional to $\sqrt{\alpha_s}$ which is the same for all quarks of a different flavor, as shown in (c) and (d). (e) Illustrates the vertices (c) and (d) in terms of lines of color

and which do not interact via electromagnetic interaction, nor via weak interaction. These objects are the *gluons*.

In quantum chromodynamics (QCD), it is hypothesized that the *color* is equivalent to the electric charge in QED; therefore, the interaction takes place between two colored quarks by exchanging a bi-colored gluon. In QCD, the quark-antiquark-gluon vertex (qqg), shown in Fig. 11.11b, has the same structure as the QED vertex eey , shown in Fig. 11.11a. The probability amplitude of the electromagnetic eey vertex is proportional to $\sqrt{\alpha}$, while that of the QCD vertex is proportional to $\sqrt{\alpha_s}$. Note that the strong coupling constant is the same for all quarks of a different flavor. It is therefore independent of the quark “flavor” (see Fig. 11.11b, c, d). The interpretation of a qqg vertex in terms of lines of color is shown in Fig. 11.11e.

It is assumed that the interaction between two quarks is mediated by the exchange of a massless gluon of spin 1. It is also hypothesized that the interaction between two quarks is invariant under the exchange of color. This implies that the three quarks of different colors are described by the symmetry group $SU(3)_C$. Note that the classifications in multiplets (octets, decuplets) in the static quark model of hadrons (Sect. 7.7) is based on the quark flavor and the approximate symmetry, $SU(3)_{flavor}$. The quark symmetry $SU(3)_C$ is considered to be exact.

The bosons that mediate the strong interaction between quarks, the gluons, must necessarily have a color and an anticolor charge in order to explain the neutrality of hadrons. There are three colors and three anticolors. Therefore, each gluon has a *color* (r, b, g) and an *anticolor* ($\bar{r}, \bar{b}, \bar{g}$), that is,

$$r\bar{b}, r\bar{g}, b\bar{g}, b\bar{r}, g\bar{r}, g\bar{b}, (r\bar{r} - g\bar{g})\sqrt{2}, (r\bar{r} + g\bar{g} - 2b\bar{b})/\sqrt{6}. \quad (11.88)$$

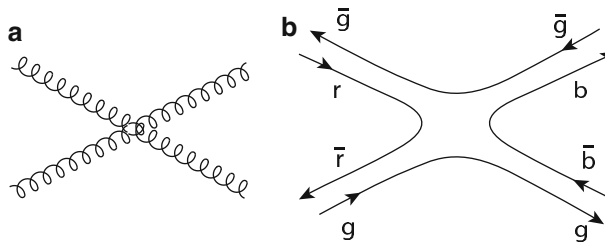


Fig. 11.12 (a) Vertex $gggg$ and (b) illustration in terms of lines of color

With three colors and three anticolors, one can form a color octet plus a color singlet. The color singlet

$$\frac{r\bar{r} + g\bar{g} + b\bar{b}}{\sqrt{3}} \quad (11.89)$$

does not carry color and cannot mediate an interaction between color charges. This interaction can only be mediated by the remaining 8 gluons of the octet.

As previously said, the color charge for the strong interaction is the analogue of the electric charge for the electromagnetic interaction. Both forces are mediated by massless vector bosons (photon or gluons); however, for the electromagnetic interaction, there are 2×1 charge types (positive and negative) and one *neutral* mediator boson (the photon), and in QCD, there are 2×3 charge types (three colors and three anticolors) and 8 *colored* mediator bosons (with color and anticolor). These considerations lead to significant differences between QCD and QED.

A fundamental difference between QED and QCD is due to the fact that gluons carry color and anticolor charges: they can thus interact with each other. In addition to the vertex $q\bar{q}g$, there is a vertex ggg as shown in Fig. 5.3. The vertex $gggg$ (see Fig. 11.12a, b) is also foreseen. These vertices make QCD richer than QED and allow for the possibility of hadronic states formed only by gluons (the *glueballs*) and of hybrid states such as $q\bar{q}g$. However, they also make QCD mathematically more complex. Note that in QED, “photon-photon” interactions are not directly possible, but only through pairs of electric charges, as shown, for example, in the diagram of Fig. 11.13.

In addition to cases similar to QED (e.g., the repulsive force between two quarks of the same color and the attractive force between quarks with color and anticolor), in QCD, different colors may give rise to an attractive force if the quantum state is antisymmetric, and a repulsive force if it is symmetric under the interchange of quarks. This means that the favorite state of three quarks is the state with three quarks of different colors, $q_r q_b q_g$, that is, the colorless state of baryons.

At small distances (corresponding to large momentum transfers, i.e., at high Q^2), α_s is small enough to allow perturbative methods of calculation in analogy with QED. However, at large distances (low Q^2), one has $\alpha_s \sim 1$ and perturbative methods (and first order Feynman diagrams) can no longer be used to make calculations. The hadron masses and most of the hadronic processes at low Q^2 cannot be simply derived from QCD.

Fig. 11.13 $\gamma\gamma$ interaction through a charged fermion box

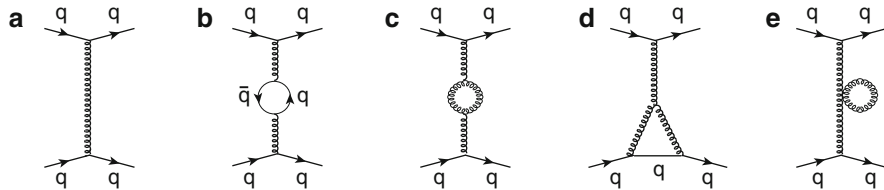
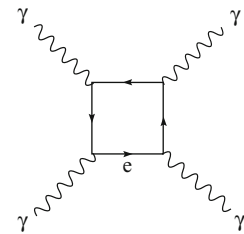
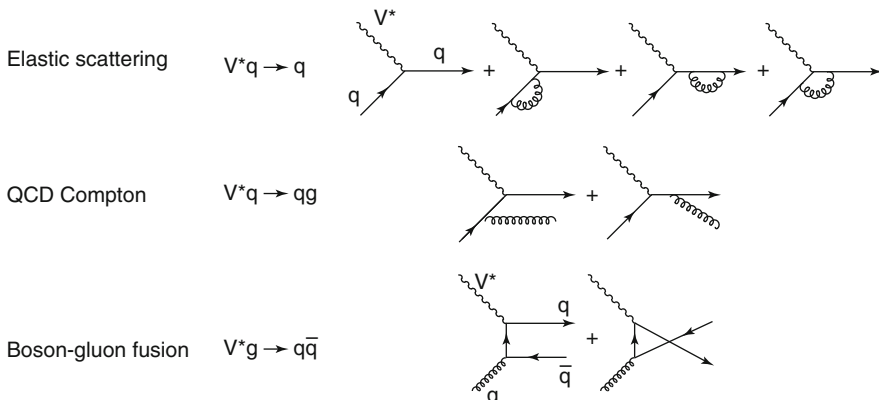


Fig. 11.14 Modifications to the simplest gluon propagator (a). In (b), one has a fermion loop ($q\bar{q}$) as in QED. In (c), (d), and (e), the boson contributions not present in QED are shown

11.9.2 Color Charge Screening in QCD

In QCD, the color charge screening is similar to that of an electric charge in QED. However, besides fermionic loops, there are also bosonic loops producing an “antiscreening” which dominates the situation (see Fig. 11.14).

It follows that α_S is a “running coupling constant” [11W04]. At the lowest order of perturbative QCD (i.e., first order in α_S), the structure functions receive contributions from the following elementary processes (V^* is a virtual boson, γ, Z^0, W^\pm):



Several parameterizations of α_S as a function of Q^2 are possible, but all depend on a free parameter to be determined experimentally since it cannot be predicted by

the theory (as the mass and electric charge of the electron in QED). In the version in which the free parameter (dimensionally, an energy in the natural unit system) is called Λ_{QCD} , one has

$$\alpha_S(Q^2) = \frac{12\pi}{(11N_c - 2N_f) \ln \left(\frac{Q^2}{\Lambda_{QCD}^2} \right)} \quad (11.90)$$

with $N_c = \text{number of colors} = 3$ and $N_f = \text{number of kinematically accessible flavors}$ (for example, $N_f = 5$ at $Q^2 = m_Z^2$ since the *top* quark mass is larger than the Z^0 boson mass). From measurements (see Sect. 11.9.4), it results that $\Lambda_{QCD} \simeq 200 \text{ MeV}$ and α_S decreases with increasing Q^2 . While it has a value ~ 10 (1) for energies of the order of 100 (1,000) MeV, one has $\alpha_S(m_\tau) \simeq 0.36$, $\alpha_S(m_Z) \simeq 0.12$ (Fig. 11.15). In the limit $Q^2 \rightarrow \infty$, one has $\alpha_S \rightarrow 0$, that is, the so-called *asymptotic freedom* which consists of a fundamental proof regarding the non-abelian nature of QCD (due to the interaction terms between gluons).

The increase in effective color charge with the separation distance between quarks can be considered as an effect due to the vacuum. It could be the cause of the *confinement* of quarks and gluons in hadrons. For $r \geq 10^{-13} \text{ cm}$, the attractive force between two quarks is large and roughly constant with r (a situation similar to that in electromagnetism between the two plates of a capacitor). This is called *infrared slavery*.

Due to the antiscreening effect, the vacuum around an isolated color charge is unstable. This may result in the hadronization phenomenon, i.e., the transformation of quarks in hadrons. However, the confinement is still not understood at the fundamental level and the existence of free quarks is not fully excluded. Note that in conditions of high energy and high density, the deconfinement phase with the formation of a *quark-gluon plasma* should take place.

11.9.3 Color Factors

In QED, the electromagnetic coupling “force” between two quarks of electric charge e_1, e_2 is equal to $e_1 e_2 \alpha$ ($e_1, e_2 = +2/3$ or $-1/3$). Similarly, in QCD, the strong coupling “force” between two color charges via the exchange of a gluon is $\frac{1}{2}|c_1 c_2| \alpha_S = C_F \alpha_S$, where C_F is the so-called *color factor*.

The color factor for the interaction between two blue quarks can be calculated as follows, see (11.88): only gluons that contain the color term $b\bar{b}$, i.e., only $(r\bar{r} + g\bar{g} - 2b\bar{b})\sqrt{6}$, have to be taken into consideration. In this case, one has $c_1 c_2 = \left(-\frac{2}{\sqrt{6}}\right) \left(-\frac{2}{\sqrt{6}}\right) = \frac{4}{6} = \frac{2}{3}$. Therefore, the color factor is $C_F = \frac{1}{2}|c_1 c_2| = \frac{1}{2} \cdot \frac{2}{3} = \frac{1}{3}$. By analyzing all other possibilities, it is found that for two quarks of the same color (or of different color), $c_1 c_2 = P - \frac{1}{3}$, with $P = \pm 1$ depending on whether the two quarks are in a symmetric or antisymmetric color state.

In a baryon, the interaction between each quark pair concerns antisymmetric states because it is necessary to have an antisymmetric final state. Therefore, for each pair, one has $c_1 c_2 = -\frac{4}{3}$ and thus $C_F = \frac{2}{3}$.

For a $b\bar{b}$ meson changing into $r\bar{r}$ or $g\bar{g}$, the color factor is $C_F = \frac{1}{2}$. For a meson which exchanges a gluon in a singlet state, the color factor is instead $C_F = \frac{4}{3}$. In conclusion, the general rule is

$$\begin{cases} \text{for } q\bar{q}: \alpha_S \text{ is replaced by } \frac{4}{3}\alpha_S \\ \text{for } qqq: \alpha_S \text{ is replaced by } \frac{2}{3}\alpha_S. \end{cases}$$

11.9.4 The Strong Coupling Constant α_S

The strong coupling constant, α_S , as the fine structure constant and the universal Fermi constant, is a free parameter of the theoretical model and must be experimentally determined. QCD predicts a well-defined dependence of α_S on the energy scale Q of the interaction, and makes predictions about various phenomena that allow one to determine its value. Experimental methods which measure α_S and verify the QCD predictions are (the value of Q corresponding to the process is also indicated):

- Hadronic decays of the τ lepton: $\tau \rightarrow \nu_\tau + \text{hadrons}$ ($Q = 1.77 \text{ GeV}$)
- Evolution of the nucleon structure functions measured in inelastic scattering of e, μ, ν on nucleons ($Q = 2 \div 50 \text{ GeV}$)
- Jet production in the inelastic scattering $ep \rightarrow eX$ ($Q = 2 \div 50 \text{ GeV}$)
- Analyses of the energy levels of bound states $q\bar{q}$ (quarkonium) ($Q = 1.5 \div 5 \text{ GeV}$)
- Decays of the vector mesons Υ ($Q = 5 \text{ GeV}$)
- Hadronic cross-section of the annihilation $e^+e^- \rightarrow \text{hadrons}$ ($Q = 10 \div 200 \text{ GeV}$)
- Fragmentation function of jets produced in $e^+e^- \rightarrow \text{hadrons}$ ($Q = 10 \div 200 \text{ GeV}$)
- Hadronic decays of the Z^0 boson ($Q = 91 \text{ GeV}$)
- Jet production in $pp, p\bar{p}$ interactions ($Q = 50 \div 300 \text{ GeV}$)
- Photon production in $pp, p\bar{p}$ interactions ($Q = 30 \div 150 \text{ GeV}$)

The results for some of these processes are illustrated in Fig. 11.15, which shows that the “constant” α_S decreases with increasing of the energy scale Q .

11.10 The Standard Model: A Summary

Let us summarize the main points of the Standard Model (SM) of the microcosm. It includes the electroweak interaction described by the symmetry group $[\text{SU}(2)_L \times \text{SU}(1)_Y]$ and the strong interaction described by the symmetry group $\text{SU}(3)_C$.

Fig. 11.15 Strong coupling “constant” α_s as a function of the centre-of-mass energy. The line shows a fit to the experimental data [P08]

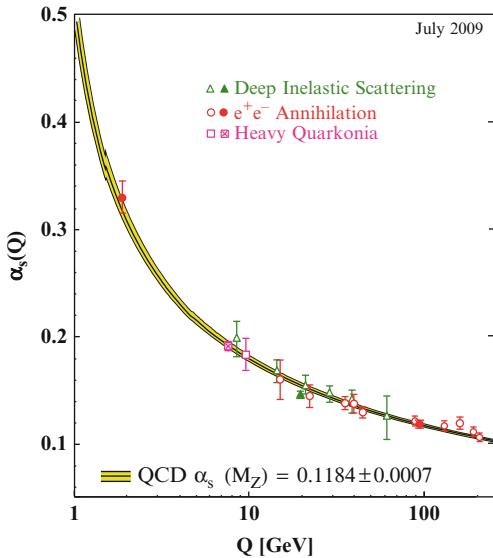


Table 11.4 Couplings in the Standard Model

Vertex	Coupling proportional to:
$\gamma f \bar{f}$	$e \gamma^\mu Q_f$
$Z f \bar{f}$	$\frac{e}{2 \cos \theta_w \sin \theta_w} \gamma^\mu (v_f - a_f \gamma^5)$
$H f \bar{f}$	m_f/v
$H Z^0 Z^0$	m_Z^2/v
$H W^+ W^-$	$2m_W^2/v$

The couplings of the vector boson Z^0 to fermions and the couplings of the scalar Higgs boson H^0 to the W^\pm and Z^0 vector bosons are listed in Table 11.4. Electroweak and strong interactions have a similar structure and are mediated via the vector bosons shown in Table 11.5. The strong interaction mediators, the gluons, carry a color charge and an anticolor charge and can interact between them, giving rise to the ggg and $gggg$ vertices. The mediator of the weak interaction, the vector bosons Z^0 and W^\pm , carry a weak charge and can also interact between themselves (vertex $Z^0 W^+ W^-$). The gravitational interaction is not included in the SM.

The electromagnetic and weak interactions are interpreted as two different aspects of a unified theory describing the electroweak interaction. The electromagnetic and weak charges are related via the Weinberg angle.

The range of the electromagnetic interaction is infinite because the photon is massless. The range of the weak interaction at low energies is about 10^{-3} fm = 10^{-16} cm because of the large mass of the mediator bosons W^\pm, Z^0 . The mediators of the strong interaction, the gluons, are also massless. However, the range of the strong force is limited to about 1 fm because of the strong interaction between

Table 11.5 The three fundamental interactions of the SM of the microcosm have couplings through different charge types and are mediated by vector bosons ($J = 1$) which are massless or have a mass around 100 GeV; the parity P is conserved in two of the three interactions

Interaction	Coupling with	Exchanged bosons	Mass (GeV/c ²)	J^P
EM	Electric charge	Photon (γ)	0	1 ⁻
Weak	Weak charge	W^\pm, Z^0	$\sim 10^2$	1
Strong	Color charge	8 gluons (g)	0	1 ⁻

Table 11.6 In the SM, the fundamental fermions are leptons and quarks with spin 1/2; they are grouped into three “families” (three “generations”). Quarks have a fractional electric charge and red, blue or yellow color charge. There are no right-handed neutrinos. The right-handed quarks and charged leptons have $I_W = 0$

Fermions	Family			Electric charge	Color	Weak isospin		Spin
	1	2	3			Left-handed	Right-handed	
Leptons	v_e	v_μ	v_τ	0	—	1/2	—	1/2
	e	μ	τ	-1	—	1/2	0	1/2
Quarks	u	c	t	+2/3	r, b, g	1/2	0	1/2
	d	s	b	-1/3	r, b, g	1/2	0	1/2

gluons. This interaction is responsible for the confinement of quarks and gluons in hadrons, and for the nonexistence of free quarks and gluons.

The fundamental fermions are the quarks and leptons, as shown in Table 11.1. They have spin 1/2 and are grouped in three *families* (*generations*), as illustrated in Table 11.6. Remember that each fermion has a corresponding antifermion as mentioned in the introduction of this chapter. On the basis of the precision measurements of the Z^0 width, one can conclude that there are only three families of massless (or light) neutrinos. The strong isospin is only important for the strong interaction; for the strong isospin, the six different quark flavors form a doublet ($I = 1/2$, quarks u, d) and four singlets ($I = 0$, quarks s, c, b, t).

The Standard Model has received strong experimental confirmation. However, an essential element of the SM, the Higgs boson (H^0), has not yet been observed. The search is now started at the LHC, see Sect. 10.10. Precision measurements in e^+e^- collisions at $\sqrt{s} \sim m_Z$ constrain the H^0 mass to a relatively low value. There are many unanswered questions surrounding the Standard Model: (1) There is a large number of free parameters (about 18, depending on how they are counted; they are the fundamental fermion and boson masses, the coupling constants g, g', α_S , the coefficients of the CKM matrix; these parameters are not given in the SM and must be measured experimentally). (2) Why are there exactly three families of fermions? (3) How can the neutrino masses be introduced? (4) Does the Higgs boson *really* exist? (5) In vacuum, the Higgs field acquires a nonzero value (11.60) that permeates the whole space. Does it affect the energy density of the universe?

Chapter 12

CP-Violation and Particle Oscillations

12.1 The Matter-Antimatter Asymmetry Problem

The CP transformation combines the charge conjugation C and parity P operators (Sect. 6.8). Under CP , a left-handed electron (e_L^-) becomes a right-handed positron (e_R^+). If CP is an exact symmetry, the laws of nature would be completely identical for matter and antimatter. Most of the observed phenomena are symmetric with respect to C and P , and consequently symmetric to CP . Exceptions are the weak interactions (WI), which violate C and P *maximally*. This means that a W boson couples with a left-handed electron e_L^- , but not with the particle P -conjugated (e_R^-) or C -conjugated (e_L^+). However, the same boson couples with the CP -conjugated particle, the e_R^+ . This seems to suggest that the weak interaction preserves CP . On the contrary, it has been known for many years that the CP symmetry is violated in some rare processes, as found for neutral K in 1964. In particular, the K_L^0 meson decays more often in the $\pi^- e^+ \bar{\nu}_e$ channel than in the $\pi^+ e^- \nu_e$, with a very small asymmetry of about 0.3%. Recently, a similar effect was found for beauty mesons with a larger asymmetry.

Closely linked to CP is the time reversal transformation T : the CPT transformation is a fundamental symmetry of physical laws. The violation of symmetry T is also observed in the decay of neutral K . Within the Standard Model (Chap. 11), the CP symmetry violation is introduced through complex phases. In particular, a simple phase factor appears in the 3×3 CKM (Sect. 8.14.3) unitary matrix that describes the transformation of an *up*-type quark into a *down*-type quark by the exchange of a W vector boson.

In 1967, Sakharov realized that the CP -violation is a necessary condition for *baryogenesis* (Sect. 13.6), i.e., the dynamic process generating matter-antimatter asymmetry in the Universe. **The Universe seems to be made of matter, with almost no antimatter.** This implies a particle-antiparticle asymmetry and suggests that CP could not be a symmetry of all fundamental interactions. Despite

the phenomenological success of the mechanism that describes the CP -violation in the Standard Model, there are probably additional, still unknown, sources of CP -violation that explain the matter-antimatter asymmetry in the Universe.

The recent discovery that neutrinos have small mass seems to imply that there is a source of CP -violation in the leptonic sector in addition to the hadronic one. The studies of neutrino oscillations could provide information on *leptogenesis*. The search for new processes that would violate the CP symmetry is currently one of the most important experimental efforts in particle physics. These studies involve the decay of mesons, the measurement of the electric dipole moment of neutrons, electrons and nuclei, and neutrino oscillations.

In Sects. 12.2 and 12.3, we will first describe the $K^0 - \bar{K}^0$ system followed by the similar $B^0 - \bar{B}^0$ system (Sect. 12.5). Neutrino oscillations, namely, the possible transformation of a neutrino of one type into another type (for example, $\nu_\mu \rightarrow \nu_\tau$), simultaneously violating two leptonic numbers, will be described in Sect. 12.6. While $K^0 - \bar{K}^0$ and $B^0 - \bar{B}^0$ mixings are included in the Standard Model, the neutrino mixings require theories with massive neutrinos that enlarge the Standard Model in some way.

12.2 The $K^0 - \bar{K}^0$ System

The K^0 and \bar{K}^0 mesons are part of the meson nonet $J^P = 0^-$ and are strangeness eigenstates. An important property of the two neutral mesons is that they have different production energy thresholds. The K^0 meson can be produced in association with the Λ^0 hyperon in the strong interaction reaction

$$\pi^- p \rightarrow \Lambda^0 K^0. \quad (12.1)$$

The threshold energy of this reaction is 0.91 GeV in the c.m. The \bar{K}^0 meson can only be produced at higher energies by (for example) the strong interaction reaction

$$\pi^+ p \rightarrow \bar{K}^0 K^+ p \quad (12.2)$$

which has an energy threshold of 1.5 GeV in the c.m. Even higher energies are needed to produce a \bar{K}^0 in combination with an antihyperon. K^0 and \bar{K}^0 are therefore distinguishable particles. It is possible to determine if a K^0 or a \bar{K}^0 has been produced by observing the associated particles. Furthermore, once produced, it is possible to distinguish one from the other because when interacting with target nuclei, they produce particles with opposite strangeness. Also the cross-sections are different with $\sigma(K^0 N) < \sigma(\bar{K}^0 N)$ because there are much more available final states for \bar{K}^0 interactions. For the K^0 ,

$$\begin{aligned} K^0 p &\rightarrow K^0 p, K^+ n \\ K^0 n &\rightarrow K^0 n. \end{aligned}$$

For the \bar{K}^0 ,

$$\begin{aligned}\bar{K}^0 p &\rightarrow \bar{K}^0 p, \pi^+ \Lambda^0, \pi^+ \Sigma^0, \pi^0 \Sigma^+ \\ \bar{K}^0 n &\rightarrow \bar{K}^0 n, K^- p, \pi^0 \Lambda^0, \pi^+ \Sigma^0, \pi^0 \Sigma^+, \pi^- \Sigma^+.\end{aligned}$$

The \bar{K}^0 can be considered as the antiparticle of K^0 , the K^- as the antiparticle of K^+ : this is evident when the K are expressed in terms of their valence quarks and antiquarks, that is, $K^+ = u\bar{s}$, $K^- = \bar{u}s$; $K^0 = d\bar{s}$, $\bar{K}^0 = \bar{d}s$. K^0 and \bar{K}^0 are *strangeness eigenstates*.

The two neutral K mesons are observed to decay by WI into $\pi\pi$ or in $\pi\pi\pi$ states, following the same rules observed for other meson and baryon decays. The decay into two pions in the final state has a lifetime much shorter than that with three pions in the final state.

We know that the same particle **cannot decay into either two or three pions**: the final states with two and three pions are CP eigenstates with different eigenvalues. The pions are produced in a state of total angular momentum $J=0$. In Sect. 6.5, we have seen that the parity of a state with n pions is $P(n\pi) = (-1)^n$, while the pions are C eigenstates with eigenvalue +1. The $\pi\pi$ state is then CP eigenstate with eigenvalue +1, while the state $\pi\pi\pi$ is a CP eigenstate with eigenvalue -1.

Virtual transitions via WI are allowed between K^0 and \bar{K}^0 . Virtual transitions between a charged particle and the corresponding antiparticle are forbidden by conservation of the electric charge; they are also forbidden between a baryon and the corresponding antibaryon by conservation of the baryonic number. Transitions between K^0 and \bar{K}^0 violate strangeness ($\Delta S = 2$), which is conserved in the electromagnetic and strong interactions, but not in the WI. Virtual transitions $K^0 \leftrightarrow \bar{K}^0$ may be described by special Feynman diagrams, as discussed in the next section.

A pure K^0 beam can be obtained at c.m. energies of ~ 1 GeV, that is, just above the threshold of reaction (12.1), though below the threshold for reaction (12.2). Due to the allowed WI transitions between K^0 and \bar{K}^0 , this pure K^0 beam at $t=0$ evolves after some time into a superposition of K^0 and \bar{K}^0 expressed as

$$|K(t)\rangle = \alpha(t)|K^0\rangle + \beta(t)|\bar{K}^0\rangle. \quad (12.3)$$

Physical states decaying through WI are, in principle, not eigenstates of the charge conjugation C , parity P , or strangeness S operators. They may eventually be eigenstates of the CP operator. An appropriate phase can be chosen so that the application of the CP operator on the K^0 and \bar{K}^0 states at rest gives

$$CP|K^0\rangle = +|\bar{K}^0\rangle \quad (12.4)$$

$$CP|\bar{K}^0\rangle = +|K^0\rangle. \quad (12.5)$$

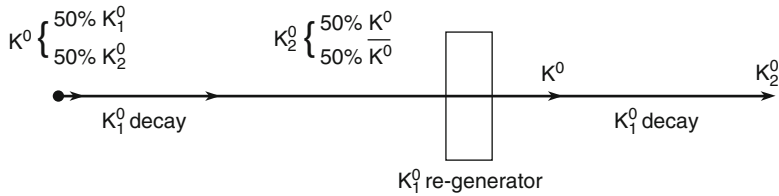


Fig. 12.1 Schematic diagram of an experiment highlighting the fluctuations in strangeness

From Eqs. 12.4 and 12.5, it is evident that K^0 and \bar{K}^0 are not CP eigenstates. Let us now build two linear combinations that are CP eigenstates, for example,

$$|K_1^0\rangle = (|K^0\rangle + |\bar{K}^0\rangle)/\sqrt{2}, \quad |K_2^0\rangle = (|K^0\rangle - |\bar{K}^0\rangle)/\sqrt{2}. \quad (12.6a)$$

From (12.6a), one has

$$K^0 = \frac{|K_1^0\rangle + |K_2^0\rangle}{\sqrt{2}}, \quad \bar{K}^0 = \frac{|K_1^0\rangle - |K_2^0\rangle}{\sqrt{2}}. \quad (12.6b)$$

We can now verify that $|K_1^0\rangle$ and $|K_2^0\rangle$ are CP eigenstates with eigenvalues $+1$ and -1 , that is,

$$\begin{cases} CP|K_1^0\rangle = (CP|K^0\rangle + CP|\bar{K}^0\rangle)/\sqrt{2} = (+|\bar{K}^0\rangle + |K^0\rangle)/\sqrt{2} = |K_1^0\rangle \\ CP|K_2^0\rangle = (CP|K^0\rangle - CP|\bar{K}^0\rangle)/\sqrt{2} = (|\bar{K}^0\rangle - |K^0\rangle)/\sqrt{2} = -|K_2^0\rangle. \end{cases} \quad (12.7)$$

The K_1^0 and K_2^0 states do not have definite strangeness. The $\pi\pi$ ($\pi\pi\pi$) state has $S = 0$ and is a CP eigenstate with eigenvalue $+1$ (-1). For this reason, if CP is conserved in the weak interaction, the K_1^0 decays into 2π , and the K_2^0 decays in 3π . Because of the larger phase space available for $K_1^0 \rightarrow 2\pi$ than for $K_2^0 \rightarrow 3\pi$, the K_1^0 lifetime is much smaller than that of K_2^0 .

12.2.1 Time Development of a K^0 Beam. K_1^0 Regeneration. Strangeness Oscillations

Suppose one has an initially pure K^0 beam produced in the reaction (12.1) just above threshold (see Fig. 12.1). For the strong interaction, the K^0 beam is a pure strangeness $S = +1$ state. For the weak interaction, the beam consists of 50% of K_1^0 mesons and 50% of K_2^0 . After about 10^{-9} s, measured in the K^0 rest system, almost all K_1^0 have disappeared (if there are no relativistic effects, it corresponds to about 30 cm in the laboratory frame). Now, the intensity of the K^0 beam is halved and the beam is predominantly composed of K_2^0 . For the strong interaction, the

beam is now composed of 50% of K^0 and 50% of \bar{K}^0 , that is, it is as if the \bar{K}^0 were “generated.” If this particle beam interacts with matter, the \bar{K}^0 component will be preferentially absorbed because it has a larger cross-section than for K^0 . As a consequence, the K_1^0 are regenerated.

The mathematical description of the time development of the K^0 beam requires the use of complex amplitudes. The relative phase between K_1^0 and K_2^0 for a given energy remains constant if the two particles have the same mass. However, K_1^0 and K_2^0 have slightly different masses because of their difference in the weak coupling. An analogous effect was found for the neutron and proton: they have different masses due to the EM interaction.

The wave function of a steady state with mass m contains the phase term $e^{-i\frac{E}{\hbar}t}$ where $E = mc^2$ if the system is at rest. In the case of a state that decays with a lifetime $\tau = \hbar/\Gamma$, the wave function contains an additional phase factor $e^{-\Gamma t/2\hbar} = e^{-t/2\tau}$. The amplitude probability of such a wave function is thus proportional to $e^{-t/\tau}$ (see discussion in Sect. 7.5). In the rest system (using here and later $\hbar = c = 1$, so that $\tau = 1/\Gamma$), the total phase of the wave function can be written as e^{-iMt} , where M is the complex quantity $M = m - i\Gamma/2$. At the time $t = 0$, when K^0 are generated through Eq. 12.1, we have

$$|K^0(0)\rangle = [|K_1^0(0)\rangle + |K_2^0(0)\rangle]/\sqrt{2} ; \quad |\bar{K}^0(0)\rangle = 0 . \quad (12.8)$$

At time t , it evolves as

$$|K_1^0(t)\rangle = |K_1^0(0)\rangle e^{-iM_1 t}, \quad |K_2^0(t)\rangle = |K_2^0(0)\rangle e^{-iM_2 t} \quad (12.9a)$$

$$|K^0(t)\rangle = \frac{1}{\sqrt{2}} [|K_1^0(0)\rangle e^{-iM_1 t} + |K_2^0(0)\rangle e^{-iM_2 t}] \quad (12.9b)$$

with $M_1 = m_1 - i\Gamma_1/2 = m_1 - i/2\tau_1$, $M_2 = m_2 - i\Gamma_2/2 = m_2 - i/2\tau_2$; m_1 and m_2 represent the masses of K_1^0 and K_2^0 , τ_1 and τ_2 their respective lifetimes.

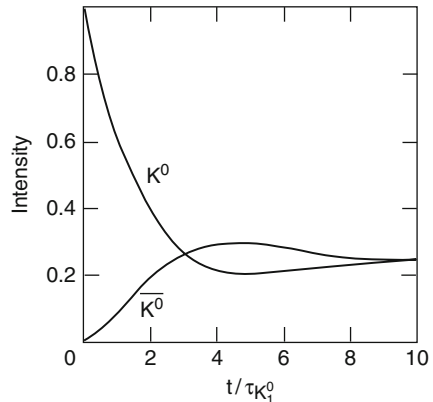
As a consequence of (12.9), a series of interference effects appears: they are the so-called *strangeness oscillations*. The intensity of the beam is given by the wave function times its complex conjugate. Starting with a pure K^0 state, i.e., $|K_1^0(0) = K_2^0(0) = K^0(0)/\sqrt{2}$, at the time t , one has

$$I_{K_1^0}(t) = \langle K_1^0(t)|K_1^{0*}(t)\rangle = \langle K_1^0(0)|K_1^{0*}(0)\rangle e^{-\Gamma_1 t} = I_1(0)e^{-\Gamma_1 t} .$$

For the relative intensity of the K^0 , one has (remember that $I_{K^0}(0) = \langle K^0(0)|K^{0*}(0)\rangle = 1$)

$$\begin{aligned} P_{K^0 \rightarrow K^0}(t) &= \frac{I_{K^0}(t)}{I_{K^0}(0)} = \langle K^0(t)|K^{0*}(t)\rangle = \\ &= \left[\frac{(\langle K_1^0(t)| + \langle K_2^0(t)|)(|K_1^{0*}(t)\rangle + |K_2^{0*}(t)\rangle)}{\sqrt{2}\sqrt{2}} \right] = \\ &= \frac{1}{4} [e^{-\Gamma_1 t} + e^{-\Gamma_2 t} + 2e^{-[(\Gamma_1 + \Gamma_2)/2]t} \cos(\Delta m t)] \end{aligned} \quad (12.10a)$$

Fig. 12.2 Intensity oscillations of K^0 and of \bar{K}^0 , starting from a pure K^0 state. Equations 12.10a, b have been used with $\Delta m_K/m_K = 0.7 \cdot 10^{-14}$



where $\Delta m = m_2 - m_1$, $I_{\bar{K}^0}(0) = 0$, $I_{K^0}(0) = 1$. In the last step, the property of the complex exponential, $e^{iy} = \cos y + i \sin y$, is used. Similarly, one has

$$P_{K^0 \rightarrow \bar{K}^0}(t) = \frac{I_{\bar{K}^0}(t)}{I_{\bar{K}^0}(0)} = \frac{1}{4} [e^{-\Gamma_1 t} + e^{-\Gamma_2 t} - 2e^{-[(\Gamma_1 + \Gamma_2)/2]t} \cos(\Delta m t)]. \quad (12.10b)$$

To illustrate the meaning of (12.10a, b), let us assume that K^0 and \bar{K}^0 are stable particles; this means (by definition of $M_{1,2}$ in (12.9)) that $\Gamma_1 = \Gamma_2 = 0$. It follows that

$$P_{K^0 \rightarrow K^0}(t) = \frac{1}{2} [1 + \cos(\Delta m t)] = \cos^2\left(\frac{\Delta m t}{2}\right) \quad (12.10c)$$

$$P_{K^0 \rightarrow \bar{K}^0}(t) = \frac{1}{2} [1 - \cos(\Delta m t)] = \sin^2\left(\frac{\Delta m t}{2}\right). \quad (12.10d)$$

At the initial time ($t = 0$), only K^0 are present; with increasing time (i.e., when particles move away from the production point), the probability of finding \bar{K}^0 increases. For $t = \pi/\Delta m$ (in natural units), only \bar{K}^0 are present in the beam; at $t = 2\pi/\Delta m$, only K^0 are present. This is the phenomenon of *particle oscillations*. The fact that Γ_1, Γ_2 are nonzero real numbers causes the intensity to exponentially decrease (as in the damped oscillatory phenomena), but does not change the frequency of beats, which depends on Δm .

The time evolution of the K^0 and \bar{K}^0 intensities is illustrated in Fig. 12.2. The mass difference between K_1^0 and K_2^0 was found to be extremely small ($\Delta m = 3.7 \times 10^{-6}$ eV). Their lifetimes are instead very different: $\tau_{K_2^0} \simeq 600 \tau_{K_1^0}$, due to the energy available in the phase space of the process, i.e., the kinetic energy available in three-particle ($K_2^0 \rightarrow 3\pi$) or two-particle ($K_1^0 \rightarrow 2\pi$) decays. Since a small *CP*-violation was experimentally found, the general framework is modified and the above description is only approximately valid.

To understand how a mismatch of the waves may change the flavor eigenstate, let us use an analogy. In optics, a distinction between “base colors” (for instance red, blue and green) and “compound colors” can be made. For example, purple is a mixture of red and blue. Now, imagine a given source of a “purple wave.” Purple (corresponding in the analogy to a flavor eigenstate) is obtained by mixing the red and blue basic colors (that correspond to mass eigenstates). The emitted wave has a percentage of red and blue waves with initial values in order to provide, in the mixture, the right shade of purple. The propagation can affect the basic red and blue colors differently. If they propagate with the same velocity, their overlap gives the same purple color everywhere. If they propagate with different velocities, their intensity is different from point to point. This corresponds to different resulting colors seen by observers in different positions. The word “oscillation” does not refer to the fact that particles are represented by waves, but rather that the observable color (= flavor eigenstate) changes with the distance from the source, with an oscillatory law. At certain points, the wave may even appear to an observer as purely red (or blue).

12.3 CP -Violation in the $K^0 - \bar{K}^0$ System

In 1964, Cronin, Fitch (Nobel laureate in 1980) and colleagues experimentally observed that a small K_2^0 fraction decays in 2π . This is inconsistent with the fact that K_2^0 is a CP eigenstate, as it should always decay into three pions. In their experiment, a pure K^0 beam of ~ 1 GeV/c momentum was injected into a 15 m length vacuum tube. All K_1^0 decayed before reaching the end of the pipe since $l_{K_1^0} = \gamma\beta c\tau_{K_S^0} \simeq 6$ cm. At the end of the tube, only K_2^0 decays in 3π were expected. A few K_2^0 decays in $\pi^+\pi^-$ and $\pi^0\pi^0$ were also observed. This result represented the first experimental evidence of CP -violation. Following this observation, a slight modification is needed in the discussion presented above. The particles with longer and shorter lifetimes were denoted as K_L^0 and K_S^0 respectively, with $\tau_S = (89.53 \pm 0.05) \times 10^{-12}$ s; $\tau_L = (51.14 \pm 0.21) \times 10^{-9}$ s (L and S stand for *long* and *short*). They are now considered as the *mass eigenstates*, leaving the names K_2^0 , K_1^0 for the *CP eigenstates* [12B95]. In addition to the $K_L^0 \rightarrow 2\pi$ decay, a charge asymmetry in the semileptonic decays of K_L^0 was also found, see (12.26).

The $K^0 - \bar{K}^0$ propagation represents a very precise interferometer, which can highlight the small CP -violation in the K_L^0 system. Due to the relevant historical point of view, the $K^0 - \bar{K}^0$ system is used in the following to describe the time evolution formalism needed to extract the small quantities producing CP -violation. The formalism can easily be generalized for other mesons made of heavier quarks, as the more recently experimentally studied D , B , B_S mesons.

12.3.1 The Formalism and the Parameters of CP-Violation

The CP -violation can be included in the basic equations of meson oscillations assuming that the Hamiltonian of the weak interaction is not invariant under CP . The formalism presented in Sect. 12.2 can be generalized: the Hamiltonian eigenstates are not eigenstates of the CP operator and the physical states are a superposition of states with CP eigenvalues +1 and -1.

The time evolution of the system $\psi = \begin{pmatrix} K^0 \\ \bar{K}^0 \end{pmatrix}$ (eigenstates for the strong interaction) is given as usual by $i \frac{\partial \psi(t)}{\partial t} = H\psi(t)$, with

$$H = M = m - \frac{i}{2}\Gamma \quad (12.11a)$$

or in the explicit form:

$$M = \begin{pmatrix} m_{11} - i\Gamma_{11}/2 & m_{12} - i\Gamma_{12}/2 \\ m_{21} + i\Gamma_{21}/2 & m_{22} - i\Gamma_{22}/2 \end{pmatrix}. \quad (12.11b)$$

Due to the CPT invariance, one has $\langle K^0 | M | K^0 \rangle = \langle \bar{K}^0 | M | \bar{K}^0 \rangle$, $m_{11} = m_{22}$ and $\Gamma_{11} = \Gamma_{22}$. If CP is conserved, one has $m_{12} = m_{12}^*$ and $\Gamma_{12} = \Gamma_{12}^*$, yielding to the already obtained Eqs. 12.10a, b.

The two eigenstates of the new Hamiltonian (12.11a) are called the *mass eigenstates*, namely,

$$|K_S^0\rangle = p|K^0\rangle + q|\bar{K}^0\rangle \quad (12.12)$$

$$|K_L^0\rangle = p|K^0\rangle - q|\bar{K}^0\rangle. \quad (12.13)$$

Since $|K^0\rangle$ and $|\bar{K}^0\rangle$ are linear combinations of CP eigenstates $|K_1^0\rangle$ and $|K_2^0\rangle$ (12.6b), the mass eigenstates can also be expressed as linear combinations of CP eigenstates

$$|K_S^0\rangle = \frac{|K_1^0\rangle + \varepsilon|K_2^0\rangle}{\sqrt{1+|\varepsilon|^2}} = \frac{1}{\sqrt{2(1+|\varepsilon|^2)}} \left[(1+\varepsilon)|K^0\rangle + (1-\varepsilon)|\bar{K}^0\rangle \right] \quad (12.14)$$

$$|K_L^0\rangle = \frac{|K_2^0\rangle - \varepsilon|K_1^0\rangle}{\sqrt{1+|\varepsilon|^2}} = \frac{1}{\sqrt{2(1+|\varepsilon|^2)}} \left[(1+\varepsilon)|K^0\rangle - (1-\varepsilon)|\bar{K}^0\rangle \right]. \quad (12.15)$$

If CP is conserved, one must have $\varepsilon = 0$ (or $p = q$) and $|K_S^0\rangle = |K_1^0\rangle$, $|K_L^0\rangle = |K_2^0\rangle$.

The ε parameter is a complex number ($\varepsilon = |\varepsilon|e^{i\varphi}$) representing the deviation of K_L^0 and K_S^0 from CP -eigenstates, i.e., the degree of CP -violation.

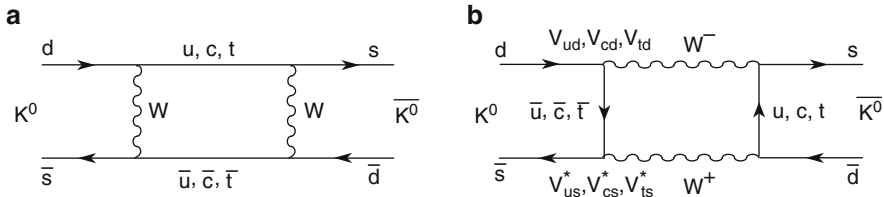


Fig. 12.3 (a), (b) Box diagrams illustrating the $K^0 \leftrightarrow \bar{K}^0$ transitions with $\Delta S = 2$. Note the matrix elements $V_{ud}, \dots, V_{us}^*, \dots$. With two exchanged W , these processes are of second order for the weak interaction

12.3.1.1 Direct and Indirect CP -Violation

The K_L^0 decay into 2π occurs via CP -violation in the mixing of the strong interaction eigenstates during their propagation. This implies a second order process in terms of the weak interaction coupling constant (the exchange of two W vector bosons is needed, with a $\Delta S = 2$ strangeness change). The corresponding Feynman diagrams are the so-called *box* diagrams shown in Fig. 12.3. The CP -violation with $\Delta S = 2$ is called *indirect*. It is measured by the (complex) quantity ε in (12.14) and (12.15).

The CP -violation can also occur through a term in the Hamiltonian (and, consequently, in Feynman diagrams) with $\Delta S = 1$, i.e., a single “conversion” of the type $s \rightarrow d$. This transition occurs with the so-called *penguin diagram* shown in Fig. 12.4, dominated by the exchange of a t quark. This figure actually represents a set of three diagrams because the gluon exchanged at the bottom of the diagram can be replaced by a photon or a Z^0 . The diagram with a gluon exchange is dominant since $\alpha_s \gg \alpha_{EM}, \alpha_{WI}$. However, for *top* mass $m_t \simeq 180$ GeV, the probability of a Z^0 exchange increases and interferes destructively with the exchange of gluons. For this reason, the penguin diagram contribution to CP -violation is relatively small. It is measured by the (complex) quantity ε' defined below. The CP -violation due to $\Delta S = 1$ transitions is called *direct*.

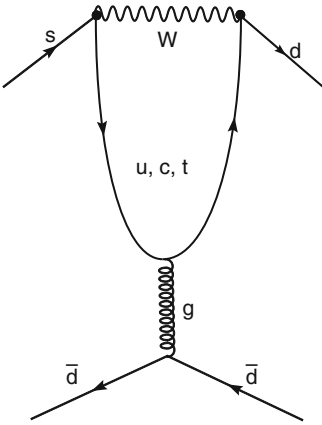
From the experimental point of view, the direct and indirect CP -violation can be highlighted both in nonleptonic decays and in semileptonic decays of mesons.

Nonleptonic decays. Let us consider the nonleptonic decay amplitudes $A(K^0 \rightarrow \pi\pi) = \langle K^0 \rightarrow \pi\pi |, A(\bar{K}^0 \rightarrow \pi\pi) = \langle \bar{K}^0 \rightarrow \pi\pi |$. The amplitude ratios for $\pi^+\pi^-$ and $\pi^0\pi^0$ decays are respectively

$$\eta_{+-} = |\eta_{+-}| e^{i\varphi_{+-}} = \frac{A(K_L^0 \rightarrow \pi^+\pi^-)}{A(K_S^0 \rightarrow \pi^+\pi^-)} \quad (12.16)$$

$$\eta_{00} = |\eta_{00}| e^{i\varphi_{00}} = \frac{A(K_L^0 \rightarrow \pi^0\pi^0)}{A(K_S^0 \rightarrow \pi^0\pi^0)} . \quad (12.17)$$

Fig. 12.4 Penguin diagram illustrating transitions with $\Delta S = 1$ ($s \rightarrow d$) whose probability amplitude contains a term that produces a small CP -violation



It can be shown [P08] that these ratios are related to both CP -violation parameters ε and ε' , that is,

$$\eta_{+-} = |\eta_{+-}|e^{i\varphi_{+-}} = \varepsilon + \varepsilon' \quad (12.18)$$

$$\eta_{00} = |\eta_{00}|e^{i\varphi_{00}} = \varepsilon - 2\varepsilon' \quad (12.19)$$

where $|\varepsilon| \ll |\varepsilon'|$. Experimentally, both the intensity and the phase of the amplitudes (12.16) and (12.17) can be measured through the interference of decays in $\pi^+\pi^-$ (and in $\pi^0\pi^0$) as a function of proper time. The observable quantity is the *asymmetry* defined as

$$A_{\pi\pi}(t) = \frac{P_{K^0 \rightarrow \pi\pi}(t) - P_{\bar{K}^0 \rightarrow \pi\pi}(t)}{P_{K^0 \rightarrow \pi\pi}(t) + P_{\bar{K}^0 \rightarrow \pi\pi}(t)} \quad (12.20)$$

where $P_{K^0 \rightarrow \pi\pi}(t) \equiv \langle K^0 \rightarrow \pi\pi | K^0 \rangle$ and $P_{\bar{K}^0 \rightarrow \pi\pi}(t) \equiv \langle \bar{K}^0 \rightarrow \pi\pi | \bar{K}^0 \rangle$; after some algebra, from (12.20), one can derive

$$A_{\pi\pi}(t) = 2\text{Re}\varepsilon + \frac{2|\eta_{\pi\pi}|e^{[(\Gamma_S - \Gamma_L)t/2]}}{1 + |\eta_{\pi\pi}|^2 e^{[(\Gamma_S - \Gamma_L)t]}} \cos(\Delta m t - \varphi_{\pi\pi}). \quad (12.21)$$

Here, ($\pi\pi$ stands for both $\pi^0\pi^0$ or $\pi^+\pi^-$). Figure 12.5 shows an example of such an interference in the $\pi^+\pi^-$ decay channel. Since (12.14) and (12.15) are not CP eigenstates, we may imagine that the component, which still decay into 2π , is the K_L^0 . The K_L^0 state contains a small fraction of K_1^0 (12.15), and this tiny fraction decays into 2π . From experiments carried out at CERN, Brookhaven, Argonne and SLAC laboratories, it was measured that $|\varepsilon| \simeq 2.3 \cdot 10^{-3}$ and $\phi \simeq 45^\circ$ (i.e., $\text{Re } \varepsilon \simeq \text{Im } \varepsilon$).

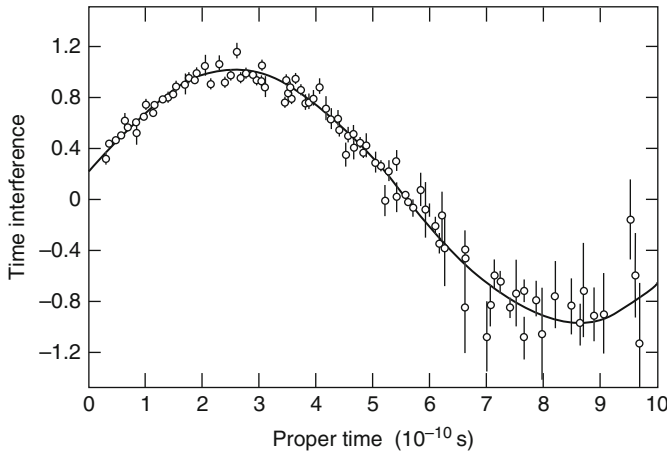


Fig. 12.5 Time interference (asymmetry) in the decay of K_L^0 and K_S^0 in $\pi^+\pi^-$ as a function of the K_S^0 proper time (see Eq. 12.20)

While it has been known since 1964 that $|\varepsilon| > 0$, for many years, there were experimental discrepancies about the fact that ε' was different from zero. Today [P08], the issue is solved. The ratio ε'/ε was determined by measuring the double ratio R (Problem 12.4)

$$R = \frac{|\eta_{00}|^2}{|\eta_{+-}|^2} = \frac{\Gamma(K_L \rightarrow \pi^+\pi^-)}{\Gamma(K_S \rightarrow \pi^+\pi^-)} \Big/ \frac{\Gamma(K_L \rightarrow \pi^0\pi^0)}{\Gamma(K_S \rightarrow \pi^0\pi^0)} \simeq 1 - 6 \frac{\varepsilon'}{\varepsilon}. \quad (12.22)$$

A few years ago, two high precision experiments (KTeV at Fermilab and NA48 at the CERN SPS) measured $\text{Re}(\frac{\varepsilon'}{\varepsilon})$ with an accuracy of the order $\sim 2 \cdot 10^{-4}$. Both experiments measured the K_S^0 and K_L^0 decays into $\pi^+\pi^-$ and $\pi^0\pi^0$, deriving the result through the relation (12.22). The two experiments agreed on the value of $\text{Re}(\frac{\varepsilon'}{\varepsilon})$, finally proving the existence of direct CP -violation. It was found [P08] that

$$\begin{cases} |\eta_{+-}| = (2.233 \pm 0.010) \cdot 10^{-3} \\ \varphi_{+-} = (43.52 \pm 0.05)^\circ \end{cases} \quad \begin{cases} |\eta_{00}| = (2.222 \pm 0.010) \cdot 10^{-3} \\ \varphi_{00} = (43.50 \pm 0.06)^\circ \end{cases} \quad (12.23)$$

From (12.18), (12.19) and (12.22), it was obtained that

$$|\varepsilon| = (2.229 \pm 0.010) \cdot 10^{-3} \quad (12.24)$$

$$\text{Re}(\varepsilon'/\varepsilon) = (1.65 \pm 0.26) \cdot 10^{-3}. \quad (12.25)$$

Here, we briefly discuss the experimental setup of the NA48 experiment at CERN. It simultaneously used two nearly collinear K_S and K_L beams and measured the four decay channels that appear in the ratio R of (12.22). The two beams were produced by 450 GeV protons from the SPS. Because of the different average decay lengths of 110 GeV/c momentum K_L ($\lambda_L = 3.4$ km) and K_S ($\lambda_S = 5.4$ m), the K_L and K_S were produced in two separate targets at 126 m and 6 m before the beginning of the decay region, respectively. Each proton pulse [about 10^{12} protons per impulse (ppi) of 2.4 s] was divided in two. Most protons were hitting the first target: the K_S decayed rapidly, and from the first target, there were about $10^7 K_L$ per pulse directed to the decay region. A small fraction of protons (about $3 \cdot 10^7$ ppi) arrived at the second target, where a beam of about $10^2 K_S$ per pulse was produced.

The $K \rightarrow \pi^+ \pi^-$ decays were measured with a spectrometer that used a magnet and a drift chamber system. For $K \rightarrow \pi^0 \pi^0$ decays, the γ 's from the π^0 decay were measured in a 10 m^3 homogeneous calorimeter filled with liquid krypton. This detector was highly segmented, with an energy resolution of better than 1% at energies above 10 GeV and a time resolution of ≤ 1 ns.

Nonleptonic decays. The semileptonic decay is a channel that can be studied by measuring the asymmetry (l stands for muon or electron), that is,

$$A_L = \frac{\Gamma(K_L \rightarrow \pi^- l^+ \nu_l) - \Gamma(K_L \rightarrow \pi^+ l^- \bar{\nu}_l)}{\Gamma(K_L \rightarrow \pi^- l^+ \nu_l) + \Gamma(K_L \rightarrow \pi^+ l^- \bar{\nu}_l)}. \quad (12.26)$$

Taking the sign of the lepton charge as a reference, a nonzero A_L value shows in an independent way that the K_L decay into “matter” and “antimatter” is different. In terms of the CP -violation parameters (see Problem 12.5), the measurements (averaged between muons and electrons) provide

$$A_L \simeq 2\text{Re}(\varepsilon) = (3.32 \pm 0.06) \cdot 10^{-3}, \quad (12.27)$$

which is consistent with what is obtained for the nonleptonic decays.

12.4 What is the Reason for CP -Violation?

Within the Standard Model, the CP -violation is introduced through the so-called Kobayashi–Maskawa mechanism which predicts the existence of a phase factor in the 3×3 matrix (8.62b). The nonzero value of the phase is the *dominant source* of CP -violation in meson decay.

Remember that the mixing of the three quark generations in the weak interaction is described by the 3×3 matrix called the *Cabibbo–Kobayashi–Maskawa* (CKM matrix). The probability of each possible quark flavor transition due to WI is therefore specified by the CKM matrix (see Chap. 8). For example, the square of the matrix element V_{ud} gives the probability that a *up* quark turns into a *down* quark. The weak interaction between *antiquarks* is ruled by the complex-conjugated CKM matrix. If the CKM matrix does not contain imaginary elements (i.e., all real elements), quarks and antiquarks would behave exactly in the same way for the WI.

The nine elements of the CKM matrix are not independent. For example, an *up*-type quark can only convert via W^+ exchange into one of the three quarks with $-1/3$ electric charge (i.e., d, s, b); the sum of the three probabilities must be equal to one. Under these constraints, the CKM matrix can be expressed in terms of only four parameters: three real numbers for the mixing angles, and one imaginary phase, which makes the *CP*-violation possible.

In Chap. 8, two possible parameterizations of the CKM matrix were presented. A widely used approximation of the CKM matrix (8.67) is the Wolfenstein parametrization which displays the hierarchy of the three mixing angles $\theta_{12}, \theta_{23}, \theta_{13}$, which have¹ $s_{12} \gg s_{23} \gg s_{13}$. The sine of the Cabibbo angle $s_{12} = \lambda$ ($\simeq 0.23$) can be used as an expansion parameter (i.e., the other elements can be expressed in terms of powers of λ):

$$V = \begin{pmatrix} V_{ud} & V_{us} & V_{ub} \\ V_{cd} & V_{cs} & V_{cb} \\ V_{td} & V_{ts} & V_{tb} \end{pmatrix} = \begin{pmatrix} 1 - \frac{1}{2}\lambda^2 & \lambda & A\lambda^3(\rho - i\eta) \\ -\lambda & 1 - \frac{1}{2}\lambda^2 & A\lambda^2 \\ A\lambda^3(1 - \rho - i\eta) & -A\lambda^2 & 1 \end{pmatrix} + O(\lambda^4) \quad (12.28)$$

where A, ρ, η are real numbers and represent (with λ) the four independent parameters of the matrix. In particular, η is the *CP*-violating phase.

A simple way to visualize the relations between the elements of the CKM matrix was proposed by J. Bjorken and C. Jarlskog in 1988 through the so-called *unitarity triangle*. The request that the CKM matrix is unitary leads to relations between its elements, for example,

$$V_{ud}V_{ub}^* + V_{cd}V_{cb}^* + V_{td}V_{tb}^* = 0. \quad (12.29)$$

Each term of (12.29) is a complex number that can be represented in a Cartesian plane: the real part is represented along the x -axis and the complex part is the ordinate. The sum behaves exactly as the sum of three vectors adding to zero: drawing a triangle in the xy -plane, the tip of the third vector ends where the first begins. The three angles (called α, β, γ) and the length of the sides correspond to relations between elements of the CKM matrix (see Fig. 12.6). The height of the triangle depends on the value of the imaginary phase η in (12.28). If $\eta = 0$, the three summands in (12.29) are real numbers and the triangle degenerates to a segment along the x -axis.

¹Here, as elsewhere, we use the notation $s_{12} = \sin \theta_{12}, c_{12} = \cos \theta_{12}$, etc.

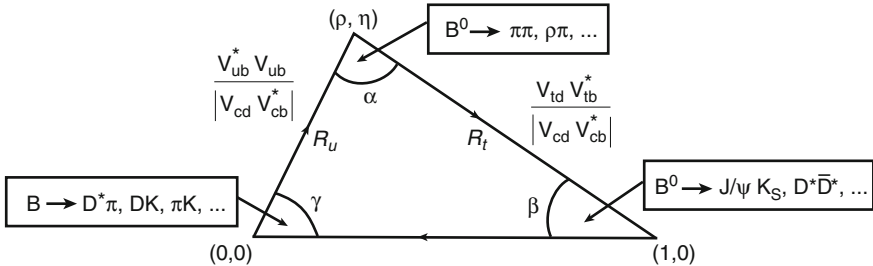


Fig. 12.6 Unitarity triangle. Inner angles α, β, γ can be determined from measurements of CP -violation in decays of mesons with a b quark. The R_u side is defined as the edge between the α and γ angles and the R_t side is defined as the edge between the α and β angles

The values of the CKM matrix elements are such that a larger degree of CP -violation is expected for mesons with a *bottom* quark with respect to the neutral kaons system. This implies that particles with a b quark behave differently than antiparticles with a \bar{b} antiquark.

Early studies on $B^0 - \bar{B}^0$ mixing were carried out by UA1 at the CERN $Sp\bar{p}S$ collider, ARGUS at DESY and by the LEP experiments. Thanks to precision measurements performed at B-factories (see next section), the predictions of the Standard Model were verified with a high degree of accuracy. The CP -violation observed in the $B^0 - \bar{B}^0$ system is compatible with the parameter obtained from the $K^0 - \bar{K}^0$ system. However, some pieces of the puzzle are still not understood, for example, the degree of CP -violation is in fact not large enough to explain the observed asymmetry between matter and antimatter in the universe.

12.5 CP -Violation in the $B^0 - \bar{B}^0$ System

The formalism introduced for the $K^0 - \bar{K}^0$ system can be applied to the $B^0 - \bar{B}^0$ case. There are two types of B^0 mesons: the “normal” B_d^0 and the “strange” B_s^0 , that is,

$$B_d^0 = \bar{b}d, \bar{B}_d^0 = b\bar{d} \quad (12.30)$$

$$B_s^0 = \bar{b}s, \bar{B}_s^0 = b\bar{s}. \quad (12.31)$$

Let us consider the $B_d^0 - \bar{B}_d^0$ system (denoted as $B^0 - \bar{B}^0$ to simplify the notation). Transitions $B^0 \leftrightarrow \bar{B}^0$ can occur via the diagrams of Fig. 12.7. As for the neutral K

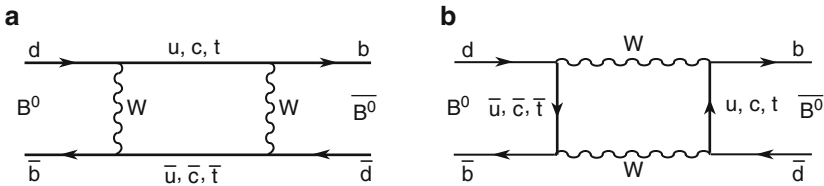


Fig. 12.7 Box diagrams illustrating the transitions (*mixing*) $B^0 \leftrightarrow \bar{B}^0$

mesons, the neutral B mesons have mass eigenstates different from the strong flavor eigenstates B^0, \bar{B}^0 . The mass eigenstates are

$$|B_{\pm}\rangle = p|B^0\rangle \pm q|\bar{B}^0\rangle. \quad (12.32)$$

The kaon mass eigenstates are distinguished primarily by their lifetime, which strongly depends on the energy available in the phase space. This quantity is different for the decay into two or three pions. For the B mesons, the lifetimes differ by a small amount and the states are distinguished primarily by their masses.

Starting at $t = 0$ with a pure B^0 or \bar{B}^0 state, the time evolution is

$$|B^0(t)\rangle = g_+(t)|B^0\rangle + \frac{q}{p}g_-(t)|\bar{B}^0\rangle \quad (12.33a)$$

$$|\bar{B}^0(t)\rangle = g_+(t)|\bar{B}^0\rangle + \frac{p}{q}g_-(t)|B^0\rangle \quad (12.33b)$$

where

$$g_{\pm}(t) = \frac{1}{2}e^{-iM_{\pm}t} e^{-\frac{1}{2}\Gamma_{\pm}t}[1 \pm e^{-i\Delta M t} e^{\frac{1}{2}\Delta\Gamma t}] \quad (12.34)$$

and $\Delta M = |M_+ - M_-|$, $\Delta\Gamma = |\Gamma_+ - \Gamma_-|$. This means that flavor eigenstates oscillate with a time-dependent probability proportional to $|g_{\pm}(t)|^2$.

Only a small fraction of B^0, \bar{B}^0 is subject to CP -violating decay. To observe these interesting decays, an enormous number of B mesons must be produced through dedicated accelerators called *B-factories*. The primary objective of B-factories is to measure the parameters of the unitarity triangle and, in particular, the β angle of Fig. 12.6.

The specific process used to measure the β angle is the time-dependent asymmetry in the decay of a initial $B^0\bar{B}^0$ pair produced by the decay of the $\Upsilon(4s)$ resonance into a common CP eigenstate. The initial $B^0\bar{B}^0$ state evolves coherently until one of the two mesons, which we call B_{tag} , decays at t_1 in a final state f_{tag} . If the B^0 is B_{tag} (as in Fig. 12.8), the second meson must be a \bar{B}^0 at the time t_1 , and it can decay at a later time t_2 into a CP eigenstate, denoted as f_{CP} . This state can be, for instance, a J/ψ (the meson formed by $c\bar{c}$) plus a K_S ($f_{CP} = J/\psi K_S$). This decay has a $BR \sim 0.5 \times 10^{-3}$, and occurs about once in 2,000 cases. The B_{tag} decay products

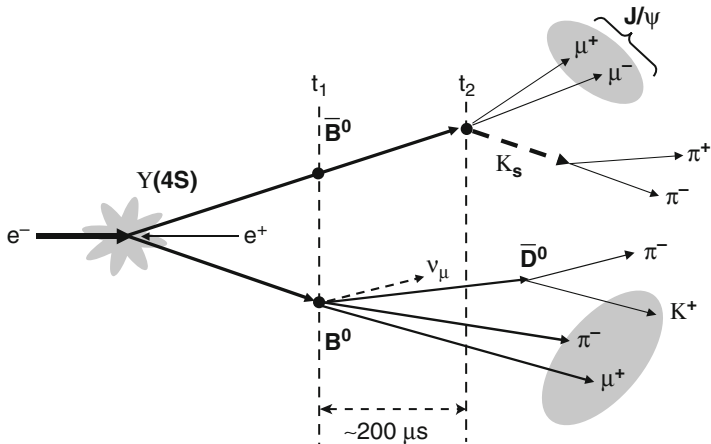


Fig. 12.8 At a B-factory, electrons and positrons collide with just enough energy to produce a $\Upsilon(4S)$, which immediately decays (through strong interaction) to B^0, \bar{B}^0 . The e^- has a higher energy than the e^+ (asymmetric collider), and thus the two B mesons move along the direction of the electron beam before decaying within a few ps (10^{-12} s). The CP -violation is measured through the B -meson decays to J/ψ plus K_S , followed by the J/ψ decay into a muon pair and the K_S decay into a pion pair. However, since either a B^0 or a \bar{B}^0 can produce these decays (for instance, the \bar{B}^0 at the time t_2), the decay of the other B meson in the event must be accurately measured (or *tagged*) in order to establish *which is which*. Here, the presence of a μ^+ in the vertex at t_1 identifies the B^0 through its semileptonic decay. The position at which the two B mesons decay must be determined precisely in order to establish how long the particles lived between t_1 and t_2 . The Standard Model predicts that, on average, B^0 mesons decay slightly later than \bar{B}^0 mesons, by an amount that depends on the angle β of the unitarity triangle [12G07]

at t_1 must be *tagged* in order to establish if it is a B^0 or a \bar{B}^0 . In the figure, the presence of a μ^+ in the vertex at t_1 identifies the B^0 through its semileptonic decay (see Problem 12.6).

The time interval $\Delta t = t_2 - t_1$ (see Fig. 12.8) between the two decays is measurable if the $\Upsilon(4s)$ is produced with a “boost” $\beta\gamma \gg 1$ along the collision z -axis (which is achieved using asymmetric colliders). Δt can be determined from the measurement of the z -distance between the decay vertices: $\Delta t \simeq (z_2 - z_1)/\beta\gamma c$.

The Standard Model predicts that, on average, B^0 mesons decay slightly later than \bar{B}^0 mesons. This asymmetry can be calculated as a function of time; according to the parameters of the CKM matrix (12.28), this asymmetry is

$$A(t) = \frac{\Gamma(\bar{B}^0 \rightarrow f_{CP}) - \Gamma(B^0 \rightarrow f_{CP})}{\Gamma(\bar{B}^0 \rightarrow f_{CP}) + \Gamma(B^0 \rightarrow f_{CP})} = -\eta_{CP} \sin 2\beta \sin \Delta M_d t \quad (12.35)$$

where $\Gamma(\bar{B}^0(B^0) \rightarrow f_{CP})$ is the branching ratio for $\bar{B}^0(B^0)$ in $f_{CP} = J/\psi K_S$ at a certain time t after production, $\eta_{CP} = \pm 1$ is the CP eigenvalue of the f_{CP} state,

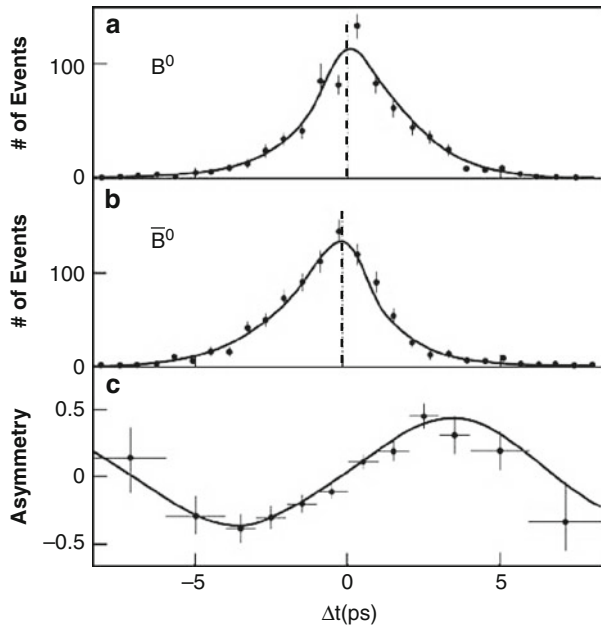


Fig. 12.9 The B^0, \bar{B}^0 mesons behave differently when they decay. The decay rate of the B^0 (a) and \bar{B}^0 (b) meson is described by an exponential curve. However, CP -violation, combined with the B^0, \bar{B}^0 mixing properties, produces a sinusoidal modulation in the exponential decay. This sinusoidal behavior changes sign between the B^0 and \bar{B}^0 meson, observable in the shapes of their decay rates. (c) Dividing the difference between the two decay rates by their sum, the asymmetry which provides a direct measurement of the angle β in the unitarity triangle is obtained [12H03]

ΔM_d is the mass difference between the two mass eigenstates determined by the $B^0 - \bar{B}^0$ mixing.

Measurements of the unitarity triangle parameters, and particularly of $\sin 2\beta$, were recently performed by the Belle and BaBar collaborations. The Belle detector is installed at the Japanese KEKB e^+e^- asymmetric collider, with 3.5 GeV positron and 8 GeV electron beams [12A01]. The BaBar detector used the PEP-II facility at Stanford (United States) where 3.1 GeV e^+ collided against 9 GeV e^- [12D01].

The decay time difference distributions between events in which the *tagging* is respectively due to a B^0 or a \bar{B}^0 are shown in Fig. 12.9 for the BaBar data. The asymmetry is clearly visible if the difference between the two distributions is divided by their sum. The sinusoidal modulation was measured with a fit to the data. The Belle and BaBar results are consistent within errors, and from the combination of the two experiments [P08], the following measurement was obtained, that is,

$$\sin 2\beta = 0.681 \pm 0.025. \quad (12.36)$$

The value $\beta = 21.0^\circ \pm 1.0^\circ$ is compatible with that obtained from the CP -violation in a neutral kaon system. The remaining angles of the unitarity triangle,

involving other elements in the CKM matrix, are more difficult to measure. For instance, $\sin 2\alpha$ cannot be simply measured tagging the $B^0 \rightarrow \pi^+ \pi^-$ decay, as the asymmetry in this decay is not simply proportional to $\sin 2\alpha$. The third angle, γ , may be determined by measuring the asymmetry in the $B^0 \rightarrow DK$ decay (where D is a meson containing a c quark). However, the measurement is extremely difficult because of the small branching ratio (BR) in this channel ($BR \sim 10^{-6}$). The value of the two angles are $\alpha = 92^\circ \pm 7^\circ$ and $\gamma = 82^\circ \pm 20^\circ$ [12G07]. Within errors, the sum of the three angles is equal to 180° .

The CP -violation parameter η in (12.28) can be estimated not only from the measurements of the unitarity triangle angles, but also from the triangle area. The triangle sides are proportional to the number of decays in the appropriate channels. From the experimental point of view, the measurement of the R_u side, between the α and γ angles, is extremely difficult because of the small value of the matrix element: $|V_{ub}| = (3.5 \pm 0.2) \times 10^{-3}$ (see Fig. 12.6). This implies that a B meson decay into mesons containing an up-quark is extremely rare (see also Fig. 8.20). The measurement of the R_t side, between the α and β angles, involves the very small V_{td} matrix element for the transition of a meson with a t -quark into mesons with a d -quark. The energies involved in B-factories are actually too low to produce mesons containing a t -quark; this channel can only be studied at higher energy colliders.

12.5.1 Future Experiments

The LHC will provide more information about the CP -violation in the B sector. The BaBar and Belle experiments detected millions of B -mesons per day; the expected rate at the LHC will be of the order of 10^6 mesons per second. The LHCb experiment (one of the four detectors installed at the CERN LHC collider) will measure the unitarity triangle parameters with high precision, and in particular, the γ angle. The proton-proton collisions, however, intrinsically have a much higher background event rate with respect to $e^+ e^-$ machines and the interesting events will be more difficult to select.

Waiting for the LHC results, the matter-antimatter asymmetry observed in the Universe stimulates new experimental ideas. A *Super flavor Factory*, which is an asymmetric $e^+ e^-$ collider similar to the current B-factories with a 100 times larger luminosity, was proposed by the international scientific community for precision measurements of the unitarity triangle parameters.

12.6 Neutrino Oscillations

The Standard Model of the microcosm includes three flavors of massless and left-handed neutrinos, denoted as ν_e, ν_μ, ν_τ ; a neutrino of one type cannot transform into a neutrino of another type. Three degenerate massless particles are surprising and

cannot explain the difference amongst themselves and the reason for the L_e, L_μ, L_τ lepton number conservation. In some Grand Unified models (the theory suggesting the unification of the electroweak interaction with the strong one, Chap. 13), neutrinos have nonzero masses (although small) with a possible relation of the type $m_{\nu_e} : m_{\nu_\mu} : m_{\nu_\tau} = m_e^2 : m_\mu^2 : m_\tau^2$. The possibility of neutrino oscillations (in fact, $\nu \rightleftharpoons \bar{\nu}$) was first suggested by Bruno Pontecorvo in 1957. The possible transformation of a neutrino of a given flavor into a different flavor was only proposed later. As a consequence of this hypothesis, the neutrino should have a nonzero mass. Neutrino mixing and oscillations can be formally treated in the same manner as already seen for the $K^0 - \bar{K}^0$, $B^0 - \bar{B}^0$ systems.

It is not correct to speak of ν_e, ν_μ, ν_τ masses. The ν_e, ν_μ, ν_τ states are defined as *weak flavor eigenstates* which must be considered in particle decays (for example, in $\pi^+ \rightarrow \mu^+ \nu_\mu$) and in particle interactions (e.g., $\nu_\mu n \rightarrow \mu^- p$). For the neutrino propagation, we shall consider the *mass eigenstates* denoted as ν_1, ν_2, ν_3 . According to quantum mechanics, the flavor eigenstates, $|\nu_f\rangle$ ($f = e, \mu, \tau$), are linear combinations of mass eigenstates $|\nu_j\rangle$ ($j = 1, 2, 3$):

$$|\nu_f(t)\rangle = \sum_j U_{fj} |\nu_j(t)\rangle. \quad (12.37)$$

In vacuum, the mass eigenstates $|\nu_j\rangle$ propagate independently, that is,

$$|\nu_j(t)\rangle = e^{-E_j t} |\nu_j(0)\rangle. \quad (12.38)$$

For a given momentum, the eigenstates $|\nu_j\rangle$ propagate with different frequencies: in (12.38), the energies $E_j = \sqrt{p^2 + m_j^2}$ (in natural units) of the mass eigenstates are slightly different for ν_1, ν_2, ν_3 for nondegenerate massive neutrinos.

12.6.1 The Special Case of Oscillations Between Two Flavors

Let us consider the simplest case of only two neutrino flavors, for example, the pair² ν_μ, ν_τ . Each state is a linear combination of the two mass eigenstates ν_2, ν_3 . The flavor and mass eigenstates are related by a unitary transformation with one mixing angle θ , namely,

$$\begin{pmatrix} \nu_\mu \\ \nu_\tau \end{pmatrix} = \begin{pmatrix} \cos \theta & \sin \theta \\ -\sin \theta & \cos \theta \end{pmatrix} \begin{pmatrix} \nu_2 \\ \nu_3 \end{pmatrix}. \quad (12.39)$$

²The same formalism applies to ν_e, ν_μ or ν_e, ν_x , with $x = \mu, \tau$.

Then,

$$\begin{cases} |\nu_\mu\rangle = \cos\theta|\nu_2\rangle + \sin\theta|\nu_3\rangle \\ |\nu_\tau\rangle = -\sin\theta|\nu_2\rangle + \cos\theta|\nu_3\rangle \end{cases}. \quad (12.40)$$

The flavor eigenstates ν_μ, ν_τ are generated in decay processes (and can be observed when they interact); the propagation in vacuum is determined by the energies of the mass eigenstates (12.38), that is,

$$\begin{cases} |\nu_2(t)\rangle = e^{-iE_2t}|\nu_2(0)\rangle \\ |\nu_3(t)\rangle = e^{-iE_3t}|\nu_3(0)\rangle \end{cases}. \quad (12.41)$$

Consider the case in which, at $t = 0$, only ν_μ are present (produced, for instance, in charged pion decays), that is,

$$\begin{cases} |\nu_\mu(0)\rangle = \cos\theta|\nu_2(0)\rangle + \sin\theta|\nu_3(0)\rangle \\ |\nu_\tau(0)\rangle = -\sin\theta|\nu_2(0)\rangle + \cos\theta|\nu_3(0)\rangle = 0 \end{cases}. \quad (12.42)$$

From these relations, with simple algebra, one can derive

$$\begin{cases} |\nu_2(0)\rangle = \cos\theta|\nu_\mu(0)\rangle \\ |\nu_3(0)\rangle = \sin\theta|\nu_\mu(0)\rangle \end{cases}. \quad (12.43)$$

At any successive time t , from (12.40), one has

$$|\nu_\mu(t)\rangle = \cos\theta|\nu_2(t)\rangle + \sin\theta|\nu_3(t)\rangle. \quad (12.44)$$

Placing (12.41) into (12.44), one obtains

$$|\nu_\mu(t)\rangle = \cos\theta e^{-iE_2t}|\nu_2(0)\rangle + \sin\theta e^{-iE_3t}|\nu_3(0)\rangle, \quad (12.45)$$

and using (12.43), one finally gets

$$|\nu_\mu(t)\rangle = \cos^2\theta e^{-iE_2t}|\nu_\mu(0)\rangle + \sin^2\theta e^{-iE_3t}|\nu_\mu(0)\rangle. \quad (12.46)$$

The probability density is obtained by multiplying (12.46) by its complex conjugate, that is,

$$\begin{aligned} |\langle\nu_\mu(t)|\nu_\mu(t)\rangle| &= I_\mu^0\{\cos^4\theta + \sin^4\theta + \sin^2\theta\cos^2\theta[e^{i(E_3-E_2)t} + e^{-i(E_3-E_2)t}]\} \\ &= I_\mu^0\left\{1 - \sin^22\theta \cdot \sin^2\left[\frac{(E_3-E_2)t}{2}\right]\right\} \end{aligned} \quad (12.47)$$

where $I_\mu^0 = |\langle\nu_\mu(0)|\nu_\mu(0)\rangle| = 1$. Given the small neutrino mass ($m_j \ll E_j$), $E_j \simeq p + \frac{m_j^2}{2p}$. The momentum p is the same for the two mass eigenstates, and thus

$$E_3 - E_2 \simeq (m_3^2 - m_2^2)/2p \simeq \Delta m^2/2E \quad (12.48)$$

with $\Delta m^2 = (m_3^2 - m_2^2)$. Equation 12.47 represents the probability that the ν_μ remains a ν_μ at a given time t , that is, $|\langle \nu_\mu(t) | \nu_\mu(t) \rangle| = P(\nu_\mu \rightarrow \nu_\mu)$. The probability that the ν_μ transforms itself into a ν_τ is $P(\nu_\mu \rightarrow \nu_\tau)$. These two probabilities are

$$\begin{cases} P(\nu_\mu \rightarrow \nu_\mu) = 1 - \sin^2 2\theta \cdot \left[\sin^2 \left(\frac{E_3 - E_2}{2} \right) t \right] = 1 - \sin^2 2\theta \cdot \sin^2 \left(\pi \frac{L}{L_{osc}} \right) \\ P(\nu_\mu \rightarrow \nu_\tau) = 1 - P(\nu_\mu \rightarrow \nu_\mu) = \sin^2 2\theta \cdot \sin^2 \left(\pi \frac{L}{L_{osc}} \right) \end{cases} \quad (12.49)$$

where

$$L_{osc} = \frac{4\pi p}{\Delta m^2} \simeq \frac{4\pi E}{\Delta m^2} = 2.48[\text{km}] \frac{E[\text{GeV}]}{\Delta m^2[\text{eV}]^2}. \quad (12.50)$$

is the *neutrino oscillation length*, Δm^2 is expressed in eV², $L \simeq ct$ is the distance (in km) between the ν_μ production and the ν_μ (or equivalently the ν_τ) observation points; the neutrino energy E is in GeV. The factor 2.48 results from this choice of units. Thus in (12.49)

$$\left(\pi \frac{L}{L_{osc}} \right) = \left(1.27 \frac{\Delta m^2[\text{eV}]^2 L[\text{km}]}{E[\text{GeV}]} \right).$$

To observe the largest ν_μ disappearance (or ν_τ appearance) the argument of the sine must be equal to $\pi/2$. For $E \simeq 1$ GeV, $\Delta m \simeq 0.05$ eV, the distance between the observer and the neutrino production point must be $L \simeq 10^3$ km.

There are no theoretical estimates for θ ; the first guess was $\theta \simeq \theta_C$, where θ_C is the small Cabibbo angle. However, we shall see that neutrino oscillation experiments show that the angle is near maximum for the $\sin^2 2\theta$ function, i.e., $\theta \sim 45^\circ$.

12.6.2 Three Flavor Oscillations

In the case of three flavors, the mixing between flavor and mass eigenstates is described by the 3×3 unitary matrix (12.37). As for the mixing among quarks, the unitary matrix can be parameterized as (8.62b), which is reported here for simplicity³ as

³The neutrino mixing matrix differs from that of quarks since there are, in addition to a phase angle that would allow the CP -violation in the leptonic sector, two other phase angles. They have consequences if the neutrino is a Majorana particle, namely, if the neutrino is identical to its antiparticle. This problem is not described here but detailed explanations can be found in [P08].

Table 12.1 Experiments for neutrino oscillations. The columns report: the source of neutrinos; some of the most significant experiments; the section in the book where they are described; the neutrino flavour at the source; the mean path length from the source to the detector; the minimum value of Δm^2 which can be measured

Source	Experiments	See Sect.	Neutrino Type	\bar{E} (GeV)	L (km)	Δm_{\min}^2 (eV 2)
Reactor ¹	Chooz, ...	12.9	$\bar{\nu}_e$	10^{-3}	1	10^{-3}
Reactors	KamLand	12.7	$\bar{\nu}_e$	10^{-3}	100	10^{-5}
Accelerator	Chorus, Nomad	12.8.1	$\nu_\mu, \bar{\nu}_\mu$	1	1	~ 1
Accelerator	K2K, MINOS, Opera	12.8.1	$\nu_\mu, \bar{\nu}_\mu$	1	300–700	10^{-3}
Atmospheric ²	SK,Soudan	12.8	$\nu_{\mu,e}, \bar{\nu}_{\mu,e}$	1	$10-10^4$	$10^{-1}-10^{-4}$
Atmospheric ³	SK,MACRO	12.8	$\nu_\mu, \bar{\nu}_\mu$	10	10^2-10^4	$10^{-1}-10^{-3}$
Sun	SK,SNO,Gallex,...	12.7	ν_e	10^{-3}	10^8	10^{-11}

¹ Chooz and Palo Verde are concluded. Double Chooz, Daya Bay and Reno are in preparation. They are mainly devoted to measure the θ_{13} mixing angle.

² The neutrino flavour is detected from the contained event topology.

³ Measured by ν_μ -induced upgoing muons

$$U_{fj} = \begin{pmatrix} c_{12}c_{13} & s_{12}c_{13} & s_{13}e^{-i\delta} \\ -s_{12}c_{23} - c_{12}s_{23}s_{13}e^{i\delta} & c_{12}c_{23} - s_{12}s_{23}s_{13}e^{i\delta} & s_{23}c_{13} \\ s_{12}c_{23} - c_{12}s_{23}s_{13}e^{i\delta} & -c_{12}s_{23} - s_{12}c_{23}s_{13}e^{i\delta_{13}} + c_{23}c_{13} \end{pmatrix} \quad (12.51)$$

(the usual abbreviations, e.g., $s_{13} = \sin \theta_{13}$, are used). The numerical values of the matrix components were measured in various experiments. The possibility of CP -violation in the leptonic sector is introduced by a phase parameter, δ , which presently is unknown. The possibility of its future measurement depends on the value of s_{13} , which determines the CP -violation amplitude.

Convincing experimental evidence for neutrino oscillations exists in:

- *Atmospheric neutrinos* ($\nu_\mu \rightarrow \nu_\tau$), that is, neutrinos produced by the interaction of cosmic rays with the atmosphere;
- *Solar neutrinos*, i.e., electron neutrinos produced by nuclear reactions in the Sun;
- Muon neutrinos produced at accelerators, with detectors placed at $L \simeq 250$ km and $\simeq 735$ km;
- Electron antineutrinos from nuclear reactors, with $L \sim 180$ km.

The experimental results (see Table 12.1 for the minimum Δm^2 value that can be tested) discussed in the following sections can be treated with good approximation with the formalism of two flavor oscillations if one of the mass eigenvalues is much larger than the other two.

12.6.3 The Approximation for a Neutrino with Dominant Mass

The more general formulas for the probability of three flavor neutrino oscillations are rather complicated [12L01]. They are obtained from (12.37), with the matrix U

with three mixing angles and one complex phase presented in (12.51). The formulas can be greatly simplified if there is a *hierarchy* between the neutrino masses, for example,

$$m_3 \gg m_2 > m_1, \quad (12.52)$$

yielding to (see also Fig. 12.17)

$$|\Delta m_{13}^2| \simeq |\Delta m_{23}^2| \gg |\Delta m_{12}^2|. \quad (12.53)$$

In this situation, there are basically two characteristic oscillation lengths given by (12.50), and that involving $|\Delta m_{12}^2|$ ($L_{12} \simeq E/\Delta m_{12}^2$) is longer. In this case, there is a range of E and L values such that short fluctuations (i.e., those relating to $|\Delta m_{23}^2|$) are active, while the long oscillation have not yet developed. The probability of short oscillation can be approximated by

$$P(\nu_\alpha \rightarrow \nu_\beta) = 4|U_{\alpha 3}|^2 |U_{\beta 3}|^2 \sin^2\left(\frac{\Delta m_{13}^2}{4E} L\right). \quad (12.54)$$

This formula is similar to the two flavor oscillations (12.49), and the probability oscillates with a single frequency, related to the mass difference $|\Delta m_{13}^2| \simeq |\Delta m_{23}^2|$. The amplitude probabilities only depend on the elements of the third column of the mixing matrix U . Explicitly, one has

$$P(\nu_e \rightarrow \nu_\mu) = 4|U_{e 3}|^2 |U_{\mu 3}|^2 \sin^2\left(\frac{\Delta m_{13}^2}{4E} L\right) = s_{23}^2 \sin^2 2\theta_{13} \sin^2\left(\frac{\Delta m_{13}^2}{4E} L\right) \quad (12.55a)$$

$$P(\nu_e \rightarrow \nu_\tau) = 4|U_{e 3}|^2 |U_{\tau 3}|^2 \sin^2\left(\frac{\Delta m_{13}^2}{4E} L\right) = c_{23}^2 \sin^2 2\theta_{13} \sin^2\left(\frac{\Delta m_{13}^2}{4E} L\right) \quad (12.55b)$$

$$P(\nu_\mu \rightarrow \nu_\tau) = 4|U_{\mu 3}|^2 |U_{\tau 3}|^2 \sin^2\left(\frac{\Delta m_{13}^2}{4E} L\right) = c_{13}^4 \sin^2 2\theta_{23} \sin^2\left(\frac{\Delta m_{13}^2}{4E} L\right). \quad (12.55c)$$

As we shall see in the discussion of experimental data (Sect. 12.8), condition (12.53) is verified. Results from atmospheric neutrinos (*atm*) and solar neutrinos (\odot) demonstrated that $\Delta m_{atm}^2 \gg \Delta m_\odot^2$. In addition, the current experimental results provide a very small θ_{13} ($< 10^\circ$). Thus, in Eq. 12.55, the term $\sin^2 2\theta_{13} \sim 0$ and only the third equation is nonvanishing.

The situation described by (12.55c) corresponds to the atmospheric neutrino oscillations, where $|\Delta m_{13}^2| \simeq |\Delta m_{23}^2| \simeq \Delta m_{atm}^2$ and $\theta_{23} \simeq \theta_{atm}$. In the case

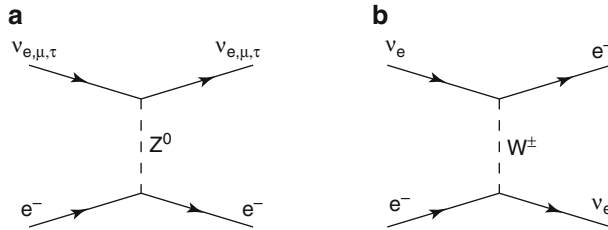


Fig. 12.10 Feynman diagrams for (a) the ν_e , ν_μ and ν_τ scattering on electrons through a neutral current weak interaction and (b) the charged current scattering of a ν_e on e^-

of atmospheric neutrinos, muon neutrinos oscillate into tau neutrinos, while the electron neutrinos are practically not affected by oscillations.

The other extreme case corresponds to the situation where $\frac{\Delta m_{13}^2}{4E}L \gg 1$ (always assuming $\Delta m_{13}^2 \simeq \Delta m_{23}^2$). This situation corresponds to the detection of electron neutrinos from a nuclear reactor (e.g., KamLAND); the short oscillations are active, and the quantity $x = (\Delta m_{13}^2 L / 4E) \simeq (\Delta m_{23}^2 L / 4E)$ is the argument of the $\sin^2(x)$ function. Because $x \gg 1$, $\sin^2(x)$ is rapidly oscillating, and only its average value is effective. In this case, long-type oscillations are observed, where the electron neutrino survival probability is given by

$$P(\nu_e \rightarrow \nu_e) \simeq c_{13}^4 P + s_{13}^4 \quad (12.56)$$

with

$$P = 1 - \sin^2 2\theta_{12} \sin^2 \left(\frac{\Delta m_{12}^2}{4E} L \right). \quad (12.57)$$

Because of the small value of θ_{13} in (12.56), $c_{13}^4 \simeq 1$, $s_{13}^4 \simeq 0$ and the electron neutrino oscillations can be described by the same formula used for two flavor oscillations.

Note that oscillations of electron neutrinos were first observed using solar neutrinos rather than reactor neutrinos. However, a complication is present for solar neutrinos since their propagation occurs not only in vacuum (on their way to the Earth), but also inside matter, that is, from the Sun core to the Sun surface.

12.6.4 Neutrino Oscillations in Matter

When neutrinos propagate in matter, the different behavior of ν_e with respect to ν_μ and ν_τ must be taken into account. For a full discussion, see [B89]. The Feynman diagrams with a Z^0 exchange are the same for ν_e , ν_μ and ν_τ ; the diagram with W^\pm exchange only exists for the ν_e (see Fig. 12.10). This different contribution to

the scattering amplitudes corresponds to a different *refraction index* of the ν_e with respect to ν_μ and ν_τ (MSW effect, from the names of the discoverers Mikheyev–Smirnov–Wolfenstein) [12M79]. Let us consider the case of two neutrinos, that is, ν_e and ν_μ . In dense matter, the mass eigenstates ν_1 , ν_2 are not related to the flavor eigenstates via the relations (12.40), but by linear combinations with coefficients that depend on the electron density ρ in matter. The effective mixing is modified by the presence of matter and, under certain conditions, a *resonant effect* can take place. For example, all the ν_e could transform in the ν_2 mass eigenstate. In this case, the ν_2 will continue to propagate as such, without further oscillations.

This certainly seems the case for electron neutrinos with MeV energies produced in the center of the Sun. Following the ν_e on their journey to the Earth, they first pass through 700,000 km of solar matter, then 150 million km into space. Near the Sun's core, the electron density is very high, but decreases by several orders of magnitude as the neutrinos reach the Sun's surface. Electron neutrinos produced by nuclear fusion reactions (see Sect. 14.10) slowly oscillate, while they are subject to charged and neutral current interactions. Because of the MSW effect, when they pass through a solar region with appropriate density, a resonant conversion ν_e into ν_2 occurs. The conversion probability depends on the neutrino energy and on the electron density in matter. Thus, a large fraction of ν_e is transformed into the mass eigenstate ν_2 . These neutrinos travel in the (almost) vacuum space between the Sun surface and the detectors on Earth without any further oscillations.

On Earth, the ν_2 interact with a certain probability as ν_e , ν_μ , ν_τ ; the probability is determined by the *composition* of ν_2 in terms of flavor eigenstates (we will see that this probability is around 33% for each state). CC interactions of ν_μ and ν_τ cannot be observed by ground detectors because they do not have enough energy to produce the muon or tau rest mass.

12.7 Neutrinos from the Sun and Oscillation Studies

According to the Standard Solar Model, the energy emitted is due to a series of thermonuclear reactions that occur in the center of the Sun. This “thermonuclear reactor” is much smaller than the size of the star. The emitted photons (with MeV energies) undergo a large number of collisions and take a very long time to reach the Sun's surface (~ 0.2 million years). The visible light emitted by the Sun originates from a well defined surface, the solar photosphere, which defines the visible size of the Sun. A large fraction of the energy is emitted in the form of neutrinos produced by the reactions illustrated in Fig. 12.11a. The corresponding energy spectrum is shown in Fig. 12.11b. Most of the neutrinos are produced by the $pp \rightarrow de^+\nu_e$ reaction, with energies below 0.42 MeV. The few higher energy neutrinos (up to 14 MeV) come from the 8B decay. Monochromatic neutrinos are also produced, for instance, in the 7Be decay.

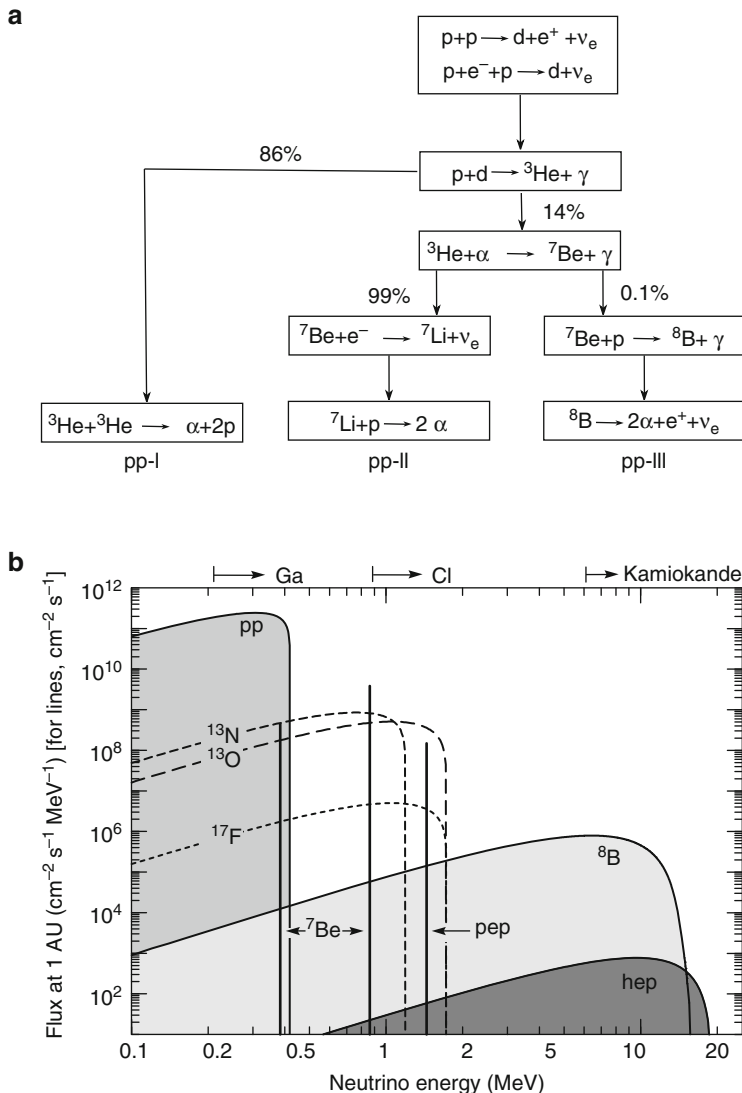


Fig. 12.11 (a) The main chain of nuclear reactions that occur in the center of the Sun. (b) The energy spectrum of solar neutrinos arriving on Earth: the solid lines indicate the neutrinos coming from the most important reactions of the *pp* cycle, the dashed and dotted lines indicate the neutrinos from the CNO cycle, Sect. 14.10

Most of the dedicated experiments measure the ν_e flux. The first experiment, designed by R. Davis (Nobel laureate in 2002), began to produce data in the early 1970s. The measured solar neutrino flux was lower than that expected from the knowledge of astrophysics and nuclear properties of the Sun. This observed

deficit had two possible interpretations. The first possibility was an astrophysical overestimate of the solar neutrino production. The second was that on the way from the center of the Sun to the Earth, transitions had occurred between the solar ν_e to different flavor neutrinos (ν_μ , ν_τ) that could not be observed in the experiment. Over the years, the second interpretation of the measured deficit was found to be correct.

The Davis experiment was a radiochemical underground experiment located in the Homestake mine in South Dakota. A large tank containing 680 t of organic liquid (perchloroethylene) was used as a target. The nuclear transmutation induced by solar neutrinos was $\nu_e + {}^{37}\text{Cl} \rightarrow {}^{37}\text{Ar} + e^-$. The radioactive ${}^{37}\text{Ar}$ is a gas which was extracted from the target, purified and counted. For this reason, the experiment was denoted as “radiochemical.” The reaction has an energy threshold of 814 keV. Therefore, only neutrinos from the ${}^8\text{B}$ decay and from the electron capture in ${}^7\text{Be}$ can be detected (see Fig. 12.11). The experimental results with the ${}^{37}\text{Cl}$ showed a ν_e flux equal to about one third of that predicted by the Standard Solar Model. This was the beginning of the solar neutrino problem.

In the early 1990s, two different radiochemical experiments (GALLEX at Gran Sasso in Italy, and SAGE in Russia) started operation: both used the ${}^{71}\text{Ga}$ and were sensitive to neutrinos with energies above 233 keV, through charged current interaction $\nu_e + {}^{71}\text{Ga} \rightarrow {}^{71}\text{Ge} + e^-$. The ${}^{71}\text{Ge}$ was extracted from the liquid target in the gaseous form GeCl_4 , chemically purified, and converted to GeH_4 gas for counting. The detection of solar neutrinos with $E_\nu > 233$ keV includes the neutrinos produced in the $p + p \rightarrow d + e^+ + \nu_e$ reaction. The results showed without a doubt that in the Sun’s core, a “fusion power plant” is active. These two radiochemical experiments also reported a significant deficit of solar neutrinos.

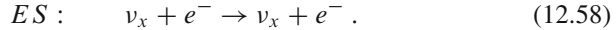
A different detection strategy which confirmed the deficit was used by the Kamiokande experiment (and after by SuperKamiokande) in Japan: neutrinos interacting via elastic scattering on electrons $\nu_x e^- \rightarrow \nu_x e^-$ were detected in a large water tank. Their energy threshold was about 7 MeV, corresponding to the neutrinos coming from the ${}^8\text{B}$ (Fig. 12.11).

The combined results indicate that there are “missing” neutrinos from the Sun, when data are compared to theoretical models. However, not one of the experiments mentioned above was able to conclusively prove that the lack of solar electron neutrinos was due to the oscillation phenomenon. They were all ν_e *disappearance experiments*. Neutrino *appearance experiments* should be able to observe neutrinos of flavor different from ν_e . The ν_μ (or ν_τ) appearance through charged current (CC) interactions produces the corresponding charged lepton. Nevertheless, the muon (or tau) rest mass is much larger than the energy corresponding to solar neutrinos, and the CC reaction cannot occur. The problem was solved by the SNO experiment, which measured the fraction of $\nu_\mu + \nu_\tau$ in the neutrino flux from the Sun using their neutral current (NC) interactions.

The SNO experiment. The Sudbury Neutrino Observatory (SNO) in Canada recorded data from 1999 until 2006. It was able to detect Cherenkov light emitted by charged particles crossing the detector, filled with 1,000 t of heavy water (D_2O) and

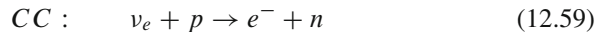
surrounded by 1,500 t of normal water used for screening purpose. The reactions that occur in normal water are:

1. The elastic scattering on electron (ES), as in SuperKamiokande:



The ES occurs through a Z^0 exchange for all neutrino flavors, and through a W^\pm exchange in the case of ν_e (see Fig. 12.10). The ES is sensitive to neutrinos of any flavor but the cross-section for nonelectronic neutrinos is largely reduced: $\sigma(\nu_{\mu,\tau}e \rightarrow \nu_{\mu,\tau}e) \simeq \sigma(\nu_e e \rightarrow \nu_e e)/6.5$. In practice, the ES is dominated by ν_e interactions and the measured solar neutrino flux is $\phi(\nu_e) + [\phi(\nu_{\mu,\tau})/6.5]$

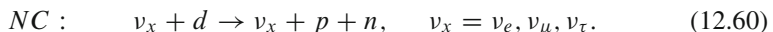
2. The ν_e CC interaction on proton (inverse β -decay), see Sect. 8.6.1:



which only occurs for ν_e through a W^\pm exchange.

In addition, in the heavy water, the following NC reaction also take place:

3. Deuterium dissociation through a Z^0 exchange:



A ~ 2 MeV photon is emitted as a result of the d dissociation in $p + n$. A salt which increases the probability of neutron capture was dissolved in the detector (as for the Cowans and Raines experiment, see Sect. 8.5). The 8 MeV γ emitted after the neutron capture produces an e^+e^- pair, which emits Cherenkov light that can be detected.

In all cases, the neutrino energy is of the order of a few MeV; also for SNO, the neutrino flux from the reaction involving the 8B is measured. The total incident neutrino flux $\nu_e + \nu_\mu + \nu_\tau$ was obtained through the reactions (12.60). This number is independent from any kind of oscillations. The ν_e flux was measured using the reaction (12.59). SNO reported for the ratio is $R = [\phi(\nu_e)/(\phi_{tot} = \phi(\nu_e + \nu_\mu + \nu_\tau))]$, that is,

$$R = \frac{\phi(\nu_e)}{\phi(\nu_e + \nu_\mu + \nu_\tau)} = 0.340 \pm 0.023_{stat} \pm 0.030_{syst} . \quad (12.61)$$

This result clearly indicates that $\phi(\nu_\mu + \nu_\tau)$ is nonzero, providing a definitive proof that some of the solar electron neutrinos, on their way to the Earth, changed flavor. On the other hand, the *total* number of solar neutrinos is conserved. The Standard Solar Model [B89] provides a neutrino flux from the Sun due to the reaction of 8B :

$$\phi_{tot}(\nu)^{SSM} = 5.49^{+0.95}_{-0.89} \times 10^6 \text{ cm}^{-2}\text{s}^{-1} \quad (12.62)$$

(to be compared with $6.5 \times 10^{10} \text{ cm}^{-2}\text{s}^{-1}$ due to the sum of all the nuclear reactions inside the Sun). The total number of neutrinos measured by SNO via the reaction (12.60) is

$$\phi(\nu_e + \nu_\mu + \nu_\tau)^{SNO} = 4.94 \pm 0.21_{\text{stat}} \pm 0.36_{\text{syst}} \times 10^6 \text{ cm}^{-2}\text{s}^{-1}. \quad (12.63)$$

The results from all the experiments mentioned above indicate that the flux of electron neutrinos is reduced by a factor from 2/3 to 1/2. This is due to the fact that in addition to the neutrino oscillation in vacuum from the Sun's surface to the Earth, the matter effect plays a significant role for high energy solar neutrinos, like those from ${}^8\text{B}$ decay, with energies larger than $\sim 8 \text{ MeV}$.

The KamLAND and Borexino experiments. The results obtained using solar neutrinos were confirmed by the KamLAND experiment in Japan. The detector had 1,000 t of liquid scintillator, and was located in the same Kamioka mine as the SuperKamiokande experiment. The KamLAND was a *long baseline experiment* (see Sect. 12.8.1) detecting $\bar{\nu}_e$ produced by a large number of nuclear reactors in the central region of Japan (the experiment was located, on average, 180 km from the reactors). Most of the electric power in Japan (more than 60 GW) is generated by nuclear power plants. Nuclear reactors produce $\bar{\nu}_e$ in the β^- decay of neutron-rich fission fragments. The flux and the energy spectrum of antineutrinos depend on the reactor power and on the isotopic composition of the fissile material. KamLAND was a $\bar{\nu}_e$ disappearance experiment which studied the flux and the energy spectrum of positrons produced in the interaction. Their results in terms of neutrino oscillation parameters (in this case, the $\bar{\nu}_e$ oscillations occur almost in vacuum) are in good agreement with the results obtained using solar neutrinos (Fig. 12.12).

The operation of the Borexino experiment at the Gran Sasso Laboratory in Italy began in 2007. The Borexino detector detects the monochromatic neutrinos ($E_\nu = 0.862 \text{ MeV}$) from the electron capture of ${}^7\text{Be}$ in the Sun. It uses liquid scintillator and the detection of neutrinos is performed through the elastic scattering (ES) on electrons. ${}^7\text{Be}$ neutrinos leave the Sun with an energy of 0.862 MeV. For such low energies, the matter effect is almost negligible, and the oscillation probability of these neutrinos is described, as in vacuum, by Eq. 12.49 (replacing μ with e). In practice, it is expected that for ${}^7\text{Be}$ neutrinos, $P(\nu_e \rightarrow \nu_e) = 0.6$. The first Borexino data [12B08], taken with a 100 ton target, reported $47 \pm 7_{\text{stat}} \pm 12_{\text{syst}}$ counts per day. Assuming neutrino oscillations with the reduction factor mentioned above, 49 ± 4 counts per day are expected; this number is in good agreement with the measured value (even if the experimental uncertainties are still large).

Discussion of the Solar Neutrino Results. The formula for neutrino oscillations in vacuum (12.49) depends on two unknown parameters (Δm^2 and θ), which, in principle, can be zero (in this case, there are no oscillations). The formula depends on two other parameters (the distance L between the neutrino production and observation points and the neutrino energy) which can be estimated or measured by experiments. Since the characteristics of solar neutrino experiments and of

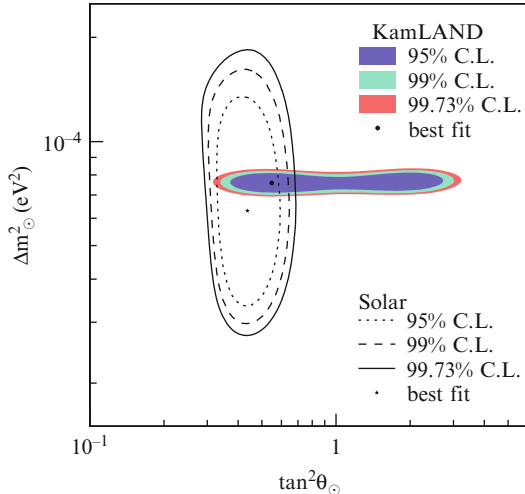


Fig. 12.12 Compendium of the current situation for the oscillations of solar neutrinos. The contour plots are shown in the parameter space $(\tan^2 \theta_\odot, \Delta m_\odot^2)$ where the x-axis is the square of the tangent of the mixing angle and the y-axis is the mass difference squared. The combination of solar neutrino experiments and the KamLAND results [P08] are shown separately

KamLAND meet those for the *neutrino with a dominant mass* discussed above, the formula that describes the oscillations is (12.57), with $\Delta m_{12}^2 = \Delta m_\odot^2$ and $\theta_{12} = \theta_\odot$. The experimental results presented as contour plots in the $(\tan^2 \theta_\odot, \Delta m_\odot^2)$ parameters space are shown in Fig. 12.12. The results of the combination of solar neutrino experiments and of KamLAND are shown separately. There is an overlap region allowed by all experiments. The combined analyses provide the preferred values (point indicated as *best fit* in the figure)

$$\Delta m_\odot^2 = (7.59 \pm 0.21) \times 10^{-5} \text{ eV}^2 \quad ; \quad \tan^2 \theta_\odot = 0.47 \pm 0.06. \quad (12.64)$$

12.8 Atmospheric ν_μ Oscillations and Experiments

Cosmic rays [G90] are protons and heavier atomic nuclei coming from outer space and constantly bombarding the Earth's upper atmosphere where they interact, producing secondary particles. A fraction of these secondary particles decay, giving rise to ν_μ and ν_e in a ratio of about two to one (see Fig. 12.13a). These *atmospheric neutrinos* have energies $> 100 \text{ MeV}$ and are produced in the atmosphere 10–20 km above the ground. Below 100 TeV, the atmospheric ν -flux is almost unaffected when passing through the Earth. Experiments can detect both upward- and downward-going neutrino-induced leptons [12C98] (neutrino from *above* and *below* in the following). At the end of the 1980s, the IMB and Kamiokande experiments found abnormalities in the ν_μ/ν_e ratio, while other smaller size experiments found no

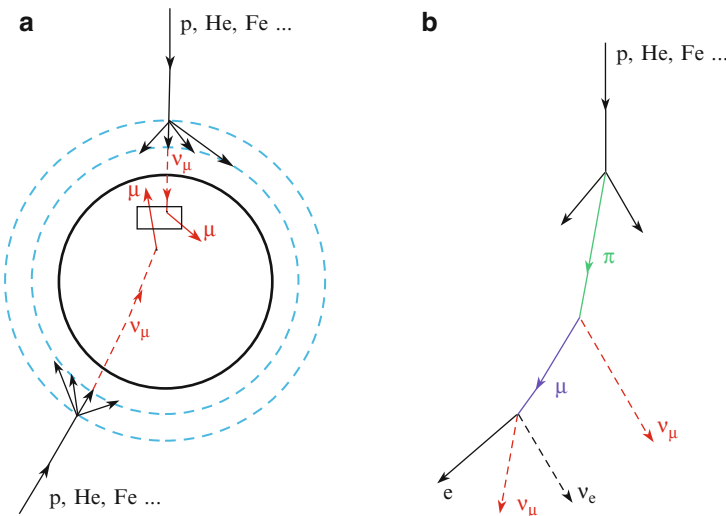


Fig. 12.13 Atmospheric neutrinos. Cosmic rays interact in the upper atmosphere, producing particle showers. Some decay of these secondary particles produces ν_μ and ν_e . The neutrinos originate from an atmospheric layer of 10–20 km thickness. A large underground detector can detect neutrinos coming from above. These downward-going neutrinos have traveled tens of kilometers and had no “time” to oscillate. Instead, neutrinos coming from the other hemisphere (upward-going neutrinos) have traveled $L \simeq 10^4$ km and have oscillated. Only the CC ν_μ interactions are shown in (a). Interactions of $\nu_e \rightarrow e$ inside the detectors can also be measured

deviations. In 1995, the MACRO experiment published experimental results on a deficit of ν_μ from below.

In 1998, SuperKamiokande (SK) [12F98], MACRO [12A98] and Soudan 2 [12S98] presented new results with definitive indications for oscillations. These observations included the number of muon neutrinos from different directions (i.e., different values of the neutrino path length L); SK and Soudan 2 also measured the ratio between the number of ν_μ and ν_e . The number of electron neutrinos was roughly in agreement with the prediction; the number of muon neutrinos coming from below was lower, while the number of ν_μ from above was in agreement with the expectations.

The oscillations between two neutrino flavor eigenstates (12.49) indicate that the probability depends on the ratio $L/\langle E_\nu \rangle$, where L is the distance between the neutrino production and observation points (i.e., $L \sim 10$ km for neutrinos coming from above, $L \sim 10^4$ km for neutrinos coming from below). The energy E_ν of a single neutrino cannot be measured. Therefore, one uses an average energy, $\langle E_\nu \rangle$, obtained from Monte Carlo simulations for a certain topology of detected neutrinos. CC events in which the produced particles remain entirely contained in the detector have $\langle E_\nu \rangle \sim 0.5$ GeV; partially contained events (typically, a few GeV muon exits the detector) have $\langle E_\nu \rangle \sim 5$ GeV. The events in which the neutrino interacts below the detector producing an upward through-going muon have $\langle E_\nu \rangle \sim 50$ GeV.

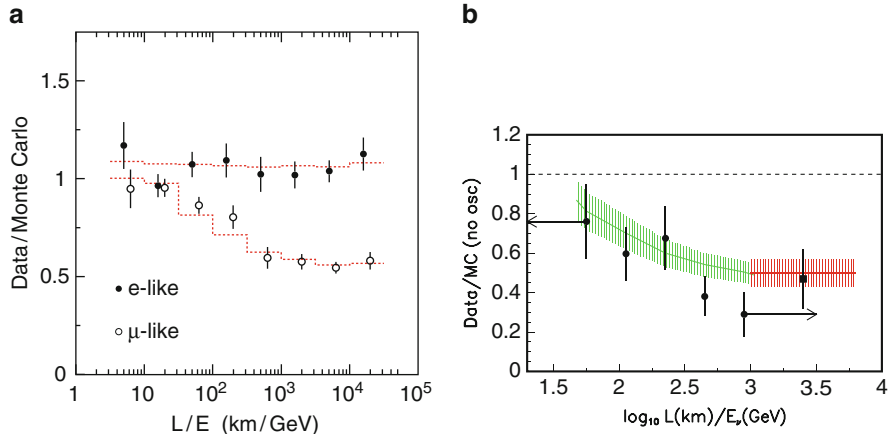


Fig. 12.14 (a) Ratio between the numbers of “e-like” (full circles) and “ μ -like” (open circles) events measured and predicted by Monte Carlo (MC) in the absence of oscillation, as a function of $L/\langle E_\nu \rangle$ in the SuperKamiokande experiment. The dotted lines represent the Monte Carlo (MC) predictions assuming $\nu_\mu \rightarrow \nu_\tau$ oscillations. (b) Ratio R of the numbers of ν_μ -induced events, measured and predicted by Monte Carlo with (line with error band) and without (dashed line at $R = 1$) neutrino oscillations in MACRO. The points with error bars represent data

In agreement with the oscillation hypothesis, the ratio of the measured and predicted numbers of ν_μ events decreases when $L/\langle E_\nu \rangle$ increases (see Fig. 12.14). It can be deduced that during the journey through the Earth, a fraction of ν_μ oscillates into neutrinos of another type.

As for solar neutrinos, atmospheric neutrino measurements provide information on the mass difference of neutrinos involved in the oscillations. These measurements are presented in Fig. 12.14. For the ν_e flavor (see Fig. 12.14a), the results are compatible with the no-oscillation hypothesis and one concludes that the ν_e did not oscillated. The results obtained for the ν_μ and ν_τ flavors instead show a clear deficit with respect to the no-oscillation hypothesis. The ν_μ and ν_τ must therefore have oscillated. Moreover, since $\Delta m_{atm}^2 \gg \Delta m_{23}^2$, Eq. 12.55 are still valid.

Information on $\Delta m_{23}^2 = \Delta m_{atm}^2$ and on the mixing angle $\theta_{23} = \theta_{atm}$ were obtained by the MACRO, Soudan 2 and SK experiments. The corresponding parameter space allowed for neutrino oscillations is shown in Fig. 12.15. The data indicate that the preferred values correspond to a mass difference $\Delta m_{atm}^2 = 0.0024 \text{ eV}^2$ and to a maximal mixing $\sin^2 2\theta_{atm} = 1$.

The **SuperKamiokande** (SK) experiment is a large cylindrical detector containing 50,000 t of water. The detector is divided into two regions; in the inner region, 11,200 photomultipliers (PMT), 20 inches (50.8 cm) in diameter, detect faint flashes of light produced by the Cherenkov effect from electrically charged particles passing through. The external region offers a shielded

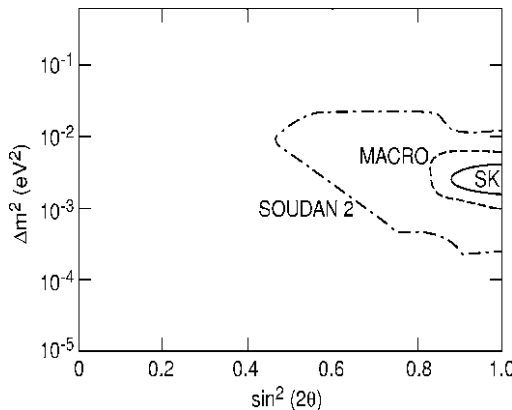


Fig. 12.15 Soudan2, MACRO and SK contour plots of the regions compatible with atmospheric neutrino oscillations in the ($\sin^2 2\theta_{atm}$, Δm_{atm}^2) parameter space

volume for cosmic rays and is used for anticoincidence. The fiducial detector mass is 22,500 t. SuperKamiokande is located 1,000 m underground in the Kamioka mine in Japan. As mentioned, the experiment also measured solar neutrinos. In 2001, an accident destroyed more than half of the PMTs. SK came back into operation in 2003 using about 5,000 PMTs, with a slightly lower energy resolution. Now (2011), it is once again fully efficient.

MACRO was a large apparatus ($12 \text{ m} \times 9.3 \text{ m} \times 76.6 \text{ m}$) in the Gran Sasso underground laboratory in Italy. It had a modular structure of six modules of $12 \times 12 \times 9.4 \text{ m}^3$ and took data from 1994 to 2000. The bottom part contained layers of limited streamer tubes (LST) interleaved with passive material plus two layers of liquid scintillator detectors and one plane of nuclear track detectors. The top part of the apparatus was empty and had a “roof” with four horizontal planes of LST and another liquid scintillator layer. Vertically, the apparatus was surrounded by a liquid scintillator plane and six lateral planes of LST.

12.8.1 Long Baseline Experiments

Long baseline high energy experiments are needed to probe, with well-controlled ν_μ beams, the small mass difference $\Delta m_{23}^2 \simeq 2 \times 10^{-3} \text{ eV}^2$ obtained with atmospheric neutrinos. To achieve this goal, typical values of $L \sim 1,000 \text{ km}$ and $E_\nu \sim 1 \text{ GeV}$ are needed.

Before the discovery of neutrino oscillations in solar and atmospheric neutrinos, two *short baseline experiments* were carried out at CERN: CHORUS and NOMAD. These two detectors were exposed to a high-energy ν_μ beam, and had $L \sim 1$ km. Their goal was to search for neutrino oscillations with $\Delta m^2 \sim 1$ eV, by performing disappearance and appearance measurements. The results were null, because they were designed to explore a range of Δm^2 values that Nature had not chosen.

Following the results of MACRO, SK and Soudan2, several *long baseline* experiments became operational. In Japan, the K2K (KEK to Kamioka) neutrino experiment took data from 1999 to 2004: muon neutrinos were produced at the 12 GeV protosynchrotron at KEK, and were detected after a 250 km path by the SuperKamiokande detector. In America, the MINOS experiment uses an intense ν_μ beam which is sent from Fermilab's Main Injector to the MINOS detector in the Soudan mine (Minnesota), located about 730 km away. The results of the two experiments are in perfect agreement with the underground measurements of atmospheric neutrinos. Both MINOS and K2K measure the neutrino-induced muon energy spectrum, confirming a distortion consistent with what is expected assuming neutrino oscillations.

Since 2008, the *long baseline CERN to Gran Sasso* project (CNGS) exploits the high-intensity and high-energy ν_μ beam produced at the CERN SPS and directed to the Gran Sasso Laboratory. The neutrino energy is fairly well-determined and the distance is $L \simeq 730$ km. At the Gran Sasso underground laboratory, the OPERA experiment [12A10] measures the ν_μ and (possibly) the ν_τ appearance. The peculiarity of the CNGS project is the possibility to measure the *appearance* of ν_τ in a ν_μ pure beam, removing any alternative (or exotic) hypothesis different from oscillations in ν_τ for atmospheric neutrinos.

OPERA is a hybrid, high-precision tracking detector that uses passive nuclear emulsions and electronic devices. The detectors are distributed inside 1.3 kton of passive material, needed for a sufficient neutrino interaction rate. Each cell consists of a thin sheet of lead (1 mm thick), alternating with a pair of emulsion layers, each of 44 μm thickness. The emulsions are glued on opposite sides of a plastic support of 200 μm thickness. The basic element, called a brick, consists of 56 cells. Each brick has $(10.2 \times 12.7)\text{ cm}^2$ area and 7.5 cm thickness, followed by two scintillator planes acting as an electronic tracker. The scintillators reconstruct the interaction vertex of the muon neutrino with a ~ 1 cm accuracy. This is sufficient to locate the brick where the interaction took place. The experiment is organized in two supermodules for a total of about 150,000 bricks. Each supermodule is followed by a muon spectrometer, drift tubes and resistive plate chambers. The spectrometer identifies muons, measuring the momentum and the sign of the charge.

The τ^- search is carried out both in the leptonic decay channels ($\tau^- \rightarrow e^- + \nu_\tau + \bar{\nu}_e$), ($\tau^- \rightarrow \mu^- + \nu_\tau + \bar{\nu}_\mu$) and in the hadronic channel

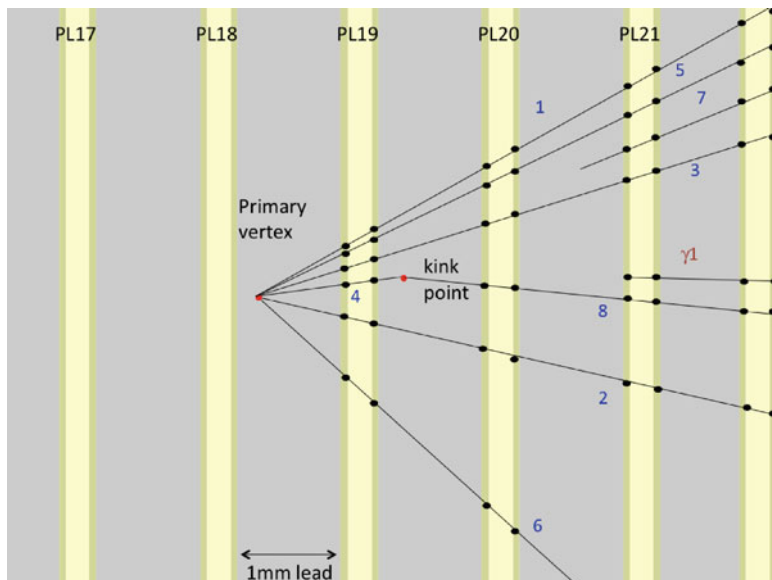


Fig. 12.16 Display of the OPERA τ^- candidate event [12A10]. At the interaction (primary) vertex, one has the reaction $\nu_\tau + N \rightarrow \tau^- + 5$ charged tracks. The τ^- (track 4) decays after a ~ 1 mm flight path, giving rise to a visible kink

$(\tau^- \rightarrow \pi^- + \nu_\tau)$. Hadrons can also be produced in ν_μ interactions. Hadrons containing charmed quarks, for example, the Λ_c^+, D^+ , are an important background source. The lifetime and the kinematics of the decay of these particles are similar to those of τ^- decay. However, the presence of a muon in these hadronic events is a clear signature that a CC ν_μ interaction took place; in this case, the event is not considered as a ν_τ candidate. Spectrometers are needed to establish the presence and the electric charge of the muon: a μ^+ arises from the decay of a charmed particle, a μ^- from the τ^- decay. Assuming $\Delta m_{23}^2 = 2.5 \times 10^{-3} \text{ eV}^2$ and $\sin^2 2\theta_{23} = 1$, 11 τ events are expected within five years with an estimated background of 0.5 event. In July of 2010, the OPERA Collaboration presented the first event candidate of a ν_τ appearance in a ν_μ beam. Particle physics is constantly evolving (see Fig. 12.16).

12.9 Effects of Neutrino Oscillations

The fact that neutrinos have mass, although small, is important and requires changes in the Standard Model of the Microcosm. With three neutrino mass eigenstates, ν_1, ν_2, ν_3 , there are three mass differences Δm_{ij}^2 related by

$$\Delta m_{23}^2 + \Delta m_{12}^2 + \Delta m_{31}^2 = 0. \quad (12.65)$$

Current measurements have identified two of the three mass differences: Δm_\odot^2 in the case of solar neutrinos (and KamLAND) (see Fig. 12.12), and Δm_{atm}^2 in the case of atmospheric neutrinos (and K2K, MINOS), (see Fig. 12.15). The experiments cannot indicate whether the two mass eigenstates which propagate from the Sun (whose masses differ by Δm_\odot^2) are *above* or *below* with respect to Δm_{atm}^2 (in Fig. 12.17, they are assumed to be *below*). The two possibilities are sometimes referred to as *normal hierarchy* or *inverted hierarchy*. The ability to discriminate between the two options could be solved with a beam of neutrinos from accelerators passing through a large quantity of matter. In Fig. 12.17, the various neutrino flavor content for each mass eigenstate are shown ($|\langle v_f | v_i \rangle|^2 = |U_{fi}|^2$). For simplicity, the figure ignores the small (and unknown) proportion of v_e in v_3 .

The v_e fraction in v_3 corresponds to $|U_{e3}|^2 = |U_{13}|^2 = s_{13}^2$ in the (12.51) matrix. This quantity is currently only bounded by the data as $|U_{e3}|^2 < 0.032$. A future precision measurement of this quantity is crucial: in the U matrix (12.51), the phase δ can be the origin for *CP*-violation in neutrino oscillations. This quantity enters in the matrix U only combined with s_{13} . The possible discovery of such violation is a very hard task from the experimental point of view.

Since s_{13} is small ($\theta_{13} < 10^\circ$), the approximation of neutrino with a dominant mass (Sect. 12.6.2) implies that the mixing angle measured with the disappearance of atmospheric neutrinos θ_{atm} corresponds to $\theta_{23} = 45^\circ \pm 8^\circ$, while that measured with the disappearance of solar neutrinos $\theta_\odot \simeq \theta_{12} = 34.5^\circ \pm 1.7^\circ$. The very large values of θ_{12}, θ_{23} show that the mixing of leptons has a very different behavior from that of quarks, where all mixing angles in the CKM matrix are small.

One of the most important quantities to be measured with precision is θ_{13} , which determines the fraction of v_e in v_3 . An experiment able to measure this angle must have $L/E \sim O(10^3 \text{ km/GeV})$, and must exploit v_e . Proposals were made for

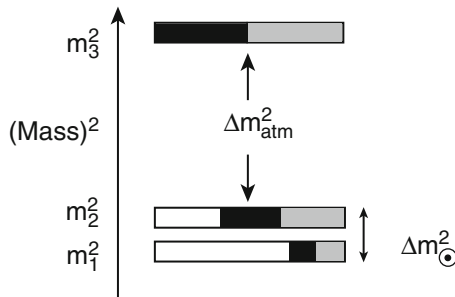


Fig. 12.17 Mass spectrum of the three neutrinos v_1, v_2, v_3 (from bottom to top), assuming $m_{v_3} > m_{v_2} > m_{v_1}$. Since the weak interaction eigenstates v_e, v_μ, v_τ are a linear combination of mass eigenstates, experiments can determine the v_e, v_μ, v_τ percentage in v_1, v_2, v_3 . This percentage is represented by shadings in the drawing. The v_3 is 50% v_μ (in black) e 50% v_τ (gray). The v_2 is about 1/3 v_e (white), 1/3 v_μ , 1/3 v_τ . Finally, the v_e dominate in the v_1 [P08]

(anti)electron neutrinos from reactors, with $L \sim 1$ km, and the study of possible $\nu_\mu \rightarrow \nu_e$ with L equal to hundreds of km (experiments Double Chooz, Reno, Daya Bay). If θ_{13} is not too small, the CP -violation in neutrinos could be studied through the difference between $P(\nu_\alpha \rightarrow \nu_\beta) - P(\bar{\nu}_\alpha \rightarrow \bar{\nu}_\beta)$. This corresponds to different oscillation behavior for neutrino and antineutrino beams. The experiment would require a super intense (but conventional, Sect. 8.7) beam of neutrinos (and antineutrinos).

The last remark is that neutrino oscillations are sensitive to the differences *between neutrino mass eigenstates*, but not to the *neutrino masses*. With three families and the hierarchy shown in Fig. 12.17 (or the reverse one), the mass of the heaviest of the three mass eigenstates is equal to $\sqrt{\Delta m_{atm}^2} \simeq 0.04$ eV. In this case, neutrinos which are so abundant in the Universe, have masses that play a marginal role for the “missing mass” (see Chap. 13). However, it may well be that the three neutrinos have average mass relatively higher, with small mass differences between eigenstates. In this case, their mass would play an important role in the Universe. Cosmology put an upper limit to neutrino masses, with a range depending on assumptions of different cosmological models, that is,

$$\sum_i m_i < (0.17 - 2.0)\text{eV}. \quad (12.66)$$

The asymmetry between baryons and antibaryons in the Universe could not have developed without some CP -violation in the early stages of the Universe evolution (which we describe in the next chapter). The only known source of CP -violation (in the quark mixing) is not sufficient to explain the observations. Thus, a CP -violation in the leptonic sector could be responsible for the observed matter/antimatter asymmetry, and this makes the study of neutrino oscillations an important connection between the microcosm and the macrocosm.

Chapter 13

Microcosm and Macrocosm

The “*Standard Model*” (SM) of the microcosm, the model of strong and electroweak interactions, is a gauge theory in which the fundamental fermions are leptons and quarks; it is based on the $SU(3)_C \times \{SU(2)_L \times U(1)_Y\}$ symmetry group. For energies below ~ 100 GeV, the $\{SU(2)_L \times U(1)_Y\}$ symmetry is spontaneously broken through the Higgs mechanism, and the three weak vector bosons (W^+, W^-, Z^0) acquire mass. The mediators of the strong interaction (eight gluons) and that of the electromagnetic interaction (the photon) remain massless.

The predictions of the SM have been verified with great precision, particularly at LEP (see Chap. 9). The SM is an excellent description of the phenomena of the microcosm (at least until $\sqrt{s} \simeq$ a few hundred GeV), although an essential element (the Higgs boson) remains to be discovered and studied.

There are many reasons, however, to believe that the SM is incomplete and represents a valid theory at relatively low energies:

1. The SM has many free parameters not derived from the theory (the masses of leptons, quarks and gauge bosons; the mass of the Higgs boson; the coupling constants; ...).
2. The three family structure remains unexplained.
3. In the same family, there are two leptons and two quarks without any real justification, even if this parallelism gives rise to the cancellation of divergences.
4. It does not contain gravity.
5. There are several unresolved “aesthetic” mathematics and physics problems. For example, the electric charge of the fundamental fermions and bosons is quantized in multiples of $1/3e$, without a deeper justification.
6. There is the *hierarchy* problem. The scale of a possible unification with gravity is the order of 10^{19} GeV. One wonders why the masses of vector bosons (about 100 GeV) can be much smaller.
7. The matter-antimatter asymmetry observed in the Universe is not really justified by the CP violation allowed within the SM.

For these reasons, more comprehensive models that contain the SM, in the low energy limit, were sought. Some of these models consider quarks and leptons as

objects made of more elementary particles (*composite models*); in some models, the Higgs and the W^\pm, Z^0 bosons are also regarded as composite; other models are based on more complete symmetries, for example, the *supersymmetry*, or attempting a true unification of electroweak and strong interactions in terms of a single symmetry group (*Grand Unified Theories, GUTs*). Finally, some models are even trying to include gravity (*supergravity, SUGRA*). In the following, we will be briefly discuss, in a simplified and qualitative way, some of these models.

The natural energy scale in most models (supersymmetry, composite models) is the TeV, while it is much higher in others ($\sim 10^{15}$ GeV for GUTs and $\sim 10^{19}$ GeV for Supergravity). There may also be intermediate scales of the order of 10^{10} eV. Research related to supersymmetric particles refer to the TeV scale, which are accessible with the LHC. Energies associated with the GUT theories cannot be reached with accelerators on Earth. Therefore, “relic” particles produced in the early moments of the Universe (e.g., magnetic monopoles) as well as rare phenomena such as proton decay should be searched for.

In the past, some connections between the microcosm and macrocosm have been highlighted, though only recently were such connections understood and was their importance fully appreciated. In general, our increasing knowledge of the submicroscopic phenomena allows us to better understand the early Universe, even if sometimes the opposite occurred. The most important connection is that needed to understand what happened in the early Universe, just after the Big Bang. When the Universe was very small, it could be considered as a hot gas of highly energetic particles. As the Universe expanded (in four dimensions), it cooled down (the average energy of its constituents decreased) and it passed through several phase transitions where the nature of the particles involved in the “gas of the Universe” varied [W08].

Unified theories of fundamental interactions have been developed in the context of particle physics, and then applied to describe the evolution of the Universe after the Big Bang. For subnuclear physicists, the first moments of the Universe represent the equivalent of a limitless energy accelerator! Collisions at LEP have reproduced situations that were typical, some 10^{-10} – 10^{-9} s after the Big Bang, while the collisions studied at the LHC ($\sqrt{s} = 14$ TeV) correspond to typical situations of about 10^{-12} – 10^{-11} s after the Big Bang.

13.1 The Grand Unification

As mentioned in point (3) of the introduction, in a single fermion family of the Standard Model, there are two quarks and two leptons. We may think that quarks and leptons are different manifestations of a single particle. This would suggest that there is a connection between the strong force acting between quarks and the electroweak interaction between leptons and between quarks. Quarks and leptons can be member of a multiplet; amongst the members of the multiplet, in addition

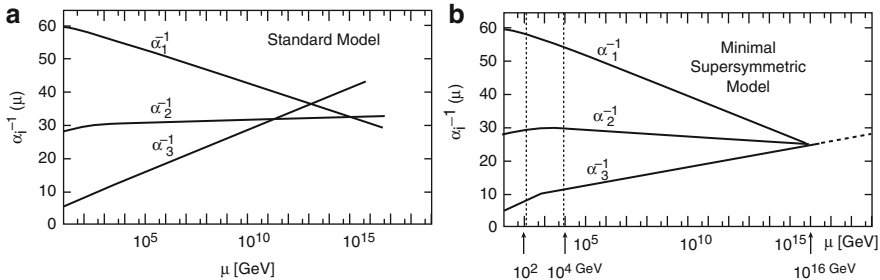


Fig. 13.1 Energy dependence of the inverse of the coupling constants $g, g', g_S (= \alpha_1, \alpha_2, \alpha_3)$ up to 100 GeV and their extrapolation to the energy of 10^{15} GeV: (a) according to the simplest model and (b) including the supersymmetry in the form of the Minimal SuperSymmetric Model (MSSM)

to the strong and weak interaction between quarks, to the weak interaction between leptons, a new interaction between a quark and a lepton should exist. In this way, we can think of a real unification of the fundamental forces, the electroweak and the strong (only gravity would be left out).

Another indication in favor of *Grand Unified Theories* arises from the evolution with energy of the inverse of the three coupling constants $g = e / \sin \theta_w$, $g' = e / \cos \theta_w$, $g_S = \sqrt{4\pi \alpha_S}$ (see Fig. 13.1a). When energy increases, the three constants start to converge and if the dependence with respect to the energy does not change, they should reach an almost equal value at the enormous energy of about 10^{15} GeV [13D94, 13L94].¹

To incorporate quarks and leptons in one family, the symmetry group should be enlarged. This group contains the known fundamental particles and explains the Grand Unification; below 10^{15} GeV, it must give rise to the symmetries of the Standard Model through spontaneous symmetry breaking; therefore, one must have, for example,

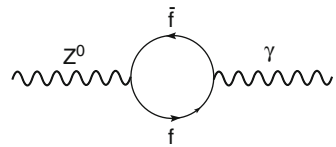
$$\text{SU}(5) \xrightarrow{10^{15}\text{ GeV}} \text{SU}(3)_C \times \text{SU}(2)_L \times \text{U}(1)_Y \xrightarrow{10^2\text{ GeV}} \text{SU}(3)_C \times \text{U}(1)_{EM}. \quad (13.1)$$

The special group of unitary symmetry $\text{SU}(5)$ is the simplest GUT symmetry group; it is symmetric for rotations in a five-dimensions inner space. The spontaneous breakings in (13.1) explain how a single unified force at very high energies spontaneously breaks in the strong and electroweak interactions at 10^{15} GeV first, and then in the three known interactions at 10^2 GeV. To explain the symmetry breaking at 10^{15} GeV, a mechanism similar to the Higgs mechanism should be introduced. New (and still undiscovered) vector bosons are needed.

Quarks and leptons of the first family are naturally contained in the symmetry group $\text{SU}(5)$. The group $\text{SU}(5)$ has a representation containing a five-dimensions

¹This extrapolation over 13 orders of magnitude is probably pure speculation.

Fig. 13.2 $Z^0\gamma$ coupling through a fermion–antifermion loop



multiplet and a 5×5 matrix. The five-dimensions multiplet is of the type R , i.e., with right-handed particles. The 5×5 matrix is antisymmetric, thus with only ten independent particles of type L , i.e., left-handed:

$$5_R = \begin{pmatrix} d_r \\ d_b \\ d_g \\ e^+ \\ \bar{v}_e \end{pmatrix}_R \quad (5 \times 5)_L = \begin{pmatrix} 0 & \bar{u}_g & \bar{u}_b & u_r & d_r \\ 0 & \bar{u}_r & u_b & d_b & 0 \\ 0 & u_g & d_g & 0 & e^+ \\ 0 & e^+ & 0 & 0 & 0 \end{pmatrix}_L. \quad (13.2a)$$

The indices r , b , g indicate the colors (r = red, b = blue, g = green). Other multiplets refer to the antiparticles of the multiplets (13.2a) and are of the type

$$\bar{5}_L = \begin{pmatrix} \bar{d}_r \\ \bar{d}_b \\ \bar{d}_g \\ e^- \\ v_e \end{pmatrix}_L \quad (5 \times 5)_R = \begin{pmatrix} 0 & u_g & u_b & \bar{u}_r & \bar{d}_r \\ 0 & u_r & \bar{u}_b & \bar{d}_b & 0 \\ 0 & \bar{u}_g & \bar{d}_g & 0 & e^- \\ 0 & e^- & 0 & 0 & 0 \end{pmatrix}_L. \quad (13.2b)$$

Quark fractional charge. The total charge of each particle multiplet must be equal to zero, that is, $Q(d_r + d_b + d_g + e^+ + \bar{v}_e) = (-1/3 - 1/3 - 1/3 + 1 + 0) = 0$, and similarly for the determinant of the matrix (13.2a, b) on the right. This implies that the charge of quarks must be a fraction of that of the leptons and that the proton charge must be equal and opposite in sign to the electron charge, $Q_p = -Q_e$.

Doubllets $(v_e, e^-)_L$, $(u, d')_L$. GUT theories explain the classification of leptons and quarks in doublets, for example, $(v_e, e)_L$, $(u, d')_L$, and explain the relations between electric charges, such as, $Q(v) - Q(e) = Q(u) - Q(d)$.

Prediction for $\sin^2\theta_w$. The diagram of Fig. 13.2 shows the mixing of the Z^0 boson with the photon γ through a fermion–antifermion loop. It may be considered as a mixing similar to the $K^0 - \bar{K}^0$ mixing introduced in Sect. 12.2.

The coupling of the Z^0 to the $f\bar{f}$ pair is $I_3 - Q \sin^2 \theta_w$ (11.75a); the coupling of the γ to the $f\bar{f}$ pair is Q ; for the GUT $\bar{5}$ representation, we have (antiquark L states have $I_3 = 0$)

Particles	I_3	Q
\bar{d}_r	0	+1/3
\bar{d}_b	0	+1/3
\bar{d}_g	0	+1/3
e	-1/2	-1
ν_e	+1/2	0
$_L$		

The sum of the couplings for the five members of the multiplet is

$$\Sigma_5 Q(I_3 - Q \sin^2 \theta_w) = 0. \quad (13.3a)$$

Since Z^0, γ are orthonormal states, $\langle Z^0 | \gamma \rangle = 0$, and Eq. 13.3a gives

$$\sin^2 \theta_w = \frac{\Sigma Q I_3}{\Sigma Q^2} = \frac{3}{8}. \quad (13.3b)$$

This is larger compared to the measured value at $\sqrt{s} = 91$ GeV ($\sin^2 \theta_w \simeq 0.23$), but it refers to the GUT unification energy scale, $\sim 10^{15}$ GeV. If the corrections shown in Fig. 13.1 are applied to the coupling constants g, g' , one has $\sin^2 \theta_w (\sqrt{s} = 91 \text{ GeV}) \simeq 0.21$, which is in better agreement with the measured value.

13.1.1 Proton Decay

The gauge bosons generate transitions between the members of a multiplet. Considering, for instance, the quintet $\bar{5}$ in (13.2b): gluons generate transitions between quarks; the W^\pm bosons generate transitions between e^- and $\bar{\nu}_e$ (and between quarks of different flavor). In SU(5), massive bosons (denoted X, Y) must exist. They generate transitions between quarks and leptons, violating both the baryonic and the leptonic number conservation. The proton decays through diagrams like that illustrated in Fig. 13.3, with the exchange of massive X, Y bosons ($m_{X,Y} \sim 10^{15}$ GeV).

The experimental results obtained with large underground water Cherenkov detectors containing thousands of tons of water or with sampling calorimeters with about 1,000 tons of iron, showed that the average proton lifetime is very long, that is, $\tau_p(p \rightarrow \pi^0 e^+) > 8.2 \cdot 10^{33}$ years. Calculations based on SU(5) diagrams like that of Fig. 13.3 predict a lower lifetime, $\sim 10^{30}$ years. Despite its beauty, it seems that

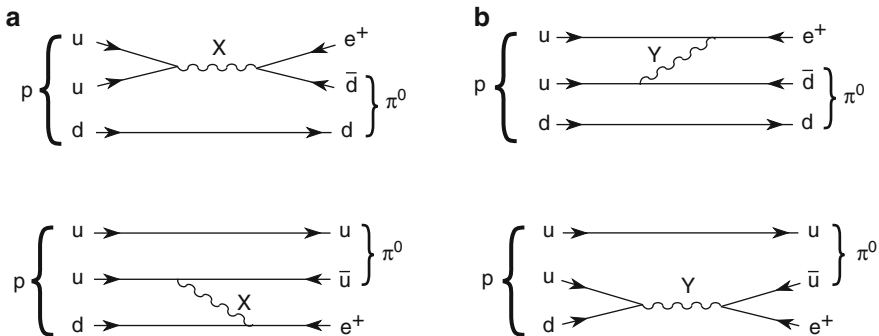


Fig. 13.3 Illustrative diagrams of proton decay, $p \rightarrow e^+ \pi^0$ in GUT theories, by exchanging (a) an X boson (with electric charge $+4/3$) and (b) a Y boson (with charge $+1/3$) of SU(5)

the simplest GUT model based on SU(5) should be rejected. There are indeed other models based on more complex groups, for example, SO(10), which have more parameters and provide longer lifetimes. The combination of the supersymmetry with GUT allows one to consider the $p \rightarrow K^+ \nu$ decay as the most probable. This leads to a longer proton lifetime, about 10^{33} year (the current experimental limit [P10] is $\tau_p > 6.7 \cdot 10^{32}$ year).

13.1.2 Magnetic Monopoles

GUT theories require the existence of supermassive *magnetic monopoles* (MMs). They could be created as point-like topological defects at the time of the Grand Unification symmetry breaking into subgroups (one of which is the $U(1)_Y$ group) at 10^{15} GeV (13.1). These MM should have a mass m_M equal to the mass of the massive X, Y bosons, divided by the unified coupling constant α at 10^{15} GeV:

$$m_M \simeq \frac{m_X}{\alpha} \sim \frac{10^{15}}{0.03} \sim 3 \times 10^{16} \text{ GeV}. \quad (13.4)$$

The MM magnetic charge g is predicted by the Dirac relation

$$e g = n \hbar c \quad (13.5)$$

where n is an integer. If we take as the elementary electric charge that of the electron and $n = 1$, we have $g = 68.5e$ in the symmetric unit system of Gauss. The magnetic charge g is therefore huge. The introduction of MMs in the Maxwell equations produce a complete symmetry between electric and magnetic fields; the symmetry is “numerically broken” by the value of magnetic charge, much larger than the electric one, and by the incredibly large mass of MMs, $m_M \sim 10^{17}$ GeV.

The MM production mechanism and their current abundance in the Universe is an additional problem. MMs with masses so large cannot be produced by any accelerator, present or predictable, even in the distant future. They could only be produced in the early Universe, in the phase transition when the GUT symmetry group breaks into subgroups containing U(1). The MMs would be produced as almost point-like topological defects. Their number in the Universe depends on the number of causally disconnected regions. In cosmological models without *inflation* (see Sect. 13.6), the number is high; if the Universe went through an inflationary phase, the number of regions not causally related would be small and the number of MMs would be very low. Another production mechanism is through high energy particle collisions immediately after the phase transition, for example, through $e^+e^- \rightarrow M\bar{M}$. This mechanism may persist for a limited time period after the phase transition because the average energy per particle decreased quickly over time.

Thus far, all magnetic monopole searches give negative results [13G84].

13.1.3 Cosmology. First Moment of the Universe

As mentioned in the case of magnetic monopoles, the basic ideas of Grand Unified Theories influenced the cosmology of *the first instants of the Universe*. The model for the point-like origin of the Universe (the *Big Bang*) predicts that the huge initial temperature decreased as the Universe expanded. Electroweak and strong interactions were unified from $\sim 10^{-44}$ to $\sim 10^{-35}$ s, when the Universe was in a high symmetry state. As the temperature decreased, phase transitions occurred. This happens, for instance, for a magnetic substance: at a high temperature, there is no preferred direction; when the temperature decreases below the Curie point, the material loses the rotational symmetry. Magnetic domains appear: this corresponds to a more ordered phase, but with a lower degree of symmetry. Something similar happened (see Sect. 13.6) at $t = 10^{-35}$ s, corresponding to a temperature of 10^{15} GeV ($\simeq 10^{28}$ K). In this (almost certainly exothermic) phase transition, many important events occurred in the Universe evolution: an exponential expansion; the production of magnetic monopoles and other particles; the decay of the X and Y bosons, and the origin of the baryon asymmetry.

Let us briefly analyze this last point. GUT theories provide processes with violation of the baryon and lepton numbers. A small CP violation is also foreseen: the X, Y bosons decay, producing a number of particles slightly larger than the number of antiparticles. With the successive particle-antiparticle annihilation, the small particle excess (small in percentage, but large in number) will produce the present Universe made of matter and no antimatter, and with a baryon-to-photon ratio equal to $\eta = n_B/n_\gamma \simeq 10^{-9}\text{--}10^{-10}$. The photons are mainly the photons of the cosmic microwave background (CMB) radiation that fills the entire Universe. Today, the CMB has a temperature of 2.7 K, corresponding to $\sim 10^{-4}$ eV. While the number of photons is much larger than that of the baryons, the mass

energy of baryons (~ 940 MeV per baryon) dominates the total visible energy. GUT theories are currently the only ones that easily explain the small n_B/n_γ value.

13.2 Supersymmetry (SUSY)

The transformations seen thus far link particles of the same type; in general, they “rotate” bosonic (or fermionic) states in other bosonic (or fermionic) states. *Supersymmetries* transform (rotate) a bosonic state into a fermionic one and vice versa. If these transformations exist, they would imply that bosons and fermions are different manifestations of a unified state: fermions and bosons would be in the same multiplet. These transformations are foreseen by *supersymmetric theories* which represent a new form of unification. A supersymmetric operation changes by $1/2$ the spin of particles, leaving the electric and color charges unchanged.

Supersymmetry has a cultural interest in itself; it also addresses some of the difficulties of Grand Unified theories. Without supersymmetry, it is indeed difficult to understand why the known fundamental particles are so light with respect to the Grand Unification scale at $\sim 10^{15}$ GeV. Supersymmetry solves this *hierarchy* problem as well as the problem of divergences (for example, the radiative corrections to the Higgs boson mass) [13L94]. In *supergravity* theories (SUGRA), the supersymmetric concepts lead to the unification with gravity.

According to supersymmetry, every known boson has a fundamental fermionic partner with spin differing by $1/2$ unit, and any fundamental fermion has a bosonic partner with spin differing by $1/2$. The supersymmetric partners of the particles are called *sparticles*. However, it seems impossible to connect the known fundamental bosons and fermions. The sparticles must be new objects: they are expected to be heavier than any known particle. This is a consequence of a supersymmetry breaking: corresponding particles and sparticles should otherwise have the same mass.

Supersymmetries postulate the existence of an operator U which transforms a fermion into a boson by varying the spin by $1/2$ unit, and vice versa:

$$\begin{aligned} U|\text{fermion}\rangle &= |\text{boson}\rangle \\ U|\text{boson}\rangle &= |\text{fermion}\rangle. \end{aligned} \tag{13.6}$$

The boson-fermion symmetry implies the existence of doublets containing a quark q and its supersymmetric partner, denoted as *squark* \tilde{q} (scalar quark), and similarly for a lepton and the corresponding boson, the *slepton* \tilde{l} (scalar lepton):

$$\begin{pmatrix} q \\ \tilde{q} \end{pmatrix}, \begin{pmatrix} l \\ \tilde{l} \end{pmatrix} \quad \text{with spin } \begin{pmatrix} 1/2 \\ 0 \end{pmatrix}. \tag{13.7}$$

Table 13.1 Fundamental particles and their supersymmetric partners. Only the Higgs bosons of the MSSM are considered

Particle, $R = +1$			Sparticle, $R = -1$		
Particle	Spin	Charge	Sparticle	Spin	S-name
e	1/2	-1	\tilde{e}	0	selectron
μ	1/2	-1	$\tilde{\mu}$	0	smu
τ	1/2	-1	$\tilde{\tau}$	0	stau
ν	1/2	0	$\tilde{\nu}$	0	sneutrino
q	1/2	2/3, -1/3	\tilde{q}	0	squark
g	1	0	\tilde{g}	1/2	gluino
γ	1	0	$\tilde{\gamma}$	1/2	photino
Z^0	1	0	\tilde{Z}	1/2	zino
H_u^0, H_d^0	0	0	$\tilde{H}_u^0, \tilde{H}_d^0$	1/2	neutral higgsino
H_u^+, H_d^-	0	± 1	$\tilde{H}_u^+, \tilde{H}_d^-$	1/2	charged higgsino
W^\pm	1	± 1	\tilde{W}^\pm	1/2	wino
G	2	0	\tilde{G}	3/2	gravitino

Sparticles couple with fields with the same coupling constant as the particles. For example, the couplings qqg , $\tilde{q}\tilde{q}\tilde{g}$, ggg , $\tilde{g}\tilde{g}\tilde{g}$ are always α_S . Similarly, there exist doublets for every vector boson and its supersymmetric partner, that is,

$$\begin{pmatrix} \gamma \\ \tilde{\gamma} \end{pmatrix}, \begin{pmatrix} Z^0 \\ \tilde{Z}^0 \end{pmatrix}, \begin{pmatrix} W^+ \\ \tilde{W}^+ \end{pmatrix}, \begin{pmatrix} W^- \\ \tilde{W}^- \end{pmatrix} \text{ with spin } \begin{pmatrix} 1 \\ 1/2 \end{pmatrix}. \quad (13.8)$$

The Higgs boson has spin $S = 0$; its supersymmetric partner has spin $S = 1/2$.

The notation for boson partners is as follows: starting from the ordinary name, the suffix *ino* is added, that is, photon \rightarrow photino, $Z^0 \rightarrow$ zino, $W^+ \rightarrow$ wino, Higgs \rightarrow higgsino.

13.2.1 Minimal Standard Supersymmetric Model (MSSM)

Table 13.1 gives an overview of fundamental particles and their supersymmetric partners. It refers to the Minimal Supersymmetric Standard Model (MSSM), the simplest supersymmetric model (the only one we consider in the following). Also, Table 13.2 refers to the MSSM. In this model, at least two complex doublets of Higgs bosons $\begin{pmatrix} H_u^+ \\ H_d^+ \end{pmatrix}$ and $\begin{pmatrix} H_u^0 \\ H_d^0 \end{pmatrix}$ should be introduced to generate the masses of “up” and “down” type quarks and the masses of the charged leptons. Supersymmetric neutral states should mix as we saw in Chap. 12 for other systems. The four neutral fermions $\tilde{\gamma}$, \tilde{Z} , \tilde{H}_u^0 , \tilde{H}_d^0 are not mass eigenstates; the latter are the *neutralinos* $\tilde{\chi}_1^0$, $\tilde{\chi}_2^0$, $\tilde{\chi}_3^0$, $\tilde{\chi}_4^0$, expressed as a mixing of the type:

$$\tilde{\chi}_{1,2,3,4}^0 = a\tilde{\gamma} + b\tilde{Z} + c\tilde{H}_u^0 + d\tilde{H}_d^0 \quad (13.9)$$

Table 13.2 “Normal” fundamental particles and supersymmetric partners; right-handed particles are included. The mass eigenstates resulting from the mixing between sparticles are also indicated

<u>Quark</u>		<u>Squark</u>			
(spin 1/2)	$\begin{pmatrix} u \\ d \end{pmatrix}_L$	u_R	d_R	(spin 0)	$\begin{pmatrix} \tilde{u} \\ \tilde{d} \end{pmatrix}_L$
	$\begin{pmatrix} c \\ s \end{pmatrix}_L$	c_R	s_R		$\begin{pmatrix} \tilde{c} \\ \tilde{s} \end{pmatrix}_L$
	$\begin{pmatrix} t \\ b \end{pmatrix}_L$	t_R	b_R		$\begin{pmatrix} \tilde{t} \\ \tilde{b} \end{pmatrix}_L$
<u>Leptons</u>		<u>Sleptons</u>			
(spin 1/2)	$\begin{pmatrix} v_e \\ e \end{pmatrix}_L$	e_R	(spin 0)	$\begin{pmatrix} \tilde{v}_e \\ \tilde{e} \end{pmatrix}_L$	\tilde{e}_R
	$\begin{pmatrix} v_\mu \\ \mu \end{pmatrix}_L$	μ_R		$\begin{pmatrix} \tilde{v}_\mu \\ \tilde{\mu} \end{pmatrix}_L$	$\tilde{\mu}_R$
	$\begin{pmatrix} v_\tau \\ \tau \end{pmatrix}_L$	τ_R		$\begin{pmatrix} \tilde{v}_\tau \\ \tilde{\tau} \end{pmatrix}_L$	$\tilde{\tau}_R$
<u>Gauge bosons</u>		<u>Gauginos</u>			
(spin 1)	g		(spin 1/2)	\tilde{g}	
	γ			$\tilde{\gamma}$	
	Z			\tilde{Z}	
	W^\pm			\tilde{W}^\pm	
<u>Higgs bosons</u>		<u>Higgsinos</u>			
(spin 0)	h^0, H^0, A^0		(spin 1/2)	$\tilde{H}_u^0, \tilde{H}_d^0$	
	H^+, H^-			$\tilde{H}_u^+, \tilde{H}_d^-$	

with different coefficients for $\tilde{\chi}_1^0, \tilde{\chi}_2^0, \tilde{\chi}_3^0, \tilde{\chi}_4^0$. Similarly, the two charged Higgsinos $\tilde{H}_u^+, \tilde{H}_d^-$ and the two winos \tilde{W}^+, \tilde{W}^- are not mass eigenstates; the mass eigenstates are the *charginos* $\tilde{\chi}^+$ and $\tilde{\chi}^-$ expressed as mixings of the type:

$$\tilde{\chi}^+ = a' \tilde{W}^+ + b' \tilde{H}_u^+, \quad \tilde{\chi}^- = a'' \tilde{W}^- + b'' \tilde{H}_d^-. \quad (13.10)$$

Since no sparticle has been experimentally observed, a new quantum number, the *R-parity*, is introduced in order to provide the supersymmetric particles with some properties that make them (currently) inaccessible. R-parity is equal to $R = (-1)^{3B+L+2S}$, where B is the baryon number, L the lepton number, and S the spin. Most SUSY models require the conservation of R and then predict the existence of a stable supersymmetric particle with a minimum mass (the “Lightest Supersymmetric Particle,” LSP). There are other models where R can be violated. In the MSSM, R-parity is conserved; $R = +1$ is assigned to known particles and $R = -1$ to the supersymmetric partners, that is,

$$\begin{aligned} R|\text{supersymmetric particle}\rangle &= -|\text{supersymmetric particle}\rangle \\ R|\text{particle}\rangle &= +|\text{particle}\rangle. \end{aligned}$$

The general situation can be more complex, as the right-handed states, such as, e_R , q_R , could give sparticles different from the left-handed ones, as shown in Table 13.2.

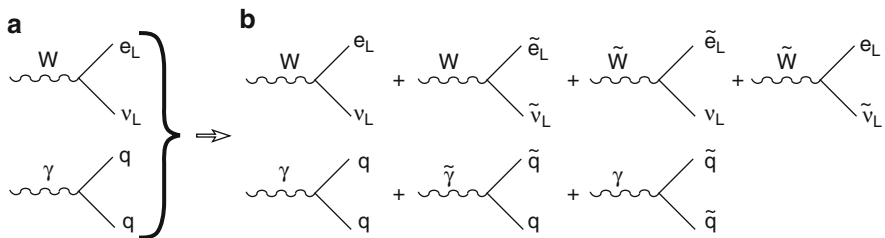


Fig. 13.4 (a) Fundamental Feynman diagrams in the SM and (b) with the introduction of supersymmetric partners. Antiparticles are not indicated. Here L (Left) represents the particle helicity

13.2.1.1 The Higgs Sector of the MSSM

In the MSSM, two complex doublets of Higgs bosons provide eight degrees of freedom. Three degrees of freedom are used to give mass to the W^+ , W^- , Z^0 . The Higgs sector in the MSSM contains five bosons (and their supersymmetric partners) that correspond to the remaining five degrees of freedom. The Higgs bosons have been called h^0 , H^0 , H^+ , H^- with even CP and A^0 with odd CP . With $m_{h^0} < m_{H^0} < m_{H^\pm}$, the h^0 boson can be identified with the scalar Higgs boson H^0 of the Standard Model, introduced in Chap. 11.

In summary, one can observe from Table 13.2 that in the MSSM:

1. The number of particles doubles.
2. The supersymmetric partner of known gauge bosons corresponds to the *gauginos*.
3. Three *sfermion* families correspond to the three fermion families.
4. In the Higgs sector, there are two doublets leading to five Higgs bosons and five Higgsinos.

13.2.1.2 Fenomenology

Calculations in the MSSM use the same Feynman rules of the Standard Model, adding the contribution of diagrams in which particles are replaced by their superpartners. The substitution of particles with sparticles must be made in pairs for angular momentum conservation. Boson-fermion couplings are illustrated in Fig. 13.4.

Since in the MSSM model the R-parity is a conserved quantum number, all vertices include superpartner pairs. Three conclusions can be drawn:

1. The supersymmetric partners are produced in pairs from normal particles.
2. There is always a supersymmetric particle in the decay products of a supersymmetric particle.
3. The lightest supersymmetric particle (LSP) is stable; it is usually assumed that the LSP is the neutralino $\tilde{\chi}_1^0$ which is neutral both for electric and color charges;

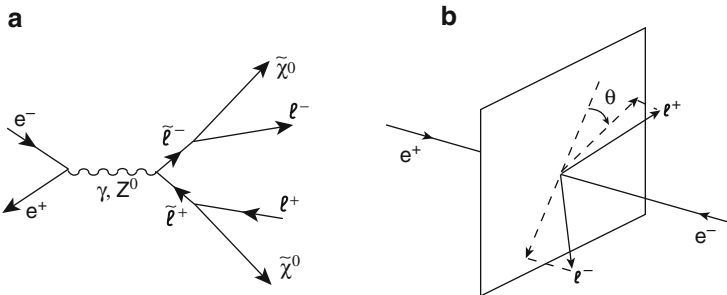


Fig. 13.5 (a) Feynman diagram for the slepton–antislepton pair production followed by the slepton decay: $\tilde{\ell}^- \rightarrow \ell^- \tilde{\chi}^0$ and $\tilde{\ell}^+ \rightarrow \ell^+ \tilde{\chi}^0$ ($\ell = e, \mu, \tau$). For $\ell = e$, the diagram where a $\tilde{\chi}_1^0$ is exchanged in the t -channel also contributes. (b) Sketch of an event which produces an acoplanar slepton–antislepton pair. The acoplanarity angle θ is the angle between the projections of the ℓ^- and ℓ^+ momenta in the plane perpendicular to the e^+ and e^- beams

the neutralino could therefore be an important component of dark matter in the Universe (see Sect. 13.6). For special mixing conditions, the LSP could correspond to the *sneutrino*.

Supersymmetry is not visible in nature and therefore must be “broken,” at least at the currently accessible energies. As the Standard Model, supersymmetric theories cannot predict the values of the particle masses, but once they have been experimentally determined, one can calculate all other quantities. Recent phenomenological supersymmetric models predict supersymmetric particles with masses between 100 and 1,000 GeV; these are searched for at the LHC.

Many searches for supersymmetric particles at $\bar{p}p$, ep , e^+e^- colliders have been carried out, up to now with negative results; only lower limits on their mass were determined. These limits (at the 95% confidence level) are presented in Table 13.3.

With the introduction of supersymmetry, the extrapolation of the interaction coupling constants to 10^{15} GeV have better behavior: the three constants appear to converge towards a common point, as shown in Fig. 13.1b.

13.2.1.3 Searches for Charged Sleptons

Let us briefly discuss an example of a typical SUSY particle search. Figure 13.5a shows the Feynman diagram for the production of charged scalar leptons $e^+e^- \rightarrow \gamma, Z^0 \rightarrow \tilde{\ell}^+\tilde{\ell}^-, \rightarrow \tilde{\mu}^+\tilde{\mu}^-$.

The sleptons decay in the corresponding charged leptons plus a neutralino, $\tilde{\ell}^\pm \rightarrow \ell^\pm \tilde{\chi}^0$; the $\tilde{\chi}^0$ (subject only to weak interaction) leaves the detector unobserved. The topology of the signal events (Fig. 13.5b) consists of two acollinear and acoplanar charged leptons, plus missing energy and momentum. The sleptons $\tilde{\ell}_R$ and $\tilde{\ell}_L$ are different particles with different masses. The most stringent experimental limits

generally apply to $\tilde{\ell}_R$, whose mass is expected to be smaller than that of $\tilde{\ell}_L$. There may also be special conditions in the MSSM parameters space for which $m_{\tilde{\ell}_L} = m_{\tilde{\ell}_R}$.

13.2.2 Supergravity (SUGRA). Superstrings

GUT theories, including normal supersymmetric theories, do not incorporate the gravitational interaction. Gravitation becomes important for energies of the order of the Planck mass, 10^{19} GeV, corresponding to a size of 10^{-33} cm. Such energies existed in the early Universe until the Planck time, 10^{-43} s.

A complete theory must contain quantum gravity. Its inclusion presents important difficulties, connected both to the quantization and to divergences. The latter cannot be easily removed by renormalization procedures, as in the supersymmetric theories. The supersymmetric theory of gravity, called *quantum supergravity* or SUGRA, has local gauge invariance. In some models, the lightest supersymmetric particle is assumed to be the gravitino.

Finally, theories in which the particles are very small size objects, for example, *strings*, in particular closed strings, have been formulated. These theories succeeded in incorporating quantum gravity. The *string theories* concern both bosonic states and supersymmetric theories (*superstrings theories*). They should be formulated in a space with many dimensions (at least ten); it is not obvious how to switch to the four dimensions of the ordinary space (the other six dimensions must be “hidden”) [13G00].

13.3 Composite Models

The existence of three families of quarks and leptons suggests the existence of possible substructures in quarks and leptons. The situation could be similar to that already encountered with atoms, nuclei and hadrons. There are other reasons to consider substructures. In some models quarks, leptons and gauge bosons are composite objects. For example, in the model of Salam and Pati, quarks and leptons are composed of three objects called *prequark* or *preons*; in the model of Harari, they are composed of three objects called *rishons*, which means “fundamental” in Hebrew. There are several difficulties in these theories associated with the very small dimensions of prequarks (much less 10^{-16} cm, also their orbits must be less than 10^{-16} cm) and with the need for an additional force that binds the prequarks. In another model, prequarks are *dions*, namely, particles with both electric and magnetic charges; in other models, the prequarks are so close together that the gravitational force is also involved.

Table 13.3 Searches for new particles. Lower mass limits in GeV [P10, 13w1, 13w2] at the 95% confidence level obtained in searches at LEP and other high-energy colliders (Tevatron and HERA). The LEP limits are obtained by combining the results of the four LEP experiments. If the combination does not exist, we refer to the best limit from a single experiment

Particle	Symbol	LEP limit (GeV)	Other limits (GeV)
Charged sleptons ^a	$\tilde{e}, \tilde{\mu}, \tilde{\tau}$	99.9, 94.9, 86.6	
Sneutrino	$\tilde{\nu}$	94 (DELPHI)	
Neutralino (LSP)	$\tilde{\chi}^0$	50.3	
Charginos	$\tilde{\chi}^\pm$	103.5	117 (D0)
Scalar quarks	\tilde{b}, \tilde{t}	99, 98	222, 176 (D0)
Gluinos	\tilde{g}	26.9 ^b	308 (D0)
SM Higgs	H_{SM}^0	114.4	
MSSM Higgs	h^0	92.8	100 (CDF)
	A^0	93.4	100 (CDF)
	H^\pm	78.6	
Higgs (charge = 2)	$H^{\pm\pm}$	99 (OPAL)	136 (CDF)
Excited leptons	e^*, μ^*, τ^*	208, 190, 185 (OPAL)	255 (H1), 221 (CDF)
Excited neutrinos	ν^*	190 (L3)	158 (ZEUS)
Excited quarks	q^*	200	775 (D0)
Scalar leptoquarks ^c	LQ	98 (OPAL)	229 (D0)
Vector leptoquarks ^c	LQ	98 (OPAL)	240 (D0)

^aFor supersymmetric particles, the limits are usually obtained within the MSSM; in some cases, the limits are within a specific model

^bLimit for a light gluino (stable)

^cAssociated pair production

Several searches for particle substructures or excited states have been carried out, all with negative results so far. The lower limits on their masses are presented in Table 13.3.

Excited leptons. They would correspond to excited states of known leptons that could be produced in pairs or individually: $e^+ e^- \rightarrow e^{*+} e^{*-}$, $e^+ e^- \rightarrow e^{*+} e^-$. Excited leptons could decay electromagnetically,

$$e^* \rightarrow e\gamma, \quad \mu^* \rightarrow \mu\gamma, \quad \tau^* \rightarrow \tau\gamma, \quad (13.11)$$

without violating the three lepton numbers. These decays were not observed at a sensitivity level of about 10^{-4} .

Decays with violation of lepton numbers. Quarks and leptons of the second and third family can be thought of as excited states of quarks and leptons of the first family. In this case, decays of the type

$$\mu \rightarrow e\gamma, \quad \tau \rightarrow e\gamma, \quad \mu \rightarrow eee \quad (13.12)$$

could be possible and the electron and muon, or electron and tau leptonic numbers are violated. These decays were not observed, resulting in the following stringent upper limit [13M10]:

$$\frac{\Gamma(\mu \rightarrow e\gamma)}{\Gamma(\mu \rightarrow e\nu\nu)} < 310^{-11}. \quad (13.13)$$

The τ could also decay in $\mu\pi$, $\tau \rightarrow \mu\pi$, violating the muon and tau leptonic numbers (also this decay channel has never been observed).

Excited neutrinos could be the weak isospin partners of excited charged leptons. They could be produced in pairs or individually and could then decay with the emission of a photon: $e^+e^- \rightarrow \nu^*\bar{\nu}^* \rightarrow \nu\bar{\nu}\gamma\gamma$, $e^+e^- \rightarrow \nu^*\bar{\nu} \rightarrow \nu\bar{\nu}\gamma$.

Excited quarks. An excited quark could decay into a quark and a photon, $q^* \rightarrow q\gamma$, or a quark and a gluon, $q^* \rightarrow qg$; the relative frequency should be approximately 1–10. In the first case, $q^* \rightarrow q\gamma$, an isolated high energy photon would be present in the final state. In e^+e^- collisions, events with one or more high energy photons could come from excited quarks, but also from the bremsstrahlung of a beam e^- (or e^+) or from the bremsstrahlung from a q (\bar{q}) in the final state.

Leptoquarks. Leptons and quarks are classified in a similar way with respect to the family structures and weak isospin multiplets. The Standard Model does not explain this parallelism, although it is necessary for the cancellation of divergent terms. This suggests that there could be a deeper correlation between quarks and leptons. In models that go beyond the SM, new particles that mediate the interaction between quarks and leptons may exist. This occurs naturally in GUT models, at very high energies. In some SM extensions, the existence of *leptoquark bosons* (LQ) are foreseen. LQ are color triplets with both lepton and baryon number, electric charge 1/3, 2/3 and relatively low masses. These LQ s decay and couple with a lepton and a quark. According to various models, LQ s are scalar (spin = 0) or vector (spin = 1) particles, and their coupling with leptons and quarks depends on the model. LQ s were introduced for the first time [13P74] in an attempt to consider the lepton number as a fourth color. In the simplest model, the interactions involving LQ s conserve baryon and lepton numbers and respect the symmetry of the Standard Model. In this case, the only free parameters are the LQ masses and their couplings with the fermions.

LQ s produced in pairs have been searched for in e^+e^- collisions, as shown in Fig. 13.6a:

$$e^+ + e^- \rightarrow LQ + \overline{LQ}, \quad LQ \rightarrow \ell + q, \quad \overline{LQ} \rightarrow \bar{\ell} + \bar{q}. \quad (13.14)$$

In this case, the LQ decay modes into eq , μq , τq were used. These combinations should conserve the “family number,” i.e., the pairs must involve ℓ and q only of the same family.

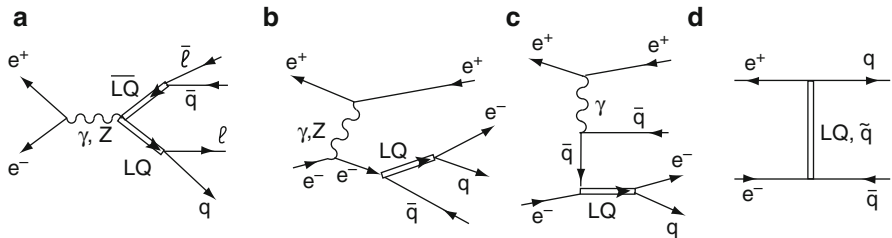


Fig. 13.6 Feynman diagrams for leptoquark production and decay in e^+e^- collisions. The leptoquark can be produced (a) in pairs (any LQ type) (b) and (c) individually (in this case, the leptoquarks belong to the first family and only couple with charged leptons). (d) Indirect effects due to the (virtual) exchange of a leptoquark of the first family in the t -channel

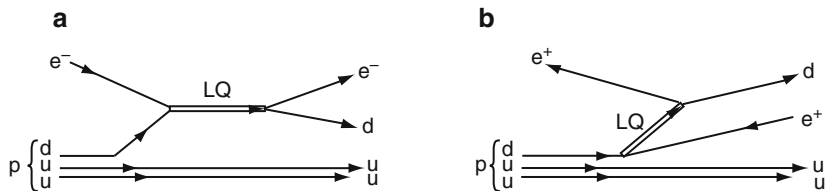


Fig. 13.7 Feynman diagrams for leptoquarks of the first family produced in ep collisions: (a) LQ formation, (b) LQ exchange in the t -channel

Individually produced LQ s were also searched for in (see Fig. 13.6b,c):

$$e^+ + e^- \rightarrow e^+ + q + LQ \rightarrow e^+ + e^- + q + \bar{q} \quad (13.15)$$

as well as indirect effects due to the exchange of a leptoquark of the first family in the t -channel (Fig. 13.6d). Electron–positron (ep) collisions, as in the HERA collider (Chap. 10), offer an easier way to search for leptoquarks of the first family (Fig. 13.7), that is,

$$e + p \rightarrow LQ + q + q \rightarrow e^+ + d + q + q. \quad (13.16)$$

In this case, a resonant system (eq) with an enhanced cross-section could be formed. The events should have a high energy lepton, a jet of hadrons at large angles and a “spectator jet” in the final state. Events are therefore similar to those of a typical deep inelastic collision.

13.4 Particles, Astrophysics and Cosmology

Cosmology has recently acquired the characteristics of an experimental discipline [13W07]. Particles with their fundamental interactions, astrophysics and cosmology

have become closely related fields. The submicroscopic phenomena allow us to better understand the evolution of the Universe and astrophysics, and vice versa. For example:

- The understanding of atomic and molecular phenomena clarified the light spectrum emitted by the Sun (and more generally by the stars), the chemical composition of the solar atmosphere and led to the discovery of helium.
- The knowledge of nuclear phenomena explain the energy source of the Sun and of the stars. At the center of a star there is a “furnace” where nuclear fusion reactions take place (Sect. 14.10).
- Nuclear and subnuclear physics allow us to understand the structure of particular celestial bodies in extreme conditions, for example, white dwarfs, neutron stars and stellar gravitational collapses (Problem 13.6).

A deep connection exists between *cosmic rays* and subnuclear physics [G90]. Primary cosmic rays mainly consist of high energy protons and atomic nuclei which, coming from outside of the solar system, interact with the nuclei of the Earth’s atmosphere. In an interaction, many particles (some of them unstable) are produced (*secondary cosmic rays*). The understanding of the origin of cosmic rays, their acceleration mechanisms, the interaction processes with interstellar material and the Earth’s atmosphere is based on the knowledge of nuclear and subnuclear physics. However, the reverse is also true: many particles were discovered in secondary cosmic rays.

Particle and astrophysics: the example of neutrino telescopes [13C10].

Astrophysics has experienced an extraordinary development in recent decades thanks to new techniques that allowed the transition from limited observations of the visible band of the electromagnetic spectrum to other wavelengths: from the radio and infrared waves on one side, to X-rays and γ -rays on the high energy side. The information that these observations can provide to the mechanisms that take place in astrophysical objects such as supernova remnants (SNR), pulsars (PLS), active galactic nuclei (AGN) and others is unfortunately incomplete, as it is limited to electromagnetic processes. Cosmic particle accelerators (in the galaxy and outside our galaxy) capable of accelerating protons and nuclei as observed in the cosmic rays (CR) must therefore exist .

The CR spectrum extends with amazing regularity up to 10^{20} eV, with a power law of the form $d\Phi/dE \simeq E^{-\gamma}$, with $\gamma = 2.7$ for energies up to $\sim 10^{15}$ eV. This behavior can be explained by the so-called “Fermi mechanism” acceleration process. Accelerated protons and nuclei (hadronic processes) may interact with ambient nuclei or with the gas of photons giving rise to π and K mesons. The π^0 (with very short lifetime) produces a photon pair; the π^\pm decay in charged leptons, neutrinos and antineutrinos (Problem 13.1). It is not an easy task to distinguish the photons produced in hadronic processes from those produced in purely electromagnetic processes (by high

energy electron bremsstrahlung or inverse Compton). A clear evidence for the presence of hadronic processes in astrophysical objects (the “smoking gun” for the discovery of CR sources) could only come from the observation of neutrinos from the decay of charged pions. The detection of high energy neutrinos and antineutrinos is mandatory for a comprehensive understanding of many astrophysical processes taking place in our Galaxy and particularly extragalactic objects such as AGNs and those cosmic objects that give rise to gamma-ray bursts (GRBs).

The small cross-section is the reason for the modest neutrino attenuation in crossing the dense layers around the astrophysical objects where they are produced. Neutrinos reach the Earth after traveling enormous galactic/intergalactic distances. A 100 GeV neutrino has a cross-section of $6.7 \times 10^{-7} \mu\text{b}$, which means that it can travel on average through a thickness of 24 million km of water before undergoing an interaction. The small neutrino cross-section requires the use of huge detectors, for example, those consisting of a large volume of water (sea or lake) or even ice. It is estimated that an instrumented volume of about 1 km^3 of ice or water is needed to be sensitive to the neutrino flux from a cosmic source.

The most efficient way to search for astrophysical neutrinos is through the detection of charged current interactions of muon neutrinos, with a muon in the final state. The muon is the particle with the longest range (Chap. 2): a 200 GeV muon can travel about one kilometer of water. Moreover, at high energies, the muon essentially retains the original direction of the neutrino (the average deflection angle is less than 0.1° for 1 TeV neutrino). A detector measuring the muon direction can therefore be used to trace back the ν emission source.

The μ is detected through the Cherenkov light produced when the relativistic particle crosses a transparent and dense medium, as deep sea water or deep ice. A suitable array of photomultiplier tubes (PMT) can be used for the detection of photons emitted by the muon; from the PMT positions and photon arrival times, dedicated algorithms can trace back the muon direction. Only upward-going muons are unambiguously originated from neutrino interactions. Neutrinos (in association with charged leptons) produced by CR interactions with atmospheric nuclei represent an irreducible background for cosmic neutrinos. Even if a detector is located under 2–3 km of water/ice, the number of muons produced by cosmic ray interactions in the atmosphere above the detector is overwhelming by more than five orders of magnitude than that produced by atmospheric neutrinos. Unlike traditional astronomy, neutrino astronomy examines the sky underground, on the other side of the Earth!

A neutrino telescope buried under the Antarctic ice is almost completed (2010); this telescope will study the northern hemisphere sky. To observe the southern celestial hemisphere (where the galactic center is located, with its potentially interesting sources), the construction of a 1 km^3 -scale

neutrino telescope in the Mediterranean Sea is planned in the next few years. The ANTARES neutrino telescope near the French coast is a smaller scale experiment ($\sim 1/50 \text{ km}^3$) in operation since May of 2008.

Particles and cosmology. The study of the dynamics of the stars in the galactic halos and of galaxies in galaxy groups showed that the quantity of matter in the Universe must be much larger than that observed with astronomical instruments. Matter which does not produce any electromagnetic radiation is denoted as dark matter; its nature is still unknown. It is likely that a part of the dark matter consists of celestial bodies like the planet Jupiter and gas clouds (baryonic dark matter); another part could consist of a “gas” of cold, weakly interacting and massive particles, see Sect. 13.5.

The knowledge of the fundamental interactions between particles is needed to understand the dynamics of the first moments of the Universe (Sect. 13.6). As a result of what happened in the early moments, different types of “relic” particles may be now present in the Universe (as for the case of magnetic monopoles, Sect. 13.1.2). After the phase transition corresponding to the formation of atoms (about 300,000 years after the Big Bang), the decoupling of electromagnetic radiation and matter took place. The Universe is uniformly filled with a microwave electromagnetic radiation, the cosmic microwave background, with a frequency spectrum typical of that of a 3 K blackbody radiation [W08].

Similarly, about 1 s after the Big Bang, the decoupling of neutrinos from the rest of matter and radiation occurred. These relic neutrinos should have a temperature of about 2 K and the density number would be about 300 cm^{-3} (~ 50 for each neutrino and antineutrino type). Relic neutrinos are not currently observable. As discussed in Sect. 12.9, cosmology allows one to set upper limits to the neutrino masses. Neutrinos with a very small mass should be distributed almost uniformly in the Universe; on the contrary, if the ν mass is of the order of a few eV, they would form halos around galaxy groups. This has consequences regarding the dynamics of galaxy formations, and the limit on the ν mass is derived from the observed distributions.

13.5 Dark Matter

The Universe is observed using electromagnetic waves of different frequencies emitted by celestial bodies (in the optical band first, then in the radio, infrared, X-rays and γ -rays). It is very likely that a majority of the matter in the Universe does not emit electromagnetic radiation. The existence of this invisible matter, the

dark matter (DM), was indirectly highlighted through its gravitational interaction with ordinary matter, which emits electromagnetic radiation.

Evidence for the existence of dark matter in spiral galaxies emerges from the analysis of the revolution speeds of stars and gas clouds in the galactic halo as a function of the distance from the center of the galaxy. Spiral galaxies, like our own galaxy, contain $\sim 10^{11}$ stars, arranged in the form of a central nucleus and a flattened rotating disk. The revolution speed of a mass m star around the center of the galaxy is determined by the condition of stable orbits, equating the gravitational force with the centrifugal force, that is,

$$\frac{G_N m M_r}{r^2} = \frac{mv^2}{r} \quad (13.17)$$

from which:

$$v(r) = \sqrt{\frac{G_N M_r}{r}}. \quad (13.18)$$

M_r is the total mass of stars and interstellar material within the distance r from the center of the galaxy. Most of the stars of a spiral galaxy are located in the central spherical bulge with radius r_s . If $\bar{\rho}$ is the average density of stars in the bulge, we have $M_r = \bar{\rho} \cdot \frac{4}{3}\pi r^3$ for $r < r_s$; it follows that

$$v(r) = \sqrt{\frac{4}{3}\pi G_N \bar{\rho} r} \approx r \text{ for } r < r_s. \quad (13.19a)$$

If all the galaxy mass is assumed inside the bulge, then $M_r \simeq \text{constant}$ for $r > r_s$, and

$$v(r) \approx 1/\sqrt{r} \text{ for } r > r_s. \quad (13.19b)$$

The observed matter distribution in the bulge and disk leads to a revolution speed of the stars as shown by the dashed line in Fig. 13.8 for the spiral galaxy NGC3198. The figure also shows the contribution of a possible dark matter halo. The experimental data obtained using the Doppler effect are indicated with black dots. From the figure it is evident that at high r , the measured velocities $v \simeq 200 \text{ km s}^{-1}$ are larger than those obtained using (13.18), also including the additional contribution of stars in the disk. There must be a contribution from a halo of dark matter. Similar results are obtained by measuring the speed of stars in other spiral galaxies. Evidence for the presence of dark matter also exists for elliptical galaxies and for galaxy clusters.

One of the major achievements of “experimental cosmology” is the series of precision measurements of cosmic microwave background (CMB). In 1992, the COBE satellite measured the black body spectrum (at a temperature of 2.725 K) of the background radiation. The measurements confirmed that any deviation from a Planck curve was smaller than 1/10,000, as expected (J.C. Mather and G.F. Smoot, Nobel laureates in 2006). The deviations from a perfect black body

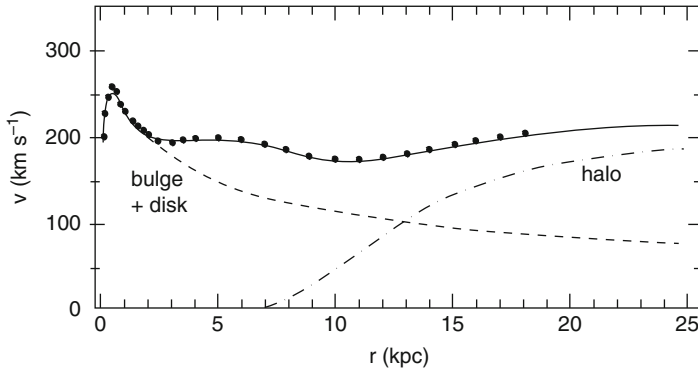


Fig. 13.8 The points indicate the measured rotation speeds of stars in the spiral galaxy NGC3198, versus their distance r from the galactic center. The *dashed line* represents the expected contribution based on the visible matter in the galactic nucleus (bulge) and in the galactic disk; the *dotted-dashed line* includes the contribution of a halo of dark matter. The *solid line* is a fit to experimental data assuming visible matter in the bulge and disk and dark matter in the halo

spectrum were measured with experiments placed on balloons (BOOMERanG [13B00], MAXIMA). Recently, the WMAP experiment on a satellite measured the temperature differences in the CMB radiation with high precision. The measured anisotropies are used to estimate the Universe's geometry, content, and evolution; test the Big Bang model and the cosmic inflation theory. Cosmology closely connects the curvature of the Universe with its matter density $\Omega = \rho/\rho_c$, where ρ_c is the *critical density of the Universe*:

$$\rho_c = \frac{3H^2}{8\pi G_N} = \frac{3(100 h_0 \text{ km s}^{-1} \text{Mpc}^{-1})^2}{8\pi G_N} \simeq 1.9 \cdot 10^{-29} h_0^2 \text{ g cm}^{-3} \quad (13.20)$$

where $H = 100h_0 \text{ km/s/Megaparsec}$ is the Hubble constant, $h_0 \simeq 0.71$.

The recent WMAP results have shown that (1) the Universe is 13.7 billion years old (with 1% margin of error); (2) the cosmological scenario which includes a period of cosmic inflation is in agreement with the observations; (3) the Hubble constant is $H = 100h_0 = 71 \pm 4 \text{ km/s/Megaparsec}$; (4) $\Omega_{tot} = 1$.

In particular, the matter density Ω can be expressed as the sum of different density terms:

1. Visible baryonic matter: $\Omega_{vis} \simeq 0.005$.
2. Nonvisible baryonic matter: $\Omega_b \simeq 0.046$.
3. Nonbaryonic dark matter: $\Omega_{DM} \sim 0.23$.
4. (from which neutrinos: $\Omega_\nu \sim 0.003 - 0.1$).
5. “Quintessence”(dark energy) $\Omega_Q \sim 0.72$.

The “Quintessence” (or dark energy) is still an unknown form of energy that permeates the space and tends to increase the expansion rate of the Universe. We will return to this topic at the end of this chapter.

No experiment has ever provided direct information on the nature of dark matter. The *baryonic* fraction of DM could be astrophysical bodies in their terminal phase (*remnants*) as white dwarfs, neutron stars and black holes. They could also be smaller objects, with insufficient mass ($0.1 m_{\odot}$, where m_{\odot} indicates the mass of the Sun) to become stars (Jupiter-like planets); these massive compact objects are called *MACHO*. The research in galactic halos (via effects like *gravitational lensing*) indicates that such objects with $m < 0.1 m_{\odot}$ exist, but that their total mass is much smaller than that of the dark matter halo. MACHOs are probably not important at the cosmological level, and they are almost certainly negligible even at the level of the internal dynamics of galaxy structure and formation.

There are other arguments in favor of the existence of nonbaryonic DM. For example, the study of nucleosynthesis of light nuclei at the cosmic time $t \simeq 200$ s leads to the value $\Omega < 0.02$ if only baryonic matter is considered. It is noteworthy that without nonbaryonic DM, it is difficult to construct models of galaxy formation starting from small fluctuations, like those observed in the cosmic microwave background. The nonbaryonic DM could be a gas of weakly interacting particles, classified as *hot* or *cold* particles depending on whether they were relativistic or not at the time of galaxy formation. If these DM particles are in thermal equilibrium with baryons and radiation, they are classified as hot or cold DM if their mass is smaller or larger than ~ 1 keV, respectively. Models with cold DM are better reproducers of the observed large scale structure of our Universe.

An interesting candidate for cold DM is the stable SUSY particle, the lightest neutralino, with a mass of the order of 100 GeV; it manifests itself as a *Weakly Interacting Massive Particle* (WIMP). A WIMP can be directly detected through elastic interaction with nuclei in scintillators, solid state detectors, etc.; the recoil nucleus will deposit a few keV of energy large enough to be measured.

There is currently a continuous development of larger and more sophisticated detectors (particularly cryogenic detectors) that can provide accurate measurements of temperature rise due to WIMP energy loss by ionization or excitation. The main problem is to distinguish genuine WIMPs interaction from background due to the ambient radioactivity. To unambiguously distinguish a possible WIMP signal from the background, the DAMA experiment [13B08] at the Gran Sasso Laboratory exploits the peculiarities of the “wind” which produces a WIMP annual modulation. Our galaxy should be surrounded by a WIMPs halo and our solar system (which is moving at a speed of about 230 km/s compared to the galactic system) should be continuously hit by a WIMPs “wind.” As the Earth moves around the Sun, the flux of WIMPs, if any, should be maximum in June (when the revolution speed of the Earth adds to the speed of the solar system in the galaxy) and minimum in December (when the two velocities have opposite directions). Data collected for 7 years suggest the presence of an annual modulation. This modulation can be explained by a contribution of WIMPs with mass of about 10 GeV. Other experiments (using different experimental techniques) do not confirm this signal, but the discussion is still open.

WIMPs are also searched for by using indirect methods: massive WIMPs can be slowed down by elastic collisions and captured by a celestial body (like the Earth or the Sun). If WIMPs collect in the nuclei of these celestial bodies, a higher concentration is expected, and WIMP–antiWIMP annihilation can take place. This annihilation would produce particles that decay into high energy ν_μ that could be detected in large underground detectors and in neutrino telescopes, resulting in high energy muons from $\nu_\mu N \rightarrow \mu^- + X$, with direction coming from the center of the Earth (or the Sun).

Another searched particle is the *axion*, that is, a particle theoretically predicted in models beyond the SM whose mass should be $\sim 10^{-5}$ eV. Axions would be nonrelativistic even if they have low mass. They are searched through their conversion into photons in a nonuniform magnetic field.

13.6 The Big Bang and the Primordial Universe

According to the *Big Bang model*, the expansion of the Universe originated from a “primordial explosion,” from a space-time singularity of very high density and temperature. Starting from the Big Bang, the Universe can be considered as a gas of particles rapidly expanding. Our knowledge on particle physics, fundamental constituents and interactions, helps us to understand what probably happened. Theories on the unification of fundamental interactions have been applied to describe the evolution of the Universe immediately following the Big Bang.

To imagine the nature of the expansion, the example of the swell of a balloon is used. Inflating the balloon, the distance between any pair of points drawn on its surface increases. A hypothetical two-dimensional observer located at one point on the balloon surface would see all other points moving away from his position in all directions. Other observers on the balloon surface will observe the same recession. There is no privileged point: the expansion has no center within the two-dimensional surface. For two-dimensional observers on a spherical surface, the Universe is finite and unrestricted in the sense that a flat individual can move in a fixed direction and, continuing, will return to the starting point. According to general relativity, the Universe expansion happens in four dimensions; it is difficult for us to see the fourth dimension, as it is difficult for the two-dimension observers to visualize their third dimension.

The Big Bang model is mainly based on three experimental facts: (1) the recession of galaxies; (2) the cosmic microwave background and (3) the ratio of helium–hydrogen abundance.

Cosmic microwave background radiation. The Universe is uniformly filled with a cosmic microwave background radiation generated at the time of H and He atoms formation, when the temperature of the Universe had dropped to 4,000 K (*time of atoms formation*). As the radiation no longer had enough energy to further ionize the

atoms, the Universe became transparent and from that moment, matter (i.e., atoms) and electromagnetic radiation were independent. The corresponding present number density of photons, about 400 cm^{-3} , represents the largest number of particles in the Universe. When increasing time, the Universe expanded and cooled down to its present status. The expansion causes an increase in the distance between two successive wave crests. A longer wavelength corresponds to lower photon energy.

Helium abundance in the Universe. Direct observation indicates that the helium present in every galaxy, in any direction and at any distance, corresponds to 20–24% of the visible baryonic mass. This is explained assuming that helium (and other light elements, for example, D , 3He , 7Li , 7Be) was produced in the early moments of the Universe. Heavier nuclei have been synthesized in heavy stars, see Sect. 14.10.

The picture of the Universe before the helium formation (200 s after the Big Bang) was as follows: the temperature was about 10^9 K and a large number of photons, a relatively small number of protons, neutrons and electrons were in statistical equilibrium. A large number of neutrinos were also present, but with negligible influence because of the low neutrino interaction cross-section with matter. The interaction between neutrons and protons formed *deuteron* nuclei with energy release; but deuteron were dissociated through $\gamma + d$ collisions and immediately split into their constituents n and p . When the temperature fell below one billion degrees, the photon energy kT was no longer able to break the deuteron nuclei. Then, a series of nuclear reactions undisturbed by the photons began; the reactions led to the formation of helium, the more stable between light nuclei, and of a relatively small number of other light nuclei elements. The time at which they were produced is called the *nucleosynthesis phase of light elements*.

The evolution after the Big Bang. As for the above description of the nucleosynthesis of light elements, the state of the Universe at any given moment is determined by statistical mechanics laws. Additional information exists regarding the number density of particles present, their temperature (i.e., their average kinetic energy), and how they interact. This information can be obtained by making extrapolations based on the knowledge of the interactions among particles at lower energies, and assuming conservation laws. It is assumed that all the conserved physical quantities (charge, baryonic and leptonic numbers, ...) were zero at the beginning. At some point, during a phase transition, some process (yet unknown) which allowed the matter to dominate over antimatter must have occurred.

We will show the evolution of the early moments of the Universe using a set of “snapshots” taken at increasing times. We must remember that our knowledge decreases when approaching the Big Bang. The broad outlines of the Universe history, illustrated in Fig. 13.9 and described below, are clear, but perhaps many “details” remain to be defined.

1. **Cosmic time $t_1 = 0$** , about 13.7 billion years ago. The Big Bang happens, i.e., the singularity at the origin of the Universe. From this moment, the Universe expands. All conserved quantum numbers are equal to zero. Probably, the total energy is also equal to zero because the kinetic energy, i.e., the energy of motion, is equal and opposite to the gravitational potential energy.

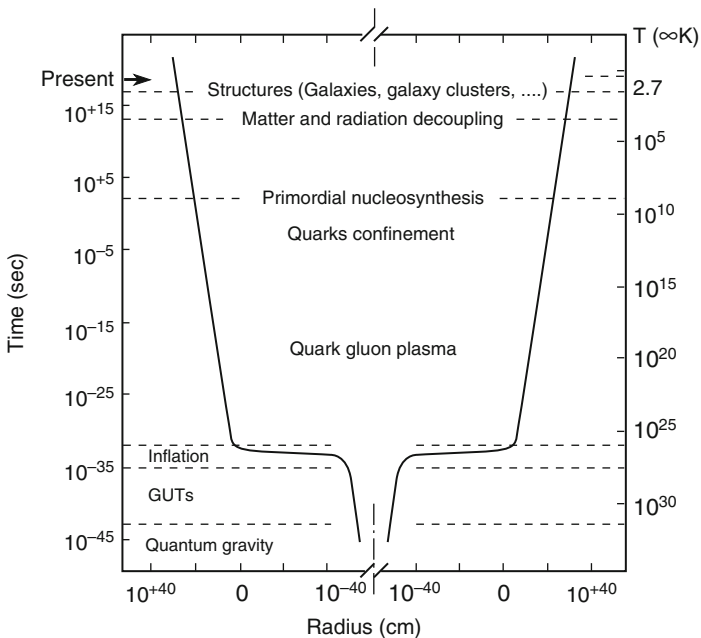


Fig. 13.9 One possible way to describe the evolution of the Universe: temperature (T) and time (t) versus the parameter R_0 that can be identified as the “radius” of the Universe. Note the inflationary phase, when the Universe expanded exponentially

2. **First phase transition at $t_2 = 10^{-43}$ s (Planck time).** The temperature is $T_2 \simeq 5 \cdot 10^{31}$ K; the average kinetic energy of each particle is $\bar{E}_2 \simeq 10^{19}$ GeV. It is the moment when particles are generated. For times smaller than the Planck time, quantum mechanical fluctuations did not allow one to consider particles as separate entities and the gravitation was unified with the Grand Unified interaction. Up to this moment, the emitted gravitational waves were absorbed; from this time, they are free to propagate.
3. **From 10^{-43} to 10^{-35} s.** The Universe (if quarks and leptons are the ultimate constituents of matter) is a gas of quarks and leptons, antiquarks and antileptons, and of X, Y bosons, the mediators of the Grand Unification interaction (if they exist). In this case, leptons and quarks behave like members of the same family; a quark can transform into a lepton (or vice versa).
4. **Second phase transition at $t_4 \simeq 10^{-35}$ s.** The temperature is $T_4 \simeq 5 \cdot 10^{27}$ K, $\bar{E}_4 \simeq 10^{15}$ GeV per particle. The era of the Grand Unification of the strong with the electroweak interaction (from t_2 to t_4) ends with a phase transition. Transitions from a quark to a lepton (or vice versa) are no longer possible. Interactions of quarks became very different from those of the leptons. This is the GUT transition, during which new particles can be created, for example, the *magnetic monopoles*. At $t = t_4$, the *electroweak era* started. According to some models, the phase transition at $t = t_4$ began with a hyper-

expansion (or *inflation*) of the Universe. Inflation is expected to have reduced the number of magnetic monopoles, and made the Universe “flat,” isotropic and causally connected. Inflation has increased with a superluminal speed at a region of about 10^{-25} cm to 100 m in a very small fraction of time.

5. **From 10^{-35} to 10^{-10} s.** Strong and electroweak interactions are different, and quarks and leptons behave as different objects; the X, Y bosons decay into quarks and leptons. Their decay leads to an asymmetry between matter and antimatter, with a slight predominance of the former. During this period (electroweak era), it seems that nothing happens: it is a short time interval that corresponds to a large energy range. Many physicists defined this time interval as *the desert*. Maybe the desert will “flourish,” if new particles (e.g., supersymmetric particles) with masses of the TeV order are discovered.
6. **Third phase transition at $t_6 = 10^{-10}$ s.** The temperature is $T_6 \simeq 1.5 \cdot 10^{15}$ K, $\bar{E}_6 \simeq 200$ GeV. The electroweak era ends: after this moment, the electromagnetic and weak forces are different from each other.
7. **Fourth phase transition at $t_7 = 10^{-6}$ s.** *Particle–antiparticle* annihilations begin. As a result of $q\bar{q}$ and e^+e^- annihilations, there is the disappearance of antimatter, leaving a number (relatively limited) of quarks and electrons. Before t_7 , there was a plasma of q, \bar{q} , gluons (*quark-gluon plasma*), plus electrons.
8. **Fifth phase transition at $t_8 = 10^{-4}$ s.** The temperature is $T_8 = 1.5 \cdot 10^{12}$ K, $\bar{E}_8 \simeq 0.2$ GeV. This phase transition corresponds to *quarks confinement* to form baryons. Leading up to this moment, quarks are free particles. Now, u, d -type quarks combine in triplets to form protons and neutrons (maybe also the few remaining \bar{q} join in triplets to form \bar{p} and \bar{n}). The difference in the number of quarks and antiquarks is now a difference between the number of p and \bar{p} (and between n and \bar{n}).
9. **From 10^{-4} to 1.1 s.** The Universe is dominated by particles with masses smaller than 6 MeV: electrons, positrons, neutrinos, antineutrinos and photons. The Universe is still so hot and dense that neutrinos interact quickly and are in thermodynamic equilibrium with e, γ . Their abundances are almost equal. The number of p and n is instead very small, about one in every billion of γ (or e^- or ν). The number of n is almost equal to that of p .
10. **Sixth phase transition at $t_{10} = 1.1$ s.** The temperature is $T_{10} \simeq 1.4 \cdot 10^{10}$ K, $\bar{E}_{10} \simeq 2$ MeV; the *neutrino decoupling* happens. The average energy of neutrinos, as that of any other particle, and the neutrino interaction probability (cross-section) decrease; the matter density decreases as well with increasing time. As a result, the neutrinos at $t = t_{10}$ do not interact frequently with the rest of the matter and become independent.

The neutron has a mass slightly larger than that of the proton: this did not play a role when the typical energies were high. In the collisions, a neutron could transform into a proton with an equal probability than that for the reverse reaction. The mass difference between n and p produces a difference in the reaction probabilities at the kinetic energies of this period. Just before neutrino decoupling, the reaction $\nu_e n \rightarrow e^- p$ was more likely than the reverse reaction. There was therefore a relative increase in the number of protons. At $t = 1.1$ s,

there is about 24% of neutrons and 76% of protons. In a pn collision, a deuterium nucleus can be formed: $np \rightarrow d\gamma$. The deuteron is rapidly broken into its constituents by a photon interaction $\gamma d \rightarrow np$.

11. **Seventh phase transition at $t_{11} = 4$ s.** The temperature is $T_{11} \simeq 4 \cdot 10^9$ K, $\bar{E}_{11} \simeq 0.5$ MeV per particle: the e^+e^- pair annihilation begins. Photons have an energy below the energy required to produce e^+e^- pairs. There is no compensation for electron and positron losses due to their annihilation. The e^- and e^+ disappear rapidly, only a small number of electrons, the excess over the e^+ , remains. The number of remaining electrons is exactly equal to that of protons. The released energy in the annihilation process heats the particles that are coupled together (photons, but not neutrinos). The photons reach an average temperature 35% higher than that of neutrinos.
12. **From 4 to 200 s.** Positrons disappear from the Universe. The number of neutrons relative to that of protons continues to decrease, due to their β -decay ($n \rightarrow pe^-\bar{\nu}_e$). At this stage, the main components of the Universe are $\gamma, \nu, \bar{\nu}$ with a (relatively) small percentage of e^-, p, n (an electron/proton for every billion photons.)
13. **Eighth phase transition at $t_{13} \simeq 200$ s.** The temperature is $T_{13} \simeq 10^9$ K, $\bar{E}_{13} \simeq 140$ keV per particle: it is the phase when the *nucleosynthesis* of deuterium, helium and other light elements (which have already been discussed above) takes place. From this moment, there is nuclear matter, with 24% helium and 76% of protons (in weights).
14. **From $t_{13} = 200$ s to $t_{14} \simeq 10,000$ years.** The Universe mainly contains photons and neutrinos. There is a (relatively) small amount of matter. There are no more free neutrons. The radiation continues to cool down as well as matter. Matter is in the form of a gas of electrically charged particles (protons and electrons). A plasma of electrons and protons is the fourth state of matter (after solid, liquid and gaseous states). It is still abundant today because it is the dominant state inside the stars.
15. **$t_{15} \simeq 10,000$ years.** Matter and radiation energy densities are equal: $\rho_{matter} = \rho_{radiation}$. The *radiation era*, which had originated just after the Big Bang, ends and the *matter era* (that continues today) begins. In the era of matter, energy is dominated by matter, i.e., the energy associated with the rest mass mc^2 . However, in the radiation era, the particle kinetic energies were much higher than the energy associated with the mass. Atoms cannot form yet: if a proton captures an electron to form a hydrogen atom, shortly after, a collision with a photon breaks the binding.
16. **Ninth phase transition at $t_{16} \simeq 300,000$ years.** The temperature is $T_{16} \simeq 4,000$ K, $\bar{E}_{16} \simeq 0.5$ eV per particle: this is the time of *atom formation*. The photon energy is so low that photons are no longer able to break atoms. In a relatively short time, electrons combine with protons to form hydrogen atoms, and with helium nuclei to form helium atoms. As the photons are no longer absorbed by atoms, the Universe becomes transparent to electromagnetic radiation, which is now decoupled from the matter and has an “independent

- life.” The WMAP (see Sect. 13.5) measurement of the temperature differences in the Cosmic Microwave Background radiation refers to this moment.
17. **$t_{17} \simeq 1$ billion of years.** The average particle energy is $E_{17} \sim 0.1$ eV. The *galaxy formation* starts. Galaxies and galaxy clusters form, then the first stars. Clouds of matter were formed by fluctuations in the matter spatial distribution; gravitation starts to form *protostars*. Over time, as the gas cloud compresses, the temperature at the center increases until it becomes so high that thermonuclear reactions can be initiated. Hydrogen is burned, and as a consequence, helium is produced as “ash.” The starlight starts to illuminate the Universe. The average wavelength of the cosmic microwave background became large, corresponding to infrared radiation.
 18. **$t_{18} \simeq$ few billion years.** The first supernovae explode, launching a large quantity of material containing heavy elements (synthesized within the stars) in the interstellar space.
 19. **$t_{19} \simeq 9$ billion years.** The Sun and its planets, including the Earth, start to form by gravitational contraction. The material collected by our cloud mostly contains hydrogen and helium, the material produced at the beginning of the Universe; there are also significant quantities of materials such as iron, synthesized in massive stars which have already exploded.
 20. **$t_{20} \simeq 13.7$ billion years.** Approximately 1 million years ago (or less), the *Homo sapiens* began to wonder how our Universe was made.

Current size of the Universe. In conclusion, it can be assumed that the Universe has a radius of about 13.7 billion light years and consists of about 100 billion galaxies; each galaxy is made of about 100 billion stars. Taking into account the mass of each star, the observable Universe is made of about 10^{80} protons. However, this should account for less than 5% of matter and energy: most of the matter/energy is still invisible to us. The number of cosmic background radiation photons is about a billion times the number of protons.

One might ask: **what existed before the Big Bang?** There can be no answer that physically makes sense because you cannot get any information for the time before the Big Bang. However, the inflation mechanism might suggest that there are many “parallel Universes.”

Expansion accelerated or decelerated. In 1998, two astrophysicist teams began to study the motion of distant galaxies by observing the final stage of some of their bright stars (type I supernovae). They found that these galaxies are moving away from us more slowly than expected from the Hubble law [13S04]. The observed light has left the galaxies a few billion years ago: looking further away in the Universe, we observe objects at increasingly younger ages. In the spirit of the standard model of the Big Bang, gravity slows the motion of bodies that are moving away from each other. Therefore young “objects” should move faster away from us than older objects. The results from type I supernovae indicate the opposite, namely, that the Universe is now expanding faster than in the past. This is an outstanding result whose consequences are not completely understood in the standard models of the Microcosm and Macrocosm.

To obtain this situation, a field that tends to accelerate objects in the Universe should probably be present. This (unknown) energy field would contribute to approximately 70% of the Universe energy density. The name of *quintessence* or *dark energy* is given to this energy field. In the future, if the type I supernovae results are definitively confirmed by other independent methods, several concepts about the Universe, particularly those relating to its future evolution, will probably need to be revised.

The future of the Universe. What can be said concerning the future evolution of the Universe? If the actual density of matter is smaller (or equal) than the critical value, then the Universe will continue to forever expand. If it is larger, the Universe would reach a maximum expansion and then have a contraction, leading to a final implosion. The recent results from WMAP and others indicate that the actual density of matter is exactly equal to the critical density, and that the Universe is flat. In the far future, the stars, having finished their nuclear fuel, will go off one after the other, and the Universe would become dark, without visible light. In the very far future, one could have the proton decays and even later blacks hole “evaporation.”

Chapter 14

Fundamental Aspects of Nucleon Interactions

14.1 Introduction

The periodic table of elements (the Mendeleev table, Appendix A.1) is the most extraordinary demonstration of the interconnection between the microcosm and macrocosm, or between particle physics, astrophysics and cosmology. Following the Standard Model of the macrocosm (Sect. 13.6), 3 min after the Big Bang, matter in the Universe was primarily composed of hydrogen (92%), helium (8%) nuclei (*primordial nuclei*) and electrons. Today, on Earth, every element of the periodic table is present, from hydrogen ($Z = 1$) to uranium ($Z = 92$). As we shall show in this chapter, all nonprimordial nuclei up to iron are formed inside stars, in the processes of stellar nucleosynthesis. The release of these elements in the Universe occurs through the gravitational collapse of massive stars, followed by the envelope expulsion (supernova). Nuclei heavier than iron are formed through neutron capture processes, followed by β -decay. Most of the produced nuclei are radioactive. Only those with long or very long lifetimes have survived. All the others were transformed into stable nuclei.

In this chapter, we shall review the basic properties of nuclei, their structure (distributions of electric charge and mass, volume) and the interactions between nucleons (i.e., between neutrons and protons) to form the nuclei. The interaction between nucleons cannot be described by a simple potential energy function. As the molecules are formed by *neutral objects* (the atoms) and bound by residual electromagnetic interactions, nuclei are formed in a similar way by objects which are *neutral* for the strong interactions. Protons and neutrons have no *color charge*. Nuclei are bound by a kind of residual strong interaction. Their interaction cannot be formalized in a simple way from the mathematical point of view.

However, we shall see that a formula that parameterizes a fundamental quantity, the *nuclear binding energy*, can be written. The higher the binding energy, the more stable is the nucleus. The properties of the nuclear binding energy not only influence the physics of nuclei, but also the structure and the stellar evolution.

Table 14.1 Distribution of stable nuclei as a function of the atomic number Z (number of protons), the number of neutrons N and the mass number $A = Z + N$

A	Z	$N = A - Z$	Number of stable nuclei
Even	Even	Even	157
Odd	Even	Odd	53
Odd	Odd	Even	50
Even	Odd	Odd	4
		Total	264

It is not necessary to consider nuclear physics in terms of quarks and gluons, even if protons and neutrons are made of quarks. In classical nuclear physics, the existence of quarks can be ignored as well as the existence of meson and hadron resonances. A nucleus consists of nucleons that somehow behave as almost free particles, although they are in a high density medium (about 10^{38} nucleons/cm 3). The average kinetic energies of nucleons in the nucleus are of the order of 20 MeV (Sect. 14.3.1), which is considerably smaller than the energy scales of elementary particles. The hadron composition in terms of quarks and gluons should only be taken into account in a deeper description of nuclear physics. Moreover, under particular conditions of energy density, such as those that can be reached during the collision between two very high energy heavy nuclei, quarks could become free and nuclear matter should behave as a plasma of *quarks and gluons*.

The chemical elements existing in nature are a finite number: they are those that appear in the periodic table of elements. Each element has a nucleus with a definite electric charge (i.e., number of protons). In the laboratory, it was possible to artificially create some nuclei, called *transuranic*. In the Mendeleev table, their position is higher than that occupied by uranium. However, these artificial nuclei have relatively small lifetimes. The stable nuclei observed in Nature are 264; the number of those unstable is larger than 1,500. Their number is increasing every year, as more refined experimental techniques allow one to observe unstable nuclei with shorter and shorter lifetimes. The nuclei can be classified in terms of the number of protons Z (the *atomic number*), the number of neutrons N and the number of nucleons A ($A = Z + N = Z$ protons plus N neutrons) (the *mass number*). By sorting the nuclei on the basis of Z and N , the stable nuclei are distributed as shown in Table 14.1. The largest number of stable nuclei occur when both Z and N are even. The number of nuclei with Z even and N odd is approximately equal to that with Z odd and N even. The content of Table 14.1 is evidence that the nuclear force is independent of whether the nucleons are protons or neutrons.

The fundamental properties of nuclear physics are more complicated than those of atomic physics. Our knowledge of nuclear interactions is, in any case, advanced enough to conclude that the chemical elements everywhere in the Universe are the same as those found on Earth. It does not exist, therefore, some elusive stable element with physics properties unknown on Earth (e.g., the *unobtanium* on the Pandora planet of the *Avatar* movie).

The physics laws are universal; from nuclear physics, we know that the nuclei (and thus the atoms) on Earth are the same as those that found elsewhere in the

Universe. From nuclear, atomic physics and astrophysics we also know that the chemical composition of planetary systems may not be very different from that of our Solar System. We do not know indeed if there is intelligent life beyond our Solar System, anywhere else in the Universe. We are also unaware of the biology of this hypothetical intelligent species, nor of their reproduction modality. Reproduction can occur similar to life on Earth, with the union of two individuals of different sexes: having seen the success and repeatability of natural laws, this assumption might be plausible. In this case, the hypothetical aliens will probably exchange a *golden* gift and not an *iron* object as a token of love. Also, in this planetary system, the ratio between the number of gold nuclei with respect to iron nuclei will be 10^{-6} – 10^{-5} , and gold will be a precious good. If in addition, there is on the gift a brilliant transparent stone made of carbon atoms in a particular lattice arrangement, we think that the hypothetical individuals of this planet will have a good chance of successfully transmitting their genes .

14.2 General Properties of Nuclei

In 1911, Rutherford, studying the transmission of alpha particles (He nuclei) in a thin layer of gold (Au), realized that they were also scattered at large angles (up to 180° , i.e., backward). At that time, the Thomson model of the atom was generally accepted: it assumed that the electrons are *drowned* in a positive charge distributed throughout the volume of the atom. Such a charged sphere is not able to significantly deviate a particle with a mass equal to 7,300 electron masses. To obtain deviations such as those observed, it must be hypothesized that the positive charge is concentrated in a much smaller volume.

The interpretation of emission spectra of atoms and the Rutherford experiment are at the base of the Bohr–Sommerfeld atomic model:

- The atom consists of a nucleus of charge $+Ze$.
- Z electrons, each with a charge $-e$, are bound to the nucleus by the Coulomb potential.
- The nucleus mass is much greater than the electron mass.
- The electric charge of the nucleus is concentrated in a region of space much smaller than the size of the atom.

After the discovery of the neutron (1932), it was realized that the nuclei are bound states of subconstituents nearly equal in mass, with N neutrons and Z protons. The interaction between the nuclear constituents has characteristics very different from the electromagnetic interaction. In particular, the forces holding the nucleus together are called *nuclear*; nuclear forces do not depend on the electric charge and they have an interaction range of about 10^{-15} m. The order of magnitude of the nuclear binding energy is the MeV; it is straightforward to estimate that to maintain two protons at a distance of $r \sim 1$ fm against the Coulomb repulsion, an energy of $U > e^2/r \sim 1$ MeV is needed. Quantities that characterize the atomic nuclei and

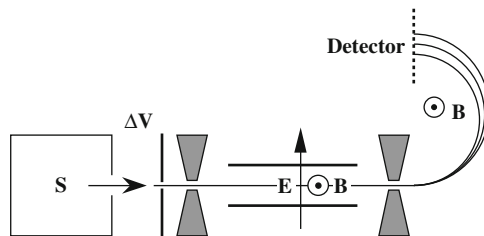


Fig. 14.1 Operation principle of a mass spectrometer. The ionized nuclei are emitted from the source S ; they enter, through a collimator, in a region with electric field E and magnetic field B . Because of E , the ion is subject to an upward force, whose module is ZeE . Meanwhile, due to the magnetic field, it is deflected downward with a force $ZevB$ (c.g.s. units). The second collimator selects only those particles for which the two forces cancel each other (those for with $v = E/B$). After the second collimator, only the magnetic field B is present. The Lorentz force deflects the ions with a curvature radius R which can be experimentally measured

give information on their structure are: mass, radius, spin; the electric charge, the magnetic dipole moment, the electric quadrupole moment.

Nuclei are indicated with the symbolic name of the element X (e.g., H for hydrogen, Fe for iron). The *atomic number* Z (and therefore the electric charge of the nucleus) is written as a subscript on the left. The *mass number* A is placed on the top left:

$$_A^Z X. \quad (14.1)$$

Electric Charge of Nuclei. The electric charge of nuclei is measured by studying the X-ray emission spectra of electrons in inner orbitals (K orbital); these electrons are not affected by the electromagnetic shielding effect by the electrons arranged in the outer orbitals. In 1913, Moseley established a relationship between the frequencies of X-rays and the atomic number, that is,

$$h\nu = \frac{3}{4}R_y(Z - 1)^2 \quad (14.2)$$

where $R_y = m_e c^2 \alpha^2 / 2 = 13.6 \text{ eV}$ is the Rydberg constant. Moseley's law ordered all known elements in the Mendeleev table, showing that the nuclear electric charge is a multiple of the elementary electric charge e .

Mass of the nuclei. The mass of the nuclei is determined by measuring their trajectory in an electric and a magnetic field. The mass spectrometer, firstly developed by Aston in 1920 (Nobel laureate in 1922), was gradually improved to achieve a precision measurement of $\Delta M/M \sim 10^{-6}$. The operating principle is shown in Fig. 14.1. Ions emitted from the source S are accelerated by an electric field E orthogonal to a magnetic field B . Both E and B are also orthogonal to the

ion trajectory in order to only select nuclei with electric charge $q = Ze$ and speed $v = E/B$; after the second collimator, there is only the magnetic field. The mass M of the nucleus is determined by measuring the curvature radius R of the trajectory curved by the Lorentz force ($qvB = Mv^2/R$)

$$M = \frac{qB}{v}R = \frac{qB^2}{E}R. \quad (14.3)$$

To reduce systematic uncertainties, the measurements are usually done by comparison amongst nuclei that have very small mass difference. An instructive online applet of a mass spectrometer can be found in [14w1].

The mass spectrometer is also used to separate isotopes of the same element and to measure their relative abundance. Carbon, for example, exists in Nature as two isotopes with relative abundance of 98.89% ($^{12}_6C$) and 1.11% ($^{13}_6C$). The atomic weight of natural carbon corresponds to the mean value $\bar{A} = 12.01$. For historical reasons, the *atomic mass unit* (AMU), denoted as u , is often used in nuclear physics. It is defined by the relation $12u = \text{mass of the isotope 12 of carbon}$. In these units, the mass of the hydrogen atom is

$$M(^1_1H) = 1.007825 u = 938.783 \text{ MeV}/c^2.$$

The conversion factor between the units is

$$1 u = 931.494 \text{ MeV}/c^2. \quad (14.4)$$

The number at the bottom of each element of the Mendeleev table in Appendix A.1 shows the value of the nuclear mass in AMU. For practical reasons, the proton rest mass ($m_p = 938.271 \text{ MeV}/c^2$) is also be used as mass unit.

14.2.1 The Chart of Nuclides

Nuclei with the same value of Z and different values of A have the same atomic properties: chemical reactions depend almost exclusively on Z . For this reason, nuclei with the same number of protons are called *isotopes* (because they occupy the same position in the Mendeleev table of elements). Nuclei with the same value of A and different values of Z are called *isobars* (because they have approximately equal mass). In terms of variables (N, Z) , the stable nuclei are concentrated in a narrow band, called *stability valley* (Fig. 14.2), indicating a correlation between the electric charge and the number of constituents.

The bond due to the strong interaction between $(n-n)$ and $(p-p)$ pairs is identical. It is different for $(p-p)$ pairs because the protons repel electromagnetically. For low values of A , nuclei have $N = Z$; starting from $A \simeq 40$, the fraction of neutrons increases.

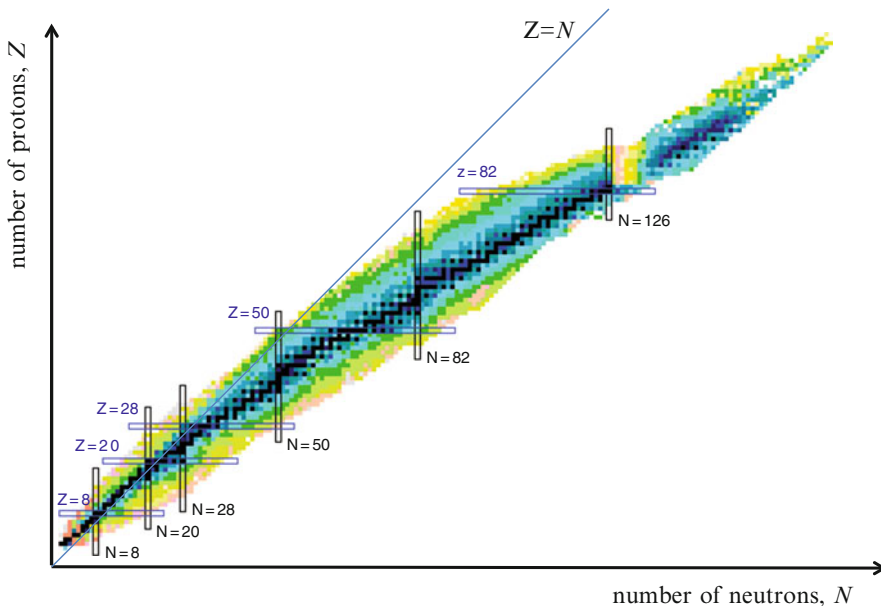


Fig. 14.2 Chart of nuclides. The nuclide lifetime increases as the darkness of the square. The stable nuclei are shown in *black* in the middle. The *bars* show the nuclei with *magic numbers*, Sect. 14.3.3 (Adapted from the interactive and color chart, which is available at the Brookhaven National Laboratory website [14w2])

14.2.2 Nuclear Binding Energy

The equivalence between mass and energy ($E = mc^2$) is not appreciable in atomic physics. The reason is that the binding energies (of the order of eV, i.e., $2 \times 10^{-5} m_e$) are much smaller than the masses of the particles. The relation $E = mc^2$ becomes important in nuclear physics, where the energies involved may represent a significant fraction of the rest masses of the nucleons. For this reason, it is sometimes convenient to express both energies and masses in natural units $\hbar = c = 1$ (see Appendix A.2), that is in MeV.

In the formation of a bond (atomic or nuclear), energy is gained because a more stable system is obtained. The energy released should be compensated by the decrease of the final mass, with respect to the sum of the initial masses of the elements. For example, the bound state with the smaller nuclear mass is the deuterium nucleus (deuteron); the deuteron is a hydrogen isotope made by one proton and one neutron ($Z = 1, A = 2$). In this case, the mass is decreased by 2.224 MeV; it is a small amount compared to $m_p + m_n$, but not quite negligible ($\sim 0.2\% m_p$).

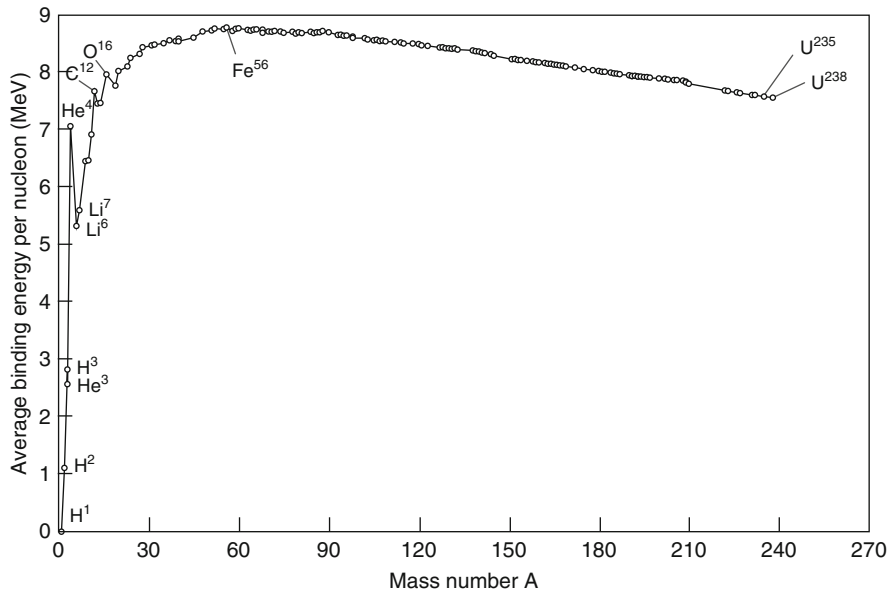


Fig. 14.3 The measured binding energy (BE) per nucleon of stable nuclei measured as a function of A . The peaks correspond to particularly stable nuclei. The curve has a maximum at $A \sim 60$

The binding energy (BE) is defined as the difference between the mass of the nucleus and the sum of the masses of the constituent nucleons:

$$M_{\text{nucleus}} = \sum_{k=1}^A m_k - BE = (Zm_p + Nm_n) - BE. \quad (14.5)$$

The helium nucleus 4_2He (also called α particle) is a particularly stable configuration whose binding energy is equal to 28.298 MeV. The binding energy of nuclei with small A is not a regular function. For $A > 12$, the binding energy is approximately proportional to the number of nucleons (Fig. 14.3), with

$$\frac{BE}{A} \sim 8 \text{ MeV/nucleon}. \quad (14.6)$$

This relation has a justification in the framework of the nuclear drop model (see Sect. 14.3.2).

14.2.3 Size of the Nuclei

The term *nuclear radius* needs to be correctly defined through the operational specification of *what is measured* and of *the measurement method*. Information

on *spatial distribution of nuclear matter* and on the *nuclear interaction range* are obtained with different methods: diffusion experiments (with α particles, neutrons, protons, electrons); spectroscopy of nuclear levels; analysis of nuclear binding energies; study of nuclear decays. In this section, we shall mainly focus on the scattering of particles on nuclei.

In Rutherford scattering (Sect. 4.7.1), the closest approach of a particle depends on the scattering angle θ . Rutherford and Chadwick already noted a large deviation from the expected Coulomb cross-section for a point-like charge when the transferred momentum is high, i.e., when the distance of closest approach is comparable with the range of nuclear forces (see Sect. 7.1.1).

Since the first measurements, it was found that the nuclear radius R is proportional to the cubic root of the atomic weight A :

$$R = R_0 A^{1/3} \quad R_0 \simeq 1.2 \times 10^{-13} \text{ cm.} \quad (14.7)$$

Using particle accelerators, it was possible to reach higher transferred momenta, and to study the structure of nuclei and nucleons in more detail (see Chap. 10). The information obtained depends on the type of particle used as a probe. α particles and protons are subject both to the Coulomb interaction and to the nuclear interaction. The neutrons are subject to the nuclear interaction only (the magnetic dipole interaction is negligible at low energy).

Distribution of the electric charge density. The electrons do not have nuclear interactions and electron scattering experiments give detailed information on the electric charge distribution, on the nucleus electromagnetic radius and on their magnetization. Using high energy electrons, $E_e = 100\text{--}1,000 \text{ MeV}$, the electromagnetic form factors of nuclei (Sect. 10.4) were measured. From the form factors, the electric charge density $\rho(r)$ and the nucleus magnetization $\mathbf{M}(r)$ can be deduced. The elastic cross-section of electrons on nuclei decreases as the transferred momentum increases. This is roughly compatible with the expected behavior from a uniform charge distribution in a sphere of radius R . A more accurate parameterization of the electric charge density inside the nucleus is obtained with a spherically symmetric distribution, that is,

$$\rho(r) = \frac{\rho_0}{1 + e^{(r-R)/t}}. \quad (14.8)$$

This is known as the *Woods–Saxon* distribution. It depends on two parameters: R represents the value of the radius where the charge density is $\rho(r) \geq \rho_0/2$; t measures the thickness of the region where the charge density decreases rapidly. For nuclei with large A , one approximately has

$$R = (1.18A^{1/3} - 0.48) \text{ fm}, \quad t = 0.55 \text{ fm.}$$

Distribution of nuclear matter. Neutron–nucleus scattering experiments are used to study the distribution of nuclear matter and of the nucleus mean square radius.

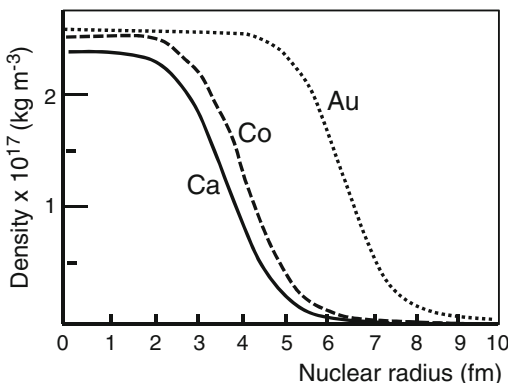


Fig. 14.4 Distribution of matter density as a function of the nuclear radius for some nuclei. The curves represent the parameterization of the experimental data with the Wood–Saxon function (14.8)

The differential cross-section for the elastic scattering of a neutron on a nucleus (n -nucleus) shows, as a function of the scattering angle, peaks and valleys typical of a diffraction pattern. Indeed, the interaction can be interpreted in a quantum-mechanical treatment (optical model of the nucleus) which describes the perturbation of the nucleus on the incident neutron in terms of a potential well¹ and an absorption term. The problem may be analyzed by solving the Schrödinger equation with a *potential well* which is described by a complex function. This corresponds to the optical analogue of a semitransparent sphere, which diffuses and absorbs light. The results for the nucleus radius can be summarized in a formula similar to (14.8) with the following parameters:

$$R = 1.2A^{1/3} \text{ fm}, \quad t = 0.75 \text{ fm}.$$

There is a surprising agreement between the electromagnetic form of the nucleus and the shape of nuclear potential, which depends on the distribution of nuclear material in the nucleus and on the nuclear force range. Figure 14.4 shows the distribution of matter density $\rho(r)$ for different nuclei.

All measurement methods, even different from those mentioned, give consistent results. From these measurements, the following conclusions can be drawn:

- The nuclear matter distribution is approximately equal to the electric charge distribution.
- To a good approximation, the distributions have spherical symmetry.
- Charge and matter distributions are approximately uniform in a sphere of radius R .

¹A potential well is the region surrounding a local minimum of the potential energy.

- The mean square radius distributions are proportional to $R = R_0 A^{1/3}$, with $R_0 \simeq 1.2 \times 10^{-13} \text{ cm}$.
- The value of R_0 depends only slightly on the measurement method.
- The *nuclear volume* is proportional to the number of nucleons, $R^3 \propto A$.
- The density of nuclear matter is high: the mass of the nucleon is equal to $\sim 1.7 \times 10^{-27} \text{ kg}$, and the nuclear density is $\rho_N = 2.4 \times 10^{17} \text{ kg m}^{-3}$, i.e., 2.4×10^{14} times that of water.

14.2.4 Electromagnetic Properties of the Nuclei

The electromagnetic properties of the nuclei are described by the charge density $\rho(\mathbf{r}; t)$ and the current density $\mathbf{j}(\mathbf{r}; t)$, in the region with radius R . The nuclei are subject to the action of electric and magnetic fields produced by charges and currents of the atomic electrons as well as to the action of external fields. The charge and current densities have the nucleus spin direction (\mathbf{I}) as symmetry axis. The electromagnetic field produced by atomic electrons has the direction of the total angular momentum as its symmetry axis.

The proton and the neutron have spin $s = 1/2$ and magnetic moment $\mu_p \mathbf{s}$ and $\mu_n \mathbf{s}$ respectively, as described in Sect. 7.14.4. It is useful to define the gyromagnetic factor $g \equiv \mu/\mu_N$ as the ratio between the intensity of the magnetic moment and the nuclear magneton $\mu_N = \frac{|e|\hbar}{2m_p} = 3.15 \times 10^{-8} \text{ eV/T}$. The magnetic moment of the nucleus is induced by the magnetic moments of individual nucleons and by the orbital motion of protons. Also in this case, it is parallel to the nuclear spin \mathbf{I} . The gyromagnetic factor of the nucleus, g_I , can be positive or negative, that is,

$$\mu_N = g_I \mu_N \mathbf{I}. \quad (14.9)$$

Different methods are used to measure the magnetic moment of the nuclei. They are based on the interaction of the nuclear magnetic dipole moment with the atomic magnetic fields or with artificial magnetic fields.

14.3 Nuclear Models

Unlike the atomic model, there is no a single model able to explain all nuclear properties. The reasons are mainly due to the fact that a massive central body representing the center of attraction is not present; in addition, the analytical form of the potential is not known. In this section, we shall describe some of the different, but complementary, nuclear models.

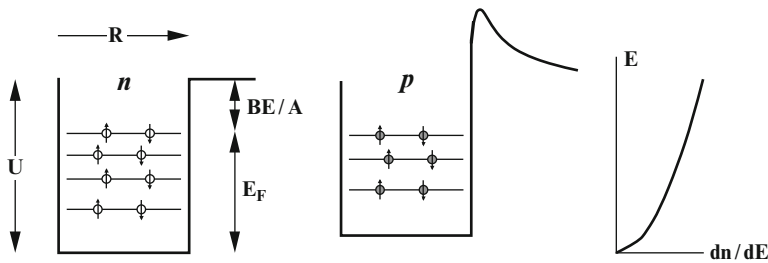


Fig. 14.5 Potential well model for protons and neutrons in a nucleus and evolution of the nucleon energy as a function of the state density dn/dE

14.3.1 Fermi Gas Model

The Fermi model is a statistical model based on the following assumptions:

1. The nucleons are spin 1/2 fermions (in a nucleus, Z protons and $N = A - Z$ neutrons) which move freely, like a gas, within the nucleus.
2. A single nucleon is subject to the collective action of all other nucleons. This action is represented by a spherically symmetric potential well $U(r)$ in a region of size $R = R_0 A^{1/3}$.
3. The nucleons gas is degenerate, i.e., the kinetic energy is much larger than the thermal energy kT . The nucleons are in the state of lowest accessible energy for the Pauli exclusion principle.

Based on these simple assumptions, the Fermi model provides information on the state density (Fig. 14.5) and on the nucleon kinetic energy for nuclei with A large enough ($A > 12$) to use statistical criteria. The number of states for a spin $s = 1/2$ fermion is calculated from the number density:

$$dn = (2s + 1) \frac{dV d\Omega p^2 dp}{h^3}.$$

Integrating over the solid angle ($\int d\Omega = 4\pi$) and volume ($V = 4/3\pi R_0^3 A$), and recalling that $h = 2\pi\hbar$ and $(2s + 1) = 2$, one has

$$dn = \frac{2 \cdot 4\pi V}{8\pi^3 \hbar^3} p^2 dp = \frac{4}{3\pi} \left(\frac{R_0}{\hbar} \right)^3 A p^2 dp. \quad (14.10)$$

The maximum of the momentum is called the *Fermi momentum*, and it is determined by requiring that the integral of (14.10) matches the number of protons (or neutrons) in the volume V :

$$\int dn_p = \frac{4}{9\pi} \left(\frac{R_0}{\hbar} \right)^3 A p_p^3 = Z; \quad \int dn_n = \frac{4}{9\pi} \left(\frac{R_0}{\hbar} \right)^3 A p_n^3 = (A - Z), \quad (14.11)$$

and

$$p_p c = \left(\frac{9\pi}{8} \right)^{1/3} \frac{\hbar c}{R_0} \left(\frac{2Z}{A} \right)^{1/3}; \quad p_n c = \left(\frac{9\pi}{8} \right)^{1/3} \frac{\hbar c}{R_0} \left(\frac{2(A-Z)}{A} \right)^{1/3}. \quad (14.12)$$

The numerical values of p_n and p_p can be derived assuming that $2Z/A \simeq 2$, $(A-Z)/A \simeq 1$ and $R_0 = 1.25$ fm. One finds

$$p_p = p_n \simeq 240 \text{ MeV/c}. \quad (14.13)$$

The corresponding kinetic energy is called the *Fermi energy* = $E_F = p_p^2/2M_p \simeq 30$ MeV (a comparable value is obtained for the neutron). The nonrelativistic approximation used here is sufficiently accurate. For heavy nuclei, the Fermi energy of neutrons is slightly larger than that of protons since $2(A-Z)/A > 1$. For example, for uranium ($Z = 92$, $A = 238$), the proton and neutron Fermi energies are respectively $E_{F_p} = 28$ MeV and $E_{F_n} = 32$ MeV. The depth of the potential well is the sum of the Fermi energy and the binding energy per nucleon, that is,

$$U = E_F + BE/A; \quad BE/A \simeq 8 \text{ MeV/nucleon} \rightarrow U = (35 - 40) \text{ MeV}.$$

For protons, the potential well is deformed by the electrostatic energy that produces a potential barrier that has a dependence $\sim 1/r$ for $r > R$ (Fig. 14.5).

The average kinetic energy per nucleon \overline{E}_C can be calculated (adding and mediating the contributions of p and n) from (14.10)

$$\overline{E}_C = \frac{\int (p^2/2m)dn}{\int dn} \simeq 20 \cdot \left[1 + \frac{5}{9} \left(\frac{A-2Z}{A} \right)^2 \right] \text{ MeV}. \quad (14.14)$$

\overline{E}_C slightly depends on the asymmetry term $\Delta = [(A-2Z)/A]^2$. When $2Z \simeq A$, as for light nuclei, $\Delta = 0$. For heavy nuclei, the average kinetic energy has a minimum for $Z = A/2$; it increases when an excess of neutrons is present. The correction factor Δ contributes only by 3% to the average kinetic energy per nucleon for the case of $^{238}_{92}U$.

14.3.2 Nuclear Drop Model

The nuclear drop model is a collective model of the nucleus which describes the nuclear binding energy with a few parameters. The model uses analogies with a liquid droplet and is based on the following assumptions:

- The interaction energy between two nucleons is independent on the nucleon type.
- The interaction is attractive at a short-range, R_{int} (as in the case of a liquid droplet in which the molecules have dipole–dipole interactions).

- The interaction is repulsive at distances $r \ll R_{int}$.
- The binding energy of the nucleus is proportional to the number of nucleons.

From these considerations, a formula for the binding energy may be obtained. It takes into account a main *volume term* and some correction factors.

Volume term. Each nucleon is strongly related to only the few nearby nucleons. The binding energy of the nucleus is not proportional to the sum of the interaction energy between all nucleon pairs (which is proportional to $A(A - 1) \simeq A^2$), but to the sum on only *nearby* nucleon pairs. Each pair is contained within an interaction volume, V_{int} , smaller than the total volume of the nucleus. This fact is explained by the *short-range* hypothesis of nuclear force. Under these conditions, the binding energy is $\propto A$, $BE = +a_0 A$.

Surface term. The binding energy is reduced by a *surface effect* since the nucleons on the nuclear surface have fewer neighboring nuclei with respect to the inner ones and are therefore less bound. The surface of the nuclear volume is proportional to $A^{2/3}$; thus, the corresponding negative correction factor can be written as $-a_1 A^{2/3}$.

Coulomb repulsion. The Coulomb repulsion between protons contributes to reducing the binding energy. Measurements of electromagnetic form factors show that the nuclei have approximately a uniform charge distribution. The electrostatic energy of a sphere of radius R with uniform charge density is proportional to the charge contained in the sphere, and inversely proportional to $R \sim A^{1/3}$. Thus, the correction term for the binding energy associated with the Coulomb repulsion is $-a_2 Z^2 / A^{1/3}$.

Term due to the exclusion principle (or asymmetry term). The binding energy is further reduced due to the contribution of the kinetic energy of nucleons: the higher the kinetic energy, the lower the binding energy. The estimate based on the Fermi gas model can be used. It takes into account the effect of fermion statistics and the Pauli exclusion principle that favors nuclear configurations with equal numbers of protons and neutrons. The average kinetic energy per nucleon is given by (14.14); the total kinetic energy of the nucleus with A nucleons is a constant, plus a correction term proportional to $[(A - 2Z)^2 / A]$. For $A/2 = Z$, the correction term is equal to zero; it becomes increasingly important as we move away from the symmetry condition $Z = N$. The binding energy contribution due to this factor is $-a_3[(A - 2Z)^2 / A]$.

Term due to configurations. It is experimentally observed that there is a systematic difference between configurations of nuclei with odd or even number of protons and neutrons (Table 14.1). It is necessary to introduce a correction term in the formula, like $a_4 / A^{1/2}$, to take this effect into account. The value and sign of a_4 are such that

	A	Z	$N = A - Z$	$\pm a_4$ (MeV)
(More stable)	Even	Even	Even	+12.6
(Intermediate)	Odd			0
(Less stable)	Even	Odd	Odd	-12.6

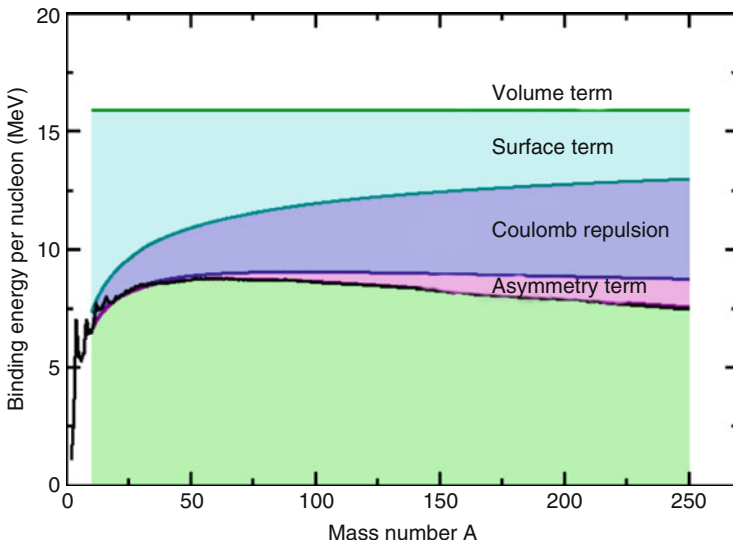


Fig. 14.6 Contribution of various terms of the Weizsäcker formula for the binding energy per nucleon as a function of A . The surface, Coulomb and symmetry terms are subtracted to the volume term. The figure does not consider the configuration term

Table 14.2 Values [14w3] of the constants in the Weizsäcker formula. a_4 takes into account the fact that the nucleus is even-even, even-odd or odd-odd

a_0	a_1	a_2 (MeV)	a_3	a_4
15.74	17.61	0.71	23.42	$\pm 12.6, 0$

The final result of all considered terms gives the Weizsäcker formula of the binding energy as a function of A and Z :

$$BE = a_0 A - a_1 A^{2/3} - a_2 \frac{Z^2}{A^{1/3}} - a_3 \frac{(A - 2Z)^2}{A} \pm \frac{a_4}{A^{1/2}}. \quad (14.15)$$

The value of the five parameters a_0, \dots, a_4 are obtained from a fit to the experimental data (see Fig. 14.6). The parameters have the dimension of energy and are measured in MeV. The values are given in Table 14.2.

From the binding energies, the masses of the nuclei can be obtained using (14.5) (Bethe and Weizsäcker formula). This formula gives the nucleus masses as a function of A , Z and of the parameters a_0, \dots, a_4 . The values calculated with (14.15) show relatively large deviations from experimental data for small A . Fewer discrepancies are observed for large A because the nuclear binding is particularly strong for certain values of Z and N . These values are denoted as *magic numbers*: since neither the Fermi gas model nor the nuclear drop model can explain them, it is necessary to introduce an additional nuclear model, the *shell model*.

14.3.3 Shell Model

The liquid drop model gives a fairly good description of the nuclear binding energy. It also offers a qualitative explanation of nuclear fission, as discussed in Sect. 14.9. The Fermi gas model is required to justify some numerical values such as the asymmetry term $[(A - 2Z)^2/A]$ in (14.15). The shell model potential is chosen as a simple three-dimensional square well, different for protons and neutrons. It explains further experimental facts such as the existence of particularly stable nuclei. In this model, the nucleons can move freely within the nucleus on quantum orbits. This is consistent with the idea that they are subject to a *global effective potential* created by the sum of the contributions of other nucleons.

Once again, the electromagnetic case can be used as a prototype. Indeed, the atomic model (based on a Coulomb potential with radial symmetry, angular momentum quantization and the Pauli principle) successfully reproduces the phenomenology of atoms: energy levels and valence. In addition, some elements (noble gases, as helium ($Z = 2$), neon ($Z = 10$), argon ($Z = 18$), krypton ($Z = 36$), ...) are characterized by a total angular momentum $J = 0$, high electron binding energies and low chemical reactivity.

Particularly stable nuclei are observed when the number of protons, Z , or the number of neutrons, $N = A - Z$ is equal to 2, 8, 20, 28, 50, 82, 126 (*magic numbers*). Nuclei with magic numbers have special features, for example, (1) many isobar nuclei exist; (2) nuclear spin $I = 0$, and null magnetic dipole and electric quadrupole moments; (3) high nuclear binding energy; (4) small nuclear cross-section. The last two properties are more evident in doubly magic nuclei such as 4_2He , $^{16}_8O$, $^{40}_{20}Ca$... $^{208}_{82}Pb$.

The goal of the shell model is to reproduce the magic numbers by solving the Schrödinger equation with a particular potential. The problem has a number of difficulties because the shape of the nuclear potential is not exactly known. Moreover, if a potential with radial symmetry is assumed, the center of symmetry is not well defined since all the nucleons are the source of the nuclear field. Finally, it is not obvious how to extend to the nucleons in the nucleus

the concept of orbital. The Pauli principle and the success of the Fermi gas model can help: if the nucleons gas is strongly degenerate, each nucleon is in a given quantum state and does not interact with another nucleon but with an exchange mechanism. This leads to an equation of motion for the single nucleon, independent of what happens to the other nucleons (*independent particle model*).

The eigenstates for a particle of mass m in a spherically symmetric potential $U(r)$ are $\psi(r, \theta, \phi) = R_{nl}(r)Y_{lm}(\theta, \phi)$ where $Y_{lm}(\theta, \phi)$ are the *spherical harmonic functions*. They are obtained by solving the radial Schrödinger equation,

$$\left[-\frac{\hbar^2}{2m} \frac{d^2}{dr^2} + U(r) + \frac{\hbar^2 \ell(\ell+1)}{2mr^2} \right] u(r) = Eu(r), \quad (14.16)$$

with $u(r) = u_{nl}(r) = rR_{nl}(r)$. One possible choice for $U(r)$ is the Woods–Saxon potential:

$$U_{WS}(r) = -\frac{U_0}{1 + e^{(r-R)/t}}, \quad (14.17)$$

which reproduces the matter distribution in the nucleus (14.8). This choice allows one to numerically solve the equation; it determines a sequence of particularly stable states with the sequence 2, 8, 20, 40, 70, 112, ...

Another important progress was made by Mary Meyer and Hans Jensen (Nobel laureate in 1963) by introducing in the potential a term for the *spin-orbit interaction*, that is,

$$U_r = U_{WS}(r) + U_{LS}\boldsymbol{\ell} \cdot \mathbf{s}. \quad (14.18)$$

This term is suggested by the observation that the interaction between nucleons has a strong dependence on the spin state. Unlike the atomic interaction, the spin-orbit term in nuclei has no origin from the magnetic dipole moment interaction with the magnetic field produced by the motion of charges. Such a term would move the energy levels by smaller quantities than those observed.

Figure 14.7 shows the energy levels obtained by solving (14.16) with the two potentials mentioned above, in addition to the simplest case of a *harmonic oscillator* potential type.

The shell model which assumes independent particles (*Independent Particle Shell Model*), besides the magic numbers, can make predictions on the spin, parity, magnetic dipole and electric quadrupole moments of the nuclei. Given the simplicity of the model, these predictions are not very accurate, but provide a useful base for further improvements.

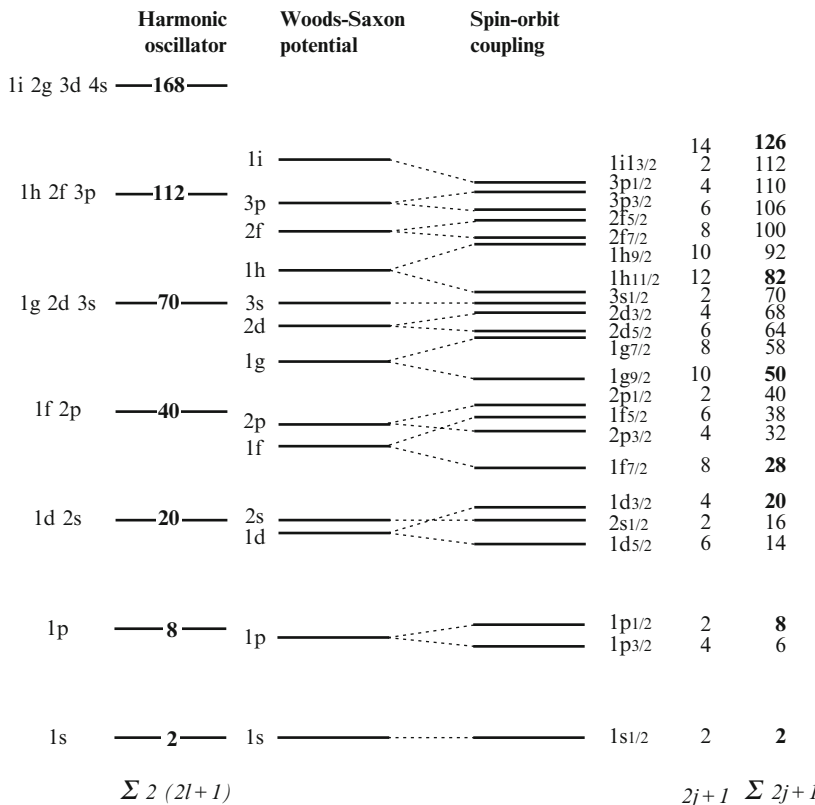


Fig. 14.7 Energy levels and magic number sequences obtained by solving (14.16) using a harmonic oscillator potential, the Woods–Saxon potential of (14.17) and the potential with a spin-orbit coupling term (14.18). The last one reproduces the observed sequence of magic numbers

14.4 Properties of Nucleon-Nucleon Interaction

In the previous section, we described some approximations which explain most of the features and physical properties of nuclei. Similarly, there are phenomenological formulations of the nucleon-nucleon potential; however, they do not allow an analytical solution of the problem. The interactions between nucleons depend on many factors: distance between nucleons, relative speed, spin, angular momentum. . . . A single simple formula (analogous to the Coulomb potential) from which the characteristics of the interactions between nucleons can be derived does not exist. The reason is due to the fact that the strong force acts (see Sect. 11.9) via gluon exchange between quarks. The residual interaction between nucleons

is analogous to the Van der Waals electromagnetic force between two neutral atoms or molecules. Indeed, in a first approximation, a nucleon is *neutral* (without color) for the strong interaction as an atom is neutral for the electromagnetic interaction.

Some properties of nucleon-nucleon interactions can be obtained from the analysis of the nucleus binding energy, from the characteristics of the deuteron and from the nucleon-nucleon elastic scattering at low energy. The deuteron is the simplest nuclear state and it represents the analogous of the hydrogen atom for the electromagnetic interaction for the nuclear interaction. The deuteron binding energy ($BE = 2.225 \text{ MeV}$) is however too low to form excited states. The main properties of interactions between nucleon pairs are:

1. *The interaction is attractive, short-range and can be described by a central potential $U(r)$.* The shape of the potential is not known a priori; different choices, for example, the square well, the Woods-Saxon potential or the harmonic oscillator potential, lead to similar conclusions for some observables using as input parameters: radius of the potential $R < 2 \text{ fm}$, depth of the potential $U_0 \simeq 40 \text{ MeV}$;
2. *The interaction is symmetric and independent with respect to the electric charge.* The study of binding energies and of energy levels of isobaric mirror nuclei show that the proton-proton, neutron-neutron and neutron-proton interactions are similar. The same conclusion is reached by comparing the $p - p$, $n - n$, $p - n$ elastic scattering at low energy. This property involves the conservation of isospin in nuclear interaction;
3. *The interaction is invariant under parity and time reversal transformations.* As a result (Table 6.3), the nuclei have neither electric dipole moment, nor a magnetic or quadrupole moment;
4. *The interaction depends on the spin.* The nucleon-nucleon state with spin $I = 0$ (singlet) has different properties from that with spin $I = 1$ (triplet), suggesting a spin-dependent interaction:

$$U_S(r) = U_s(r)\mathbf{s}_1 \cdot \mathbf{s}_2 - U_t(r)\mathbf{s}_1 \cdot \mathbf{s}_2 \quad (14.19)$$

which is attractive in the triplet (t) and repulsive in the singlet state (s);

5. *The interaction also has a noncentral potential term.* To account for the magnetic dipole moment and the electric quadrupole moment of the deuteron, it is assumed that it is a mixed state, i.e., a superposition of states of even angular momentum L . However, a potential with radial symmetry does not produce stationary degenerate eigenstates with different values of L . Therefore, the nucleon-nucleon interaction must also include a nonradial term (*tensor potential*), $U_T(\mathbf{r})$. Since the only defined direction is that of the spin, the tensor potential can be built with combinations which depend on spin and distance, for example, $(\mathbf{s} \cdot \mathbf{r})$ or $(\mathbf{s} \times \mathbf{r})$, which are invariant under parity and time reversal transformations;
6. *The interaction is repulsive at small distances, $r \ll R$.* Nuclei have energy and volume proportional to the number of nucleons: the nucleus cannot be

compressed. This implies that in addition to the attractive potential with range R , there is a repulsive potential at a distance $r \ll R$. This is confirmed by the study of nucleon-nucleon scattering: the potential is attractive at low-energy while the potential becomes repulsive at intermediate energy ($p_{cm} > 400 \text{ MeV}/c$, corresponding to $r < 0.5 \text{ fm}$). The effect is related to the Pauli exclusion principle: two nucleons with the same quantum numbers cannot be in the same position. A repulsive potential can be constructed with the same combinations of spin operators that generate the tensor potential;

7. *Exchange forces are acting between the nucleons.* The differential elastic proton-proton cross-section shows a symmetry between θ and $\pi - \theta$ because the particles are identical. The same phenomenon is observed in the case of elastic neutron-proton scattering at intermediate energy. This effect cannot be justified under the dynamics of the process. The deflection angle is related to the impulse transferred in the collision: $\theta \simeq \Delta p / p \simeq \text{Potential Energy/Kinetics Energy}$. The large angle scattering should not be allowed when the kinetic energy increases, contrary to what is observed. This effect can be explained if there are exchange forces acting on the coordinates and the spin of the nucleons.

All experimental indications agree on the fact that the nuclear interactions between $p - p$, $p - n$, $n - n$ pairs are equal. In this case, the proton and the neutron can be considered as a single particle, the *nucleon*, which exists in two states of charge, eigenstates of the isospin operator.

14.5 Radioactive Decay and Dating

The discovery of natural radioactivity in 1896 by Henri Becquerel (Nobel laureate in 1903) is at the origin of nuclear physics. It took many years to understand the nature of the nuclear decay which occurs in several ways:

- α decay: emission of helium nuclei.
- β decay: emission of electrons (or positrons) and neutrinos.
- γ decay: emission of electromagnetic radiation.
- Fission: scission into two or more nuclei.

In the early years of radioactive decay research, it was proven that the decay is of stochastic nature. The *activity*, defined as the number of decays per time unit, decreases exponentially with time. This evidence led to the conclusion that radioactive decay is not originated by mutation of the chemical substance, but that it results from several successive processes involving individual nuclei. The law of the radioactive decay (Sect. 4.5.2) can be interpreted on the assumption that the decay probability per time unit: (1) it is independent of time; (2) it is a property of the substance and of the decay process; (3) in a substance containing N nuclei, the decay probability per time unit of a single nucleus does not depend on N .

Recalling (4.42), if N_o is the number of nuclei at $t = 0$, the number of nuclei at time t is $N(t) = N_o e^{-t/\tau}$ where τ is the nucleus lifetime. The goal of *fundamental interaction* theories is to determine the value of τ according to fundamental laws and a few free parameters. For instance, the weak interaction predicts the lifetime of the β decay from the Fermi constant and the energy available in the final state.

In nuclear physics, the *half-life* $t_{1/2}$ is usually more frequently used than the lifetime τ . The half-life is defined as the time interval in which the number of nuclei is halved. It is easy to verify that

$$t_{1/2} = \tau \ln 2 = 0.693\tau. \quad (14.20)$$

The activity $A(t)$ of a substance (number of decays per time unit) is therefore

$$A(t) = \frac{dN(t)}{dt} = \frac{N_o e^{-t/\tau}}{\tau}. \quad (14.21)$$

The commonly used unit for the activity is the *Curie*, defined as the activity of one gram of radium: $1 \text{ Ci} = 3.7 \cdot 10^{10}$ decays/s. The nucleus $^{226}_{88}Ra$ decays by emitting α particles with 4.9 MeV kinetic energy; its half-life is $t_{1/2} = 1,602$ years. The lifetime is then $\tau_{Ra} = 7.3 \cdot 10^{10}$ s. The activity of one gram of $^{226}_{88}Ra$ (containing $N_A/226$ nuclei, where N_A is the Avogadro's number) is

$$A_{Ra} = \frac{N_A}{226\tau_{Ra}} = \frac{6.02 \cdot 10^{23}}{(226)(7.3 \cdot 10^{10})} = 3.7 \cdot 10^{10} \text{ s}^{-1}.$$

The unit for the radioactivity in the International System is the *Becquerel*, which corresponds to one decay per second, $1 \text{ Bq} = 0.27 \cdot 10^{-10} \text{ Ci}$.

14.5.1 Cascade Decays

Environmental radiation is mainly due to the natural decay of elements with very long lifetime: U, Th, K, and decays of, for example, their *children*, *grandchildren*. A major contribution comes from a gaseous element, the radon, which originates from the chains of thorium-uranium.

The radon is a noble and radioactive gas formed by the decay of radium in the uranium decay chain. Being an α emitter, radon is a very heavy gas and is considered extremely dangerous to the human health if inhaled. The most stable isotope, the ^{222}Rn , has a lifetime of 3.8 days. One of the main risk factors of radon is linked to the fact that it accumulates within housing

and becomes a major cause of lung cancer (it is estimated that this is the second leading cause of cancer after smoking). Radon is a chemically inert element (as a noble gas) soluble in water. Because its concentration in the atmosphere is usually extremely low, the natural water surfaces in contact with the atmosphere (springs, rivers, lakes, ...) release radon, in very limited quantities but continuously, through volatilization.

Because of its solubility in water, radon is present in the soil and can accumulate in some construction materials, especially volcanic tuff or granite. It emerges from the construction materials and dissipates in the environment, accumulating in enclosed spaces (especially, wineries and rooms without sufficient aeration) and becoming dangerous. A simple protection method against the accumulation of this gas is the ventilation of rooms, especially when they are underground or in direct contact with the soil.

When a generic nucleus produced in a decay is also radioactive, cascade decays are produced. This phenomenon mainly affects the heavy nuclei that give rise to radioactive chains: the nucleus of a radioisotope, after the decay, becomes an isotope of a different element which is often unstable. A chain ends when a stable isotope is formed. In nature, we know three main decay chains: starting from ^{238}U (see Fig. 14.8), from actinium and from thorium, all ending to lead isotopes. There are also artificial radioactive chains, amongst which the most important is that of plutonium produced in nuclear reactors. Radioisotopes are part of the natural radioactive chains, or can be produced by cosmic ray interactions in the atmosphere.

If $\tau_1 = 1/\lambda_1$ is the lifetime of the decay $nucleus_1 \rightarrow nucleus_2$ which in turn decays with lifetime $\tau_2 = 1/\lambda_2$, one has:

$$dN_1 = \lambda_1 N_1(t)dt \quad dN_2 = \lambda_2 N_2(t)dt. \quad (14.22)$$

Suppose that at the beginning ($t = 0$), daughter type 2 nuclei are absent ($N_2(0) = 0$) and $N_1(0) = N_0$. The number of nucleus two decays depends on how many nuclei are generated by the decay of nucleus 1 and on its activity ($N_2 \sim dN_2/dt$). Then,

$$N_2(t) = ae^{-\lambda_1 t} + be^{-\lambda_2 t}. \quad (14.23)$$

The production rate of the type 2 nuclei at $t = 0$ is equal to the activity of type 1 nuclei. This allows one to determine the constants a, b in (14.23) with the following initial conditions:

$$\begin{aligned} N_2(t = 0) &= a + b = 0 \\ (dN_2/dt)_{t=0} &= (dN_1/dt)_{t=0} = -a\lambda_1 - b\lambda_2 = \lambda_1 N_0 \end{aligned} \quad (14.24)$$

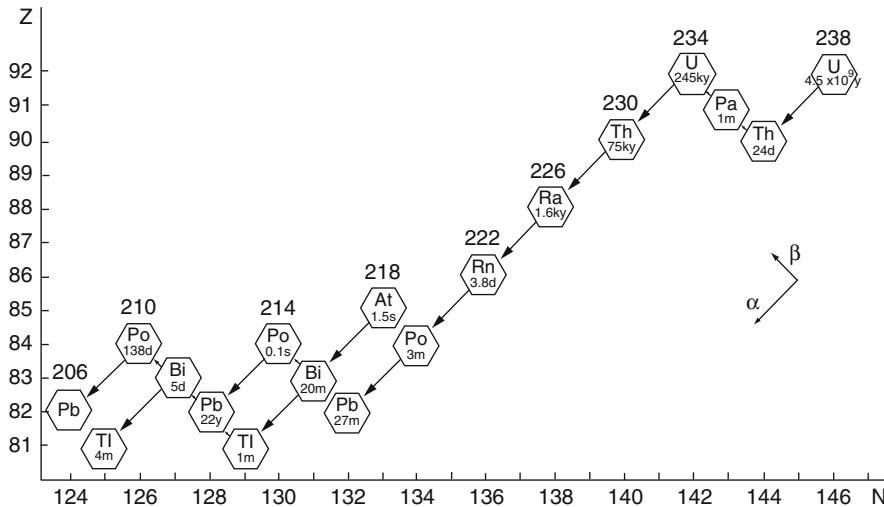


Fig. 14.8 Decay chain of the ^{238}U isotope. The arrows towards the bottom left indicate the α decays, with a variation of -2 in Z ; upward arrows indicate β decay, with a variation of $+1$ in Z . The half-life is indicated inside the box of each element (d = days, m = months, y = years) (Data from [14w2])

from which the activities can be obtained (see also Exercise 14.10):

$$A_1(t) = N_0 \lambda_1 e^{-\lambda_1 t}; \quad A_2(t) = N_0 \frac{\lambda_1 \lambda_2}{\lambda_2 - \lambda_1} (e^{-\lambda_1 t} - e^{-\lambda_2 t}). \quad (14.25)$$

14.6 γ Decay

A nucleus in an excited state can decay to the ground state, or to a lower energy state, by emission of electromagnetic radiation, that is,



The differences between the nuclear energy levels are typically in the range 0.1–10 MeV. This energy is shared between the photon energy E_γ and the kinetic energy T_N of the recoil nucleus ${}^A_Z X$ (note that $T_N \ll E_\gamma$ with very few exceptions). In the γ decay, angular momentum and parity of the nucleus are conserved. The measurement of the emitted radiation provides information on energy levels and on the spin and parity of nuclear states.

Multipole radiation. The γ radiation is usually observed at distances very large compared to the size of the nucleus; the wavelength is typically $\lambda = 2\pi\hbar c/E_\gamma = 10^2\text{--}10^4\text{ fm}$. The approximation for the development of the electromagnetic field

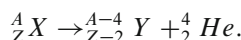
in terms of multipoles are therefore valid. The electromagnetic field produced by static charges and time-dependent currents can be obtained as the Fourier transform of the frequency ω components. The multipole development is characterized by the value of the angular momentum l of the emitted radiation. The power radiated at the frequency ω depends on the electric E_{lm} and magnetic B_{lm} moments of order 2^l .

The transition probability due to electric $\langle f_N | E_{lm} | i_N \rangle$ and magnetic $\langle f_N | B_{lm} | i_N \rangle$ multipoles corresponds to the matrix elements M_{lm} obtained from the perturbation theory (see Sect. 4.3). The calculation is analytically difficult because, in general, the radial wave function is unknown. Moreover, the Pauli exclusion principle (a nucleon cannot go in an already occupied state) prevents large variations of the nucleon wave function. The calculation is simplified, assuming that the radiated emission is related to the angular momentum variation of the wave function while the radial part is almost unchanged. A value for the decay constant $\lambda = 1/\tau$ for each matrix element W_{lm} can be obtained. This technique is called the *Weisskopf estimate of the decay constant*, and produces values which are approximate, but can provide useful information to distinguish the different γ decay modes. Typical values range from $\lambda(B_4) \sim 10^{-5} s^{-1}$ to $\lambda(E_1) \sim 10^{14} s^{-1}$.

14.7 α Decay

Most of the heavy nuclei decay emitting positively charged particles. This phenomenon was studied since the early 1900s by M. Curie and E. Rutherford. In 1909, Rutherford, carrying out an experiment in which a substance was decaying in vacuum, observed that the accumulating gas was helium. This observation allowed the identification of the α particles with the helium nuclei. The decay occurs with the expulsion of the α particle from a nucleus with large atomic weight A . Systematic studies made in the following years showed that α particles emitted by different radioactive nuclei, all have a kinetic energy of the order of a few MeV. On the contrary, the nuclei lifetime range over many orders of magnitude with approximately exponential dependence on the α particle energy E_α . The main features of the α decay are

- The majority of nuclei with $A > 200$ have an α decay.
- α particles are helium nuclei which are very stable and with a binding energy $BE = 28.3$ MeV.
- α particles emitted from a given nucleus are monochromatic since it is a two-body decay:



- The kinetic energy of α particles varies in a small range, typically $4 < E_\alpha < 9$ MeV.

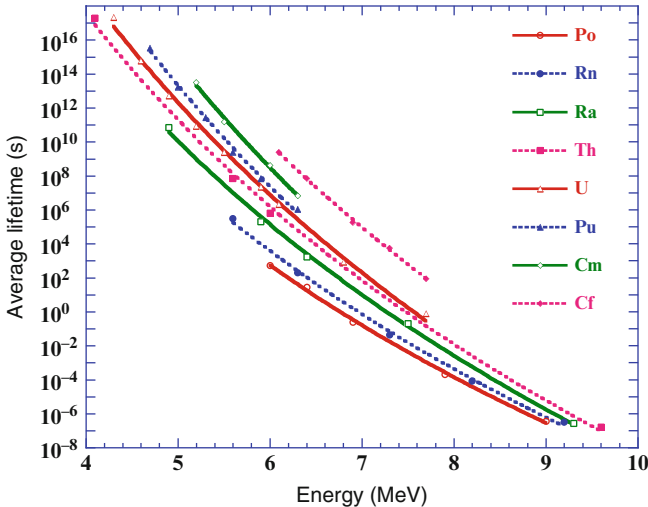


Fig. 14.9 α -decay average lifetime τ as a function of the energy E_α . τ varies over 20 orders of magnitude, from microseconds to billions of years, due to the strong dependence on E_α in the tunneling effect. There is also a small dependence on the mass number A

- The lifetime τ has a strong dependence on the kinetic energy of the α particles. The lifetimes change by more than 20 orders of magnitude (Fig. 14.9) for E_α ranging from 4 to 9 MeV, according to the empirical Geiger–Nuttal law,

$$\log_{10}(1/\tau) = a - bZE_\alpha^{-1/2}. \quad (14.27)$$

- For the same energy E_α , the lifetime increases with the mass number A . The α -emission can be understood from the following assumptions:
 - The nucleus ${}_Z^AX$ is a bound state composed of the nucleus ${}_Z^{A-4}Y$ and an α particle; this assumption is justified by the fact that the He nucleus is a strongly bound state.
 - The potential of the system ${}_Z^{A-4}Y - \alpha$ is represented by a spherically symmetric potential well for $r < R$ plus the Coulomb potential for $r > R$ (Fig. 14.10):

$$U(r) = -U_0 \quad (r < R); \quad U(r) = \frac{2(Z-2)e^2}{r} \quad (r \geq R).$$

- The α particle inside the potential well has positive energy, equal to the kinetic energy $E = E_\alpha$ after the decay.

For a nucleus with $A > 200$, the radius and depth of the potential well are respectively of the order of $R \simeq 7\text{--}8 \text{ fm}$ and $U_0 \simeq 40 \text{ MeV}$; the height of the Coulomb barrier potential is $U(R) \simeq 30 \text{ MeV}$. Therefore, the α particle with energy $E_\alpha < U(R)$ cannot overcome the Coulomb potential barrier.

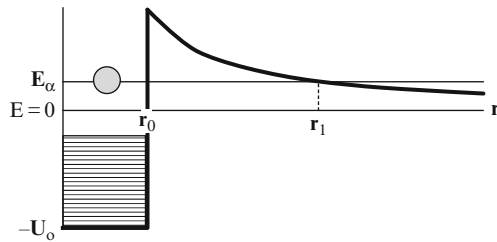


Fig. 14.10 Sketch of characteristic variables (used in the text) in the Gamow model for the α decay

In quantum mechanics, the α particle can cross the potential barrier by *tunneling effect*. This hypothesis was developed by Gamow (and, independently, by Gurney and Condon) in 1928 and can reproduce with a good approximation the empirical Geiger–Nuttal law (14.27). This was one of the first successes of the newly born quantum mechanics theory.

14.7.1 Elementary Theory of α Decay

A description of the tunneling effect in the Gamow model can be found in any advanced text of quantum mechanics (e.g., [G03]). Here, we shall summarize the most relevant features. Inside the potential well, the α particle has positive energy E_α and oscillates hitting the barrier with a frequency f . The decay probability per time unit can be determined by multiplying the frequency f with the probability T to cross the barrier through tunneling effect:

$$1/\tau = \lambda = fT. \quad (14.28)$$

Classically, a particle with energy E_α inside a potential well of height $U_0 > E_\alpha$ would have no escaping chance. In quantum mechanics, the transmission coefficient T through the one-dimensional potential barrier of height U and width L can be calculated using the Schrödinger equation. It is found that $T \simeq e^{-2[2m(U-E_\alpha)]^{1/2}L}$. In the case of a symmetric three-dimensional spherical potential barrier, one has

$$T \simeq e^{-2G}; \quad G = \frac{1}{\hbar} \int_R^{r_1} [2m(U(r) - E_\alpha)]^{1/2} dr \quad (14.29)$$

where G is called the Gamow factor. The integral must be extended to the interval in which $U(r) = \frac{2(Z-2)e^2}{r} \geq E_\alpha$; R is the radius of the potential well and r_1 is the distance for which $U(r_1) = E_\alpha$ (see Fig. 14.10).

The Gamow factor may be calculated according to the electric charge Ze in the nucleus, the radius $R = R(A)$ and the energy E_α of the α particle, that is,

$$G = 2(Z - 2)[e^2/(\hbar c)] \left[\frac{2mc^2}{E_\alpha} \right]^{1/2} [\pi/2 - 2(R/r_1)^{1/2}] \quad (14.30)$$

where $e^2/(\hbar c) = \alpha_{EM} = 1/137$ is the electromagnetic coupling constant, see (4.6b). The frequency with which the α particle oscillates within the potential well depends on the ratio between its velocity v_α and the radius R . Since the α particle is a boson, its motion is not decelerated (i.e., “braked” through some term which reproduces a *friction*) within the potential well. The relationship between total energy $E_\alpha + U_0$ and speed is

$$v_\alpha = [2(E_\alpha + U_0)/m]^{1/2} = c[2(E_\alpha + U_0)/mc^2]^{1/2}. \quad (14.31)$$

By inserting numerical values, typical velocities are $v_\alpha \simeq 0.15c$.

Since the lifetime (14.28) depends on $T = e^{-2G}$ and on v_α/R , from (14.30) and (14.31), one finds

$$\frac{1}{\tau} \propto \frac{c}{R} [2(E_\alpha + U_0)/mc^2]^{1/2} \cdot e^{-4(Z-2)e^2/(\hbar c)[\frac{2mc^2}{E_\alpha}]^{1/2}}. \quad (14.32)$$

The following relationship can be obtained:

$$\log_{10} \frac{1}{\tau} = a - bZE_\alpha^{-1/2} \quad (14.33a)$$

which is exactly the Geiger–Nuttal law, where τ is expressed in years and the a, b parameters are given by

$$a = 1.61; \quad b = 28.9 + 1.6Z^{2/3}. \quad (14.33b)$$

This relation reproduces the observed dependence of the lifetime on the α particle energy and it accounts for the variation of τ on more than 20 orders of magnitude. It also explains that the α emission with energy $E_\alpha < 4$ MeV has a very long lifetime, such that the phenomenon is virtually undetectable. The experimental results show that, at energy $E_\alpha = \text{constant}$, the lifetime increases with the mass number. Indeed, as A raises, both the electrical charge and the nuclear radius increase. These increase the Gamow factor which depends on the height and width of the potential barrier.

14.7.2 Lifetime Calculation of the $^{238}_{92}U$ Nucleus

The expected lifetime of the nucleus $^{238}_{92}U$ can be calculated as an example. Using (14.7), the value of its radius is $R \simeq 9.3$ fm. The mass is $m = m_\alpha = 3.7 \times 10^3$ MeV

and the measured value of $E_\alpha = 4.2 \text{ MeV}/c^2$. From (14.31), $f = v_\alpha/R = 2.3 \times 10^{21} \text{ s}^{-1}$ is obtained. The distance r_1 is determined by requiring that the Coulomb potential corresponds to the energy E_α , i.e., $90 \times 2 \times e^2/r_1 = 4.2 \text{ MeV}$, from which one finds that $r_1 = 63 \text{ fm}$. From (14.30), we can instead calculate the Gamow factor

$$G = (2 \times 90)[1/137][2 \times 3.7 \cdot 10^3 / 4.2]^{1/2} [\pi/2 - 2(9.3/63)^{1/2}] = 42.9.$$

The transmission factor is $T = e^{-2G} = 5.43 \cdot 10^{-38}$. The decay rate λ and the half-life $t_{1/2}$ are respectively

$$\lambda = fT = 2.3 \cdot 10^{21} \times 5.4 \cdot 10^{-38} = 1.2 \cdot 10^{-16} \text{ s}^{-1} \quad (14.34a)$$

$$t_{1/2} = \frac{\ln 2}{\lambda} = 5.6 \cdot 10^{15} \text{ s} = 1.8 \cdot 10^8 \text{ y}. \quad (14.34b)$$

The observed lifetime of $^{238}_{92}U$ (4.47×10^9 years) is approximately 25 times larger than the value obtained with the previous calculation. Note that the Gamow factor is usually large, $G \sim 30\text{--}50$, and that even a small uncertainty in the parameters involves a large change in e^{-2G} . The most uncertain parameter is the radius R used to calculate the Gamow factor since the α emitting nuclei have large A and irregular configurations. We have assumed spherical nuclei, but we know that many high-mass nuclei are not spherical. A small increase in the value of R significantly changes the value of T . Finally, the α decays can produce variations in the nuclear spin and parity, if the α particle is emitted with orbital angular momentum ℓ . In this case, in addition to the Coulomb potential, the centrifugal potential $\hbar^2 \ell(\ell+1)/2mr^2$ should be considered. This term increases the potential barrier, and consequently the nuclear lifetime.

14.8 β Decay

Rutherford observed (at the beginning of last century) the emission of negatively charged particles, which were called β particles and later identified as electrons. In the following years, the experimental results showed that a nucleus changes its atomic number after β -emission. β decays occur in both light and heavy nuclei with lifetimes varying from milliseconds to billion years. In 1919, Chadwick showed that the nuclei emit electrons with a continuum energy distribution; in a transition,

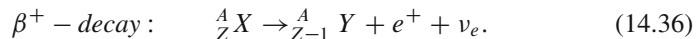


the *maximum of the electron energy* is approximately equal to the difference in mass between nuclei

$$E_{max} \simeq (M_X - M_Y)c^2.$$

If the emitted electrons are not atomic electrons, the process must originate in the nucleus itself and since the nuclei do not contain electrons, the process corresponds to a variation of the nucleus. In 1933, Sargent analyzed the dependence of the decay lifetime on the emitted electrons energy. He observed that, for energies $E_{max} \gg m_e c^2$, the lifetime is proportional to E_{max}^5 (Sect. 8.4.2).

To conserve energy and momentum in the β decay, energy must be emitted in the form of neutral radiation in addition to the electron and the nucleus Y . This is the *Pauli hypothesis for the neutrino*, see Sect. 8.2. The β decay is then a three-body process:



A β decay conserves the atomic number A constant, see Eqs. 14.35, 14.36. The phenomenon can be explained in terms of the binding energy BE (14.15). All systems tend to the value of minimum energy. The mass of a nucleus (14.5) is the sum of the constituents masses minus the binding energy. If we consider the Weizsäcker mass formula as a function of Z , for each given value of A , there is a parabola (if A is odd) or two parabolas (if A is even) with the concave side opening up, that is,

$$M(A, Z) = Nm_n + Zm_p - BE(Z, A) = (b_0 + b_1 A \pm a_4/A^{1/2}) - b_2 Z + b_3 Z^2 \quad (14.37)$$

[b_0, \dots, b_3 are constants depending on a_0, \dots, a_3 of (14.5)]. The β decay transforms the nucleus (Z, A) in a nucleus which differs by one unit of Z . The nucleus moves to a location in the parabola closer to the minimum which corresponds to a more stable position.

Nuclei with A odd. If A is odd, $a_4 = 0$ and the nuclei are located on a single mass parabola, such as, in Fig. 14.11a which refers to $A = 101$. There is a stable nucleus, ${}_{44}^{101} Ru$, with the highest binding energy. All isobars have smaller binding energies and higher masses with respect to the stable nucleus. Decays occurring on the left side of the minimum are β^- , while those on the right side are β^+ . The β^+ decay is only possible within a nucleus because the rest mass of the neutron is larger than that of the proton.

Nuclei with A even. The isobars with even mass number form two separate parabolas: one for even-even nuclei, the other for odd-odd nuclei. They are separated by twice the energy of the configuration term $a_4 = 12.6$ MeV. Sometimes, there is more than one β stable even-even nucleus. For example, in the case of $A = 106$ (as shown in Fig. 14.11b), there are ${}_{46}^{106} Pd$ and ${}_{48}^{106} Cd$. The first is truly stable, as it corresponds to the minimum of the parabola. The isotope Cd could instead transform via double β decay in ${}_{48}^{106} Cd \rightarrow {}_{46}^{106} Pd + 2e^+ + 2\nu_e$. However, the probability for this process is so small (second order in the weak interaction

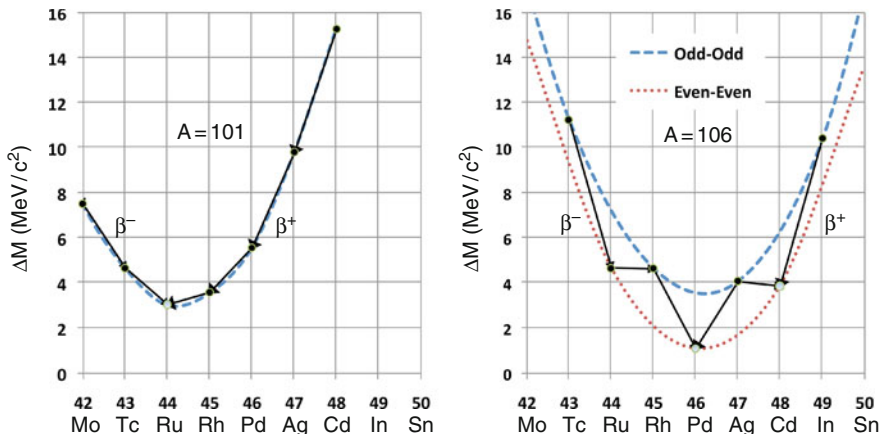


Fig. 14.11 β decay mass parabola (a) for a nucleus with odd- A ($A = 101$) and (b) for a nucleus with even- A ($A = 106$). The ordinate scale shows the relative mass difference between states, corresponding to the energy available for the $(e^-, \bar{\nu}_e)$ or (e^+, ν_e) pairs in the β decays denoted by arrows. The stable states are $^{101}_{44}Ru$, with $BE/A = 8.601$ MeV/nucleon and $^{106}_{46}Pd$, with $BE/A = 8.579$ MeV/nucleon [14w2]

coupling constant) that $^{106}_{48}Cd$ can be considered as stable. The odd-odd nuclei with $A > 14$ are never stable, as they always have a near even-even nucleus more strongly bound. Only the light nuclei 2_1H , 6_3Li , $^{10}_5B$, $^{14}_7N$ are stable (see Table 14.1), as the increase of the energy asymmetry term would exceed the decrease of the energy term due to the configuration.

14.8.1 Elementary Theory of Nuclear β -Decay

The transition probability of the neutron β decay (which corresponds to the elementary process (14.35)) has already been calculated in Sect. 8.3; the same formalism with a few appropriate changes can be applied to (14.36). The transition probability is given by

$$dW^\pm(p) = \frac{G_F^2 c^3}{2\pi^3 \hbar} |\mathcal{M}|^2 (Q - T_e)^2 p^2 F^\pm(Z, E) dp \quad (14.38)$$

(note the dependence on [Energy⁵]). The square matrix element $|\mathcal{M}|^2$ is dimensionless; it depends on the wave functions of neutrons and protons in nuclei. The Pauli exclusion principle, the isospin multiplicity of the new nuclear state and the multiplicity of nuclear spin states must be taken into account in the calculation of $|\mathcal{M}|$. Compared to the expression for the neutron β decay (Sect. 8.3), a corrective function $F^\pm(Z, E)$ depending on the atomic number and electron energy was introduced in (14.38). It takes into account the effect of electron interaction with

the Coulomb field of the nucleus. The effect is different for the β^- and β^+ decays, for which the potential is attractive in the former and repulsive in the latter. The term $F^\pm(Z, E)$, which relates to the density of final states, was first calculated by Fermi.

The lifetime τ for the β decay can be derived by integrating (14.38)

$$\frac{1}{\tau} = \int dW^\pm = \frac{(m_e c^2)^5}{2\pi^3 \hbar} G_F^2 |\mathcal{M}|^2 f^\pm(Z, E). \quad (14.39)$$

The dimensional dependence on $[Energy]^5$ has been absorbed in $(m_e c^2)^5$. $f^\pm(Z, E)$ is a (dimensionless) function which depends on $F^\pm(Z, E)$, on the nuclear electric charge and on the integration upper limit for the electron momentum. Although it can be calculated on the basis of nuclear models, when the decay energy is $E_{max} \gg m_e c^2$, the electron has a large momentum and $F^\pm(Z, E) \simeq 1$. In this case, $p_{max}c \simeq E_{max}$, and the approximation $f^\pm(Z, E) = (E_{max}/m_e c^2)^5/30$ (as for the neutron) can be used. If $E_{max} \gg mc^2$, the nuclear lifetime depends on the fifth power of the maximum energy available in the final state, in agreement with the Sargent rule:

$$\frac{1}{\tau} \simeq \frac{E_{max}^5}{60\pi^3 \hbar} G_F^2 |\mathcal{M}|^2. \quad (14.40)$$

This strong dependence on E_{max} explains why the β decay lifetime ranges from fractions of seconds to billions of years.

14.9 Nuclear Reactions and Nuclear Fission

In a nuclear reaction, two particles or two nuclei change their state as a result of their interaction

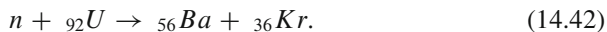


Q indicates the mass difference between the initial and final states, $Q = (m_a + m_b - m_c - m_d)c^2$. Reactions with $Q > 0$ are called *exothermic*: mass is converted into kinetic energy of the final state. Reactions with $Q < 0$ are *endothermic*: kinetic energy is converted into mass. Due to the short range of the nuclear interaction and if the initial particles have electric charges, energy must be provided to overcome the Coulomb repulsion. In nuclear reactions, in addition to energy and momentum, the angular momentum, the electric charge, the baryonic number, the strong isospin, the charge conjugation and the parity are conserved. The first nuclear reaction causing a substance transmutation was observed by Rutherford in 1919 using α particles (emitted in polonium decays) with a kinetic energy sufficient to compensate the negative value of Q and the Coulomb repulsion in the reaction $\alpha + {}^{14}_7 N \rightarrow {}^{17}_8 O + p; \quad Q = -1.19 \text{ MeV}$.

An important experimental breakthrough came in 1932 when the neutron was discovered by Chadwick in the reaction $\alpha + {}_4^9 Be \rightarrow {}_6^{12} C + n$; $Q = +5.71 \text{ MeV}$. This discovery opened new possibilities for investigation of the nuclear structure and of the nuclear interactions. Indeed, neutrons are not affected by the Coulomb repulsion and nuclear reactions can occur with very little kinetic energy. In addition to nuclear interaction, there are reactions caused by weak or electromagnetic interactions which play a key role in the mechanism of nucleosynthesis and energy production in stars.

14.9.1 Nuclear Fission

The neutron discovery was followed by an intense activity to produce nuclear reactions initiated by neutrons. E. Fermi (Nobel laureate in 1938 for this work) studied neutron capture reactions to produce heavy nuclei and their β decays. In 1938, O. Hahn and F. Strassmann observed that elements with atomic number approximately equal to half that of uranium are produced in collisions of neutrons with uranium nuclei, e.g.,



In 1939, L. Meitner and O. Frisch hypothesized that the production of elements with intermediate atomic number was due to the heavy nuclear fission induced by neutron capture.

Spontaneous fission. For elements in the periodic table, the *spontaneous fission* (i.e., not induced by external factors)



is prevented by the nuclear attractive potential. This can be deduced from the nuclear drop model which predicts that only nuclei with $Z^2/A > 47$ may be subject to spontaneous fission.

Fission induced by neutrons. The situation can change drastically if a heavy nucleus captures a neutron. In this case, the nucleus can split into two. The decrease in the nuclear binding energy (14.15), due to variations of the negative terms, allow solutions for which the nuclear fission from ${}_{Z}^A N$ to two nuclei ${}_{Z_1}^{A_1} X$, ${}_{Z_2}^{A_2} Y$ (with $A_1 + A_2 = A$, $Z_1 + Z_2 = Z$) is energetically favored.

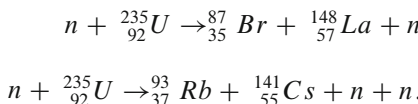
Bohr and Wheeler determined some properties of spontaneous fission and n induced fission using the nuclear drop model:

- For nuclei with $Z^2/A > 47$, i.e., $Z \geq 130-140$, the energy difference after the fission is positive; the nuclei are unstable and undergo spontaneous fission (indeed, they do not exist in nature).

- For nuclei near the instability threshold, i.e., with $A \simeq 100$, the energy change due to neutron capture is not sufficient to cause fission.
- For heavier stable nuclei, $A \geq 240$, the energy variation induced by neutron capture is sufficient to cause fission.
- The activation energy $EB - Q$ needed to ignite the fission can be calculated; it is different for odd- A and even- A nuclei.

Uranium fission. Natural uranium is composed of two isotopes: $^{238}_{92}U$ and $^{235}_{92}U$, with relative abundances of 99.28% and 0.72%. The fission of $^{235}_{92}U$ is initiated by capture of thermal² neutrons with a cross-section: $\sigma^{235} \simeq 580 \text{ b}$. The fission of $^{238}_{92}U$ is initiated by neutrons with kinetic energy $T_n > 1.8 \text{ MeV}$ with a much smaller cross-section: $\sigma^{238} \simeq 0.5 \text{ b}$. The typical energy released in a nuclear fission is $Q = 210 \text{ MeV}$, yielding an efficiency $Q/M_U = 210 \text{ MeV}/220 \text{ GeV} \simeq 10^{-3}$.

Nuclei with $A_X \sim 90$, $A_Y \sim 145$ are produced in the final state, for example, one has



In addition, an average number $\bar{n} \sim 2.5$ of *immediate neutrons* with kinetic energy $T_n \simeq 2 \text{ MeV}$ are also produced. The term *immediate neutrons* indicates that fission occurs with very short reaction times (10^{-16} – 10^{-14} s) and that the neutron emission is accompanied by the emission of photons with energy $E_\gamma \simeq 8 \text{ MeV}$. The remaining energy is in the form of kinetic energy of the two emitted nuclei. Usually, these nuclei have an excess of neutrons and reach the stability valley in the $A - Z$ plane through β emission. The energy released in the β decays is on average $E_\beta \sim 20 \text{ MeV}$, from which approximately 12 MeV are carried away by the antineutrinos. Therefore, the fission reaction is a source of neutrons, photons, electrons and antineutrinos.

One may wonder why the $^{235}_{92}U$ is more efficient than other isotopes in the fission reaction induced by neutron capture. In the case of $^{235}_{92}U$, the intermediate state $^{236}_{92}U$ is formed; the mass difference is

$$\Delta M^{235} = M({}_{92}^{235}U) + m_n - M({}_{92}^{236}U) = 6.5 \text{ MeV}.$$

The activation energy of the $^{235}_{92}U$ fission is 6.2 MeV; therefore, the neutrons do not need to have kinetic energy and the $^{235}_{92}U$ fission is obtained with thermal neutrons. In the case of the $^{238}_{92}U$ isotope, the intermediate state $^{239}_{92}U$ is formed; the mass difference is

$$\Delta M^{238} = M({}_{92}^{238}U) + m_n - M({}_{92}^{239}U) = 4.8 \text{ MeV}.$$

²Thermal neutrons are obtained slowing down neutrons; after a number of elastic collisions with light nuclei in a neutron moderator at a given temperature, neutrons arrive at about this energy level, provided that they are not absorbed.

The activation energy for the $^{238}_{92}U$ fission is 6.6 MeV; hence, to enable the fission of this isotope, neutrons with kinetic energy $T_n > 1.8$ MeV are required. In the case of uranium, the term a_4 in (14.15) plays a decisive role. In the neutron capture reaction, the even-even nuclei, for example, $^{236}_{92}U$ and $^{238}_{92}U$, become even-odd nuclei. An additional energy equal to $a_4/A^{1/2} = 12.6 \text{ MeV}/\sqrt{236} \simeq 0.8 \text{ MeV}$ should be provided. Instead, the nucleus $^{235}_{92}U$ becomes an even-even nucleus after neutron capture, but the same amount of energy ($\simeq 0.8 \text{ MeV}$) now becomes available. Note that the difference between the binding energies in the two cases reflects the difference between $\Delta M^{235} - \Delta M^{238}$.

14.9.2 Fission Nuclear Reactors

A fission reaction typically produces an average number of neutrons > 1 ; these neutrons may subsequently induce new fission reactions. Conditions for self-powered chain reactions can be created to produce energy by fission. The first nuclear pile was built by Fermi and collaborators in 1942. A nuclear reactor based on controlled fission reactions are used to produce: (1) energy; (2) neutron sources for research and medical purposes; (3) radio-isotopes or other fissile substances, for example, $^{239}_{94}Pu$ or $^{233}_{92}U$. Uncontrolled chain reactions are the basis for nuclear bombs.

A typical nuclear reactor for energy production is based on chain reactions in uranium. By $^{235}_{92}U$ fission reaction, each produces an average of $\simeq 200 \text{ MeV}$ and 2.5 neutrons. The cross-section of neutron capture is small and only thermal neutrons are efficiently captured by $^{235}_{92}U$ to produce successive fission reactions. For this reason, it is necessary to moderate neutrons, forcing them to lose energy in successive collisions with light nuclei. From the construction point of view, the core of a uranium nuclear reactor consists of a moderator material and of enriched uranium, i.e., a kind of uranium in which the percent composition of $^{235}_{92}U$ is increased typically at 3% level (in nature, this isotope has an abundance of 0.7%).

To moderate neutrons, materials containing low Z nuclei are used, e.g., H_2O , D_2O (the so-called *heavy water*) or C . Carbon is not very efficient, but can be distributed effectively in the fuel. The Chernobyl energy power plant in the former USSR used carbon as a moderator. The water (normal or heavy) is also an efficient heat exchanger to cool the reactor. The hydrogen nuclei in the molecule of water are also very efficient to moderate neutrons; there is a disadvantage due to the high cross-section of the competitive reaction $n + p \rightarrow^2_1 H + \gamma$, that reduces the neutron budget. The deuterium nucleus present in heavy water (instead of hydrogen) has a much smaller cross-section for the process $n + ^2_1 H \rightarrow ^3_1 H + \gamma$, but it produces radioactive tritium that must be filtered out from the cooling system.

With a proper combination of fuel and moderator, the situation in which there is on average one thermal neutron per fission is reached. This is the so-called *critical reactor* situation. Preventing that this factor exceeds unity and that the reactor reaches the super-critical situation with the risk of failures, materials with

high capture cross-section for thermal neutrons must be inserted. The most suitable material is cadmium.

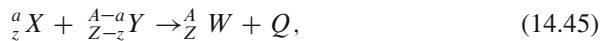
One gram of $^{235}_{92}U$ produces, in a critical reactor,

$$1 \text{ g} (^{235}_{92}U) = \frac{6 \times 10^{23}}{235} \times 200 \text{ MeV} \simeq 0.8 \times 10^{11} \text{ J}, \quad (14.44)$$

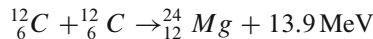
approximately three times the energy produced in the combustion of a ton of coal. The energy associated with nuclear processes is in fact ~ 6 orders of magnitude higher than the energy associated with chemical (= electromagnetic) reactions that govern combustion processes.

14.10 Nuclear Fusion in Astrophysical Environments

In a fusion reaction, two light nuclei combine to form a nucleus with larger atomic weight. The binding energy of nuclei BE (14.15) as a function of the mass number A shows that the fusion reaction,



produces free energy $Q > 0$ if $d(BE)/dA > 0$, corresponding to nuclei with $A < 60$ (i.e., nuclei lighter than iron). Due to the short range of nuclear interaction, the fusion reaction can only occur if the nuclei have sufficient initial kinetic energy to compensate the Coulomb repulsion in order to bring the two nuclei in contact. For example, the reaction



is exothermic, but requires that the two carbon nuclei initially have an energy that overcomes the Coulomb repulsion. The activation energy E_a corresponds to ($A = 12$, $Z = 6$, $R_0 = 1.2 \text{ fm}$)

$$E_a \geq \frac{Z^2 e^2}{R} = \frac{Z^2 e^2}{2R_0 A^{1/3}} = 9 \text{ MeV}. \quad (14.46)$$

Spending 9.0, 13.9 MeV are produced. The efficiency ($Q/2M_C \simeq 6 \cdot 10^{-4}$ in this example) is inversely proportional to the mass of the merging nuclei. Energy released in fusion reactions transforms in kinetic energy of the nuclei; if there is a force field capable of confining the nuclei, the temperature increases until equilibrium is reached. In the equilibrium phase, the fusion reactions are self-sustained and produce energy. Stable confinement situations are present in the cores of stars, and (hopefully) in future *nuclear fusion reactors*.

For light nuclei with $Z \simeq A/2$, the required temperature to compensate the Coulomb repulsion (14.46) is

$$E_a \sim kT = \frac{A^{5/3}e^2}{8R_0} \simeq 0.14 \times A^{5/3} \text{ MeV} \quad T \simeq 1.6 \times 10^9 \times A^{5/3} \text{ K}. \quad (14.47)$$

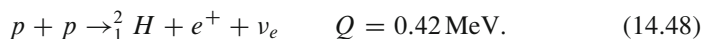
However, the energy of the nuclei in the Maxwell velocity distribution tail and the tunneling probability make nuclear fusion possible even at lower temperatures.

14.10.1 Fusion in Stars

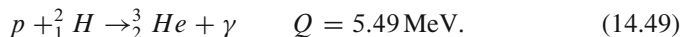
The Sun (like all main sequence stars) produces energy by fusion (see Fig. 12.11a): four protons form a helium nucleus releasing about 26 MeV with a very high efficiency, $26 \text{ MeV}/(2m_p + 2m_n) = 0.007$. The temperature inside the Sun is $T \simeq 1.5 \times 10^7 \text{ K}$, corresponding to a proton kinetic energy of $E_p \simeq 1.3 \text{ keV}$, much lower than the Coulomb repulsion energy $\simeq 0.8 \text{ MeV}$. The force field that holds the nuclei in the star core is due to the gravitational pressure of matter present in the outer layers. A star is a system in equilibrium between pressure due to gravity and pressure due to radiation produced by fusion reactions in the core.

The material formed in the early phase of the universe, at the time of the *primordial nucleosynthesis* (Sect. 13.6), was in mass by 3/4 of protons, 1/4 helium nuclei and traces of heavier *Li, Be, B* elements. Gravitational attraction and fluctuations in particle density caused condensations of matter with the formation of *protostars*. When in the center of a protostar, the density becomes sufficiently high and the fusion cycle starts.

The first reaction of the cycle occurs through weak interaction, that is,



The cross-section for this low energy process is extremely small, $\sigma \sim 10^{-55} \text{ cm}^2$: this is why the stars burn very slowly. The reaction in which the formed deuteron interacts with a proton occur via strong interaction and has a large cross-section:



Thus, the produced deuterons are immediately transformed. When the density of ${}_2^3 He$ nuclei is high enough, the reaction



starts and one helium nucleus plus two protons are formed; the latter are available to start other cycles. Further reactions of the cycle, particularly those producing neutrinos, are shown in Fig. 12.11. The proton–proton cycle can be summarized as

$$4p \rightarrow {}_2^4 He + 2e^+ + 2\nu_e \quad Q = 24.7 \text{ MeV.} \quad (14.51)$$

To this value of Q , 2 MeV must be added due to the annihilation of the two positrons. Neutrinos do not energetically contribute to star equilibrium because they have a low interaction probability and immediately escape. Since each neutrino has an average energy $\bar{E} \sim 0.3$ MeV which is subtracted, the total energy balance of the cycle is about 26 MeV. The measurement of solar neutrino flux (Sect. 12.7 and Exercise 14.7) provided important information not only on the neutrino physics properties, but also on how the fusion process occurs in the Sun and on the properties of our star (Standard Solar Model [B89]).

Due to many other processes, the energy produced by fusion propagates to the surface of the Sun, the photosphere. The diffusion time of photons from the stellar core to the photosphere (taking into account the γ -p cross-section) is of the order of 10^5 – 10^6 years.

The Sun has converted hydrogen to helium for roughly 5×10^9 years. The value of solar mass and the emitted power indicate that it will continue for about as many years. A star with roughly the solar mass, when hydrogen is exhausted, tends to contract and to increase its density; this happens because the radiation produced by the fusion reactions is no longer able to balance the gravitational pressure. With contraction, the gravitational energy is converted into kinetic energy of the nuclei: the temperature increases and further fusion reactions may be ignited.

The critical point is the carbon formation. In a star composed mainly of ${}_2^4 He$ nuclei, ${}^8 Be$ is continuously formed. ${}^8 Be$ has a mass which is slightly larger than twice the ${}_2^4 He$ mass, that is, ${}_2^4 He + {}_2^4 He \rightarrow {}_4^8 Be$; $Q = -0.09$ MeV. Once formed, it splits again into two ${}_2^4 He$ nuclei. When the ${}_2^4 He$ density is extremely high, a fusion reaction forming carbon nuclei in an excited state occurs with a resonant cross-section: ${}_2^4 He + {}_4^8 Be \rightarrow {}_6^{12} C^*$. The excited state C^* immediately decays to the ground state. The carbon abundance in the universe is relatively high and it may also be present in stars that have not exhausted the proton cycle. In the presence of protons, the nucleus ${}^6_6 C$ acts as a *catalyst* for another cycle, similar to the proton–proton cycle, that produces energy transforming protons into helium nuclei: the CNO cycle.

Reaction	Q (MeV)
$p + {}_{6}^{12} C \rightarrow {}_{7}^{13} N + \gamma$	1.94
${}_{7}^{13} C \rightarrow {}_{6}^{13} C + e^+ + \nu_e$	1.20
$p + {}_{6}^{13} C \rightarrow {}_{7}^{14} N + \gamma$	7.55
$p + {}_{7}^{14} N \rightarrow {}_{8}^{15} O + \gamma$	7.29
${}_{8}^{15} O \rightarrow {}_{7}^{15} N + e^+ + \nu_e$	1.94
$p + {}_{7}^{15} N \rightarrow {}_{6}^{12} C + {}_{2}^4 He$	4.96

Finally, one has $4p \rightarrow {}_2^4 He + 2e^+ + 3\gamma + 2\nu_e$ with a total energy balance of about 26 MeV. The ${}_{\text{6}}^{12}C$ nucleus is strongly bound and is the starting point for the formation of heavier nuclei through fusion; for example,

Reaction	Q (MeV)	E_C (MeV)
${}_{\text{2}}^4 He + {}_{\text{6}}^{12} C \rightarrow {}_{\text{8}}^{16} O + \gamma$	7.16	3.6
${}_{\text{2}}^4 He + {}_{\text{8}}^{16} O \rightarrow {}_{\text{10}}^{20} Ne + \gamma$	4.73	4.5
${}_{\text{2}}^4 He + {}_{\text{10}}^{20} Ne \rightarrow {}_{\text{12}}^{24} Mg + \gamma$	9.31	5.4

Note that the Coulomb potential barrier E_C increases with the atomic number. The probability of each reaction is inversely proportional to E_C and the relative nuclear abundance decreases with increasing A .

When helium is exhausted as a fuel, the star tends to contract again (if massive enough), increasing density and temperature. It can start a new fusion cycle using carbon and oxygen as fuel. The potential barrier is respectively 9.0 and 14.6 MeV; to sustain the following fusion reactions, temperatures $T \geq 10^9$ K are required.

Reaction	Q (MeV)
${}_{\text{6}}^{12} C + {}_{\text{6}}^{12} C \rightarrow {}_{\text{10}}^{20} Ne + \alpha$	4.62
${}_{\text{6}}^{12} C + {}_{\text{6}}^{12} C \rightarrow {}_{\text{11}}^{23} Na + p$	2.24
${}_{\text{6}}^{12} C + {}_{\text{6}}^{12} C \rightarrow {}_{\text{12}}^{23} Mg + n$	-2.61
${}_{\text{6}}^{12} C + {}_{\text{6}}^{12} C \rightarrow {}_{\text{12}}^{24} Ne + \gamma$	13.93
${}_{\text{8}}^{16} O + {}_{\text{8}}^{16} O \rightarrow {}_{\text{14}}^{28} Si + \alpha$	9.59
${}_{\text{8}}^{16} O + {}_{\text{8}}^{16} O \rightarrow {}_{\text{15}}^{31} P + p$	7.68
${}_{\text{8}}^{16} O + {}_{\text{8}}^{16} O \rightarrow {}_{\text{16}}^{31} S + n$	1.46
${}_{\text{8}}^{16} O + {}_{\text{8}}^{16} O \rightarrow {}_{\text{16}}^{32} S + \gamma$	16.54

In the above reactions, in addition to the heavy nuclei, photons, protons, neutrons and α particles are also produced. These particles have energies high enough to produce other heavy nuclei from ${}_{\text{14}}^{28} Si$ and ${}_{\text{16}}^{32} S$ nuclei. These reactions are energetically favored when compared to fusion reactions, for example, ${}_{\text{14}}^{28} Si + {}_{\text{14}}^{28} Si \rightarrow {}_{\text{28}}^{56} Ni + \gamma$, that require an even higher temperature.

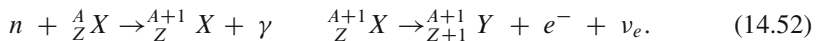
14.10.2 Formation of Elements Heavier than Fe in Massive Stars

Nucleosynthesis from nuclear fusion proceeds until the formation of nuclei with $A \leq 60$. The heavier elements up to iron are only synthesized in massive stars with $M > 8M_\odot$. Near the end of its life, the star begins to convert the silicon core into iron and nickel (this phase lasts a few days). Once the star core is

made primarily of iron, further compression of the core does not ignite nuclear fusion anymore; the star is unable to thermodynamically support its outer envelope made of concentric shells of silicon, sulfur, oxygen, neon, carbon, helium and hydrogen (in order from the innermost to the outermost part). As the surrounding matter falls inward under gravity, the temperature of the core is so high that the iron disintegrates with a large absorption of energy (core cooling) into helium nuclei, neutrons and protons. As can be seen in Fig. 14.3, the transformation of iron nuclei into heavier or lighter elements is endothermic, and energy must be provided. Now, the electron capture on protons becomes favored and electron neutrinos are produced as the core gets neutronized (a process known as *neutronization*).

The core cooling deprives the star of the energy power that allowed the balance with the gravitational pull of falling matter. The rest of the star, without the support of the radiation, collapses, compressing the star nucleus. When the core reaches densities of above 10^{12} g/cm³, neutrinos are trapped in the so-called neutrinosphere. The collapse continues until 3–4 times the density of ordinary nuclei is reached, after which the inner core rebounds sending a shock-wave across the outer stellar shells. This shock-wave loses energy heating the matter that it crosses. Particle–antiparticle annihilation (mainly e^+e^-) is a source of neutrino–antineutrino pairs of all flavors. In this way, 99% of the star binding energy is released in the form of neutrinos in a few tens of seconds.

The shock wave generates local compressions that trigger new interactions. The formation of nuclei heavier than iron (from silver, platinum, gold, mercury up to uranium) is induced by neutron capture and β^- decay:



Charged particles such as p or α cannot be easily captured due to the additional Coulomb barrier. The neutron capture can occur when free neutrons are available, just immediately after the supernova explosion. In particular, nickel and cobalt are produced; the fluorescence due to their radioactive decay is the primary cause of the visible light observed by astronomers in the first weeks after the supernova explosion.

The relative abundance of heavy nuclei depends on the lifetime τ_n for the neutron capture and on the lifetime τ_β for the β decay:

- If $\tau_n \gg \tau_\beta$, the nucleus ${}_{Z+1}^{A+1} X$ formed by neutron capture has enough time to undergo a β^- decay; the nucleus tends to stabilize along the stability valley. Since the probability of neutron capture $\sim 1/\tau_n$ is small, the reactions occur at a low rate and are classified as *s-processes* (*s* = slow).
- If $\tau_n \ll \tau_\beta$, the newly formed nucleus does not decay immediately; after subsequent neutron captures, the isotopes move away from the stability valley (${}_{Z+1}^{A+1} X \rightarrow {}_{Z+1}^{A+2} X \rightarrow {}_{Z+1}^{A+3} X \rightarrow \dots$). The number of neutrons increases and thus the instability for β^- decay. Since the probability of neutron capture is large and the reactions occur with a high rate, these are called *r-processes* (*r* = rapid).

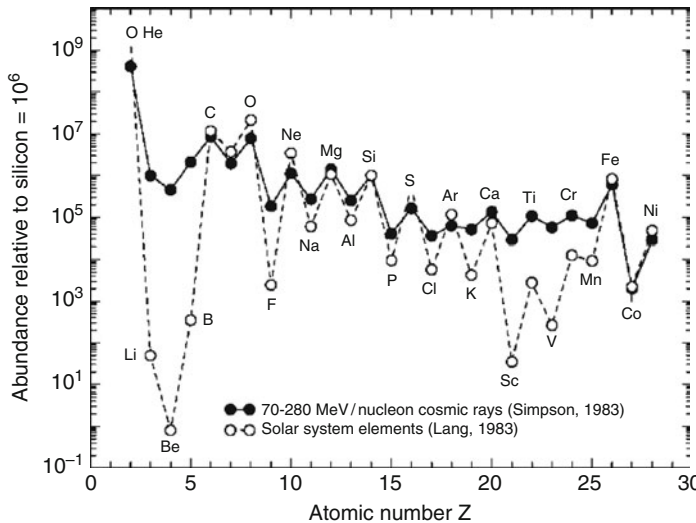


Fig. 14.12 Relative abundance with respect to silicon of elements in the Solar System and in Cosmic Rays. The correlation between the relative abundances leads to the hypothesis that the mechanisms that accelerate the CR and those that produce planetary systems are closely related. The discrepancies (the CR abundance of elements such as Li , Be , B) are explained by the CR diffusion processes and interaction within our galaxy [14S83]. Elements heavier than Fe are much rarer since they are formed during the phases of stellar gravitational collapses. Nuclei with $Z > 40$ have an abundance relative to iron of 10^{-7} – 10^{-5}

Even today, most of the material in the universe is made of hydrogen ($\sim 75\%$) and helium ($\sim 24\%$) nuclei formed in the primordial nucleosynthesis. Stellar nucleosynthesis does not increase the abundance of light nuclei (lithium, beryllium and boron) as these elements act as catalysts of nuclear reactions that occur when the star is on the *main sequence*. The Li , Be , B abundances in the Solar System (and in the universe) are generally very small for this reason. The most abundant nuclei are those formed with α particle capture (carbon, oxygen, neon, magnesium, silicon ...) and nuclei with binding energy close to the maximum $A \sim 60$ (iron, nickel).

The nuclei with $A > 60$ have relative abundance decreasing with A . Some exceptions (peaks in the relative abundance) correspond to the nuclei with *magic numbers*. Figure 14.12 shows the relative abundance of elements in the Solar System compared with that of Cosmic Rays (CR). The similarities between the two distributions indicate that astrophysical sources that accelerate CR have chemical composition similar to that of our Solar System. The explanation is probably related to the fact that astrophysical mechanisms that accelerate the galactic CR (supernova explosions) are closely correlated with those that can give rise to planetary systems. The CR surplus of elements such as Li , Be , B are due to the effects of propagation (fragmentation) of C , N , O present in Cosmic Rays in the interactions with the protons of the interstellar medium, see Problem 14.9.

14.10.3 Earth and Solar System Dating

Another example of the close interconnection between nuclear physics and astrophysics is the possibility of estimating the age of the Sun and of the time required for the formation of our planetary system. It is believed that the Solar System was formed from a cloud of gas and dust (with a diameter of about 100 astronomical units, see Appendix A.5, and a mass about two to three times that of the Sun). The cloud was hit by a shock wave generated by the explosion of a nearby star (supernova) with mass at least ten times that of the Sun. The shock wave caused the compression of the gas and dust cloud that, because of the gravitational attraction, began to pull inward other material forming the solar nebula. In the process of contraction, as a result of the gravitational attraction, pressure, magnetic fields and rotation, the nebula was flattened into a protoplanetary disk with a protostar at its center. In the protoplanetary disk, various planets were formed.

In the inner region of the planetary system in formation (which includes the zone where the Earth is now), the temperature was too high to allow condensation of volatile molecules such as water and methane. Only relatively small rocky bodies were formed (mainly by compounds with high melting point, such as silicates and metals) that will evolve later in planets of terrestrial type. Externally, “gas giants” Jupiter and Saturn developed, while Uranus and Neptune captured less gas and condensed around nuclei of ice.

At the center of the system, the Sun started to shine when the pressure due to gravity was high enough to cause the activation of fusion reactions in the protostar. A strong stellar wind began to remove most of the gas and dust. Thanks to their huge mass and large distance, the “gas giant” planets kept their atmosphere. The current atmosphere in terrestrial planets is the result of volcanism and impacts with other celestial bodies.

The dating of the Earth is possible through measurements of radioactive decay. Heavy elements in the Solar System were formed in a relatively small time, during the gravitational collapse of the massive star that triggered the formation of the Sun. The theory of heavy element nucleosynthesis [14B57] hypothesizes that nuclei such as the ^{187}Re , ^{232}Th , ^{235}U are synthesized by neutron capture (the *r-process*) from the lighter elements expelled by the gravitational collapse. The various models discussed in [14T98] assume, in the formation, a ratio $(^{235}U/^{238}U)_r = 1.35 \pm 0.30$.

The concentration of heavy elements is now different from the original one because each isotope has a different half-life. The present ratio between these elements depends on the time T from their synthesis; it is measured in rocks of the Earth, of the Moon and in meteorites. We can assume that $T = \tau_f + \tau_{SS}$, where τ_f is the time between the supernova explosion that originated the Solar System and the birth of the Solar System (and Earth), and τ_{SS} is the age of the Solar System (and Earth).

The calculation can be specifically performed for the important case of uranium isotopes. The lifetime of the ^{238}U isotope is $\tau_{238} = 6.43 \times 10^9$ years, larger than the lifetime of the ^{235}U isotope, equal to $\tau_{235} = 1.01 \times 10^9$. Therefore, the ratio

$^{235}U/^{238}U$ is decreased today: it is $(^{235}U/^{238}U)_0 = 7.2 \times 10^{-3}$ and is known with great accuracy (error of the order of the percent) through measurements made on terrestrial and lunar rocks and on meteorites.

It is easy to verify that the current ratio of concentrations should be

$$\left(\frac{^{235}U}{^{238}U}\right)_0 = \left(\frac{^{235}U}{^{238}U}\right)_r \cdot \left(\frac{e^{-T/\tau_{235}}}{e^{-T/\tau_{238}}}\right). \quad (14.53)$$

Inserting numerical values, one obtains

$$T = \tau_f + \tau_{SS} = 6.3 \times 10^9 \text{ years}. \quad (14.54)$$

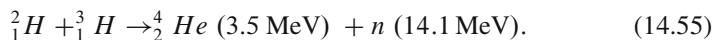
Techniques of estimating τ_{SS} also exist. One of them is based on the fact that the ^{238}U isotope (as shown in Fig. 14.8) ends in the ^{206}Pb stable isotope, while the ^{235}U isotope terminates in the ^{207}Pb stable isotope. From the measured ratio, $\tau_{SS} = 4.5 \times 10^9$ years is obtained. The formation process of the Sun and of our planetary system lasted about 1.8 billion years.

14.11 Nuclear Fusion in Laboratory

Concerning the production of energy, the fusion process has a larger efficiency than fission. Using light nuclei as a fuel, fusion produces no radioactive waste nuclei. However, in laboratory, it is much more difficult to achieve and maintain temperature and density conditions able to produce energy by fusion. The Coulomb potential barrier increases with atomic number Z and for light nuclei is typically $\simeq 1$ MeV. This value is reduced if the tunneling probability is considered, but still energies $\simeq 10$ keV (i.e., temperatures $\sim 10^8$ K) should be reached to merge two light nuclei. Under these conditions, the atoms are completely ionized (plasma of ions and electrons). The electrons in the high-density plasma are accelerated by the strong electric fields of nuclei and emit bremsstrahlung radiation. The power radiated is proportional to Z^2 and it subtracts energy from the plasma. The conditions to achieve fusion reactions in laboratory and to produce energy are:

- To use nuclei with small atomic number Z .
- To operate at high temperature, $T > 10^8$ K.
- To operate at high density.
- To use reactions with large cross-sections and high energy yield.

The most promising reaction is the deuterium-tritium reaction:



The energy yield is approximately 340 GJ per gram of reagent, equivalent to 8 tons of oil.

However, since the nuclei have a positive electrical charge and therefore repel each other, it is necessary to spend energy to bring them close together. The best solution is to heat a deuterium-tritium mixture up to very high temperatures (of the order of 100–200 million degrees). To minimize the loss of heat, any contact with the vessel wall where the gas is contained must be avoided. On the other hand, already at 10^5 K, atoms and molecules are dissociated into electrons and positive nuclei (plasma). In plasma, interactions occur through long-range electromagnetic fields resulting from the contribution of many charged particles (collective effects). Only a small fraction of collisions leads to close contact between two nuclei and thus to fusion. Two key conditions are necessary for controlled fusion:

- To heat the plasma up to temperatures T necessary to efficiently produce fusion reactions.
- To contain and thermally confine the plasma in order to minimize the particle and energy losses. An equilibrium between energy deposited in the plasma by the fusion products and power loss must be reached (this situation is called *ignition*).

These conditions are achieved when the product $n\tau T$ exceeds the specific threshold value of the considered fusion reaction. n is the number density of the plasma and τ the energy confinement time. The result can be obtained either with high density plasmas confined for a short time (inertial confinement), or with low density plasma and high confinement time. In the latter case, the plasma confinement is achieved by magnetic fields. The fields guide the charged particles motion within the combustion chamber along trajectories that do not intersect the walls. The former technical approach is the so-called *inertial fusion*, while the second is *magnetic fusion*.

The ITER project. The prototype machine for the magnetic confinement is the Tokamak. It has the form of a toroidal ring around which a set of coils are symmetrically arranged to generate a toroidal magnetic field; the magnetic field guides charged particle motion. Within the machine, the vacuum is produced and the fuel with a low density (10^{20} particles/m³) is injected. The walls of the ring act as a container for gas and must absorb the heat from the hot plasma during operation. In 1988, a common design project (called ITER) [14w4] was initiated between Europe, USA, (former-)USSR and Japan. The effort is devoted to verify the technical possibility of fusion reactions to produce energy; to the research and development of the necessary key technologies; to the construction of a prototype reactor. In November 2006, representatives of the ITER (European Union, China, Japan, India, Republic of Korea, Russia, USA) signed an agreement for the construction of the machine, after a long negotiation period. The construction of ITER began in Cadarache (France) in early 2007. The program foresees the development of the experimental activities for a 25 year period, which includes 10 years for

construction. A period of 6 years is scheduled at the end for dismantling and transportation of radioactive waste (produced in the interaction of neutrons with the containment materials) in a suitable site. Construction costs are estimated at five billion euros.

ITER is the first machine having the production of electricity from fusion as an objective, with 500 MW pulse of 400 s duration; the conditions are such that the plasma heating from the helium nuclei produced by fusion reactions will exceed that generated by external circuits. This prototype machine is designed to generate thousands of pulses per year and to test the key technologies for a fusion power plant, in particular:

- *The superconducting magnet system, necessary to limit the power dissipation.*
- *The fuel loading process in the reaction chamber and the simultaneous extraction of produced particles.*
- *The plasma heating and its control with auxiliary power to hopefully achieve long operating cycles and, if possible, stable operation.*
- *The disposal of the energy generated and of the burned fuel.*
- *The recovery of tritium.*
- *The monitoring of the functioning and operational safety.*

The success of ITER will be essential to determine if nuclear fusion³ will replace hydrocarbons efficiently and possibly with a minor environmental impact.

³The fuel material of nuclear fusion is the deuterium which is virtually available to every nation from the sea.

Appendix A

- A.1 Periodic Table
- A.2 The Natural Units in Subnuclear Physics
- A.3 Basic Concepts of Relativity and Classical Electromagnetism
- A.4 Dirac Equation and Formalism
- A.5 Physical and Astrophysical Constants

A.1 Periodic Table [P08]

4. PERIODIC TABLE OF THE ELEMENTS

Table 4.1. Revised isotopic abundances of the elements (bottom) as weighted by atomic masses relative to the mass of the carbon-12 isotope, defined to be exactly 12 unified atomic mass units (u). Errors range from 1 to 9 in the last digit quoted. Relative isotopic abundances often vary considerably, both in nature and in the laboratory. However, although no stable isotope exists, the mass of the longest-lived isotope of that element can be taken as its atomic mass. For elements 11–12, the atomic numbers are given. Adapted from the Commission of Atomic Weights and Isotopic Abundances, "Atomic Weights and Isotopic Abundance of the Elements 1995," Pure and Applied Chemistry, 68, 2239 (1996), and G. Audi and A. H. Wapstra, "The 1993 Mass Evaluation," Nucl. Phys. A, 566, 1 (1993).

A.2 The Natural Units in Subnuclear Physics

In particle physics, it is convenient to use the natural units system in which the fundamental physical quantities are mass, velocity and angular momentum. The unit system becomes very appropriate when you choose $\hbar = c = 1$. In this system, all physical quantities are expressed in terms of a power of mass $[M]$. The extension to thermodynamics is made by putting $K = 1$, where K is the Boltzmann constant. This allows a significant reduction regarding the notation; at the end, it is always possible by dimensional analysis, for example, insert the correct \hbar and c factors to write the result in the more usual units (see Problems in Chap. 1).

Let us examine the implications of this choice, that is, $\hbar = c = 1$.

- Consequences of $c = 1$.** The choice $c = 1$, since the speed has dimensions $[c] = [v] = [LT^{-1}]$, implies that length and time have equal dimensions:

$$[L] = [T]$$

Similarly, given the relativistic relation between energy and momentum

$$E^2 = p^2 c^2 + m^2 c^4,$$

the choice $c = 1$ implies that energy, mass and momentum have the same dimension. Momentum is usually expressed in units $\text{MeV}/c \rightarrow \text{MeV}$ and the mass in units $\text{MeV}/c^2 \rightarrow \text{MeV}$. Thus, the proton has mass 938.27 MeV , meaning that $m_p c^2 = 938.27 \text{ MeV}$ (remember that $c = 2.9979 \cdot 10^8 \text{ m s}^{-1}$).

- Consequences of $\hbar = 1$.** The numerical value of the reduced Planck constant is $\hbar = 6.582 \cdot 10^{-22} \text{ MeV s}$. \hbar has the dimension

$$[\hbar] = [\text{Energy} \cdot \text{time}] = [ML^2 T^{-1}].$$

By considering $\hbar = 1$ dimensionless, the units of mass, length and time are related. Since $[L]$ and $[T]$ are equivalent because of the choice $c = 1$, we obtain for the mass

$$[M] = [L^{-2} T] = [L^{-1}] = [T^{-1}].$$

In this way, in the natural unit system, the mass is the only independent physical quantity. Moreover, if we decide to choose the GeV to measure the mass in the natural unit system, lengths and times are expressed in GeV^{-1} .

Numbers to remember. The following numeric values are useful for the conversion to/from natural units ($1 \text{ b} = 10^{-24} \text{ cm}^2$), that is,

$$\hbar c = 6.582 \cdot 10^{-22} \cdot 3 \cdot 10^8 \text{ MeV s m s}^{-1} = 197.33 \text{ MeV fm}$$

$$(\hbar c)^2 = (0.19733 \cdot 10^{-13})^2 \text{ GeV}^2 \text{ cm}^2$$

$$= 0.38938 \text{ GeV}^2 \text{ mb} = 0.38938 \cdot 10^{-27} \text{ GeV}^2 \text{ cm}^2$$

$$(\hbar c)^3 = (0.19733 \cdot 10^{-13})^3 \text{ GeV}^3 \text{ cm}^3 = 7.684 \cdot 10^{-42} \text{ GeV}^3 \text{ cm}^3.$$

The conversion factors to switch from the natural units to the International System units are determined by an appropriate dimensional analysis.

GeV⁻¹ → m. Remembering that $\hbar c = 197.33 \text{ MeV fm} = 0.19733 \text{ GeV fm} = 1.9733 \cdot 10^{-16} \text{ GeV m}$, in natural units, $\hbar = c = 1$, we get

$$1 \text{ GeV}^{-1} = 1.9733 \cdot 10^{-16} \text{ m.}$$

GeV⁻¹ → s. Remember that if $\hbar = 6.582 \cdot 10^{-25} \text{ GeV s}$, since $\hbar = 1$, we get

$$1 \text{ GeV}^{-1} = 6.582 \cdot 10^{-25} \text{ s.}$$

GeV → kg. Remember that if $1 \text{ eV} = 1.6022 \cdot 10^{-19} \text{ J}$, $1 \text{ GeV} = 1.6022 \cdot 10^{-10} \text{ J}$, we get

$$1 \frac{\text{GeV}}{\text{c}^2} = \frac{1.6022 \cdot 10^{-10}}{(2.997925 \cdot 10^8)^2} \frac{\text{J}}{\text{m}^2 \text{s}^{-2}} = 1.7827 \cdot 10^{-27} \text{ kg } (\sim m_p).$$

In summary, we have:

$$\begin{aligned} 1 \text{ GeV}^{-1} &= 6.582 \cdot 10^{-25} \text{ s} = 1.9733 \cdot 10^{-16} \text{ m} \\ &= (1.780 \cdot 10^{-27} \text{ kg})^{-1} = (1/1.160 \cdot 10^{13}) \text{ K}^{-1} \\ [M] &= [E] = [p] = [L^{-1}] = [T^{-1}] = [\text{K}]. \end{aligned}$$

A.3 Basic Concepts of Relativity and Classical Electromagnetism

A.3.1 The Formalism of Special Relativity

We recall some aspects of the special relativity formalism. The fundamental laws of physics have the same form in all inertial reference systems (the equations are *covariant*). The Lorentz transformation with velocity v along the z axis can be written as

$$\begin{cases} ct' = ct \cosh \theta - z \sinh \theta \\ z' = -ct \sinh \theta + z \cosh \theta \\ x' = x, \quad y' = y \end{cases} \quad (\text{A.1})$$

with $\tanh \theta = v/c = \beta$, $\cosh \theta = \gamma$, $\sinh \theta = \beta \gamma$.

As $\cos i\theta = \cosh \theta$, $\sin i\theta = i \sinh \theta$, the Lorentz transformation (A.1) can be considered as a rotation of an imaginary angle $i\theta$ in the (ict, z) plane.

Covariant notations are used in different forms, and sometimes (\mathbf{r}, ict) or (\mathbf{r}, ct) without $i = \sqrt{-1}$ is preferred. The majority prefers

$$(ct, \mathbf{r}) = (x^0, x^1, x^2, x^3) = x^\mu \quad (\text{A.2})$$

$$\left(\frac{E}{c}, \mathbf{p}\right) = (p^0, p^1, p^2, p^3) = p^\mu \quad (\text{A.3})$$

with the basic invariant $E^2/c^2 - \mathbf{p}^2 = m^2c^2$ for a free particle of rest mass m . Any quantity that behaves as (ct, \mathbf{r}) is called *four-vector*. In many cases, the natural units with $\hbar = c = 1$ are used and the units of space and time (or energy and momentum) in the four-vectors are the same.

The *scalar product between four-vector* $A^\mu = (A^0, \mathbf{A})$, $B^\mu = (B^0, \mathbf{B})$ can be written as

$$A \cdot B = A_\mu B^\mu = A^\mu B_\mu = \eta_{\mu\nu} A^\mu B^\nu = \eta^{\mu\nu} A_\mu B_\nu. \quad (\text{A.4})$$

The metric tensor $\eta_{\mu\nu}$ is defined as $\eta_{00} = 1$, $\eta_{11} = \eta_{22} = \eta_{33} = -1$, and the other components = 0 (and similarly for $\eta^{\mu\nu}$; note that $\eta_{\mu\nu}\eta^{\mu\nu} = 4$); Eq. A.4 understands a sum over the index μ, ν .

A^μ is a *contravariant vector* and A_μ is a *covariant vector*. Note that the spatial part of A^μ is \mathbf{A} , while the spatial part of A_μ is $-\mathbf{A}$. A particular nomenclature is defined for

$$\partial^\mu = \frac{\partial}{\partial x_\mu} = \frac{1}{c} \left(\frac{\partial}{\partial t}, -\nabla \right) \quad \partial_\mu = \frac{\partial}{\partial x^\mu} = \frac{1}{c} \left(\frac{\partial}{\partial t}, \nabla \right), \quad (\text{A.5})$$

transforming respectively as $x^\mu = (ct, \mathbf{x})$ and $x_\mu = (ct, -\mathbf{x})$. Forms like $E \rightarrow i\hbar \frac{\partial}{\partial t}$, $\mathbf{p} \rightarrow -i\hbar \nabla$ are written in covariant form as $p^\mu \rightarrow i\hbar \partial^\mu$. By ∂_μ and ∂^μ , one has the D'Alembert operator in covariant form, that is,

$$\square = \partial_\mu \partial^\mu = \frac{1}{c^2} \frac{\partial^2}{\partial t^2} - \nabla^2$$

Examples of scalar products (Lorentz invariant quantities) are¹:

$$p^\mu x_\mu = P \cdot X = p \cdot x = Et - \mathbf{p} \cdot \mathbf{x} \quad (\text{A.6})$$

$$p^\mu p_\mu = P \cdot P = P^2 = p \cdot p = p^2 = (E/c)^2 - \mathbf{p}^2. \quad (\text{A.7})$$

The repeated indices are balanced to the left and right of the equation (or on the bottom and on the top) and repeated indices appear as an upper and lower index.

¹The four-vectors are usually defined with capital letters (for example, P), but also with lowercase letters (for example, p).

For a free particle, one has $P^2 = m^2c^2$ (we say that the particle is “on mass shell”). The square of the total energy in the center of mass is called the s variable and is written as

$$s = (p_1 + p_2)^\mu(p_1 + p_2)_\mu = (p_1 + p_2)^2 = (P_1 + P_2)^2 = E_{cm}^2. \quad (\text{A.8})$$

Finally, the equations that describe the transformations of electric and magnetic field components as a result of coordinate transformations (A.1) are

$$\begin{cases} E'_z = E_z \\ E'_y = \gamma(E_y + \beta B_x) \\ E'_x = \gamma(E_x - \beta B_y) \end{cases} \quad \begin{cases} B'_z = B_z \\ B'_y = \gamma(B_y - \beta E_x) \\ B'_x = \gamma(B_x + \beta E_y). \end{cases} \quad (\text{A.9})$$

They show that it is impossible to consider the electric field and the magnetic field as independent entities.

A.3.2 The Formalism of Classical Electromagnetism

The classical theory of electromagnetism defines the fields **E** and **B** that obey the *Maxwell equations*. They allow us to calculate **E**, **B** once we know the charge density ρ and the current density **j**. In the Gauss system of units (c.g.s.), the Maxwell's equations are

$$\begin{cases} \nabla \cdot \mathbf{E} = 4\pi\rho \\ \nabla \cdot \mathbf{B} = 0 \\ \nabla \times \mathbf{E} = -\frac{1}{c} \frac{\partial \mathbf{B}}{\partial t} \\ \nabla \times \mathbf{B} = \frac{4\pi}{c} \mathbf{j} + \frac{1}{c} \frac{\partial \mathbf{E}}{\partial t} \end{cases} \quad (\text{A.10})$$

where $\rho = dq/dv$, $\mathbf{j} = \rho \mathbf{v} = [dq/(dt dS)]\hat{n}$ are respectively the charge density and current density and \hat{n} is the unit vector normal point by point to the surface S . In a vacuum, $\epsilon = \mu = 1$ and it is not necessary to define the vectors **D** e **H**. The volume element can be written in one of the following notations: $d v = d^3x = d^3r$. The force acting on a charge q moving with velocity **v** is

$$\mathbf{F} = q \left(\mathbf{E} + \frac{\mathbf{v}}{c} \times \mathbf{B} \right). \quad (\text{A.11})$$

One can say that there are Coulomb forces between stationary electric charges and additional forces (magnetic) between moving charges. Accelerated electric charges emit electromagnetic radiation, which can then be diffused or absorbed by bodies containing electric charges.

The fields \mathbf{E} , \mathbf{B} can be expressed in terms of a scalar potential φ and a potential vector \mathbf{A}

$$\begin{cases} \mathbf{E} = -\nabla\varphi - \frac{1}{c}\frac{\partial\mathbf{A}}{\partial t} \\ \mathbf{B} = \nabla \times \mathbf{A} \end{cases} . \quad (\text{A.12a})$$

In relativistic notation, we consider the contravariant four-vector position $x^\mu = (ct, \mathbf{x})$, energy-momentum $p^\mu = (E/c, \mathbf{p})$, current density $J^\mu = (c\rho, \mathbf{j})$, potential $A^\mu = (\varphi, \mathbf{A})$ and the antisymmetric tensor

$$F^{\mu\nu} = \frac{\partial A^\nu}{\partial x_\mu} - \frac{\partial A^\mu}{\partial x_\nu} = \partial^\mu A^\nu - \partial^\nu A^\mu. \quad (\text{A.12b})$$

The (A.12b) expressed in tensor form the equations relating the fields and potentials described by (A.12a). In the vacuum, in covariant form, Maxwell's equations are not homogeneous, that is,

$$\begin{cases} \nabla \cdot \mathbf{E} = 4\pi\rho \\ \nabla \times \mathbf{B} = +\frac{\partial \mathbf{E}}{\partial t} + \frac{4\pi}{c}\mathbf{j} \end{cases} \quad \square A^\mu = \frac{4\pi}{c} J^\mu \begin{cases} -\nabla^2 \mathbf{A} + \frac{1}{c^2} \frac{\partial^2 \mathbf{A}}{\partial t^2} = \frac{4\pi}{c} \mathbf{j} \\ -\nabla^2 \varphi + \frac{1}{c^2} \frac{\partial^2 \varphi}{\partial t^2} = 4\pi\rho \end{cases} \quad (\text{A.13})$$

and are written in tensor form through a single equation, that is,

$$\partial_\mu F^{\mu\nu} = \frac{4\pi}{c} J^\nu, \quad F^{\mu\nu} = \begin{pmatrix} 0 & -E_x & -E_y & -E_z \\ E_x & 0 & -B_z & B_y \\ E_y & B_z & 0 & -B_x \\ E_z & -B_y & B_x & 0 \end{pmatrix} \quad (\text{A.14a})$$

where J^ν ($\nu = 0, 1, 2, 3$) are the four components of the four-vector charge density and current density.

For the two homogeneous equations

$$\begin{cases} \nabla \cdot \mathbf{B} = 0 \\ \nabla \times \mathbf{E} = -\frac{1}{c} \frac{\partial \mathbf{B}}{\partial t}, \end{cases}$$

the tensor form is

$$F_{[\mu\nu,\lambda]} = 0, \quad \text{or} \quad \sum_{\mu,\lambda,\rho=0}^3 \epsilon^{\mu\lambda\rho\sigma} \frac{\partial F_{\lambda\rho}}{\partial x^\mu} = 0 \quad (\text{A.14b})$$

where $F_{[\mu\nu,\lambda]} = \partial_\lambda F_{\mu\nu}$ and the parenthesis indicates the sum over all cyclic permutations with sign, $F_{[\mu\nu,\lambda]} = \partial_\lambda F_{\mu\nu} + \partial_\mu F_{\nu\lambda} + \partial_\nu F_{\lambda\mu}$. $\epsilon^{\mu\lambda\rho\sigma}$ is the completely antisymmetric Ricci tensor with $\epsilon^{0123} = 1$.

The expression of the covariant electromagnetic tensor is obtained by $F_{\mu\nu} = \eta_{\mu\lambda} \cdot \eta_{\gamma\nu} F^{\lambda\gamma}$, with $\eta^{\mu\nu}$ matrix of the metric , namely,

$$\eta^{\mu\nu} = \begin{pmatrix} 1 & 0 & 0 & 0 \\ 0 & -1 & 0 & 0 \\ 0 & 0 & -1 & 0 \\ 0 & 0 & 0 & -1 \end{pmatrix}. \quad (\text{A.15})$$

$F_{\mu\nu}$ is obtained from $F^{\mu\nu}$ by changing $\mathbf{E} \rightarrow -\mathbf{E}$ and $\mathbf{B} \rightarrow \mathbf{B}$, i.e., the electric field is described by a polar vector and the magnetic by an axial one.

A.3.3 Gauge Invariance of the Electromagnetism

One important property of the electromagnetic field is the *gauge invariance*. The observable fields \mathbf{E} and \mathbf{B} are invariant if φ and \mathbf{A} change in the following way:

$$A^\mu \rightarrow A'^\mu = A^\mu - \partial^\mu \Lambda \begin{cases} \varphi \rightarrow \varphi' = \varphi - \frac{1}{c} \frac{\partial \Lambda}{\partial t} \\ \mathbf{A} \rightarrow \mathbf{A}' = \mathbf{A} + \nabla \Lambda. \end{cases} \quad (\text{A.16})$$

These transformations are called *gauge transformations*. The scalar function Λ can be a constant (then one has a *global gauge invariance*) or a function that varies from point to point (*local gauge invariance*).

From the relation $\mathbf{B} = \nabla \times \mathbf{A}$, it is evident that the vector potential is defined, leaving its divergence as a free parameter. The choice $\nabla \mathbf{A} = 0$ identifies the class of the so-called *Coulomb gauge*. The choice adopted here, $\nabla \mathbf{A} + \frac{1}{c} \frac{\partial \varphi}{\partial t} = 0$, is called the *Lorentz gauge*. One has $\nabla \mathbf{A}' + \frac{1}{c} \frac{\partial \varphi'}{\partial t} = 0$ if we request that the scalar function Λ satisfies $\square \Lambda = 0$.

The electromagnetic field can be described by the four-vector potential $A^\mu(x^\mu)$ that obeys (A.13), which can be written in the form

$$\square A^\mu(x^\mu) = \frac{4\pi}{c} J^\mu(x^\mu).$$

In vacuum, without sources, one has

$$\square A^\mu = 0 \Rightarrow \frac{1}{c^2} \frac{\partial^2 \mathbf{A}}{\partial t^2} - \nabla^2 \mathbf{A} = 0,$$

and the solution is

$$A^\mu = e^\mu e^{iq \cdot x} \Rightarrow \vec{A} = \hat{\mathbf{e}} A_0 \exp[-i(\mathbf{K} \cdot \mathbf{r} - \omega t)]$$

where A_0 represents the amplitude, $\omega = 2\pi\nu$ is the pulsation, \mathbf{K} is the wave-vector which represents the direction of wave propagation, and $\hat{\mathbf{e}}$ represents the polarization vector which indicates the direction along which the field \mathbf{E} oscillates.

A.4 Dirac Equation and Formalism

A.4.1 Derivation of the Dirac Equation

The Klein–Gordon equation (4.12) contains second derivatives with respect to time and space coordinates; it is adequate for particles of integer spin (such as the photon, in the limit $m = 0$). Dirac proposed an equation that would satisfy the energy-momentum relativistic relation ($E^2 = p^2 + m^2$), but containing only first order space-time derivative. It is considered to be an equation of the type $E\psi = i\hbar\frac{\partial}{\partial t}\psi = H\psi$. The simplest linear operator for the Hamiltonian H is (here, we always use the units $c = 1$)

$$H = \boldsymbol{\alpha} \cdot \mathbf{p} + \beta m \quad (\text{A.17})$$

where $\boldsymbol{\alpha} = (\alpha_1, \alpha_2, \alpha_3)$ is a vector quantity and β a scalar one; they are defined so that $H^2 = p^2 + m^2$. This is verified if

$$\alpha_i^2 = 1; \quad \beta^2 = 1; \quad (\alpha_i \alpha_j + \alpha_j \alpha_i) = 0; \quad (\alpha_i \beta + \beta \alpha_i) = 0. \quad (\text{A.18})$$

Since the quantities α_i and β anticommute between them, they cannot be simple numbers, but must be matrices of size at least 4×4 . As a consequence, the function ψ is a column vector with four components (spinor). The explicit form of $\boldsymbol{\alpha}$ and β is not unique and we follow the representation of Dirac–Pauli:

$$\boldsymbol{\alpha} = \begin{pmatrix} 0 & \boldsymbol{\sigma} \\ \boldsymbol{\sigma} & 0 \end{pmatrix}; \quad \beta = \begin{pmatrix} \mathbf{1} & 0 \\ 0 & -\mathbf{1} \end{pmatrix} \quad (\text{A.19})$$

where $\boldsymbol{\sigma}$ are the 2×2 Pauli matrices:

$$\sigma_1 = \sigma_x = \begin{pmatrix} 0 & 1 \\ 1 & 0 \end{pmatrix}, \quad \sigma_2 = \sigma_y = \begin{pmatrix} 0 & -i \\ i & 0 \end{pmatrix}, \quad \sigma_3 = \sigma_z = \begin{pmatrix} 1 & 0 \\ 0 & -1 \end{pmatrix} \quad (\text{A.20})$$

and $\mathbf{1}$ is the 2×2 identity matrix.

The Dirac equation can be as well represented with the matrices α_i and β , with the matrices γ^μ defined as

$$\boldsymbol{\gamma} = \beta \boldsymbol{\alpha}; \quad \gamma^i = \beta \alpha_i \quad (i = 1, 2, 3); \quad \gamma^0 = \beta. \quad (\text{A.21})$$

In this way, it is easy to show (Problem 4.9) that the eigenvalue equation $E\psi = i\hbar\frac{\partial}{\partial t}\psi = H\psi$ can be written as

$$i\hbar\gamma^0\frac{\partial}{\partial t}\psi + i\hbar\boldsymbol{\gamma}\cdot\boldsymbol{\nabla}\psi - m\psi = 0. \quad (\text{A.22})$$

If we use the four-vector notation,

$$\left(\frac{\partial}{\partial t}, \boldsymbol{\nabla}\right) \equiv \left(\frac{\partial}{\partial x_o}, \frac{\partial}{\partial x_i}\right) \equiv \frac{\partial}{\partial x_\mu} \equiv \partial_\mu, \quad (\text{A.23})$$

the (A.22) can be written in a compact form as

$$i \sum_\mu \gamma^\mu \frac{\partial}{\partial x_\mu} \psi - m\psi = 0; \quad \mu = 0, \dots, 3. \quad (\text{A.24a})$$

If the sign of summation over μ is implied, the most compact form is

$$(i\gamma^\mu \partial_\mu - m)\psi = 0. \quad (\text{A.24b})$$

From (A.21), it follows that $(\gamma^0)^2 = 1$, $(\gamma^i)^2 = -1$, $\gamma^\mu \gamma^\nu = -\gamma^\nu \gamma^\mu$ and the γ^μ matrices can be expressed as

$$\gamma^k = \begin{pmatrix} 0 & \sigma_k \\ -\sigma_k & 0 \end{pmatrix} \text{ with } k = 1, 2, 3; \quad \gamma^0 = \gamma_0 = \begin{pmatrix} \mathbf{1} & 0 \\ 0 & -\mathbf{1} \end{pmatrix}; \quad \gamma^5 = \begin{pmatrix} 0 & \mathbf{1} \\ \mathbf{1} & 0 \end{pmatrix} \quad (\text{A.25a})$$

or explicitly, as

$$\gamma^0 = \begin{pmatrix} 1 & 0 & 0 & 0 \\ 0 & 1 & 0 & 0 \\ 0 & 0 & -1 & 0 \\ 0 & 0 & 0 & -1 \end{pmatrix}, \quad \gamma^1 = \begin{pmatrix} 0 & 0 & 0 & 1 \\ 0 & 0 & 1 & 0 \\ 0 & -1 & 0 & 0 \\ -1 & 0 & 0 & 0 \end{pmatrix}, \quad \gamma^2 = \begin{pmatrix} 0 & 0 & 0 & -i \\ 0 & 0 & +i & 0 \\ 0 & +i & 0 & 0 \\ -i & 0 & 0 & 0 \end{pmatrix},$$

$$\gamma^3 = \begin{pmatrix} 0 & 0 & 1 & 0 \\ 0 & 0 & 0 & -1 \\ -1 & 0 & 0 & 0 \\ 0 & 1 & 0 & 0 \end{pmatrix}. \quad (\text{A.25b})$$

In addition, the γ^5 matrix is defined as

$$\gamma^5 = \gamma_5 = i\gamma^0\gamma^1\gamma^2\gamma^3 = \begin{pmatrix} 0 & 0 & 1 & 0 \\ 0 & 0 & 0 & 1 \\ 1 & 0 & 0 & 0 \\ 0 & 1 & 0 & 0 \end{pmatrix} \text{ with } \gamma_5^2 = 1; \quad \gamma^5\gamma^\mu + \gamma^\mu\gamma^5 = 0. \quad (\text{A.25c})$$

A.4.2 General Properties of the Dirac Equation

Before discussing solutions, some important properties of the Dirac equation are shown.

Invariance property. The Dirac Hamiltonian H (A.17) commutes with the *angular momentum operator* \mathbf{J} : $[H, \mathbf{J}] = 0$ (Problem 4.10), where

$$\mathbf{J} = \hbar \mathbf{l} + \frac{1}{2} \hbar \boldsymbol{\sigma}. \quad (\text{A.26})$$

H also commutes with the pseudoscalar *generalized helicity operator* Λ :

$$\Lambda = \begin{pmatrix} \frac{\boldsymbol{\sigma} \cdot \mathbf{p}}{p} & 0 \\ 0 & \frac{\boldsymbol{\sigma} \cdot \mathbf{p}}{p} \end{pmatrix} \quad (\text{A.27})$$

so that $[H, \Lambda] = 0$ (see Problem 4.11). The helicity operator also commutes with the momentum $[\Lambda, \mathbf{p}] = 0$. The Dirac Hamiltonian can inherently describe the motion of particles with half-integer spin with spin oriented along the direction of motion, as discussed in detail in Sect. A.4.4.

Adjoint equation. Let us separate the (A.24) in the space-like and time-like part:

$$i \gamma^0 \frac{\partial}{\partial t} \psi + i \gamma^k \frac{\partial}{\partial x_k} \psi - m \psi = 0 \quad (\text{A.28})$$

with $k = 1, 2, 3$. We define the adjoint spinor as:

$$\overline{\psi} \equiv \psi^\dagger \gamma^0 = \psi^{T^*} \gamma^0. \quad (\text{A.29})$$

It can be verified that the Hermitian conjugate of (A.28) can be written as

$$i \frac{\partial}{\partial t} \overline{\psi} \gamma^0 + i \frac{\partial}{\partial x_k} \overline{\psi} \gamma^k + m \overline{\psi} = 0 \quad (\text{A.30})$$

which is defined as the *adjoint Dirac equation*. By multiplying (A.28) to the left by $\overline{\psi}$ and (A.28) to the right by ψ and summing, one obtains

$$\frac{\partial}{\partial t} (\overline{\psi} \gamma^0 \psi) + \frac{\partial}{\partial x_k} (\overline{\psi} \gamma^k \psi) \equiv \frac{\partial}{\partial x_\mu} (\overline{\psi} \gamma^\mu \psi) = 0, \quad (\text{A.31})$$

representing the continuity equation similar to that adopted in the case of the Schrödinger equation in Chap. 4 (4.10) if we define

$$J^\mu \equiv (\overline{\psi} \gamma^\mu \psi). \quad (\text{A.32})$$

The adjoint function has the remarkable property of allowing for the construction of relativistically invariant quantities, for example, (A.32).

The Lagrangian density for a Dirac field. The Lagrangian L of a system is a function that summarizes the dynamics of the system. If the Lagrangian is known, then the equations of motion can be derived. The time integral of the Lagrangian is called *action*, and is denoted by S .

In field theory, the Lagrangian density \mathcal{L} is defined as the quantity which must be integrated over all space-time to get the action $S = \int \mathcal{L} d^4x$. The Lagrangian is then the spatial integral of the Lagrangian density. The Dirac equation is the *equation of motion* for a suitable Lagrangian density obtained from variational calculus (see Problem 11.1). The Lorentz-invariant Lagrangian density with (A.24b) as solution is simply

$$\bar{\psi}(i\gamma^\mu \partial_\mu - m)\psi = 0. \quad (\text{A.33})$$

The modern point of view is to start with a Lagrangian (or the action) as the fundamental quantity from which field equations are derived (as we did in Chap. 11 for the Lagrangian density of the electroweak theory).

Relativistically invariant quantities. A Lorentz transformation between two inertial reference systems along the x axis with relative velocity $\beta = v/c$ can be expressed in the following form:

$$x'_\mu = \sum_v a_{\mu v}(\beta) x_v; \quad a_{\mu v} = \begin{pmatrix} (1-\beta^2)^{-1/2} & -\beta(1-\beta^2)^{-1/2} & 0 & 0 \\ \beta(1-\beta^2)^{-1/2} & (1-\beta^2)^{-1/2} & 0 & 0 \\ 0 & 0 & 1 & 0 \\ 0 & 0 & 0 & 1 \end{pmatrix}. \quad (\text{A.34})$$

There is Lorentz-invariance of the Dirac equation if there exists a function $\psi'(x'_\mu)$ which satisfies equation A.24 in the new coordinates x'_μ :

$$i \sum_\mu \gamma^\mu \frac{\partial}{\partial x'_\mu} \psi' - m \psi' = 0; \quad \mu = 0, \dots, 3. \quad (\text{A.35})$$

It can be shown that this function exists and can be represented as

$$\psi' = S\psi; \quad \text{with } S^{-1} \gamma^\mu S = \sum_v a_{\mu v} \gamma^v. \quad (\text{A.36})$$

S is an operator that only acts on the spinor of ψ .

By combining the matrices γ with the wave function ψ and its adjoint, five objects mutually independent and relativistically invariant can be built. These are shown in table Sect. 8.16.1, in column “currents.” See Problem 8.15.

Reversal of space coordinates and parity P. We have seen in Sect. 6.4 that the operation of inversion of space coordinates is generated by the operator P called

parity. Let us apply the reversal of space coordinates $\mathbf{r} \rightarrow -\mathbf{r}$ to the Dirac equation (A.28):

$$\left(i\gamma^0 \frac{\partial}{\partial t} - i\gamma^k \frac{\partial}{\partial x_k} - m \right) \psi(-\mathbf{r}, t) = 0. \quad (\text{A.37})$$

$\psi(-\mathbf{r}, t)$ is a wave function with the space coordinates reversed, and is **not** a solution of the Dirac equation (note the sign of the discrepancy between the space and time components of (A.28) and (A.37)). One should therefore seek a wave function with the space coordinates reversed that is: (1) the solution of the Dirac equation, and (2) Lorentz-invariant. To this purpose, let us multiply the (A.37) to the left with γ^0 and use the property $\gamma^0\gamma^k = -\gamma^k\gamma^0$:

$$\left(i\gamma^0 \frac{\partial}{\partial t} + i\gamma^k \frac{\partial}{\partial x_k} - m \right) \gamma^0 \psi(-\mathbf{r}, t) = 0. \quad (\text{A.38})$$

By comparison of (A.28) and (A.38), we have

$$\gamma^0 \psi(-\mathbf{r}, t) \equiv \psi(\mathbf{r}, t); \quad \gamma^0 \psi(\mathbf{r}, t) \equiv \psi(-\mathbf{r}, t). \quad (\text{A.39})$$

This equation shows that the operator γ^0 represents the parity operator (which reverses the space coordinates) for the wave function solutions of the Dirac equation.

Time reversal operator T. Similar to the parity operator, it can be shown that under reversal of time coordinate (Sect. 6.7), the equation $\psi(\mathbf{r}, -t)$ does not satisfy the Dirac equation, while

$$\gamma^3 \gamma^1 \psi^*(\mathbf{r}, -t) = \psi(\mathbf{r}, t); \quad \gamma^1 \gamma^3 \mathcal{K} \psi(\mathbf{r}, t) = \psi(\mathbf{r}, -t) \quad (\text{A.40})$$

does. \mathcal{K} is the operator of complex conjugation: $\mathcal{K}\psi \equiv \psi^*$. As a consequence,

$$\gamma^1 \gamma^3 \mathcal{K} \quad (\text{A.41})$$

represents the operator which reverses the time for the wave function solutions of the Dirac equation.

Charge conjugation and parity operator CP. Less straightforward, is the proof (see, for example, [Be08]) that the operator

$$i\gamma^2 \mathcal{K} \quad (\text{A.42})$$

represents the operator which transforms the spinor $\psi(\mathbf{r}, t)$ into the spinor with opposite energy, momentum and spin, that is,

$$(i\gamma^2 \mathcal{K}) \psi_+ = \psi_-(-\mathbf{p}). \quad (\text{A.43})$$

Recalling the definition of charge conjugation and parity operator CP (Sect. 6.8), if $\psi(\mathbf{r}, t)$ represents the particle state, $i\gamma^2 \mathcal{K} \psi$ is the corresponding antiparticle state. Then, the operator turns, for example, the neutrino state (= spinor with positive energy) with negative helicity, into an antineutrino state (= spinor with negative energy) with positive helicity, see Fig. 6.3.

A.4.3 Properties of the Dirac Equation Solutions

The Dirac equation is a set of four equations, each of which must have a solution. These solutions are normally written in the following form:

$$\psi = ue^{i(\mathbf{p}\cdot\mathbf{r}-Et)} = ue^{-ip_\mu x^\mu} \quad (\text{A.44})$$

where the space-time dependence $e^{i(\mathbf{p}\cdot\mathbf{r}-Et)} \equiv e^{-ip_\mu x^\mu}$ is separated from that depending on the spin u . The four component spinors u are constants and correspond to 4×1 matrices. There is a very useful representation, namely,

$$\psi = \begin{pmatrix} \phi \\ \chi \end{pmatrix} e^{i(\mathbf{p}\cdot\mathbf{r}-Et)} \quad (\text{A.45})$$

where ϕ and χ are two component spinors. As an exercise (Problem 4.12), we demonstrate that inserting (A.45) in the Dirac equation results in

$$\phi = \frac{\boldsymbol{\sigma} \cdot \mathbf{p}}{E - m} \chi \quad (\text{A.46a})$$

$$\chi = \frac{\boldsymbol{\sigma} \cdot \mathbf{p}}{E + m} \phi, \quad (\text{A.46b})$$

forming a homogeneous system which admits solution only if $E^2 - p^2 - m^2 = 0$. We obtain again a quadratic relation, similar to that already obtained with the Klein–Gordon equation whose solutions are

$$E = \pm \sqrt{p^2 + m^2}, \quad (\text{A.47})$$

including solutions with negative energy. Dirac suggested that all states with negative energy are fully occupied. The creation of a e^+e^- pair is explained as the transition (induced by a photon with energy $E_\gamma > 2m_e c^2$) of an electron in a negative energy state into a positive energy state. The lack of an electron (a *hole*) in this *sea* of particles with negative energy represents a positron.

An additional difficulty arises from the consideration that if all the negative energy states are filled, the energy of the vacuum state is $-\infty$. Dirac solved this issue, assuming that measurable quantities correspond to a variation with respect to the vacuum state, in analogy with the classical potential energy. As the measured

values are deviations from the vacuum state, the Dirac theory cannot predict mass and electric charge of particles. This aspect (*renormalization*) is common to all field theories.

The homogeneous system (A.46) has two dependent variables (χ, ϕ) which are crossed in the equations and give rise to four solutions (taking into account the sign of energy). The $2 + 2$ solutions are

$$\text{for } E = |E| : \quad \phi = \frac{\sigma \cdot \mathbf{p}}{|E| - m} \chi; \quad \chi = \frac{\sigma \cdot \mathbf{p}}{|E| + m} \phi; \quad (\text{A.48a})$$

$$\text{for } E = -|E| : \quad \phi = -\frac{\sigma \cdot \mathbf{p}}{|E| + m} \chi; \quad \chi = \frac{\sigma \cdot \mathbf{p}}{m - |E|} \phi. \quad (\text{A.48b})$$

The choice of the independent spinor (ϕ or χ) is guided by physics considerations.

Nonrelativistic limit. Let consider the nonrelativistic limit where $\mathbf{p} \rightarrow 0$ and $E \rightarrow m + p^2/2m$. Then,

$$\frac{p}{|E| - m} \rightarrow \frac{p}{p^2/2m} \rightarrow \infty, \quad \frac{p}{|E| + m} \rightarrow 0. \quad (\text{A.49})$$

In this case, the (A.48) become

$$\text{for } E > 0 : \quad \chi \rightarrow 0; \quad |\phi| \gg |\chi| \quad (\text{A.50a})$$

$$\text{for } E < 0 : \quad \phi \rightarrow 0; \quad |\chi| \gg |\phi|. \quad (\text{A.50b})$$

Since two solutions vanish, we consider the two remaining as arbitrary functions. To represent them, as the Dirac equation describes spin 1/2 particles, for ϕ, χ , we choose the eigenstates of the operator σ_3 (the projection of the third component of the spin operator), that is,

$$\sigma_3 \phi = \pm \phi; \quad \sigma_3 \chi = \pm \chi. \quad (\text{A.51})$$

It is straightforward to verify that the eigenstates can be written as

$$\begin{aligned} \phi_R &= \begin{pmatrix} 1 \\ 0 \end{pmatrix}; \quad \phi_L = \begin{pmatrix} 0 \\ 1 \end{pmatrix} \\ \chi_R &= \begin{pmatrix} 1 \\ 0 \end{pmatrix}; \quad \chi_L = \begin{pmatrix} 0 \\ 1 \end{pmatrix} \end{aligned} \quad (\text{A.52})$$

where the indices L and R will be clarified in the following. With this choice, the four solutions of the Dirac equation are

$$\text{for } E = |E| : \quad \psi_+ \equiv N u_+ e^{i(\mathbf{p} \cdot \mathbf{r} - Et)} = N \left(\begin{pmatrix} \phi \\ \frac{\sigma \cdot \mathbf{p}}{|E| + m} \phi \end{pmatrix} \right) e^{i(\mathbf{p} \cdot \mathbf{r} - |E|t)} \quad (\text{A.53a})$$

$$\text{for } E = -|E| : \quad \psi_- \equiv N u_- e^{i(\mathbf{p} \cdot \mathbf{r} - Et)} = N \begin{pmatrix} -\frac{\sigma \cdot \mathbf{p}}{|E|+m} \chi \\ \chi \end{pmatrix} e^{i(\mathbf{p} \cdot \mathbf{r} + |E|t)} \quad (\text{A.53b})$$

where $N = \sqrt{\frac{m+|E|}{2|E|}}$ is a normalization factor derived from the condition $\psi^\dagger \psi = 1$. It is easy to show that the four solutions (A.53) are mutually orthogonal. The meaning of the four component spinors u_+, u_- is evident in the limit $p \rightarrow 0$:

$$u_+ = \begin{pmatrix} \phi \\ 0 \end{pmatrix}; \quad u_- = \begin{pmatrix} 0 \\ \chi \end{pmatrix}. \quad (\text{A.54})$$

Since ϕ, χ are eigenstates of σ_3 , we interpret u_+, u_- as eigenstates of the spin operator, which in a generalized form is

$$\tilde{\sigma}_3 = \begin{pmatrix} \sigma_3 & 0 \\ 0 & \sigma_3 \end{pmatrix}. \quad (\text{A.55})$$

Relativistic limit. The relativistic limit is represented by the condition $m \rightarrow 0$; $|E| \rightarrow p$. It is easy to show that the spinors u of (A.53) become

$$u_+ = \begin{pmatrix} \phi \\ \chi \end{pmatrix} = \begin{pmatrix} \phi \\ \frac{\sigma \cdot \mathbf{p}}{p} \phi \end{pmatrix} \quad (\text{A.56a})$$

$$u_- = \begin{pmatrix} \phi \\ \chi \end{pmatrix} = \begin{pmatrix} -\frac{\sigma \cdot \mathbf{p}}{p} \chi \\ \chi \end{pmatrix}. \quad (\text{A.56b})$$

The function ϕ in the lower part of the four-dimensional spinor u_+ is the eigenstate of the helicity operator $\frac{\sigma \cdot \mathbf{p}}{p}$. Indeed, taking the z axis coincident with the direction of the momentum $\mathbf{p} = (0, 0, p_3)$, we have

$$\frac{\sigma \cdot \mathbf{p}}{p} \phi = \sigma_3 \phi = \pm \phi, \quad (\text{A.57})$$

depending on $\phi = \begin{pmatrix} 1 \\ 0 \end{pmatrix} \equiv \phi_R$, or $\phi = \begin{pmatrix} 0 \\ 1 \end{pmatrix} \equiv \phi_L$. Similarly, χ in the upper spinor component u_- represents the helicity eigenstate, though with reversed signs of the eigenvalues, namely,

$$-\frac{\sigma \cdot \mathbf{p}}{p} \chi \equiv -\sigma_3 \chi = \pm \chi. \quad (\text{A.58})$$

With the choices we made, the two upper and lower components of the four-dimensional spinor u_+ (u_-) are respectively associated with the eigenstates of the spin and helicity operators (helicity and spin). Below, to highlight the different orientation of the spins, we will use the notations u_{+r}, u_{-r}, u_{+l} and u_{-l} .

A.4.4 Helicity Operator and States

The two pairs of Dirac equation solutions (A.48) are functions of the momentum \mathbf{p} and correspond to both positive and negative energy eigenvalues. Their eigenstates are the two component spinors (A.48). Because the four solutions are independent (as seen in Sect. A.4.2), another independent observable that commutes with the Hamiltonian exists. This is the *generalized helicity*² operator:

$$\Lambda = \begin{pmatrix} \frac{\sigma \cdot \mathbf{p}}{p} & 0 \\ 0 & \frac{\sigma \cdot \mathbf{p}}{p} \end{pmatrix}. \quad (\text{A.59})$$

The operator Λ commutes with \mathbf{p} and the Hamiltonian: $[\Lambda, \mathbf{p}] = 0$, $[\Lambda, H] = 0$, and therefore it represents a constant of motion (Sect. 6.3). The helicity operator has two eigenvalues, $\lambda = \pm 1$, which distinguish eigenstates with the same energy eigenvalue.

Relativistic case (particle with null mass). Let us now verify the effect of the generalized helicity (A.59) on the helicity eigenstates (A.57) of the spinor u_+ (A.56a). This corresponds to the relativistic limit where the mass of the particle is negligible. In particular, if we consider the momentum oriented along the z -axis, one has $\mathbf{p} = (0, 0, p_3)$, and

$$\Lambda u_+ = \begin{pmatrix} 1 & 0 & 0 & 0 \\ 0 & -1 & 0 & 0 \\ 0 & 0 & 1 & 0 \\ 1 & 0 & 0 & -1 \end{pmatrix} \begin{pmatrix} 1 \\ 0 \\ \frac{p_3}{|E|+m} \\ 0 \end{pmatrix} = + \begin{pmatrix} 1 \\ 0 \\ \frac{p_3}{|E|+m} \\ 0 \end{pmatrix} = u_+. \quad (\text{A.60})$$

In practice, the spinor u_+ (solution with positive energy) with the spin along the direction of the momentum is the eigenstate of the operator Λ with eigenvalue $\lambda = +1$. We call this state $(u_+)_{\lambda=+1} \equiv u_{+r}$. Similarly, the other three states will be u_{+l}, u_{-r}, u_{-l} .

With this momentum orientation, it is easy to verify that the operator (A.59) can be expressed as $\Lambda = \Lambda_R + \Lambda_L$, where

$$\Lambda_R \equiv \frac{1 + \gamma^5}{2} = \frac{1}{2} \begin{pmatrix} \mathbf{1} & \mathbf{1} \\ \mathbf{1} & \mathbf{1} \end{pmatrix} \quad (\text{A.61})$$

$$\Lambda_L \equiv \frac{1 - \gamma^5}{2} = \frac{1}{2} \begin{pmatrix} \mathbf{1} & -\mathbf{1} \\ -\mathbf{1} & \mathbf{1} \end{pmatrix}. \quad (\text{A.62})$$

²Note that the polarization and the helicity operators $\frac{\sigma \cdot \mathbf{p}}{p}$ are defined on two-component spinors (separately describing the fermions and antifermions). Sometimes, the generalized helicity operator is called *chirality*. The chirality is an operator acting on a four-component spinor.

The matrix array γ^5 is defined in (A.25c). The operators defined above are Hermitian and have the properties of projection, that is, $\Lambda_R + \Lambda_L = 1$, $\Lambda_R \Lambda_L = \Lambda_L \Lambda_R = 0$, $\Lambda_R \Lambda_R = \Lambda_R$, $\Lambda_L \Lambda_L = \Lambda_L$. Applying the projectors to the eigenstates u_+ and u_- (A.56), it is easy to verify that

$$\Lambda_L u_{+r} = 0; \quad \Lambda_R u_{+r} = \begin{pmatrix} 1 \\ 1 \end{pmatrix} \phi_R \quad (\text{A.63a})$$

$$\Lambda_L u_{+l} = \begin{pmatrix} 1 \\ -1 \end{pmatrix} \phi_L; \quad \Lambda_R u_{+l} = 0. \quad (\text{A.63b})$$

Depending on the fact that the four-components spinor u has spin parallel or antiparallel to the momentum³, one has

$$u_{+r} = \Lambda_R u_{+r} \quad (\text{A.64a})$$

$$u_{+l} = \Lambda_L u_{+l}. \quad (\text{A.64b})$$

Λ_L is the projection operator of the negative helicity state (or *Left-handed*, L) and the operator Λ_R is the projection operator of the positive helicity state (or *Right-handed*, R). Taking into account (A.57, A.58), where the particle mass is $m = 0$, the spinor u is intrinsically the eigenstate of helicity $+1$ or of helicity -1 . This is not true in the case of massive particles.

The projection operators applied to the spinor of negative energy produce similar effects to (A.63). For $|E| < 0$, the operator Λ_L extracts from u_- the state of positive helicity (right-handed) and Λ_R the state of negative helicity (left-handed).

Remember that the matrix γ^0 is the parity operator for a Dirac spinor: u changes its helicity state under the application of this operator:

$$\gamma^0 u = \begin{pmatrix} 1 & 0 \\ 0 & -1 \end{pmatrix} \begin{pmatrix} \phi \\ \chi \end{pmatrix} = \begin{pmatrix} \phi \\ -\chi \end{pmatrix}. \quad (\text{A.65})$$

Particle with mass. Let us assume once again that the momentum \mathbf{p} of the particle is along the z axis and initially consider positive energy solutions (A.48). In this case, one can show that

$$\sigma \cdot \mathbf{p} \phi_R = p \phi_R; \quad \sigma \cdot \mathbf{p} \phi_L = -p \phi_L, \quad (\text{A.66})$$

³Sometimes, the states with *up* and *down* spins are indicated as spin \uparrow or spin \downarrow .

and it can be verified that

$$\Lambda_L u_{+l} = \frac{1}{2} \left(1 + \frac{p}{|E| + m} \right) \begin{pmatrix} 1 \\ -1 \end{pmatrix} \phi_L \quad (\text{A.67a})$$

$$\Lambda_R u_{+l} = \frac{1}{2} \left(1 - \frac{p}{|E| + m} \right) \begin{pmatrix} 1 \\ 1 \end{pmatrix} \phi_L. \quad (\text{A.67b})$$

Being both projections that are not null, $u_{+l} = \Lambda_L u_{+l} + \Lambda_R u_{+l}$ appears to be composed of a superposition of positive and negative helicity states, with different weights. If we define the probability of finding the lepton described by the spinor u_{+l} in the left and right-handed helicity state with (respectively) the relative weights P_l and P_r , that is,

$$P_l \equiv |\Lambda_L u_{+l}|^2 = \frac{1}{2} \left(\frac{|E| + m + p}{|E| + m} \right)^2 \quad (\text{A.68a})$$

$$P_r \equiv |\Lambda_R u_{+l}|^2 = \frac{1}{2} \left(\frac{|E| + m - p}{|E| + m} \right)^2, \quad (\text{A.68b})$$

the average helicity of the state can be defined as

$$\langle h \rangle \equiv \frac{P_r - P_l}{P_r + P_l}. \quad (\text{A.69})$$

Introducing the (A.68) into (A.69), we obtain that the average helicity for a fermion (= spinor with positive energy) with left-handed helicity is

$$\langle h \rangle = -\frac{p}{|E|} = -\frac{v}{c} = -\beta. \quad (\text{A.70})$$

Using similar calculations, it can be verified that the other spinors are a superposition of positive and negative helicity states. The corresponding average helicity values are reported here below.

	Particle		Antiparticle	
	u_{+l}	u_{+r}	u_{-r}	u_{+l}
h ($m = 0$)	-1	+1	+1	-1
$\langle h \rangle$ ($m \neq 0$)	$-\beta$	$+\beta$	$+\beta$	$-\beta$

As discussed in Sect. 8.16, the experiments agree with the fact that neutrinos (antineutrinos) (case $m = 0$) have helicity -1 ($+1$), while the electron (positron) has helicity $-\beta$ ($+\beta$). The Hamiltonian describing the interaction must take into account the suppression of the unobserved states, as it was done in the $V - A$ theory.

A.5 Physical and Astrophysical Constants [P08]

1. PHYSICAL CONSTANTS

Table 1.1. Reviewed 2007 by P.J. Mohr and B.N. Taylor (NIST). Based mainly on the “CODATA Recommended Values of the Fundamental Physical Constants: 2006” by P.J. Mohr, B.N. Taylor, and D.B. Newell (to be published in Rev. Mod. Phys. and J. Phys. Chem. Ref. Data). The last group of constants (beginning with the Fermi coupling constant) comes from the Particle Data Group. The figures in parentheses after the values give the 1-standard-deviation uncertainties in the last digits; the corresponding fractional uncertainties in parts per 10^9 (ppb) are given in the last column. This set of constants (aside from the last group) is recommended for international use by CODATA (the Committee on Data for Science and Technology). The full 2006 CODATA set of constants may be found at <http://physics.nist.gov/constants>.

Quantity	Symbol, equation	Value	Uncertainty (ppb)
speed of light in vacuum	c	299 792 458 m s ⁻¹	exact*
Planck constant	\hbar	6.626 068 96(33) × 10 ⁻³⁴ J s	50
Planck constant, reduced	$\hbar \equiv \hbar/2\pi$	1.054 571 628(53) × 10 ⁻³⁴ J s – 6.682 118 98(16) × 10 ⁻²² MeV s	50 25
electron charge magnitude	e	1.602 176 487(40) × 10 ⁻¹⁹ C = 4.803 204 27(12) × 10 ⁻¹⁰ esu	25, 25
conversion constant	$\hbar c$	197.326 9631(49) MeV fm	25
conversion constant	$(\hbar c)^2$	0.389 379 304(19) GeV ² mbarn	50
electron mass	m_e	0.510 998 910(13) MeV/c ² = 9.109 382 15(45) × 10 ⁻³¹ kg	25, 50
proton mass	m_p	938.272 013(23) MeV/c ² = 1.672 621 637(83) × 10 ⁻²⁷ kg – 1.607 276 466 77(10) u = 1836.152 672 47(80) m_e	25, 50 0.10, 0.43
deuteron mass	m_d	1875.612 793(47) MeV/c ²	25
unified atomic mass unit (u)	(mass ¹² C atom)/12 = (1 g)/(N _A mol)	931.494 028(23) MeV/c ² = 1.660 538 782(83) × 10 ⁻²⁷ kg	25, 50
permittivity of free space	$\epsilon_0 = 1/\mu_0 c^2$	8.854 187 817 ... × 10 ⁻¹² F m ⁻¹	exact
permability of free space	μ_0	4π × 10 ⁻⁷ N A ⁻² = 12.566 370 614 ... × 10 ⁻⁷ N A ⁻²	exact
fine-structure constant	$\alpha = e^2/4\pi\epsilon_0\hbar c$	7.297 332 5376(50) × 10 ⁻³ = 1/137.035 999 679(94) [†]	0.68, 0.68
classical electron radius (e^- Compton wavelength)/2π	$r_e = e^2/4\pi\epsilon_0 m_ec^2$	2.817 940 2894(68) × 10 ⁻¹⁸ m	2.1
Bolz radius ($m_{\text{min}} \rightarrow \infty$)	$\tilde{r}_e = \hbar/m_ec = r_e\alpha^{-1}$	3.861 592 6459(53) × 10 ⁻¹³ m	1.4
wavelength of 1 eV/c particle	$a_{ee} = 4\pi r_0\hbar^2/m_ec^2 = r_e\alpha^{-2}$	0.529 177 208 59(36) × 10 ⁻¹⁰ m	0.68
Rydberg energy	$hcR_\infty = m_ec^4/2(4\pi\epsilon_0)^2\hbar^2 = m_ec^2\alpha^2/2$	1.239 841 875(31) × 10 ⁻⁶ m	25
Thomson cross section	$\sigma_T = 8\pi r_e^2/3$	13.605 691 92(34) eV	25
Bolz magneton	$\mu_B = \hbar/e m_e$	0.665 245 8558(27) barn	4.1
nuclear magneton	$\mu_N = \hbar/2m_p$	5.788 381 7555(79) × 10 ⁻¹¹ MeV T ⁻¹	1.4
electron cyclotron freq./field	$\omega_{cy}^B/B = e/m_e$	3.152 451 2326(45) × 10 ⁻¹⁴ MeV T ⁻¹	1.4
proton cyclotron freq./field	$\omega_p^B/B = e/m_p$	1.758 820 150(44) × 10 ¹¹ rad s ⁻¹ T ⁻¹	25
gravitational constant [‡]	G_N	6.674 28(67) × 10 ⁻¹¹ kg ⁻¹ s ⁻² = 6.708 81(67) × 10 ⁻³⁹ $\hbar c$ (GeV/c ²) ⁻²	1.0 × 10 ⁵ 1.0 × 10 ⁵
standard gravitational accel.	g_N	9.806 65 m s ⁻²	exact
Avogadro constant	N_A	6.022 141 79(30) × 10 ²³ mol ⁻¹	50
Boltzmann constant	k	1.380 650(24) × 10 ⁻²³ J K ⁻¹ = 8.617 343(15) × 10 ⁻⁵ eV K ⁻¹	1700 1700
molar volume, ideal gas at STP	$N_A k(273.15 \text{ K})/(101 325 \text{ Pa})$	22.413 996(39) × 10 ⁻³ m ³ mol ⁻¹	1700
Wien displacement law constant	$b = \lambda_{\text{max}}T$	2.897 7685(51) × 10 ⁻³ m K	1700
Stefan-Boltzmann constant	$\sigma = \pi^2 k^4/60\hbar^3 c^2$	5.670 400(40) × 10 ⁻⁸ W m ⁻² K ⁻⁴	7000
Fermi coupling constant ^{**}	$G_F/(hc)^3$	1.166 37(1) × 10 ⁻⁵ GeV ⁻²	9000
weak-mixing angle	$\sin^2 \theta(W_Z) (\overline{\text{MS}})$	0.231 19(14) ^{††}	6.5 × 10 ⁵
W^\pm boson mass	m_W	80.398(25) GeV/c ²	3.6 × 10 ⁵
Z^0 boson mass	m_Z	91.1876(21) GeV/c ²	2.3 × 10 ⁴
strong coupling constant	$\alpha_s(m_Z)$	0.1176(20)	1.7 × 10 ⁷
$\pi = 3.141 592 653 589 793 238$	$e = 2.718 281 828 459 045 235$	$\gamma = 0.577 215 664 901 532 861$	
1 in ≡ 0.0254 m	1 G ≡ 10 ⁻⁴ T	1 eV = 1.602 176 487(40) × 10 ⁻¹⁹ J	$kT \text{ at } 300 \text{ K} = [38.681 685(68)]^{-1}$ eV
1 A = 0.1 mm	1 dyne = 10 ⁻⁵ N	1 eV/c ² = 1.782 661 758(44) × 10 ⁻³⁶ kg	0 °C = 273.15 K
1 barn ≡ 10 ⁻²⁸ m ²	1 erg ≡ 10 ⁻⁷ J	2.997 924 58 × 10 ³ esu = 1 C	1 atmosphere ≡ 760 Torr ≡ 101 325 Pa

* The meter is the length of the path travelled by light in vacuum during a time interval of 1/299 792 458 of a second.

† At $Q^2 = 0$. At $Q^2 \approx m_W^2$, the value is $\sim 1/128$.

‡ Absolute lab measurements of G_N have been made only on scales of about 1 cm to 1 m.

** See the discussion in Sec. 10. ^{††}Electroweak model and constraints on new physics.[†]

†† The corresponding $\sin^2 \theta$ for the effective angle is 0.23149(13).

2. ASTROPHYSICAL CONSTANTS AND PARAMETERS

Table 2.1. Revised May 2008 by E. Bergner and D.E. Groom (LBNL). The figures in parentheses after some values give the one standard deviation uncertainties in the last digit(s). Physical constants are from Ref. 1. While every effort has been made to obtain the most accurate current values of the listed quantities, the table does not represent a critical review or adjustment of the constants, and is not intended as a primary reference. The values and uncertainties for the cosmological parameters depend on the exact data sets, priors, and basis parameters used in the fit. Many of the parameters reported in this table are derived parameters or have non-Gaussian likelihoods. The quoted errors may be highly correlated with those of other parameters, so care must be taken in propagating them. Unless otherwise specified, cosmological parameters are best fits of a spatially-flat Λ CDM cosmology with a power-law initial spectrum to WMAP 3-year data alone [2]. For more information see Ref. 3 and the original papers.

Quantity	Symbol, equation	Value	Reference, footnote
speed of light	c	$299\,792\,158 \text{ m s}^{-1}$	exact 4
Newtonian gravitational constant	G_N	$6.6743(7) \times 10^{-11} \text{ m}^3 \text{ kg}^{-1} \text{ s}^{-2}$	[1]
Planck mass	$\sqrt{\hbar G_N/c^3}$	$1.220\,89(6) \times 10^{19} \text{ GeV}/c^2$ $= 2.176\,44(11) \times 10^{-8} \text{ kg}$	[1]
Planck length	$\sqrt{\hbar G_N/c^3}$	$1.616\,24(8) \times 10^{-35} \text{ m}$	[1]
standard gravitational acceleration	g_N	$9.806\,65 \text{ m s}^{-2}$	exact 1 ^a
jansky (flux density)	Jy	$10^{-26} \text{ W m}^{-2} \text{ Hz}^{-1}$	definition
tropical year (equinox to equinox) (2007)	yr	$31\,556\,925.2 \text{ s} \approx \pi \times 10^7 \text{ s}$	[5]
sideral year (fixed star to fixed star) (2007)		$31\,558\,149.8 \text{ s} \approx \pi \times 10^7 \text{ s}$	[5]
mean sideral day (2007) (time between vernal equinox transits)		$23^h\,56^m\,04\,090\,53$	[5]
astronomical unit	AU, A	$149\,597\,870\,700(3) \text{ m}$	[6]
parsec (1 AU/1 arc sec)	pc	$3.055\,677 \times 10^{16} \text{ m} = 3.262 \dots \text{ ly}$	[7]
light year (deprecated unit)	ly	$0.3066 \dots \text{ pc} = 0.946\,053 \dots \times 10^{16} \text{ m}$	
Schwarzschild radius of the Sun	$2G_N M_\odot/c^2$	$2.953\,250\,077\,0(2) \text{ km}$	[8]
Solar mass	M_\odot	$1.988\,4(2) \times 10^{30} \text{ kg}$	[9]
Solar equatorial radius	R_\odot	$6.9551(3) \times 10^8 \text{ m}$	[10]
Solar luminosity	L_\odot	$3.842\,7(1) \times 10^{26} \text{ W}$	[11]
Schwarzschild radius of the Earth	$2G_N M_\oplus/c^2$	$8.870\,055\,881 \text{ mm}$	[12]
Earth mass	M_\oplus	$5.972\,6(6) \times 10^{24} \text{ kg}$	[13]
Earth mean equatorial radius	R_\oplus	$6.378\,137 \times 10^6 \text{ m}$	[5]
luminosity conversion (deprecated)	L	$3.02 \times 10^{28} \times 10^{-0.4} M_{\odot,\text{bol}} \text{ W}$ ($M_{\odot,\text{bol}}$ = absolute bolometric magnitude) — bolometric magnitude at 10 pc)	[14]
flux conversion (deprecated)	\mathcal{F}	$2.52 \times 10^{-8} \times 10^{-0.4} m_{\odot,\text{bol}} \text{ W m}^{-2}$ ($m_{\odot,\text{bol}}$ = apparent bolometric magnitude) — $-2.5 \log_{10} f_\nu - 56.10$ (for f_ν in $\text{W m}^{-2} \text{ Hz}^{-1}$) $= -2.5 \log_{10} f_\nu + 8.90$ (for f_ν in Jy)	from above
ABbsolute monochromatic magnitude	AB	$-2.5 \log_{10} f_\nu - 56.10$ (for f_ν in $\text{W m}^{-2} \text{ Hz}^{-1}$) $= -2.5 \log_{10} f_\nu + 8.90$ (for f_ν in Jy)	[15]
Solar velocity around center of Galaxy	Θ_0	$220(20) \text{ km s}^{-1}$	[16]
Solar distance from Galactic center	R_0	$8.0(5) \text{ kpc}$	[17]
local disk density	ρ_{disk}	$3.12 \times 10^{-24} \text{ g cm}^{-3} \approx 2.7 \text{ GeV}/c^2 \text{ cm}^{-3}$	[18]
local halo density	ρ_{halo}	$2-13 \times 10^{-25} \text{ g cm}^{-3} \approx 0.1-0.7 \text{ GeV}/c^2 \text{ cm}^{-3}$	[19]
present day CMB temperature	T_0	$2.725(1) \text{ K}$	[20]
present day CMB dipole amplitude		$3.358(17) \text{ mK}$	[21]
Solar velocity with respect to CMB		$369(2) \text{ km/s}$ towards $(\ell, b) = (263.86(4)^\circ, 48.24(10)^\circ)$	[21]
Local Group velocity with respect to CMB	vLG	$627(22) \text{ km s}^{-1}$ towards $(\ell, b) = (276(3)^\circ, 30(3)^\circ)$	[22]
entropy density/Boltzmann constant	s/k	$2.889.2 (T/2.725)^3 \text{ cm}^{-3}$	[14]
number density of CMB photons	n_γ	$410.5 (T/2.725)^3 \text{ cm}^{-3}$	[23]
present day Hubble expansion rate	H_0	$100 \text{ h km s}^{-1} \text{ Mpc}^{-1}$ $= h \times (9.777\,752 \text{ Gyr})^{-1}$	[24]
present day normalized Hubble expansion rate ^b	\dot{h}	$0.73(3)$	[2,3]
Hubble length	c/H_0	$0.923\,063 \times 10^{26} \text{ h}^{-1} \text{ m} \approx 1.27 \times 10^{26} \text{ m}$	
scale factor for cosmological constant	$c^2/3H_0^2$	$2.852 \times 10^5 \text{ h}^{-2} \text{ m}^2$	
critical density of the Universe	$\rho_c = 3H_0^2/8\pi G_N$	$2.775\,366\,27 \times 10^{11} \text{ h}^2 M_\odot \text{ Mpc}^{-3}$ $= 1.873\,35(19) \times 10^{-29} h^2 \text{ g cm}^{-3}$ $= 1.053\,68(11) \times 10^{-5} h^2 (\text{GeV}/c^2) \text{ cm}^{-3}$	[2,3]
pressureless matter density of the Universe ^d	$\Omega_m = \rho_m/\rho_c$	$0.128(8) h^{-2} \approx 0.24$ (WMAP3) $0.132(\gamma) h^{-2} \Rightarrow 0.27(2)$ (ALL mean)	[2,3]
baryon density of the Universe ^d	$\Omega_b = \rho_b/\rho_c$	$0.0223(7) h^{-2} \approx 0.0425$	[2,3]
dark matter density of the universe ^d	$\Omega_{dm} = \Omega_m - \Omega_b$	$0.105(8) h^{-2} \approx 0.20$	[2]
dark energy density of the Universe ^d	Ω_Λ	$0.73(3)$	[25]
Hubble length	c/H_0	$0.925\,063 \times 10^{26} \text{ h}^{-1} \text{ m} \approx 1.27 \times 10^{26} \text{ m}$	
radiation density of the Universe ^d	$\Omega_\gamma = \rho_\gamma/\rho_c$	$2.471 \times 10^{-5} (T/2.725)^4 h^{-2} \approx 4.6 \times 10^{-5}$	[23]
neutrino density of the Universe ^d	Ω_ν	$0.0005 < \Omega_\nu h^{-2} < 0.023$ $< 0.001 < \Omega_\nu < 0.05$	[26]
total energy density of the Universe ^d	$\Omega_{\text{tot}} = \Omega_m + \dots + \Omega_\Lambda$	$1.011(12)$	[2,27]

References

[Note] Writing a book is a complex task, simply because it requires the knowledge of the existing literature, from which we are inevitably in great debt to. Below is a list of texts, reviews and some specialized works. The works used in different parts of this book are referred to within square brackets in the general bibliography section and ordered by year (the last two characters). Those more specific references are divided between chapters, whose number is denoted by the first character. We frequently refer to web pages: in this case, they are indicated by the lower case character [w], followed by a progressive number. We avoided mentioning old historical papers because they are generally difficult to find. In the book, the Nobel laureates are quoted with the indication of the year, and the reference is not duplicated. We strongly recommend reading the Nobel lectures, which are all available at: http://nobelprize.org/nobel_prizes/physics/laureates/

General Bibliography

- [H84] Halzen, F., Martin, A.D.: Quarks and Leptons. Wiley, New York (1984). ISBN: 978-0471887416
- [S86] Segrè, E.: Nuclei and Particles. Benjamin-Cummings Pub Co. (1977). ISBN: 978-0805386011. Also in Italian: Nuclei e particelle. Zanichelli, Bologna (1986). ISBN: 978-8808056283
- [L87] Leo, W.R.: Techniques for Nuclear and Particle Physics Experiments. Springer, Berlin (1994). ISBN: 978-3540572800
- [P87] Perkins, D.H.: Introduction to High Energy Physics, 4th edn. The Edinburgh building, Cambridge CB2 8RU, UK (2000). ISBN: 978-0521621960
- [K88] Krane, K.S.: Introductory Nuclear Physics. Wiley, New York (1988). ISBN: 978-0471805533
- [A89] Aitchison, I.J.R., Hey, A.J.G.: Gauge Theories in Particle Physics, 3rd edn. Taylor & Francis, New York/Philadelphia (2002). ISBN: 978-0750308649
- [B89] Bachall, J.N.: Neutrino Astrophysics. Cambridge University Press, Cambridge (1989). ISBN: 978-0521379755. The Solar Standard Model is also described on the website: <http://www.sns.ias.edu/~jnb/>
- [C89] Cahn, R.N., Goldhaber, G.: The Experimental Foundations of Particle Physics. The Edinburgh building, Cambridge CB2 8RU, UK (1989). ISBN: 978-0521521475
- [G90] Gaisser, T.K.: Cosmic Rays and Particle Physics. Cambridge University Press, Cambridge (1991). ISBN: 978-0521339315
- [G91] Guidry, M.: Gauge Field Theories. Wiley, New York (1991). ISBN-13: 978-0471353850

- [H91] Hughes, I.S.: Elementary Particles, 3rd edn. The Edinburgh building, Cambridge CB2 8RU, UK (1991). ISBN: 978-0521407397
- [W91] Williams, W.S.C.: Nuclear and Particle Physics (1991). ISBN: 978-0198520467
- [L92] Longair, M.S.: High Energy Astrophysics, 2nd edn. Cambridge University Press, Cambridge (1992). ISBN: 978-0521387736 (Vol. I); ISBN: 978-0521435840 (Vol. II)
- [D94] Das, A., Ferbel, T.: Introduction to Nuclear and Particle Physics. Wiley, New York (1994). ISBN: 978-0471571322
- [M94] Martin, B.R., Shaw, G.: Particle Physics, 2nd edn. Wiley, New York (1997). ISBN: 978-0471972853
- [P95] Povh, B., Rith, K., Scholz, C., Zetsche, F.: Particles and Nuclei. An Introduction to the Physical Concepts, 6th edn. Springer, Berlin (2008). ISBN: 978-3540793670
- [J99] Jackson, J.D.: Classical Electrodynamics. Wiley, New York (1999). ISBN: 978-0471309321
- [G03] Gasiorowicz, S.: Quantum Physics, 3rd edn. Wiley, New York (2003). ISBN: 978-0471057000
- [B04] Basdevant, J.L., Rich J., Spiro, M: Fundamentals in Nuclear Physics. Springer, 2004, ISBN 0-387-01672-4
- [B08] Bettini, A.: Introduction to Elementary Particle Physics. Cambridge University Press, Cambridge (2008). ISBN: 978-0521880213
- [Be08] Bendiscioli, G.: Fenomeni Radioattivi. Springer, Milan (2008) (in Italian). ISBN: 978-8847008038
- [P08] Amsler, C., et al., (Particle Data Group): Review of particle physics. Phys. Lett. **B667**, 1 (2008)
- [W08] Weinberg, S.: Cosmology. Oxford University Press, Oxford (2008)
- [P10] Nakamura, K., et al., (Particle Data Group): Review of particle physics J. Phys. G. **37**, 075021 (2010). Phys. Lett. **B667**, 1 (2008). Available at: <http://pdg.lbl.gov/>

Chapter 2

- [2C70] Charpak, G., Rahm, D. Steiner, M.: Some developments in the operation of multiwire proportional chambers. Nucl. Instrum. Methods. **80**, 13 (1970)
- [2S77] Sauli, F.: Principles of Operation of Multiwire Proportional and Drift Chambers. CERN/EP 77-09. European Organization for Nuclear Research, Geneva (1977). <http://cdsweb.cern.ch/record/117989>
- [2L07] Lagniel, J.-M.: Status of the hadron therapy projects in Europe. DOI 10.2109/PAC.2007.4440335. Also in <http://hal.in2p3.fr/in2p3-00169261/en/>
- [2w1] <http://www.tera.it/>
- [2w2] “The Particle Detector BriefBook” <http://physics.web.cern.ch/Physics/ParticleDetector/BriefBook/>

Chapter 3

- [3w1] Didactic website on bubble chambers (Introduction to the BC): http://teachers.web.cern.ch/teachers/archiv/HST2005/bubble_chambers/BCwebsite/
- [3w2] <http://cdsweb.cern.ch/record/39469>

Chapter 4

- [4T73] ’t Hooft, G., Veltman, M.: Diagrammar. CERN Report 73-9, Geneva (1973). <http://cdsweb.cern.ch/record/186259/files/>
- [4A08] Avignone, F.T., Elliott, S.R., Engel, J.: Double beta decay, Majorana neutrinos, and neutrino mass. Rev. Mod. Phys. **80**, 481–516 (2008) arXiv:0708.1033 [nucl-ex]

Chapter 7

- [7S63] Shafer, J.B., et al.: Spin and parity of the 1385-MeV resonance. *Phys. Rev. Lett.* **10**, 179 (1963)
- [7G76] Giacomelli, G.: Total cross sections and elastic scattering at high energies. *Phy. Rep.* **23C**, 124 (1976)
- [7B79] Barber, D.P., et al.: Test of universality of charged leptons. *Phys. Rev. Lett.* **43**, 1915–1918 (1979)
- [7P04] Perl, M.L., Lee, E.R., Loomba, D.: A brief review of the search for isolatable fractional charge elementary particles. *Mod. Phys. Lett. A* **19**, 2595–2610 (2004)

Chapter 8

- [8B78] The Pauli letter is extracted from: Brown, L.M.: The idea of the neutrino. *Phys. Today* **31**, 23–28 (1978)
- [8B83] Bizzeti, P.G.: Weak interactions in nuclei. *La Rivista del Nuovo Cimento* **6**(12), 1–64 (1983)
- [8A84] Ademollo, M.: Cabibbo theory and current algebra. *La Rivista del Nuovo Cimento* **7**(1), (1984). doi: 10.1007/BF02724333
- [8B84] Bertin, A., Vitale, A.: Pure leptonic weak processes. *La Rivista del Nuovo Cimento* **7**(7), (1984). doi: 10.1007/BF02724331
- [8F84] Focardi, S., Ricci, R.A.: Historical introduction. The beta-decay and the fundamental properties of weak interactions. *La Rivista del Nuovo Cimento* **6**(11), (1983). doi: 10.1007/BF02740918
- [8G84] Goggi, G.: Gauge vector bosons and unified electroweak interaction. *La Rivista del Nuovo Cimento* **7**(4), (1984). doi: 10.1007/BF02724354
- [8P84] Palmonari, F.: Nonleptonic weak interactions. *La Rivista del Nuovo Cimento* **7**(9), (1984). doi: 10.1007/BF02724346
- [8Pu84] Pullia, A.: Structure of charged and neutral weak interactions at high energy. *La Rivista del Nuovo Cimento* **7**(2), (1984). doi: 10.1007/BF02724329
- [8V84] Bertin, A., Vitale, A.: Strangeness-conserving semi-leptonic weak processes. *La Rivista del Nuovo Cimento* **7**(8), (1984). doi: 10.1007/BF02724332
- [8G10] Grodzins, L.: The tabletop measurement of the helicity of the neutrino, *Il Nuovo Saggatore* **26**(5–6), 23 (2010) . On line on: <http://prometeo.sif.it/papers/online/sag/026/05-06/pdf/05-percorsi.pdf>

Chapter 9

- [9BH82] Bloom, E., Feldman, G.: Quarkonium. *Sci Am.* **246**, 66–77 (1982)
- [9M98] Montagna, G., Nicrosini, O., Piccinini, F.: Precision physics at LEP. *La Rivista del Nuovo Cimento* **21**(9), 1–162 (1998). Also: hep-ph/9802302
- [9B00] Brandt, D., Burkhardt, H., Lamont, M., Myers, S., Wenninger, J.: Accelerator physics at LEP. *Rep. Prog. Phys.* **63**, 939–1000 (2000). Also: CERN-SL-2000-037-DI
- [9A01] Abbiendi, G., et al., (OPAL Coll.): Measurement of the mass and width of the W boson in e+e- collisions at 189 GeV. *Phys. Lett. B* **507**, 29 (2001). Also: arXiv:hep-ex/0009018v1
- [9L03] LEP and SLD Coll. A Combination of preliminary electroweak measurements and constraints on the Standard Model. LEPEWWG/2003-02, hep-ex/0312023.
- [9H04] Heister, A., et al., (ALEPH Coll.): Studies of QCD at e^+e^- centre-of-mass energies between 91 GeV and 209 GeV. *Eur. Phys. J. C* **35**, 457 (2004)
- [9w1] The LEP Electroweak working group. <http://lepewwg.web.cern.ch/LEPEWWG/Welcome.html>
- [9w2] The LEP QCD annihilations working group. <http://lepqcd.web.cern.ch/LEPQCD/annihilations/>

Chapter 10

- [10G93] Giacomelli, G., Giacomelli, P.: Particle searches at LEP. *La Rivista del Nuovo Cimento* **16**(3), 1 (1993). doi: 10.1007/BF02832334
- [10P02] Hagiwara, K., et al., (Particle Data Group): Review of particle physics. *Phys. Rev. D* **66**, 010001 (2002)
- [10A09] ALEPH, CDF, D0, DELPHI, L3, OPAL, SLD Collaborations, the LEP Working Group, the Tevatron Electroweak Working Group, and the SLD Electroweak and Heavy flavor Group. Precision electroweak measurements and constraints on the standard model [arXiv:0911.2604 \[hep-ex\]](https://arxiv.org/abs/0911.2604).
- [10C11] The CMS Collaboration. Measurement of W^+W^- production and search for the Higgs Boson in pp Collisions at $\sqrt{s} = 7$ TeV. *Phys. Lett. B* **699** (2011) 25–47. [arXiv:1102.5429 \[hep-ex\]](https://arxiv.org/abs/1102.5429)
- [10L11] LHC Higgs Cross Section Working Group, Dittmaier, S., Mariotti, C., Passarino, G., Tanaka, R. (eds.): *Handbook of LHC Higgs Cross Sections: 1. Inclusive Observables*, CERN-2011-002 CERN, Geneva (2011), [arXiv:1101.0593 \[hep-ph\]](https://arxiv.org/abs/1101.0593)
- [10w1] The Physics of RHIC. <http://www.bnl.gov/rhic/physics.asp>

Chapter 11

- [11A84] Altarelli, G.: Future perspectives in particle physics. *La Rivista del Nuovo Cimento* **7**(3), (1984). doi: 10.1007/BF02724328
- [11W04] Wilczek, F.A.: Asymptotic freedom: from paradox to paradigm. http://nobelprize.org/nobel_prizes/physics/laureates/2004/wilczek-lecture.pdf

Chapter 12

- [12M79] Mikheyev, S.P., Smirnov, A.Y.: *Nuovo Cimento* **19**, 17 (1986) ; Wolfenstein, L.: *Phys. Rev. D* **20**, 2634 (1979)
- [12B95] Paver, N.: Aspects of CP violation in neutral kaon decays. In: *Proceedings of the 4th School on Non-accelerator Particle Astrophysics*, p. 34. World Scientific, Singapore (1995)
- [12A98] Ambrosio, M., et al., (MACRO Coll.): Measurement of the atmospheric neutrino-induced upgoing muon flux using MACRO. *Phys. Lett.* **434**, 451 (1998)
- [12C98] Carrigan, R.A., Giacomelli, G., Paver, N. (eds.): *Proceedings of the 5th School on Non-Accelerator Particle Astrophysics*. Ed. Università di Trieste, Trieste (1999):
 - Giacomelli, G., Spurio, M.: Atmospheric neutrinos and neutrino oscillations, p. 146 ([hep-ph/9901355](https://arxiv.org/abs/hep-ph/9901355));
 - Cecchini, S., Sioli, M.: Cosmic ray muon physics, p. 201;
- [12F98] Fukuda, Y., et al., (SuperKamiokande coll.): Evidence for oscillation of atmospheric neutrinos. *Phys. Rev. Lett.* **81**, 1562 (1998)
- [12S98] Sanchez, M., et al., (Soudan 2 Coll.): Measurement of the L/E distributions of atmospheric ν in Soudan 2 and their interpretation as neutrino oscillations. *Phys. Rev. D* **68**, 113004 (2003)
- [12A01] Abe, K., et al.: Observation of large CP violation in the neutral B meson system. *Phys. Rev. Lett.* **87**, 091802 (2001)
- [12D01] Dorfan, J.: BaBar results on CP violation. *Int. J. Mod. Phys. A* **17**, 2925 (2002)
- [12L01] Lipari, P.: Introduction to neutrino physics. 1st CERN - CLAF School of High-energy Physics, Itacuruca, Brazil, (2001). <http://cdsweb.cern.ch/record/677618>
- [12H03] Harrison, P.: Nature's flawed mirror. *Phys. World* **16**(7), 27 (2003)
- [12G07] Gershon, T.: A triangle that matters. *Phys. World* **20**(4), 24 (2007)
- [12B08] Bellini, G., et al., (BOREXino Coll.): Measurement of the solar 8B neutrino flux with 246 live days of Borexino and observation of the MSW vacuum-matter transition. *Phys. Rev. D* **82**, 033006 (2010) . Also: [arXiv:0808.2868 \[astro-ph\]](https://arxiv.org/abs/0808.2868)

- [12A10] Agafonova, N.: et al., (OPERA Coll.): Observation of a first ν_τ candidate in the OPERA experiment in the CNGS beam. Phys. Lett. B **691**, 138–145 (2010). Also: arXiv:1006.1623 [hep-ex]

Chapter 13

- [13P74] Pati, C., Salam, A.: Lepton number as the fourth color. Phys. Rev. D **10**, 275 (1974)
- [13G84] Giacomelli, G.: Magnetic monopoles. La Rivista del Nuovo Cimento **7**(12), 1 (1984)
- [13D94] De Boer, W.: Grand Unified theories and supersymmetry in particle physics and cosmology. Prog. Part. Nucl. Phys. **33**, 201 (1994). Also: arXiv:hep-ph/9402266v5
- [13L94] Lopez, J., Nanopoulos, D.V., Zichichi, A.: A layman's guide to SUSY GUT. La Rivista del Nuovo Cimento **17**(2), 1 (1994). Also in: <http://cdsweb.cern.ch/record/255084/>
- [13B00] De Bernardis, P., et al.: A flat universe from high-resolution maps of the cosmic microwave background radiation. Nature **404**, 955 (2000)
- [13G00] Greene, B.: The Elegant Universe: Superstrings, Hidden Dimensions, and the Quest for the Ultimate Theory. Vintage Series, Random House Inc., New York (2000) ISBN: 978-0375708114
- [13S04] Riess, A.G., et al., (Supernova Search Team Coll.): Type Ia supernova discoveries at $z > 1$ from the Hubble space telescope: Evidence for past deceleration and constraints on dark energy evolution. Astrophys. J. **607**, 665–687 (2004). Also: astro-ph/0402512.
- [13W07] Spergel, D.N., et al., (WMAP Coll.): Wilkinson microwave anisotropy probe (WMAP) three year results: Implications for cosmology. Astrophys. J. Suppl. **170**, 377 (2007). Also: astro-ph/0603449.
- [13B08] Bernabei, R., et al., (DAMA Coll.): First results from DAMA/LIBRA and combined results with DAMA/NaI. Eur. Phys. J. C **56**, 333 (2008). Also: arXiv:0804.2741 [astro-ph]
- [13C10] Chiarusi, T., Spurio, M.: High-energy astrophysics with neutrino telescopes. Eur. Phys. J. C **65**, 649–710 (2010)
- [13M10] J. Adam et al. (MEG Collaboration). A limit for the $\mu \rightarrow e\gamma$ decay from the MEG experiment. Nucl. Phys. B834 (2010), 1–12
- [13w1] The SUSY LEP working group. <http://lepsusy.web.cern.ch/lepsusy/www/>
- [13w2] The Higgs LEP working group. <http://lephiggs.web.cern.ch/LEPHIGGS/papers/index.html>

Chapter 14

- [14B57] Burbidge, E.M., Burbidge, G.R., Fowler, W.A., Hoyle, F.: Synthesis of the elements in stars. Rev. Mod. Phys. **29**, 547 (1957). This historical article is jokingly referred as B^2FH
- [14S83] Simpson, J.A.: Elemental and isotopic composition of the galactic cosmic rays. Annu. Rev. Nucl. Part. Sci. **33**, 323 (1983)
- [14T98] Truran, J.W.: The age of the universe from nuclear chronometers. Proc. Natl. Acad. Sci. U.S.A. **95**, 18–21 (1998). This paper was presented at a colloquium entitled The Age of the Universe, Dark Matter, and Structure Formation whose proceedings are available at http://www.nap.edu/catalog.php?record_id=6237
- [14w1] <http://www.physics.brocku.ca/applets/MassSpectrometer/index.html>
- [14w2] National Nuclear Data Center, information extracted from the NuDat 2 database. <http://www.nndc.bnl.gov/nudat2/>
- [14w3] Bertsch, G., Bulgac, A., Luo, A., McDaniel, C.: Liquid Drop Model of Nuclear Binding Energy. <http://128.95.95.61/~intuser/ld3.html>
- [14w4] Fusion for Energy (F4E) is the European Union's Joint Undertaking for ITER and the Development of Fusion Energy. <http://fusionforenergy.europa.eu/>

Index

A

Absorber, 43, 243

Absorption coefficient, 140

Accelerator, 45

- circular, 49, 50

- electrostatic, 49

- linear, 49

Acoplanarity angle, 396

Action, 470

Activity, 433, 434

AdA storage ring, 229

Adjoint Dirac equation, 469

Adjoint spinor, 469

ALEPH, 239

ALICE, 305

α

- decay, 433, 437

- particles, 95, 417

α_S , 237

Amplifier, 33–35

Analog-to-digital converter (ADC),
34

Anderson, C.D., 3, 4

Angular momentum
orbital, 159
total, 159

Angular resolution, 96

Annihilation, 270

Antibaryon, 143

Antiparticle, 2

Antisymmetric wave function, 110

Associated production, 155, 156

Aston, V., 418

Asymmetry, 203

Asymmetry term, 426, 427

Asymptotic freedom, 108, 342

ATLAS, 305

Atmospheric neutrino, 368

- oscillations, 376

Atom, 1, 5–9

Atomic

- nucleus, 11, 25

- number, 13, 15, 20

- system, 157

- weight, 15

Atomic mass unit (AMU), 419

Attenuation, 141

- coefficient, 22

Average helicity, 477

Axial meson, 125

Axial-vector

- current, 227

- interaction, 223

Axion, 407

B

Bacher, R., 183

Baker, E.B., 190

Balmer formula, 237

Bandwidth, 37

Baryogenesis, 347

Baryon, 111, 135

Baryonic number, 54

Baryon number, 111, 125, 144, 157

- conservation, 103

- violation, 391

Beam, 50

- intersecting, 52

Becquerel, H., 433

Bessel function, 300

β decay, 103, 433, 441

β inverse

- decay, 197

- process, 184

- Bethe–Bloch formula, 15
 Bethe, H.A., 183, 190
 Bethe–Heitler formula, 20, 25
 B-factories, 360
 Bhabha scattering, 92, 98
 Big Bang, 3, 9
 model, 391, 407
 Bilinear forms, 223
 Binding energy (BE), 421
 Bjorken, J.D., 276, 359
 Bjorken scaling, 290
 law, 277
 Blackett, P., 3
 B-meson tagging, 361, 362
 Bohr
 atom, 161, 237
 classical formula, 15
 magneton, 99
 Bohr–Sommerfeld atomic model,
 417
 Boltzmann constant, 6
 Bose–Einstein statistics, 1, 110
 Boson, 1, 10, 111
 Boson–fermion symmetry, 392
 Bosonic
 particle, 85
 propagator, 85
 Bottomonium, 237
 Bottom quantum number, 169
 Bra, in Dirac notation, 115
 Branching ratio, 89
 Branching ratio for Σ decays, 209
 Breit–Wigner
 equation, 148
 formula, 221
 resonance, 148
 Bremsstrahlung, 13, 20–21, 77, 92, 247
 Brookhaven National Laboratory,
 234
 Bubble chamber, 31, 33, 40–42, 214
 Bunch, 50
- C**
 Cabibbo angle, 211–213, 228, 367
 Cabibbo–Kobayashi–Maskawa matrix,
 359
 Cabibbo, N., 211, 212
 Callan–Gross relation, 279
 Calorimeter, 42–44
 homogeneous, 44
 sampling, 44, 242
 Cascade decays, 434–436
- Center-of-mass
 energy, 142
 system, 47, 52
 CERN, 10, 199, 214, 220, 229, 230, 239, 252,
 296, 305
 SPS, 199
 CERN to GS project, CNGS, 380
 Chadwick, J., 4, 182, 422, 441, 445
 Chamberlain, O., 143
 Charge
 asymmetry, 353
 conjugation, 126
 division method, 34
 density, 464
 multiplicity, 296, 302
 renormalization, 337
 Charged current, 103–105, 180
 Charged pion decay, 205
 Charmed quark, 215
 Charmonium, 238
 Charm quantum number, 61, 169
 Charpack, G., 34
 Cherenkov counter, 32, 39
 threshold, 40
 Chirality, 475
 Christenson, J., 131
 Circuit, 35
 CKM
 matrix, 218, 359
 mixing angles, 218
 Classical electron radius, 96
 Clebsh–Gordan coefficients, 153
 CMS, 305
 CNO cycle, 450
 Cobalt experiment, 202
 Coherent scattering, 25
 Collider, 97
 Collision length, 140
 Collisions
 e^+e^- , 229
 lepton-lepton, 229
 Color, 157, 233
 charge, 107, 108
 factor, 221, 342
 field, 317
 force, 339
 quantum number, 232
 singlet, 161, 339
 space, 322
 triplet, 399
 Composite model, 386, 397
 Compton
 edge, 24

- effect, 78
scattering, 22–24
- Confinement, 342, 345
- Conservation
angular momentum, 113
of the electric charge, 60
energy, 115
energy and momentum, 181, 182,
185, 262
isospin, 138
laws, 46, 61, 69, 113
of the lepton number, 199
linear momentum, 113
parity, 121
strangeness, 154
- Continuity equation, 469
- Coordinate space, 86
- Cork, B., 144
- Cosmic microwave background radiation,
403, 407
- Cosmic time, 8, 408
- Coupling constant, 102
- Cowan, C., 191
- CP, 128
eigenstate, 215, 353
violation, 131, 347
- CPT
invariance theorem, 132
- Creation and destruction operators, 227
- Creation of particles, 46
- Critical energy, 20, 26
- Cronin, J.W., 353
- Cross-section, 4, 29
- C shell correction, 15
- Curie, M., 437
- Current density, 464, 465
- Curvature radius, 62
- D**
- D'Alembert operator, 463
- Dalitz plot, 146
- Dalitz, R.H., 145
- Dallaporta tetrahedron, 211
- Dark
energy, 413
matter, 403
- Davis, R., 372
- Dead time, 31
- de Broglie
equation, 62
relation, 45
wavelength, 221, 235
- Debye, 183
- Decay
of charged particles, 67
constant, 36
fraction, 89
length, 358
mode, 89
- Deep inelastic scattering (DIS), 136, 279
- Delayed coincidence, 192
- DELPHI, 239
- Density
effect, 15
of electric charge in nuclei, 422
of Lagrangian, 114
of magnetization in nuclei, 422
of states, 84
- DESY, 229
- Detailed balance principle, 122, 123
- Detector
dead time, 31
efficiency, 31
energy resolution, 32
response time, 31
spatial resolution, 32
- Deuterium, 411
- Deuteron, 122, 432
- Differential elastic cross-section, 94
- Diffractive scattering, 296
- Digital (or logic) signal, 34
- Dion, 397
- Dipole, 2
form factor, 275
formula, 275
magnetic, 126
transition, 121
- Dirac
equation, 81
fermion, 222
notation, 115
relation, 390
sea, 81
theory, 99, 227, 473
- Dirac, P., 4, 81
- Discovery of particles, 3
- Distribution
function, 272
of nuclear matter, 422
time, 59
- Doppler effect, 404
- Drell–Yan
model, 171
process, 305
- Drift
chamber, 30
time, 35

Duality, wave-particle, 45
 Dynode, 36

E
 Earth and Solar System dating, 454
 Eigenstate, 157
 Einstein, A., 313
 Einstein equation, 46
 Elastic
 process, 314
 scattering, 94, 95, 269
 Electric
 charge, 2, 7, 9, 10
 charge of nuclei, 418
 field, 317
 form factor, 273
 signal, 30, 35
 Electromagnetic
 calorimeter (ECAL), 42
 cascade, 25, 42
 coupling constant, 76
 interaction, 1, 74, 222
 properties of the nucleus, 424
 radius of the nucleus, 422
 shower, 25
 wave, 50
 Electron, 1
 classical radius, 15, 24
 Electronic neutrino, 4
 Electrostatic separator, 55
 Electroweak interaction, 3, 73
 Elementary particle, 1, 81
 Elliptic galaxy, 404
 Endothermic nuclear reactions, 444
 Energy
 of an accelerator, 48
 distribution, 24
 loss, 12
 loss through excitation, 20
 loss through ionization, 13
 loss through radiation, 18, 43
 resolution, 32
 response, 24
 Equation
 de Broglie, 62
 Dirac, 81
 eigenvalue, 115, 118, 120
 Hamilton, 115
 Heisenberg, 116
 Klein-Gordon, 136
 Klein-Nishina, 24
 Lagrange, 113, 114

Maxwell, 464
 Schrödinger, 79
 Evolved QCD, 294
 Exchange
 force, 433
 process, 75
 Excitation, 6, 12
 energy, 6
 energy loss, 12
 potential, 32
 Exothermic nuclear reactions, 444
 Expectation value, 115, 173

F
 Fall time, 38
 Fermi
 β decay theory, 184
 coupling constant, 106, 186
 energy, 426
 gas model, 425
 mechanism, 401
 momentum, 425
 statistics, 233
 transitions, 196, 201, 227
 weak interaction theory, 180, 214
 Fermi-Dirac statistics, 1, 110
 Fermi, E., 69, 106, 179, 183, 444, 445, 447
 Fermilab, 10, 199, 229, 236, 296, 306, 380
 Fermion, 2, 110
 Feynman
 diagram, 74, 76, 90
 scaling, 279
 Feynman, R.P., 222, 279
 Fine structure, 237
 constant, 76, 334
 First instants of the Universe, 391
 Fission, 433
 chain reaction, 447
 energy, 447
 induced by neutrons, 445
 nuclear, 28
 nuclear reactor, 447
 Fitch, V.L., 353
 Flavor, 168
 eigenstates, 367
 lepton number conservation, 198
 of quarks, 233
 Fluorescence, 35
 Flux return, 240
 Force particle, 1, 8
 Form factor, 272
 electric, 273

- magnetic, 273
- proton, 270
- Forward-backward asymmetry, 254
- Forward detector, 243
- Four-vector, 465
- Fragmentation, 268
 - function, 268
- Frascaty Laboratory, 229
- Free mean path, 25
- Friedman, J.L., 277
- Frisch, O., 445
- Fusion
 - inertial, 456
 - in laboratory, 455
 - magnetic, 456
 - photon-gluon, 293
- G**
- Galaxy
 - cluster, 404
 - formation, 412
- γ
 - decay, 433, 436
 - rays, 7, 28, 39
- Gamow factor, 439
- Gamow, G., 439
- Gamow-Teller transitions, 195, 196, 201, 227
- Gargamelle experiment, 214
- Garwin, R.L., 202
- Gauge
 - invariance, 78, 132, 318
 - in QED, 318
 - in SU(2), 320
 - in SU(3), 320
 - theory, 78, 326, 385
 - transformation, 133, 318, 319
- Gauginos, 395
- Gauss-cgs system, 13
- Gauss theorem, 13
- Geiger counter, 30, 32, 33
- Geiger-Nuttal law, 438, 440
- Gell-Mann, M., 159, 176, 215, 222
- Gell-Mann-Nishijima relation, 318
- Generalized coordinates, 114
- Generalized helicity, 475
- General properties of nuclei, 417
- General relativity, 102
- GIM mechanism, 215, 234
- Glashow, S.L., 215
- Glauber model, 304
- Glueball, 178
- Gluon, 2, 4, 7–9, 314, 339
 - fusion, 306
- Golden rule, 85
- Goldhaber experiment, 205
- Goldhaber, M., 204, 205
- Goldstone boson, 326
- Gradient operator, 79
- Grand Unified Theory (GUT), 3, 10, 386, 387
- Gran Sasso Laboratory, 379, 380
- Gravitational
 - force, 76
 - interaction, 1
 - lensing, 406
- Graviton, 2, 102
- Gravity, 102
- GUT. *See* Grand Unified Theory (GUT)
- Gyromagnetic ratio, 100, 337
- H**
- Hadron, 1
 - jet, 268, 291
 - spectroscopy, 176
 - therapy with nuclei, 18
- Hadron-hadron collisions, 142
- Hadronic
 - calorimeter (HCAL), 42, 43
 - cascade, 43
 - interaction eigenstate, 215
 - process, 401
 - resonance, 142, 144, 416
- Hadronization, 105, 246, 268, 293
- Hahn, O., 445
- Half-life, 110, 434
- Hamilton equations, 115
- Hamiltonian, 115, 117, 120
- Heavy
 - quark, 215, 234
 - water, 447
- Heisenberg
 - equation, 116
 - representation, 116
- Heisenberg, W., 137
- Helicity, 204, 270
 - factor in π decay, 227
 - of the neutrino, 204, 205
 - operator, 201
- HERA, 295
- Hess, V., 3
- Hierarchy problem, 385
- Higgs
 - boson, 2, 9, 262, 325
 - potential, 325

Higgs (*cont.*)
 vacuum expectation value, 326
 High transverse momentum, 296
 Hofstadter, R., 274
 Hybrid state, 178
 Hypercharge, 169, 318, 334
 Hyperfine structure, 237
 Hyperon, 1, 4, 158
 decay, 103

I

Iliopoulos, J., 215
 Impact parameter, 13, 93–95
 Inclusive reaction, 292
 Independent particle model, 430
 Inelastic collision, 6
 Inelasticity, 283
 Inertial fusion, 456
 Infinite force range, 95
 Inflation, 410
 of the Universe, 391
 Integrated luminosity, 293, 300
 Intensity of an accelerator, 48
 Interaction
 between nucleons, 415
 spin-orbit, 237
 spin-spin, 237
 International System of Units, 74
 Intersecting Storage Rings (ISR), 296
 Intranuclear cascade, 304
 Intrinsic angular momentum, 110
 Invariance
 Poincaré, 114
 spatial rotation, 113
 time-translation, 114
 Invariant rotation, 115
 Inversion
 space, 120
 time, 122
 Ionization, 8, 12, 30
 chamber, 30, 32
 detector, 29, 31
 energy, 8
 energy loss, 12
 potential, 15, 31
 Isobar, 419, 442
 Isoscalar nucleus, 172
 Isospin
 conservation, 138
 multiplet, 137, 158
 singlet, 139, 163
 Isotope, 419
 Isovector field, 320

J

Jarlskog, C., 359
 Jensen, H., 430
 Jet, 232, 245, 308
 spectator, 268
 target, 268
 JET chamber, 240
 J/Ψ, 234

K

Kendall, H.W., 277
 Ket, in Dirac notation, 115
 Kinetic energy, 6
 Klein–Gordon equation, 136
 Klein–Nishina equation, 24
 K⁰ neutral meson, 348
 oscillation, 348
 Knock-on electrons, 19
 Kobayashi, M., 218

L

L3, 239
 Laboratory system, 47–48
 Lagrange equations, 113, 114
 Lagrangian, 114, 470
 density, 114, 470
 Lamberston, G.R., 144
 Lamb shift, 337
 Laser, 110
 Lattes, C.M.G., 4
 Lattice QCD, 176
 Leading order, 92
 Lederman, L.M., 198, 202
 Lederman, M.L., 236
 Lee, T.D., 201
 Left-handed
 lepton, 204
 particle, 223
 Legendre polynomials, 120
 LEP, 220, 229, 230, 239, 249, 305
 detectors, 239
 phase II, 257
 Leptogenesis, 348
 Lepton, 1, 111, 135
 family, 198
 number, 111
 conservation, 103
 violation, 391
 universality, 239, 245, 251
 Leptonic
 weak current, 226
 WI process, 208

- Lepton–nucleon
 collision, 293
 scattering, 267, 294
- Leptoquark, 399, 400
- LHC, 10, 229, 304, 345
- LHCb, 305
- Lifetime, 1, 88
- Light
 guide, 35, 37
 speed, 50
- Local invariance, 320
- Long baseline experiment, 379
- Longitudinal polarization of the spin, 201
- Lorentz
 force, 62
 transformation, 223
- Low transverse momentum, 296
- Luminescence, 35
- Luminometer, 241, 243
- Luminosity, 52, 53, 99, 242, 300
- Luminous efficiency, 36
- M**
- MACHO, 406
- MACRO experiment, 380
- Magic numbers, 429
- Magnetic
 dipole, 126
 moment, 2
 form factor, 273
 fusion, 456
 monopole, 74, 390, 410
 quadrupole, 55
- Magneton nuclear, 174
- Maiani, L., 215
- Main sequence, 453
- Majorana, E., 81
- Manhattan project, 184, 191
- Maskawa, T., 218
- Mass
 difference, 168
 eigenstate, 219, 353, 367
 of the nuclei, 418
 spectrometer, 418
- Matrix
 element, 77
 γ , 226
 metric, 466
- Matter
 era, 411
 particle, 1
- Matter-antimatter asymmetry, 347
- Maxwell equations, 81, 464
- Mean free path, 140
- Meitner, L., 445
- Mendeleev table, 416
- Merey, M., 430
- Meson
 pseudoscalar, 163
 scalar, 178
 tensor, 178
 vector, 165
- Microstrip detector, 31, 32, 38
- Microvertex detector, 242
- Millikan, R., 177
- Mills, R.L., 321
- Minimal standard supersymmetric model (MSSM), 393
- Minimum bias
 event, 221
 trigger, 298
- Mixing
 angle, 165
 of quarks, 359
- Model of multihadronic production, 256
- Möller scattering, 92
- Momentum space, 86, 93
- Monte Carlo method, 31
- Mott formula, 270
- MSSM. *See* Minimal standard supersymmetric model (MSSM)
- MSW effect, 370
- Multiplicity, charged, 55
- Multiplier, 35
- Multi-prong decay, 69
- Multiwire proportional chamber, 30
- Muon, 1, 59
 decay, 189
 neutrino, 4, 198
- N**
- Neddermeyer, S.H., 4
- Neutral current, 103–105, 180, 323
 interaction, 373
 WI process, 217
- Neutralino, 406
- Neutrino, 4
 appearance, 380
 appearance experiment, 373
 Dirac, 81
 disappearance experiment, 373
 energy spectrum, 181
 helicity, 204
 interaction length, 198
 Majorana, 81

- Neutrino (*cont.*)
 - mass, 348
 - mass eigenstate, 371
 - mean free path, 198
 - mixing angle θ_{12} , 376, 382
 - mixing angle θ_{13} , 368
 - mixing angle θ_{23} , 378
 - oscillation, 348
 - telescope, 401
 - two-component theory, 205
- Neutrino beam, 199, 214
 - broad-band, 199
 - narrow-band, 199
- Neutrino-nucleon cross-section, 288
- Neutron
 - β decay, 103
 - interaction, 28
 - moderation, 447
 - star, 7, 401
- Neutronization, 452
- Newton, 101, 102
- Nishijima, K., 159
- Noble gases, 429
- Noether's theorem, 113, 114
- Nonleptonic WI process, 208, 210
- Nuclear
 - absorption, 123
 - binding energy, 420, 421
 - bomb, 191
 - capture, 28
 - collision, 29
 - drop model, 426
 - emulsion, 30
 - fission, 28, 444, 445
 - force, 106
 - fusion, 7, 448
 - fusion in stars, 401
 - fusion reactor, 448
 - magneton, 174
 - model, 424
 - physics, 28, 29, 49
 - radius, 421
 - reaction, 444
 - reactor, 184
 - spin, 195
 - transition, 195
- Nucleon, 135, 433
- Nucleon-nucleon interaction, 431
- Nucleosynthesis, 406, 408, 411
- Nucleus-nucleus collision, 303
- Nuclide chart, 419
- Number of light neutrino families, 251
- O
 - Occhialini, G.P.S., 4
 - Off mass shell, 91
 - On mass shell, 91, 220, 464
 - OPAL, 239
- P
 - Pair
 - annihilation, 411
 - production, 22, 23, 25
 - Pais, A., 215
 - Parity, 119, 159
 - conservation, 121, 223
 - violation, 4, 201
 - experiment, 201, 202
 - in weak interactions, 205
 - Particle
 - decay, 88
 - real, 91
 - virtual, 91
 - Particle-antiparticle
 - asymmetry, 347
 - parity, 125
 - symmetry, 128
 - Parton model, 266, 279, 288, 291
 - Pauli
 - exclusion principle, 110, 433
 - letter, 181
 - neutrino hypothesis, 181–182, 442
 - Pauli, W., 4, 181, 183
 - Periodic table of elements, 415
 - Perl, M.L., 238
 - Perturbative theory, 76
 - Phase
 - space, 146, 166
 - factor, 105, 110
 - transition, 132
 - velocity, 50
 - Phosphorescence, 35
 - Photocathode, 35–37
 - quantum efficiency, 37
 - response, 37
 - Photoelectric effect, 22, 78
 - Photographic method, 33
 - Photomultiplier, 35–36
 - Photon, 1
 - propagator, 99
 - Piccioni, O., 144
 - Pion decay, 226
 - Pion-nucleon collision, 142, 171
 - Planck
 - constant, 45
 - length, 102

- mass, 102
time, 397, 409
- Poltergeist project, 190
- Pomeranchuk theorem, 298
- Pomeron exchange, 296
- Pontecorvo, B., 365
- Position resolution, 38
- Positron, 66
- Positronium, 237
- ortho-, 237
 - para-, 237
- Potential
- central, 85
 - Coulomb, 76
 - electrostatic, 78
 - static, 80
 - tensor, 432
 - well, 423
- Powell, C.F., 4
- Preon, 397
- Primary cosmic rays, 3
- Primordial
- deuterium, 411
 - helium, 411
 - nucleosynthesis, 449
- Production
- of associated particles, 155
 - of quark pairs, 232
- Propagator, 77
- Proportional counter, 30
- Proton
- decay, 386
 - form factor, 270
- Protostar, 412
- Pseudoscalar meson, 125
- Puppi triangle, 189
- Q**
- QCD. *See* Quantum chromodynamics (QCD)
- QED. *See* Quantum electrodynamics (QED)
- Quantum chromodynamics (QCD), 161, 107, 139, 313
- Quantum electrodynamics (QED), 78, 107
- checks, 99
- Quark, 1, 227, 230
- b, 237
 - c, 234
 - confinement, 410
 - distribution function, 286
 - dynamic structure, 136
 - flavor, 104, 135
- fragmentation function, 293
- sea, 136
- valence, 157, 176
- Quark-gluon plasma, 304, 305, 416
- Quintessence, 413
- R**
- Radiation, 11
- era, 411
 - length, 20, 25, 26
- Radiative
- correction, 100, 329, 335
 - event, 258
 - process, 234
- Radioactive
- decay, 2, 179, 227
 - decay law, 88
 - nucleus, 69
 - series, 435
- Radiochemical experiment, 373
- Radon, 434
- Range, 16
- of action, 29
- Ratio R, 233
- Rayleigh
- collision, 22, 23
 - scattering, 22, 23, 25
- Reactor neutrino, 368
- Reines, F., 191
- REL. *See* Restricted Energy Loss (REL)
- Renormalizable theory, 262
- Renormalization, 335
- Representation
- Heisenberg, 115
 - Schrödinger, 115
- Residual strong interaction, 135
- Resolution in energy, 44
- Resonance, 110
- baryonic, 150
 - elastic, 150
 - formation, 151
 - hadronic, 148, 235
 - J/ψ , 235
 - meson, 231
 - production, 151
- Response
- to luminous radiation, 37
 - time, 31
- Rest mass, 463
- Restricted Energy Loss (REL), 19
- Reverse reaction, 122
- Richter, B., 234

- Right-handed
lepton, 204
particle, 224
- Rise time, 31, 37
- Rishons, 397
- Rosenbluth formula, 274
- Rosenbluth, M., 272
- R-parity, 394
- R-process, 452, 454
- Rubbia, C., 220
- Running of the coupling constant, 317
- Rutherford
elastic scattering, 95
formula, 95
scattering, 93, 270, 422
- Rutherford, E., 95, 417, 422, 437, 441, 444
- S**
- Sakharov, A.D., 347
- Sargent, B.W., 442
- Sargent rule, 189
- Scalar potential, 465
- Scale breaking effect, 293
- Scaling
Bjorken, 290
invariance violation, 291
- Scattering
amplitude, 105
angle, 95
- S-channel, 151
- Schrödinger
equation, 79
representation, 115
- Schwartz, M., 198
- Schwinger, J., 78
- Scintillation
counter, 30, 34, 203
detector, 34
- Scintillator, 34
inorganic, 36
organic, 36
plastic, 36
- Sea quark, 136, 172, 267
- Second Fermi golden rule, 85
- Second quantization, 78
- Segrè, E., 143
- Selection rules, 121
for nonleptonic decays, 210
- Semiconductor, 37
detector, 38
- Semileptonic WI process, 208, 209
- Sfermion, 395
- Shell
correction, 15
model, 429
- Shock wave, 39
- Short baseline experiment, 380
- Singlet spin state, 196
- SLAC. *See* Stanford Linear Accelerator Center (SLAC)
- Slepton, 392
- SNO experiment, 373
- Solar neutrino, 368, 373
problem, 373
- Solar System, 454
- Solid angle, 40, 55
- Space-like photon, 91
- Space phase, 122
- Spark chamber, 33
- Spatial resolution, 31, 32
- Spectator, 31, 32
jet, 268
quark, 103
- Spectroscopy of heavy mesons, 237
- Spherical harmonics, 120
- Spin, 110
magnetization, 203
quantization, 177
space, 159
statistics, 118, 161
- Spinor, 81, 227
- Spin-orbit interaction, 430
- Spin-parity, 122
- Spiral galaxy, 404, 405
- Spontaneous
fission, 445
symmetry breaking, 314, 325
- S-process, 452
- Squark, 392
- Stability, 110
valley, 419
- Stable
nuclei, 416
particles, 2
- Standard deviation, 46
- Stanford Linear Accelerator Center (SLAC), 229, 234, 239, 249, 277
- Standard Model, 220, 254, 347
of Microcosm, 9, 313
- Standard Solar Model, 371
- Star, 7
- Static quark model, 135, 157, 170
- Steinberger, J., 198
- Stellar
gravitational collapse, 401
nucleosynthesis, 414, 453, 454

- Strangeness, 4, 61, 135, 154
 conservation, 154
 eigenstate, 349
 oscillation, 350
- Strange particle, 60, 154
 decay, 154, 208
 production, 156
- Strassmann, F., 445
- String theory, 397
- Strong
 coupling constant, 296
 hypercharge, 158
 interaction, 1, 101, 106
 isospin, 54
- Structure function, 267, 268
- Supergravity (SUGRA), 386, 392, 397
- SuperKamiokande experiment, 378
- Supernova, 454
- Superposition model, 304
- Supersymmetric theory, 392
- Supersymmetry (SUSY), 386, 392
- Surface term, 427
- Symmetry group, 317
- Synchrocyclotron, 49
- T**
- Target jet, 268
- Tau neutrino, 199
- Taylor, R.E., 277
- T-channel, 214
- Temperature, 5
- Tevatron, 10, 199, 306
- Theory-experiment comparison, 86
- Thermal equilibrium, 406
- Thermal neutron, 446
- Third lepton family, 198
- Thomson
 atomic model, 417
 collision, 22
 cross-section, 23
 formula, 24
- Three-body decay, 83
- Three neutrino flavor oscillations,
 367
- Three-prong decay, 69
- Threshold detector, 40
- Time
 projection chamber (TPC), 30
 resolution, 31
 reversal, 122, 129
- Time-like photon, 91
- Time-of-flight (TOF), 242
 spectrometer, 57
- Ting, S., 234
- Tomonaga, S., 78
- Top quantum number, 159
- Total elastic cross-section, 94
- Townsend discharge, 33
- TPC, 33
- Transferred four-momentum, 222
- Transition probability, 73, 78, 82, 89, 92
- Transuranic nuclei, 416
- Trigger, 35
- Tunneling effect, 438
- U**
- Ultimate constituent, 1, 2, 5, 9
- Uncertainty, 45
 principle, 101
 relation, 75
- Uncontrolled chain reaction, 447
- Unification relations, 335
- Unit, 30
- Unitarity
 limit violation, 316
 triangle, 359
- Unitary
 group, 157, 319
 matrix, 320, 324
 operator, 116
 symmetry, 387
 transformation, 365
- Universality
 of fermions, 227
 of leptons, 239
 quark-lepton, 219
 of weak interactions,
 187, 211
- Unstable
 nuclei, 416
 particle, 46
 particle decay, 46
- Uranium fission, 446
- V**
- Vacuum
 pipe, 50
 polarization, 335, 337
- Valence quark, 157, 176, 266
- van der Meer, S., 220
- V-A theory, 207, 222
- Vector
 boson, 2, 73, 105, 223
 boson fusion, 306, 307
 interaction, 223

- Vector (*cont.*)

meson, 125

potential, 465
- Vertex, 86, 154

chamber, 242

factor, 86
- Violation

of the baryonic number, 57
- Virtual

particle, 101

transition, 349
- Volume term, 427
- W**
- W

mass, 262

vector boson, 220
- Wave

amplitude, 80

function, 115

intensity, 315

operator, 227
- Wavelength, 30
- Wave-particle duality, 45
- Weak

baryonic current, 227

charge, 103

charged current, 213

current, 223

interaction, 1, 71, 103, 179

neutral current, 213

Weakly Interacting Massive Particle (WIMP), 406
- Weinberg angle, 329, 334, 344
- Weinrich, M., 202
- Weisskopf formula, 170
- Weizsäcker formula, 442
- WIMP. *See* Weakly Interacting Massive Particle (WIMP)
- WI process

charged current, 103–105, 180

leptonic, 208

neutral current, 103–105, 180, 217

nonleptonic, 208

semileptonic, 208
- Woods-Saxon

distribution, 422

potential, 430
- World War II, 137, 183
- Wu experiment, 202
- Wu, M., 202, 203
- X**
- X-rays, 7
- Y**
- Yang, C.N., 201, 321
- Yukawa, 136, 137

meson, 137

model, 80
- Yukawa, H., 4
- Z**
- Z^0

hadronic width, 250

lifetime, 251

peak, 254

vector boson, 213, 220

width, 250
- Zweig, G., 177
- Zweig rule, 166